A STUDY OF NUCLEAR EFFECTS USING FORWARD-RAPIDITY HADRON PRODUCTION AND DI-HADRON ANGULAR CORRELATIONS IN $\sqrt{S_{NN}} = 200$ GEV D+AU AND P+P COLLISIONS WITH THE PHENIX DETECTOR AT RHIC

BY

BEAU ANTHONY MEREDITH

DISSERTATION

Submitted in partial fulfillment of the requirements
for the degree of Doctor of Philosophy in Physics
in the Graduate College of the
University of Illinois at Urbana-Champaign, 2011

Urbana, Illinois

Doctoral Committee:

Professor Jen-Chieh Peng, Chair
Associate Professor Matthias Große Perdekamp, Director of Research
Professor John Stack
Professor Russ Gianetta

Abstract

Measurements using the PHENIX forward detectors at the Relativistic Heavy Ion Collider (RHIC) in high-energy deuteron-gold (d+Au) collisions enable us to study cold nuclear matter effects in nucleon structure at small parton-momentum fraction, or Bjorken-x. The large gluon densities in Lorentz-contracted gold nuclei enable us to search for the yet-unobserved saturation of the gluon distribution at small x, which is caused by a balance between gluon fusion and splitting. Gluon saturation is described by the Color Glass Condensate (CGC) theory [1], which predicts a suppression of inclusive particle production in heavy-ion collisions, in particular at forward rapidity, because of a decreased gluon density. In addition, it has been suggested that forward rapidity di-hadron correlations may elucidate CGC effects with two signatures that are specific predictions from CGC: awayside-yield suppression and angular broadening [2]. This thesis describes the first experimental measurements of these forward di-hadron correlations in PHENIX.

Previously, RHIC experiments have shown a suppression in the single-particle nuclear modification factors (R_{dA}, R_{cp}) for $\sqrt{s_{_{NN}}} = 200$ GeV d+Au collisions in the forward (deuteron) direction [3, 4]. Multiple theories can explain the observed suppression (including CGC), but a conclusive measurement discriminating amongst the models has yet to be carried out.

Two new forward-rapidity electromagnetic calorimeters (Muon Piston Calorimeters or MPCs, $-3.7 < \eta < -3.1$, $3.1 < \eta < 3.9$) enable the PHENIX experiment to measure the single-particle nuclear modification factors in addition to further understanding forward particle production with the forward di-hadron correlation measurements. Azimuthal correlations of di-hadron pairs at different pseudorapidities allow us to scan the x-dependence of correlated di-hadron production, which can then be used to discriminate amongst the models that compete to explain the observed levels of forward particle production. More specifically, the x-dependence of the yields and widths of the correlated peaks can be measured, rigorously testing the theoretical models that attempt to explain the forward particle production. The forward-rapidity correlations are especially interesting because it is expected that they provide a test of gluon saturation down to $x \approx 5 \times 10^{-4}$ in the Au-nucleus.

In this thesis, we present results based on the high integrated-luminosity data sample of proton-proton (p+p) and d+Au collisions at $\sqrt{s_{NN}} = 200$ GeV taken at RHIC in 2008. In order to produce the results in the relatively new MPC, a significant effort was concurrently invested into tasks related to the detector efficacy, including: improving the electromagnetic-shower reconstruction algorithm, devising and implementing the detector calibration, and creating the simulated particle-reconstruction efficiency and simulated particle-identification schemes. The relevant details of this work are shown followed by the physics analyses, which we summarize in what follows.

We first present the PHENIX $\sqrt{s_{NN}} = 200$ GeV inclusive π^0 $R_{\rm dA}$ results as well as the p+p π^0 differential cross section and the d+Au invariant yields for the pseudorapidity ranges of $3.0 < \eta < 3.4$, $3.4 < \eta < 3.8$, and $3.0 < \eta < 3.8$. We observe a similar trend in the suppression of $R_{\rm dA}$ as first observed by the BRAHMS experiment in the forward direction wherein the suppression increases with decreasing collision impact parameter [3]. We also observe a larger suppression in the higher-rapidity bin ($3.4 < \eta < 3.8$) as compared to the lower ($3.0 < \eta < 3.4$). These results are compared with the nuclear-shadowing model of Qiu and Vitev [5], and the comparison shows that nuclear shadowing alone is unable to explain the observed level of suppression.

We then proceed to show three sets of di-hadron correlation functions: two sets wherein a particle is at midrapidity ($|\eta| < 0.35$) and the other is at forward rapidity ($3.0 < \eta < 3.8$) in the MPC (termed mid-forward correlations), and another wherein both particles are detected at forward rapidity in the MPC (forward-forward correlations). For both the mid-forward and forward-forward correlations, we quantify the yields of the correlated awayside signal and form the di-hadron nuclear modification factor $J_{\rm dA}$, which is the correlated two-particle analogue of $R_{\rm dA}$. We again observe an increasing suppression with decreasing impact parameter, but in addition we see a very large suppression in $J_{\rm dA}$ that reaches $J_{\rm dA} \approx 0.1$ for the forward-forward correlations; it is these correlations that are expected to be most sensitive to gluon-saturation effects [6]. To summarize the $J_{\rm dA}$ data, the measured values are plotted versus our estimate of the parton momentum-fraction in the Au-nucleus, x_{frag}^{Au}. We observe an increasing level suppression with decreasing x_{frag}^{Au}, which would seem to support the predictions of CGC. However, predictions from other models, notably initial-state energy loss with nuclear shadowing, are necessary to eliminate other possible explanations. We also present simulation studies in the appendix that raise questions about the nature of particle production for the forward-forward correlations. In particular, the forward-forward correlated di-hadron signal in the PYTHIA p+p monte-carlo simulations does not seem to originate from di-jet production, but from some other momentum-conserving process. While PYTHIA admittedly does not correctly simulate the partonic

interactions, this study still raises questions about the nature of di-jet production in this region.

To Anna and Annette

Acknowledgments

The entire PHENIX collaboration has been extremely helpful over the course of my studies, and I would first like to thank everyone for their help and support. Listing everyone who has helped me would cause this section to look like the title page of PHENIX papers, where ~ 400 names appear, so I shall refrain from this. That said, I would like to acknowledge people with whom I have worked closely during my time at graduate school.

Amongst the individuals, I would first like to thank my advisor at UIUC, Professor Matthias Große Perdekamp for giving me the opportunity to work on interesting projects throughout my time in graduate school. I once heard the former PHENIX spokesperson use the a one-word identifier for Matthias: "Powerhouse"; this is completely accurate. His very pleasant nature, enthusiasm, and his constant barrage of new ideas make him an ideal advisor, and I am grateful that I had the opportunity to work with him.

Additionally, I would like to thank my "surrogate" advisor while at BNL, Dr. Mickey Chiu. Mickey is the backbone of the MPC hardware, software, and simulation efforts, and without him this work could not have been completed. I also thank him for his friendship.

I would like to acknowledge people that were helpful during my first years in graduate school working on the tasks related to the RPC upgrade project: thanks to Ralf Seidl, Ruihze Yang, Rusty Towell, John Hill, John Blackburn, Eric Thorsland, Andrew Glenn, Dave Northacker, Young Jin Kim, Chang Lee, Shawn Wadhams, Scott Wolin, Daniel Jumper, Dave Layton, John Koster, Alex Burnap, Nicholas Mucia, and Aaron Veicht.

I would also like to give special thanks to current and former UIUC students: Dr. John Koster, Scott Wolin, and Cameron McKinney for their work on the MPC, and for their friendship. Together, we spent countless hours slaving over the MPC calibrations and reconstruction. Special thanks goes to Donald Yang for our many discussions about computing over lunch, and for introducing me to the PHENIX computing environment. Thanks to Anselm Vossen and Martin Leitgab for being awesome members of the UIUC group.

Many thanks to Chris Pinkenburg for his willingness to modify the offline analysis framework for the

MPC analyses, push forward the calibrations, and database YAMs (Yet Another MPC calibration). Also, thanks to Carla Vale for help with data production. Thanks to Andre Kazentsev, David Kleinjan, Ken Sedgwick, and Oleg Eyser for their contributions to the MPC.

Thanks to those who gave input and feedback to the data analysis (in addition to those already mentioned): Anne Sickles, Mike McCumber, Zvi Citron, Jiangyong Jia, Andrew Adare, Justin Frantz, and Mike Tannenbaum. In addition, there are a number of phenixians that have been helpful in both pushing the research forward and giving advice, including Jamie Nagle, Craig Ogilvie, Barbara Jacak, Rich Seto and Mike Leitch. Thanks to the PPG and IRC committee for the publication: Mickey, Matthias, Mike Leitch, Terry Awes, Zvi Citron, Mike McCumber, Vlad Pantuyev, DongJo Kim, and Kyoichiro Ozawa.

Special thanks to Yuri Kovchegov, Cyrille Marquet and Dima Kharzeev for our CGC discussions. Also, thanks to Yuri and Fabio Dominguez for helpful conversations in preparing this thesis.

Lastly, I would like to thank my friends and family for their invaluable support they have given me throughout this work.

Table of Contents

List of Abbreviations and Terms

PHENIX	Pioneering High Energy Nuclear Interaction eXperiment .
RHIC	Relativistic Heavy Ion Collider.
Run8	The eighth year of physics operations at RHIC that took place in 2008. The collision species were $\sqrt{s_{NN}} = 200$ GeV d+Au and p+p.
p+p	Proton-Proton.
d+Au	Deuteron-Gold.
Au+Au	Gold-Gold.
MPC	PHENIX Muon Piston Calorimeter.
module units	2.26 cm, or the lateral dimensions of the crystals in addition to half the separation distance between adjacent crystals.
APD	Avalanche Photodiode.
LED	Light-Emitting Diode.
ADC	Analog-to-Digital Converter.
FEM	Front End Module.
AMU	Analog Memory Unit.
EMCal or EMC	PHENIX Midrapidity Electromagnetic Calorimeter.
DC	PHENIX Drift Chamber.
PC	PHENIX Pad Chamber.
BBC	Beam-Beam Counter.
MB	Minimum Bias: the PHENIX the minimum bias trigger for data acquisition is the coincidence of hits within both BBCs.
DAQ	Data Acquisition System.
LO	Leading-Order.
LL	Leading-Log.
NLO	Next-to-Leading-Order.

NLL	Next-to-Leading-Log.
QCD	Quantum Chromo Dynamics.
pQCD	perturbative Quantum Chromo Dynamics.
CGC	Color Glass Condensate.
QGP	Quark-Gluon Plasma.
VMD	Vector-Meson Dominance.
DIS	Deep Inelastic Scattering
PDF	Parton Distribution Function.
nPDF	Nuclear Parton Distribution Function - this term is used for nuclei with more than one nucleon ($A > 1$).
CF	Azimuthal Angle Two-Particle Correlation Function.
CY	Conditional or Per-Trigger Yield of the Awayside Peak in the $\Delta\phi$ Correlation Functions.
ZYAM	Zero-Yield At Minimum method for determining the pedestal in two-particle $\Delta\phi$ correlations.
mid-forward	Two-particle correlations where one particle is at midrapidity ($-0.35 < \eta < 0.35$) and the other at forward rapidity ($3.0 < \eta < 3.8$).
forward-forward	Two-particle correlations where both particles are at forward rapidity ($3.0 < \eta < 3.8$).
EM	Electromagnetic.
CG	Center-of-Gravity.
NDF	Number of Degrees of Freedom.
RMS	Root-Mean Square - equivalent in this text as the estimated standard deviation of a distribution.
QA	Quality Assurance.
MIP	Minimum Ionizing Particle.
PISA	PHENIX GEANT3 based detector simulation package.
PYTHIA	Leading-Order monte-carlo used to simulate p+p events.

List of Symbols

z	The longitudinal or beam direction.
x, y	The transverse coordinates perpendicular to the beam axis in PHENIX.
$\eta = -\ln(\tan(\theta/2))$	pseudorapidity.
$y = \frac{1}{2}\ln(\frac{E+p_z}{E-p_z})$	rapidity.
$\sqrt{s}$	Center of mass energy of the nucleus-nucleus system.
$\sqrt{s_{NN}}$	Center of mass energy per nucleon of nucleus-nucleus system.
E, p_T, p_x, p_y, p_z	Energy and momentum components; p_z is the momentum along the beam-direction.
$p_T = \sqrt{p_x^2 + p_y^2}$	Transverse momentum defined to be momentum x-y plane.
$\phi = \arcsin(p_y/p_T)$	Azimuthal angle in the transverse plane; for the azimuthal correlation functions $\Delta\phi = \phi_2 - \phi_1$, where $\phi_{1,2}$ are the angle of the two particles.
$\theta = \arccos(p_z/p_{tot})$	The angle relative to the $+z$-axis as defined in a spherical coordinate system.
x, or x_B	Bjorken x, or parton momentum fraction of proton (or nucleon).
$Y \equiv \ln(1/x)$	"Rapidity" variable commonly used by theorists to describe the evolution of the parton densities with the momentum fraction, x. This should not be confused with the rapidity (y) or pseudorapidity (η) variables.
CF	Azimuthal angle two-particle correlation function.
CY	Conditional or per-trigger yield of the awayside peak in the $\Delta\phi$ correlation functions.
$N_{\rm coll}$	Number of binary nucleon-nucleon collisions as estimated via a Glauber simulation.
$R_{\rm dA}$	Single hadron nuclear modification factor formed by taking the ratio between measured hadron yields in d+Au per $N_{\rm coll}$ and yields in p+p.
$J_{\rm dA}$	Correlated di-hadron nuclear modification factor formed by taking the ratio between measured di-hadron yields in d+Au per $N_{\rm coll}$ and di-hadron yields in p+p. In practice, the formula $J_{\rm dA} = I_{dA,trig} \times R_{dA,trig}$ is used.
$I_{\rm dA}$	Ratio of conditional yields (CY) between d+Au and p+p.

Part I

Introduction

The proton is the most prevalent nuclear system in the universe, and yet even ignoring the challenges of spin substructure the exact composition is not completely understood. Ostensibly, the proton is composed of three valence quarks which are bound together by gluons – the gauge bosons of the strong nuclear force. However, if one probes the proton substructure on small timescales, the quantum fluctuations appear as a large density of gluons and quark/anti-quark pairs fluctuating into and out of existence. This rich substructure has been of great theoretical interest; experiments with collision systems ranging from e^+/e^-, Deep Inelastic Scattering (DIS), p+p, and heavy ions have all played a role in understanding the distribution of partons (quarks and gluons) inside protons and heavier nuclei.

It is our goal in this thesis to provide experimental measurements that help to understand the substructure of nucleons bound in nuclei. In particular, using deuteron-gold (d+Au) collisions at the Relativistic Heavy Ion Collider (RHIC), we probe the low momentum-fraction (or Bjorken x) distribution of gluons in the gold nucleus, which in the rest frame appears as transient fluctuations that have little influence on collision dynamics, but when Lorentz-boosted to a high-energy frame, appear on longer time-scales and can have significant impact on the collision dynamics. Our measurements are sensitive to low-x phenomena in the Au-nucleus because we measure π^0's in the forward (deuteron-going) direction; in particular we measure the single-particle spectra and angular correlations with one forward particle and the other at both mid and forward rapidities, thereby constraining x to small ranges. By using the high-energy Au-nucleus, we look at a system wherein the parton densities are enhanced owing to the Lorentz contraction, and thus yet unobserved effects such as gluon saturation [1, 7, 8] are expected to occur at a larger x than they would in a simple p+p collisions. It is this nuclear enhancement that we exploit in our measurements wherein we compare spectra in d+Au to p+p; however, other initial-state effects such as leading- and higher-twist nuclear shadowing [9, 10, 11] and initial-state energy loss [12, 13] must also be accounted for the in the d+Au collisions to fully understand our measurements.

In this introduction, we weave together theoretical and experimental results relevant to our measurement. Our goal is to understand the parton distribution functions (PDFs) of the Au-nucleus at very low momentum fraction; hence, we begin our discussion with an introduction to DIS experiments, which have been crucial in the calculation of PDFs. We then discuss the phenomenon of nuclear shadowing and discuss some models and methods of parameterizing it. Finally, we discuss heavy-ion collisions at RHIC and how gluon saturation effects might be detected through forward-rapidity particle production in deuteron-gold collisions. We contrast the Color Glass Condensate (CGC) theory of gluon saturation with other models that make the similar predictions and discuss a set of measurements (azimuthal two-particle correlations) that will help to

distinguish amongst the competing models.

Chapter 1

Motivation

1.1 QCD

Experiments have shown that the interactions between the quarks and gluons are described by the relativistic SU(3) theory of Quantum Chromo-Dynamics (QCD) [14]. The QCD Lagrangian is

$$L_{QCD} = \bar{\psi}_i(i\gamma^\mu\partial_\mu - m_i)\psi_i - gG^\alpha_\mu\bar{\psi}_i\gamma^\mu T^\alpha_{ij}\psi_j - \frac{1}{4}G^\alpha_{\mu\nu}G^{\mu\nu}_\alpha, \tag{1.1}$$

where ψ are the spin 1/2 fermion fields (quarks) and G are the spin 1 massless boson fields (gluons). Analytic solutions to QCD remain elusive; instead there are certain regimes and techniques wherein QCD calculations can be performed. The two most prevalent schemes for calculating QCD solutions are perturbative QCD (pQCD) [15, 16] and lattice QCD [17]. Perturbative QCD can be formulated as an expansion in powers of the strong coupling constant α_s (see Fig. 1.1). At the scale of gluon exchanges in the bound state of hadrons ($\Lambda_{QCD} \approx 0.2$ GeV), $\alpha_s \sim 1$, which means a perturbative solution at fixed order will not be reasonable to describe these systems; instead, one employs the computationally intensive lattice QCD calculations which have been successful in calculating properties of nucleons such as mass and in understanding the hot, dense, de-confined state of matter formed in high-energy Au+Au collisions at RHIC known as Quark Gluon Plasma (QGP) [18, 19, 20, 21, 22]. On the other hand, asymptotic freedom of QCD shows a decrease in the strong coupling constant with a decrease in the distance scales probed [15, 16]. In the context of high-energy nucleon-nucleon collisions, the resolution of the partonic interaction is measured by the momentum transfer (q) between the initial and final state, which is inversely proportional to the distance scale probed. Asymptotic freedom is very significant for both its physical meaning and calculational applicability. From a calculational standpoint, it says that at high energies, pQCD calculations at finite orders can be used to describe interactions between partons; at low energies, QCD calculations remain difficult due to the coupling constant of order unity. Physically, it means that if one probes the nucleon structure with a low-energy interaction, the partons cannot be seen individually; rather one sees pairs (mesons) or trios of quarks

(baryons) coupled together by gluons. However, if the probe has a sufficiently high energy, the distance scale is small enough that the interactions can resolve individual partons. The charge radius of the proton is ≈ 0.8 fm, and one needs a probe of ~ 0.2 fm, or $Q^2 \sim 1$ (GeV/c)^2 to resolve the individual partons and so that α_s is small.

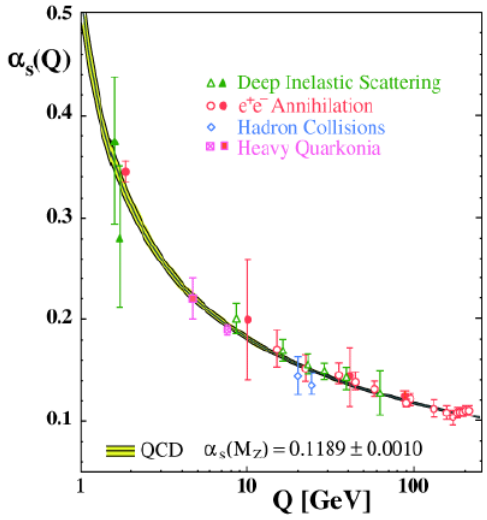

Figure 1.1: The strong coupling constant α_s versus the four-momentum transfer $Q = \sqrt{|q^2|}$ [23].

In recent years, theorists working on understanding the initial state of nucleon structure in nuclei have created a theoretical framework to solve problems in another region of QCD phase space – the low Bjorken-x region of high-energy nuclei wherein the gluon density is large. Based on experimental evidence, the gluon density at moderately small x appears to diverge faster than is physically allowable. But, when the gluon density becomes very large, the process of gluon fusion begins to balance out the gluon splitting, which slows down the divergence of the gluon distribution with decreasing x. This phenomenon is commonly known as gluon saturation [7, 8]. In the regime where gluon fusion exceeds gluon splitting, a new theory, the so-called Color Glass Condensate (CGC) [1], has been developed that performs a perturbative expansion with a characteristic saturation scale, Q_s.

1.2 The Structure of Nuclei in DIS

One of the most effective methods to understand the structure of the nucleus has been through Deep Inelastic Scattering (DIS) [24]. Though we are dealing with heavy-ion collisions in this thesis, it is useful to give a

brief introduction to DIS in the context of understanding the parton distribution functions (PDFs).

A common DIS experiment is electron (or positron)/proton scattering (see Fig. 1.2), wherein an exchange of a virtual photon occurs.

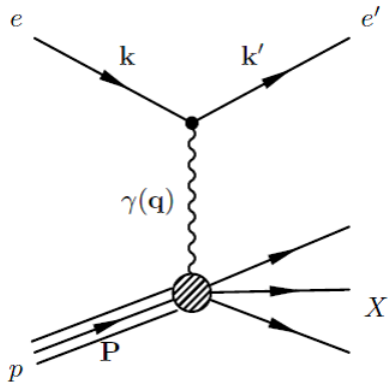

Figure 1.2: Feynman diagram for virtual photon exchange in $ep \to eX$ Deep Inelastic Scattering (DIS).

Given that p (k) is the four momentum of the incoming proton (electron), and q is the four-momentum transfer by the virtual photon, we define the following variables related to the DIS $ep \to eX$ cross section and structure functions

$$x = \frac{Q^2}{2p \cdot q} = Q^2/2M\nu, \tag{1.2}$$

$$y = \frac{p \cdot q}{p \cdot k} = \nu/E, \tag{1.3}$$

where Bjorken-x [25] can be interpreted as the fraction of the proton momentum carried by a parton, and in the proton rest frame ν is the energy of the virtual photon, making y the fraction of the electron energy transferred to the proton. If $Q^2 \equiv -q^2 \gtrsim 1$ (GeV/c)^2, the virtual photon interacts with the parton substructure rather than the proton as a whole. The DIS cross section can be parameterized by two structure functions $F_2(x, Q^2)$ and $F_L(x, Q^2)$, which are mainly related to the quark and gluon distributions, respectively. If we consider the proton as consisting only of point-like charged partons (the so-called Quark-Parton Model [26]), then we expect that the structure of the proton will be independent of the spatial resolution ($\propto 1/Q^2$) at which we probe it. We quantify this experimentally in terms of the structure function F_2, which in this

example is simply

$$F_2(x, Q^2) \approx F_2(x) = \sum_i e_i^2 x(q_i(x) + \bar{q}_i(x)), \tag{1.4}$$

where q_i and $\bar{q}_i$ are the quark and anti-quark distribution functions; i refers to the quark-flavor. These distribution functions are considered to be universal; that is, they apply for any collision system for a given x, Q^2.

F_2 and F_L are experimentally accessible through the double differential DIS cross section

$$\frac{d^2\sigma}{dxdQ^2} = \frac{2\pi\alpha^2 Y_+}{xQ^4}(F_2(x, Q^2) - \frac{y^2}{Y_+}F_L(x, Q^2)), \tag{1.5}$$

where $Y_+ = 1 + (1 - y)^2$. Here we have neglected electro-weak contributions which only are important when $Q^2 \sim M_{Z^0}^2$ and do not consider charged W-boson exchange. As indicated above, the quark-parton model predicts that F_2 should be independent of Q^2 and that $F_L = 0$, as F_L is related to the gluon field absent from the model.

Indeed, from Fig. 1.3 [27, 28, 29, 30, 31, 32] we see that for $x \approx 0.25$ this property known as Bjorken scaling [25] holds; however, for both small x and large x we see that there are scaling violations, as one can see a variation of F_2 with Q^2. These violations arise as a natural consequence of QCD and the inclusion of gluons in the proton wavefunction. Quarks are surrounded by a parton cloud, and as one views the quark structures at higher values of Q^2, we undress the quark; therefore, we view the quark as having a smaller momentum fraction x as we increase Q^2. The gluon distribution is not directly accessible via F_2 but can be determined by the scaling violation $\frac{dF_2}{d\ln Q^2} \propto \alpha_s xG(x, Q^2)$, or from measurements of F_L.

The evolution of the parton distributions between different scales, Q^2, is described by a set of equations known as DGLAP[1] evolution equations [33, 34, 35, 36] in QCD. With the help DGLAP evolution, the PDFs can be determined from experimental data sets at different Q^2. In Fig. 1.4, we show the parton distribution functions for $Q^2 = 10$ (GeV/c)^2 extracted from F_2 data of the H1 and ZEUS experiments at HERA with a Next-to-Leading-Order (NLO) QCD DGLAP analysis [30]. The input data for the analysis are shown in Fig. 1.3.

The gluon distribution found at HERA exceeds the quark distribution for $x \lesssim 0.1$ (note that $xG(x)$ is plotted in Fig. 1.4). At small x, the gluon distribution is divergent with the additional consequence of an infinite number of gluons in the proton. It has been proposed that the divergence in the gluon distribution

[1] Dokshitzer, Gribov, Lipatov, Altarelli, Parisi

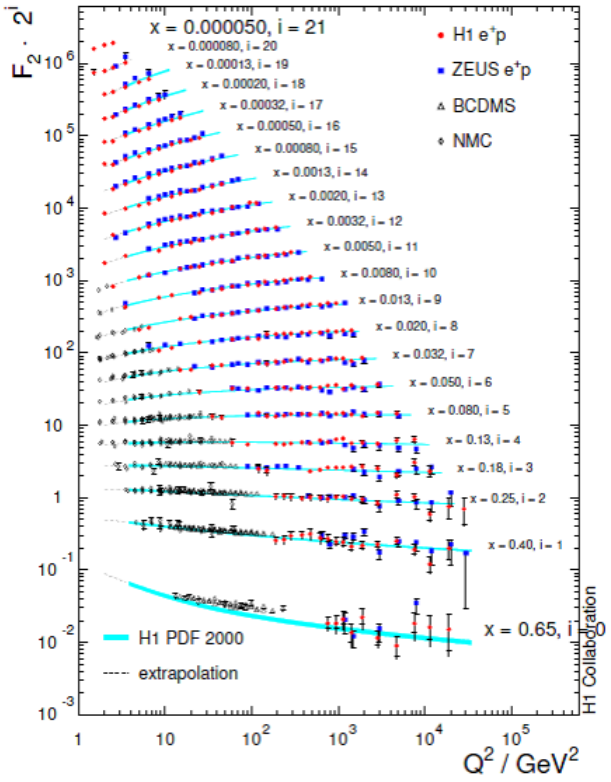

Figure 1.3: DIS F_2 data from HERA [27, 28, 29, 30], NMC [31], and BCDMS [32] as a function of Q^2 for different values of x.

at small x indicates a breakdown of DGLAP evolution at low x and Q^2 [37].

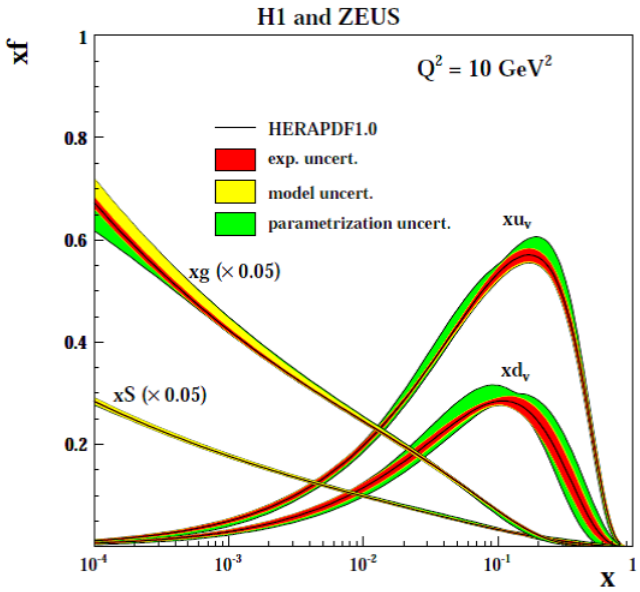

Figure 1.4: Parton distribution functions (PDFs) as determined by a HERA NLO QCD analysis as a function of x for $Q^2 = 10$ (GeV/c)^2 [30].

Next, we introduce the BFKL evolution, which evolves the parton densities versus $\ln(1/x)$, and is valid at small x at a fixed Q^2. At small x, gluon splitting is the dominant process; BFKL describes the small-x distributions by successively considering long-lived fast partons (at high x) as a source for the slow partons (resumming the leading contribution of $\ln(1/x)$ at each step in the evolution). Consider the ladder diagram in Fig. 1.5. The ladder is ordered in x, and the upper, high-x, partons can be considered static sources for the lower ones. At each step in the ladder, the probability for the emission of a gluon is $\alpha_s \int dx/x = \alpha_s \ln(1/x)$.

Figure 1.5: Gluon ladder for BFKL evolution which describes the density of partons as one goes to smaller x. The horizontal gluon lines are emitted with strong ordering in x; that is $x_0 > x_1 > \ldots x_n$.

At some point in the evolution, the density of gluons is so large that the gluon wavefunctions begin to overlap in the transverse direction and gluon recombination effects become important. This taming of the ostensibly divergent gluon distribution by gluon fusion is known as gluon saturation [7, 8], and is responsible for restoring unitarity to the BFKL cross section [38]. The Q^2 where saturation effects are expected to be relatively large is known as the saturation scale $Q_s^2 \propto 1/x^\lambda$, (see Ref. [39] for overview).

There is also a cross-over region between Leading-Order (LO) DGLAP and LO BFKL known as the DLL (double-leading-logarithm) region. BFKL resums in powers of $\ln(1/x)$, while DGLAP resums powers of $\ln(Q^2)$. The DLL approximation is valid at small x and involves a resummation of $\alpha_s \ln(Q^2) \ln(1/x)$. This extends the usefulness of LO DGLAP to small x. Because of its relative simplicity, some models describing gluon saturation have chosen to use a hybrid of DLL DGLAP and saturation [7, 8, 37], rather than the more correct BFKL and saturation [38, 39].

In Fig. 1.6 [37], we compare the extraction of the gluon density at low Q^2 from HERA data for DGLAP evolution and the hybrid DLL-DGLAP evolution with saturation effects. The CTEQ6 [40] LO gluon PDFs, based on DGLAP evolution, are shown along with a gluon distribution based on a saturation calculation called DGLAP-GRLMQ [37]. In both cases, the gluon distributions are determined by fitting the HERA data. For relatively large Q^2, the distributions are nearly the same; however, as Q^2 gets smaller, the saturation model is systematically higher and avoids the apparent failure of DGLAP evolution leading to a negative gluon distribution at small Q^2.

It is useful at this point to juxtapose the evolution in Q^2 versus that in x. To guide the discussion, we show a schematic picture of the parton densities within a nucleon for different x and Q^2 in Fig. 1.7 [39]. First, we consider the evolution of the PDFs with varying Q^2. Normal pQCD is applicable at relatively large Q^2; this is the regime wherein the size of the probe can resolve individual partons. As we increase Q^2, we probe smaller distance scales, and hence we resolve partons of decreasing size. This evolution is described by DGLAP, and most experimental data from DIS are in this kinematic region. At very small $Q^2 < \Lambda_{QCD}^2$, pQCD is no longer applicable, and hence we cannot readily interpret F_2 in terms of PDFs from DGLAP. Next we consider varying x with a fixed Q^2. At $x \approx 0.3$ with $Q^2 \gtrsim 1$ (GeV/c)^2, we probe the valence-quark distribution of the proton. As we go to smaller x with a fixed Q^2, BFKL describes the evolution of gluon distribution. At some very small x (where Q_s^2 becomes large), we enter the non-linear evolution regime in which gluon saturation becomes important, and models without a recombination mechanism are expected to fail. To date, there has been no conclusive measurement that has proven the existence of this regime; however, measurable effects should exist at sufficiently high parton densities at small x.

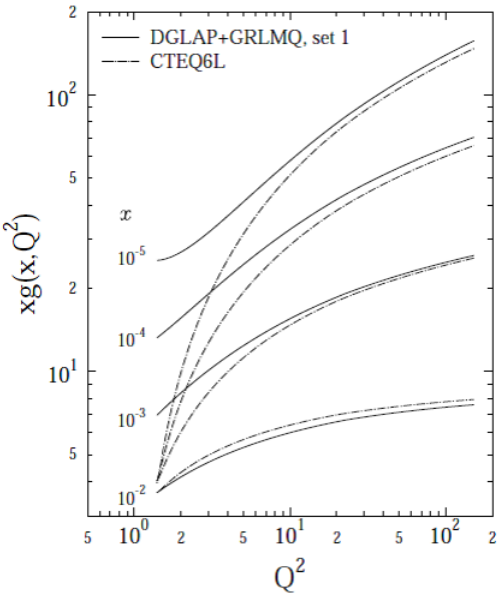

Figure 1.6: Example gluon distribution functions showing the LO CTEQ6 gPDFs [40] and the DGLAP-GRLMQ saturation model calculation [37]. The gluon recombination effects increase the gluon density at small $Q^2 \approx 1$ (GeV/c)^2 above 0 and thus one avoids the problem of a negative gluon density at small Q^2.

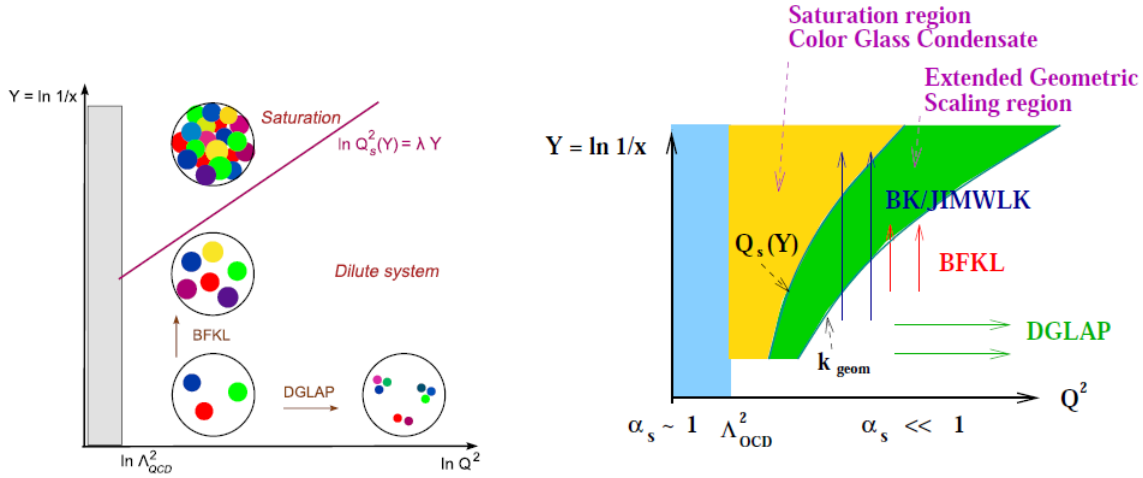

(a) (b)

Figure 1.7: Phase diagrams in $\ln(1/x)$ vs. $\ln(Q^2)$ showing where the Color Glass Condensate is expected to exist. **a.)** Illustration of how the gluon density changes with varying Q^2 and $\ln(1/x)$, **b.)** Clear "phases" of the gPDFs are shown, including the CGC and its boundary with the DGLAP regime known as the Region of Extended Scaling.

1.3 Nuclear Shadowing in DIS

Fixed target $eA \rightarrow eX$ DIS experiments [41, 42, 43, 44, 45, 46] have been performed to study nucleon structure in nuclei. Naïvely, one would expect the total cross section to scale with the number of nucleons, or $\sigma_{eA} = A\sigma_{ep}$. However, there are various effects which modify this simple picture. The nuclear modification factor for DIS is defined as

$$R^A_{F_2}(x, Q^2) = \frac{F_2^A(x, Q^2)}{AF_2^{nucleon}(x, Q^2)}. \tag{1.6}$$

In Fig. 1.8, we show the qualitative behavior of $R^A_{\mathrm{F}_2}$ as a function of x [47]. One can see the non-unity behavior of the ratio. Various regions of suppression (shadowing, EMC effect) and enhancement (anti-shadowing, Fermi-motion) have been found experimentally. At small $x \lesssim 0.1$, the suppression in $R^A_{\mathrm{F}_2}$ is known as shadowing [11]. In this thesis we focus on low-x phenomena, and so the phenomenon of nuclear shadowing is of direct relevance to our studies.

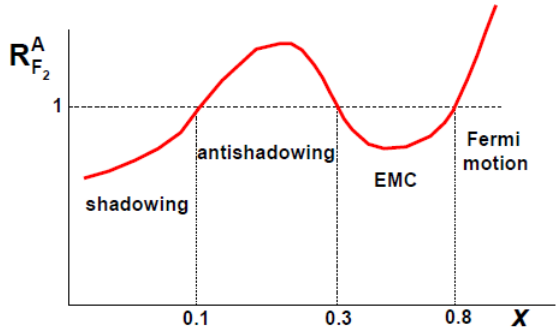

Figure 1.8: Example diagram showing the behavior of $R^A_{\mathrm{F}_2}$ as function of x. The shadowing region exists for $x \lesssim 0.1$.

Nuclear shadowing is simply the suppression of $R^A_{\mathrm{F}_2}$ and does not refer to a specific model. The origins are not completely understood, but some key features exist in most models.

Some authors take a practical approach to shadowing; they simply parameterize the measured values of F_2^A, and extract nuclear PDFs (nPDFs) using DGLAP evolution. One limitation of this approach is that the nPDFs do not represent the true parton distribution functions, but rather may incorporate final-state interactions. Additionally, gluon recombination effects at small x may be present. In Fig. 1.9, we show the ratios of the nPDFs to the proton PDFs calculated in Ref. [47], along with uncertainties as a function of x. All nPDFs (valence quarks, gluons, and sea) exhibit shadowing at small x; the low-x gluon nPDF appears to

be more suppressed but also less constrained since the gluon is not directly probed in F_2. These nPDFs can then be used to describe the initial state in heavy-ion collisions at RHIC, as the distributions are universal.

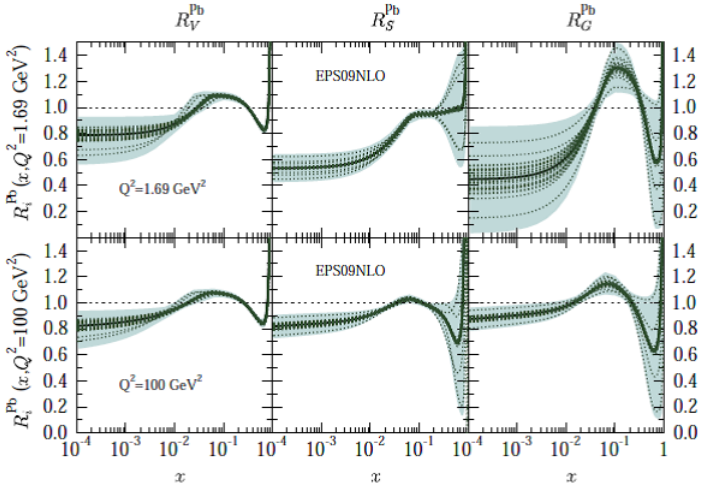

Figure 1.9: EPS09 Pb nPDFs for $Q^2 = 1.69$, 100 $(\mathrm{GeV/c})^2$ [47] for valence quarks (left), sea quarks (center), and gluons (right).

Next we briefly introduce some of the models proposed to explain shadowing. In the rest frame of the nucleus, a relatively simple shadowing mechanism arises from multiple scattering of the hadronic component ($q\bar{q}$ pair) of the virtual photon with the nucleus as discussed for example by Glauber and Gribov [48] and Armesto [11]. In nucleus rest frame, a typical scale of the $q\bar{q}$ wavefunction is $l_{coherence} = 1/2xm_{nucleon}$, and can be the length of several nucleons for sufficiently small x. When $l_{coherence} \approx r_A$ (nuclear radius) the probe will simultaneously interact with all nucleons at the same impact parameter. As an example, in Fig. 1.10, we show a diagram that represents the leading-twist[2] [14, 49] contributions to multiple scattering for a massless scalar particle colliding with a nucleus; the second diagram contributes a negative correction to the $e(p, A)$ cross section and hence provides a mechanism for shadowing [11].

In Ref. [50], predictions for low-x $R^A_{\mathrm{F}_2}$ data indicate that leading-twist shadowing effects are unable to account for the observed shadowing, and hence higher-twist effects might be necessary. The twist expands the scattering amplitude in terms of $1/Q$, and at high Q^2 the higher-twist terms are less important. The aforementioned example is a model for leading-twist shadowing, with essentially no dependence on Q^2. One mechanism that contains higher-twist effects and is valid at small x and Q^2 is known as vector-meson

[2]Twist denotes the order parameter in the operator product expansion (OPE) of the forward scattering amplitude in hard scattering. The coefficients associated with matrix elements at a given order in the expansion are the so-called Wilson coefficients and can be calculated in perturbative QCD. The twist parameter, t, in the OPE is equal to the dimension of the operator minus its spin, and governs the power suppression, $1/Q^{t-2}$, of a matrix element in the expansion [14, 49].

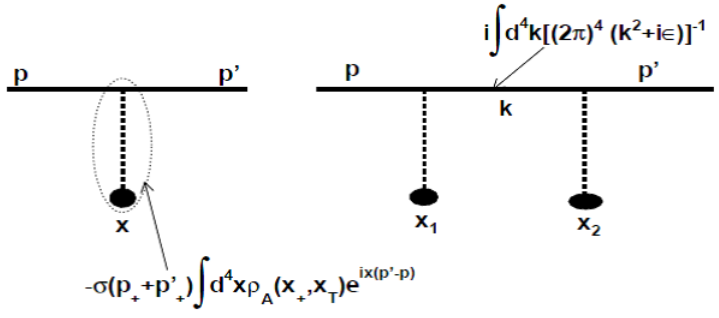

Figure 1.10: Example diagrams from Ref. [11] showing the single and double-scattering diagrams for a massless scalar particle on a nucleus. The second diagram only contributes in large nuclei when the coherence length is sufficiently large, and contributes a negative correction to the cross section.

dominance (VMD), wherein the virtual photon fluctuates into a vector meson (ω, ρ, or ϕ) and is absorbed by the exterior nucleons, thus shadowing the interior nucleons from the photon flux. When VMD effects are added to leading-twist effects, Ref. [50] observes better agreement with $R_{\mathrm{F}_2}^A$ as seen in Fig. 1.11.

Another possibility for nuclear shadowing at moderately small values of Q^2 are higher-twist QCD power corrections to multiple scattering (again coherence effects) [5]. The main result of this model is that low-x F_2^A data can be reproduced by a resummation of the higher-twist diagrams. For reasonably small corrections, the resummation effectively leads to a rescaling of $x \to x(1 + \frac{\xi^2}{Q^2}(A^{1/3} - 1))$, where $\xi^2 \approx 0.09 - 0.12$ GeV^2 is determined from fits to the data. One should note that these power corrections are enhanced by the nuclear size which originates in the coherent multiple scattering. Also, in tuning the parameter ξ, it was assumed that there were no leading-twist shadowing effects; hence this is in fact an upper bound on the shadowing corrections from higher-twist effects. In Fig. 1.12, we show $R_{\mathrm{F}_2}^A$ data and theory curves from this model.

In the Color Glass Condensate formalism for gluon saturation, the nuclear shadowing arises naturally from the evolution in x to a large density of gluons [1, 39, 51, 52]. The CGC formalism involves a resummation of all twists and takes into account gluon recombination, which is not the case for any of the other models. The phenomenon of shadowing arises from the ab initio evolution equations rather than invoking ad hoc mechanisms. The CGC formalism is complex [53], and only in recent years have the fitted model parameters become consistent across DIS and heavy-ion collision systems [51, 52]. In Fig. 1.13, we show $R_{\mathrm{F}_2}^A$ data as well as a CGC prediction for nuclear shadowing ($x < 0.01$). One can see good agreement between the CGC curves and the data.

Hence we see that there are a variety of models that predict nuclear shadowing; this phenomenon has been studied extensively, but there is still a large amount of uncertainty about its origins. It is found that

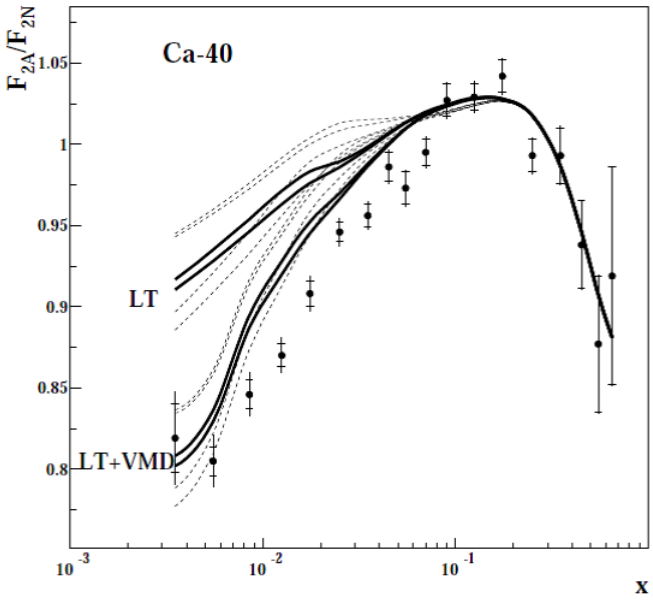

Figure 1.11: Nuclear-shadowing fits to $F_2^A/F_2^n = R^A_{F_2}$ data from DIS for leading-twist (LT) and higher-twist (VMD) effects [50].

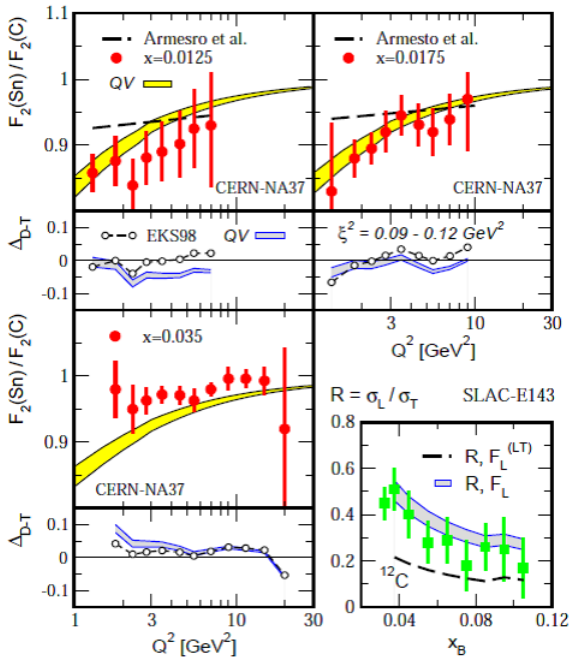

Figure 1.12: Nuclear-shadowing fits to F_2 data from the NMC experiment and $R = \frac{\sigma_L}{\sigma_T}$ data from SLAC for higher-twist shadowing (without any leading-twist effects) [5].

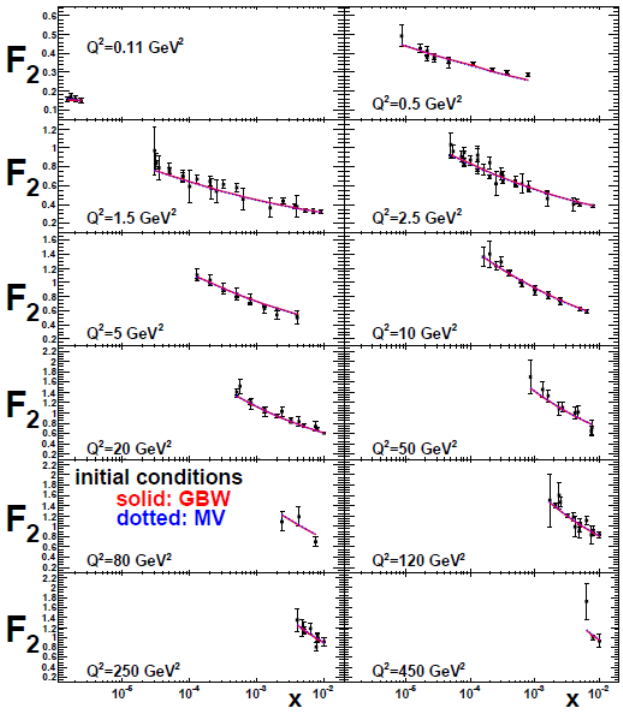

Figure 1.13: CGC fits to F_2 data from H1 and ZEUS (HERA), E665 (Fermilab), and NMC (CERN) collaborations [51].

higher-twist shadowing corrections in addition to those from leading-twist are needed to properly describe the low-x $R^A_{F_2}$ data, though it is also true that these higher-twist corrections are able to describe the shadowing without leading-twist effects [5]. CGC takes into account both leading- and higher-twist effects as well as gluon recombination effects; the match between the low-x data and theory is also quite good [51, 52]. Others have taken the approach of using DGLAP evolution with the measured structure functions F_2^A and not to consider the origin of shadowing [47]; however, if DGLAP fails at some small value of x then these models would not produce accurate nPDFs.

1.4 From DIS to Hadronic Collisions

For hadronic collisions (i.e. deuteron-gold collisions compared to a proton-proton reference), the theoretical ambiguities become even more complex than in DIS, as more effects can modify the differential cross sections of particle production. An important observation is that most shadowing models alone cannot describe the suppression observed in forward particle production in d+Au collisions as compared to p+p. However, in Ref. [52], Albacete and Marquet show that CGC calculations can quantitatively describe the observed d+Au and p+p spectra with input mainly coming from the DIS $R^A_{F_2}$ data. Thus we have an exciting opportunity at RHIC wherein we may be able to detect the onset of gluon saturation. Alternatively, in Ref. [54], the authors show that by using initial-state energy loss [12] along with the higher-twist power-corrections proposed by Qiu and Vitev [10], the measured nuclear modification factor can be reproduced. Thus, more measurements are needed to distinguish between the models and understand the origins of shadowing observed.

1.5 Hadronic Collisions

Let us consider the most basic hadronic collision system - proton-proton (p+p) collisions. Given a sufficiently large Q^2, one can calculate the pQCD differential cross section for a certain species from the parton distribution functions in both protons, the invariant amplitude for QCD Feynman diagrams, and the fragmentation functions which describe the production of hadrons from a final-state parton [14]. This is more complicated than in DIS[3] because the cross section depends on the convolution of two sets of parton distribution functions and because we have to consider the fragmentation functions. Formally, we have the following expression

[3]Semi-inclusive DIS (SIDIS) also uses fragmentation functions.

for the inclusive p+p $\rightarrow h$+X differential cross section at leading-order:

$$E\frac{d^3\sigma_{A+B\rightarrow h}}{d^3p} = \sum_{abc}\int dx_1 f_a(x_1)\int dx_2 f_b(x_2)\int \frac{dz}{z}\left(E_c\frac{d^3\sigma^{a+b\rightarrow c+X}}{d^3p_c}\right)\frac{D_{c\rightarrow h}(z)}{z}, \tag{1.7}$$

where

- a, b are the flavor of colliding partons,
- c is the flavor of one of the final state partons,
- x_1, x_2 are the Bjorken-x of the colliding partons (i.e. momentum fraction of proton carried by the partons),
- z is the fraction of the scattered quark momentum carried by the measured hadron,
- $f_a(x)$ is the probability density function for a parton with momentum fraction x and of type a,
- $D_{c\rightarrow h}(z)$ is the fragmentation function for producing a hadron from a parton of type c.

Next-to-Leading-Order (NLO) pQCD calculations for high-energy collisions have been shown to give excellent agreement with measured single particle differential cross sections in both the central and forward rapidity regions where $\sqrt{s} > 62$ GeV (see Fig. 1.14) [4, 55, 56].

When we instead consider proton-nucleus collisions (p+A), theoretical calculations have to consider the cold nuclear matter effects on the cross section including conventional nuclear shadowing [9, 10, 11], energy-loss [12, 13], and a modification of jet fragmentation [57] in addition to gluon saturation [1, 7, 8, 39, 58]. An understanding of p+A collisions is important in order to quantify the initial state in A+A collisions and to possibly detect the onset of gluon saturation, which has yet to be experimentally confirmed. We have already introduced the importance of nuclear shadowing and gluon saturation in the context of DIS collisions; next, we consider these effects in the context of heavy-ion collisions at RHIC.

1.5.1 Heavy-Ion Physics at RHIC

The Relativistic Heavy Ion Collider (RHIC) at Brookhaven National Laboratory turned on in 2000. RHIC can collide heavy ions (e.g. Au, Cu) up to a center of mass energy of $\sqrt{s_{NN}} = 200$ GeV, and polarized protons up to $\sqrt{s} = 500$ GeV [59].

The original goal of the experiments at RHIC was to search for a new, hot, dense phase of matter wherein quarks and gluons are not bound inextricably together by the strong force into states with null net color

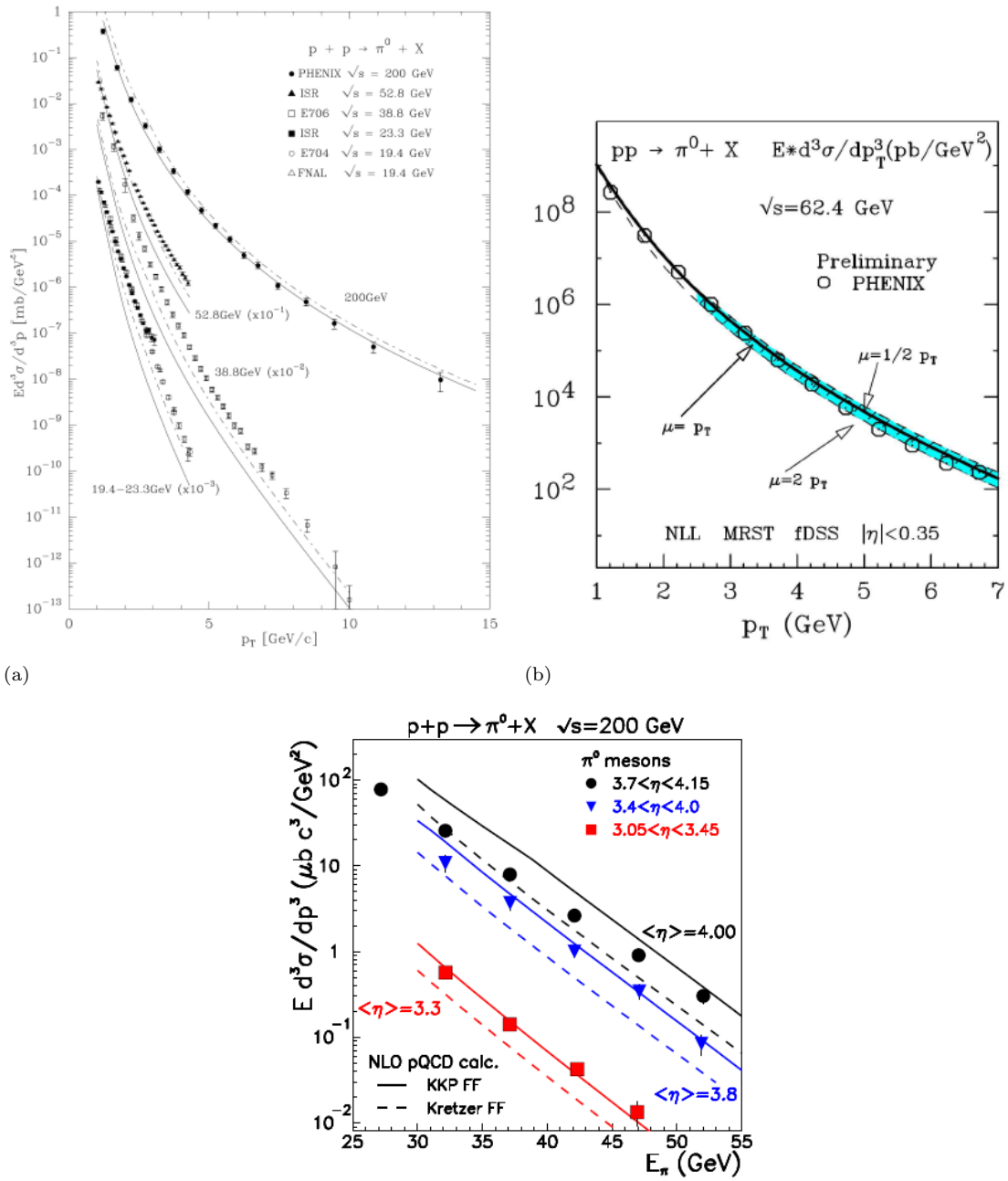

Figure 1.14: Agreement between p+p differential cross sections at midrapidity for **a.)** $\sqrt{s} = 200$ GeV [55] and **b.)** $\sqrt{s} = 62$ GeV [56] and for **c.)** forward rapidity at $\sqrt{s} = 200$ GeV [4].

charge, but instead have color degrees of freedom, now known as quark-gluon plasma (QGP) [18]. The laboratory for this search is heavy-ion collisions. Heavy-ion collisions are preferable to the simple proton-proton (p+p) system because one can obtain a much higher energy density in the collision, owing to the Lorentz-contracted nuclei (in the lab frame, the relativistic nuclei have a flattened pancake shape). The most prevalent heavy ion used in RHIC is gold (Au), and we will henceforth limit our discussion to only collision systems involving Au.

One of the main signatures of QGP is that outgoing partons lose energy exiting the colored medium [60]. At RHIC energies, for a large enough momentum transfer Q^2, the interaction of quarks and gluons can be modeled via a simple $2 \rightarrow 2$ scattering wherein momentum and energy are conserved. Because of the nature of the strong nuclear force, the outgoing partons hadronize into a spray of particles known as jets. Thus, a consequence of the parton energy loss is that one expects a reduction in the measured jet-yield at a given pseudorapidity (η) and transverse momentum (p_T).

1.5.2 Glauber Monte Carlo

To quantify the level of suppression in the jet-yield, one uses a p+p reference experiment and a Glauber model [61, 62, 63] to calculate the expected number of inelastic nucleon-nucleon collisions in the Au+Au system for all impact parameters (called N_{binary}, or N_{coll}). In the Glauber calculation we parameterize the radial distribution of nucleons within an Au-nucleus by a Woods-Saxon function

$$\rho = \rho_0 \frac{1}{1 + e^{(r-R)/a}}, \tag{1.8}$$

where $R = 6.38$ fm, $a = 0.54$ fm [62, 63].

One then simulates collisions between two nuclei. The nucleon-nucleon inelastic cross section at $\sqrt{s_{NN}} =$ 200 GeV is taken to be $\sigma_{NN} = 42$ mb, and if the colliding nucleons have a transverse separation that satisfies

$$d < \sqrt{\sigma_{NN}/\pi} \tag{1.9}$$

then the nucleons produce an inelastic collision, adding to N_{coll}. One then forms a ratio of measured particle yields in Au+Au compared to p+p scaled by $1/N_{coll}$, or

$$R_{AA}(p_T) = \frac{1}{N_{coll}} \frac{(dN/dp_T)_{Au+Au}}{(dN/dp_T)_{p+p}}. \tag{1.10}$$

1.5.3 QGP or CGC?

A suppression is indicated by $R_{AA} < 1$. In the first two years of running at RHIC it was indeed seen that there was a large suppression of $R_{AA} \approx 0.3$ for $p_T > 4$ GeV/c as seen in Fig. 1.15 [64, 65]. However, QGP was not the only proposed mechanism to bring about a suppression of jets, as other initial-state effects could also predict a suppression in R_{AA}, such as Color Glass Condensate [1]. The CGC hadron-yield suppression originates from the saturation of gluons in the initial state of the Au-nucleus (a reduced gluon distribution produces a smaller cross section, eq. 1.7), whereas QGP predicts the suppression from the final state.

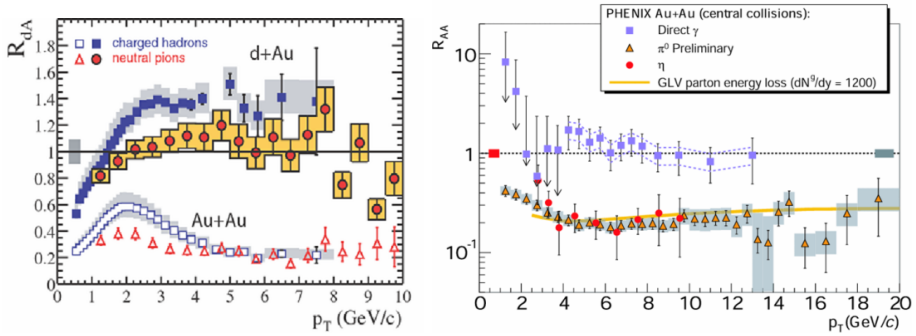

(a) (b)

Figure 1.15: Strong evidence for QGP **a.)** R_{AA} is suppressed [64, 65], while R_{dA} is not [66]. **b.)** R_{AA} for direct photons is not suppressed (photons interact via electromagnetic force and hence do not interact with the colored medium) [67].

To test between the predictions, a control experiment was devised. In deuteron-gold (d+Au) collisions, the energy density of the final state was predicted to be much lower than in the Au+Au case, and hence no QGP was expected to exist. CGC, on the other hand, predicted that the suppression should occur because the large density of gluons is still present in the initial state of the Au-nucleus. In an experimental tour de force, the PHENIX collaboration measured the nuclear modification factor R_{dA} (Figs. 1.15-1.16) and found that the result was nearly unity for hard-scattering regime ($p_T > 2$ GeV/c), indicating that in fact QGP was responsible for the suppression of R_{AA} [66, 68].

Despite its apparent failure to describe the suppression of the nuclear modification factors at midrapidity, CGC did offer an explanation of the observed suppression of R_{dA} at forward rapidities in the deuteron-going direction (see Fig. 1.17) [3, 4]. The qualitative argument is that saturation effects become more important because the forward region probes lower x in the Au-nucleus, and thus the parton densities increase. Hence the theory of CGC was provided with a new experimental testing ground in inclusive hadron production at forward rapidity.

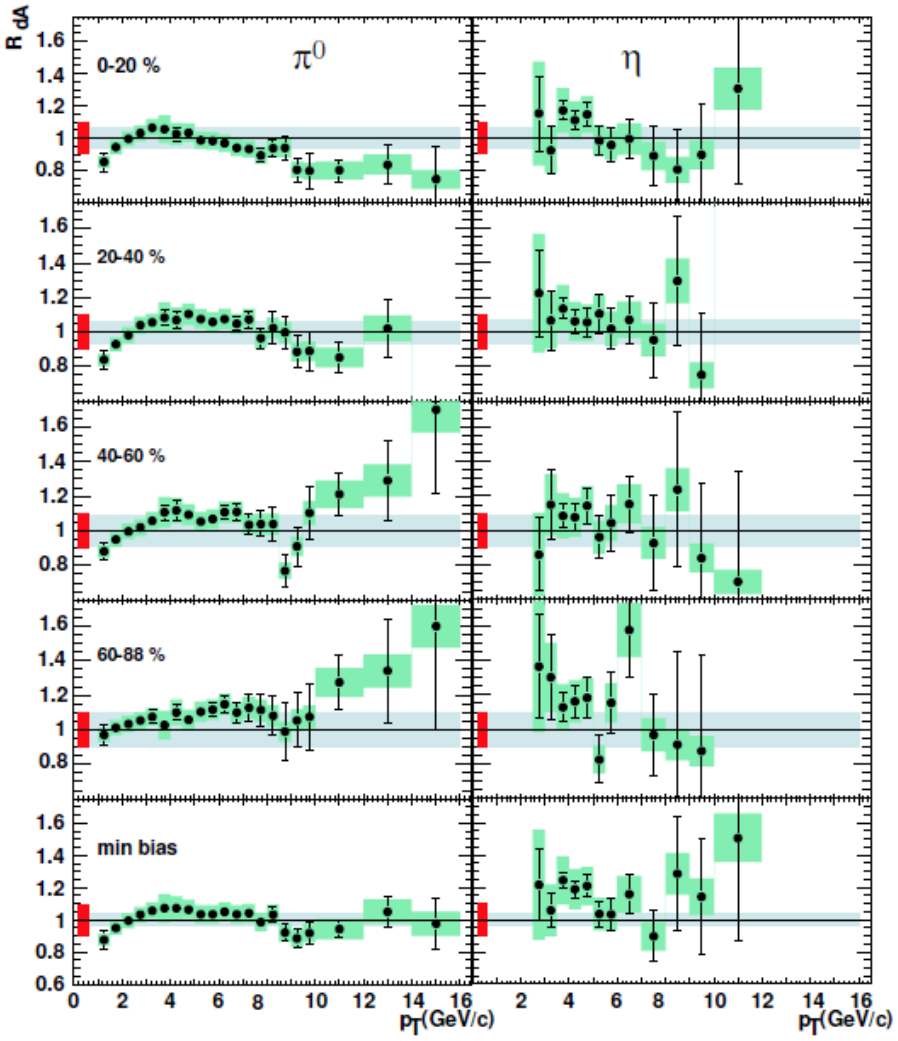

Figure 1.16: R_{dA} for neutral-pion and eta mesons for $\sqrt{s_{_{NN}}} = 200$ GeV collisions shown at midrapidity ($|\eta| < 0.35$) for different centrality bins. The $0 - 20\%$ centrality bin is on average the smallest impact parameter collision sample while the $60 - 88\%$ bin has the largest impact parameter.

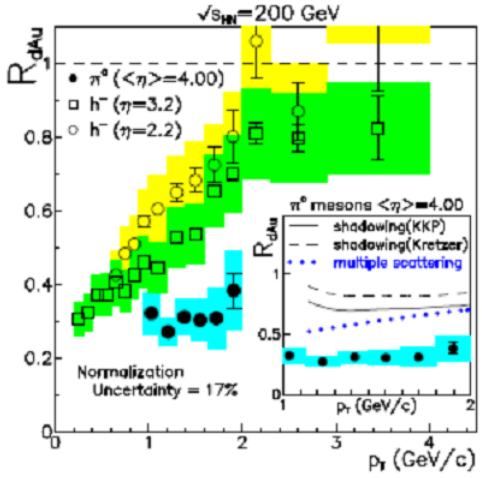

Figure 1.17: R_{dA} for neutral pions (STAR experiment) [4] and negatively charged hadrons (BRAHMS experiment) [3]. A larger suppression in R_{dA} is seen as one goes to more forward values of η. The negatively charged hadron sample is expected to be enhanced due to isospin effects, and so the level of suppression may be larger than shown by the ratio [9].

1.6 The Color Glass Condensate

We have thus far discussed gluon saturation in the context of DIS, and we now extend this discussion to heavy-ion collisions where gluon saturation is synonymous with the Color Glass Condensate theory [1]. What is the meaning of this appellation?

Color refers the color charge of the gluons.

Glass is a disordered system that can be viewed as a solid on short timescales and a liquid on long timescales. Similarly, on short timescales the partons' color fields are essentially frozen, while on long timescales they fluctuate.

Condensate refers to the fact that the gluons are expected to have their transverse momentum peaked about the saturation scale Q_s.

As we shall soon see, the phenomenology of CGC leads us to perform azimuthal angle two-particle correlation measurements to test if gluon saturation has been reached at RHIC. We must also take care to consider other model predictions in these measurements; disentangling the competing models that try to explain the forward d+Au physics is paramount to understanding if we can truly observe CGC at RHIC.

1.6.1 Gluon Wavefunction at Small Bjorken-x

As we have already discussed at some length in this introduction, the gluon distribution function inside a nucleus increases rapidly as one proceeds to small Bjorken-x. At this point, it is illustrative to describe a relatively simple physical reason for this behavior. We first consider a nucleus in its rest frame. This is a non-perturbative object containing many transient quantum fluctuations (e.g. gluons, quark/anti-quark pairs) as are allowed by the Heisenberg Uncertainty Principle. If we boost the nucleus to successively faster moving frames, these fluctuations begin to "freeze out" (exist on longer time scales) owing to the Lorentz time dilation involved in the boost. When the nucleus is boosted to a sufficiently high energy, the "frozen fluctuations" exist on a long enough time scale to become static sources for other transient fluctuations (even lower-x gluons). One can repeat this argument ad infinitum and qualitatively understand why the gluon distribution grows as one views successively smaller values of x (see Fig. 1.18) [28, 69]. Hence, this is the essence of the aforementioned BFKL evolution which evolves the PDFs in x; the number of gluons at each step in the evolution is proportional to the number at the previous step, or $\frac{\partial n}{\partial \ln(1/x)} \propto n$, giving exponential growth in the variable $Y \equiv \ln(1/x)$.

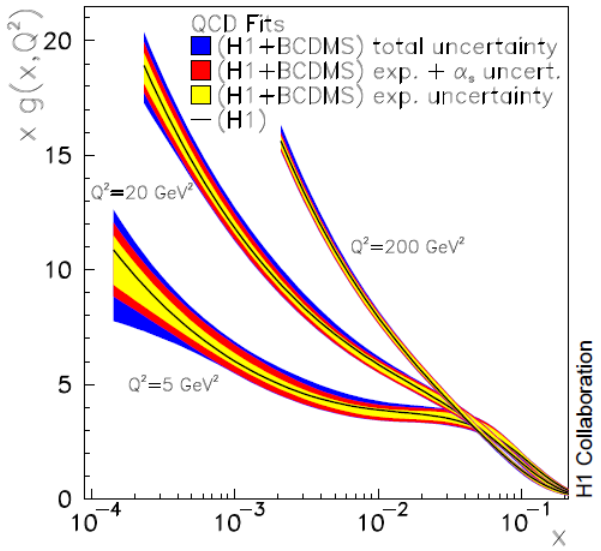

Figure 1.18: Gluon distribution function $xG(x, Q^2)$ versus x for $Q^2 = 5$, 20, and 200 (GeV/c)^2 [28].

This evolution has both phenomenological and theoretical problems at sufficiently small values of x. Phenomenologically it does not seem reasonable to have a divergent gluon distribution[4] as $x \to 0$. More

[4]Actually, this is not completely accurate; as long there is momentum conservation and the distribution does not violate the Froissart unitarity bound, the distribution is allowable [70]. This leads to a logarithmic growth in x.

specifically, what happens if the gluon density is so high that the wavefunctions overlap in the transverse plane[5]? Gluon fusion is an allowable QCD process due to the gluon self-interaction, and it would seem that there needs to be a term $\propto -n^2$ in the evolution equation to account for this. Theoretically, the problem is that the BFKL scattering matrix is not unitary. To restore the unitarity, it was found that one needs to add the aforementioned term in the BFKL evolution that corresponds to gluon recombination ($\propto -n^2$). A simplified version of the correct evolution equation (known as the Balitsky-Kovchegov or BK equation [38, 71]) is shown below:

$$\frac{\partial n}{\partial Y} = \omega\alpha_s n + \chi\alpha_s\partial_t^2 + \beta\alpha_s^2 n^2, \tag{1.11}$$

where n is the scattering amplitude (directly related to the gluon density), $Y \equiv \ln(1/x)$, and ω, χ, and β are all of order 1. The first term $\propto \alpha_s n$ is the BFKL evolution term (gluon bremsstrahlung), the second term with ∂_t^2 is a diffusion term, and the third term $\propto (\alpha_s n)^2$ is the gluon recombination term. The recombination term only becomes important when $\alpha_s n \approx 1$, and hence it can be ignored for a dilute system.

One can see the effect of the recombination term in the BK-equation on the DIS ep cross section in Fig. 1.19-a. At high energy (note that $s \approx Q^2/xy$), one can see a plateau in the cross section known as the black-disk limit[6], which originates from the gluon recombination term in eq. 1.11 slowing down the fast growth of the scattering amplitude. In Fig. 1.19-b, we show the scattering amplitude of a quark/anti-quark dipole scattering with a nucleus versus the transverse separation of the dipole $x_\perp \sim 1/Q$, which essentially shows the same behavior as Fig. 1.19-a, but in addition illustrates that the saturation scale Q_s (see section 1.6.2) is basically defined as the location where the scattering amplitude reaches half its maximum value.

Initially, the BK evolution was studied at leading order with a fixed coupling constant. The theory was able to qualitatively describe the data with certain model assumptions, but was not able to make ab initio predictions across both DIS and heavy-ion collisions. More recently, the theory has been extended to NLO with a running-coupling constant (called rcBK) [72, 73]; this has restored much of the predictive power that was found to be lacking with the LO theory.

The full description of CGC is given by the JIMWLK renormalization group equations [53]; the BK equation arises when one considers the large-N_C limit[7]. Here, the fast partons are described by a color charge density ρ, and the low-x, slow partons are described by the classical gauge fields A^μ obtained by

[5] The overlap in the longitudinal direction is governed by the de Broglie-like coherence length $l_{coherence} \propto 1/x$, which spans the longitudinal extent of the Au-nucleus for $x \lesssim 0.1$ [11]

[6] The black-disk limit means that the cross section for a sphere of radius R is $\sigma = 2\pi R^2$.

[7] $N_C = 3$ in the real world and is the number of color charges in QCD (red, green, and blue).

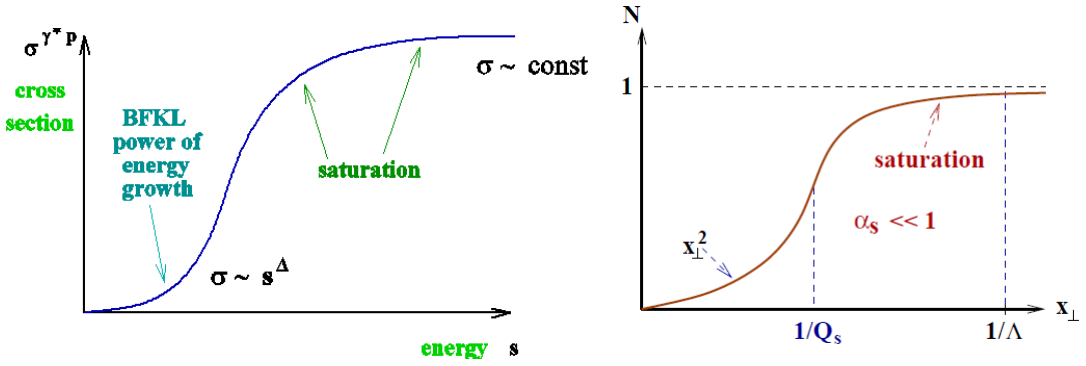

Figure 1.19: **a.)** Cross section versus $s \approx \frac{Q^2}{xy}$ for DIS ep scattering. Gluon recombination tames the rise of the BFKL cross section at large s (or small x). **b.)** Scattering amplitude of a $q/\bar{q}$ dipole scattering with a nucleus versus the transverse separation of the dipole $x_\perp \sim 1/Q$. One can see that at relatively large $x_\perp$ (or small Q^2) the amplitude saturates.

solving the Yang-Mills equation with the frozen source ρ. The functional $W_{xo}[\rho]$ is the weight of ρ, and depends on x_o, which is the scale used to separate the frozen source from the dynamic fields. The equation describing the evolution of W (JIMWLK) is

$$\frac{\partial W_{xo}[\rho]}{\partial \ln(1/x_o)} = -H[\rho, \frac{\delta}{\delta\rho}]W_{xo}[\rho], \tag{1.12}$$

where H is the JIMWLK Hamiltonian. Analytic solutions are very difficult; it has been found in numerical studies that there is little difference between solutions to the BK and JIMWLK equations [70].

1.6.2 The Saturation Scale and Geometric Scaling

The size of the gluon wavefunction is dependent upon both Bjorken-x and the four-momentum transfer squared of the interaction, Q^2. As Q^2 increases, the size of the wavefunction probed decreases. Thus at large Q^2 it is possible to fit a large density of gluons into a nucleon without observing effects from overlaps. The condition for observing CGC requires a small x and sufficiently small Q^2; this condition can be succinctly formulated in terms of characteristic scale for gluon saturation aptly named the saturation scale, $Q_s(x)$. The saturation scale describes the Q^2 boundary of the saturation regime that evolves with x (see Fig. 1.7). It is given by the value of Q^2 where the terms in the BK equation (eq. 1.11) corresponding to gluon splitting and fusion are equal [70]. Alternatively, another way to specify a saturation scale is to identify the value of $x_\perp$ in the dipole scattering amplitude where it reaches half of its maximum value, as shown in Fig. 1.19-b.

In the leading-logarithmic (LL) solutions of the BK equation, the saturation scale is related to the number of nucleons A (e.g. 197 in Au) and the momentum fraction x in the following manner:

$$Q_s^2 \propto \frac{A^{1/3}}{x^{\lambda_s}}, \tag{1.13}$$

where $\lambda_s \approx 0.2 - 0.3$ is the so-called evolution speed as determined by DIS data. The $A^{1/3}$ dependence arises from longitudinal overlaps amongst the gluon wavefunctions at small x in Lorentz contracted nuclei. The longitudinal extent of the low-x gluon wavefunction spans the entire length of the nucleus (not true at high x), and hence the gluon density increases in proportion to the number of nucleons ($\propto N_{gluons}$) at a given transverse position, which on average is $\propto A^{1/3}$. The fact that the Au-nucleus has a diameter of about 12 nucleons coupled with the spherical shape of the nucleus (in the rest frame) determines the impact parameter dependence of longitudinal gluon density. For instance, in a p+Au collision with zero impact parameter, the proton interacts with ≈ 12 nucleons, while for very peripheral impact parameters, the proton can see only one nucleon; hence, the gluon density will be 12 times greater at the center of the nucleus than at the edges. In Fig. 1.20 we show the so-called unintegrated gluon distribution $\phi(x, k_T^2)$[8] as a function of the intrinsic transverse momentum k_T of the gluons [74].

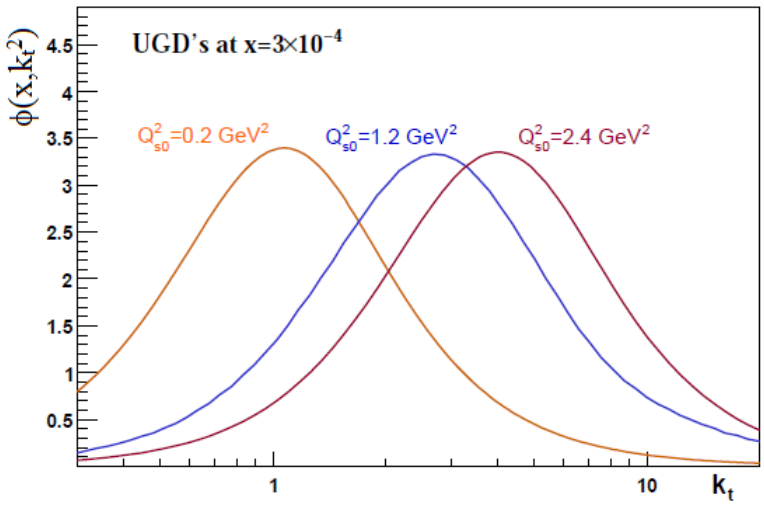

Figure 1.20: Unintegrated gluon distributions $\phi(x, k_T^2)$ for targets of thickness 1, 6, and 12 nucleons, respectively at $x = 3 \times 10^{-4}$. One can see how the saturation scale increases as the target size is increased.

The three curves in the figure correspond to the low-x ($x = 3 \times 10^{-4}$) gluon distributions for targets that

[8] $xG(x, Q^2) = \int^{Q^2} dk_T^2 \phi(x, k_T^2)$

are 1, 6, and 12 nucleons thick (corresponding to $Q_{s0}^2 = 0.2$, 1.2, and 2.4 (GeV/c)^2). Please note that in this figure, the saturation scale Q_s^2 is approximately 2-3 times greater than Q_{s0}^2 because of the evolution with x (see eq. 1.13).

This figure illustrates a key point about the measurements carried out in the context of this thesis. We enhance the saturation scale Q_s^2, or the Q^2 value at which we begin to observe saturation effects, by increasing the nuclear radius. Hence gluon saturation can occur in both the proton and the gold nucleus, but begins at larger values of Q^2 in the Au-nucleus because of the enhanced nuclear size. For example, given that we probe $x = 3 \times 10^{-4}$ (as in the figure) where we have $Q^2 \approx 4$ (GeV/c)^2, one would expect to see saturation effects in the Au-nucleus but not in the proton. Hence our measurements using d+Au collisions compared to a p+p reference exploit this difference in the saturation scale in an attempt to observe the saturation effects on the gluon distributions.

Fig 1.20 also illustrates a few important points about a "saturated" gluon density. If one performs the integral of the gluon distribution over k_T, the integral will be finite; the same is true for the x-integral. This is true simply because the nucleus cannot have an infinite momentum, though there is not restriction on having an infinite number of gluons. This, along with the Froissart unitarity bound impose restrictions on the rate of growth, and $\phi(x, k_T^2)$ must grow slower than $\ln(1/x)$ ($\ln(1/k_T)$) as x (k_T) $\to 0$ [70]. Also, one can see that the transverse momentum distribution is peaked near the value of the saturation momentum Q_s, indicating that the majority of CGC gluons have $k_T \approx Q_s$.

In addition to the $A^{1/3}$ dependence, the saturation scale is also $\propto 1/x^{\lambda_s}$, or if we let the rapidity variable $Y \equiv \ln(1/x)$, $Q_s^2 \propto e^{\lambda_s Y}$. In the leading-logarithmic BK calculation the value calculated for λ_s is about 4 times larger than the $\lambda_s \approx 0.3$ expected from DIS data. This discrepancy was found to be due to not including the next-to-leading corrections and running-coupling corrections in the BK equation [72, 75, 76]. Upon adding these corrections, it was seen that the evolution of the saturation scale was in fact

$$Q_s^2 = Q_0^2 e^{\lambda\sqrt{Y+Y_0}}, \tag{1.14}$$

where Q_0 and Y_0 are the initial conditions for Q_s^2 and Y where the evolution begins. Within the x ranges accessible at RHIC the evolution speed λ_s (defined by the logarithmic derivative $\lambda_s = d\ln Q^2/dY$) calculated in this framework was found to be very close to 0.3 [75], thus agreeing with experimental data on geometric scaling (discussed below).

At RHIC energies in the Au-nucleus, Q_s is expected to be about $1 - 2$ GeV/c [39, 52] depending upon impact parameter and x, which is a semi-hard scattering regime. If $Q^2 < Q_s^2$, saturation effects are expected

to play a role in the collision dynamics; hence to observe gluon saturation, it is beneficial to increase the saturation scale by having a large nucleus and a small momentum fraction. This makes forward-rapidity particle production (smaller x than midrapidity, see eq. 1.15) in d+Au collisions an ideal tool to search for CGC, as one can probe small x with a large nucleus free from QGP effects.

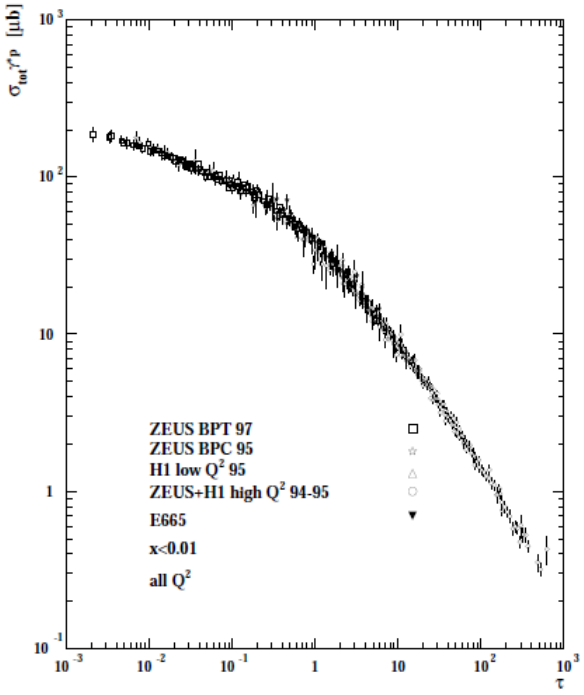

Figure 1.21: DIS $\gamma^* p$ cross section versus the scaling variable $\tau = Q_s^2(x)/Q^2$ demonstrating geometric scaling for $x < 0.01$ [77].

If we go to slightly larger $Q^2 \gtrsim Q_s^2$ at fixed $Y = \ln(1/x)$, we encounter a region of phase space known as the Region of Extended Scaling or Color Quantum Fluid [39, 58, 78, 77]; this is predicted to be the region of overlap between CGC and regular BFKL evolution (see Fig. 1.7). One prediction of this region is called geometric scaling wherein the DIS cross section scales with a single variable $\tau = Q_s^2(x)/Q^2$ instead of having independent x and Q^2 dependencies; this indeed has been observed in the data for $x < 0.01$ [77] and is shown in Fig. 1.21, wherein experimental data at different combinations of x and Q^2 can all be plotted on a single curve. From the data, this scaling directly constrains the value of the evolution speed, λ_s, between $0.2 - 0.3$. Hence, the fact that the NL CGC theory now predicts an evolution speed that is consistent with that observed in data shows that the NL corrections are necessary to properly describe the physics [72, 75, 76].

DGLAP evolution can also produce this scaling behavior, though it posits no a priori reason why the scaling should exist. As discussed, CGC, on the other hand, predicts that the scaling region should exist and makes a prediction for λ_s that is consistent with the observed parameter in the scaling data. A phase diagram of the nuclear wave function is shown in Fig. 1.7-b, and one can see that the Extended Scaling Region lies between the Saturation Region and the region described by BFKL or DGLAP.

Once we increase Q^2 sufficiently, BFKL evolution describes the evolution in $\ln(1/x)$ while DGLAP describes the Q^2 evolution. It should be noted that most phenomena in the BFKL region can be described by the DGLAP evolution and that only a few measurements are sensitive to BFKL effects exclusively.

1.6.3 Comparison between Models and Data

At RHIC, hard scattering dominates particle production at $Q^2 \gtrsim 4$ (GeV/c)^2. Because Q_s^2 is calculated to be $\gtrsim 1$ (GeV/c)^2 for the Au-nucleus at RHIC energies, hard-scattering involving gluons from the Au-nucleus in heavy-ion collisions is thought to be sensitive to CGC and BFKL evolution effects [39, 58, 78]. The absence of $R_{\rm dA}$ suppression at midrapidity would seem to negate this sentiment [66]; however we also see a suppression of R_{dA} in the forward rapidities [3, 4], thus probing lower x. Additionally, recent CGC calculations for $R_{\rm dA}$ are able to reproduce the observed spectra quite well [52] as seen in Fig. 1.22-a; the evolution speed predicted by CGC agrees with the geometric scaling data [77], and the theory parameters obtained from the fit agree well with those obtained from fitting the eA DIS data [51, 52].

However, given the present experimental evidence, other shadowing effects can also explain some of the suppression. One issue with the non-CGC shadowing models is that the predicted suppression of the forward $R_{\rm dA}$ is too low, even when including higher-twist effects[9] [9, 10, 47]. In addition to nuclear shadowing, there are models that predict an increasing energy loss as the forward-particle Feynman-x_F increases, where $x_F = \frac{p_z}{\sqrt{s}/2}$. The increasing energy loss in combination with shadowing can reproduce the level of observed suppression (see Fig. 1.22-b) [12, 13]. Another model (parton recombination) posits that because of the smaller number of soft partons in the forward region in d+Au, there will be a suppression of particles in the final state [57]. This model would be consistent with models wherein the soft particle production is suppressed in the forward direction. Hence more detailed measurements are needed to understand the suppression.

[9] See Fig. 8.1 for comparisons of Qiu-Vitev higher-twist shadowing [10] to the new PHENIX data.

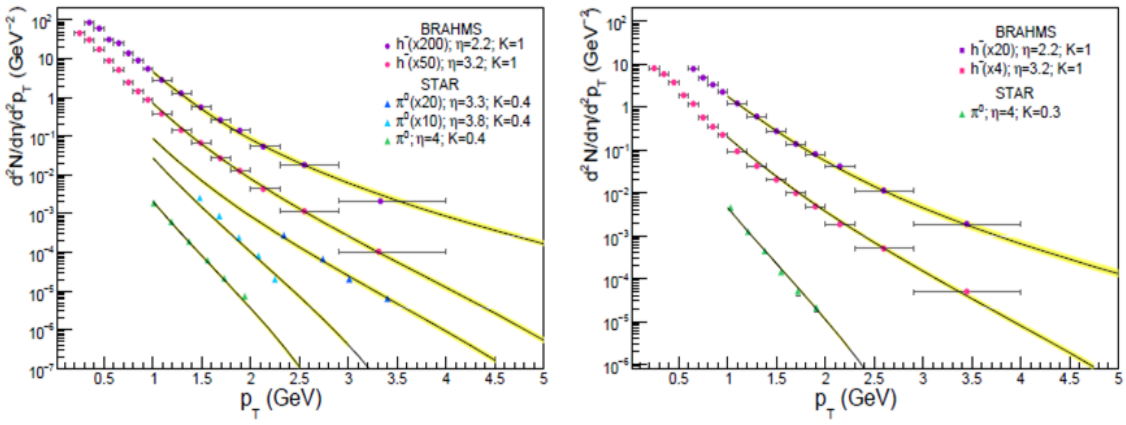

(a)

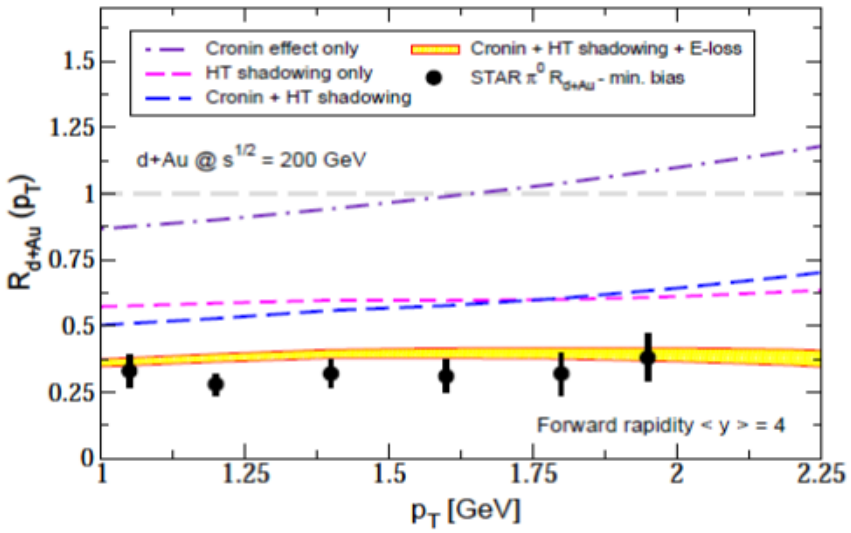

(b)

Figure 1.22: Comparison of data and theory for forward particle production at $\sqrt{s_{NN}} = 200$ GeV for **a.)** Color Glass Condensate [52] and **b.)** higher-twist shadowing with initial-state energy loss [54].

1.7 Two-Particle Correlations and CGC

Two-particle $\Delta\phi$ correlation functions [79, 80, 81, 82], which tag di-jet correlations at different ranges of x, might discriminate between CGC and other models of cold nuclear matter effects. In the simple $2 \rightarrow 2$ hard-scattering picture, the initial parton transverse momentum (k_T) is relatively small, and thus momentum conservation requires that the particles come out back-to-back in the transverse plane. Thus if we consider particles produced from opposing jets, the azimuthal angle difference ($\Delta\phi$) between the particles should be distributed about $\Delta\phi = \pi$ in an approximately Gaussian distribution. On the other hand, if the particles are produced in the same jet, $\Delta\phi$ between the particles is centered about 0 in a Gaussian distribution. An example correlation function is shown in Fig. 1.23. One can see that the correlation function is made of a *nearside* peak at $\Delta\phi = 0$ and an *awayside* peak at $\Delta\phi = \pi$ on top of a pedestal, or flat background. The pedestal arises from instances wherein the two particles are not correlated; uncorrelated hadron pairs arise from soft processes that dominate at $Q^2 \lesssim 1$ (GeV/c)^2, from different nucleon-nucleon interactions in heavy ion collisions, from multi-parton interactions, or from three-jet events.

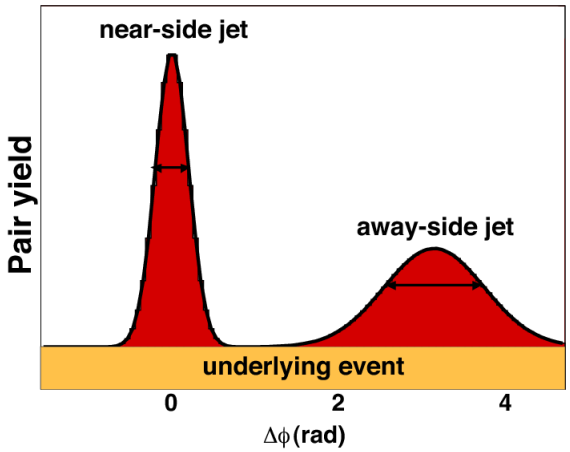

Figure 1.23: Sample two-particle $\Delta\phi$ correlation function showing the nearside peak, awayside peak, and the pedestal (or underlying event). Correlation functions separated in rapidity by $\Delta\eta \gtrsim 1.2$ do not show a nearside peak.

The nearside peak is sensitive to only the fragmentation of hadrons about the jet-axis. There is a characteristic component of the hadrons momentum transverse to the jet-axis known as $J_T \approx 0.5$ GeV/c [80] that controls the width of the peak. Thus by increasing the p_T of the two particles, the nearside peak is expected to narrow. If there were no intrinsic k_T for either of the colliding partons, the width of the awayside peak would also be dominated by the J_T; however, since there is some $\langle k_T \rangle \approx 2$ GeV/c [80] at RHIC energies,

the di-jets are not exactly back-to-back and the awayside peak broadens.

One reason that the correlation functions are interesting is that we expect CGC effects to modify the traditional $2 \rightarrow 2$ hard scattering picture. One example of this is the production of so-called monojets, or a $2 \rightarrow 1$ phenomenon, as proposed by Kharzeev, Levin, and McLerran [2]. A monojet could be from two gluons (off-shell) fusing into one final-state gluon; momentum is conserved by the recoil of the CGC gluons. There would be no awayside peak (or a decorrelated one) in the correlation function because of the $2 \rightarrow 1$ process, and thus one would expect a decrease in the yield of the awayside and angular broadening. Thus because the correlation functions have angular information and can isolate hard-scattering, one expects them to be more sensitive to CGC effects than single-particle measurements such as $R_{\rm dA}$.

Also, the correlation functions are able to probe the di-jet structure even at $p_T < 2$ GeV/c, because one can pick out the correlated part of the signal, which indicates di-jet production, from the background. Thus the Gaussian signal in the correlation functions probes hard scattering and removes the soft contributions, unlike the single-particle measurements. Maybe more importantly, by constraining the rapidities of the di-jets, one can constrain the x range to much smaller ranges and values. At leading order the following relationship holds between parton momentum fractions $x_{1,2}$ and the rapidity of outgoing jets given that parton 1 moves in the $+z$-direction (deuteron-direction) and parton 2 in the -z (Au-direction):

$$x_1 = \frac{p_{T,1}e^{y1} + p_{T,2}e^{y2}}{\sqrt{s}}, \tag{1.15}$$

$$x_2 = \frac{p_{T,1}e^{-y1} + p_{T,2}e^{-y2}}{\sqrt{s}}. \tag{1.16}$$

To reach small x_2 (x of parton in Au-nucleus), it is preferable to have two particles in the forward direction. For example, if both jets are forward with $y_{1,2} = 3.0$ and $p_{T,1,2} = 2.0$ GeV/c, we have $x_2 = \frac{4.0e^{-3}}{200} \approx 10^{-3}$. If one jet is at $y_1 = 0$ and $y_2 = 3$, $p_{T,1,2} = 2.0$ GeV/c, then $x_2 \approx \frac{2.0e^{0}}{200} = 10^{-2}$. This also demonstrates that at leading order, forward-particle production from di-jets consists of a relatively large range in x. By using two-particle correlations, we constrain x and thus are able to study nuclear effects in different ranges of x. This is paramount to understand particle production in the forward region and to probe CGC.

Let us now consider the rapidity separated angular correlations where $\eta^{mid} < |0.35|$ and $\eta^{fwd} = 3.0 - 3.8$, termed *mid-forward* correlations. In Ref. [2], the authors describe two processes that decorrelate the experimentally observed away side peak: one is the large rapidity gap emission of mini-jets, known as Mueller-Navelet Jets, decorrelating initially back-to-back partons in the subsequent parton shower [83]. The

other is the decorrelation from CGC wherein the observed jets are from multiple, independent scatterings from the CGC, which produce gluon emissions within two parton showers (see Fig. 1.24[10]).

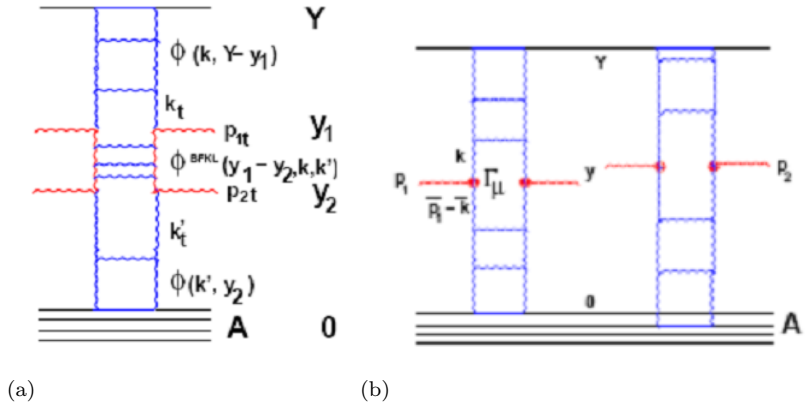

(a) (b)

Figure 1.24: BFKL ladder diagrams showing two processes by which angular broadening can occur in correlation functions. **a.)** A large rapidity gap between the detected jets (red) allows evolution to produce multiple gluons along the rapidity gap [83], **b.)** multiple scattering produces uncorrelated jets [2].

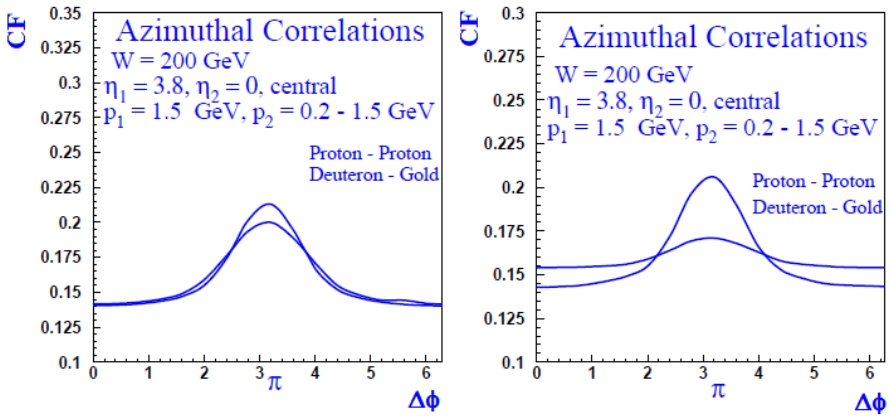

Figure 1.25: Angular decorrelations from the processes in Fig. 1.24 [2].

Thus it was predicted that the correlation functions would have a small broadening of the awayside peak both due to BFKL evolution and CGC effects as well as a decrease in the conditional yields or per-trigger yields, which are the normalized areas of the awayside peaks (see section 5.2) [2, 6, 84]. The normalization

[10] Please note that the diagrams and their complex conjugate diagrams are shown, and the vertices in the gluon ladders are in fact Lipatov vertices (see Refs. [70, 2] for more details). Also, for clarity the authors decided to highlight the detected gluon lines in red and point them away from the ladder.

involves dividing by the inclusive yield of *trigger*[11] particles. This measurement was once thought to be an extremely strong probe of CGC; however, in recent years, many theorists have questioned whether x is low enough for CGC to be applicable in this regime [85].

A first measurement of the correlated di-hadron suppression for rapidity separated hadron-pairs was performed in Ref. [86]; here PHENIX performed correlations between charged hadrons detected in the muon arms ($1.4 < \eta < 2.2$) and at midrapidity in d+Au and p+p (*mid-muon* correlations). The measurement showed an apparent lack of suppression in the nuclear modification factor $I_{\rm dA}$, the ratio of CYs between d+Au and p+p (see section 5.2 for details), and it was thought that this negated the existence of CGC at RHIC (see Fig. 1.26-a). More recently, in 2009 we presented an $I_{\rm dA}$ measurement at the Quark-Matter Conference that piqued the interest of the CGC community (see Fig. 1.26-b). We showed that for the mid-forward correlations (using the midrapidity charged hadrons and MPC π^0's), a suppression of $I_{\rm dA} \approx 0.5$ is present at small impact parameters (large $N_{\rm coll}$), and some attributed the suppression we observed to CGC [87].

How then can these two results be consistent when one indicates no suppression and the other clearly does show it? The difference between the mid-muon $I_{\rm dA}$ and mid-forward $I_{\rm dA}$ exists for two reasons:

1. The mid-muon correlations used an $I_{\rm dA}$ where the "trigger particle" was defined at the forward rapidity of the muon spectrometer, while the mid-forward correlations used the trigger particle at midrapidity,

2. The suppression of $I_{\rm dA}$ triggered at midrapidity seems to increase with increasing rapidity of the "associate" particle. Because the MPC is more forward than the Muon Arms, $I_{\rm dA}$ using the MPC should be more suppressed.

Hence it was once again thought that the mid-forward di-hadron correlations might be revealing CGC effects. However, upon communicating with one of the main theorists who performed the CGC di-hadron correlation predictions, it was conveyed that a lower x was necessary before CGC effects should show up [85].

In order to probe these very small values of x we measure correlation functions wherein both particles are at forward rapidity, termed *forward-forward* correlations; this probes the lowest value of x achievable at RHIC. Broadening effects due to CGC are expected to be large, and we also would expect the yields to be suppressed. Recent predictions that have been made using the preliminary results from PHENIX [88] and STAR [89] show an awayside peak that is greatly suppressed as seen in Fig. 1.27 [90].

[11] The distinction between the two particles is somewhat arbitrary. Usually the trigger particle is the higher-p_T particle of the pair and the associate has smaller p_T.

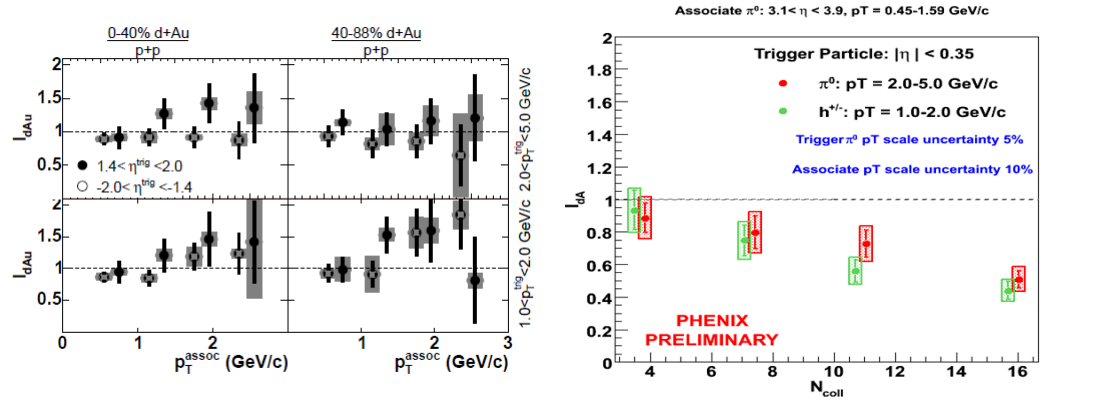

(a) (b)

Figure 1.26: I_{dA} for two-particle correlations wherein **a.)** the trigger particle is at the forward muon arm rapidity ($1.4 < \eta < 2.2$) and the associate particle is at midrapidity [86], and **b.)** the trigger particle is at midrapidity and the associate particle is at the forward MPC rapidity ($3.0 < \eta < 3.8$) [87].

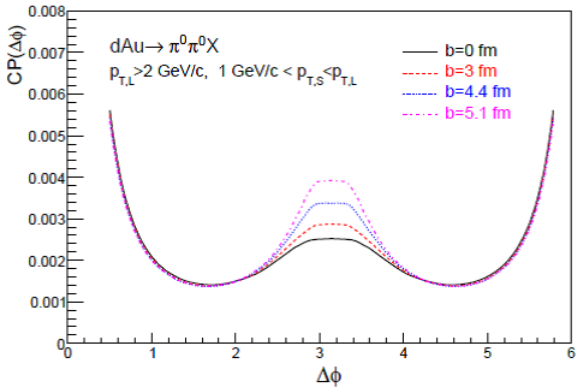

Figure 1.27: Two-particle angular correlations for forward π^0's where $2.4 < \eta_{1,2} < 4.0$ for different impact parameters. One can see a suppression in the yields as one goes to smaller impact parameters [90].

The mid-forward and forward-forward correlation functions give access to different parts of the forward particle production. The mid-forward correlations probe a higher $x_2 \approx 0.01$, while the forward-forward probe very small $x_2 \approx 0.0005$. In terms of understanding the suppression of R_{dA}, one might suppose that the mid-forward are more important because in the $2 \rightarrow 2$ hard scattering picture, the most probable rapidity configuration for a forward di-jet system is mid-forward. The measurements are complimentary in that we can understand the di-jet production in different x ranges. We would expect gluon saturation effects to be the strongest in the forward-forward correlations, because they probe the smallest values of x. Hence we are providing measurements which will help us to understand the suppression of R_{dA} and are predicted to be very sensitive to gluon saturation effects.

Chapter 2

Experimental Apparatus

2.1 RHIC

The Relativistic Heavy Ion Collider [59] at Brookhaven National Laboratory is a 3.8 km circumference storage ring used for both polarized p+p and heavy-ion collisions. It can collide protons up to a center-of-mass energy of $\sqrt{s} = 500$ GeV and heavy ions (Au, Cu, etc.) up to $\sqrt{s_{NN}} = 200$ GeV. Two counter-circulating beams have the capability to collide at six different interaction points. Presently, only the PHENIX [19] and STAR [20] experiments are operating at RHIC, though two smaller experiments (PHOBOS [22] and BRAHMS [21]) recently stopped recording data.

Figure 2.1: Aerial view of the RHIC accelerator complex.

Heavy-ion beams are created from a sputter-ion source and then accelerated by a Tandem Van Der Graff accelerator. Next, the beam is sent to a booster synchrotron followed by injection into the AGS (Alternating-Gradient Synchrotron) where it is accelerated up to $\approx$ 10 GeV/nucleon. The beam exits the AGS and is split by the transfer line into two RHIC beam lines, where the fully-ionized beams are stored until they reach full energy [59].

The original goal of the collider was to observe the transition from normal hadronic matter to a plasma of quarks and gluons that contain color degrees of freedom. Definitive proof of a plasma has been established [19, 20, 21, 22] and so RHIC has transitioned from a discovery machine into a tool for understanding the properties of the QGP, as well as to precisely measure properties of proton spin structure. Some discovery potential remains, however, in trying to observe the Color Glass Condensate [1] in d+Au collisions. The asymmetric d+Au collisions are used rather than p+Au because the magnetic rigidity ($\propto Z/A$) of the deuteron is closer to that of the Au-ion. Similar rigidities are needed because both beams pass through the DX magnets near each of the interactions points [91].

2.2 PHENIX

The PHENIX (Pioneering High Energy Nuclear Interaction eXperiment) experiment [92] at RHIC is armed with an array of detector subsystems capable of identifying photons, electrons, hadrons, and muons in different pseudorapidity ranges. The initial design of the experiment was aimed at identifying rare probes in Au+Au and p+p collisions via leptonic (electron and muon) and photonic channels. Many upgrade detectors have been added to PHENIX throughout its lifetime to increase its efficacy, but the main subsystems remain intact. PHENIX consists of a central spectrometer mainly used for identifying photons, electrons and charged hadrons at midrapidity ($-0.35 < \eta < 0.35$) [93, 94, 95] as well as two muon-spectrometer arms at forward and backward rapidities ($1.2 < |\eta| < 2.2$) [96]. From 2005 to 2007, two new forward electromagnetic calorimeters were installed in the cylindrical holes of the piston-shaped muon magnets. The Muon Piston Calorimeters (MPCs) sit at very forward rapidities ($3.1 < |\eta| < 3.9$) and are used to detect photons and hadrons that have photon-decay modes [97, 98, 99]. These forward calorimeters are useful for both spin physics [97, 98] and heavy-ion physics (especially for d+Au collisions) [87, 88, 99, 100], as the forward rapidity region probes smaller x and larger x_F than at midrapidity and has produced several interesting experimental measurements that are not satisfactorily explained by the present state of theory. In addition to the main detector subsystems and the MPCs, global event detectors exist that characterize the events [101]. In what follows, we will discuss the detector subsystems that are directly relevant for discussion of the physics results including the global detectors, the midrapidity electromagnetic-calorimeters and charged-hadron spectrometers, and the forward Muon Piston Calorimeters.

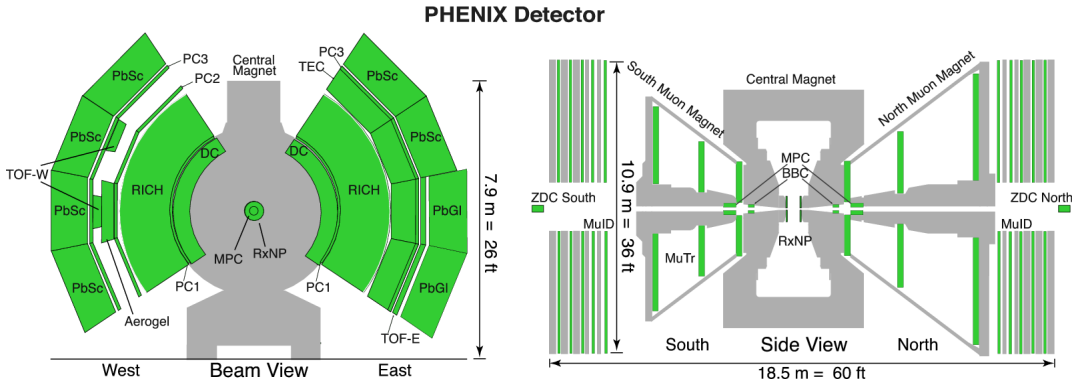

Figure 2.2: Side and beam views of PHENIX.

2.3 Global Event Detectors

The global detectors in PHENIX include the Beam-Beam Counter (BBC), Zero-Degree Calorimeter (ZDC), and Reaction Plane Detector (RXNP). The RXNP [102] is one of detectors used in heavy-ion collisions to determine what is known as the reaction plane, which is the plane defined by the set of displacement vectors that can be drawn between the nuclear centers of the colliding nuclei along their collision paths. It is useful for determining properties of heavy-ion collisions, especially when QGP is formed. The ZDCs [101] are hadronic calorimeters at $\eta \approx \pm 6$ used for detecting spectator neutrons, triggering on inelastic events as a minimum-bias trigger, and for determining event centrality (related to impact parameter). However, for d+Au collisions, only the BBC is used for the minimum-bias trigger as well as centrality determination. Also, it is not typical to characterize a d+Au event by a reaction plane. Hence we limit further discussion of global detectors to the BBCs.

The BBCs [101] sit at ± 144 cm from the nominal interaction point at $3.0 < |\eta| < 3.9$ covering 2π in azimuth. Each BBC consists of the 64 3-cm quartz radiators with a Cherenkov threshold of $\beta = 0.7$ readout by photomultiplier tubes. They are used to detect forward, charged particles. The BBCs are an extremely important set of detectors both for online (during data acquisition) and offline purposes. The timing difference between the BBCs is used to measure the online z-vertex as well as a more refined offline z-vertex. The online vertex allows one to select a sample of events that are contained within roughly 40 cm of the nominal interaction point $z = 0$ cm in all triggers that utilize the BBCs. Additionally, the sum of timing signals is the start-time, T_0, for time-of-flight measurements. The BBCs have a timing resolution of ≈ 50 ps (as compared to the average bunch-crossing time of ≈ 100 ns) and can resolve the z-vertex to within ≈ 1 cm.

The requirement that one phototube in each BBC has a hit selects a sample of events known as the minimum-bias sample and this trigger is the most basic of all PHENIX Local Level 1 (LL1) triggers [101]. In the 2008 PHENIX run (the eighth year of data-taking, or Run8), the event rate for the trigger was 100 kHz, which is far higher than the typical DAQ bandwidth of 5 kHz. Hence, many of these events are randomly discarded (other triggers exist specifically for photons, electrons, muons, etc. that also take up DAQ bandwidth). The BBCs are also used to determine the centrality of the event, which we discuss in the next section.

2.3.1 Centrality Determination

The d+Au collision system is asymmetric; we usually say the deuteron traverses in the forward-rapidity direction (towards the north BBC, or BBCN) while the gold ion moves in the backward-rapidity direction (towards the south BBC, or BBCS). It has been shown that the charge deposited in the south BBC is proportional the number of participants in the collision (N_{part}), which is correlated with the number of binary collisions, $N_{\rm coll}$, defined in section 1.5.2. The relationship between the south BBC charge and $N_{\rm coll}$ is quantitatively determined by the Glauber monte-carlo along with tuning the BBC response to match in simulation and data [61, 62, 63].

In d+Au collisions, the BBC trigger detects 88.4% of the total inelastic cross section [63]. We thus split this event sample into 88 equally-sized bins and call the bin with the highest charge the 1% bin (most central collisions or largest N_{coll}) and the bin with the lowest charge the 88% bin (most peripheral or smallest N_{coll}).

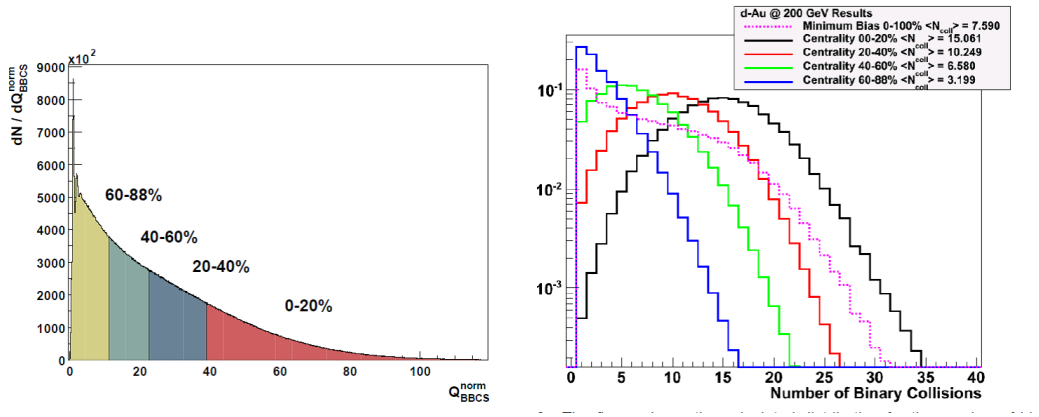

(a) (b)

Figure 2.3: **a.)** South BBC charge distribution divided into four centrality classes (0-20%, 20-40%, 40-60%, and 60-88%), **b.)** N_{coll} distributions for the centrality classes as well as the 0-100% class.

In Fig. 2.3-a, we show the charge distribution for the south BBC; here the colors represent four centrality classes (0-20%, 20-40%, 40-60%, and 60-88%). In our analysis, we use these classes and form distributions of N_{coll} for each centrality class (Fig. 2.3-b) as determined from the Glauber monte-carlo. When we discuss using a value of N_{coll} in a ratio such as $R_{\rm dA}$, we always use the average of the centrality class in question (see Fig. 2.3-b); $\langle N_{\rm coll}\rangle$ values are 15.1 ± 1.0, 10.2 ± 0.70, 6.6 ± 0.44, and 3.2 ± 0.19, respectively for the 0-20% through 60-88% centrality bins [63, 99]. For p+p, $\langle N_{\rm coll}\rangle = N_{\rm coll} = 1$.

2.4 Central Rapidity Spectrometer

The PHENIX central-rapidity (a.k.a. midrapidity) spectrometer [94, 95] has two main components:

- A charged particle tracking system (Central Magnet, Drift Chambers, multi-wire proportional chambers with pad readout, Ring Imaging Cherenkov Detectors, Time of Flight Detectors),
- A large electromagnetic calorimeter (EMCal).

The spectrometer consists of two arms which each cover $\pi/2$ in azimuth and $-0.35 < \eta < 0.35$. One can see the different components in Fig. 2.2. Some of the measurements presented in this thesis use both charged hadrons as well as π^0's from the central spectrometer, and hence we give a brief description of the relevant detectors in what follows.

2.4.1 Charged Tracking

The PHENIX Drift Chambers (DCs) [94] sit $2 - 2.4$ m away from the interaction point and consist of six planes of wires, X1, U1, V1, X2, U2, and V2. The DCs were designed to have a tracking efficiency of $> 99\%$. The X-layers are oriented along the direction of the beam, allowing a precise determination of the position ($\lesssim 150$ μm in the $r - \phi$ plane, and thus providing precise transverse momentum determination). The U- and V-layers are oriented with a stereo angle of $\pm 6^\circ$ relative to the X-layers and provide a measurement in the z-position of $\lesssim 2$ mm, which is nearly what can be obtained by the Pad Chambers.

The PHENIX Pad Chambers (PC1, PC2, PC3) [94] are multi-wire proportional counters with pad readout that reside directly behind the DCs (PC1), behind the RICH (PC2, West arm only), and directly in front of the EMCal (PC3). The PCs provide a measurement of the position in all directions (z as well as radial) and are thus used in calculating the total momentum of a track. The PCs are the only non-projective element of the central tracking system, and hence they provide a veto of spurious tracks. Together with PC1, the

PHENIX DCs provide a total momentum resolution of $\delta p/p \approx 0.7\% \oplus 0.1\% p$. PC3 is used to confirm tracks through z- and ϕ-matching cuts, while PC2 is not often used. To reconstruct tracks in the high-multiplicity Au+Au environment, a Hough transform is employed which transforms all possible tracks into $\alpha - \phi$ space (see Fig. 2.4) and finds local maxima in the track density that pass a threshold.

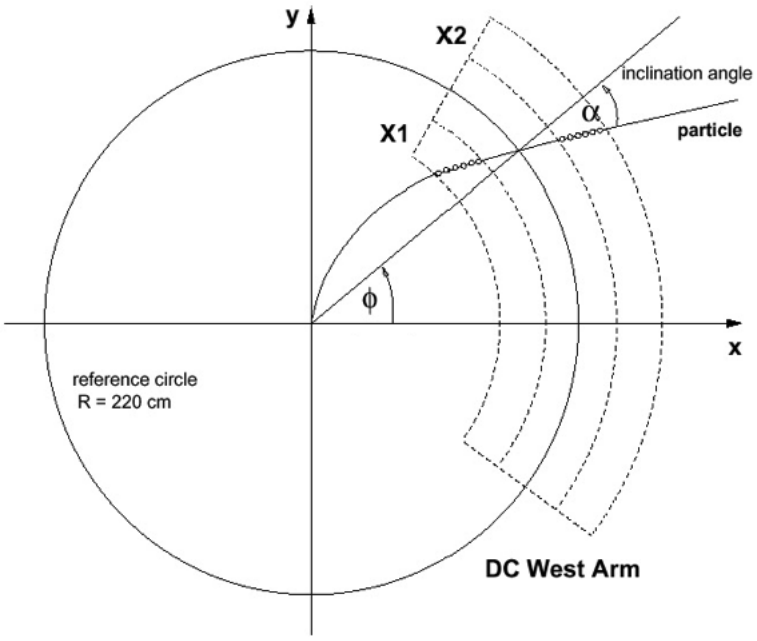

Figure 2.4: Example path of a charged particle originating from the nominal collision vertex. The track is bent by the PHENIX magnets and is detected by the Drift Chambers [94].

The last detector that we will discuss in this section is the Ring-Imaging Cherenkov detector (RICH) [94] which sits between 2.6 and 4.1 m from the center of the beam pipe. The RICH detects Cherenkov light radiated by charged particles traversing the radiator gas (CO_2 in our case) and can discriminate electrons from charged pions up to ≈ 4.7 GeV/c. For a $\beta = 1$ particle, the ring diameter is 11.8 cm and roughly 12 photons are emitted per ring through a path length of 1.2 m. The RICH is used mainly to identify electrons. Conversely, a RICH veto rejects tracks in charged-hadron identification. We expect all charged hadrons ($m > m_\pi$) to emit no Cherenkov light until they reach the pion-threshold, and hence this gives us a very pure sample of hadrons below 4.7 GeV/c [103].

2.4.2 Midrapidity Electromagnetic Calorimeter

The PHENIX EMCal [93] consists of 8 sectors (2 Pb-Glass, 6 Pb-Scintillator) and contains in total 24,768 towers. The acceptance is identical to the midrapidity tracking system wherein we have two arms that each cover $\pi/2$ radians in ϕ and $|\eta| < 0.35$. The EMCal is used to detect photons, electrons, and hadrons that decay into photons and electrons. Each PbSc (PbGl) sector consists of 72×36 (96×48) towers; the towers cover approximately 0.01×0.01 (0.008×0.008) in $\Delta\phi \times \Delta\eta$ space. The energy resolution of the PbSc (PbGl) is

$$\frac{\delta E}{E} = 8.1\%/\sqrt{E} \oplus 2.1\% \ (5.9\%/\sqrt{E} \oplus 0.8\%). \tag{2.1}$$

The PbSc (PbGl) calorimeters have sufficient granularity to completely separate two photons from the $\pi^0 \to \gamma\gamma$ decay up to $E = 12$ (17) GeV, which is well above the energy used in the analysis presented in this thesis. A photon trigger using the energy deposition into the EMCal towers is used in PHENIX to trigger on high-momentum photons ($p_T > 2$ GeV); this allows us to utilize the full luminosity of the data-taking period.

Chapter 3

Muon Piston Calorimeter

The nearly symmetrical forward- and backward-rapidity Muon Arm detectors possess large magnets shaped like pistons, as seen in Fig. 2.2. In the front of the magnets are cylindrical holes nearly 50 cm in diameter where the two Muon Piston Calorimeters (MPCs) were installed between 2006-2007 (see Fig. 2.2). A detailed introduction to the MPCs, particularly the hardware, can be found in Ref. [98]. In this chapter, we give a basic description of the MPCs and discuss the principles of calorimetry for electromagnetic showers. We then proceed to discuss the details of the clustering algorithm (used to calculate energy and position of particles) which we implemented, and next discuss how we reconstruct the invariant mass spectrum of two-photon decays. Finally, we provide details on the calibration procedure and the performance of the detector in the 2008 data-taking period.

3.1 Description

The north MPC ($3.1 < \eta < 3.9$) has 216 homogeneous $PbWO_4$ crystals while the south MPC ($-3.7 < \eta < -3.1$) has 192. Both calorimeters have a toroidal shape where the outer diameter of the frame measures ≈ 46 cm (see Fig. 3.2). The MPCs are positioned in the shadow of the BBCs (see section 2.3) at $z = \pm 220$ cm in either direction and have 2π coverage in ϕ. The tower dimensions are $2.2 \times 2.2 \times 18$ cm^3; this corresponds to a $\Delta\phi \times \Delta\theta$ acceptance of $\approx 0.01 \times 0.01$ rad^2.

$PbWO_4$ has a Moliere radius of 2.0 cm and a radiation length of ≈ 0.9 cm [104, 105], which means that the electromagnetic shower has relatively small transverse and longitudinal profiles; in fact, the Moliere radius is the world's smallest for scintillating crystals. The towers are read out by Hamamatsu avalanche photodiodes [106] (APDs) attached to the front of the crystals. Both the crystals and the APDs have temperature coefficients of $\approx -2\%/^\circ$C [106, 107], and hence the output signal is very sensitive to temperature fluctuations, as the net result is $-4\%/^\circ$C. In fact, if run at a cryogenic temperature of -25°C (as with the $PbWO_4$ PHOS calorimeter at ALICE [107, 108]), the light yield from the crystal nearly increases by a

factor of three compared with room temperature. The MPC is usually kept near room temperature, but is located near a water-cooling system for the Muon Arm magnets, and hence is subject to some fluctuations. These fluctuations are partially corrected out by the LED monitoring system [109, 110], which corrects for any changes in APD gain and crystal transparency throughout the duration of running period, but does not correct for changes in the light yield of the crystal due to temperature fluctuations. The crystals were donated by the Kurchatov Institute and were developed for the PHOS detector in ALICE [105, 107, 108]. Fig. 3.1 shows a picture of a $PbWO_4$ crystal and tower assembly, while Fig. 3.2 shows the crystals installed in the toroidal MPC frame.

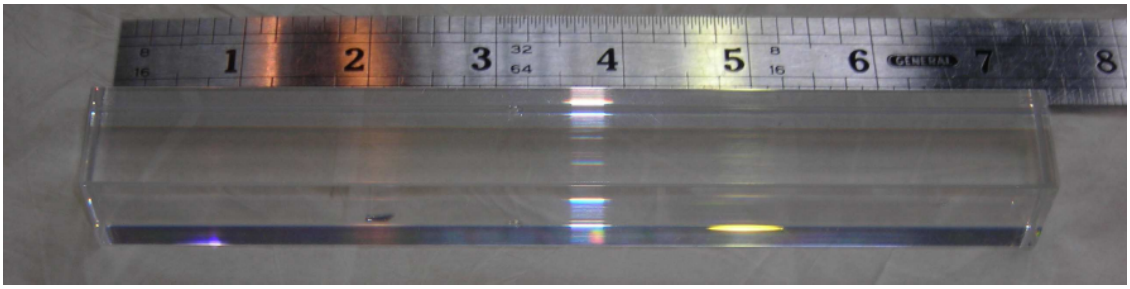

(a)

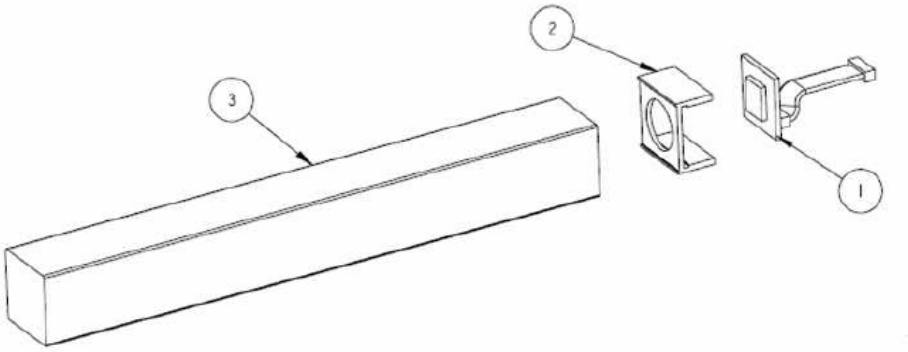

(b)

Figure 3.1: **a.)** A $PbWO_4$ crystal from the Muon Piston Calorimeter, and **b.)** MPC Tower Assembly: 1) Crystal, 2) APD Holder, 3) Avalanche Photodiode and preamp [98].

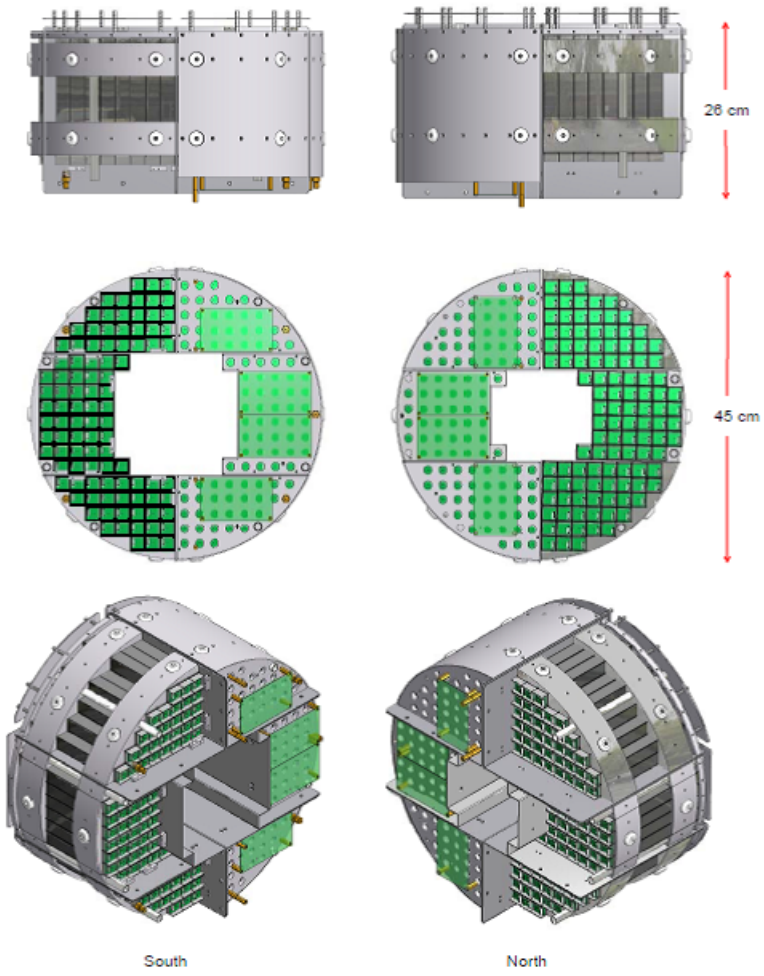

Figure 3.2: AutoCAD drawing of MPCs [98].

3.2 Readout

There are 220 towers comprising the north MPC and 196 comprising the south. The Hamamatsu avalanche photodiodes [106] (APDs) convert the scintillation light produced in $PbWO_4$ crystals into charge signals, which are amplified and sent to a driver board. The amplifiers are mounted on the backside of the small printed circuit boards that are attached to the APDs. Each driver board can supply power to the amplifiers and read back signals from up to 24 towers, and there are 10 driver boards used in each MPC for contiguous groups of towers. Because the MPC uses EMCal front end modules (FEMs), the analog charge signals are sent to a receiver board, where the signals are converted to match the input specifications of the FEMs. These signals are then sent to the FEMs (each FEM can read 144 towers, so we use 2 per MPC) where they are stored Analog Memory Units (AMUs). The FEMs have a ring buffer of 64 AMU cells for each tower, which allows us to store up to 64 events and only digitize the signals if a trigger condition is sent by the triggering system[1] [98].

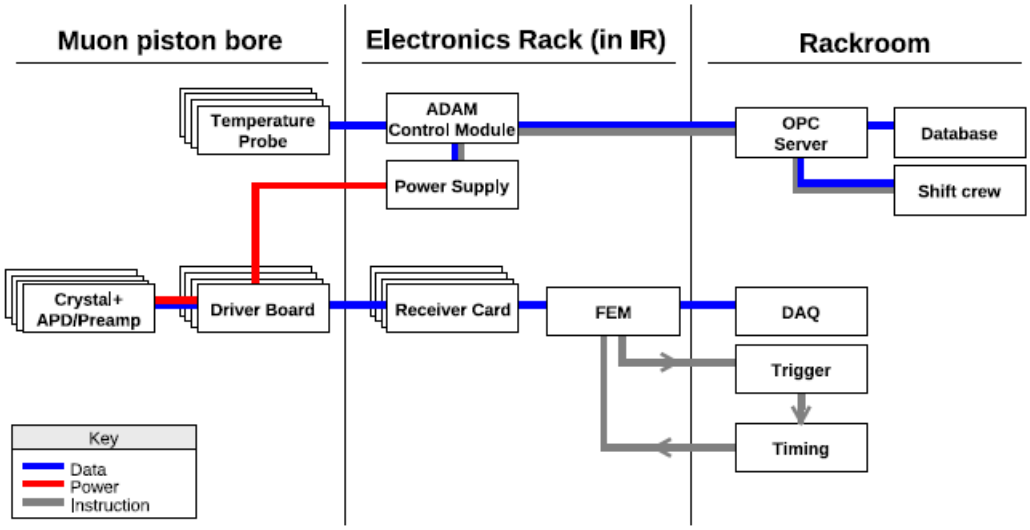

Figure 3.3: Diagram of MPC electronics from Ref. [98] showing the main components in the readout.

The data are then sent to the Data Collection Modules (data formatting and packaging), SubEvent Buffers (CPUs that hold subevents before they are assembled into full events), Assembly and Trigger Processors (CPUs that build an event by combining subevents from multiple buffers), and finally to one of six "Buffer Boxes" for temporary data storage. The final format of an event is termed PHENIX Raw Data Format

[1]The Global Level 1 trigger performs a logical OR of trigger bits for all available triggers and instructs the Master Timing Module to send signals to the Granule Timing Modules, which then send signals for all FEMs to initiate the readout.

(PRDFs); the PRDF files are the starting point for the offline reconstruction [111, 112, 113].

3.3 Offline Reconstruction

The PHENIX Raw Data Format files (PRDFs) are the lowest level file used for offline reconstruction. A data-production process is used to reconstruct hit or track information from the PRDF, and to write this information to separate files for each subsystem called nano-DSTs (Data Summary Tables). For instance, the MPC charge and timing information are written to files with the identifier DSTMPC, while the EMCal cluster data are written to files called PWGs. The data production also creates files for each trigger type (e.g. minimum-bias trigger, EMCal photon trigger, MPC Photon trigger) [114].

For the MPC, the data-production step is simple, as the charge and timing signals are transcribed from the PRDF to the nano-DST. It is only at the analysis stage that the tower charges turned into photon-candidate clusters with energy and position information. This is feasible because there are a small number of towers (416) in both MPCs. It is also beneficial because it allows the calibration process to occur on a longer timescale than allowed by data production. The final calibration procedure we established is outlined in this thesis (see section 3.10), and was only completed recently; the flexibility of the MPC reconstruction allowed us to optimize the procedure free from the deadline of the data production. For each event, the clusters are produced using the clustering algorithm (see section 3.6.2), and then are available for analysis.

3.4 Basic Principles of Calorimetry

In general, an electromagnetic calorimeter is used for detecting photons, electrons, and hadrons (mainly π^0's) with photon or electron decay modes. For the MPC, the $PbWO_4$ crystals are homogeneous, meaning that it is both an absorber and scintillator (for comparison, the midrapidity PbSc sampling calorimeter has thin alternating layers of absorber and scintillator).

When a photon (also $e^{\pm}$) is incident upon the calorimeter, its energy is spread into a shower of electromagnetic particles where the lateral size of the shower (transverse to the direction of incidence) grows as the shower particles traverse the length of the crystals. For high energy particles ($E \sim 1$ GeV), the shower proceeds through a stochastic cascade of particles created by e^+/e^- pair production (for photons) and bremsstrahlung (for $e^{\pm}$) (see Fig. 3.4 and caption for description).

Once the energy of the shower electrons and positrons decreases to the so-called critical energy (Calculation using Z=68.3 and formula from Ref. [115] yields $\epsilon \approx 9$ MeV for $PbWO_4$), or the energy at which

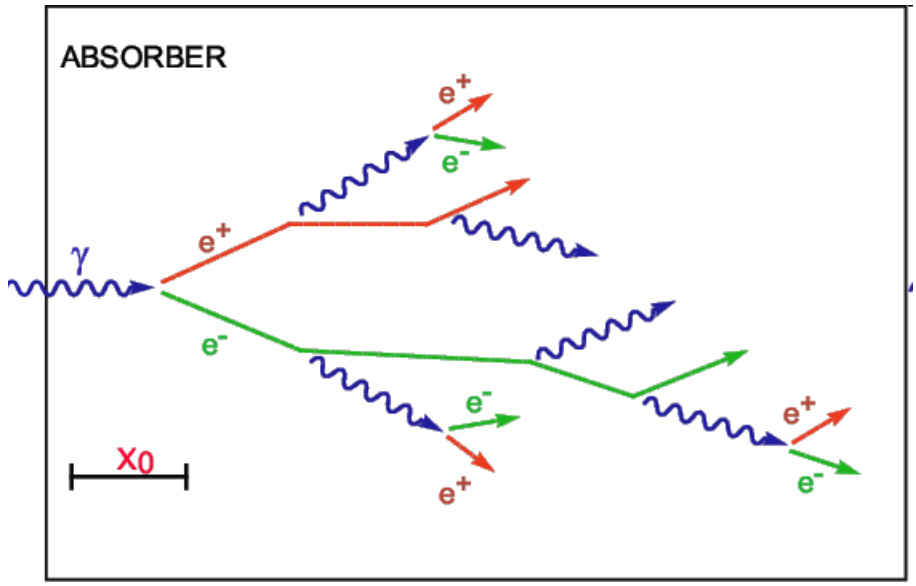

Figure 3.4: Creation of an electromagnetic shower in an absorber material for a high-energy photon incident on the absorber. The photon first interacts with the absorber and transfers its energy into an electron/positron pair. The electron and positron then interact with the absorber and radiate a photon via bremsstrahlung. This cascade continues until the electrons and positrons reach the critical energy of the material, ϵ.

ionization losses equal those from bremsstrahlung, they lose most of their energy through ionization and excitation of the crystals electrons. Many electrons are excited from the valence band into the conduction band (and holes in the opposite sense), and the subsequent relaxation process creates the scintillation light which is detected by the photosensor (in this case the APD) [115].

The electromagnetic shower can essentially be described by two parameters, the radiation length X_0 and the Moliere radius R_M. The radiation length is the distance over which an electron will lose $1/e$ of its energy due to bremsstrahlung (i.e. $E(x) = E_0 e^{-x/X_0}$). In Fig. 3.5-a, we show the longitudinal profile of an EM-shower in the $PbWO_4$ crystals [115].

One can see from the figure that most of the energy is contained within $20X_0$, the radiation length of the $PbWO_4$ crystals used in the MPC. Showers up to ≈ 100 GeV will deposit all their energy within about $25X_0$, though there is some energy dependence to the shape of the distribution; this originates from the fact that it takes more steps in a cascade for the shower particles reach the critical energy if the initial energy is higher. The energy dependence of the longitudinal profile is logarithmic; this can be understood because the process is similar to a binary tree-like branching. In a very simplistic model, at the end of the showering, all the energy E_0 is distributed equally amongst $N_{particles} = E_0/\epsilon$ with energy ϵ. If we double the energy,

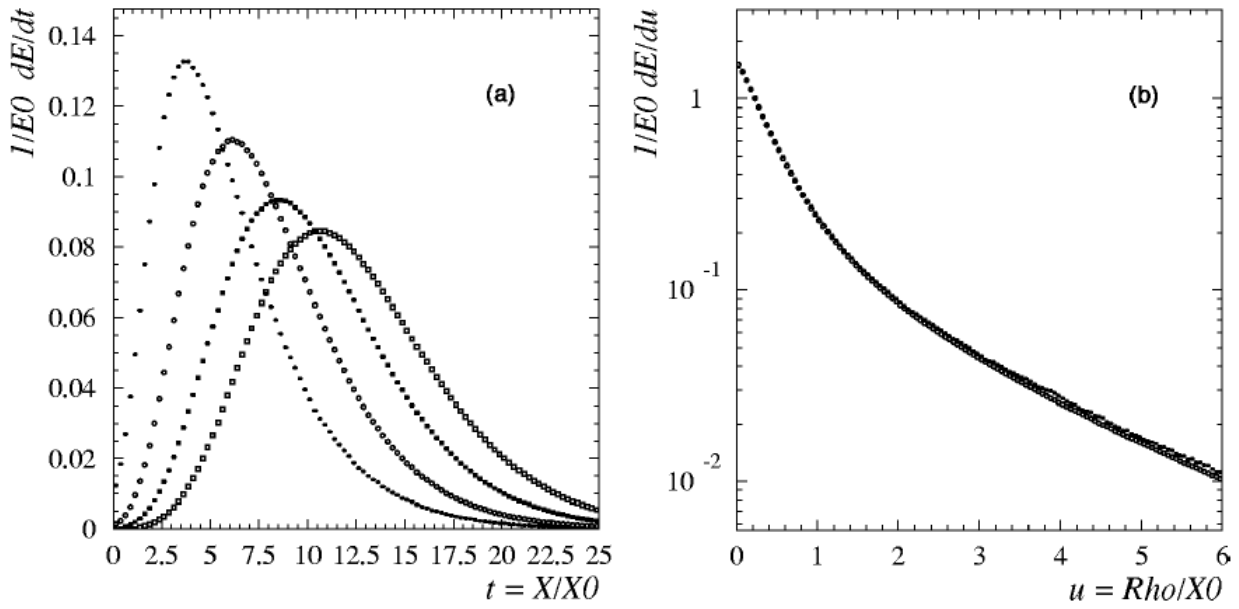

Figure 3.5: **a.)** Longitudinal shower profiles for incident electrons with E_0 of 1 GeV, 10 GeV, 100 GeV, and 1 TeV, and **b.)** Radial shower profile for an electron with E_0 of 1 GeV and 1 TeV.

we simply double the number of particles. The number of particles at the tth step is 2^t, or conversely, the number of steps is $t = \log_2 N_{particles} = \log_2(E_0/\epsilon)$ (and hence the logarithmic growth). The location where 95% of the energy is contained, $t_{95\%}$ is given in Ref. [115] as

$$t_{95\%} \simeq \ln(E_0/\epsilon) + 0.08Z + 10.1, \tag{3.1}$$

where E_0 is the initial photon-energy and Z is the atomic number of the crystal. Using this equation along with the approximations $Z \approx 68.3$ and $\epsilon \approx 9$ MeV indicates that a 1 GeV photon will deposit around 95% of its energy in the 20 radiation lengths of the MPC crystals. As the energy of the incident photon grows we expect more leakage from the back of the crystal, and thus a small energy-dependent leakage-correction is necessary (e.g. Fig. 3.10).

The lateral growth of the shower comes mainly from multiple scattering of the electrons and positions. The transverse profile the $PbWO_4$ crystals is shown in Fig. 3.5-b in units of X_0. The lateral spread is described by the Moliere radius ($R_M = 2.0$ cm for the $PbWO_4$ crystals), which is essentially the radius of an infinite cylinder that would contain 90% of the shower energy. A very simple relationship [115] exists

between the Moliere radius, radiation length, and critical energy, which is

$$R_M = 21 \text{ MeV} \times \frac{X_0}{\epsilon}. \tag{3.2}$$

The Moliere radius influences the design choices for the lateral crystal size; crystal dimensions should be such that the energy in a shower is spread over multiple crystals for good position resolution and hence the lateral dimensions should be $\lesssim R_M$.

The intrinsic uncertainty in the measured energy is based on the stochastic nature of the shower. The energy is $\propto N_{particles}$ and thus we have

$$\sigma_E \propto \sigma_{Nparticles} = \sqrt{N_{particles}} \propto \sqrt{E}. \tag{3.3}$$

Typically, one can parameterize the uncertainty of the energy in the following manner:

$$\frac{\sigma_E}{E} = \frac{a}{E} + \frac{b}{\sqrt{E}} + c. \tag{3.4}$$

Though not necessarily the standard terminology, we will use the nomenclature that follows when discussing terms in the above equation. Additionally listed are the approximate values of the terms for the 2008 MPC data.

- ***a*** The *noise term* is uncorrelated with the energy measured and is dominated by electronics noise in the MPC, $\approx 40 - 70$ MeV.
- ***b*** The *stochastic term* originates from the showering process, $\approx 2.6\%$.
- ***c*** The *calibration term* increases with the energy and is dominated by the calibration error in the MPC, $\approx 4\%$.

3.5 MPC Clustering Basics

As detailed in the previous section, when a photon or electron is incident upon a MPC crystal, the energy is converted into a shower of electrons, positrons, and photons that spreads longitudinally through the crystal's depth and laterally to the surrounding crystals. The exact distribution of energy into the different crystals is essentially determined by the radial profile (Fig. 3.5-b) and the location where the incident particle strikes the face of a calorimeter crystal.

To make our experimental measurements, we group the cluster of towers where the energy is deposited into an aptly named object called a *cluster*. It is possible to form clusters for virtually all types of particles; however, the only particles that consistently deposit the majority of their energy into the calorimeter are photons, electrons, and positrons. Hadronic interactions are suppressed by the long hadronic interaction length of the crystals, while other leptons do not experience any significant bremsstrahlung and only interact through ionization in a minimal sense (minimum ionizing particles or MIPs).

The MPC uses a similar *clustering algorithm* as the midrapidity EMCal, wherein clusters are formed by searching for those towers that have greater energy than their nearest neighbors; in other words the algorithm searches for energy local-maxima. The calorimeters have very similar calorimeter dimensions (ratio of lateral tower size to Moliere radius) as do the central PbSc EMCal towers [93], and hence the existing EMCal reconstruction code is the basis for the MPC; the algorithm implemented is somewhat based on what was done for the GAMS calorimeter by Lednev [116].

3.6 Reconstruction Algorithm

The reconstruction involves turning raw charge signals of the towers into cluster energies, positions, and parameters used for particle identification. In what follows we outline the basic scheme used for analyzing MPC data and provide an in-depth discussion of the clustering algorithm. We discuss relevant detector performance parameters and show a comparison between the data from Run8 $\sqrt{s} = 200$ GeV p+p data and simulations of $\sqrt{s} = 200$ GeV p+p events generated by PYTHIA [117] simulations that are run through the PHENIX GEANT3 [118] detector simulation package known as PISA[2] [111]. We will also discuss the parameterization of the EM-shower shape and contrast it with the EMCal algorithm.

As a reference, the main parameters created from the reconstruction algorithm are listed below.

x*, *y*, *z Log-weighted center-of-gravity lateral positions x, y and the longitudinal position z.

ecore Energy optimized for single electromagnetic clusters.

dispx*, *dispy Lateral dispersion, 2^{nd} moment of the position where the weight is the tower energy.

chi2core A χ^2/NDF variable that compares the measured shower-shape with the predicted.

[2]PHENIX Integrated Simulation Application

3.6.1 Tower Energy Calculation

A tower energy is determined by multiplying the charge signal by a gain constant, or

$$E_{tow} = g_{tow} \times Q_{tow}. \tag{3.5}$$

The charge signal is based on the output of an AMU[3]-based ADC system wherein the charge is essentially the difference between the ADC signal measured after (post) and before (pre) the event. The MPC ADCs have two dynamic ranges (hi and lo) that differ by a factor of ≈ 16, allowing one to make precise measurements for both low- and high-energy particles. The gain is determined from the calibration procedure detailed in section 3.10. The majority of gain changes are corrected by use of a LED monitoring system wherein blue (and red) light are pulsed into the crystal and the subsequent signals are measured by the APD (see section 3.10.3).

3.6.2 Clustering Algorithm

Towers that have passed the online zero-suppression cuts on the ADC values and that have an energy above the *tower-threshold* of 10 MeV are considered in the process of clustering. In the clustering algorithm, a cluster is essentially defined as a group of contiguous towers that have energy above the tower-threshold.

In each cluster there exists only one local maximum; if multiple local maxima exist within a group of contiguous towers, then one has overlapping showers, and a cluster-splitting algorithm is used in an attempt to reconstruct the original showers. In the overlap region, the splitting consists of assigning fractions of tower energies to the different clusters. We only try to distinguish shower overlaps where multiple energy maxima are visible in the towers. If two showers overlap on the same tower or neighboring towers, no attempt is made at the reconstruction stage to distinguish them.

In what follows, we outline the details used in creating clusters where we only consider towers that have energies above the tower-threshold. Please note that in this discussion we reference the usage of the radial EM shower-shapes, which are described in detail in section 3.9. The shower-shapes give the expected fraction of energy for a tower at a given radial (lateral) displacement from the cluster center.

1. "Glue" together towers and edge neighbors into a grouping that we call a "supercluster."

2. Create a cluster object for each local maximum found in the "supercluster." If only one maximum is found, then only one cluster is formed, and we skip the next step (cluster-splitting).

[3]Analog-Memory Unit

3. Given that more than one local maxima is found in the previous step, an energy-sharing procedure is used to distribute each tower's energy amongst the clusters. An initial informed guess is made for each cluster's position and energy by using the 3×3 grid of towers surrounding the cluster's local maximum. Then, for each tower in the supercluster, the lateral displacement from the different cluster centers is calculated. For a given tower, this displacement and the clusters' energies are then used to predict the fraction of the energy this tower should contribute to each cluster. The prediction assumes that the showers are electromagnetic and is calculated from the parameterized shower-shapes (section 3.9). The energy in the tower is thus shared amongst the clusters in proportion to the predicted energies for each cluster (energy is conserved in this step). The cluster energies and positions are then recalculated using the shared energies. The procedure is then repeated six times.

4. Calculations of cluster position, energy, lateral dispersion, and χ^2/NDF (measure of how electromagnetic the shower is) are performed and the variables are stored in cluster objects. These are the objects available to analyzers of the MPC data.

3.6.3 Position Calculation

The z-positions of the MPC faces are located ≈ 220 cm from the nominal z-vertex, and hence all particles incident on the MPC share the same nominal z-position. The distance from the event vertex does change on an event-by-event basis, but usually not by more than ± 40 cm.

For the MPC x- and y-measurements (normal to the incident plane), we use a relatively simple log-weighted center of gravity (CG) technique as opposed to a linear-weighted position. Both linear- and log-weighted CG positions can be written as

$$x = \frac{\sum_i x_i \times w_i}{\sum_i w_i}. \tag{3.6}$$

The difference between linear- and log-weighted positions are the weights. For the linear-weighted CG position we have

$$w_i = E_i, \tag{3.7}$$

whereas for the log-weighted CG

$$w_i = 4.0 - \ln(\frac{E_i}{\sum_i E_i}). \tag{3.8}$$

Both positions have a systematic offset from the real position by construction. However, the log-weighted position is a better measurement of the real hit position because the EM-shower's radial profile is exponential in the tails (see Fig. 3.5). Additionally, there is a correction to a particle's position based on its angle of incidence obtained from PISA simulations. Consider a track incident on the calorimeter at a non-perpendicular angle. The longitudinal direction of the ensuing shower will proceed in the direction of the incident particle. This changes the radial distribution of energy amongst the crystals, and thus changes the position calculation. In the MPC, the correction for this change is at most $\simeq 0.6$ cm. The correction we apply is

$$x = x_{cg} - x_{corr}, \tag{3.9}$$

where

$$x_{corr} = sign(x) \times 0.0326 \times (|x_{cg}| - 0.4642). \tag{3.10}$$

The position resolution of the MPC is energy and species dependent; it is approximately $2 - 5$ mm for single photons run through the PISA simulation as seen in Fig. 3.6. There is also a position dependence to the resolution, as the BBC frame and the MPC frame both create areas where the resolution is worse (see Fig. 3.7).

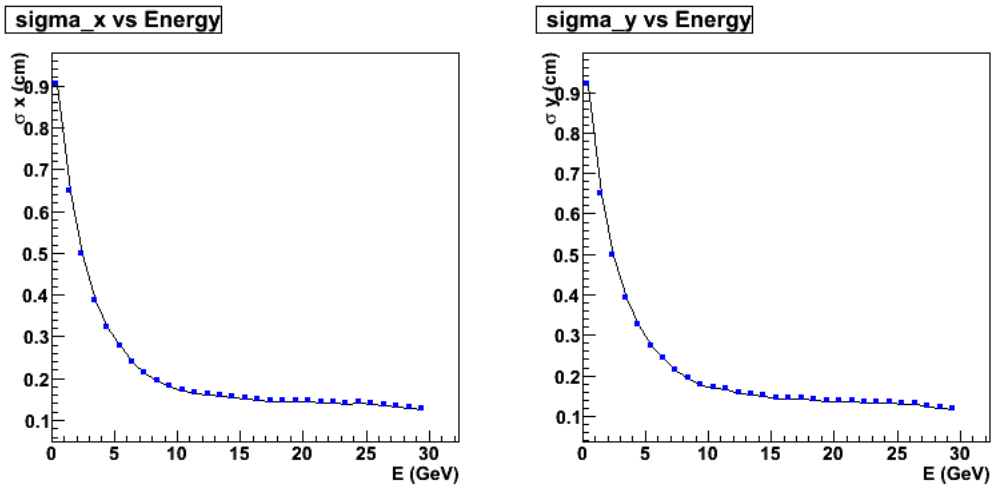

Figure 3.6: Position resolution for the north and south MPCs as a function of primary photon energy from single-photon PISA simulations.

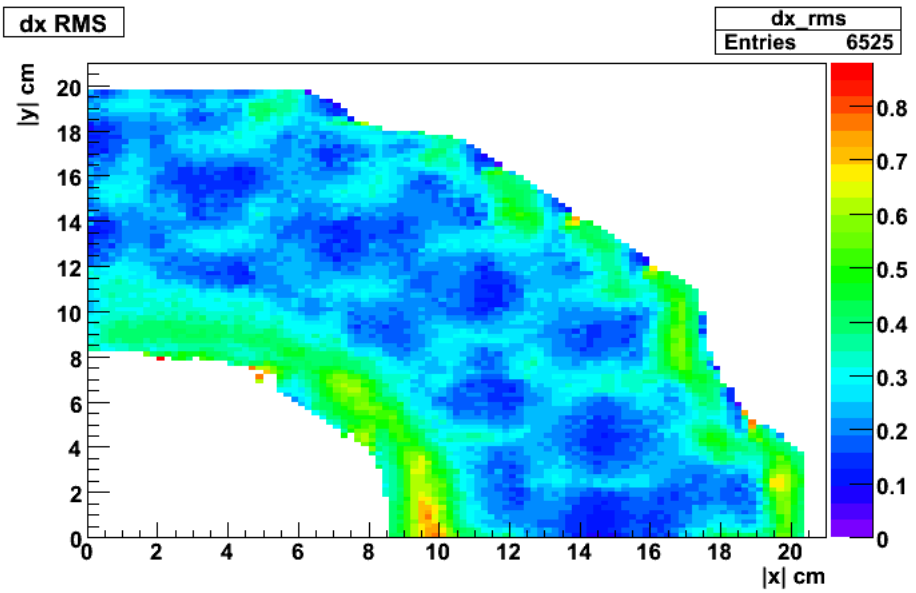

Figure 3.7: Position resolution in the north MPC as a function of reconstructed cluster position for $10 < E < 20$ GeV from single-photon PISA simulations.

3.6.4 Cluster Energy Calculation

The *ecore* variable is defined as the sum of tower energies in a subset of towers within a cluster that are predicted to have $> 2\%$ of the total energy (typically it only uses 3×3 grid of towers centered at the maximum). The prediction is based on the central position of the cluster and the radial shower-shape (see section 3.9.3) determined from simulations. This procedure is used to keep the noise at a low level in the energy calculation.

We tune *ecore* by running single-photon simulations in PISA. Photons of varying energies and hit positions are directed from the nominal collision vertex into the MPC, and the energy response is measured along with position information. The *ecore* variable is tuned such that the peak in the distribution of $E_{measured}/E_{primary}$ as seen in Fig. 3.8 is at 1 (note: $E_{primary}$ is the true energy of the photon). In this way, we correct for the $\approx 5\%$ leakage of energy out the back of the calorimeter (see eq. 3.1) as well as any deviation in *ecore* from the true energy. The low-side tails in Fig. 3.8 arise from integrating over positions where energy leakage can occur including the BBC shadow (see Fig. 3.9) and the metal frame which separates the sections of the MPCs.

The behavior of *ecore* in response to single photons run through PISA is shown in Fig. 3.10. In the simulation, a $5\% \times E$ calibration error was introduced to simulate the smearing of the gains in real data.

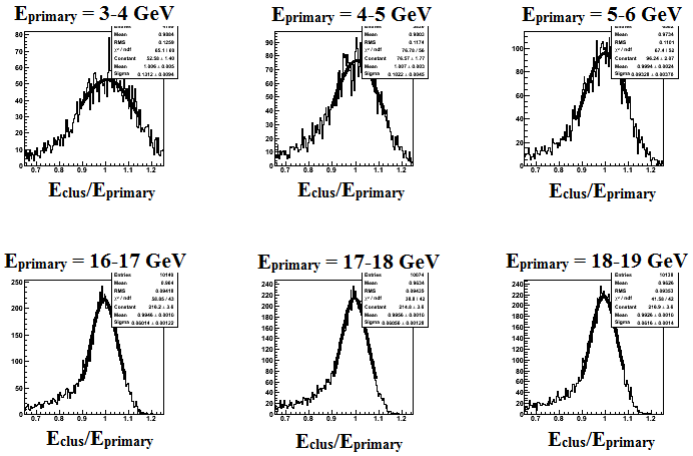

Figure 3.8: Example distributions of $E_{clus}/E_{primary}$ for different energy bins. On the top, the bins are $E_{primary} = 3-4$, $4-5$, and $5-6$ GeV, while on the bottom the bins are $E_{primary} = 16-17$, $17-18$, and $18-19$ GeV. The energy dependence of the maxima of the distributions are plotted in Fig. 3.10.

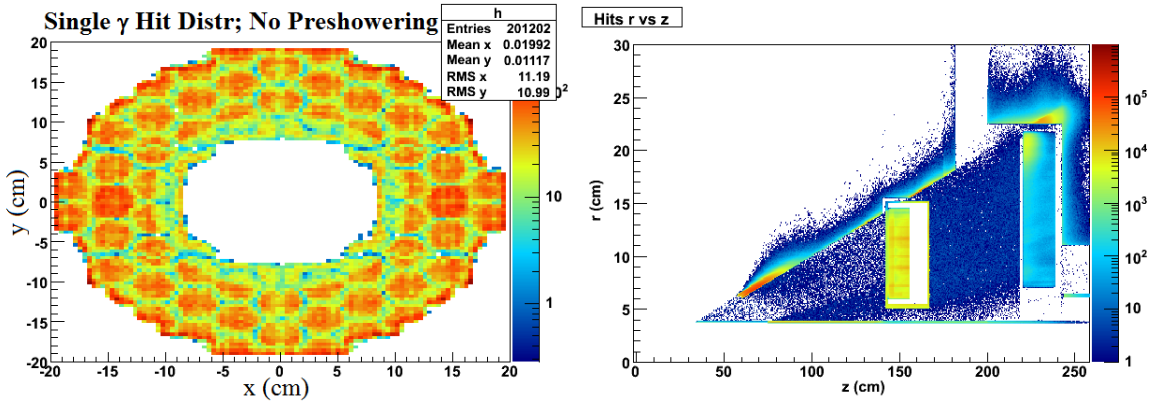

(a) (b)

Figure 3.9: **a.)** This plot illustrates the effect of the BBC frame ($z = 144$ cm) and the beam-pipe steel ($r \approx 4$ cm, $z > 75$ cm) on the cluster hit-distribution for single photons run through the MPC PISA simulation. **b.)** The PISA hit distribution of single photons directed at the MPC ($z = 220$ cm) in the $r - z$ plane, illustrating where the significant preshowering can occur.

Additionally, a 75 MeV noise contribution and a $2.62\% \times \sqrt{E}$ stochastic error were also used to smear the tower energies (see eq. 3.4). The photons were required not to preshower in any other PHENIX detectors and are distributed at least 1 cm inside of the detector edges. Additionally, we require the cluster position to be within 0.8 cm of the primary position. As seen in Fig. 3.10-a, a correction to the energy response is necessary to bring the $E_{measured}/E_{primary}$ curve to 1. The correction function used to transform Fig. 3.10-a to 3.10-b is

$$E = \frac{E_0}{0.9759 + 0.03201 \times e^{(-0.09286 E_0/0.98)}}. \tag{3.11}$$

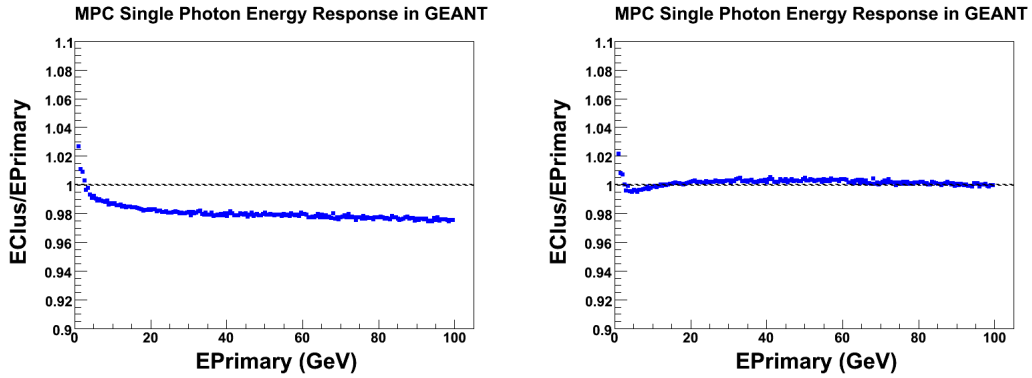

(a) (b)

Figure 3.10: Single-photon simulation behavior of *ecore* **a.)** before correction and **b.)** after correction from eq. 3.11.

One can see that there is some non-uniform behavior still remaining in the energy response that may be at most 1% above 2 GeV. This originates from a 1% difference in energy scale between the north and south calorimeters in simulation, small changes in the tower position as compared to the simulation where this function originates, and a non-optimal functional form used for the correction. However, since this 1% is not the dominant uncertainty in the energy scale (presently 2%), we accept this in our systematic error. The 2% energy-scale uncertainty encompasses number of factors including a slight difference between the eta-meson mass in data and simulation, fluctuations of the gain with time, and the factors mentioned above.

It is also interesting to observe that in Fig. 3.10-a, there is a negative slope at high energies in the energy-response curve. This is qualitatively consistent with our discussion in section 3.4. Here we discussed that the 20 radiation lengths of the MPC are only sufficient to contain about 95% of the shower energy for $E \approx 1$ GeV. As the incident particle energy increases, the shower grows longitudinally and less of it is contained within the MPC. As an exercise, we have attempted to understand this behavior with the admittedly simple

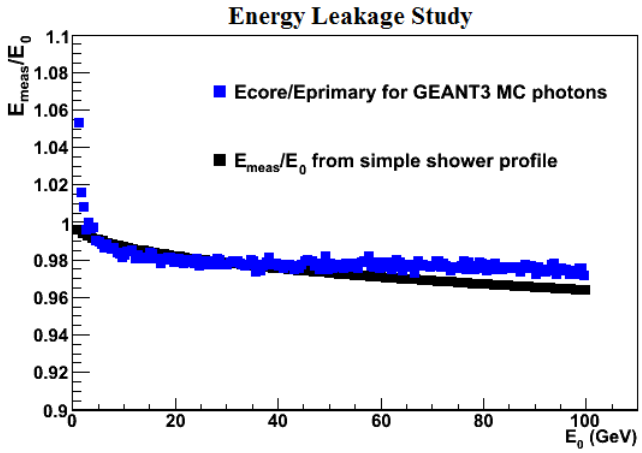

Figure 3.11: Energy-response comparison between *ecore* for single photons run through PISA (blue) and predictions using longitudinal-profile parameterizations of $PbWO_4$ crystals based on Ref. [119] (black). The reason for the negative slope at high energies is that the shower needs more length to deposit all of its energy.

parameterizations of the longitudinal profile in Ref. [119] by first calculating profiles for $PbWO_4$, and then calculating the energy deposit within $20X_0$ for different energies. The qualitative picture looks the same (see Fig. 3.11), but the negative slopes of the high-energy responses differ, as the parameterized showers seem to be slightly longer than those in the simulation. The parameterizations seem to also have the problem that they do not obey eq. 3.1, and hence perhaps they are inaccurate. The simulation studies in the figure already include a 5% leakage correction factor, and so it may be coincidental that the plots are at the same scale.

3.6.5 Lateral Dispersion and χ^2/NDF

Two important variables that can isolate electromagnetic showers from other types (e.g. hadronic showers) are the lateral dispersion and the χ^2/NDF, or chi2core. The lateral dispersion for the x-position coordinate is defined as

$$disp_x = \frac{\sum_i E_i(x_i - \bar{x})^2}{\sum_i E_i}, \tag{3.12}$$

where $\bar{x}$ is the mean value for the x-position. The dispersion can be defined with respect to the different types of positions (e.g. log- or linear-weighted CG) and there are position-dependent corrections that can be applied [120].

The radial shower-shape and fluctuations were both parameterized in simulation as described in sec-

tion 3.9. These provide the predicted energies and fluctuations in the towers of a cluster as a function or radial (or lateral) separation from the cluster center, Δr_i, and total energy in all towers of the cluster, E_{tot}. Using the shower profile and fluctuations, we construct a χ^2-like quantity as follows:

$$\chi^2 = \sum_i \frac{(E_i - E_{predicted,i})^2}{\sigma_i^2}, \tag{3.13}$$

where

$$E_{predicted,i} = f(E_{tot}, \Delta r_i),\ \sigma_i = g(E_{tot}, \Delta r_i). \tag{3.14}$$

The NDF in χ^2/NDF is simply the number of towers used in the calculations.

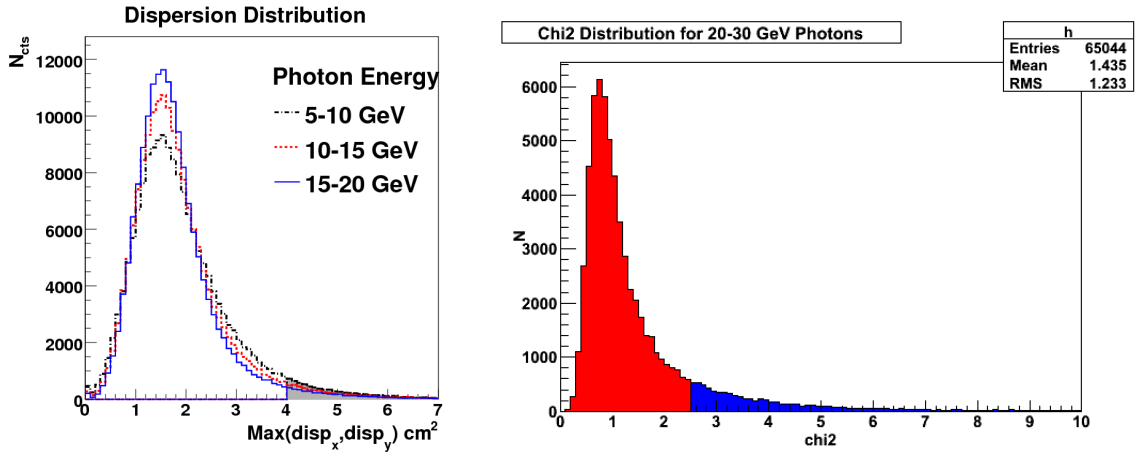

(a) (b)

Figure 3.12: Results from single-photon simulations run through PISA for **a.)**Maximum of x and y dispersions, **b.)** chi2core distributions. The counts in the shaded gray region in (a) and those shaded in blue for (b) are excluded from analysis when running over the real data so as to reject hadronic showers.

The response to single photons has been simulated using PISA; these give us a reasonable handle on what type of cuts we can make on these variables to reject non-photonic clusters. In Fig. 3.12, we show the lateral dispersion and chi2core distributions for different energy ranges of photons as indicated on the plots. The chi2core variable is the χ^2/NDF defined in eq. 3.13 and only includes contributions from towers less than 2.5 module units from the cluster center. The cuts made in analysis are chi2core < 2.5 and $Max(disp_x, disp_y) < 4.0$ module units^2; entries above these cut values are shaded gray in the dispersion histograms and in blue for the chi2core histogram.

3.7 Invariant Mass Reconstruction

In high-energy nucleus-nucleus collisions, the most abundant particles produced are the mesons with the smallest mass called pions. The charged pions ($\pi^{\pm}$) are relatively stable particles, but the neutral pions decay via the $\pi^0 \rightarrow \gamma\gamma$ decay channel 98.9% of the time. Thus, the easiest particle to detect with an EM-calorimeter is the π^0, and its invariant mass (in terms of the decay photons) can be calculated as the product of the relativistic four-vectors, or

$$m_{inv}^2 = p_\mu p^\mu = E^2 - p^2 = 2E_1E_2(1 - \cos\Delta\theta), \tag{3.15}$$

where E_1, E_2 are the photon energies and $\Delta\theta$ is the angle between the three-momentum vectors of the photons. We thus take all photon-candidate pairs (a photon candidate is a cluster that passes the cuts listed in section 4.2) and calculate their invariant mass, binning the resultant masses into a histogram. In Fig. 3.13, we show sample invariant mass plots for p+p, d+Au peripheral, and d+Au central collisions that display a pronounced π^0 peak near $m_{inv} = 0.135$ GeV/c^2. To measure the yield of π^0's, we have to subtract a combinatoric background from underneath the π^0 mass, as is shown in section 4.4.1.

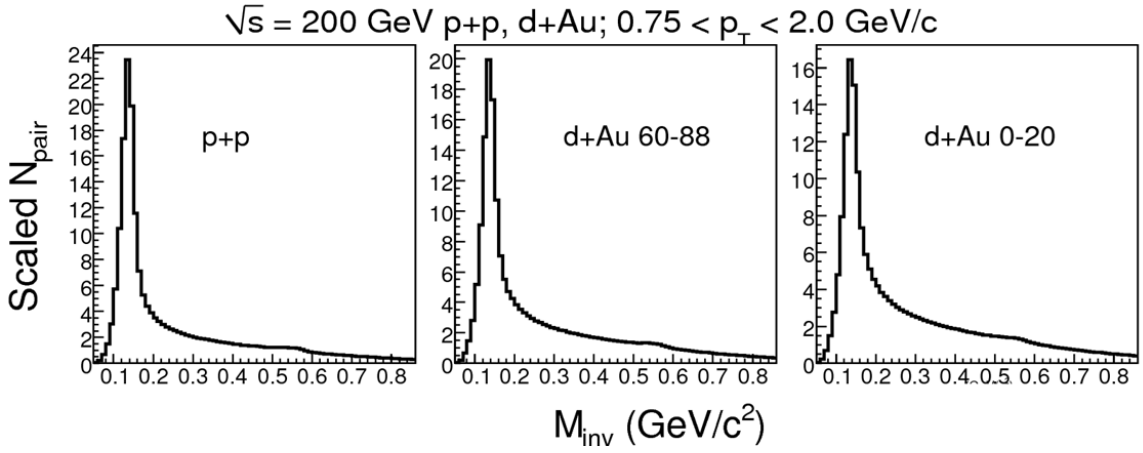

Figure 3.13: Sample invariant mass spectra for p+p, d+Au peripheral, and d+Au central collisions showing the π^0 peak around $m_{inv} = 0.135$ GeV/c^2.

The separation of the two photons decaying from a π^0 depends on the energy and the so-called energy asymmetry of the π^0. We can rewrite eq. 3.15 in terms of the total energy $E_{tot} = E_1 + E_2$ and the energy

asymmetry $\alpha = \frac{|E_1 - E_2|}{E_1 + E_2}$ and eq. 3.15 becomes

$$m_{inv}^2 = \frac{E^2}{2}(1-\alpha^2)(1-\cos\Delta\theta) \approx \frac{E^2}{2}(1-\alpha^2)(\Delta\theta^2/2). \tag{3.16}$$

The small angle approximation above ($1 - \cos\Delta\theta \approx \Delta\theta^2/2$) is valid for angles between photons detected within the MPC. Eq. 3.16 shows that for a fixed mass and energy asymmetry α, the angular separation of the photons decreases as the energy increases. Thus for sufficiently high-energy π^0's, the photons will be separated by an angle $\Delta\theta$ smaller than the granularity of the towers; subsequent clustering would then produce one cluster and the two-photon invariant mass technique becomes intractable. In the analysis presented in this thesis, a minimum separation of 2.6 cm is required for photon-candidate pairs, which with $m = 0.135$ GeV/c^2, $\alpha = 0$, gives a π^0 energy of ≈ 23 GeV. If we instead choose $\alpha = 0.6$ (which is the maximum asymmetry we have in the analysis), the energy becomes ≈ 28 GeV. Hence, the granularity of our detector imposes an upper limit on the energy of π^0's that we can detect via the two-photon decay.

One can also see from eq. 3.16 that at a fixed energy, the parameter that controls the two photons' separation angle $\Delta\theta$ is the energy asymmetry α, to which it is directly proportional. If one considers the two-photon decay in the rest frame of the π^0, one can show that the decay probability is uniform in α and that $\alpha_{max} = \beta$, the velocity of the π^0.

The minimum separation is defined by the condition $\alpha = 0$, or $E_1 = E_2$. Very large separations are possible for large values of α (e.g. > 0.9), but we use the constraint that $\alpha < 0.6$, which limits the separation to within a 20% range. The cut of $\alpha < 0.6$ ostensibly reduces our efficiency by 40%; however, many asymmetric π^0's cannot be detected with the other cuts we impose, and hence the loss is not significant.

3.8 Comparison of Data with Simulation

Detector efficiency calculations are performed using PISA [111], the GEANT3 [118] PHENIX detector simulation package. It is very important that the simulation accurately describes the detector acceptance and behavior. Detailed studies have been performed that show our detector is well described by the simulation, and in what follows we present supporting results.

In order to understand how well our simulated results match with the data, it is necessary to look at the invariant mass, χ^2/NDF, and dispersion distributions; if the distributions look significantly different, the simulations could produce significantly different efficiencies than what we should measure in the data.

Single-photon distributions in simulation are useful for understanding how to cut on the variables, but

they do not tell one how well the simulations compare to the data (unless we have a clean sample of photons). To do this, one can compare the quantities by selecting the invariant mass window of the π^0. In Figs. 3.14-3.16, we show the invariant mass distributions, dispersion distributions, and χ^2 distributions for π^0 candidates in p+p data compared to p+p PYTHIA [117] $\rightarrow$ PISA simulations in the north MPC. These distributions are shown in three energy-bins: $7-10$ GeV, $10-15$ GeV, and $15-22$ GeV. For the dispersion and χ^2 distributions, we use the π^0 mass window of 0.08 GeV/c^2 $< E <$ 0.18 GeV/c^2. The χ^2 distribution is shown for each cluster individually, while the dispersion distributions are shown as $Max(disp_1, disp_2)$, where $disp_i = Max(disp_{i,x}, disp_{i,y})$ for both clusters 1 and 2.

In the figures that follow, one can see that there is a very good match between the simulation and data, which gives us confidence that our simulation is properly describing the response of the detector for both single photons and for π^0's. This is paramount in determining acceptance and efficiency corrections.

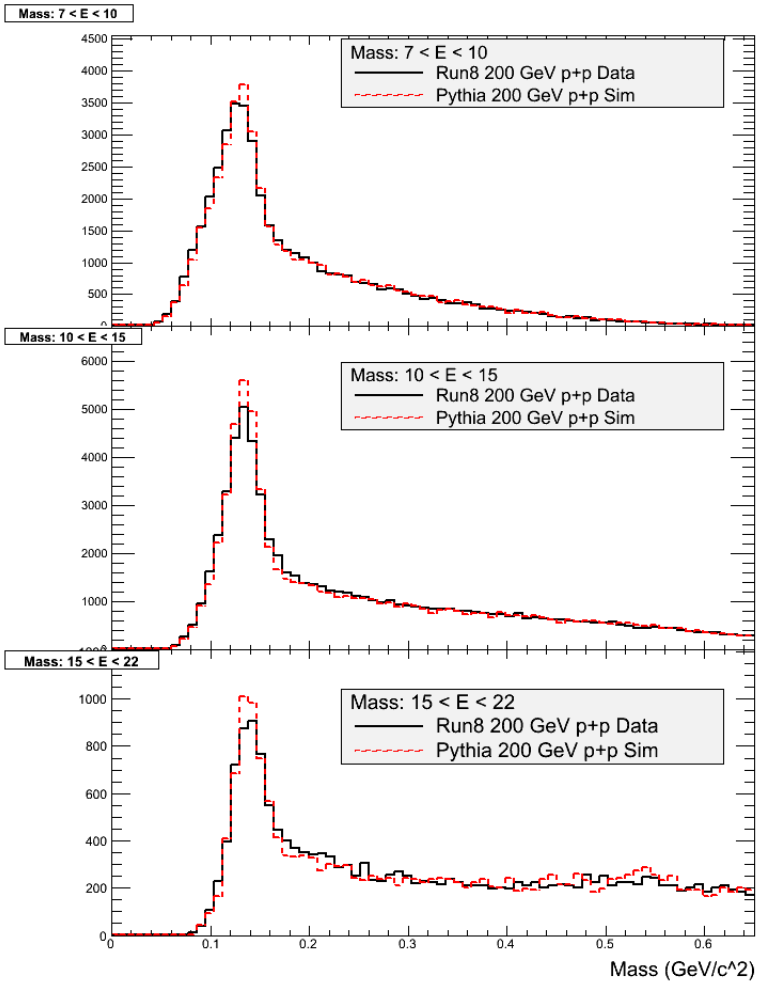

Figure 3.14: North MPC invariant mass comparison between simulation and data for three different energy bins: $7 < E < 10$ GeV, $10 < E < 15$ GeV, and $15 < E < 22$ GeV.

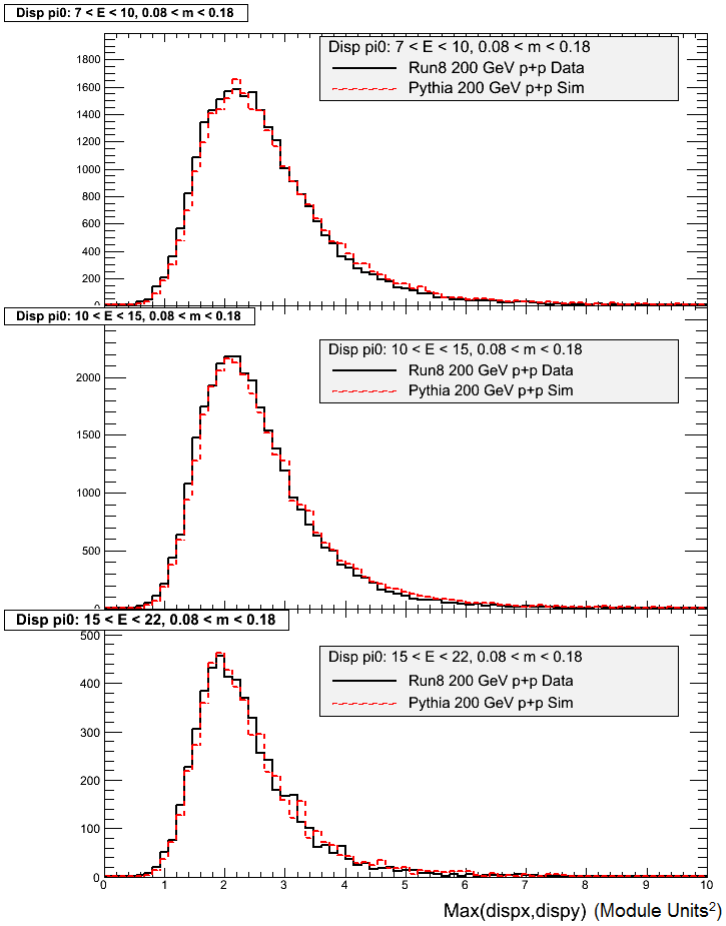

Figure 3.15: North MPC π^0 dispersion comparison between simulation and data for three different energy bins: $7 < E < 10$ GeV, $10 < E < 15$ GeV, and $15 < E < 22$ GeV.

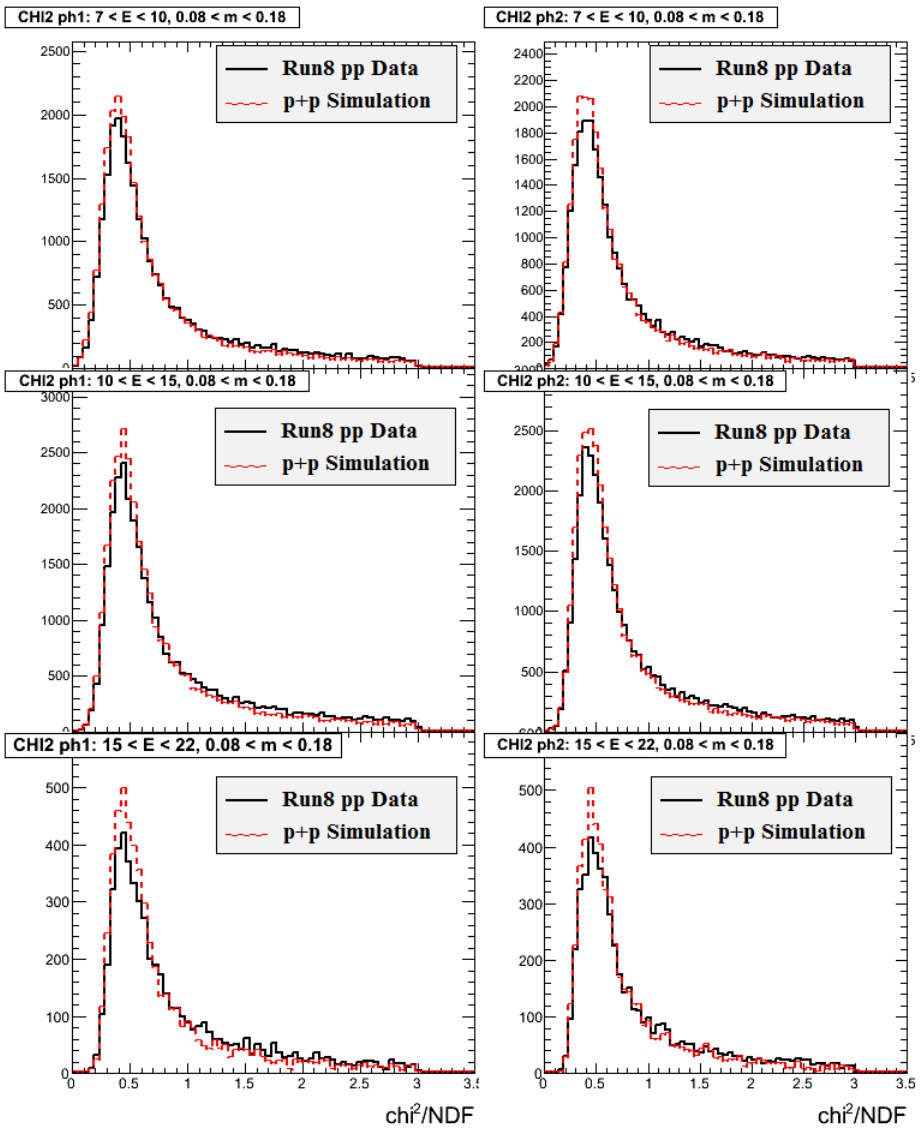

Figure 3.16: North MPC cluster χ^2/NDF comparison between simulation and data for three different energy bins: $7 < E < 10$ GeV, $10 < E < 15$ GeV, and $15 < E < 22$ GeV.

3.9 Shower Shape Parameterization and Test Beam Results

3.9.1 Introduction

Parameterization of the radial shower-shape was accomplished by simulating single photons in the MPC PISA simulations and measuring both the radial shower-shape and the associated fluctuations as a function of the primary energy. To parameterize the fluctuations, a noise term of 75 MeV was applied as well as a stochastic term of $2.62\% \times \sqrt{E}$. To produce a shower-shape at a given energy, we consider a cluster with total energy E_{tot} and tower energies $E_{tow,i}$. We form a 2-D histogram with the following axes

$$E_{frac,i} = E_{tow,i}/E_{tot}, \tag{3.17}$$

$$\Delta r_i = \sqrt{(x_i - \bar{x})^2 + (y_i - \bar{y})^2}, \tag{3.18}$$

where $\bar{x}$ and $\bar{y}$ are the log-weighted CG (eq. 3.8) cluster x- and y-positions. One then fills the histogram for each tower in the cluster. The radial shower-shape is simply a fit of E_{frac} as a function of Δr. The fluctuations are simply the spread in $E_{frac}(\Delta r)$, or the RMS (RMS $\equiv$ standard deviation in this context) of a projection in a given Δr bin. Please note that for the figures in this section, we use the notation $R \equiv \Delta r$.

3.9.2 Test Beam Data

Before discussing the parameterization of the shower-shape, let us first justify the usage of single-photon simulations for the parameterization of the shower-shape. A beam test was carried out at Fermilab with the MPC crystals, and here we present the analysis performed by A. Kazantsev [121]. Two samples of beams are used for the comparison of simulation to data: a 16 GeV electron beam, and a hadronic beam. Hadronic backgrounds in the electron beam were decreased by using a Cherenkov detector, but the exact hadronic background remaining is not known. The shower-shape for both e^- and hadrons was then created as described in the introduction above. In Fig. 3.17, one can see the side-by-side comparison of the electron sample (a) and the hadronic sample (b).

One notable observation is that in both plots there is some contamination, which in turn will slightly skew the corresponding shapes. Still, one can easily see that the energy in the electromagnetic shower is more concentrated in the center of the shower. The shower-shape parameters thus give good rejection against hadronic showers because of the distinctly different behaviors.

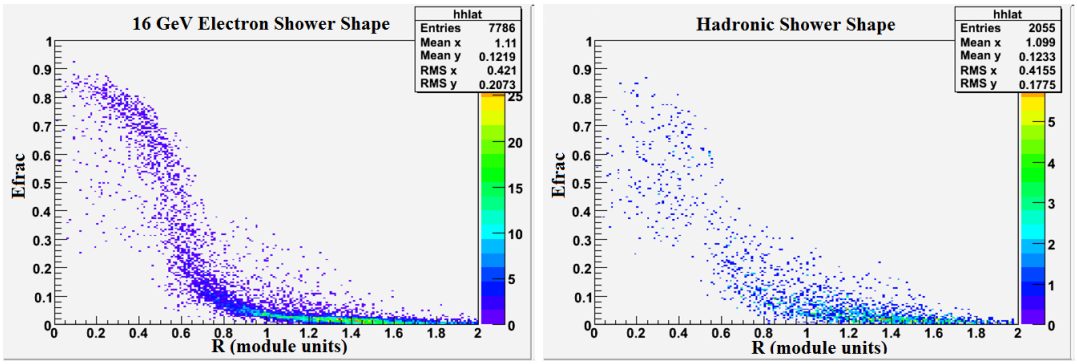

(a) (b)

Figure 3.17: Test beam shower-shapes for **a.)** 16 GeV electron sample and **b.)** the hadronic sample. The horizontal- and vertical-axis labels are Δr and E_{frac}, respectively.

In Fig. 3.18, we show the averaged electromagnetic shower-shape for both electrons (black, open circles) and hadrons (black, closed circles). The hadronic shape is distinctly different than the others; it starts at a lower value, but has less of a drop-off. Also shown are sample corrected electron shapes (colored crosses) based upon weighting the hadronic shape by different factors and subtracting this from the measured electron shape; this exercise shows how the contamination could affect the signal.

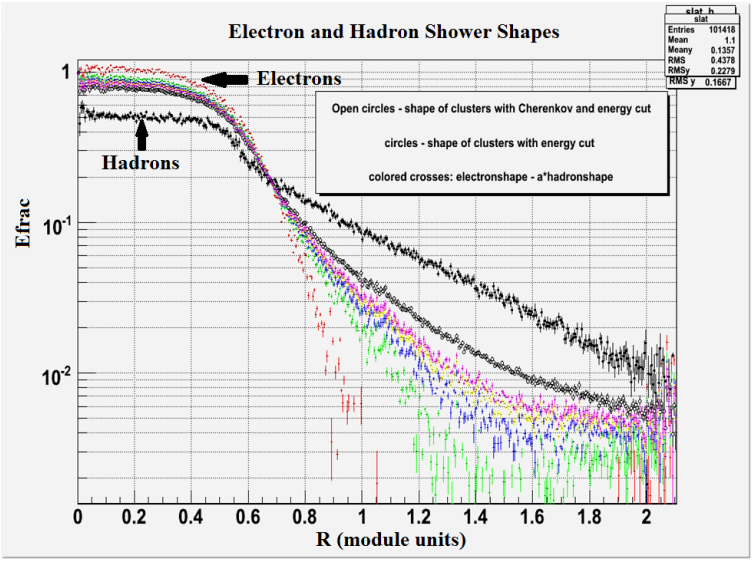

Figure 3.18: Test beam shower-shapes for electrons (black, open circles), hadrons (black, closed circles), and corrected electron shapes assuming different levels of hadronic contamination (colored crosses). The horizontal- and vertical-axis labels are Δr and E_{frac}, respectively.

Next, in Fig. 3.19, we compare a simulated shower-shape ($10 - 15$ GeV electromagnetic showers) with

the 16 GeV test beam data. Here we have the shower-shapes for the electron test beam data (open black, circles), simulation data (closed black, circles), and corrected electron test beam data (colored crosses). Please note that these corrections are not based on any measurement of the hadronic contamination, and so are admittedly not proof of an exact match between simulation and data. However, even assuming no contamination, the shapes are very similar, and hence this gives us confidence that using single-photon simulations to parameterize the shower-shape is a valid procedure.

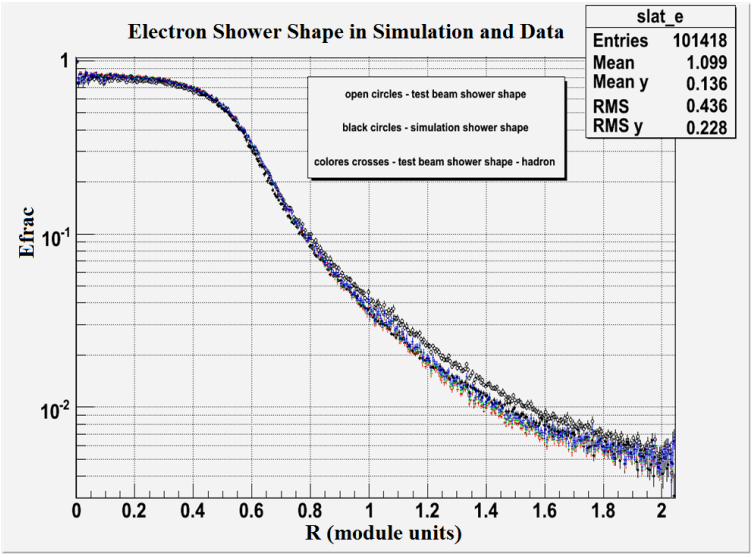

Figure 3.19: Shower-shapes for 16 GeV e^- test beam data (black, open), $10-15$ GeV simulated data (black, closed), and corrected test beam data (colored crosses). The horizontal- and vertical-axis labels are Δr and E_{frac}, respectively.

The last test-beam plot that we will discuss is shown in Fig. 3.20. Here we show that using the primary position (black) in simulation and the log-weighted position (red) in data produce similar shower-shapes. From this, one can infer that the log-weighted CG position is a very good measurement of the true position of an electromagnetic-shower producing particle.

3.9.3 Shower Shape Parameterization

The MPC analysis code is based on the pre-existing PHENIX EMCal [93] code. The EMCal shower-shape was parameterized and used in the clustering in a similar manner as in the MPC. We sought to improve the on the EMCal shower-shape parameterization, which uses a linear-weighted CG position. When the EMCal position is calculated, a minimization technique is used that has a similar position resolution as the log-weighted CG position. Thus, when the χ^2/NDF is calculated, there will always be some systematic

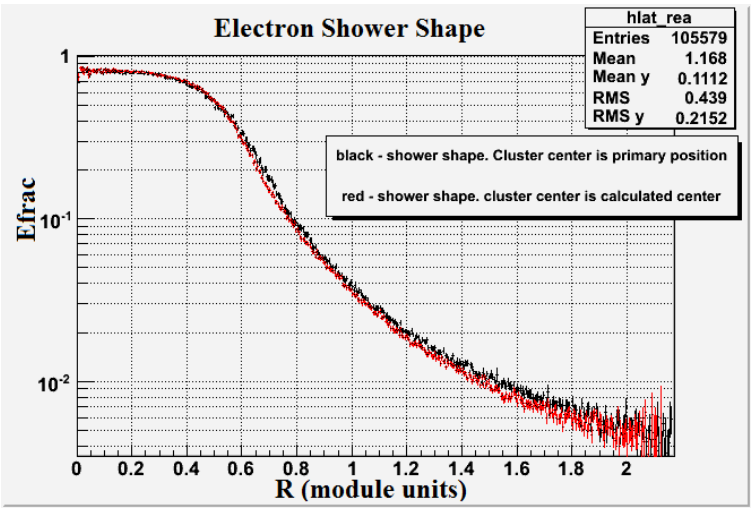

Figure 3.20: Simulated shower-shapes using primary position (black) and log-weighted CG position (red). The horizontal- and vertical-axis labels are Δr and E_{frac}, respectively.

contribution because the position used to parameterize the shape is different from the measured cluster position. However, according to the author of the analysis code [122], this difference is accounted for in the energy fluctuations of the parameterization; nevertheless, we sought to improve the parameterization and opted to use the log-weighted CG position for this. In Fig. 3.21, we show a comparison between the EMCal and MPC shower-shapes. One can see that the linear-weighted CG position does not have the plateau at small Δr as does the log-weighted CG.

In the process of parameterizing the shower-shape, it was realized that the following two distinct shower-shapes were necessary.

sharing-shape The shape that is used for the sharing of energies when clusters are merged.

χ^2-shape The shape used for the calculation of the χ^2/NDF.

The *sharing-shape* does not include fluctuations (other than stochastic) in its formulation and includes towers that have zero energy. This shape is used in the energy-sharing procedure, as this procedure tries to properly distribute the energy amongst the different towers. If the towers with zero energy were not included, the high-Δr (or R) shower-shape tails would be biased upwards. This in turn would lead to problems with the cluster-splitting procedure; towers far from the cluster position would tend to "grab" more energy than should be allocated in the sharing procedure. This shape was parameterized out to a photon energy of 60 GeV.

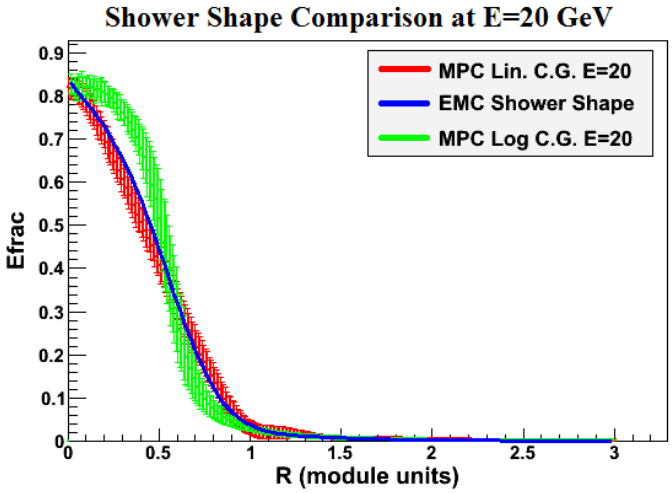

Figure 3.21: Shower-shape comparison between linear-weighted CG (red), log-weighted CG (green) in the MPC for $E = 20$ GeV single photons run through GEANT. The EMCal parameterization (blue line) is also shown for comparison and matches well with the MPC linear-weighted CG shape.

The χ^2-*shape* includes the fluctuations in its formulation and only uses towers with energies above the 10 MeV threshold, which eliminates noise. This shape is what is used for the χ^2 calculation, wherein we only consider the sample of towers that *do* have a given energy above the threshold, and is parameterized to 30 GeV. Above the range where the shapes were parameterized, 60 (30) GeV is used as the input for the sharing- (χ^2-) shape.

As it turns out, it is also useful to use the linear-weighted CG shape of the EMCal during the cluster splitting process; the reason is that the log-weighted CG shape tends to spread the energy farther away from the cluster-center, and this can have adverse effects on the sharing procedure. Hence, because the EMCal shape is in fact very similar to the MPC-shape, we use this in all but the last step of the energy-sharing procedure (see section 3.6.2), wherein we use the *sharing-shape*. Hence in our clustering we have three shapes that we use for different purposes.

The parameterization of the MPC shower-shape begins by finding suitable fit functions (see eqs. 3.21, 3.22) to fit the shower-shape and the fluctuations. We then calculate the energy dependence of the parameters in the fit functions. The EMCal fit functions (see eq. 3.19) were initially used; the shower-shape and fluctuation fit functions are

$$f_{EMC}(\Delta r) = p_0 e^{-p_1 \Delta r} + p_2 e^{-p_3 \Delta r^3}, \tag{3.19}$$

$$\sigma_{EMC}(E_{frac}) = s_0 + s_1 E_{frac} + s_2 E_{frac}^2 + s_3 E_{frac}^3. \tag{3.20}$$

Bad fits to the MPC shower-shape, however, necessitated a modification to better fit the log-weighted shape; we added an extra term of $e^{-(\Delta r)^5}$, and thus the MPC shower-shape is described by the function

$$f_{MPC}(\Delta r) = p_0 e^{-p_1 \Delta r} + p_2 e^{-p_3 \Delta r^3} + p_4 e^{-p_5 \Delta r^5}. \tag{3.21}$$

Modifications to the functional form of the fluctuations were made to optimize both the energy dependence of the fit and are shown below.

$$\sigma_{MPC}(E_{frac}) = \begin{cases} s_0 + s_1(E_{frac} - 0.4) + s_2(E_{frac} - 0.4)^2 + s_3(E_{frac} - 0.4)^3 + s_4(E_{frac} - 0.4)^4 & \Delta r < 1.2 \\ t_0 e^{-t_1 \Delta r} & \text{else} \end{cases} \tag{3.22}$$

The offset of $(E_{frac} - 0.4)$ in the polynomial equation above is significant; the terms in the polynomial get successively smaller with increasing power for $E_{frac} \in (0, 0.9)$. Without an offset, when $E_{frac} \approx 0.8 - 0.9$, the terms are of order one and the fit parameters converge to large, positive and negative values, which are not stable. This instability makes it impossible to parameterize the energy dependence of the RMS fit-parameters accurately, but is fixed by parameterizing about $E_{frac} = 0.4$.

All the parameters in eqs. 3.21-3.22 (p_i, s_i, t_i) are parameterized as functions of the cluster energy. We first show a few example fits to both the radial shower-shape and fluctuations in Figs. 3.22-3.24. We then show how well our parameterized shapes reproduce the observed shape and fluctuations in Figs. 3.25-3.27. Finally we show the fits used to extract the energy-dependent parameters in Figs. 3.28-3.29. It should be noted that these fits and parameters correspond to the χ^2-*shape*.

A few example *sharing-shapes* from our parameterization (blue) are compared to the measured shapes in Figs. 3.30-3.32; fits to the energy-dependent parameters are shown in Fig. 3.33.

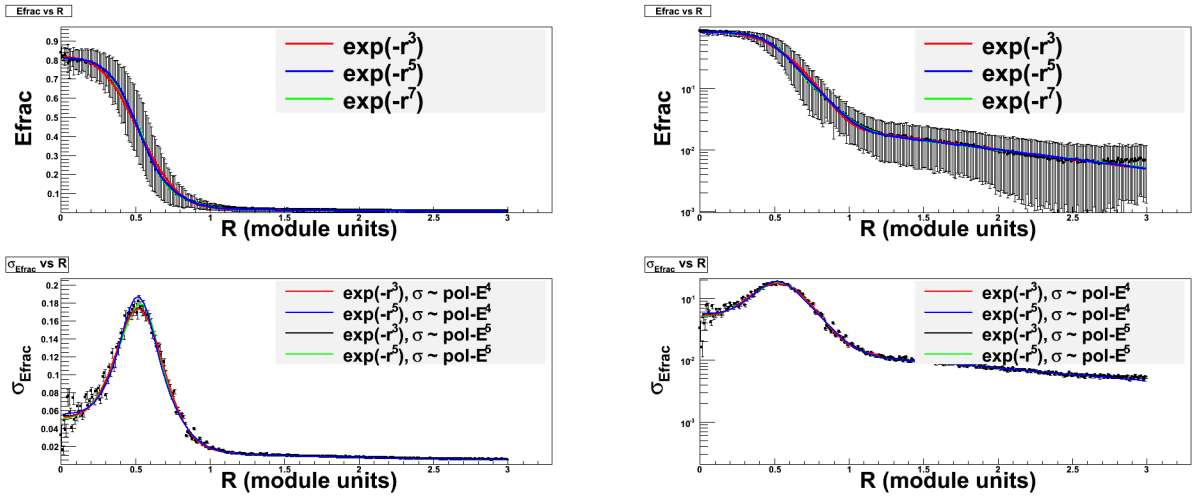

Figure 3.22: χ^2***-shape*****:** Fits to the shower-shape (top) and fluctuations (bottom) for E=5.25 GeV photons in PISA; the blue curve is functional form used for the shower-shapes. The legend refers to the leading exponential power of the functional form of the fit. The right-hand plots are the log-scale of the left.

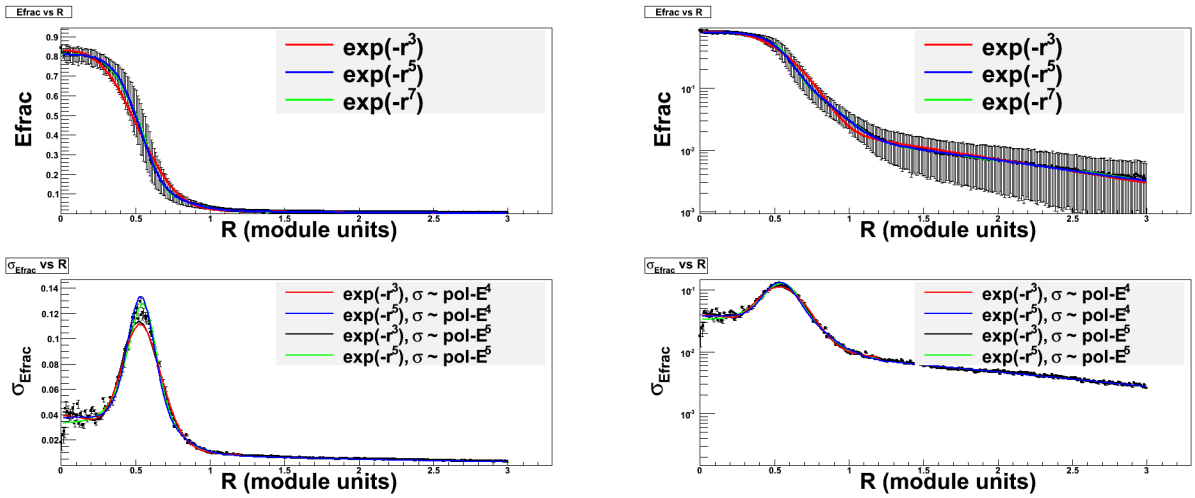

Figure 3.23: χ^2***-shape*****:** Fits to the shower-shape (top) and fluctuations (bottom) for E=10.5 GeV photons in PISA; the blue curve is functional form used for the shower-shapes. The legend refers to the leading exponential power of the functional form of the fit. The right-hand plots are the log-scale of the left.

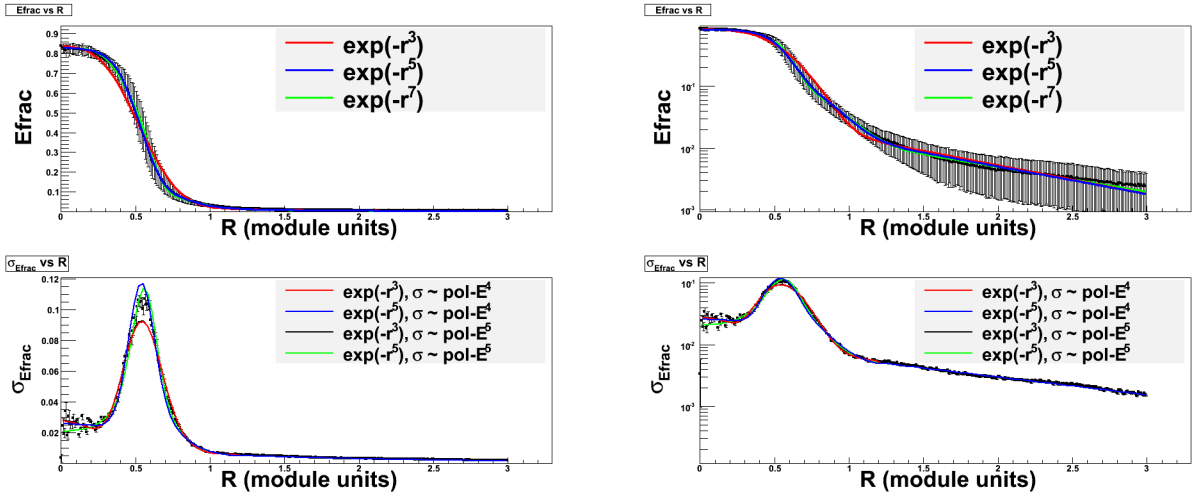

Figure 3.24: χ^2***-shape*****:** Fits to the shower-shape (top) and fluctuations (bottom) for E=20.5 GeV photons in PISA; the blue curve is functional form used for the shower-shapes. The legend refers to the leading exponential power of the functional form of the fit. The right-hand plots are the log-scale of the left.

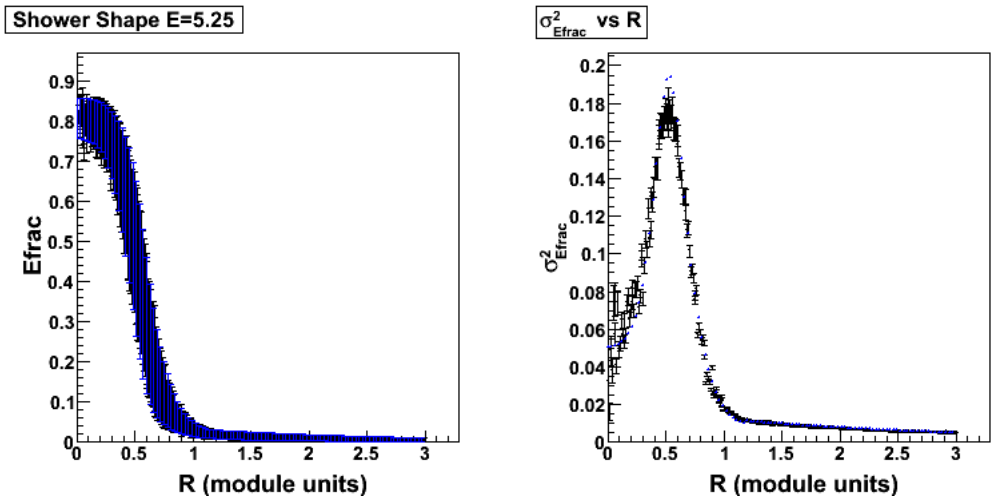

Figure 3.25: χ^2***-shape*****:** $E = 5.25$ GeV, **Left:** The parameterized shower-shape and fluctuations (blue) are plotted on top of the actual measured shape and fluctuations (black). **Right:** The parameterized (blue) and measured (black) fluctuations are plotted versus R.

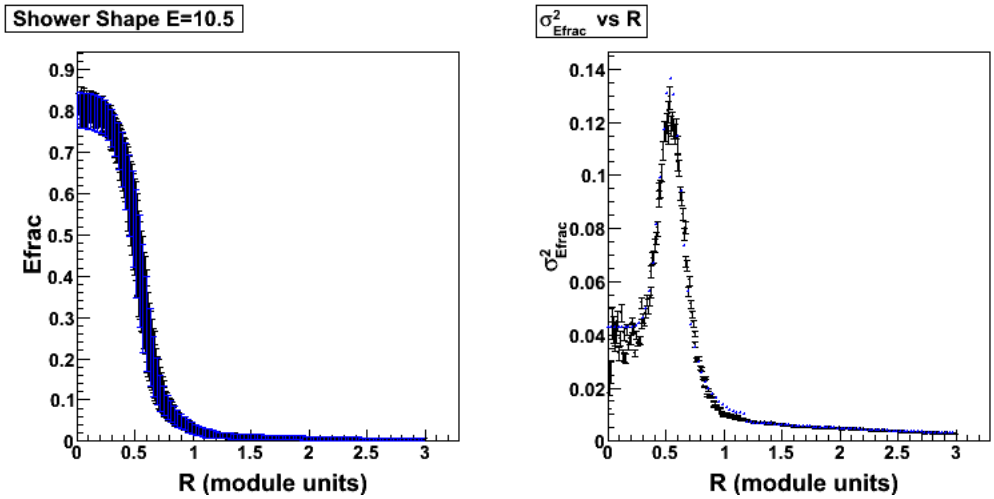

Figure 3.26: χ^2***-shape*****:** $E = 10.5$ GeV, **Left:** The parameterized shower-shape and fluctuations (blue) are plotted on top of the actual measured shape and fluctuations (black). **Right:** The parameterized (blue) and measured (black) fluctuations are plotted versus R.

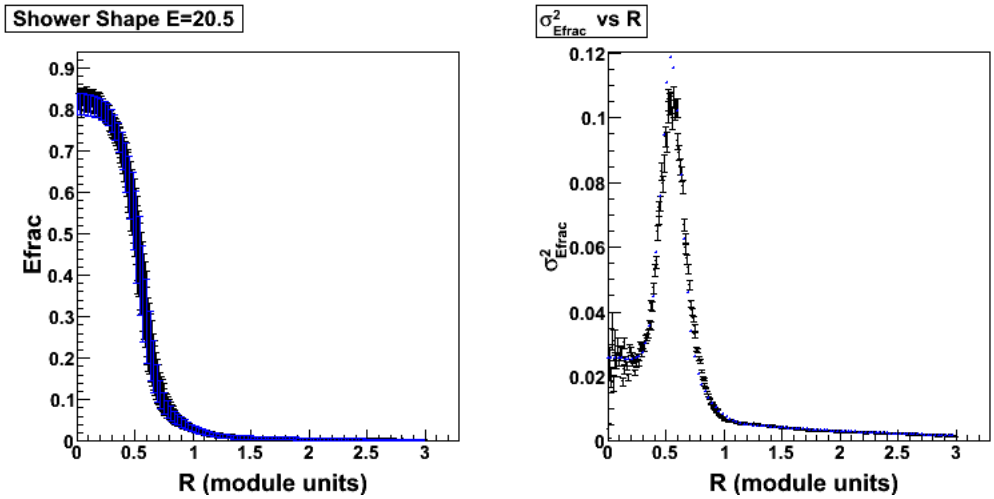

Figure 3.27: χ^2***-shape*****:** $E = 20.5$ GeV, **Left:** The parameterized shower-shape and fluctuations (blue) are plotted on top of the actual measured shape and fluctuations (black). **Right:** The parameterized (blue) and measured (black) fluctuations are plotted versus R.

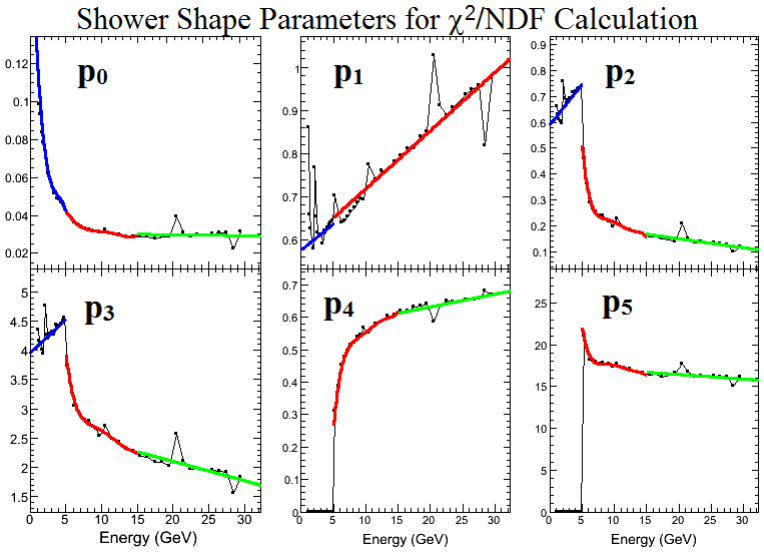

Figure 3.28: χ^2***-shape*****:** The coefficients p_i of the shower-shape in eq. 3.21 are fit as a function of energy in a piecewise fashion.

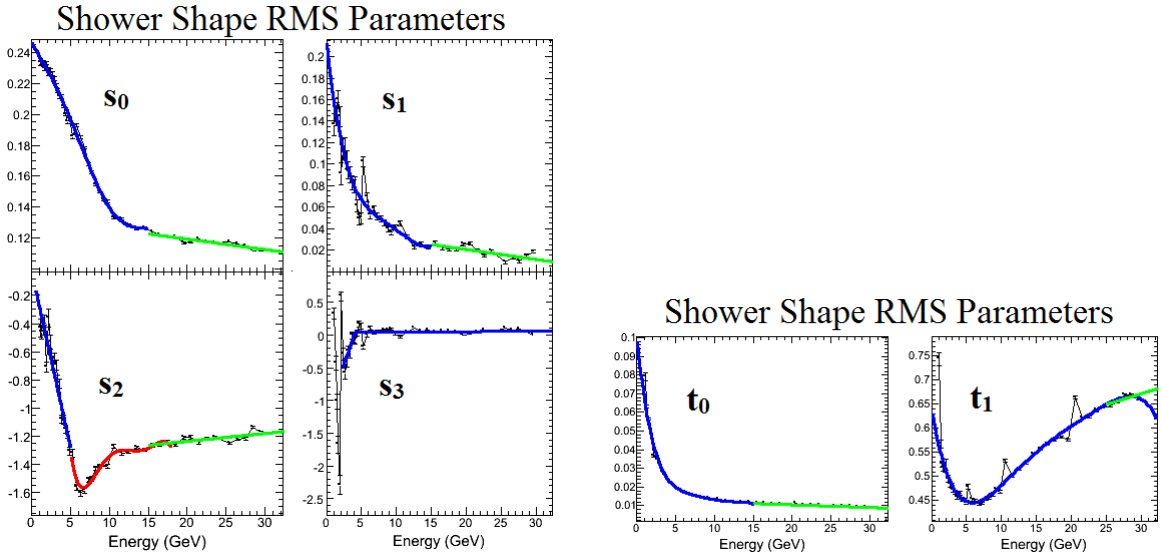

Figure 3.29: χ^2***-shape*****:** The coefficients s_i and t_i of the RMS in eq. 3.22 are fit as a function of energy in a piecewise fashion.

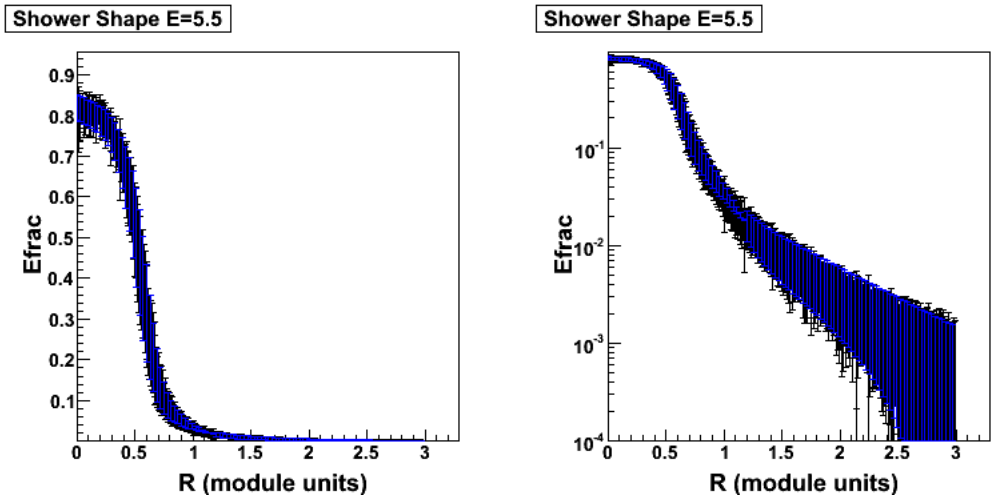

Figure 3.30: ***sharing-shape*: $E = 5.25$ GeV, Left (linear-scale), Right (log-scale):** The parameterized shower-shape and fluctuations (blue) are plotted on top of the actual measured shape and fluctuations (black).

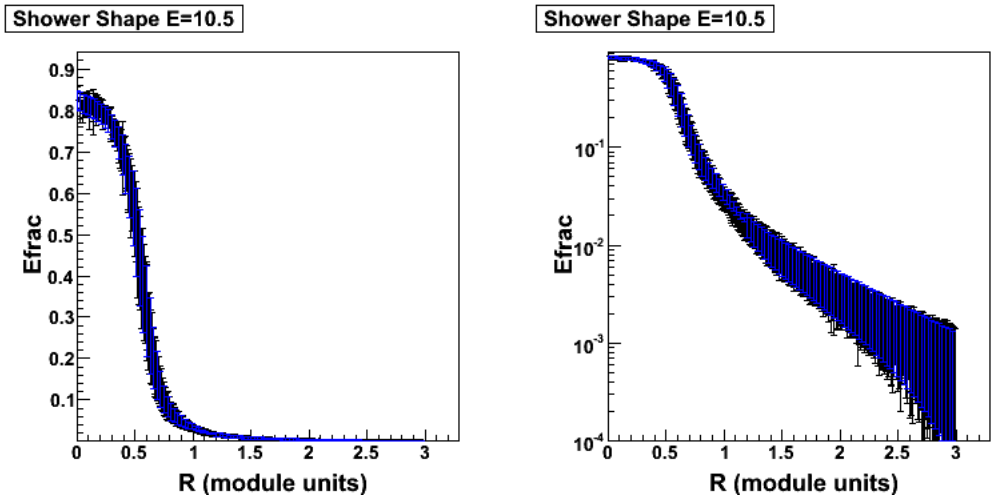

Figure 3.31: ***sharing-shape*: $E = 10.5$ GeV, Left (linear-scale), Right (log-scale):** The parameterized shower-shape and fluctuations (blue) are plotted on top of the actual measured shape and fluctuations (black).

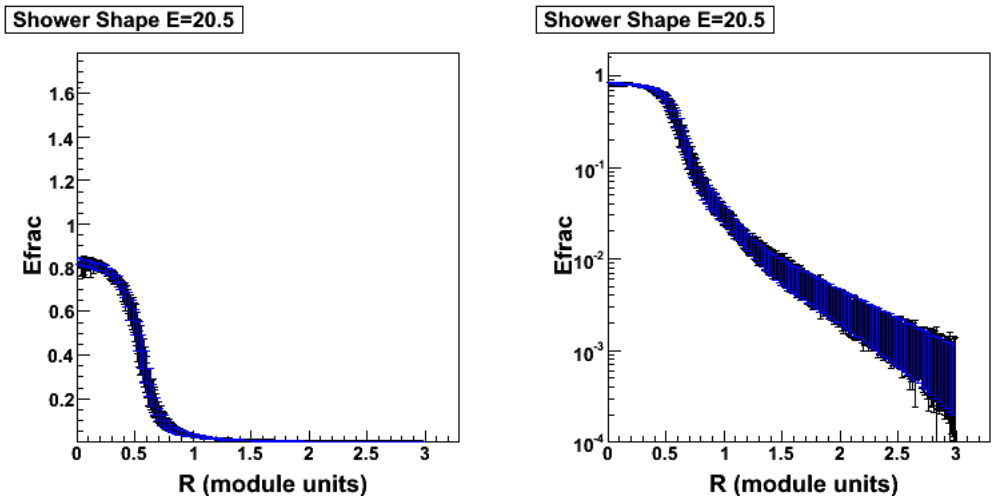

Figure 3.32: ***sharing-shape*: $E = 20.5$ GeV, Left (linear-scale), Right (log-scale):** The parameterized shower-shape and fluctuations (blue) are plotted on top of the actual measured shape and fluctuations (black).

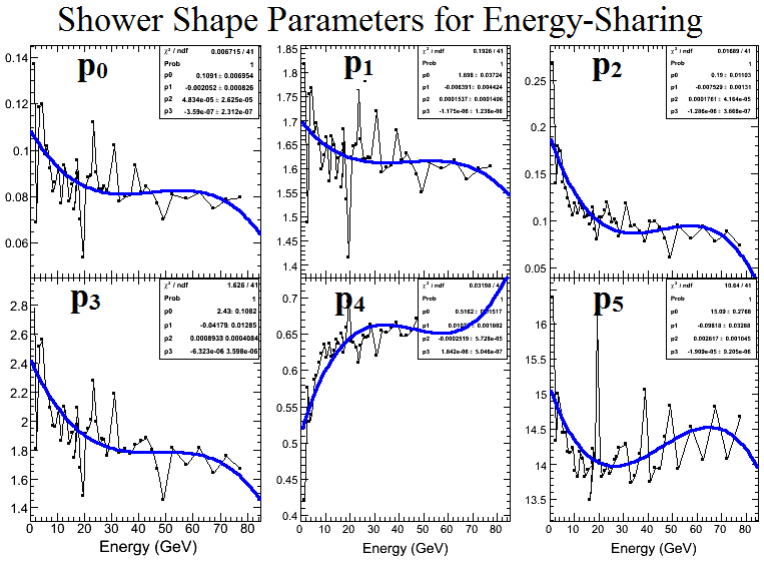

Figure 3.33: ***sharing-shape*:** The coefficients p_i of the shower-shape in eq. 3.21 are fit as a function of energy in a piecewise fashion.

3.10 MPC Calibration Procedure

Through a process of trial and error, a clear calibration procedure for the MPC has been optimized. The original Run8 calibration idea was that the Minimum Ionizing Particles (MIPs) and the so-called inverse slope technique were to give us a first order calibration and that the so-called iterative π^0 would be the final calibration.

However, it was found that the gains can shift by a significant amount on both short and long timescales. The short-term changes result mainly from temperature changes coupled with the effective 4% temperature coefficient of the towers. The long-term changes are due to a change in how the light is transmitted from the $PbWO_4$ crystal to the APD. For instance, in Run8, we see a $\approx 40 - 50\%$ gain drop from the beginning of the d+Au run to the end of the p+p run in virtually all towers (e.g. Fig. 3.35), and there are many local gain-shifts resulting from changes in temperature. The π^0 calibration is not fine enough to elucidate many of the local changes, and hence a finer gain-monitoring technique was necessary.

To improve the situation, it was decided to implement data from the LED monitoring system [98]. A blue (red) pulse of light of known intensity is sent from the back of a crystal to the APD (which sits at the front), and a charge signal is measured. The change of this signal gives us a handle on how the gain changes over time. Once the usage of the LED monitoring system was implemented to track the time-dependence of the gains, the MIP+LED calibration gave us a stable π^0 peak across all runs and was good to $\delta E/E \approx 8\%$. Additionally, by using the π^0 calibration, we were able to reduce the calibration error to $\approx 4\%$.

3.10.1 MIP Calibration

A Minimum-Ionizing Particle (MIP) is a particle that interacts with a material only through Bethe-Bloch ionization wherein a minimal amount of energy is lost through interactions with electrons. Typical MIP particles are muons and charged pions, though charged pions can also undergo hadronic interactions as well. The energy deposited depends upon a particle's path length through the material. For the 18 cm long $PbWO_4$ towers of the MPC, the average energy deposited by a MIP has been calculated to be 0.234 GeV. To observe a MIP in the MPC, one simply examines the low-energy spectra of each tower, and searches for a signal protruding from the spectral shape. This signal is enhanced by requiring that the energy deposited in the tower be correlated with a track that projects from the interaction vertex through the BBC and through the tower of interest. In Fig. 3.34, we show an example MIP peak. A tower gain value can then be determined from the correlation of the charge at which the MIP value occurs, or $g_{tow} \times Q_{tow} = 0.234$ GeV.

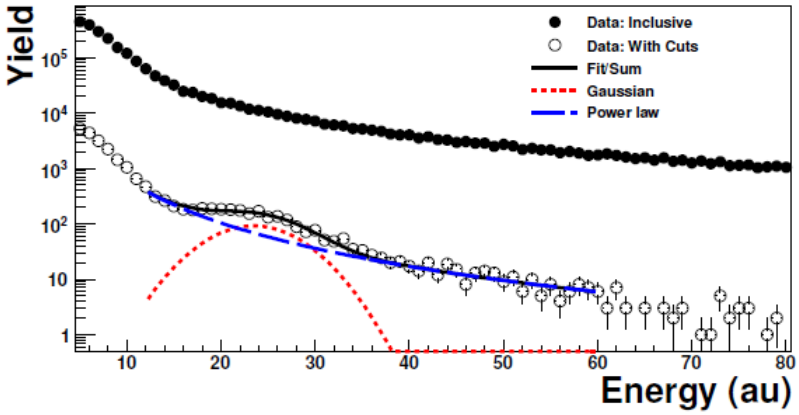

Figure 3.34: Example MIP peak and fit from Ref [98].

3.10.2 Inverse Slope or Log-Intercept

There are cases wherein towers do not have clear MIPs. When this occurs, another method can be used to determine the tower gains called the method of inverse slopes (or log-intercept depending on the fit to the charge spectrum). This calibration technique requires that some towers are well calibrated, and makes a correlation between the shape of the charge distributions and the gains of the towers. For large energies, it is expected that the behavior of the energy distribution scales as a power law in transverse momentum (at fixed rapidity) while at low energies an exponential behavior is expected. We consider these two cases and derive a correlation between the gain and the fit parameters of these two functional forms.

First, consider a power-law spectrum where $f(E) = AE^{-\alpha}$ with the gain g determined from the relation $gQ = E$. Then we have

$$f(Q) = A(gQ)^{-\alpha} = (Ag^{-\alpha})Q^{-\alpha} \tag{3.23}$$

Thus we see that by correlating the intercept in a log-log plot of $\ln(f)$ versus $\ln(Q)$ (or the prefactor in the power law) against the gain value, we obtain a correlation that can be used to calibrate towers whose gains are not fixed by the MIP. This applies to towers that are at similar pseudorapidities since the energy spectrum changes as the pseudorapidity is varied.

For an exponential function of the form $f(E) = A\exp(-\beta E)$, we have

$$f(Q) = A\exp(-\beta g Q) \tag{3.24}$$

and hence by correlating the slope in a semi-log plot of $\ln(f)$ versus Q with the gain values, we can calibrate the remaining uncalibrated towers. In practice it was found that using a power law worked better and this is what was used in the fits [123].

3.10.3 LED Calibration

The LED calibration is very straightforward. A detailed description of the system can be found in Ref. [98]. Blue and red LEDs pulse light through the crystals every 100 ns and the ADC values are measured. The light is also sent to PIN diodes which monitor the intensity; the PIN diodes correct the measured ADC values for any fluctuations in the source. The LEDs track and correct for changes in gain that occur over the running period due to changes in the amount of light a crystal transmits to the APD or due to temperature fluctuations in the APD itself. The LED system does not, however, monitor for changes in the light yield; the temperature coefficient in the $PbWO_4$ crystal is associated with the light yield and hence this is not monitored with the LED system.

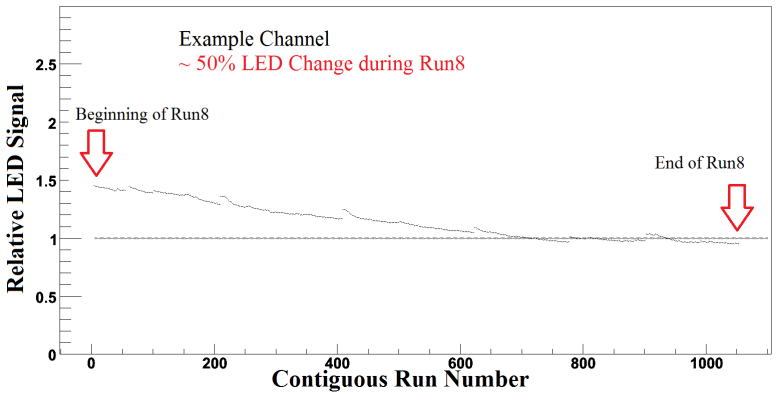

Figure 3.35: Example red LED signal throughout the 2008 run. Each data point corresponds to a data-taking period that was roughly one hour long, and the entire run lasted from November of 2007 through March of 2008. One can see a clear drop of nearly 50% over the duration of the run for this tower. The discontinuities are due to the magnets being switched off and on during shutdown periods.

The necessity of the LEDs can be seen in the $40-50\%$ gain change (as measured by the LEDs) that occurred in the 2008 running period (Fig. 3.35). Possible reasons for the gain changes include a change in the optical properties of the region between the APD and crystal or a change of the optical properties of the crystal itself. Additionally, the MPCs sit next to the water-cooling system of the muon magnets and experience relatively large variations in temperature before and after shutdown periods.

For each run, distributions of ADC values for the LEDs are measured and the mean values of the

distributions are calculated. A procedure is then carried out that eliminates outliers and the values are entered into the database. As we run over the data, we modify the gain value by $g_{tow} \rightarrow g_{tow}/LED_{tow}$. An example of the normalized LED values versus run number are shown in Fig. 3.35, and the efficacy of the LEDs can be seen by the π^0 mass remaining constant over the running period despite the 40-50% gain change (see Fig. 4.4 in section 4.3.3).

3.10.4 π^0 Calibration

The combination of MIP, inverse slope, and LED calibrations lead to an approximate 8% calibration error. By using an iterative procedure to match the π^0 mass in each tower with the expected values, we can improve this further to $\approx 4\%$.

The iterative π^0 calibration tries to match the mass of the π^0 in each tower to a mass determined by simulation. The simulations are $\sqrt{s} = 200$ GeV p+p PYTHIA events run through PISA, and we reconstruct the π^0 mass in each tower. A histogram with the two-cluster invariant mass distribution is formed for each tower. Entries into the histogram are made when a tower is the central tower of a cluster (highest energy tower). Hence, for each cluster pair, there is an entry for two different towers. The simulation has been tuned to match the electronics noise and the stochastic fluctuations with those in the data. We use a calibration error $\delta E_{calib} = 1\% \times E$ for simulation. The PYTHIA simulations (Tune A [124]) have been tuned to match the spectral shape and cross section of p+p data quite well at $\sqrt{s} \sim 1$ TeV, and this tuning seems to extrapolate down to RHIC energies and produce realistic particle rates [98]. We fit a Gaussian peak to the mass in each tower in simulation. We then try to adjust the gains in the data such that the mean value of a fit to the π^0 mass peak matches that in simulation.

Certain cuts are used on the clusters and the cluster pairs to enhance the signal-to-background ratio. A list of the cuts used in the calibration procedure are given below:

z-vertex $|z_{vtx}| < 30.0$ cm,

Minimum cluster energy $E_{clus} > 2$ GeV,

Shower-shape $\chi^2/NDF < 3$,

Lateral dispersion $Max(disp_x, disp_y) < 4.0$ module units^2,

Pair p_T $p_{T,pair} > 0.45$ GeV/c,

Pair energy 9 GeV $< E_{pair} <$ 17 GeV,

Energy asymmetry $\alpha < 0.6$.

The data are analyzed first with the gains determined from the MIPs. The gains are then adjusted by trying match the mass in data to simulation, or

$$g_{new} = g_{old} \times m_{sim}/m_{reco}. \tag{3.25}$$

Nominally speaking, $m_{sim} = 0.135$ GeV/c^2; however, we used the values determined by simulation in order to optimize the gains.

A simple Gaussian fitting procedure was used to find the value of the mass in each bin. Ideally, a subtraction of the background would be performed before fitting the peak to a Gaussian. However, it was found that a subtraction was unnecessary and that one could simply fit a small region ($\pm$25 MeV) around the maximum of the mass peak. The mean value and standard deviation are then calculated from this fit; the standard deviation is still a good measure of the width of the peak, but is not an exact measure. Seven iterations of this procedure are carried out; subsequent iterations produce changes that are $\lesssim 1\%$.

Results from a few of the iterations are shown in Figs. 3.37-3.38, and the gain changes are shown in Fig. 3.39. Additionally, the invariant mass peaks of all MPC towers are shown for the first and last iteration in Figs. 3.40-3.41.

A cursory evaluation of the efficacy of the gain-set is shown in Fig 3.36 wherein we show the invariant mass spectrum for $E_{pair} > 30$ GeV. The peak at $m_{inv} \approx 0.55$ GeV/c^2 is the eta meson; the angular separation of the photons from the $\pi^0 \rightarrow \gamma\gamma$ decay is too small to observe the decay at this energy (see section 3.7), and hence no π^0 peak is present. To evaluate the calibration error, we compare Run8 p+p data with p+p PYTHIA$\rightarrow$ PISA simulations; different calibration errors were scanned in simulation to best match the observed $\delta m/m$ of the eta-meson peak. It was necessary to use a high-energy ($E_{pair} \gtrsim 20$ GeV) peak to ensure that the peak width was not dominated by noise. It was found that the MPC has a calibration error of $\approx 4\%$, which is reasonable considering the large gain changes, temperature fluctuations, and energy leakage (along frames, out the back, and preshowering before the detector).

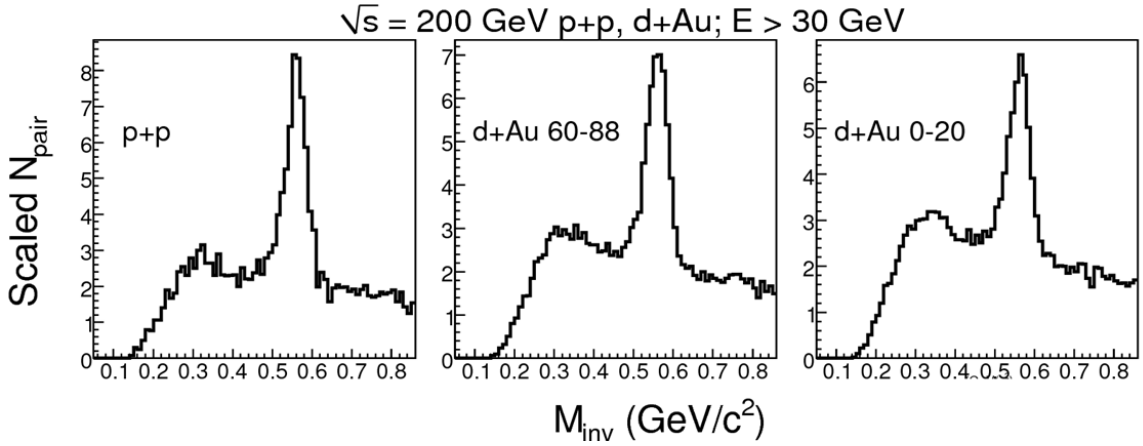

Figure 3.36: Sample invariant mass spectra for p+p, d+Au peripheral, and d+Au central collisions showing the eta-meson peak around $m_{inv} = 0.55$ GeV/c^2. The π^0 peak is not present because the energies of the cluster pairs are too high.

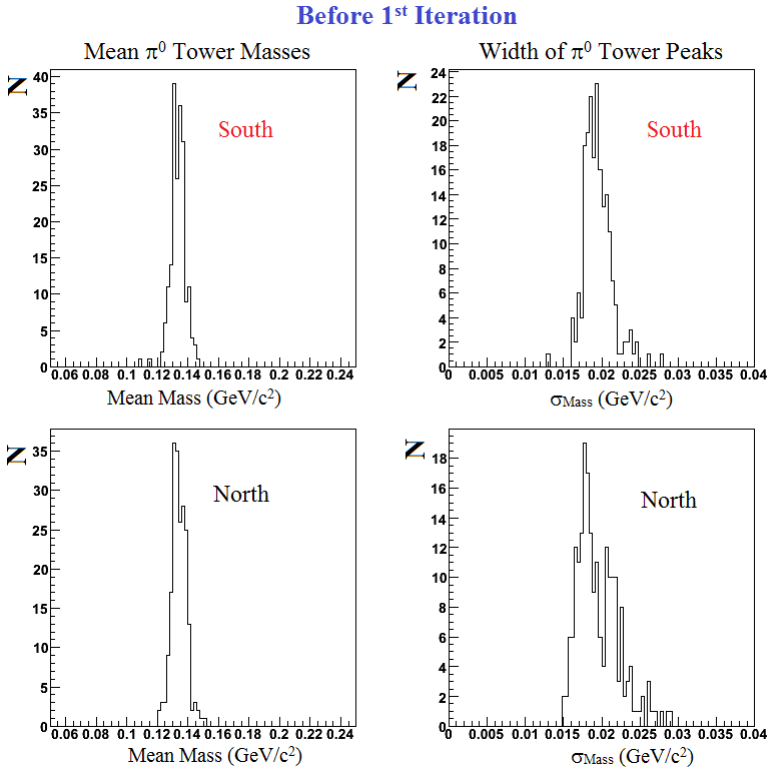

Figure 3.37: Distributions of the π^0 mean-mass values and π^0 mass-width values for towers in the south (top) and north (bottom) MPCs before the first iteration of the π^0 calibration.

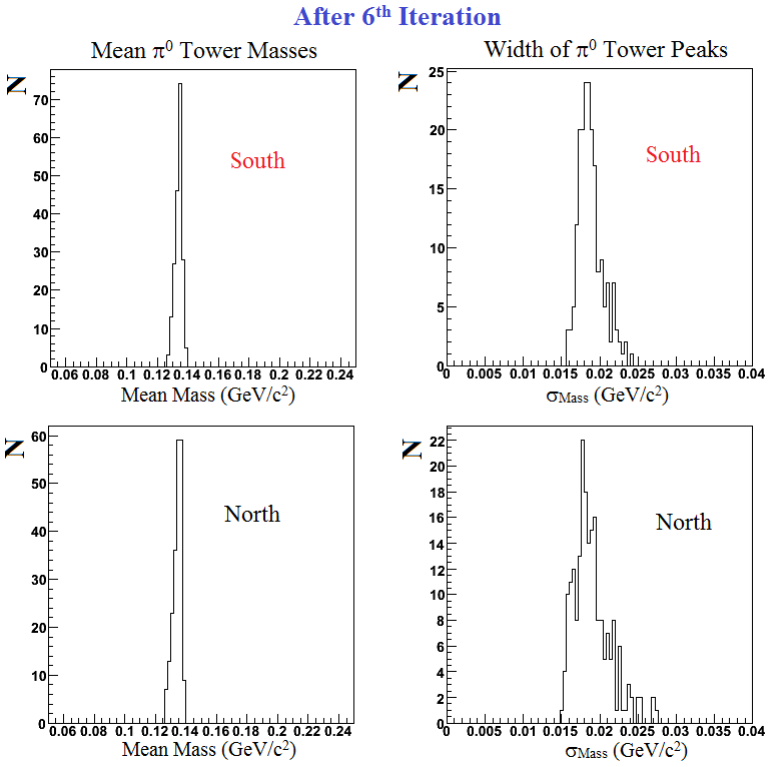

Figure 3.38: Distributions of the π^0 mean-mass values and π^0 mass-width values for towers in the south (top) and north (bottom) MPCs after the sixth iteration of the π^0 calibration.

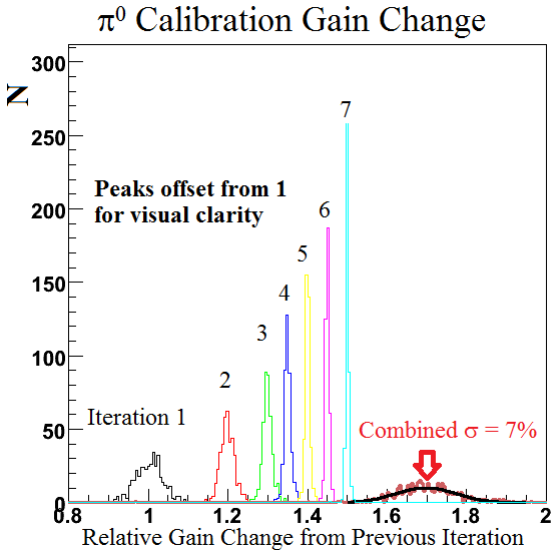

Figure 3.39: This illustrates the gain change after each iteration of the π^0 calibration. Each peak represents the gain changes relative to the previous iteration. The last peak represents the total change in the gains throughout the whole process, and has a width of $\approx 7\%$.

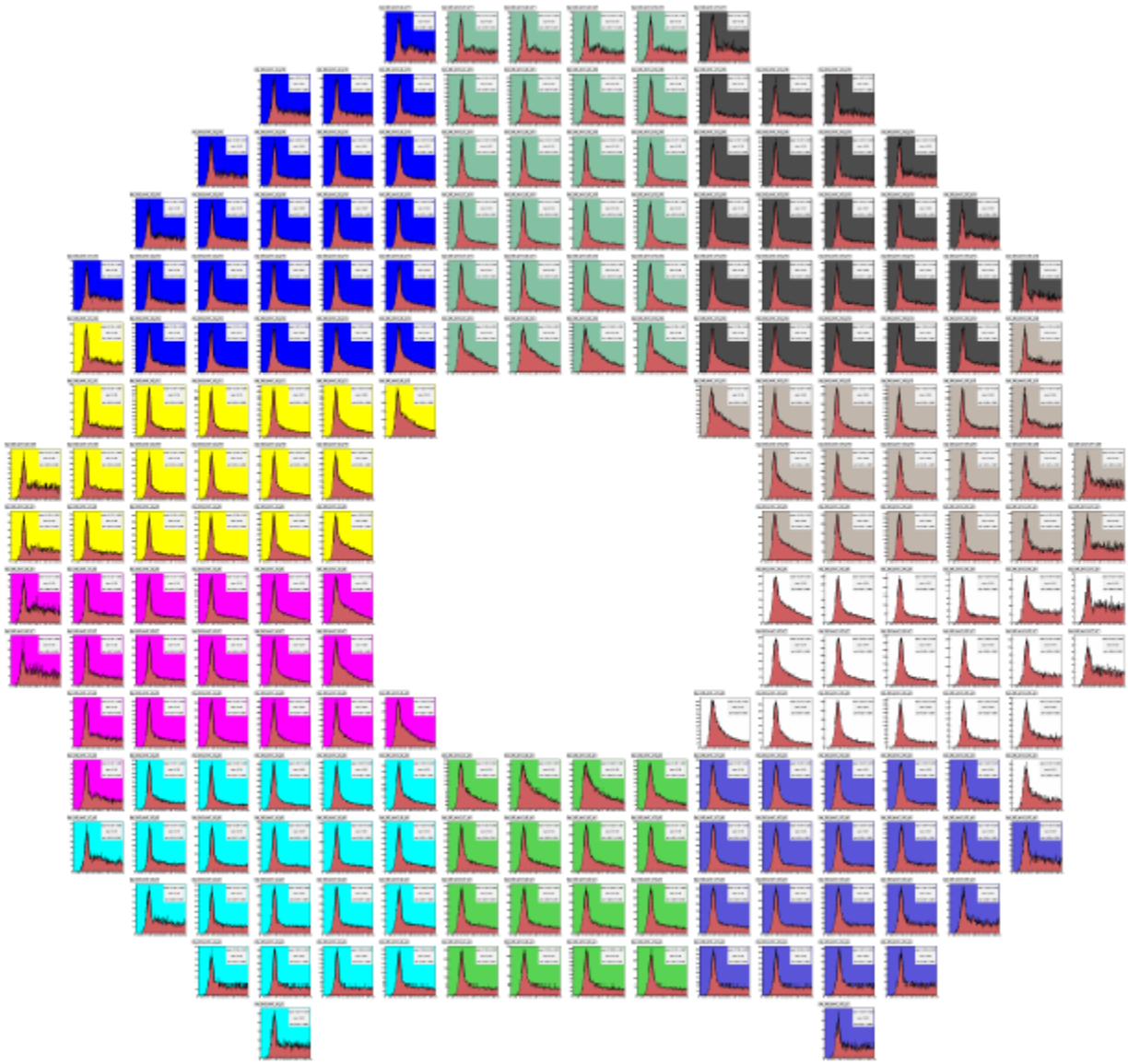

Figure 3.40: Invariant mass distributions in all north MPC towers before the iterative π^0 calibration (using only MIP and LED calibrations). The iterative procedure matches the mean value of the π^0 peak in each tower to the simulated means from simulation.

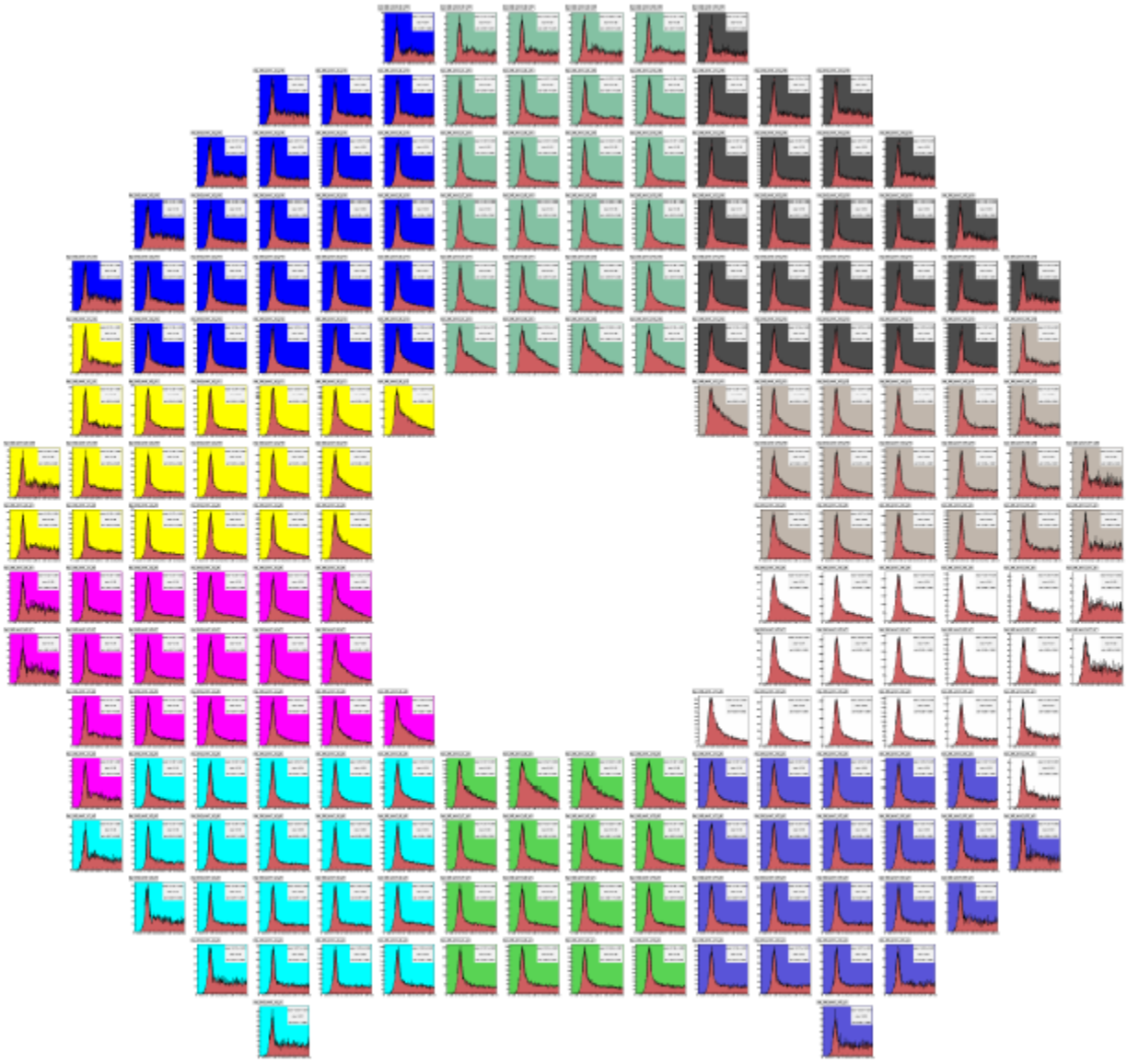

Figure 3.41: Invariant mass distributions in all north MPC towers after the iterative π^0 calibration. The iterative procedure matches the mean value of the π^0 peak in each tower to the simulated means from simulation.

Part II

Measurements

In the following chapters we present essentially four measurements that have been performed using the PHENIX MPCs; these include the inclusive p+p π^0 cross section, R_{dA}, azimuthal di-hadron correlations where one particle is detected at midrapidity and the other at forward rapidity, and finally, di-hadron correlations where both particles are detected at forward rapidities.

We first define each measurement, followed by discussing the relevant technical details. Then, we show the final results and accompany these with a discussion of the experimental impact. After all measurements have been presented, we will show a few theoretical predictions and try to discuss how these data can have an impact on our understanding of the initial state for heavy-ion collisions, the Color Glass Condensate, and cold nuclear matter effects.

Chapter 4

Forward π^0 Invariant Yields, p+p Cross Section, and $R_{\rm dA}$

4.1 Definitions

First, we define the π^0 invariant yields, which later can be simply related to the π^0 differential cross section. The invariant yield is defined as:

$$E\frac{d^3N}{d^3p} = \frac{1}{N_{inel}}\frac{1}{2\pi p_T}\frac{d^2N(p_T,\eta)}{dp_T d\eta}, \tag{4.1}$$

where N_{inel} is the total number of inelastic events. Also, it is implicit that the values of $d^2N/dp_T d\eta$ have been corrected for the bin-shift and bias-correction factors as well as for the acceptance $\times$ efficiency of the detector, or

$$\frac{1}{N_{inel}}\frac{d^2N(p_T,\eta)}{dp_T d\eta} = \frac{1}{N_{MB}}\frac{N_{\pi^0}(p_T,\eta)}{\Delta\eta\Delta p_T} \times \frac{C_{bias}\times C_{up-down}}{\epsilon}, \tag{4.2}$$

where C_{bias} is the bias-correction factor for the minimum-bias sample (see section 4.4.3), $C_{up-down}$ is the up-down correction factor (see subsection 4.4.4) that corrects for the finite bin-width and spectral shape, and ϵ is the acceptance $\times$ efficiency of the detector that includes the $\pi^0 \rightarrow \gamma\gamma$ branching ratio of 98.79% (see section 4.4.2). We also normalize the spectrum, dividing by the bin-sizes $\Delta\eta = 0.4$ or $\Delta\eta = 0.8$, and $\Delta p_T = 0.25$ GeV/c.

Next, we define the p+p differential cross section. This is simply the invariant yield multiplied by the inelastic p+p cross section at $\sqrt{s} = 200$ GeV of 42.2 mb, or

$$E\frac{d^3\sigma}{d^3p} = E\frac{d^3N}{d^3p} \times \sigma_{inel,p+p}. \tag{4.3}$$

Finally, we define the nuclear modification factor $R_{\rm dA}$ as the ratio of the invariant yields per number

binary collisions, $N_{\rm coll}$, in d+Au over p+p, or

$$R_{dA}(p_T,\eta) = \frac{1}{N_{coll}} \frac{(Ed^3N/dp^3)_{dA}}{(Ed^3N/dp^3)_{pp}}. \tag{4.4}$$

It is also useful to write $R_{\rm dA}$ in a relatively simple form in terms of the π^0 differential cross sections (written here as σ_{π^0}) and the inelastic cross sections, σ_{inel}, as shown below:

$$R_{dA}(p_T,\eta) = \frac{1}{N_{coll}} \frac{\sigma_{\pi^0,dA}/\sigma_{inel,dA}}{\sigma_{\pi^0,pp}/\sigma_{inel,pp}}. \tag{4.5}$$

$R_{\rm dA}$ written in the form of eq. 4.5 above has an analogous form in the two-particle measurements (i.e. $J_{\rm dA}$ in eq. 5.7).

4.2 MPC π^0 and High-Energy Cluster Particle Identification

In this section, we discuss the particle-identification cuts used to identify π^0's in the MPC and the quality assurance (QA) metrics used to ensure good data quality. In addition, we also discuss the cuts used to identify single high-energy clusters (e.g. π^0's with photon showers that are merged) that can be used to extend the p_T reach of the π^0 measurement. Only data taken when the detector subsystems in PHENIX were functioning properly are analyzed; otherwise, the data are excluded.

We use the 2008 RHIC Run8 p+p and d+Au datasets taken by PHENIX. The minimum-bias data is used for the invariant yield, p+p cross section and R_{dA} measurements.

4.2.1 Photon Candidate Identification

Our goal is to measure π^0's via the $\pi^0 \to \gamma\gamma$ channel, and thus we must detect the photons from the decay. Photons are identified in a calorimeter as clusters (see section 3.6), and we enhance the sample by making lateral dispersion and shower-shape cuts in order to reject hadronic contamination. Low-energy clusters are rejected because of the high level of electronics noise present (40-70 MeV/tower). Additionally, radial cuts on cluster positions are applied to ensure that it lies within the MPC acceptance; the inner radial cut also has the benefit of decreasing the combinatoric background underneath the π^0 invariant mass peak. The aforementioned cuts are summarized in the list that follows; the variables are defined in section 3.6.

Minimum cluster energy $ecore > 2$ GeV.

Radial MPC acceptance 11 cm $< r <$ 19 cm, where $r \equiv \sqrt{x^2+y^2}$.

Electromagnetic shower-shape $\chi^2/NDF < 2.5$.

Lateral dispersion $Max(dispx, dispy) < 4.0$ module units^2.

4.2.2 Neutral-Pion Identification

Neutral pions are identified by their peak in the invariant mass spectrum at $m_{inv} \approx 0.135$ GeV/c^2. The invariant mass spectrum is formed by pairing together all photon-candidate pairs and calculating their mass (see section 3.7). The following cuts are made on photon-candidate pairs to form the invariant mass spectrum:

Pair energy $7 < E_{tot} < 22$ GeV,

Cluster separation $\Delta r = \sqrt{(x_1 - x_2)^2 + (y_1 - y_2)^2} > 2.6$ cm (also, contiguous clusters must have at least one tower in between them),

Energy asymmetry $\alpha = \frac{|E_2 - E_1|}{E_2 + E_1} < 0.6$.

4.2.3 High-Energy Cluster Identification

Around $E \approx 15 - 20$ GeV, the two photon showers from a π^0 decay begin to merge into one cluster. Because π^0's are the dominant source of photons within the MPC, we can use a single cluster measurement at high energies to measure π^0's. Simulated p+p PYTHIA→PISA studies indicate that the π^0 contribution to the single-cluster spectrum for $p_T > 1$ GeV/c and $E > 15$ GeV is $\gtrsim 75\%$. Hence, single high-energy clusters are used to extend the p_T reach of π^0's beyond 2 GeV/c in the MPC.

The merging of the two photon showers from π^0's can significantly change the shower-shape, and hence no χ^2/NDF cut is applied. The lateral-dispersion distribution, on the other hand, does not change significantly, and hence the applied cut changes minimally. High-energy clusters above $E \gtrsim 30$ GeV face a problem that does not plague the low-energy ones: a fake background of high-energy clusters exists that has a comparable rate to the real clusters from a nuclear-counter effect[1]. These fake clusters usually have a single tower that contains all the energy, and it is thought that some type of particle deposits energy directly into the avalanche photo-diode, thus causing a fake signal. The fake clusters do not affect the low-energy clusters because their rate is small in comparison, and because the χ^2/NDF cut (for the photon candidates) reduces the fakes rate. To cut against these fakes, we first define E_8 to be the sum the energies of the 8 towers in the 3×3 grid surrounding the central tower. Then we take the ratio of E_8 to the central tower energy, E_{cent}, and require

[1]The source of the effect is not completely understood, but can easily be corrected for. It is thought that a large flux (e.g. spallation neutrons) of low-energy particles can actually deposit energy directly into the silicon layers of the APD and create a false signal. The rate of these fake hits is small compared to the inclusive single-cluster rate below $E \sim 20$ GeV.

that the ratio is greater than some minimum value (see below). Additionally, we require a minimum lateral dispersion to further cut against the fakes. All the cuts we make on the high-energy clusters are summarized in the list that follows.

Cluster energy $15 < E < 100$ GeV.

Minimum p_T $p_T > 1$ GeV/c.

Lateral dispersion $Max(disp_X, disp_Y) < 5.0$ module units^2.

Eliminate fakes I $E_8/E_{cent} > 0.14$.

Eliminate fakes II $\sqrt{disp_X^2 + disp_Y^2} > 0.5$ module units^2.

4.3 MPC Data Quality

4.3.1 MPC Warnmap

One of the first QA steps is to create a list of towers that are excluded from analysis known as a *warnmap* using the minimum-bias data in p+p and d+Au. To form our warnmap, we plot distribution of $\ln(N_{hits})$ versus the radial position of the tower (note: $r/z \approx 2e^{-\eta}$). The logarithm appears to vary linearly with the radius. We thus fit the correlation with a line and use least trimmed squares (LTS) regression [125] to eliminate outliers that are more than 3.5σ away from the mean value (see Fig. 4.2).

Towers in the MPC lie outside the $\pm 3.5\sigma$ band for various reasons; these include a beam-pipe support in the North MPC that blocks 14 towers and a dead tower in the South MPC, but these can be identified by other methods. One of the main reasons for this procedure is to identify poorly calibrated towers. Use of $\ln(N_{hits})$ rather than N_{hits} is thus justified because it is directly proportional to the gain error given that one has a power law or exponential spectrum, as we now justify. If we say that the energy spectrum for a given tower is $f(E) \propto E^{-a}$, then integrating over a small energy range we have $N_{hits} \propto E^{-a+1}|_i^f$. Given that the ratio of the calibration gain to the real gain is $1 + \delta g$, we have

$$N_{hits} \propto (1 + \delta g)^{-a+1} E^{-a+1}|_i^f. \tag{4.6}$$

Taking the log of both sides and assuming that δg is small, or $\ln(1 + \delta g) \approx \delta g$, we have

$$\ln(N_{hits}) \propto \ln(1 + \delta g) + C(E) \approx \delta g + C(E), \tag{4.7}$$

where $C(E)$ is a function of energy.

A similar exercise can be performed for an exponential-energy spectrum which leads to the same result above (eq. 4.7). Hence we see that for a Gaussian distribution of δg centered about 0, we would expect the distribution of $\ln(N_{hits})$ to reflect the spread in the gain; more precisely, one standard deviation of this distribution should reflect the standard deviation of the difference between the measured gains and their true values, or the calibration error. Thus, this procedure gives us a way to cut out badly calibrated towers as well as towers that do not perform properly.

Four energy-thresholds were chosen for the creation of the warnmap: 1.0, 6.0, 10.0, and 13.0 GeV. The number of counts above each threshold were put into histograms for each tower and run, and one value was established for each tower by calculating the mean across all runs. Then the linear fit with LTS regression is performed and the outliers are excluded.

There was a noisy driver board in the north MPC which caused towers to appear in the warnmap only for lower-energy thresholds ($\lesssim$ 1 GeV) due to the fact that one begins to sample the pedestal of the ADC distribution. To ensure data quality, this entire region was removed from the analysis (20 towers). Additionally, there are 14 towers in the north MPC that are blocked by a thick beam-pipe support which are also masked out (see Fig. 4.1-a). The north essentially has no other bad towers, thus indicating a good calibration. The south MPC was also calibrated well, as only four towers in total were rejected. One can see how some of the towers were rejected in Fig. 4.2. The final warnmaps for the north and south MPCs are shown in Fig. 4.1.

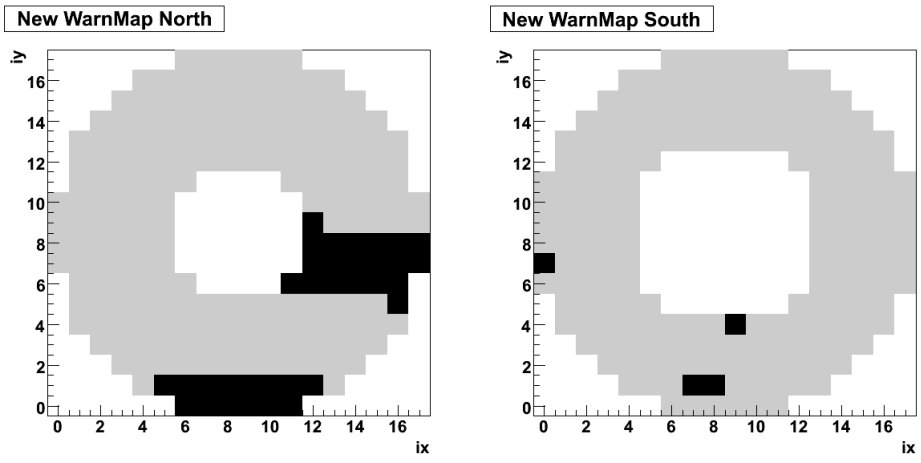

(a) (b)

Figure 4.1: Final warnmaps in both p+p and d+Au for **a.)** north MPC and **b.)** south MPC. The black towers are excluded from analysis.

4.3.2 Neutral-Pion Yield

The next QA metric is to plot the π^0-yield per minimum-bias event. We fit the *background* of the invariant mass distribution as described later in section 4.4.1 and subtract it from the *foreground*[2] distribution, leaving a Gaussian peak. We fit this distribution and integrate the yield as a function of run number (Fig. 4.3). We exclude runs that have a yield outside the red bands shown in the figure.

4.3.3 Neutral-Pion Mean

Another QA metric is the mean value of the π^0 invariant mass peak across the run (see Fig. 4.4). We accept all points which are within 1.5% of the mean value of the fit, as we claim a 2% uncertainty on our energy scale. The cuts used for this peak are the basic cuts described in section 4.2 with the requirement that $p_T > 0.75$ GeV/c. We plot the 1σ lower band to show the width of the Gaussian distribution for the π^0 peak.

4.3.4 Two-Particle $\Delta\phi$ Acceptance Functions

The last QA metric is the two-particle $\Delta\phi$ event-mixed acceptance function calculated across Run8 for two forward particles. The stability of the acceptances for p+p and d+Au are shown in Fig. 4.5; we quantify the change in acceptance by a χ^2-value which is defined as follows (See Fig. 4.6):

$$\chi^2_j/NDF = \sum_{i=1,i\neq n}^{N_{bins}} \frac{(y_{ij} - y_{in})^2}{\sigma^2_{ij}} \times 1/N_{bins}, \tag{4.8}$$

where y_{ij} is the value of the acceptance in the i^{th} $\Delta\phi$ bin for the j^{th} run, and n is a fixed run (actually set of five runs) that all χ^2-values are compared to. Stringent cuts of $\chi^2/NDF < 2$, (1.5) are used as a QA metrics for p+p (d+Au).

[2]The foreground distribution is simply the di-cluster invariant mass distribution where clusters are paired from the same event.

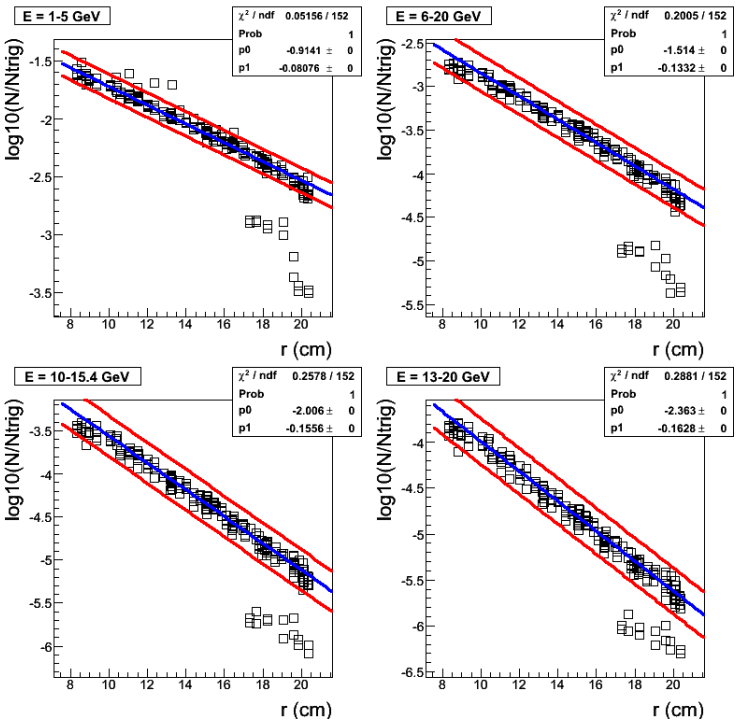

(a)

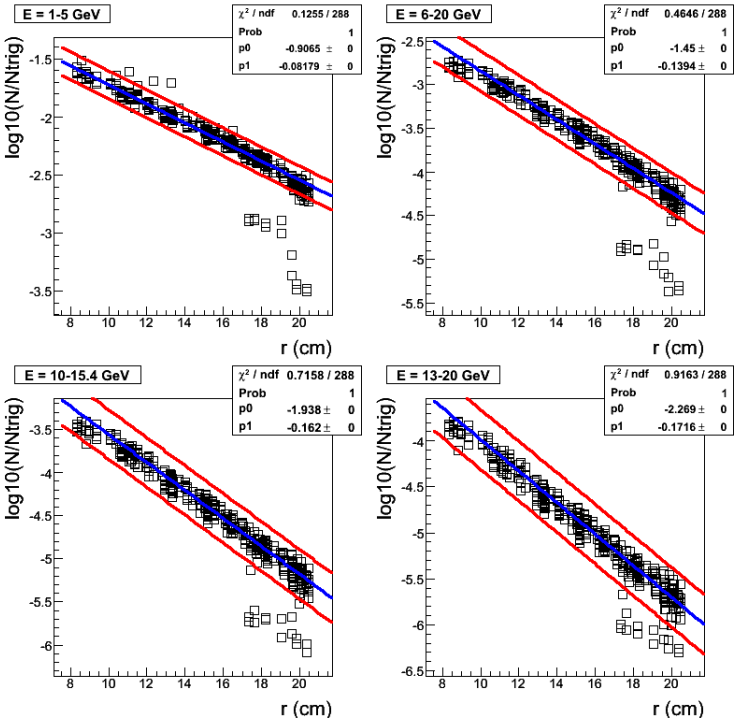

(b)

Figure 4.2: Hit distributions for p+p collisions at $\sqrt{s} = 200$ GeV in **a.)** north MPC and **b.)** north and south MPCs. The vertical axis is $\log_{10}(N_{hits}/N_{trig})$, and the horizontal axis is radial distance from the beam pipe of a given tower. The low energy-thresholds are 1, 6, 10, and 13 GeV for the plots shown. Only the towers within the red 3.5σ bands are kept (excepting for the noisy driver board in the north).

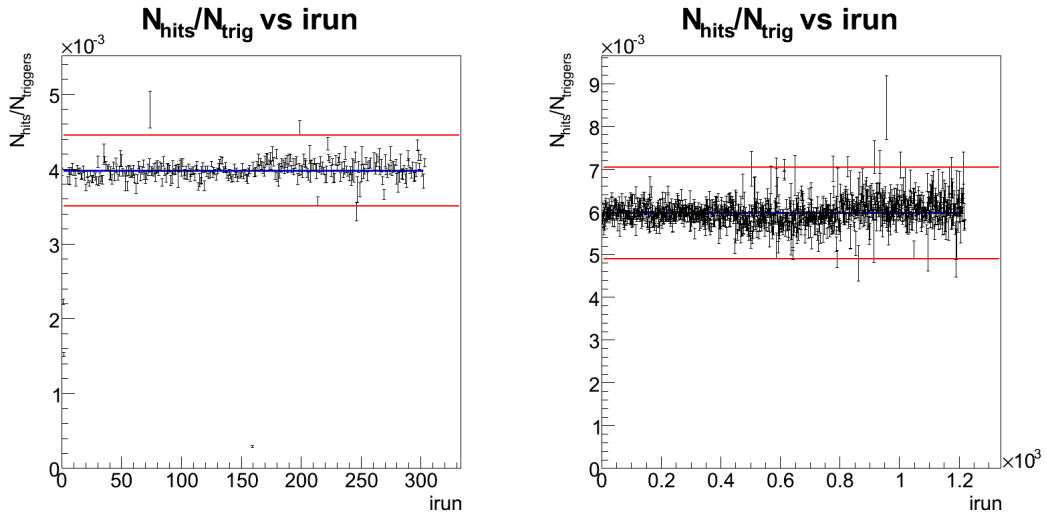

(a) (b)

Figure 4.3: The π^0-yield per min-bias event for **a.)** p+p, **b.)** d+Au 60%-88%. Data points outside the red band are excluded from analysis.

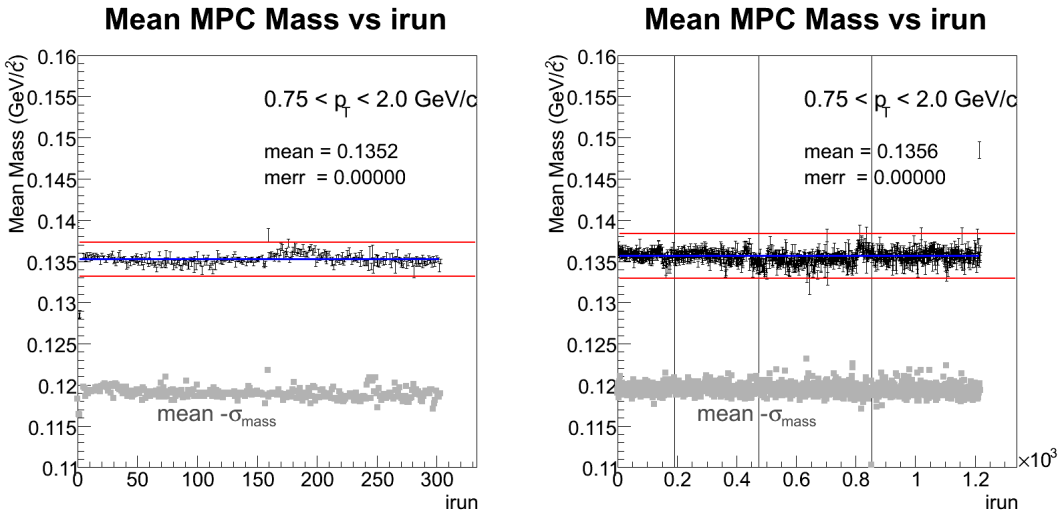

(a) (b)

Figure 4.4: The mean and standard deviation of the Gaussian fit to the π^0 invariant mass distribution for **a.)** p+p, **b.)** d+Au 60-88%.

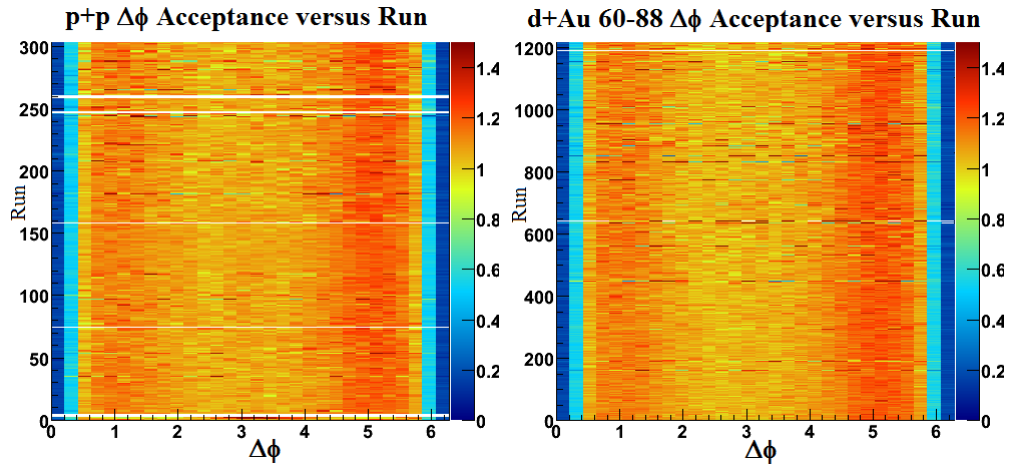

(a) (b)

Figure 4.5: The cluster/π^0 (MPC/MPC) event-mixed acceptance functions versus run number for **a.)** p+p, **b.)** d+Au. The color scale represents the value of the acceptance, which has been normalized to have an average value of 1 for a given run.

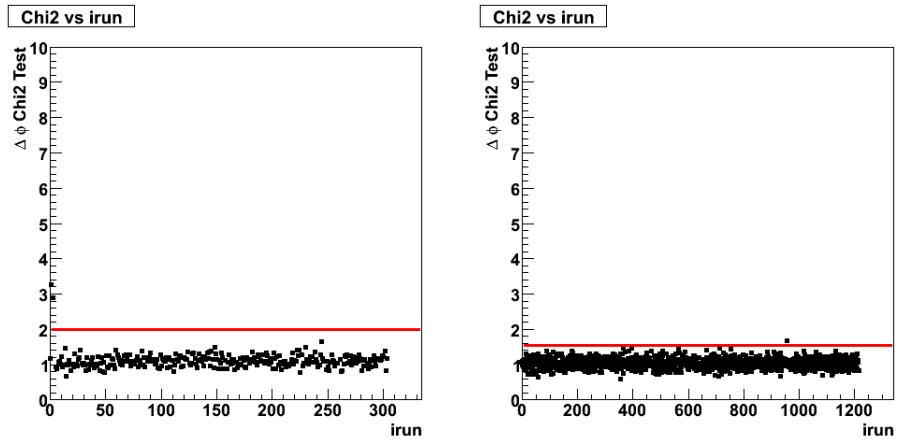

(a) (b)

Figure 4.6: The χ^2/NDF for the cluster/π^0 (MPC/MPC) mixed-event acceptance functions versus run number for **a.)** p+p, **b.)** d+Au. Data points with a χ^2/NDF value above the red line are excluded from the analysis.

4.4 Data Analysis

4.4.1 Yield Extraction

The π^0's are identified by forming an invariant mass distribution for all combinations of cluster pairs that pass the particle-identification cuts defined in section 4.2. The position and energy of the clusters are then input in the formula for the invariant mass of the $\pi^0 \to \gamma\gamma$ decay, which as a reminder is

$$m_{inv}^2 = 2E_1E_2(1 - \cos\Delta\theta). \tag{4.9}$$

The extraction of the π^0 yield from the invariant mass distributions in PHENIX is usually first attempted by a technique known as event mixing. Event mixing consists of forming an invariant mass distribution with clusters paired from different events. To distinguish between the same-event and mixed-event invariant mass distributions, they are termed foreground and background, respectively. The background will contain no mass peaks, whereas clear π^0- and η-meson peaks are present in the foreground. One usually normalizes the amplitude of the background to the foreground on both sides of the π^0 peak, careful to avoid the η-meson peak. However, in our case, there is little to normalize to on the low-mass side of the peak (e.g. Fig. 4.7), and hence we are forced to only use the higher-mass side for the normalization. In Fig. 4.7, we show the foreground (black) and event-mixed background (red) distributions normalized from $m_{inv} = 0.30 - 0.36$ GeV/c^2. The π^0 yield is obtained by subtraction of the background from the foreground and integrating the counts.

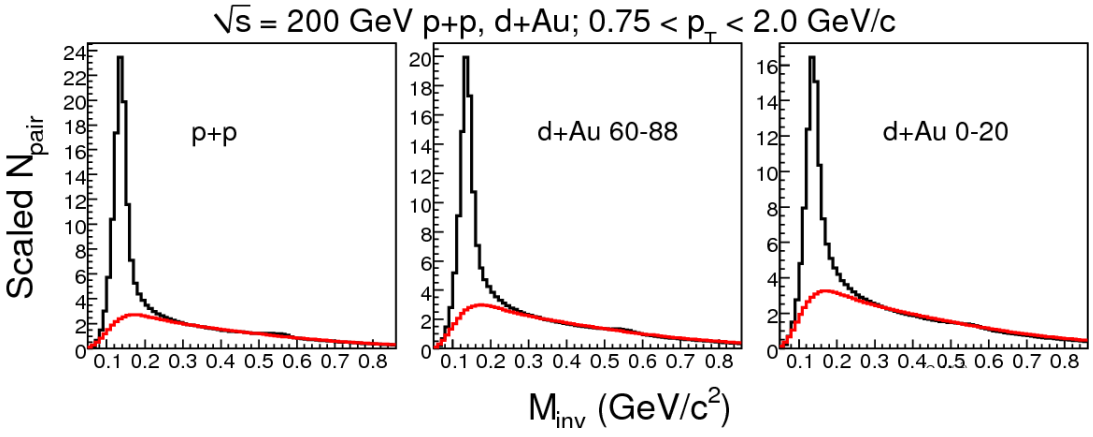

Figure 4.7: Sample invariant mass spectra (black) and mixed-event background (red) for p+p, d+Au peripheral, and d+Au central collisions showing the π^0 peak around $m_{inv} = 0.135$ GeV/c^2. The mixed-event background has been normalized from $m_{inv} = 0.30 - 0.36$ GeV/c^2. This technique underestimates the true background level in the MPC invariant mass distribution (see Fig. 4.8).

The mixed-event technique, however, has been shown in monte-carlo simulations to be incorrect for the MPC π^0-yield extraction. The PYTHIA [117] simulation package was used to produce simulated $\sqrt{s} = 200$ GeV p+p events. The events consist of partonic interactions, followed by the hadronization of the partons into particles. These particles decay until the "stable" particles remain. All particles (including partons) and their relevant kinematical properties (e.g. energy and momentum) are stored in an event record. The PYTHIA events are then run through the PHENIX GEANT3 detector simulation package known as PISA [111]. PISA takes the particles produced in PYTHIA and interacts them with the different detector geometries and materials in PHENIX. We use a version of PYTHIA (6.4 Tune A) [124] that has been tuned to match the single-particle distributions observed in Fermilab data, and hence the invariant mass distributions in simulation look very similar to those observed in data.

We developed a technique to track the simulated particle-energy deposits into clusters in the MPC. This allows one to identify decay photons from π^0's on an event-by-event basis in simulation, thus enabling one to track the background contributions to the invariant mass distribution in an exacting manner. In Fig. 4.8, we show example simulated invariant mass distributions that illustrate the failure of mixed events to describe the background. One can see that the green (mixed-event background) underestimates the true level of the background (blue). The motivation for this technique is that the yield extraction using the mixed-event background is inconsistent with the reconstruction efficiency. More specifically, when we extract the yield in p+p PYTHIA→PISA simulations and use our calculated efficiencies to correct back to the original spectrum, the result does not match with the input from PYTHIA.

Because the p+p PYTHIA→PISA simulations have very similar invariant mass distributions to the actual p+p data, they can be used as a good estimator of the background in p+p data. For d+Au collisions, linear combinations of embedded p+p PYTHIA events were used for the background, as we explain below.

Embedding in this context is the superposition of two (or more) events on top of each other. For the embedding of two p+p PYTHIA events, the event records from the different events are merged. Then, for each tower, the energy deposition from one event is added to that of the other. The last step is to form the new clusters which can have contributions from both events. Deuteron-gold collisions can be thought of as a superposition of multiple nucleon-nucleon collisions (see Fig. 2.3-b for the N_{coll} distribution); the embedding of multiple p+p events is an attempt to reproduce the effect that the underlying N_{coll} distribution has on the background level. It was found that embedding three p+p events produces an invariant mass distribution similar to d+Au 0-20% events (these have the smallest signal-to-background ratio). Hence, to describe the d+Au backgrounds, we add linear combinations of what we now term 1pp, 2pp and 3pp events (i.e. 3pp

means three p+p events embedded into each other) to match the foreground mass distribution in question (e.g. d+Au 20-40). We then add the background distributions together in the same proportion and use these for yield extraction.

The invariant mass shapes for 1pp, 2pp, and 3pp events can be seen in Figs. 4.9-4.11. In the $p_T = 0.25-0.5$ GeV/c bin, a small hump in the background of the 3pp shape (Fig. 4.11) was observed that is not reproduced in data, and hence it was reduced such that the simulated distributions better match the real data.

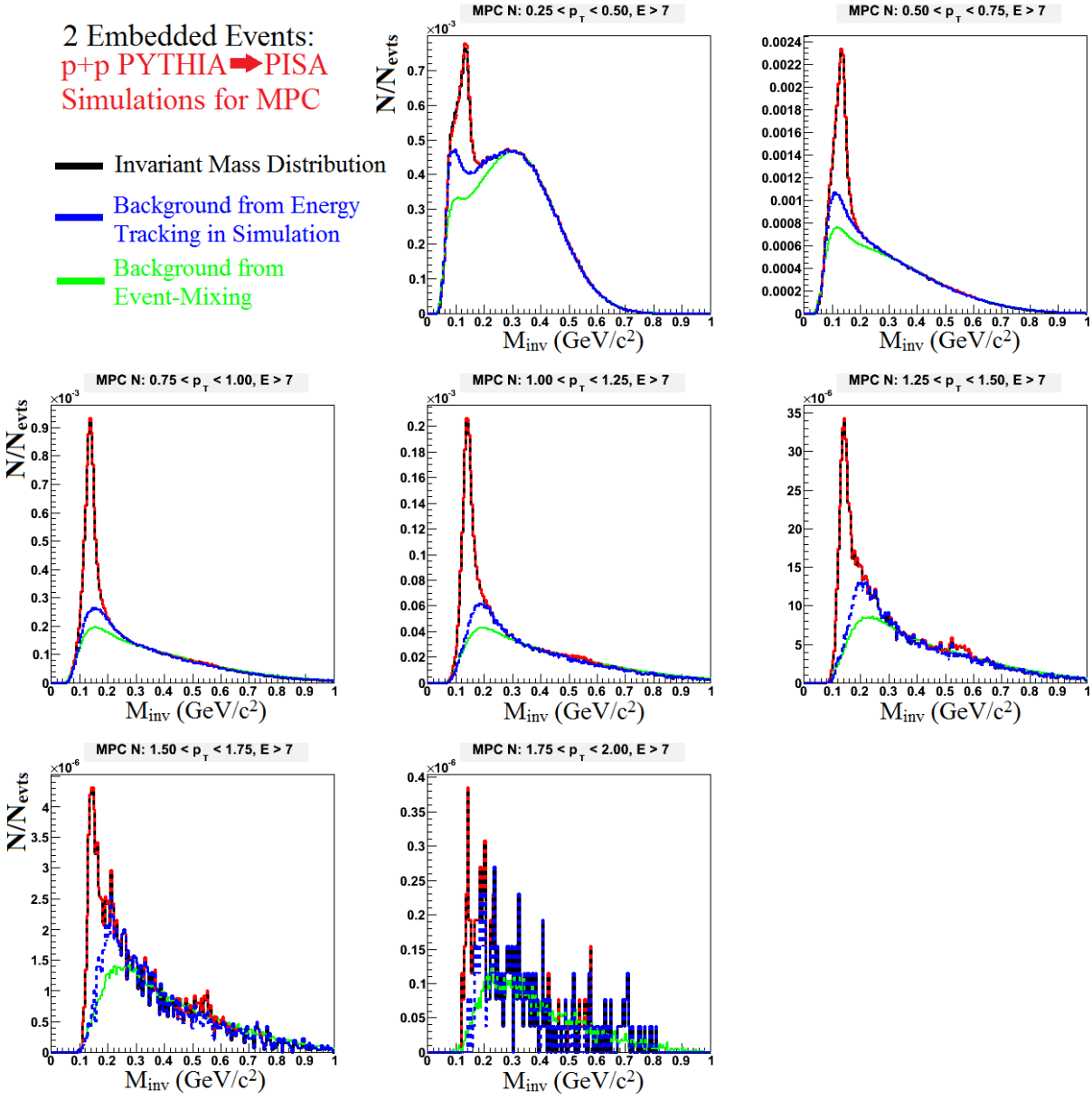

Figure 4.8: Foreground (red and black), background determined from simulation (blue), and the mixed-event background (green) for two p+p PYTHIA events embedded into each other for $3.0 < \eta < 3.8$.

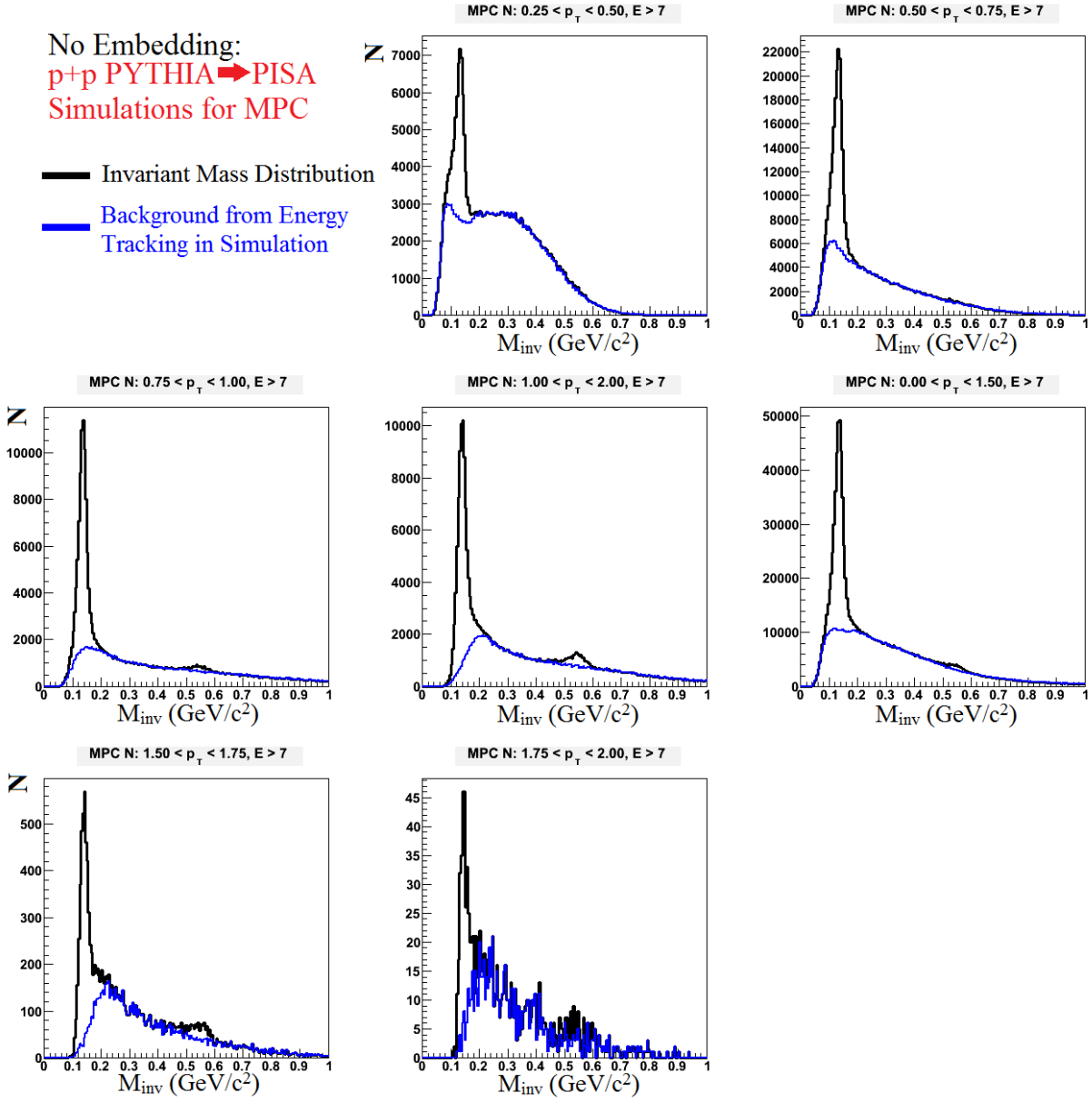

Figure 4.9: **1pp:** Foreground (black) and background determined from simulation (blue) for one p+p PYTHIA event for $3.0 < \eta < 3.8$.

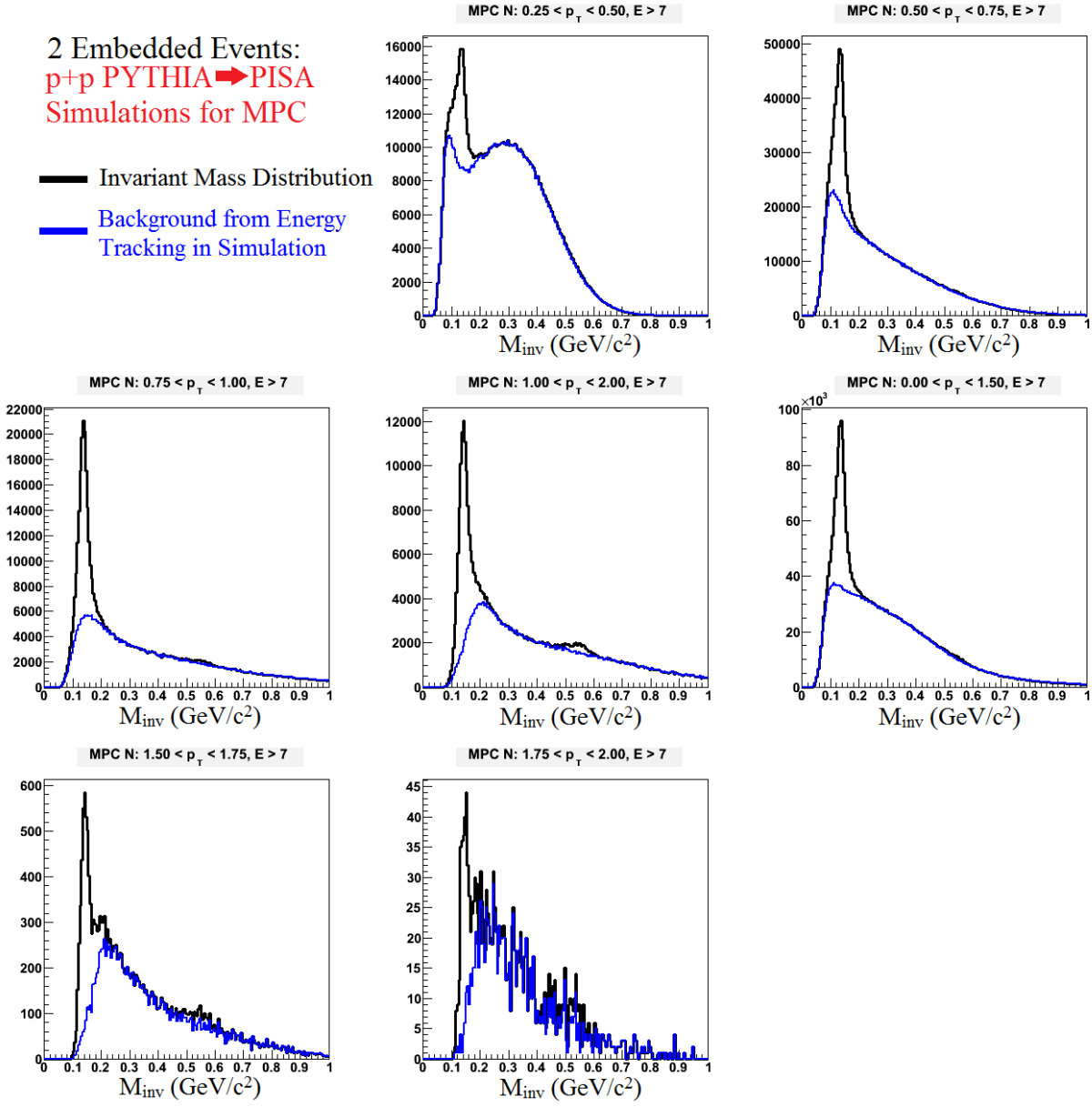

Figure 4.10: **2pp:** Foreground (black) and background determined from simulation (blue) for two p+p PYTHIA events embedded into each other for $3.0 < \eta < 3.8$.

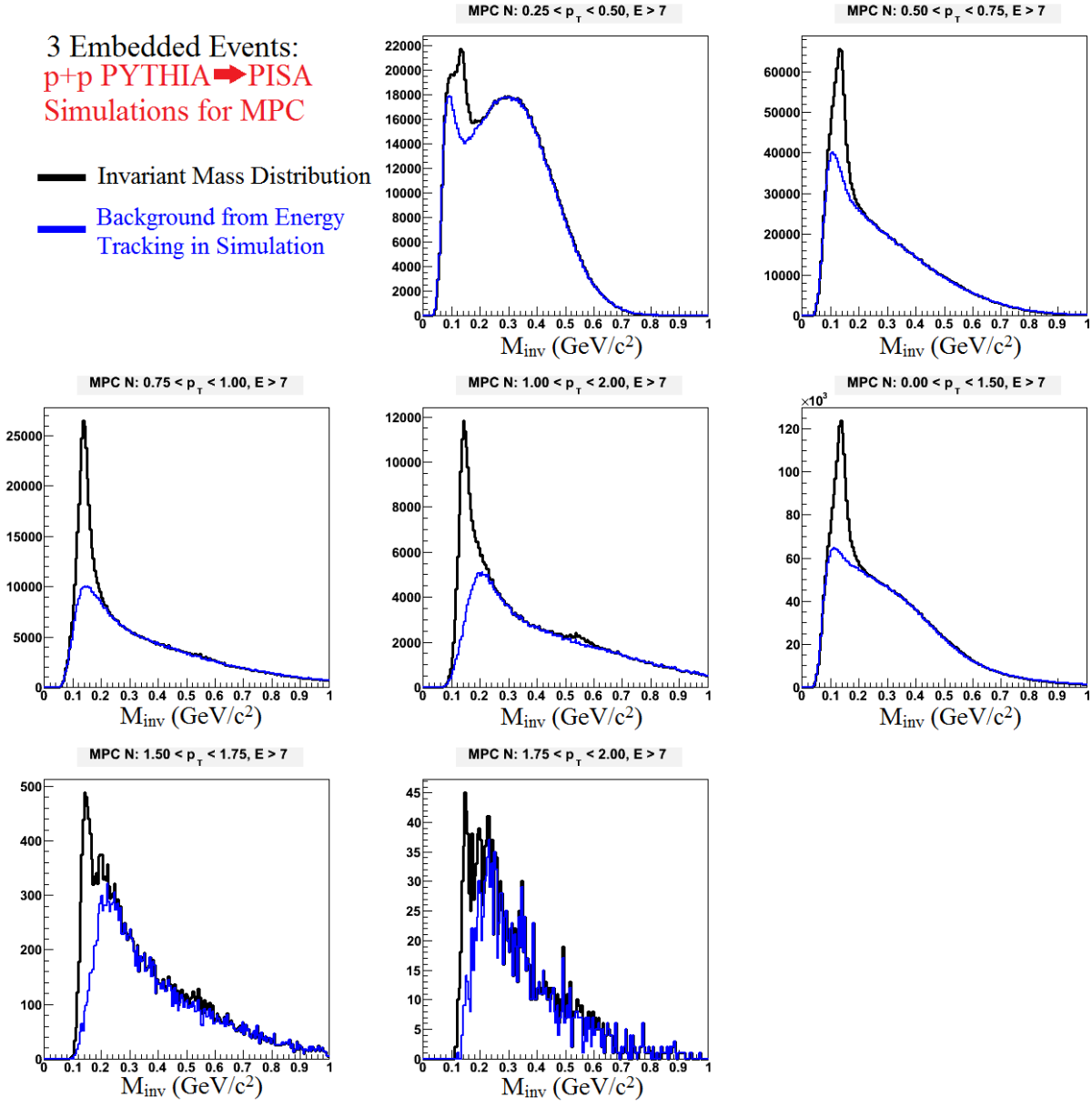

Figure 4.11: **3pp:** Foreground (black) and background determined from simulation (blue) for three p+p PYTHIA events embedded into each other for $3.0 < \eta < 3.8$.

The actual matching consists of minimizing a χ^2-like quantity between the linear combination of simulated foreground shapes and the data in the range of $m_{inv} = 0.05 - 0.4$ GeV/c^2. In particular, we first form a linear combination of the 1pp, 2pp, and 3pp foreground shapes s_i using coefficients c_{npp} as

$$s_i = c_{1pp} \times fg_{1pp,i} + c_{2pp} \times fg_{2pp,i} + c_{3pp} \times fg_{3pp,i} \tag{4.10}$$

where i is an invariant mass bin, $c_{1pp} + c_{2pp} + c_{3pp} = 1$ (we are careful to avoid double-counting), and $fg_{npp,i}$ corresponds to the simulated foreground produced by embedding $1 \leq n \leq 3$ p+p events into each other.

Then, given that d_i is the value of the data in bin i, we perform the minimization on the quantity

$$\bar{A}_{sd} \times \frac{1}{\sigma_{A,tot}} = \frac{\sum_i \frac{s_i - d_i}{s_i + d_i} \times 1/\sigma_i^2}{\sum_i 1/\sigma_i^2} \times \frac{1}{\sqrt{\sum_i \sigma_i^2}}, \tag{4.11}$$

where σ_i corresponds to the statistical uncertainty of asymmetry quantity $A_{sd} = \frac{s_i - d_i}{s_i + d_i}$, and s_i has been re-normalized such that $\sum_i s_i = \sum_i d_i$ for i in bins between $m = 0.05 - 0.40$ GeV/c^2. This procedure is akin to averaging the asymmetry value A_{sd} over all bins and dividing by the total statistical uncertainty. In practice, it was used over a more conventional χ^2-minimization because it produced better results. We thus produce a simulated shape that best matches our real data by using the linear combination of the 1pp, 2pp and 3pp shapes. The last step is to calculate our background, which is a linear combination of the simulated backgrounds with the same coefficients c_{npp} fixed from the minimization, or

$$bg_i = c_{1pp} \times bg_{1pp,i} + c_{2pp} \times bg_{2pp,i} + c_{3pp} \times bg_{3pp,i}. \tag{4.12}$$

This becomes that background we use for yield extraction.

If we look at the invariant mass plots in Fig. 4.12 for central d+Au collisions, we see that the black is the data (d_i), the red is the linear combination of shapes that best matches the data (s_i), and the blue is the linear combination of background shapes with the same coefficients as used in the matching (bg_i).

Figure 4.13 shows the value of our minimization parameter versus fractions of 2pp and 3pp events (or c_{2pp} and c_{3pp}). Here we do not allow negative coefficients $c_{npp} < 0$, and so only the triangle wherein $c_{2pp} + c_{3pp} \leq 1$ is considered. Also, since $c_{1pp} + c_{2pp} + c_{3pp} = 1$, the fraction of 1pp ($c_{1pp}$) can be thought of as lying on the diagonals; that is, when $c_{2pp} + c_{3pp} = 1$ (at the hypotenuse of the triangle), $c_{1pp} = 0$. When $c_{2pp} + c_{3pp} = 0$, then $c_{1pp} = 1$, and we are at the origin.

The simulated data consists of 50 million p+p events; hence using the simulated shapes increases the statistical error in subtracting the background. In some cases (i.e. the last two p_T bins), the statistics of

the background are not sufficient to use the histogram for subtraction. In these cases, the background is fit with a Landau distribution added to a 7^{th} degree polynomial. In appendix B.2, we show the invariant mass distributions, backgrounds, and minimization contours for all centralities and rapidity ranges ($3.0 < \eta < 3.4$, $3.4 < \eta < 3.8$, and $3.0 < \eta < 3.8$).

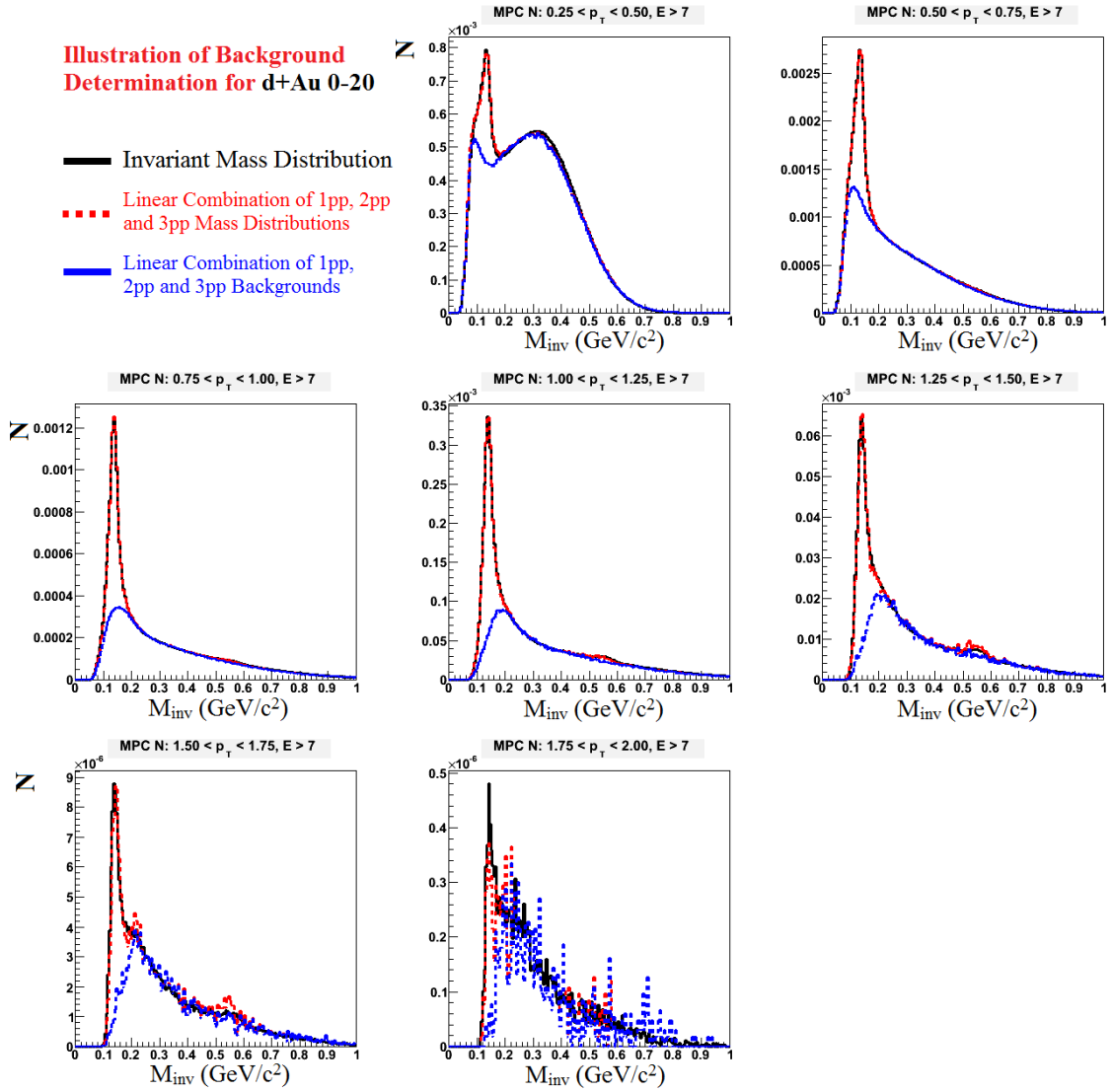

Figure 4.12: Illustration of the process for finding the background for d+Au 0-20% events, $3.0 < \eta < 3.8$. Linear combinations of the 1pp, 2pp, and 3pp shapes (red) are used that best match the data (black). The background is then the sum of the linear combinations of 1pp, 2pp, and 3pp backgrounds with the coefficents previously determined.

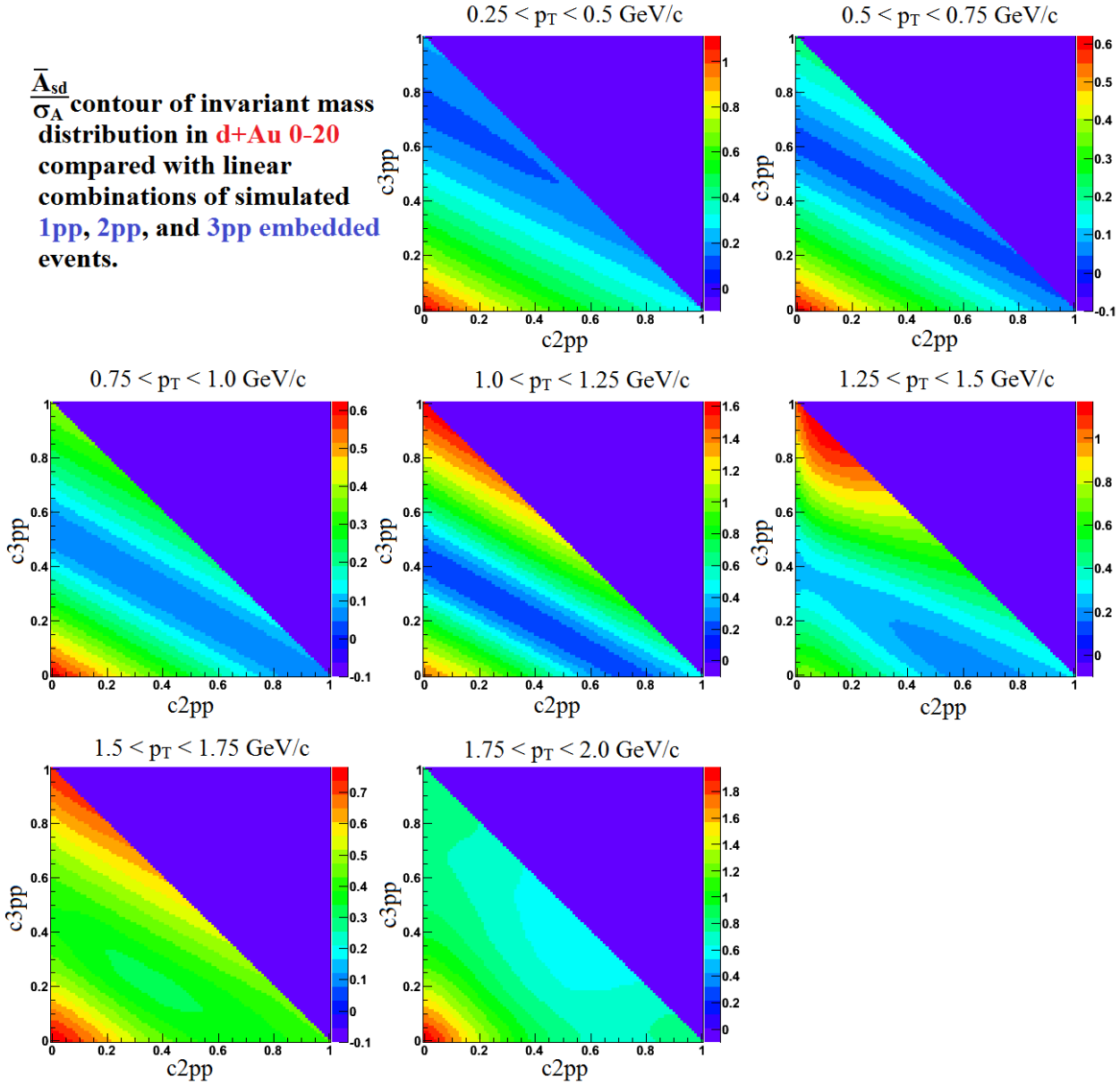

Figure 4.13: This shows the minimization contours for choosing the linear combination of 1pp, 2pp, and 3pp shapes for matching to the foreground distribution in data for d+Au 0-20% events, $3.0 < \eta < 3.8$.. The vertical axis represents the 3pp fraction (c_{3pp}) while the horizontal axis represents the 2pp fraction (c_{2pp}). The 1pp shape is constant along the diagonals, as the fraction of 1pp is $c_{1pp} = 1 - c_{2pp} - c_{3pp}$.

4.4.2 Acceptance × Efficiency

There are several different techniques that can be used to estimate the correction factor for the limited MPC acceptance and efficiency. The most basic one is to generate a sample of single-π^0 events using a single-particle generator (e.g. PYTHIA) that can generate π^0's distributed uniformly in pseudorapidity and p_T (or energy). The decay photons from the π^0's are run through PISA, and the efficiency is simply determined as

$$\epsilon(p_T, \eta) = \frac{N_{reco}(p_T, \eta)}{N_{thrown}(p_T, \eta)} \tag{4.13}$$

The reconstructed π^0's are extracted from the invariant mass distribution. If we had a perfect detector, this technique would be sufficient. However, one additionally has to account for the resolution of the detectors, which causes a smearing of the p_T and pseudorapidity bins. Also, one has to consider efficiency changes when the π^0's are detected in the presence of other particles – so-called multiplicity effects.

To estimate the multiplicity effects, we embed the single π^0's into real events (d+Au or p+p) and calculate the efficiency. The embedding procedure basically involves adding the energies in a tower from both events together, as described in the previous section.

The smearing effect from the finite detector resolution can be resolved by a number of different approaches; two common approaches include matrix inversion and iterative methods to unfold the smeared spectrum. We have chosen to use the iterative method but both will be described in what follows.

To correctly calculate the efficiencies, we have to consider the bin smearing wherein bin content that belongs to bin i ends up in bin j, along with a falling spectrum in both p_T and pseudorapidity. It is easiest to formulate the efficiency calculation in terms of a matrix-inversion problem. Given that s_i are the true yields in bin i (p_T or η bin), y_i are the measured yields in bin i, and $\bar{\epsilon}_{ij}$ is the efficiency matrix which accounts for smearing from bins $i \rightarrow j$, we have

$$\sum_j \bar{\epsilon}_{ij} s_j = y_i. \tag{4.14}$$

This efficiency matrix accounts for both the smearing of bins as well as the probability to reconstruct a π^0. To obtain s_i, we simply need to invert the matrix $\bar{\epsilon}_{ij}$. The efficiency matrix can be determined from simulation, but properly inverting the matrix and the errors can be difficult, especially because we must account for the smearing in both p_T and η.

Instead, we choose to follow PHENIX convention perform an iterative procedure. The problem can be

formulated as

$$\epsilon_i = \frac{y_i}{s_i} = \frac{\sum_j \bar{\epsilon}_{ij} s_j}{s_i}, \tag{4.15}$$

where ϵ_i is the efficiency of bin i that has accounted for all smearing (y_i has contributions from all s_j). As a simple example, for the case where there are two bins, we have

$$\epsilon_1 = \epsilon_{11} + \frac{s_2}{s_1}\epsilon_{12}. \tag{4.16}$$

This illustrates that the spectral shape must be known to measure the efficiencies, as ϵ_1 depends on both s_1 and s_2, the true values of the spectrum in these two bins (unless there is no smearing between bins 1 and 2 or $\epsilon_{12} = 0$, i.e. the perfect detector). Because the off-diagonals of the efficiency matrix are non-zero (i.e. there is smearing), a simultaneous determination of the efficiencies and the spectral shape is carried out via an iterative procedure. We begin the procedure by using the spectral shapes (in both p_T and η) measured from PYTHIA.

To "apply" the shapes, we consider the single-π^0 events distributed uniformly in p_T (what follows also applies to η). Each of the generated events is weighted according to the p_T at which the π^0 was generated. For example, given a p_T spectrum that has a value of 3 at $p_T = 0.25$ GeV/c and 1 at $p_T = 0.5$ GeV/c, each π^0 with $p_T \approx 0.25$ GeV/c is counted three times in the efficiency calculation; each π^0 with $p_T \approx 0.5$ GeV/c is counted once.

Using the two-bin example in eq. 4.16, $s_1 = 3s_2$ and thus

$$\epsilon_1 = \bar{\epsilon}_{11} + \frac{1}{3}\bar{\epsilon}_{12}. \tag{4.17}$$

Consider an other example in which true π^0 distribution is flat in p_T, or $s_1 = s_2$ and we have

$$\epsilon_1 = \bar{\epsilon}_{11} + \bar{\epsilon}_{12}. \tag{4.18}$$

These two examples illustrate that what we call the "efficiency" actually depends on the spectral shape and is not simply a property of the detector.

The iterative procedure is designed to produce the correct p_T and η spectra. The corrections to the p_T and η spectra are done separately, rather than simultaneously. Specifically, five iterations of corrections are performed on the p_T spectrum, followed by a corrective iteration to the η spectrum. This procedure is

carried out six times; thus in total there are 36 steps in the procedure. The steps of one iteration are detailed below:

1. Use p_T and η spectra from the previous iteration (0^{th} p_T, η iterations use PYTHIA) as a weight to calculate the efficiencies (eq. 4.13),
2. Correct measured yields by efficiencies to create the p_T spectrum in η bins,
3. Fit p_T spectrum with piecewise exponential/Hagedorn function from eq. 4.19,
4. Repeat steps 1-3 five times and convergence of p_T spectrum is achieved,
5. Modify linear fit to η spectrum to better match observed yields in η bins,
6. Repeat steps 1-5 six times.

The p_T fit function that describes the data well is a piecewise exponential and modified Hagedorn function, or

$$f(p_T) = \begin{cases} a_0 e^{-a_1 pT} & p_T < 0.5 \text{ GeV/c}, \\ \frac{a_0 p_T}{(e^{-a_1 p_T - a_2 p_T{}^2} + p_T/a_3)^{a_4}} & p_T > 0.5 \text{ GeV/c}. \end{cases} \tag{4.19}$$

The Hagedorn function is designed to encompass both the high-p_T power-law behavior and low-p_T exponential behavior; in practice an exponential function at low-p_T and in combination with the Hagedorn function at higher p_T fit the data quite well.

In Figs. 4.14-4.15, we show dN/dp_T for the five iterations of the p_T-corrective procedure for p+p and d+Au 0-20%. The top, left plot uses the PYTHIA input spectrum, and the subsequent plots are the iterations of the procedure. Here the black data points are for real data, while the data points shown with a dashed, blue line are the input PYTHIA spectrum. One can see in Fig. 4.14 that the PYTHIA dN/dp_T matches that in data very well.

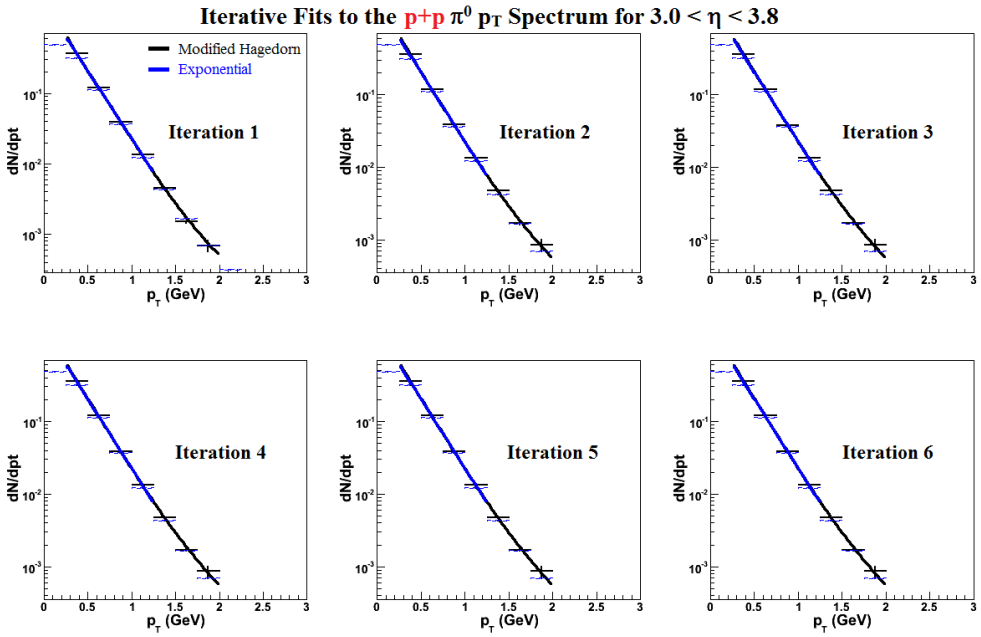

Figure 4.14: **p+p,** $3.0 < \eta < 3.8$**:** The p_T spectrum (black) and fit as a function of iteration. The dashed, blue data points are the PYTHIA p_T spectrum for a point of reference.

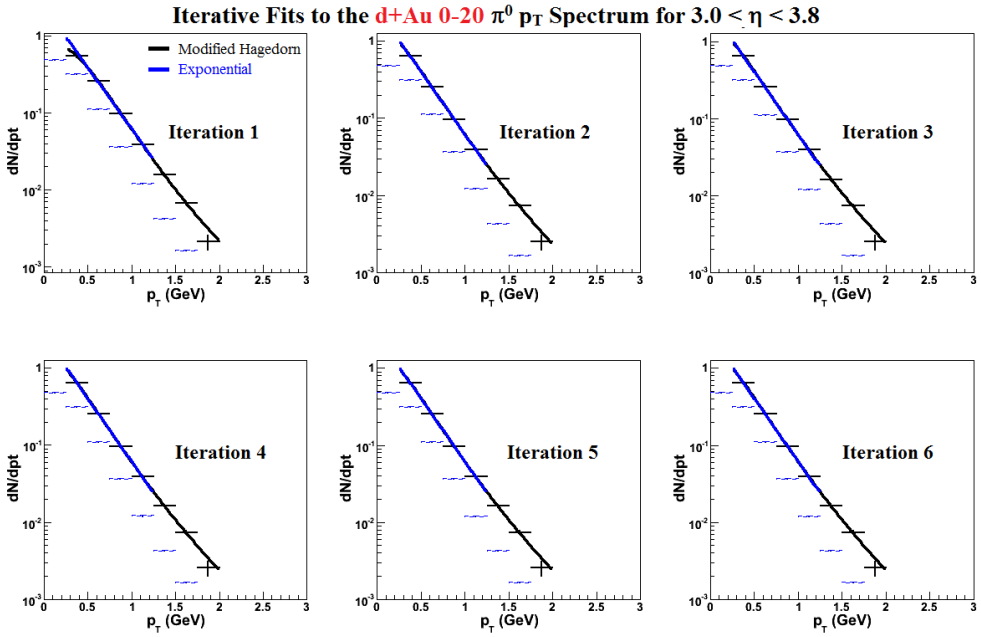

Figure 4.15: **d+Au 0-20%,** $3.0 < \eta < 3.8$**:** The p_T spectrum (black) and fit as a function of iteration. The dashed, blue data points are the PYTHIA p_T spectrum for a point of reference.

For the η distribution, we fit a simple line to the shape from PYTHIA in each p_T bin as shown by the black line in Fig. 4.16. Care is taken to ensure that the average value of the weights in the η bin equals one, so that the total weighting of the given p_T bin does not change.

The yields are measured in two pseudorapidity bins, $\eta_1 = 3.0 - 3.4$ and $\eta_2 = 3.4 - 3.8$. The measured η spectra (in each p_T bin) are compared to PYTHIA (in the two η bins); then in each pseudorapidity iteration (step 5 in the above procedure), the linear fit is modified so that the ratio of counts in the two η bins is the same as what we measure. Formally, we have

$$C(p_T) = \frac{N_2/N_1}{P_2/P_1} \tag{4.20}$$

where P_i (N_i) are the integral PYTHIA (data) yields over the p_T, η range of the η_i-bin in question. The original linear fit to the PYTHIA pseudorapidity spectrum is modified until $N_1/N_2 = P_1^*/P_2^*$, where P^* corresponds to the yield from the modified fit. Examples of the final η distributions compared to those from PYTHIA are shown in Fig. 4.16 for d+Au 0-20% data. The pseudorapidity distribution was never allowed to be negative, but rather when $\eta > \eta_{min}$ (i.e. where the distribution is 2% of the maximum value) the distribution remains flat.

The modification of the η distribution is made difficult because the p_T range accessible is different in the two pseudorapidity bins measured, as the $\eta = 3.0 - 3.4$ bin has p_T bins from $0.25 - 2.0$ GeV/c, whereas the $\eta = 3.4 - 3.8$ bin has p_T bins from $0.25 - 1.5$ GeV/c. The procedure that was carried out was to measure $C(p_T)$ in the three bins with p_T between $0.5 - 1.25$ GeV/c, and essentially use the $C(p_T)$ values of the highest and lowest p_T bins for the surrounding bins. The three "middle" p_T bins were used to avoid systematic problems; the other two p_T bins ($0.25 - 0.5$, $1.25 - 1.5$ GeV/c) common to both pseudorapidity bins have small efficiencies because simultaneous p_T and energy cuts are made. This is illustrated in Fig. 4.17, which shows what we call the "kinematic acceptance" in the p_T and η bins for the energy cuts of $7 < E < 22$ GeV. In Fig. 4.18, we show the ratio $C(p_T)$ using the 3-point fit (a) and 5-point fit (b). The 3-point fit was the actual fit that was used; the 5-point fit was used in the systematic error studies.

The final efficiencies are shown in Fig. 4.19. One can see that the increased event multiplicity of d+Au collisions has a relatively small effect on the MPC π^0 efficiency.

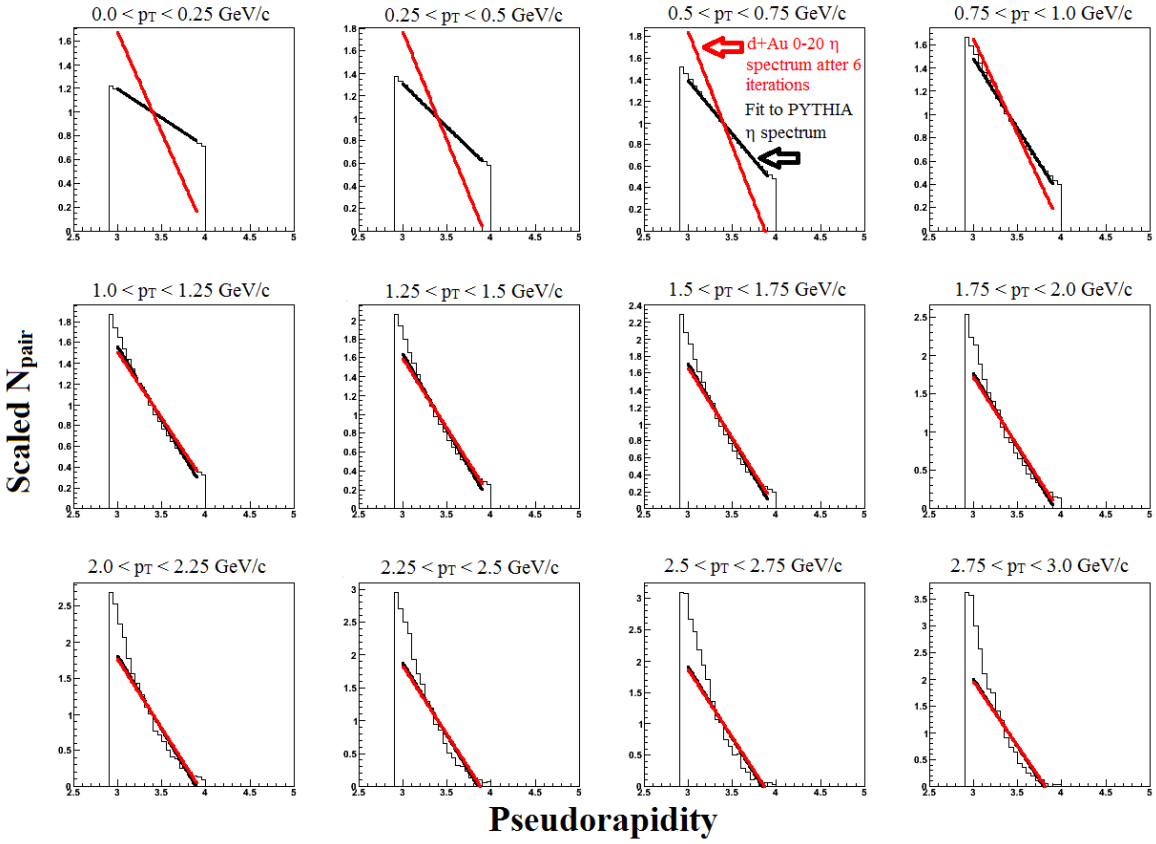

Figure 4.16: **d+Au 0-20%,** $3.0 < \eta < 3.8$**:** PYTHIA pseudorapidity distributions for p_T bins of size 0.25 GeV/c from $0 - 3$ GeV/c. The black lines are the initial fit to the PYTHIA spectrum, while the red lines are the modified distributions after all iterations of the process.

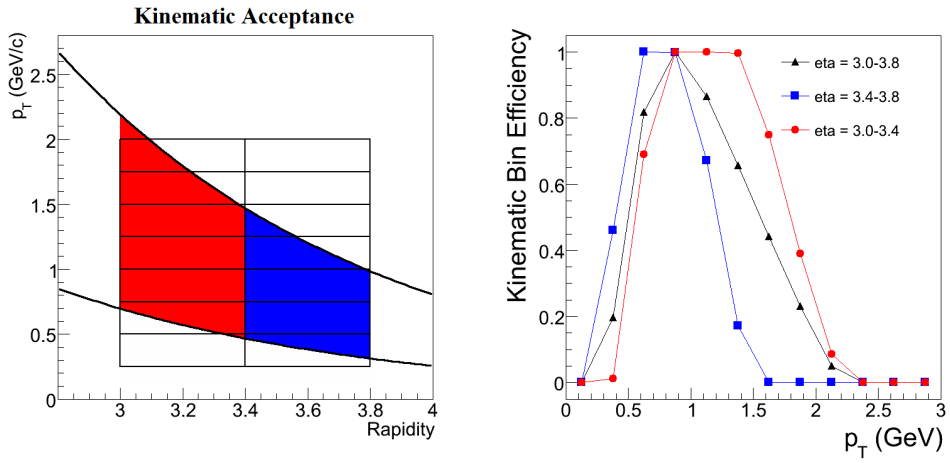

(a) (b)

Figure 4.17: **a.)** "Kinematic acceptance" diagram and **b.)** rough "kinematic acceptance" efficiency determined by simultaneously making p_T, energy, and pseudorapidity cuts in the forward region. The black curves in (a) are the location of the fixed-energy cuts of 7 GeV (lower) and 22 GeV (upper), while the black boxes represent our $p_T \times \eta$ bins.

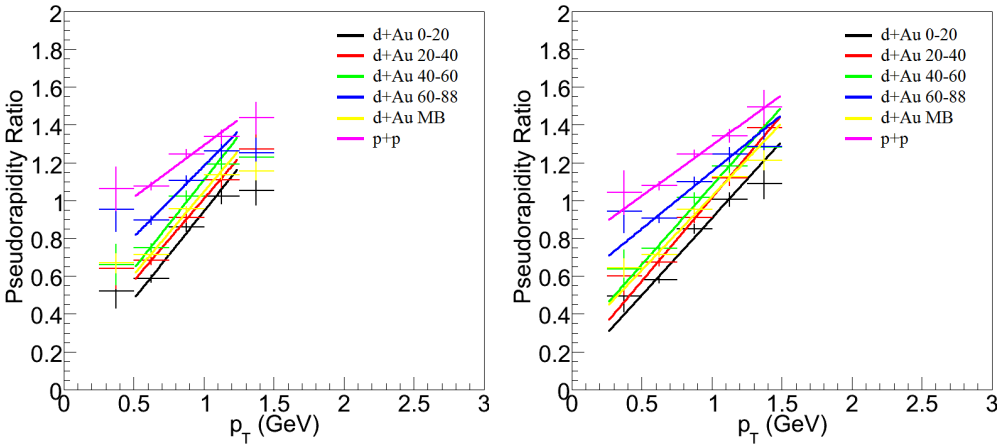

Figure 4.18: Modification factor from eq. 4.20 using **a.)** the 3-point linear fit, and **b.)** the 5-point linear fit after six iterations of the procedure.

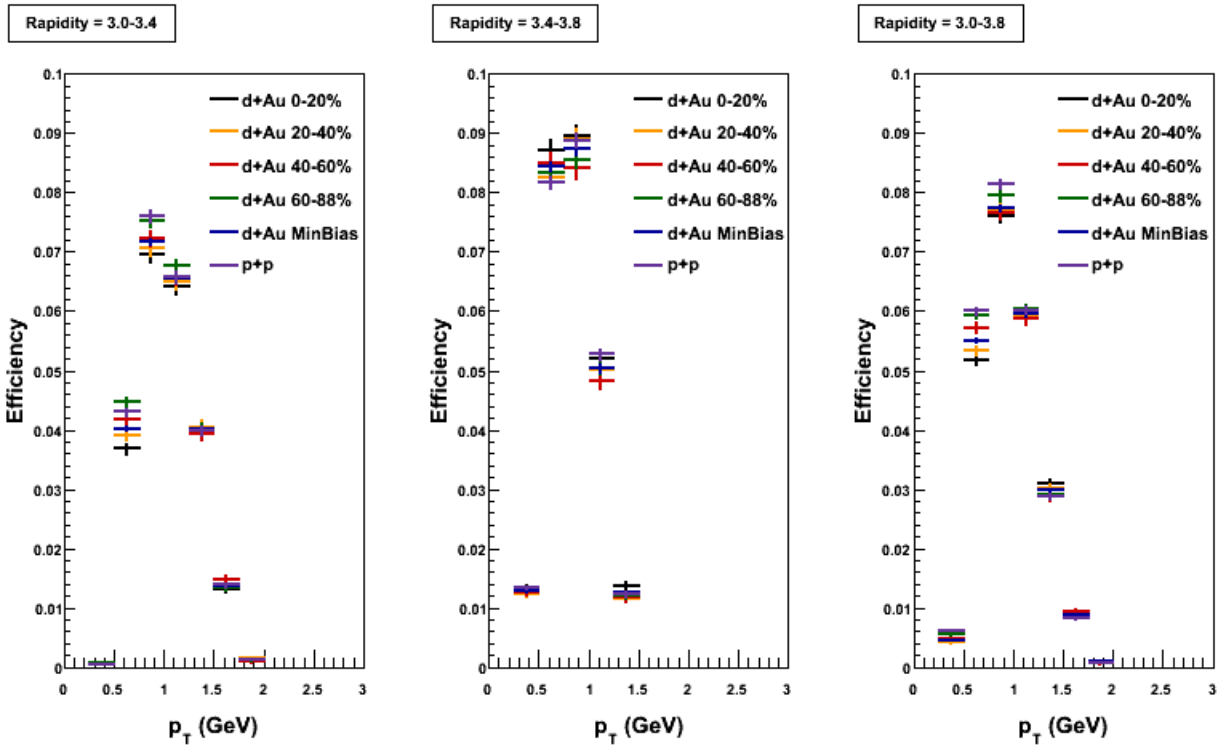

Figure 4.19: Final acceptance × efficiencies in p+p and d+Au for all centralities and rapidity intervals.

4.4.3 Bias-Correction Factor

The PHENIX minimum-bias trigger is defined by a coincidence between hits in the Beam-Beam Counters (BBCs) on either side of the interaction point. The efficiency of the minimum-bias trigger is $\approx 54\%$ in p+p collisions [126]. This means that the trigger will see only 54% of the p+p inelastic cross section in p+p collisions, or in absolute terms, ≈ 23 mb of the available 42 mb at $\sqrt{s} = 200$ GeV. This correction is applied to correct up the total number of events observed in the minimum-bias sample to the true number of inelastic p+p events, or $N_{inelastic} = N_{MB}/0.54$. For the π^0 measurement at hand, we must also correct for the π^0's that are lost by our minimum-bias selection. It has been found that when the minimum-bias trigger is 54% efficient, the π^0 efficiency is $\approx 79\%$ (the efficiencies are correlated with each other and can change as the high-voltage is changed [127]). Thus one would correct the number of π^0's to $N_{\pi^0,inel} = N_{\pi^0,mb}/0.79$.

A simple heuristic for understanding why the efficiency of the minimum-bias trigger and the π^0-efficiency within this trigger sample are so different is that the π^0 requires one detector whereas the minimum-bias sample requires at least a two-particle coincidence. Thus the efficiency for each BBC to fire individually is $\approx 74\%$, which is very similar to the π^0 efficiency. For the p+p sample, we define the bias factor to be the ratio of these correction factors, or

$$C_{bias} = \epsilon_{MB}/\epsilon_{\pi^0} \approx 0.69, \tag{4.21}$$

so that we can easily correct the minimum-bias ratio of π^0's per event to the true value, or

$$\frac{N_{\pi^0,inel}}{N_{p+p,inel}} = C_{bias} \times \frac{N_{\pi^0,MB}}{N_{p+p,MB}}. \tag{4.22}$$

In the d+Au sample, the trigger efficiency is 88.4%. This can be understood in a very simple manner. If we consider the d+Au system as a superposition of nucleon-nucleon (NN) collisions where the minimum-bias efficiency for a single NN collisions is 54%, we can calculate the overall efficiency by assuming the efficiency follows a binary distribution (e.g. if $N_{coll} = 2$, then $\epsilon_{MB} = 1 - (1 - 0.54)^2 = 0.71$). We then can use the N_{coll} distribution in Fig. 2.3-b as a weighting function and use the probabilities from the binary distribution to calculate an expectation value for the efficiency, or

$$\epsilon_{d+Au,MB} = \sum_{N_{coll}} f(N_{coll}) \times (1 - (1 - \epsilon_{p+p,MB})^2), \tag{4.23}$$

where $\sum_{N_{coll}} f(N_{coll}) = 1$.

We also consider the bias corrections for the d+Au centrality classes. As previously discussed, the centrality class is defined by dividing the BBC charge distribution in the Au-going direction (or south) into 88 bins of equal area. We define our centrality classes as 0-20%, 20-40%, 40-60%, and 60-88% (see Fig. 2.3-a). The bias-correction factor is defined in a slightly different way for these classes than for the p+p or d+Au minimum-bias samples. Within each class, the efficiency loss for the given sample is not corrected for. Instead, we consider the bias created by measuring the π^0's. Given that we measure a π^0, the nucleon-nucleon minimum-bias trigger becomes $\approx 75\%$ efficient because the charge distribution is biased to larger values. For a given centrality class, we consider both events that move into and out of a centrality class because of the bias in triggering on π^0 events, and apply a bias correction that makes the sample unbiased [63]. In Table. 4.1, we show the bias-correction factors for the p+p and d+Au samples.

Table 4.1: N_{coll}, bias factors, and inelastic p+p cross-section

species	N_{coll}	σ_{Ncoll}/N_{coll}	C_{bias}	σ_{Cbias}/C_{bias}	$\frac{\sigma_{Ncoll\times Cbias}}{N_{\rm coll}C_{bias}}$	p+p x-section
d+Au 0-20%	15.06	0.099	0.941	0.011	0.048	-
d+Au 20-40%	10.25	0.107	1.000	0.006	0.041	-
d+Au 40-60%	6.58	0.139	1.034	0.016	0.051	-
d+Au 60-88%	3.20	0.025	1.031	0.053	0.075	-
d+Au MinBias	7.59	0.028	0.889	0.001	0.034	-
p+p	1.00	0.000	0.690	0.097	0.097	42.2 mb

4.4.4 Bin-Shift Correction

To correct the yield measured in the p_T bin to the bin center, a so-called up-down correction is used [128]. The fit to the p_T spectrum (see eq. 4.19) $f(p_T)$ is used to calculate the correction for the transverse-momentum bin $p_1 \leq p_T < p_2$. The correction is the ratio of the fit function at the bin center to the average value of the function over the range of the bin, or

$$C_{up-down} = \frac{f(\frac{p_1+p_2}{2})}{1/(p_2-p_1)\int_{p1}^{p2} f(x)dx}. \tag{4.24}$$

A very easy way to calculate this comes about when one takes the functional form for the spectra to be exponential. If $f(p_T) = e^{-ap_T}$ and the width of the p_T bin is Δ, then

$$C_{up-down} = \frac{x}{\sinh x}, \tag{4.25}$$

where $x = \Delta a/2$. If the fit function behaves exponentially over the bin in question, one can still use this

formula by simply setting $a = |\frac{df(p_T)/d(p_T)}{f(p_T)}|$. As a rule of thumb, in our case $\Delta = 0.25$ and $a \approx 4$, and thus $x \approx 0.5$, which gives $R \approx 0.96$.

In Fig. 4.20, we show the bin-shift correction as a function of p_T for all centralities and pseudorapidity bins used in this analysis. The correction is quite small due to the choice of small p_T bins and the shape of the falling spectra. If we chose 0.5 GeV/c bins, then we would have a more sizable correction of $C_{up-down} \approx 0.85$.

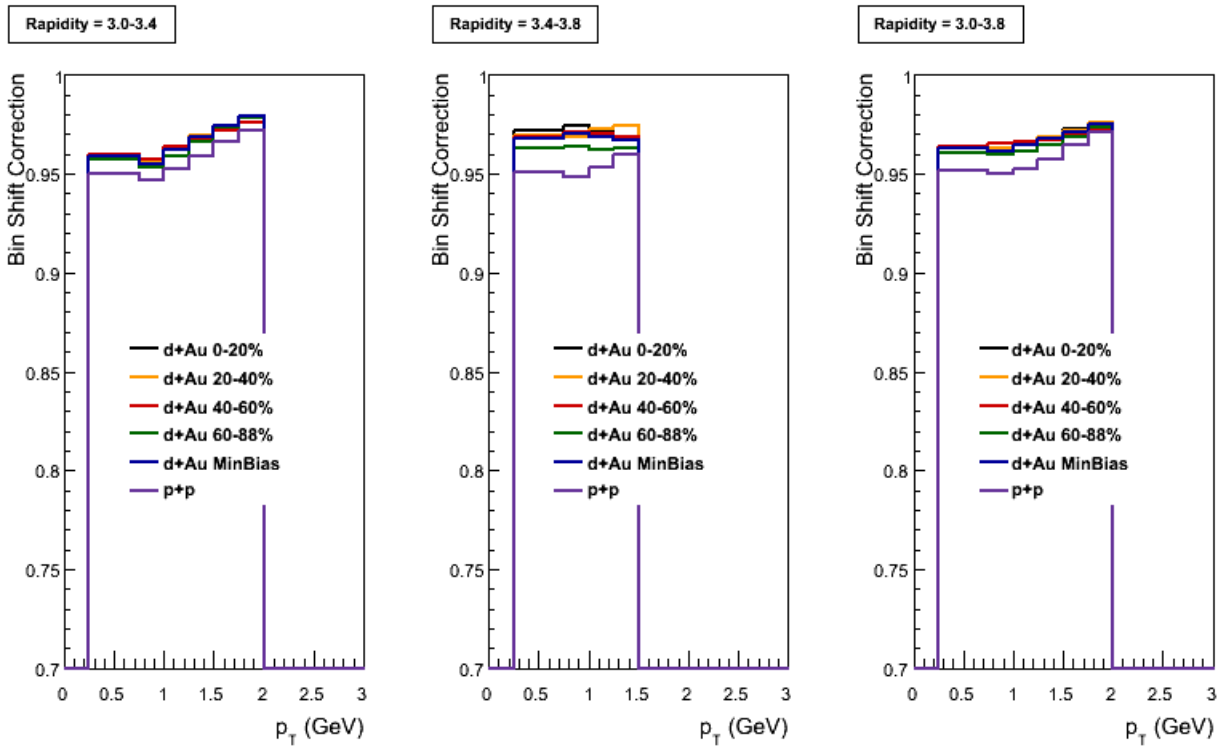

Figure 4.20: Up-down correction, $C_{up-down}$, in p+p and d+Au for all centralities and rapidity intervals.

4.5 Systematic Studies

In the following we present our systematic studies for the invariant yields, p+p cross sections, and $R_{\rm dA}$ values. Plots of the systematic errors are presented and specific values are quoted in the text. The relative errors on the invariant yields summarized in Tables B.4-B.6. Since some of the errors cancel when taking the ratio between d+Au and p+p, the errors on $R_{\rm dA}$ are different and the relative errors are shown in Tables B.7-B.9.

4.5.1 Energy Scale

As stated in section 4.3.3, we quote a scale error of $\delta E/E \approx 2\%$. We then calculate this systematic error as a function of p_T by propagating the 2% into our functional form. If we say $f(p_T) \equiv dN/dp_T$, then our systematic uncertainty from the energy scale becomes

$$\delta f(p_T) = |\frac{df(p_T)}{dp_T}| \times 0.02 \times p_T \tag{4.26}$$

Please note that if we multiply the yields by $1/p_T$ (as we do for the differential cross section and invariant yield) that the relative error increases by 2% for all p_T bins. The energy scale error on the invariant yields is shown in Fig. 4.21.

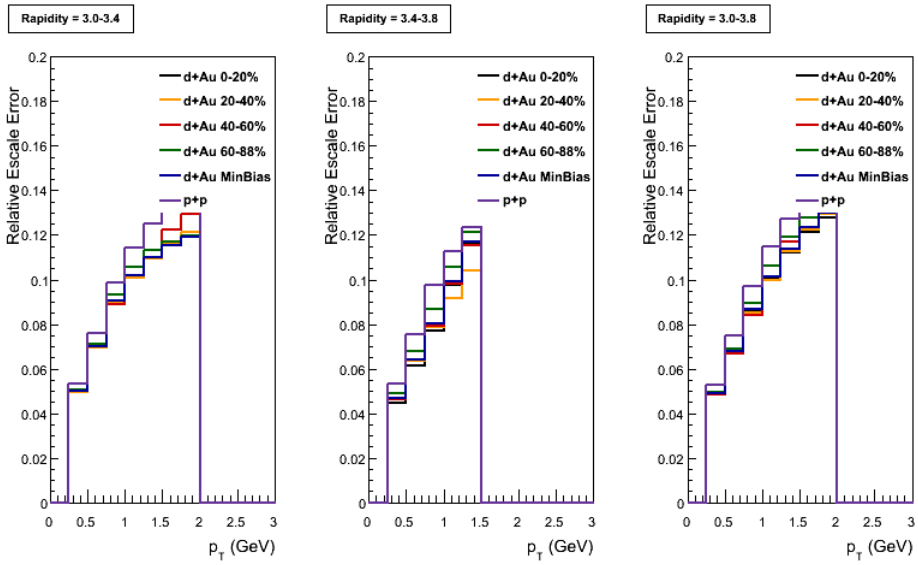

Figure 4.21: Relative energy-scale error on the invariant yields in p+p and d+Au for all centralities and rapidity intervals.

When calculating R_{dA}, much of this error cancels due to the fact that we use the same calibrations for the p+p and d+Au datasets. $R_{\rm dA}$ still exhibits a positive slope, and hence we should propagate the 2% error into this quantity. If we assume the functional form of R_{dA} is linear and has a vertical intercept at $R_{\rm dA} = 0$, then we have an error of 2%. In addition to this error, there is also a small error from the gain stability in each tower, as the LED corrections we apply to each tower can be as large as a factor 2. We estimate that this error is about 2% and quote a conservative, total systematic error on the ratio of the invariant yields as 4%.

4.5.2 GEANT

Here we try to establish the systematic error from using the GEANT3 [118] simulation to calculate the efficiency of MPC. We do this by comparing quantities between $\sqrt{s}$ = 200 GeV p+p PYTHIA $\rightarrow$ PISA simulations and the p+p data. In particular, we look at the χ^2/NDF (or chi2core) and lateral-dispersion parameters in the π^0 mass window and compare the effect of our cuts between simulation and data. One note is that the z-vertex distributions in the PYTHIA dataset are different than p+p data, and so a weighting factor was used to make them effectively the same.

We begin by making only the energy and p_T cuts in both simulation and data. The distributions are normalized such that the integral number of counts in the π^0 mass window in simulation and data are equal. In the leftmost columns of Figs. 4.22-4.26, we plot the invariant mass, χ^2/NDF, lateral dispersion, ϕ, and η distributions where we have only made the energy and p_T cuts. We then apply the analysis cuts of $\chi^2/NDF < 2.5$ and $Max(disp_1, disp_2) < 4$ and the resulting distributions are shown in the rightmost columns of the figures. The distributions in simulation and data are very similar, as the maximum difference in yields is 3% in any of the p_T bins displayed. This 3% thus goes into our systematic error for the reconstruction efficiency.

One issue with the MPC is that the beam-pipe steel can cause preshowering long before the photon reaches the MPC. This effect is z-vertex dependent as well. Fig. 4.27 shows the average number of radiation lengths that a photon traverses before reaching the MPC.

This motivates a study wherein we check the behavior of the π^0 efficiency as a function of z-vertex. To do this, we essentially employ the same procedure as above, except in a limited z-vertex range surrounding $z_{vtx} = 0$ cm. We postulate that the behavior is very similar in simulation and data near $z_{vtx} = 0$, and hence we normalize in this range. We then compare the z-vertex distributions without making any dispersion or χ^2/NDF cuts. In Fig. 4.28, we see that for $z_{vtx} < -20$ cm and $z_{vtx} > 20$ cm, there are differences in the

distributions. The directions of the differences would actually cancel when added together, but we decide to use the absolute value of the difference between the two distributions as a measure of systematic error. We find the difference to be around 6% and use this as another source of systematic uncertainty.

Finally, another possible systematic error is the use of π^0's embedded into real events to estimate multiplicity-dependent effects on the efficiency. Using p+p PYTHIA→PISA events, we have calculated the efficiencies using our embedding procedure, and used these to correct the measured yields (for the simulated data) to produce a reconstructed p_T spectrum. We have compared our reconstructed p_T spectrum to the thrown p_T spectrum and find very good match that is better than 2%. We add this contribution in quadrature to the GEANT systematic error and obtain a final error of

$$\delta f(p_T)/f(p_T) = 0.03 \oplus 0.06 \oplus 0.02 = 0.07. \tag{4.27}$$

In taking the ratio of yields between d+Au and p+p, a portion of this error will cancel. Differences between d+Au and p+p that contribute to the error of the ratio include different z-vertex distributions as well as significant changes in the LED values, which change the noise error in the tower energies. We conservatively estimate that approximately 4% of the error remains, and we quote this in our calculation of R_{dA} as the GEANT systematic uncertainty.

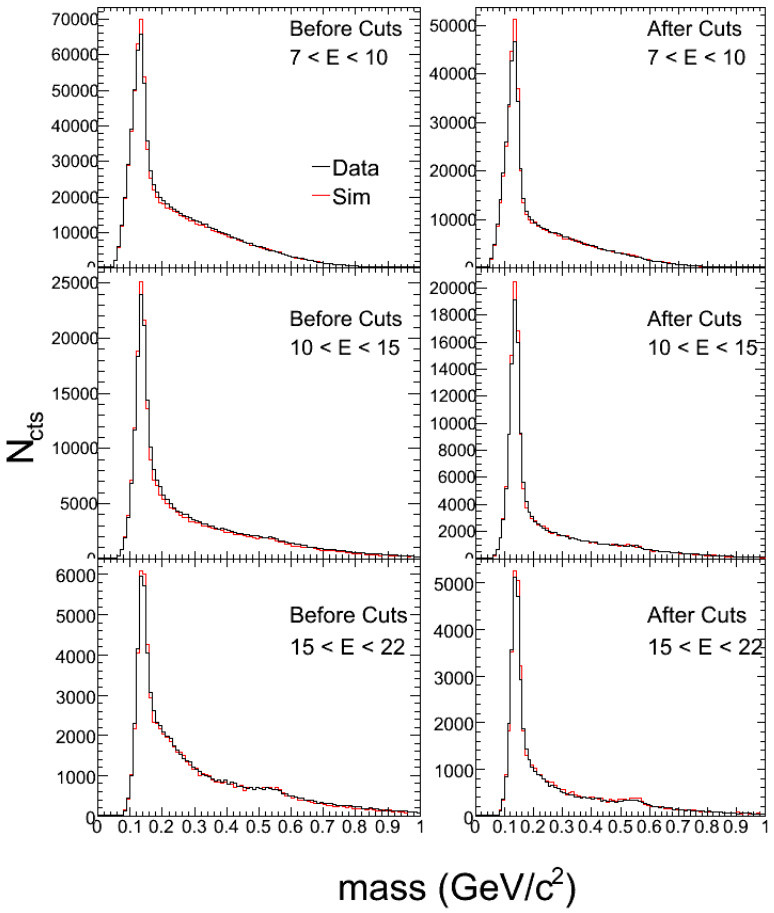

Figure 4.22: Invariant mass distributions in data (black) and p+p PYTHIA simulations (red). The counts are normalized from $m_{inv} = 0.08 - 0.18$ GeV/c in the leftmost column, where the χ^2/NDF and dispersion cuts are not made. The rightmost column shows the distributions after all cuts are made.

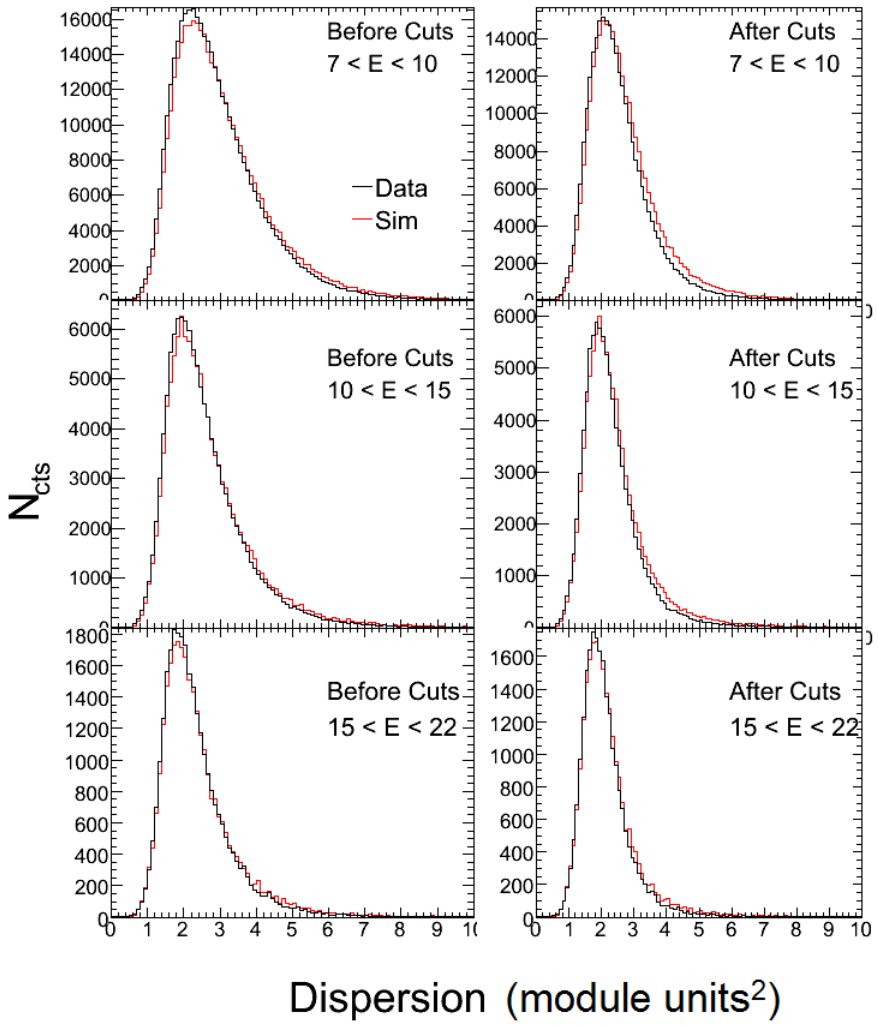

Figure 4.23: Dispersion distributions for the π^0 mass window in data (black) and p+p PYTHIA simulations (red). The counts are normalized in leftmost column, where the χ^2/NDF and dispersion cuts are not made. The rightmost column shows the distributions after all cuts are made.

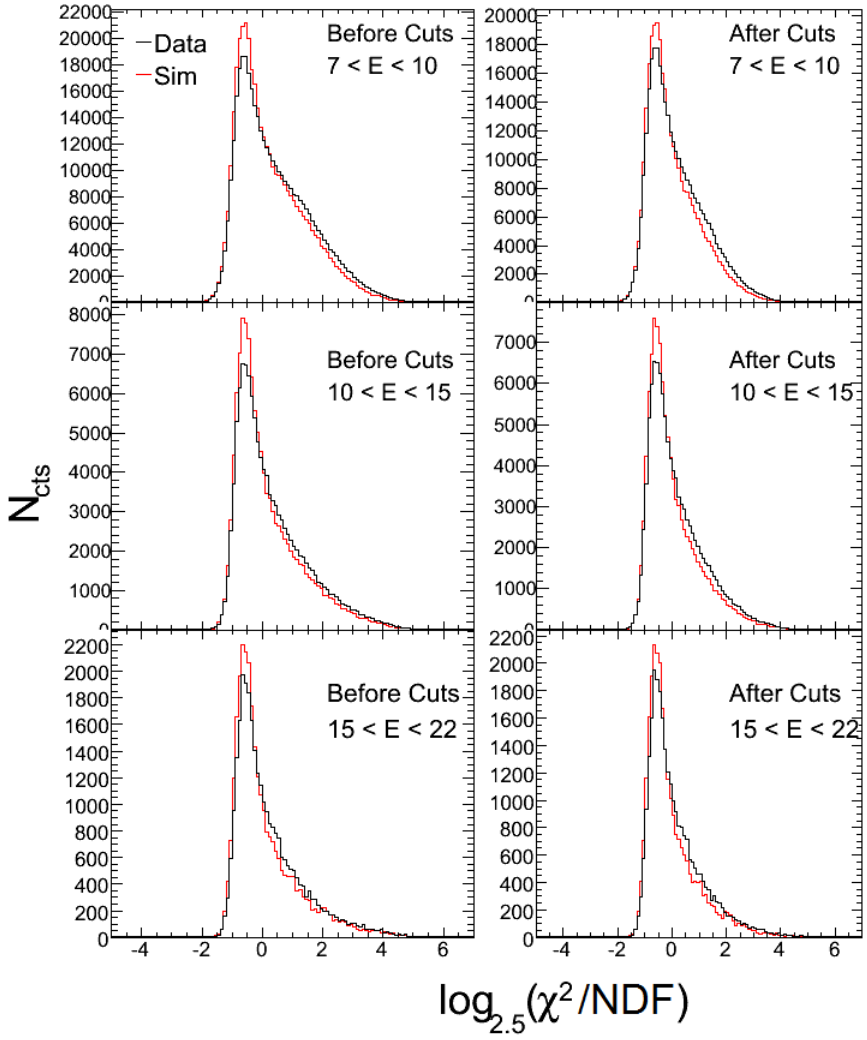

Figure 4.24: χ^2 distributions for the π^0 mass window in data (black) and p+p PYTHIA simulations (red). The counts are normalized in leftmost column, where the χ^2/NDF and dispersion cuts are not made. The rightmost column shows the distributions after all cuts are made.

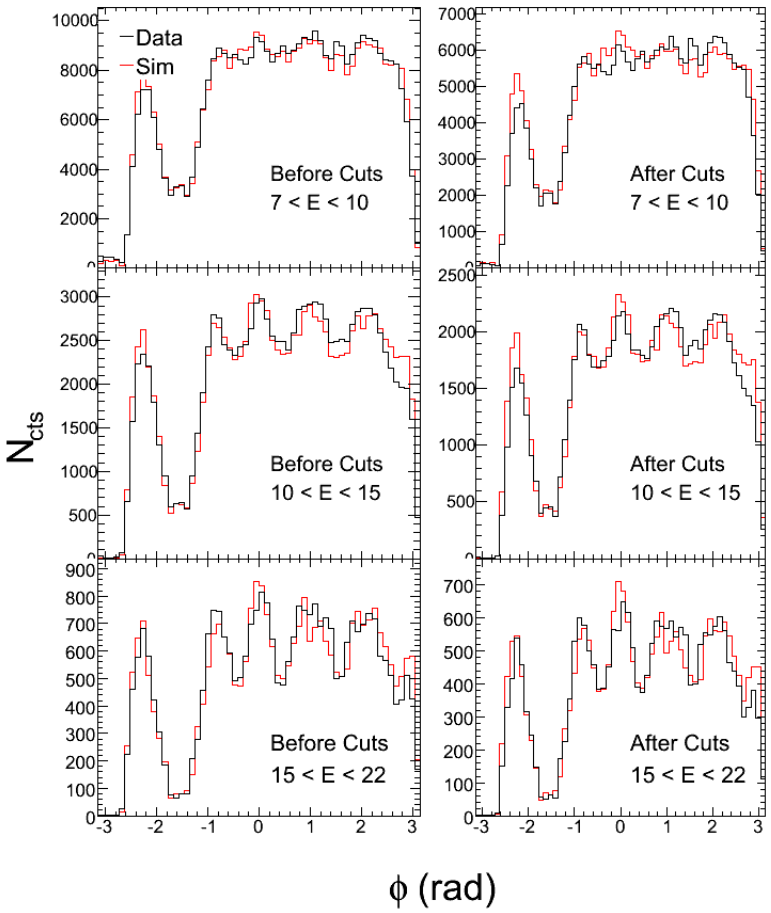

Figure 4.25: The ϕ distribution for the π^0 mass window in data (black) and p+p PYTHIA simulations (red). The counts are normalized in leftmost column, where the χ^2/NDF and dispersion cuts are not made. The rightmost column shows the distributions after all cuts are made.

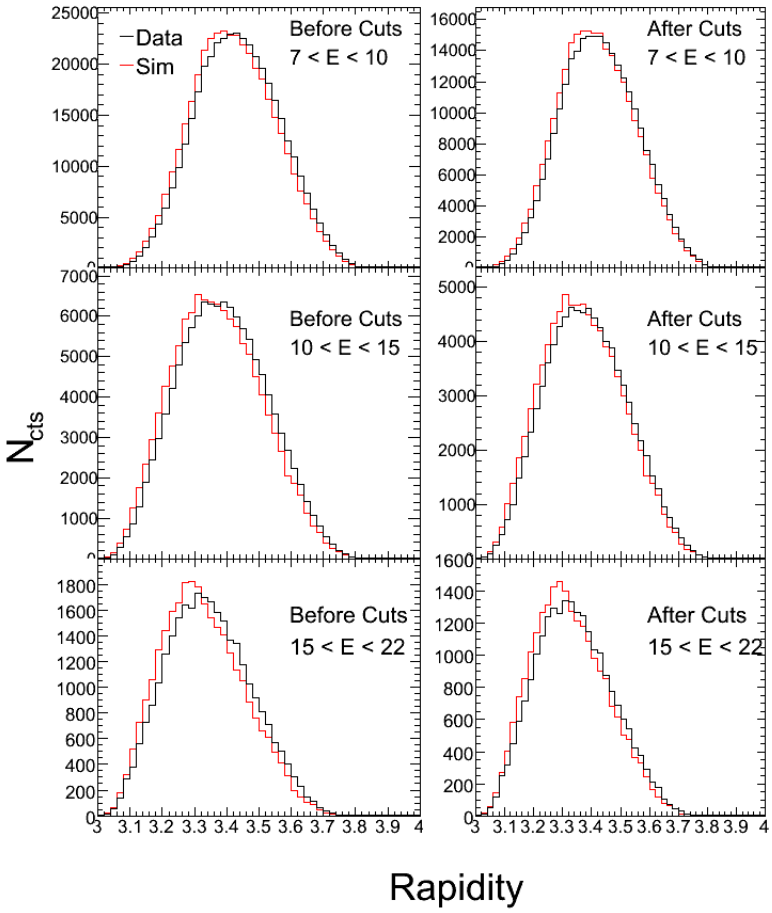

Figure 4.26: Pseudorapidity distribution for the π^0 mass window in data (black) and p+p PYTHIA simulations (red). The counts are normalized in leftmost column, where the χ^2/NDF and dispersion cuts are not made. The rightmost column shows the distributions after all cuts are made.

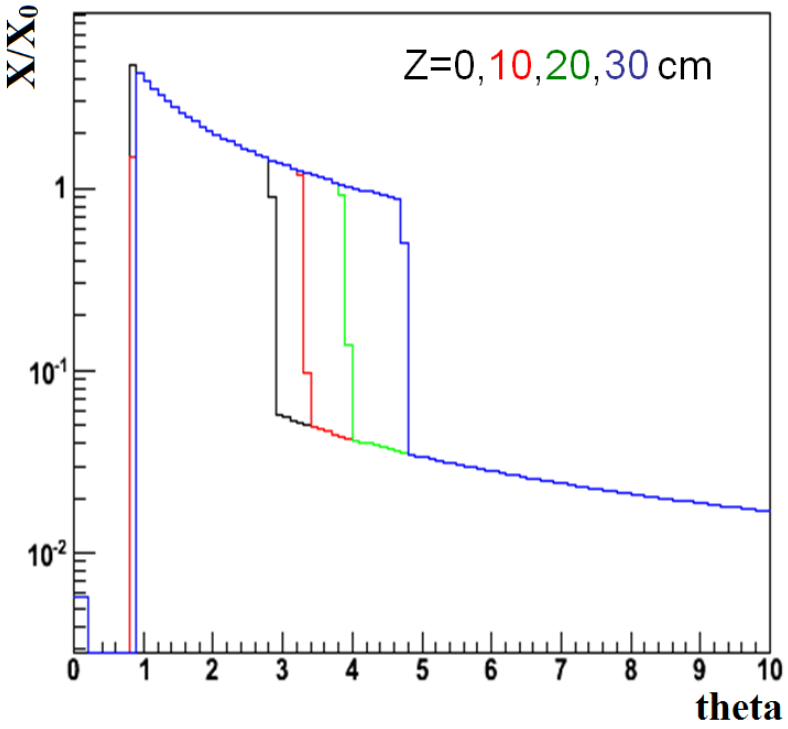

Figure 4.27: Mean number of radiation lengths traversed by a photon from the collision vertex to the MPC as a function of z-vertex and θ.

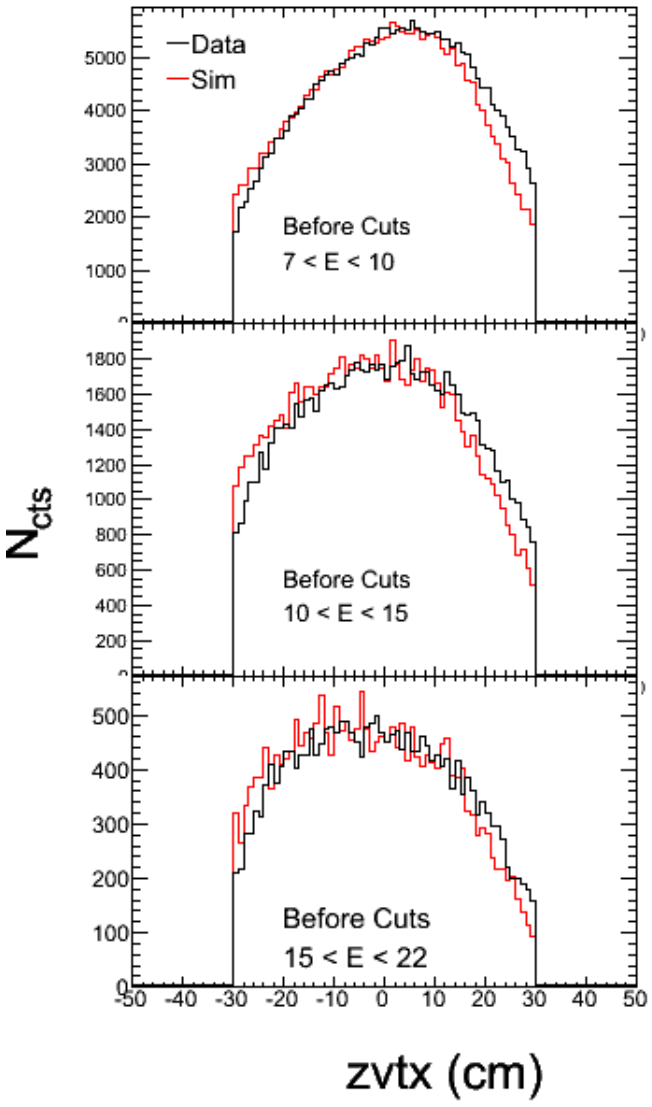

Figure 4.28: The z-vertex distribution comparison between p+p PYTHIA simulations and data in the π^0 mass window. The counts are normalized between data and simulation from -5 cm $< z_{vtx} < 5$ cm.

4.5.3 Yield Extraction

As described in section 4.4.1, we do not use mixed events to determine the background in the invariant mass spectrum but rather use the background shapes from simulation. We created a high-statistics sample of simulated p+p PYTHIA→PISA events in the MPC, and we use linear combinations of 1pp, 2pp, and 3pp events (where 3pp means we embed 3 p+p events into each other) to measure the invariant mass background. To estimate a systematic error on this procedure, we do not compare with mixed events, but rather vary the composition of our background to have different fractions of 1pp, 2pp, and 3pp events. For example, in Fig. 4.13 above we chose our background shapes by the linear combinations of the simulated distributions that minimize the contour. To gauge a systematic error, we vary the shape in a circle of radius 10% around the minimum value. We simultaneously vary the normalization range symmetrically around the nominal range of $0.25 - 0.3$ GeV/c^2 and form a distribution of the relative values of the yield. We conservatively estimate that our systematic error is 1.5 times larger than the Gaussian width of this distribution. The yield-extraction systematic errors for all centralities are plotted in Fig. 4.29.

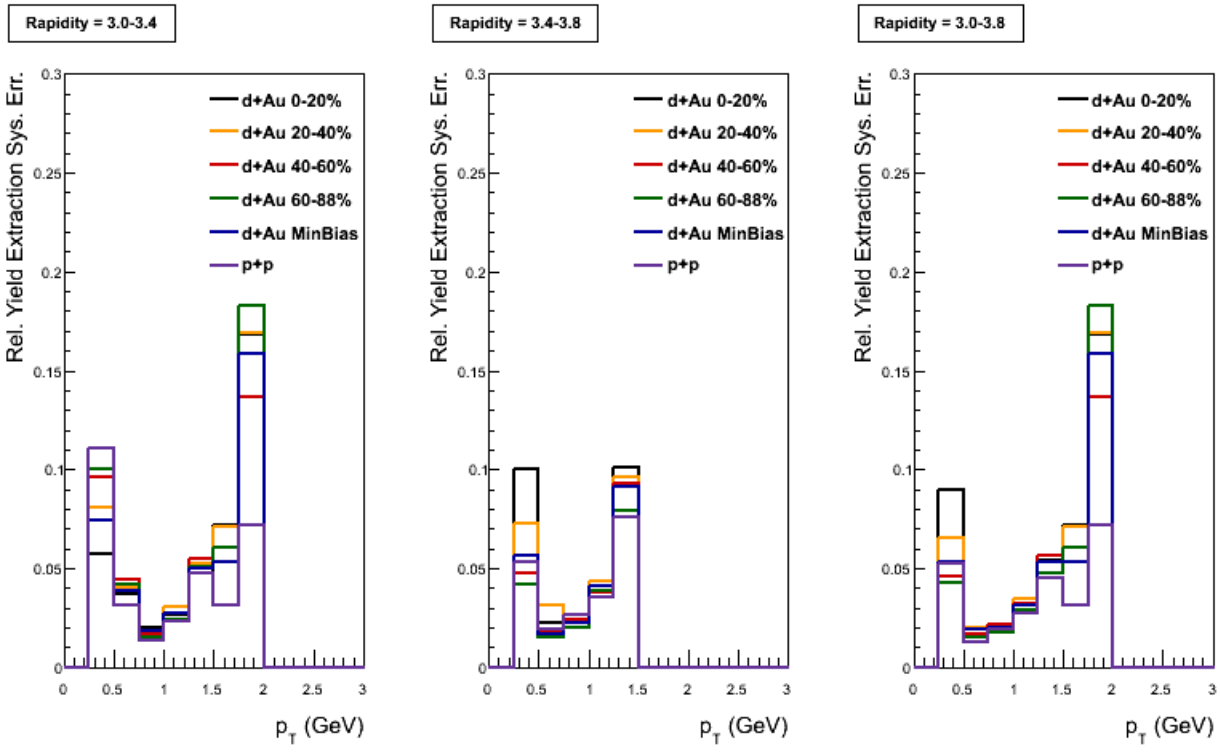

Figure 4.29: Relative systematic error on yield extraction in p+p and d+Au for all centralities and rapidity intervals.

4.5.4 Input Spectrum

The systematic error on the input spectrum would be zero if there were no smearing between different p_T and η bins. Since this is not the case, we must estimate an error for this. As described in the embedding efficiency section 4.4.2, we use an iterative procedure to calculate the correct p_T shape which consists of five steps. Then we correct the η shape, and repeat the total procedure six times. When we correct the η distribution, we do so using only three measured points as described in section 4.4.2. Thus, to calculate a systematic error, we use different input spectra and quantify how the different choice of input spectra affects our final result. In Figs. 4.30-4.31, we show the relative difference, $\frac{spec_i - spec_{meas}}{spec_{meas}}$, of the input spectra used in this study for all centralities considered. The input spectra used for systematic error evaluation are as follows:

rapidity itr6; pT itr5; fit5 Identical to the final result with the exception that a 5-point fit is used when correction the pseudorapidity distribution (see Fig. 4.18-b),

rapidity itr1; pT itr5; fit3 Identical to the final result with the exception that only one iteration is used to correct the pseudorapidity distribution,

pythia rapidity; pT itr5 We perform the five p_T-spectrum correction iterations and use the PYTHIA pseudorapidity spectrum,

+20% Increase the pseudorapidity ratio in eq. 4.20 by 20% for all p_T values, which effectively flattens the pseudorapidity distribution,

-20% Decrease the pseudorapidity ratio in eq. 4.20 by 20% for all p_T values, which effectively steepens the pseudorapidity distribution,

pure pythia weight We use p_T and η spectra obtained directly from PYTHIA.

To calculate a relative systematic error, we take half of the maximum deviation between our measured spectra and the spectra that are systematically varied. This error is plotted in Figs. 4.30-4.31 as the error bar in each bin, and in Fig. 4.32 as the value of the histogram.

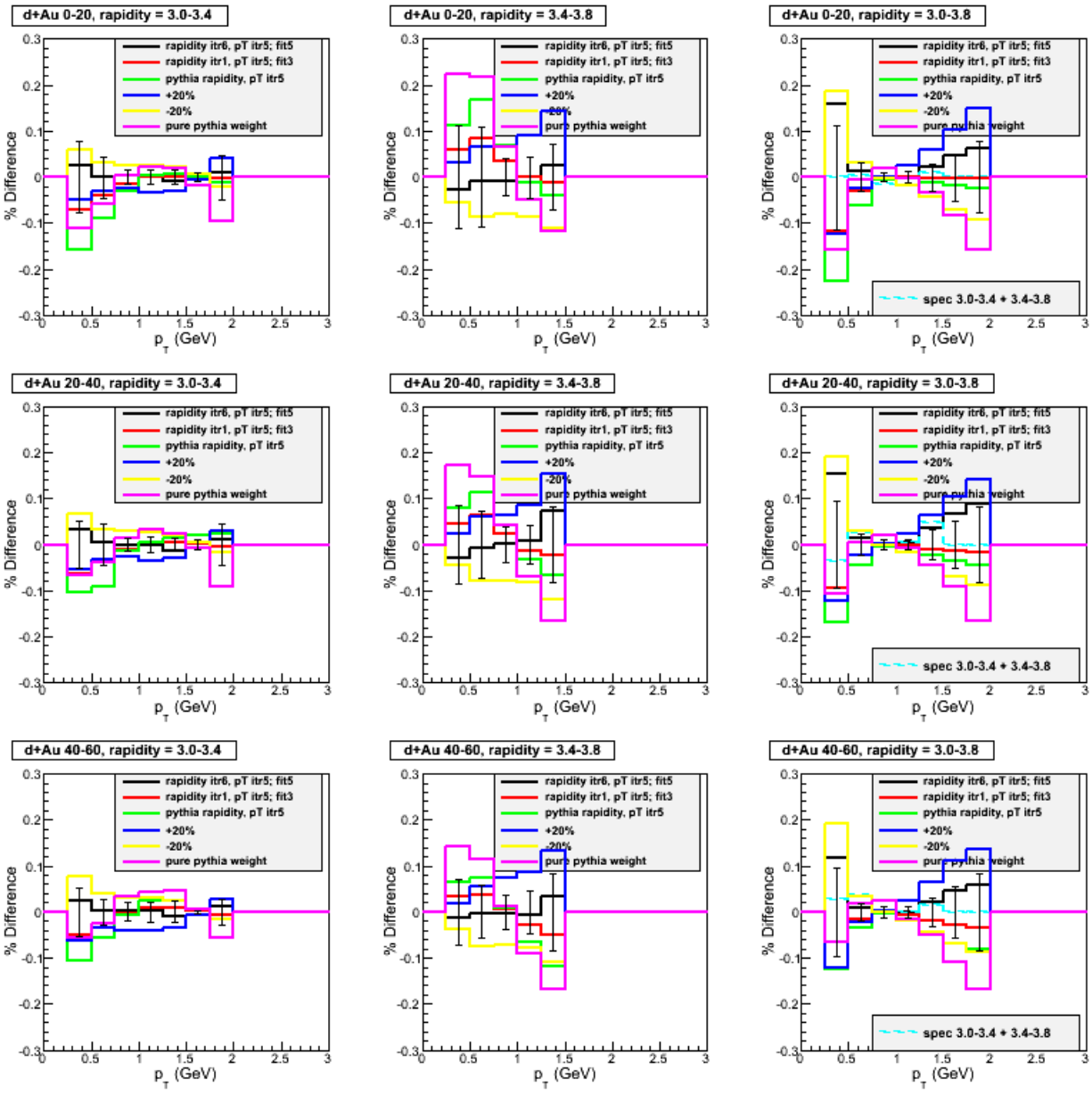

Figure 4.30: This shows relative differences of using different input spectra in the efficiency calculation for d+Au 0-20%, 20-40%, and 40-60%.

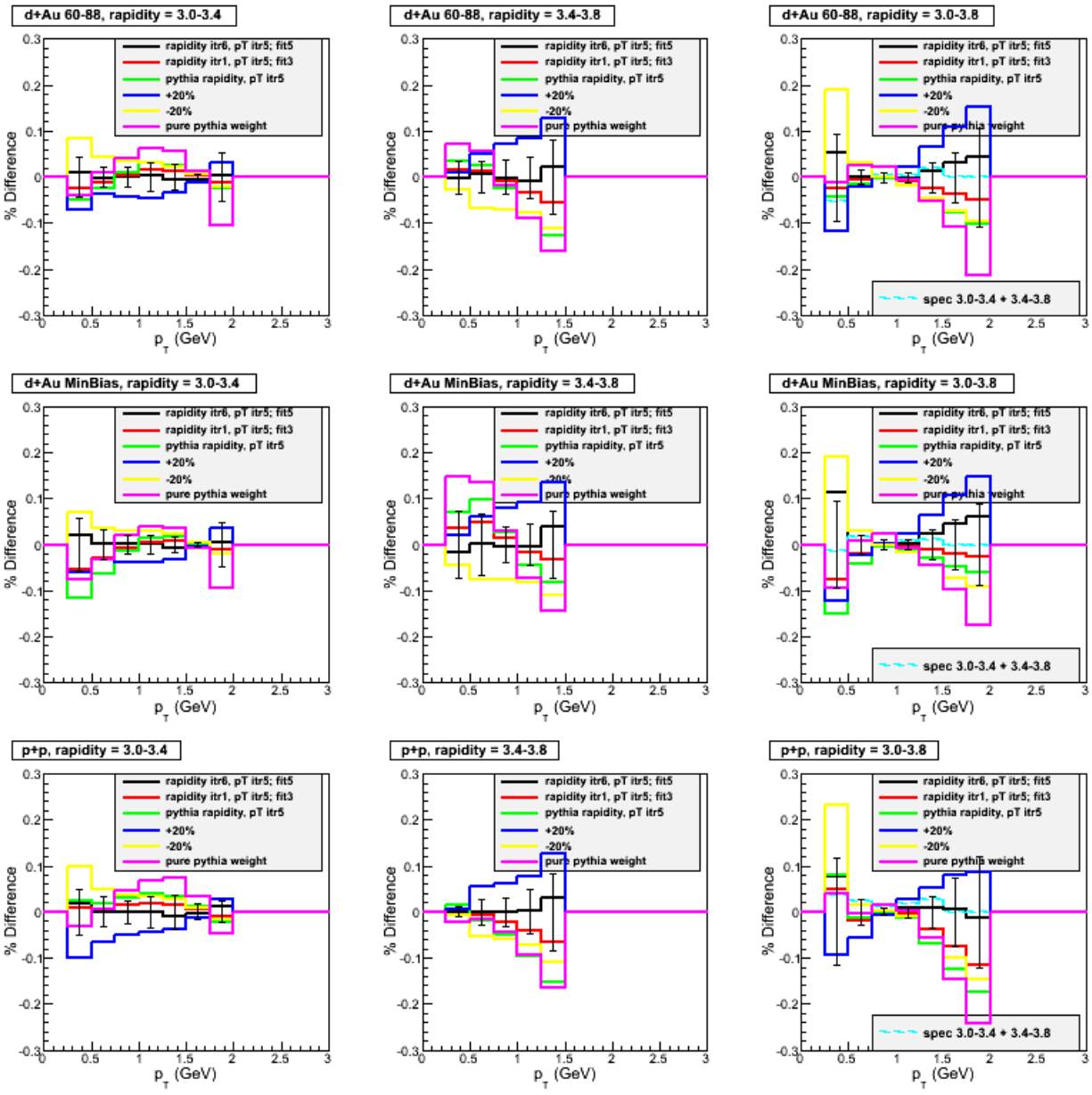

Figure 4.31: This shows relative differences of using different input spectra in the efficiency calculation for d+Au 60-88%, d+Au MinBias, and p+p MinBias.

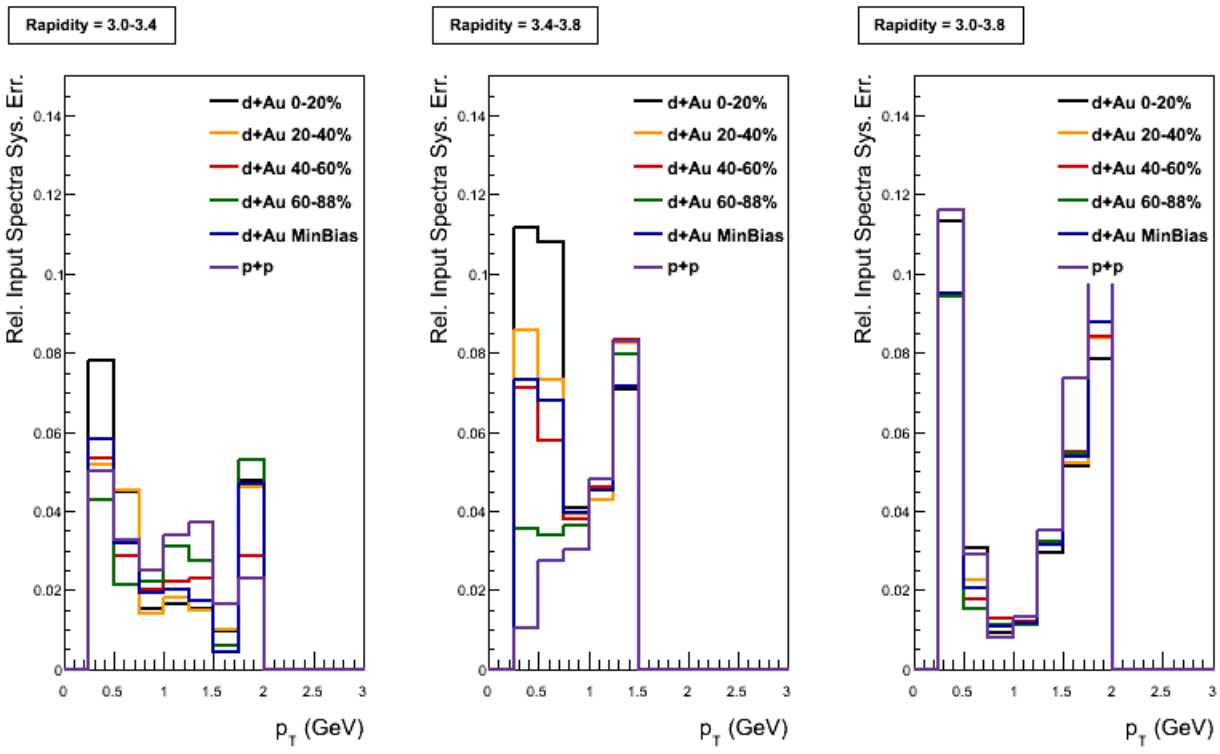

Figure 4.32: Systematic error from varying the shape of the input spectra.

4.5.5 Global Errors

The global systematic errors present in our measurement are those that correct out the triggering biases. For p+p collisions, we quote a global error of $\approx 9.7\%$ on our bias-correction factor, which is also the global error of both the π^0 invariant yields and differential cross section. For d+Au, global errors exist for both the bias-correction factors and $\langle N_{coll} \rangle$ values; these systematic errors as well as the errors for the ratio $C_{bias}/N_{\rm coll}$ were calculated in Ref. [63]. The systematic errors are summarized in Table 4.2 below; for the $R_{\rm dA}$ measurement we add the p+p global errors in quadrature with the d+Au errors.

Table 4.2: Global systematic errors for invariant yields and $R_{\rm dA}$.

	p+p	d+Au MB	d+Au 0-20%	d+Au 20-40%	d+Au 40-60	d+Au 60-88
σ_{Cbias}/C_{bias}	0.097	0.001	0.011	0.006	0.016	0.053
$\sigma_{Rda}/R_{\rm dA}$	-	0.103	0.108	0.105	0.110	0.123

4.6 Results

We present the results for the invariant yields in p+p and d+Au in the 0-20%, 20-40%, 40-60%, 60-88% and 0-100% centrality bins. We then proceed to calculate the values of the p+p cross section as well as the values of R_{dA} for all centrality bins in question.

4.6.1 MPC π^0 Invariant Yields

The invariant yields (see eq. 4.1) for all d+Au centrality classes and for p+p are shown in Fig. 4.33. The tabulation of the invariant yields and relative errors can be found in Tables B.4-B.6.

4.6.2 MPC π^0 Cross Section in p+p

We calculate the p+p cross section by simply multiplying the invariant yields by the p+p inelastic cross section, $\sigma_{pp} = 42.2$ mb. The results for this are shown in Fig. 4.34. The tabulated values and relative errors are available in Tables B.7-B.9. Please note that for the yields and p+p cross section, the π^0 branching ratio is accounted for in the efficiency calculation. Also, no feed-down correction is applied. For reference, we also plot the BRAHMS π^- data for $\eta = 2.95$, 3.3 in Fig. 4.35. One would expect our data to be very similar to that of BRAHMS, and a very reasonable match is indeed seen.

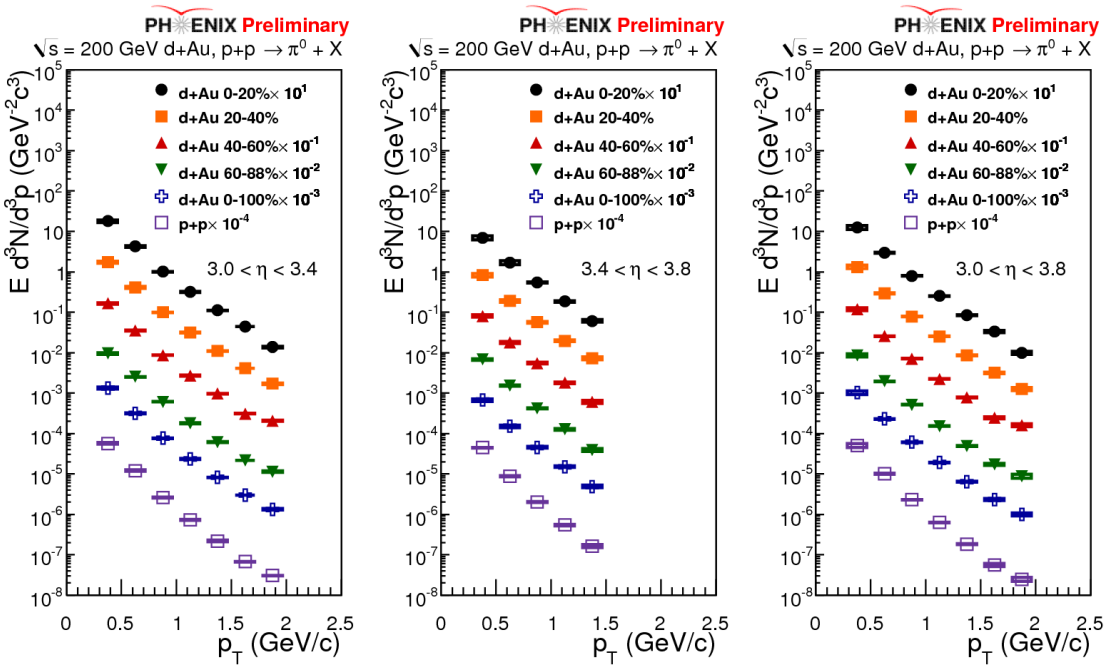

Figure 4.33: Invariant yields in p+p and d+Au for all centralities and rapidity intervals.

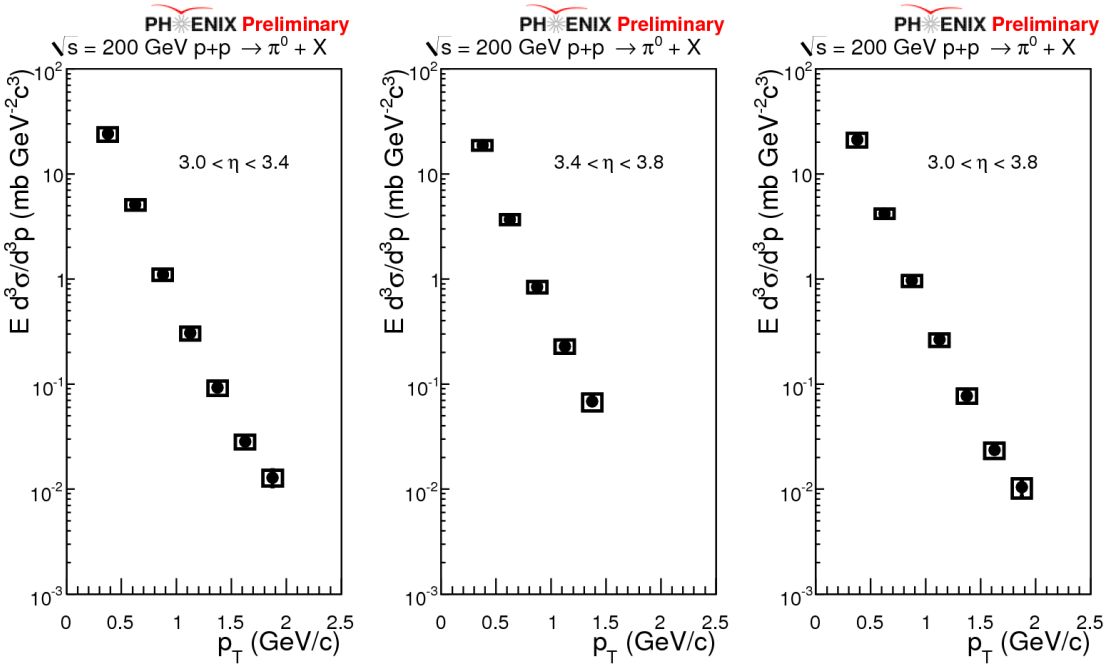

Figure 4.34: Differential cross section for $p + p \rightarrow \pi^0$ for all rapidity intervals.

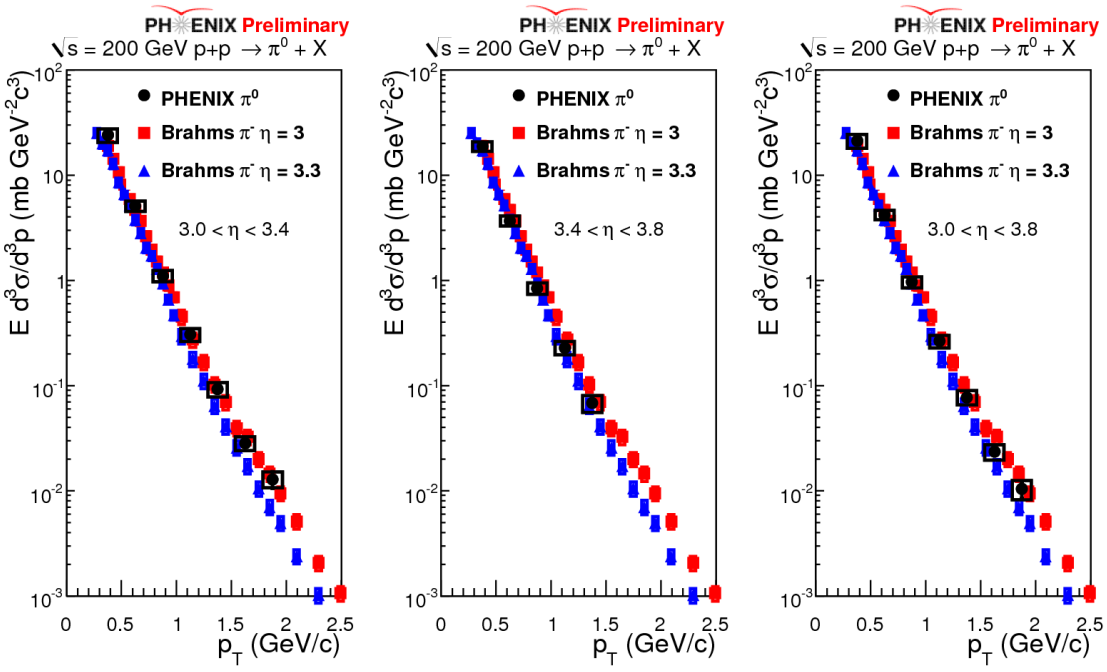

Figure 4.35: Differential cross section for $p + p \rightarrow \pi^0$ for all rapidity intervals. The PHENIX results for π^0 mesons are compared to the BRAHMS results for π^+ and π^- mesons.

4.6.3 MPC π^0 $R_{\rm dA}$

The nuclear modification factor is simply defined as the ratio of the invariant yields in d+Au over p+p scaled by $1/N_{coll}$ (see eq. 4.4). In Fig. 4.36, we show the values of R_{dA} for all centralities and rapidities. R_{dA} is largely suppressed in the most central collisions, but is much less suppressed (if at all) in peripheral collisions. Also, one can easily see increasing suppression as we go from the lower rapidity bin of $3.0-3.4$ to the higher rapidity bin of $3.4-3.8$. The tabulated values of $R_{\rm dA}$ along with their relative errors are available in Tables B.7-B.9, while the $N_{\rm coll}$ values can be found in Table 4.1.

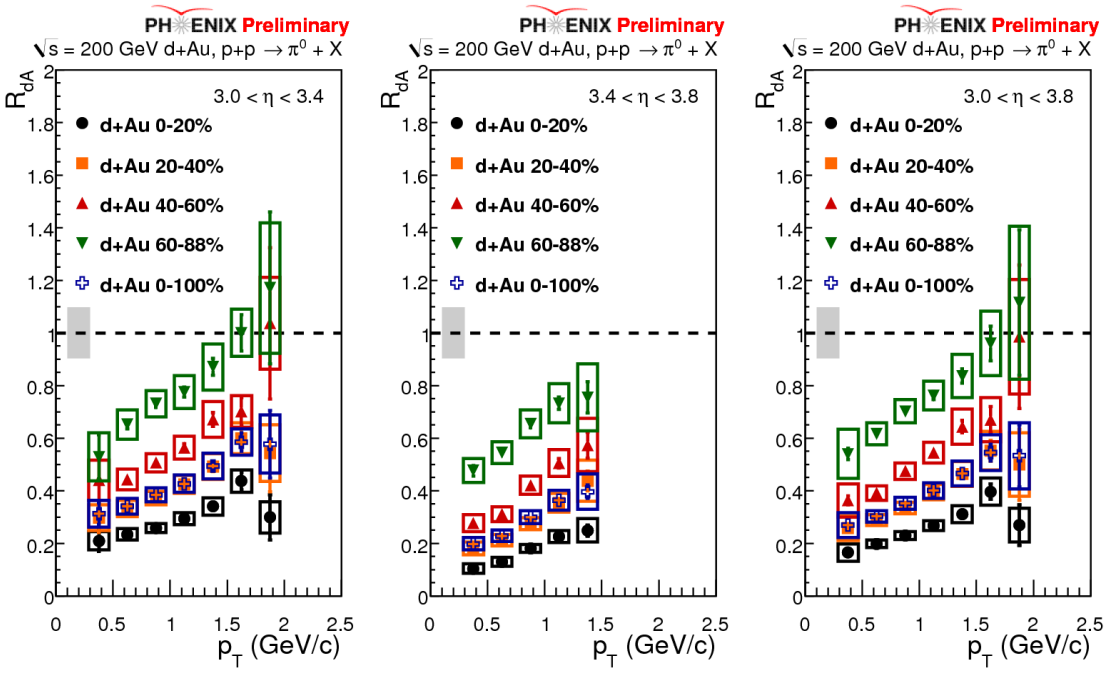

Figure 4.36: R_{dA} for all centralities and rapidity intervals. The systematic error on each point is shown by the open boxes. The gray error band at the left on each panel represents a global systematic scale error of 9.7%. Additional centrality-dependent systematic errors of 7.5%, 5.1%, 4.1%, and 4.8% for the peripheral to central bins, respectively, are not shown.

Chapter 5

$\Delta\phi$ Correlation Functions

5.1 Overview

Azimuthal angle correlation functions are the distributions of angular differences between pairs of particles in the transverse plane (or ϕ-direction) relative to the beam-axis (z). Angular correlations at $\Delta\phi = \pi$ are a corollary of momentum conservation of the outgoing jets from a simple $2 \rightarrow 2$ hard scattering picture.

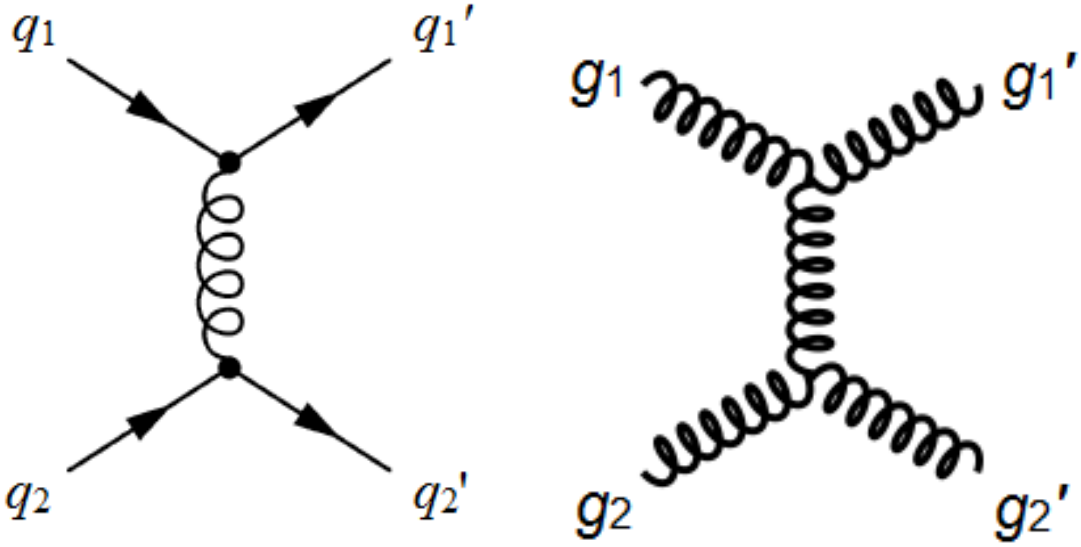

(a) (b)

Figure 5.1: Example leading-order QCD processes wherein a virtual gluon is exchanged in the scattering of **a.)** two quarks, **b.)** two gluons.

Example leading-order processes are shown in Fig. 5.1 depicting the scattering of two quarks (a) and two gluons (b) via virtual gluon exchange. At leading order in QCD, the incoming partons have no transverse momentum and hence the outgoing partons have opposing p_T vectors. The partons hadronize into jets of particles; particles from opposing jets are therefore expected to be nearly back-to-back in ϕ, and hence a

peak at $\Delta\phi = \pi$ appears in the correlation functions. Particles from the same jet have very similar angles, giving rise to a correlation at $\Delta\phi = 0$. This picture is applicable for the majority of the jets produced at RHIC energies, and allows one to measure quantities sensitive to di-jet production without directly observing jets. It should be noted that not all pairs of particles will be correlated (e.g. soft production mechanisms, multi-parton interactions); these produce a flat pedestal upon which the correlated signals sit.

The raw, measured $\Delta\phi$ distribution (termed foreground) can be described by the following expression:

$$\frac{dN^{measured}(\Delta\phi)}{d\Delta\phi} = acc(\Delta\phi) \times (jet(\Delta\phi) + bg(\Delta\phi)), \tag{5.1}$$

where $acc(\Delta\phi)$ is the pair acceptance function (defined below), $bg(\Delta\phi)$ is the flat combinatoric pedestal from uncorrelated particle production, and $jet(\Delta\phi)$ is the jet component of the $\Delta\phi$ distribution. The pair acceptance function is defined by the convolution of the single-particle ϕ distributions of the two particles, $f(\phi_1)$, $g(\phi_2)$. Given that $\Delta\phi = \phi_2 - \phi_1$, one formal expression for the acceptance function is

$$acc(\Delta\phi) = \int_0^{2\pi} d\phi_1 f(\phi_1) g(\phi_2) = \int_0^{2\pi} d\phi_1 f(\phi_1) g(\Delta\phi + \phi_1). \tag{5.2}$$

The correlation function (CF) is defined by dividing out the acceptance from the foreground distribution, or

$$CF = \frac{1}{acc(\Delta\phi)} \times \frac{dN^{measured}(\Delta\phi)}{d\Delta\phi}. \tag{5.3}$$

Correlation functions have been used extensively in PHENIX and STAR to understand the modification of di-jet production in the presence of a dense, final-state medium – the quark-gluon plasma. One of the most significant observations was the apparent disappearance of the awayside peak in Au+Au collisions [129], as seen in Fig. 5.2. The most prevalent interpretation is that one jet escapes the medium (produced near surface of medium), but that the opposing parton (in $2 \rightarrow 2$ picture) loses energy as it traverses in the opposite direction through the bulk of the colored medium. The energy losses change the direction of the parton and cause an angular decorrelation.

In addition to the QGP effects observed in the correlations, it was also thought that Color Glass Condensate (CGC) effects might cause decorrelations in the awayside peak, which should be observable in d+Au collisions. The idea behind the CGC decorrelations is that the Au-nucleus has a parton density that is enhanced by its large size; a parton from the deuteron interacts with multiple low-x gluons from the CGC. What appears is one jet and many scattered gluons. This is the so-called monojet picture of correlations in the CGC framework [2]. The monojet effect is supposed to turn on as one progresses to smaller values of

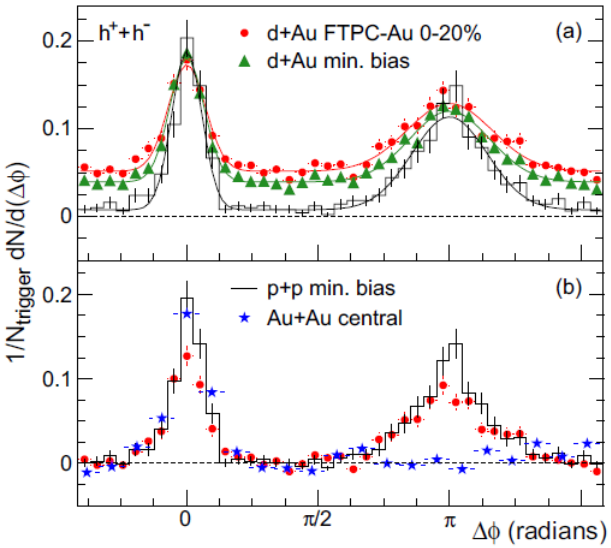

Figure 5.2: Azimuthal two-particle correlations **(top)** for d+Au central compared to d+Au minimum bias and **(bottom)** for Au+Au central compared to p+p minimum bias. The disappearance of the awayside peak in the Au+Au correlations does not occur in d+Au, indicating that a final-state effect is responsible [129].

gluon momentum fraction x in the Au-nucleus, and would predict both a *broadening* in the awayside peak width (as determined by a Gaussian fit) as well as a *suppression* in the integral yield over the awayside peak. It is thus preferable to have both jets in the forward direction (see x_2 in eq. 1.15) in order to probe small x. Previous measurements have been performed with both hadrons detected at midrapidity; it was found that little decorrelation exists in this rapidity range [130]. In this thesis, we make two azimuthal correlation measurements, the so-called *mid-forward* correlations (particles at mid and forward rapidity) and the *forward-forward* correlations (both particles at forward rapidity). In this way we scan different ranges in Bjorken-x and search for the turn on of suppression and broadening effects in two-particle correlations. These measurements also serve to provide an understanding of the suppressed $R_{\rm dA}$ observed at forward rapidity.

5.2 Quantifying Suppression

We have thus far defined the correlation functions and discussed why they are important, but have yet to describe specifically how they can be used to show that a suppression or broadening exists in the awayside peak. As discussed in section 1.7, the correlation functions can be modeled as two Gaussian peaks (at

$\Delta\phi = 0,\ \pi$) sitting atop a constant pedestal. To understand the di-jet properties, we quantify the yield and width of the awayside peak. The simplest method is to find a flat normalization region in between the nearside and awayside peaks and assume that this is the level of the pedestal; this method is termed ZYAM or Zero-Yield at Minimum [131]. Then one can simply use a two-Gaussian fit with a fixed pedestal level to extract the awayside peak properties. Another method is to allow the pedestal level to be determined from a fit. The width can be directly read off from the fits to compare between p+p and d+Au. The yield is also taken from the fit (or an integral over the awayside bins), but one must be careful to normalize the yield and correct for detector inefficiencies. In this vein, we define a quantity termed "conditional yield", CY, that is essentially the area of the awayside peak normalized to the number of "trigger" particles and corrected for the "associate" particle inefficiency. Trigger and associate are appellations given to the two particles that are in fact interchangeable; however, it is usually understood that the trigger particle is the higher-p_T particle and indicates that a jet was produced. The conditional yield can then be interpreted as the yield of correlated particles in the awayside peak that were produced given that a jet was produced with $\langle\Delta\phi\rangle = \pi$.

Thus the conditional yield is extracted by taking

$$CY = \frac{1}{N_{trig}\epsilon_a}\int_0^{2\pi} d\Delta\phi(CF_{awayside}(\Delta\phi) - bg(\Delta\phi)) \tag{5.4}$$

where N_{trig} is the number of trigger particles measured and ϵ_a is the associate particle efficiency (see section 4.4.2). It is understood here that $CF_{awayside}$ is only the peak at $\Delta\phi = \pi$ on top of the pedestal and does not include any contributions from the nearside peak. One advantage of using the conditional yield as opposed to a fully-corrected yield is that one does not need to correct for the trigger particle efficiency in the calculation.

To compare d+Au to p+p, we form the correlated di-hadron nuclear modification factor I_{dA}, which is defined to be the ratio of the conditional yield in d+Au to p+p, or

$$I_{dA} = \frac{CY_{dA}}{CY_{pp}}. \tag{5.5}$$

Additionally, we form the nuclear modification factor called J_{dA}, which is

$$J_{dA} = I_{dA} \times R_{dA,trigger}, \tag{5.6}$$

where $R_{dA,trigger}$ is measured for the trigger particle. The reason we define J_{dA} is that it is essentially the

correlated two-particle analogue of R_{dA}, as

$$J_{dA} \equiv 1/N_{coll} \frac{(N_{pair}/N_{evt})_{dA}}{(N_{pair}/N_{evt})_{pp}} \Longleftrightarrow 1/N_{coll} \frac{(N_{sngl}/N_{evt})_{dA}}{(N_{sngl}/N_{evt})_{pp}} \equiv R_{\rm dA}, \tag{5.7}$$

where $N_{\rm coll}$ is the number of binary collisions, N_{pair} is the corrected number of correlated pairs in the awayside peak, N_{evt} is the number of inelastic events, and N_{sngl} is the single particle yield for the definition of $R_{\rm dA}$.

Thus we see that $J_{\rm dA}$ is the ratio of the fully-corrected correlated pair yield per binary collision of the awayside peak between d+Au and p+p; it can be interpreted as the di-jet nuclear modification factor analogous to $R_{\rm dA}$ for single particles. Another advantage of $J_{\rm dA}$ is that the value does not depend upon the choice of trigger-particle rapidity, whereas $I_{\rm dA}$ does. In fact, it is impossible for $I_{\rm dA}$ with a forward trigger to be the same as $I_{\rm dA}$ with the midrapidity trigger given that the value of $R_{\rm dA}$ in the two regions differ.

5.3 Experimental Method

Particles are first identified as described sections 4.2, 6.1, 6.3 and buffers containing these particles are filled; each particle object holds position, energy, p_T, and ϕ information. After the buffers are filled, the order of the particles is randomized to eliminate bias from the particle ordering.

To construct a correlation function, two particle buffers are first selected (e.g. midrapidity EMCal π^0's and MPC π^0's). For each same-event pair, a histogram is filled with all values of $\Delta\phi$. If the two detectors had uniform 2π coverage in azimuth, no corrections for the two-particle acceptance $acc(\Delta\phi)$ (eq. 5.2), would be necessary. However, because there are essentially two $\pi/2$ acceptance holes that exist at midrapidity (see Fig. 2.2) and the useful MPC ϕ-acceptance is not uniform, it is necessary to calculate the two-particle acceptance. In principle this can be done using the single-particle acceptance distributions (from eq. 5.2), but complications can arise if one uses particles from the same detector and one has to make a pair cut not in the single-particle ϕ distributions; additionally one needs to keep track of the z-vertex and centrality dependencies of the ϕ-distributions. Another equivalent technique is to form mixed-event pair acceptance distributions, wherein the acceptance is calculated by measuring $\Delta\phi$ of particle pairs from different events.

In what follows, we give a brief description of the event mixing. Event-mixing objects are created; these contain the particle information from the present event in a buffer plus a fixed-size queue of past-event buffers ordered sequentially. Once each queue is filled to capacity, the event mixing ensues; we calculate $\Delta\phi$ between the particles on the current-event buffer for the trigger particle (e.g. central arm particle) and

the event-mixing queue of the associate particle (e.g. MPC π^0). The filling of the queue is FIFO (first-in, first-out) wherein the events from current event are added to the front of the queue and the events at the back of the queue are discarded. We mix events only when they fall within the same centrality and z-vertex bin. Within the centrality bins (0-20%, 20-40%, 40-60%, and 60-88%), we only mix events that are within 4-5% of each other, depending upon the centrality bin in question. The z-vertex bins are 3 cm wide, and we accept only events between $\pm$30 cm. The capacity of each queue is based upon the multiplicity of the associate particle and thus depends upon the centrality binning.

Once an acceptance function is measured, its area is normalized to 2π. This choice of normalization ensures that the normalization of the correlation function (eq. 5.3) does not depend upon the $\Delta\phi$-binning and is defined per-unit $\Delta\phi$.

Chapter 6

Mid-Forward Correlations

The first set of correlation functions we shall discuss are those wherein the trigger particle is a midrapidity hadron ($h^{\pm}$ or π^0), and the associate particle is a forward rapidity π^0 detected in the MPC. The two particles are separated in rapidity by approximately 3.3 rapidity units; jet cones have a radius of ≈ 1 unit in rapidity, and hence no peak appears at $\Delta\phi = 0$ in the correlation functions. No azimuthal anisotropy due to elliptic flow contributions [132] is expected because QGP is not formed in d+Au nor p+p collisions. Hence we only expect to have an awayside peak at $\Delta\phi = \pi$ atop a constant background.

As previously mentioned, these correlation functions were predicted to be a strong signature of CGC early on [2], though recently there has been skepticism [85, 133] as to whether CGC effects should be present given the moderately small values of $x \approx 10^{-2}$ of expected in the mid-forward system.

6.1 Charged Hadron Identification

Charged hadrons are identified for $0.5 < p_T < 4.7$ GeV/c by requiring tracks in the X-, U-, and V-layers of the PHENIX DCs and by requiring that no Cherenkov signal is present in the RICH. Electrons have a Cherenkov threshold in CO_2 of ≈ 18 MeV that is much lower than that for the lightest charged hadron, the $\pi^{\pm}$, of 4.7 GeV/c, and hence requiring a RICH veto filters electrons from the sample. As an additional criterion to reduce ghost tracks a match with the PC3 detector subsystem is also required. The uncorrected $h^{\pm}$ spectra for the d+Au centrality classes and p+p is shown in Fig. 6.1. One can see that the hadron yields increase with increasing $N_{\rm coll}$ of the centrality class in question.

6.2 Charged Hadron Data Quality

As with the MPC, a number of QA-metrics are employed to ensure data quality. We looked at the run-by-run variations in particle yields as well as looking at the mixed-event two-particle $\Delta\phi$ acceptance between hadrons and MPC π^0's. In Fig. 6.2, we show the $h^{\pm}$ yields per minimum-bias event as a function of run

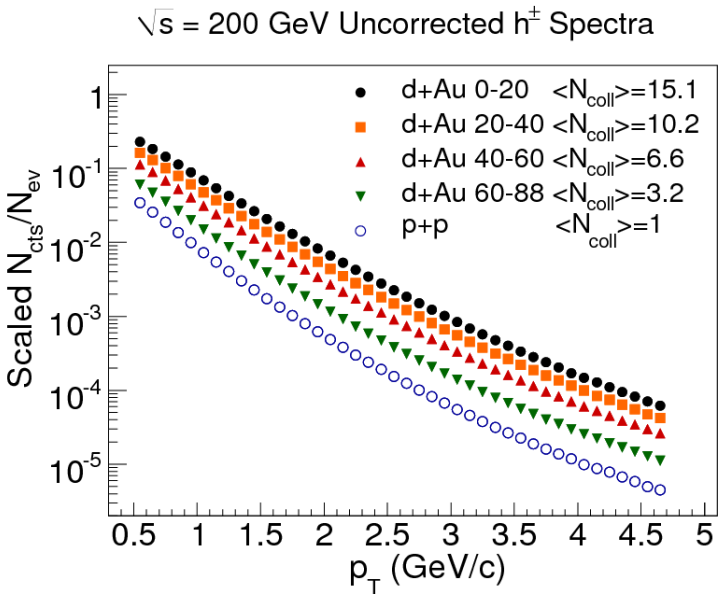

Figure 6.1: The uncorrected $h^{\pm}$ p_T spectrum for p+p and all d+Au centrality classes at midrapidity, $|\eta| < 0.35$.

number with an acceptance correction applied (the acceptance varies mainly due to inoperative regions of the DCs [134]). We exclude runs that have yields outside the red bands.

Because the midrapidity $h^{\pm}$ ϕ-acceptance changes over time (see Fig. 6.3), we calculate two-particle acceptance functions for rungroups with similar acceptances (this is an issue that does not affect the MPC data), as indicated by the blue bands in Figs. 6.4, 6.5. Here we show the p+p and d+Au two-particle acceptance χ^2/NDF for different rungroups, which have the blue lines as the rungroup boundaries. The groups shown here are also the rungroups used for event mixing. We make a χ^2/NDF cut of about $2.5 - 3$ for all plots.

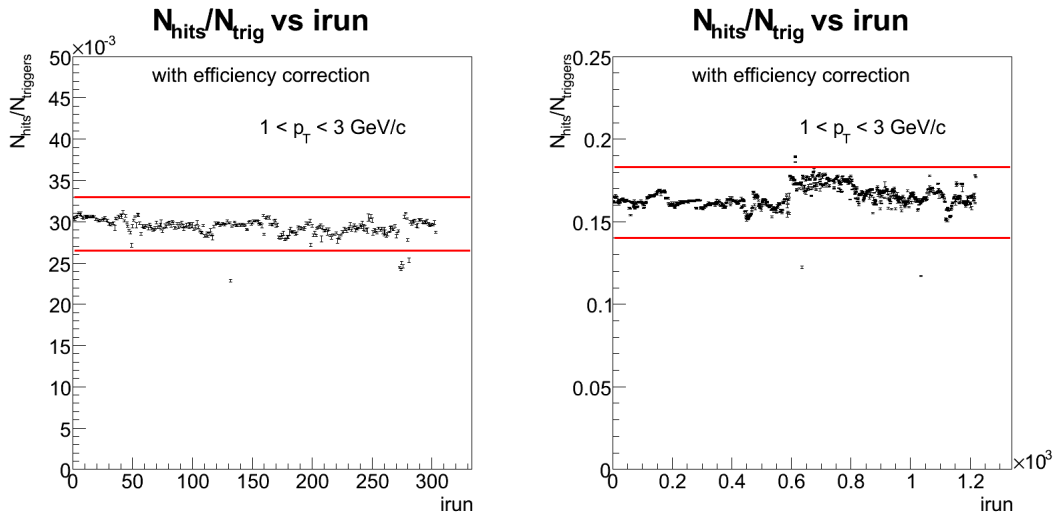

(a) (b)

Figure 6.2: The corrected central-arm $h^{\pm}$ yield per minimum-bias event versus run number for **a.)** p+p, **b.)** d+Au 60-88%. The red lines indicate the stability cuts applied for data quality.

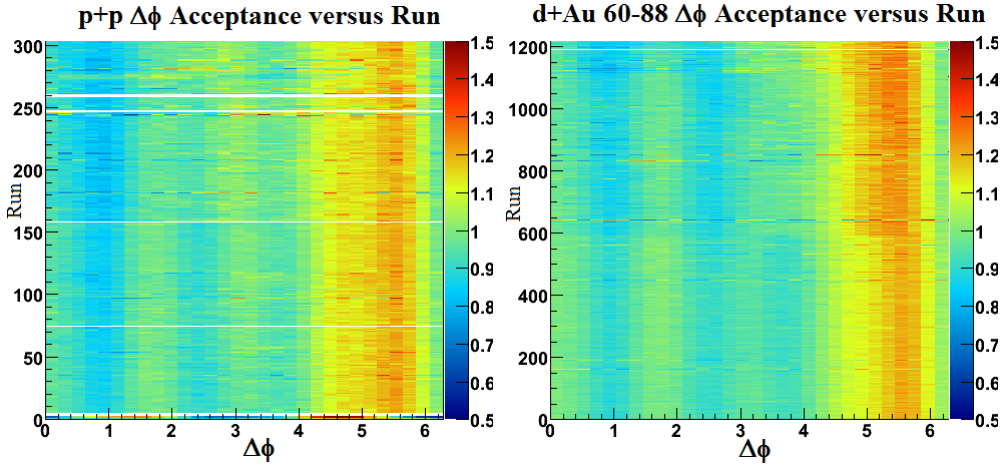

(a) (b)

Figure 6.3: The central-arm $h^{\pm}$/MPC-π^0 $\Delta\phi$ mixed-event acceptance functions versus run number for **a.)** p+p, **b.)** d+Au 60-88%. The color scale represents the value of the acceptance, which has been normalized to have an average value of 1 for a given run.

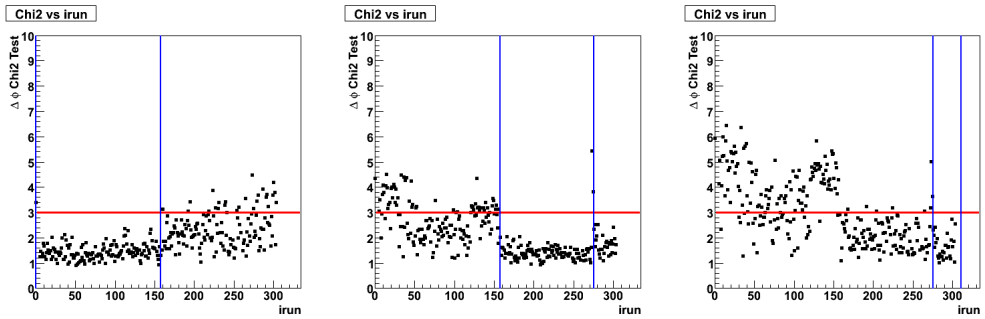

(a) (b) (c)

Figure 6.4: The χ^2/NDF for the central-arm $h^{\pm}$/MPC-π^0 $\Delta\phi$ mixed-event acceptance functions for three different run ranges in p+p. The run range for each plot is indicated by the bounding blue vertical lines, while runs that have a χ^2/NDF above the red line are excluded from analysis.

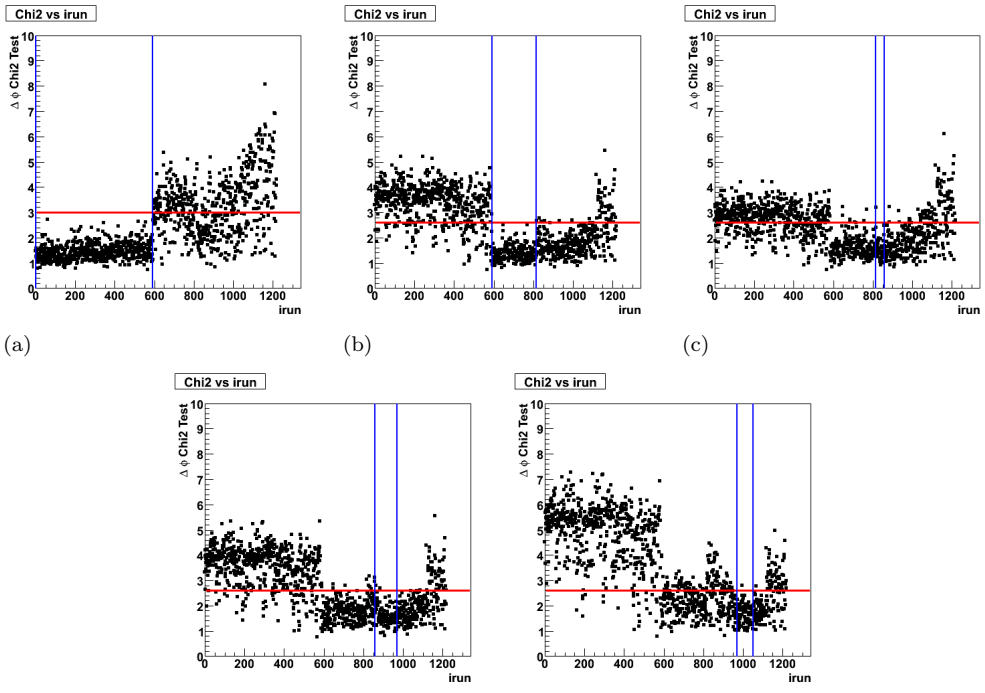

(a) (b) (c)

(d) (e)

Figure 6.5: The χ^2/NDF for the central-arm $h^{\pm}$/MPC-π^0 $\Delta\phi$ mixed-event acceptance functions for five different run ranges in d+Au. The range for each plot is indicated by the bounding blue vertical lines, while runs that have a χ^2/NDF above the red line are excluded from analysis.

6.3 EMCal π^0 Particle ID

6.3.1 Photon-Candidate Identification

We only use EMCal π^0's from the photon-triggered dataset; specifically, we require that at least one of the two clusters used is in the EMCal supermodule (12×12 group of towers read out the by the same Front-End Module) responsible for firing the trigger. Our photon-candidate clusters also have an electromagnetic shower-shape and an energy above a minimum threshold. Below, we list the specific photon-candidate identification cuts.

Minimum Cluster Energy $E_{PbGl} > 0.2$ ($E_{PbSc} > 0.1$) GeV.

Shower-shape I $\chi^2/NDF < 3.0$.

Shower-shape II $prob_{photon} > 0.02$ (This maps directly to a χ^2/NDF cut; it represents the fraction of photons rejected by the cut. In this case, we would expect to reject the 2% sample of photons that have the largest χ^2/NDF.).

6.3.2 Neutral-Pion Candidates

For π^0 candidates (cluster pairs that go into the di-cluster invariant mass spectra in the mass window of $0.1 - 0.18$ GeV/c^2), we first specify that both clusters are in the same sector of the calorimeter. We then form the di-cluster invariant mass spectra from clusters that pass the following pair cuts:

Energy asymmetry $\alpha = \frac{|E_2 - E_1|}{E_1 + E_2} < 0.8$,

Pair energy $E_1 + E_2 > 2.5$ GeV.

In Fig. 6.6, we show sample invariant mass spectra (black) of pairs that pass the above listed cuts for p+p, d+Au 0-20, and d+Au 60-88 with $4.0 < p_T < 7.0$ GeV/c. The red curve is the normalized, event-mixed background which we subtract to obtain the yields. The normalization occurs in the ranges of $m_{inv} = 0.065 - 0.09$ GeV/c^2 and $0.19 - 0.22$ GeV/c^2. Many analyses in PHENIX have used a 3^{rd} degree polynomial normalized to the areas outside the π^0 mass window for the yield extractions; we have found the difference between the polynomial and mixed-event backgrounds is $\lesssim 1\%$ (which is far less than the other systematic errors for the measurement) for all p_T bins and centrality classes, and hence using the event-mixed background was deemed acceptable. Moreover, we only use the EMCal π^0 yields in $I_{\rm dA}$ and $J_{\rm dA}$, and thus the majority of the yield-extraction systematic error will cancel in the ratio between d+Au and p+p.

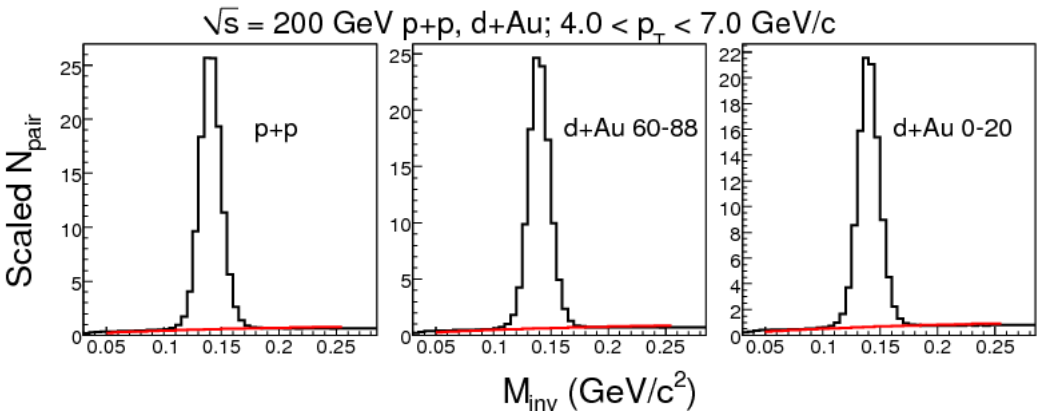

Figure 6.6: Sample EMCal invariant mass spectra (black) and mixed-event background (red) for p+p, d+Au peripheral, and d+Au central collisions showing the π^0 peak around $m_{inv} = 0.135$ GeV/c^2.

6.4 EMCal π^0 Run QA and Warnmap

The EMCal-π^0 QA-metrics are very similar to those used in the MPC in section 4.2, and they are shown below:

1. Create warnmap (Fig. 6.7),
2. Plot mean and width of π^0 invariant mass peak as a function of segment number and cut out runs outside 1% of the mean value (Fig. 6.8),
3. Extract yields through background subtraction (here we use mixed events) and plot N_{π^0}/N_{events} as a function of segment number,
4. Plot two-particle EMCal/MPC $\Delta\phi$ acceptance function versus segment,
5. Plot χ^2/NDF for the acceptance function (see eq. 4.8) and cut out runs where the two-particle $\chi^2/NDF > 3$ (Fig. 6.10).

We next expound upon a few of the items listed above. First, the EMCal warnmap determination is simpler than in the MPC because we expect a nearly uniform hit rate across all towers at midrapidity, which was not the case at forward rapidity (see Fig. 4.2). Because of the large number of towers and the uniform grid structure of the EMCal, we can also mask out towers that surround bad ones and exclude the edges without a significant loss in acceptance. In Fig. 6.7, we show the towers that have been masked in our analysis in both p+p and d+Au. We employ a similar procedure as in the MPC wherein we look at the

distribution of $\ln(N_{hits}/N_{events})$ and exclude outliers. The resulting warnmap masks out $\approx 25\%$ of the total EMCal acceptance.

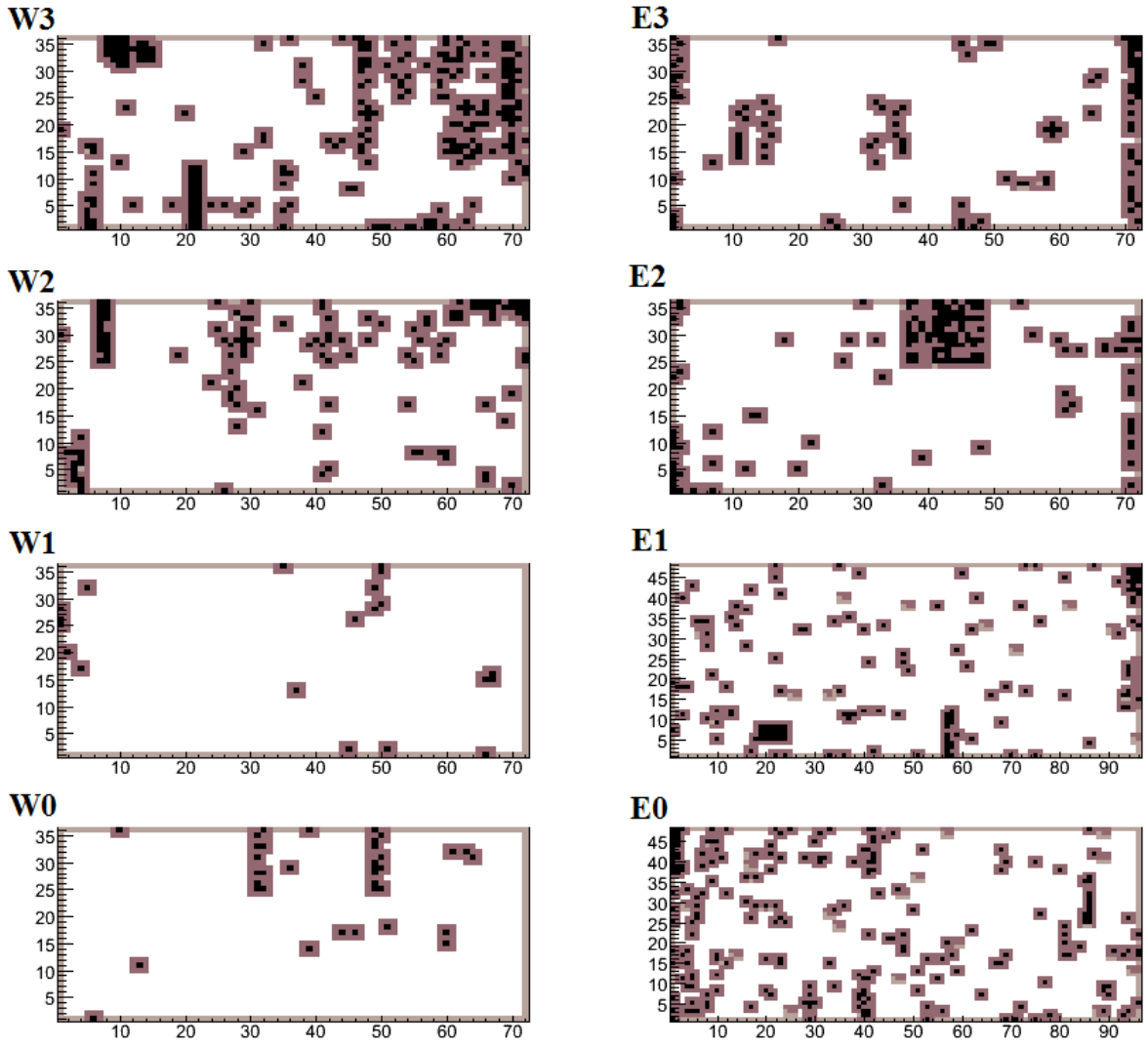

Figure 6.7: Final warnmaps for each sector of the EMCal West and East Arms. The black color indicates a tower that has a hit rate that is out of the acceptable limits. The other colors are neighboring towers that are masked off or edge towers. The PbGl sectors are E0, E1, while the rest are PbSc.

Next, in Fig. 6.8 we show the stability of the mean value of the EMCal π^0 mass peak ($p_T > 2.5$ GeV/c) across the entire run with the exclusion bands in red. We plot the 1σ lower band to show the width of the Gaussian distribution.

In Fig. 6.9, one can see that the two-particle $\Delta\phi$ acceptance functions for the EMC π^0/MPC π^0 correlations are fairly stable over time. Our χ^2 metric (Fig. 6.10) also looks reasonable for the p+p and d+Au

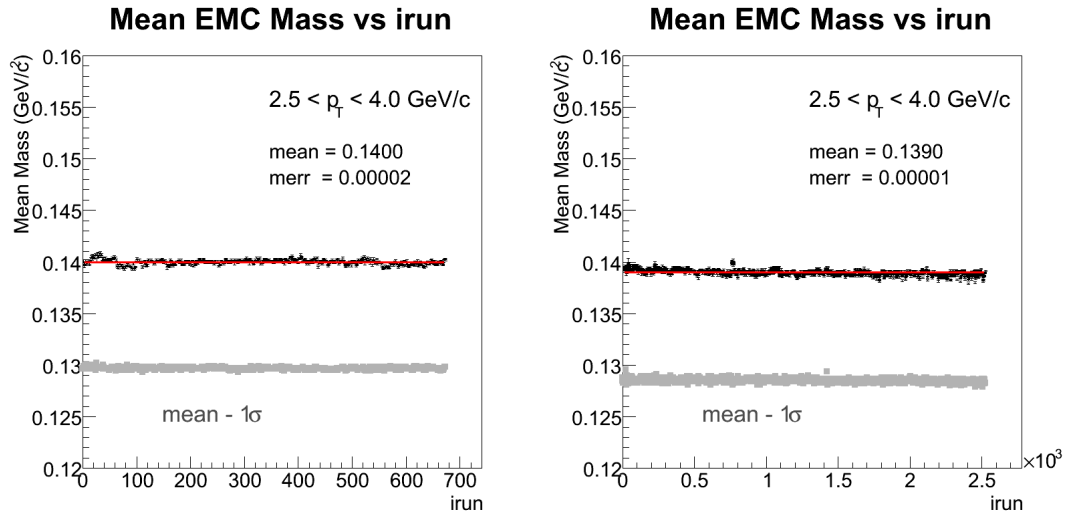

(a) (b)

Figure 6.8: The mean and standard deviation of the Gaussian fit to the EMC π^0 invariant mass distribution for **a.)** p+p, **b.)** d+Au 60-88%. The expected mass is $m_{inv} \approx 0.139$ GeV/c^2 from simulation data [135].

runs indicating that our acceptance correction is stable.

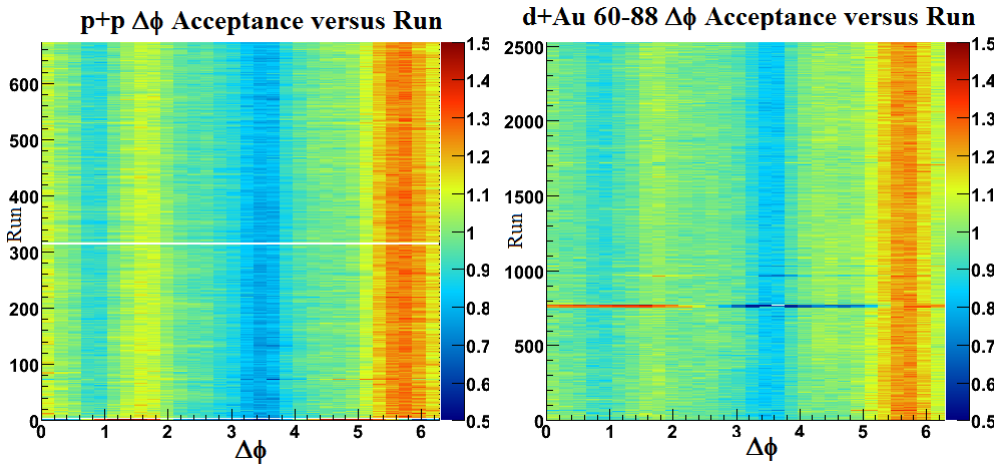

(a) (b)

Figure 6.9: The π^0/π^0 (EMC/MPC) mixed-event acceptance functions versus run number for **a.)** p+p, **b.)** d+Au. The color scale represents the value of the acceptance, which has been normalized to have an average value of 1 for a given run.

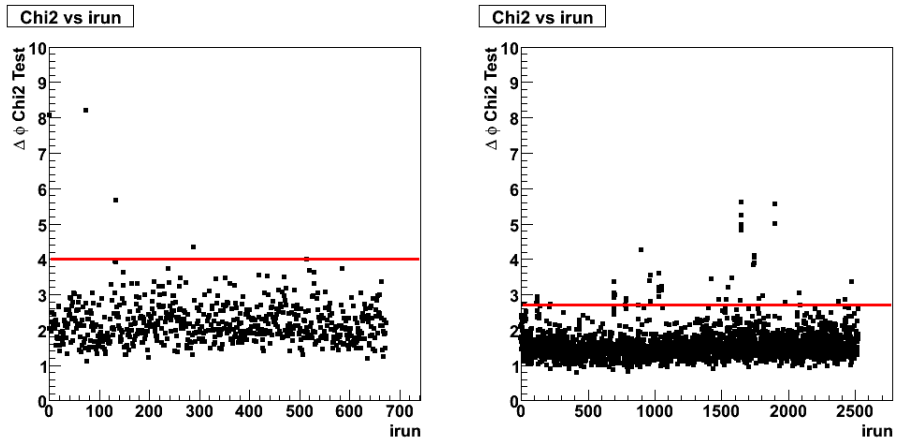

(a) (b)

Figure 6.10: The χ^2/NDF for the π^0/π^0 (EMC/MPC) mixed-event acceptance functions versus run number for **a.)** p+p, **b.)** d+Au. Runs that have a χ^2/NDF above the red line are excluded from analysis.

6.5 Data Analysis

6.5.1 Fitting Procedure

Example efficiency-corrected correlation functions for p+p are shown in Fig 6.11 for the rapidity-separated EMCal/MPC π^0/π^0 correlations. The MPC π^0-identification procedure was described in section 4.2. We fit the distribution with a constant plus a Gaussian signal. Because the correlation functions are very wide, we have to account for the periodic boundaries of $0 - 2\pi$; that is, a wide Gaussian signal will wrap around the sides of the periodic boundaries. Hence we define our signal as a periodic function; in the ideal case, we would create a function that is periodic to infinity. However, for pragmatic considerations, we only use what is termed a 5-Gaussian fit, wherein our function is the sum of five Gaussian signals atop a constant background, with each Gaussian centered at $n\pi$, $n \in \{-3, -1, 1, 3, 5\}$, or

$$f(\Delta\phi) = p_0 + \frac{p_1}{\sqrt{2\pi}\sigma} \sum_{\mu\in\{-3\pi,-\pi,\pi,3\pi,5\pi\}} e^{\frac{(x-\mu)^2}{2\sigma^2}}. \tag{6.1}$$

For correlation functions with good statistics, we observe that this fit procedure works well and usually ($\sim 95\%$ of CFs) gives answers where $\sigma \lesssim 1.3$. However, when statistics are small, the fits can systematically favor widths that are very large. Upon performing fitting tests, it is easy to see that a large-width and a low-statistics signal can produce fits whose widths deviate from the original value significantly. Also, there are cases when minimization contour for the fit is very flat, and this increases the systematic error dramatically. In both these cases, we obtain a better measurement by fixing the background level to a constant and re-fitting the correlation function. Hence for these cases when we have large widths ($\sigma > 1.3$) or large errors on the area ($> 30\%$), we use the background level from the nearest neighbor that has the same trigger p_T to calculate the background and perform the fit again with a fixed-background level. We take our new fitted error on the width and add 15% to this in quadrature. Additionally, we add a conservative 25% error[1] to the new area to account for the uncertainty in the background level.

[1] The 25% error is an upper estimate for the area error this procedure produces. The relative error on the area can be greater than the width because an increasing area will start to reduce the background level once the correlation function is wide enough.

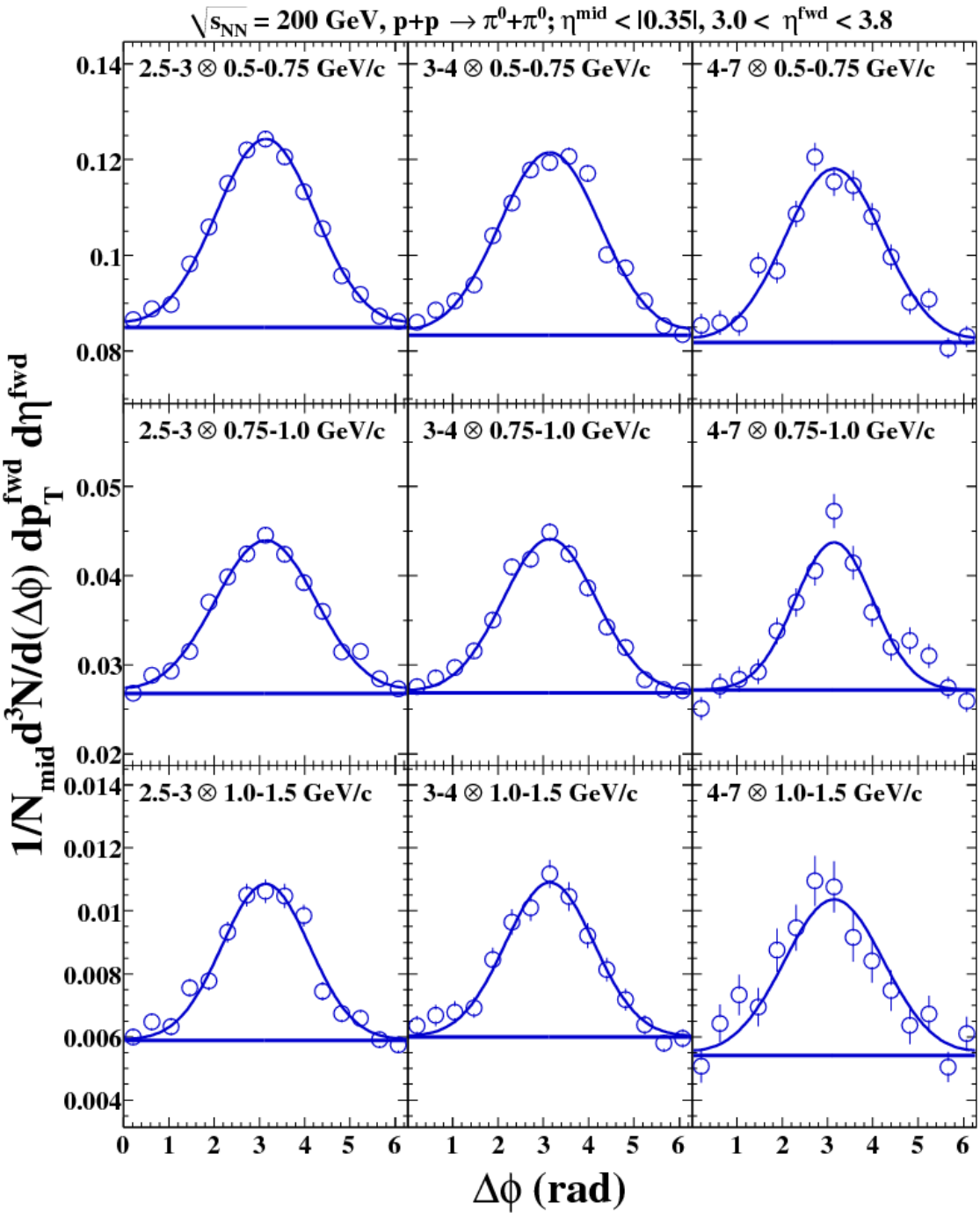

Figure 6.11: **EMC π^0/MPC π^0:** Example p+p $\Delta\phi$ correlation functions. The p_T of the trigger (EMC) and associate particle (MPC) are listed as $p_{T,trig} \otimes p_{T,assoc}$.

6.5.2 Sideband Correction

Another issue is that we have background counts underneath the π^0 peak that contribute to the correlation function. These exist in both the EMCal-π^0 ($m_{inv} = 0.10 - 0.18$ GeV/c^2) and MPC-π^0 ($m_{inv} = 0.08 - 0.18$ GeV/c^2) mass windows, though the background is larger in the MPC mass window. We try to measure only the correlation function for the π^0's, and so we must correct for these background contributions. The problem is analyzed in two different ways: 1.) measure the correlation functions of the *sidebands* (mass windows outside the π^0 range) and 2.) use p+p PYTHIA→PISA simulations. It has been found that assuming that the sidebands have a similar correlation strength (defined below in eq. 6.2) as the π^0 signal is reasonable. In practice, we employ a non-unity correction to the correlation strength (7% in p+p, 10% in d+Au), as one would naïvely expect the sidebands to contribute more than the π^0's simply because of combinatorics. Evidence that our procedure works well in simulation is shown in Figs. 6.12-6.13. These figures represent the correlation functions as determined in full PYTHIA→PISA simulations for single p+p events and two embedded p+p events, respectively. Here we have identified the exact π^0 contributions to the correlation function (red) by tracking the energy depositions in the calorimeter and also have used our corrective procedure to measure the correlation function (blue). This is a direct comparison of the true π^0 correlation function to the measured one using simulated events.

To understand the systematic error on our procedure, it is easiest to define a quantity called the correlation strength M, where for a pure signal one would have

$$N_{pairs} = (s_1 s_2) \times M_A, \tag{6.2}$$

where s_1 is the yield of trigger particles and s_2 is the number of associate particles that we measure. We need to disentangle the contributions from the background underneath both the trigger and associate particles, but we will start with a simpler exercise. Let us assume there is only a background for the associate particle (i.e. the mass background underneath the π^0 mass window), thus giving us $s_2 + b_2$ associate counts. Then we have

$$CY_{meas} = \frac{Y_{s1s2} + Y_{s1b2}}{s_1} = \frac{M_A s_1 s_2 + M_B s_1 b_2}{s_1} = M_A s_2 + M_B b_2, \tag{6.3}$$

where M_A is the correlation strength for the pure-signal correlation and M_B is the correlation strength for

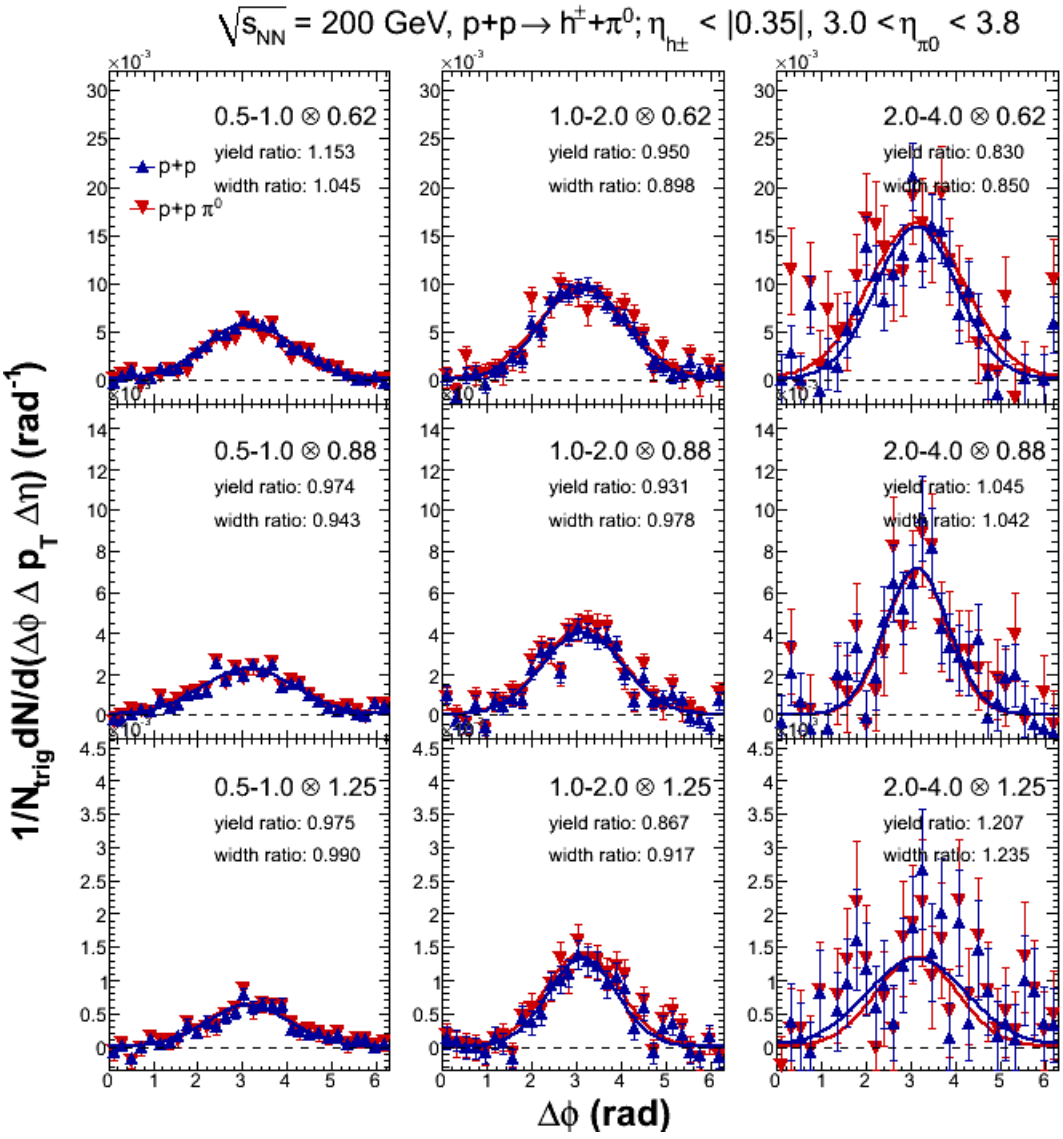

Figure 6.12: Example p+p PYTHIA→PISA $\Delta\phi$ correlation functions for the true π^0 correlation function (red) and our measured (blue). The p_T of the trigger (midrapidity $h^{\pm}$) and associate particle (MPC π^0) are listed as $p_{T,trig} \otimes p_{T,assoc}$.

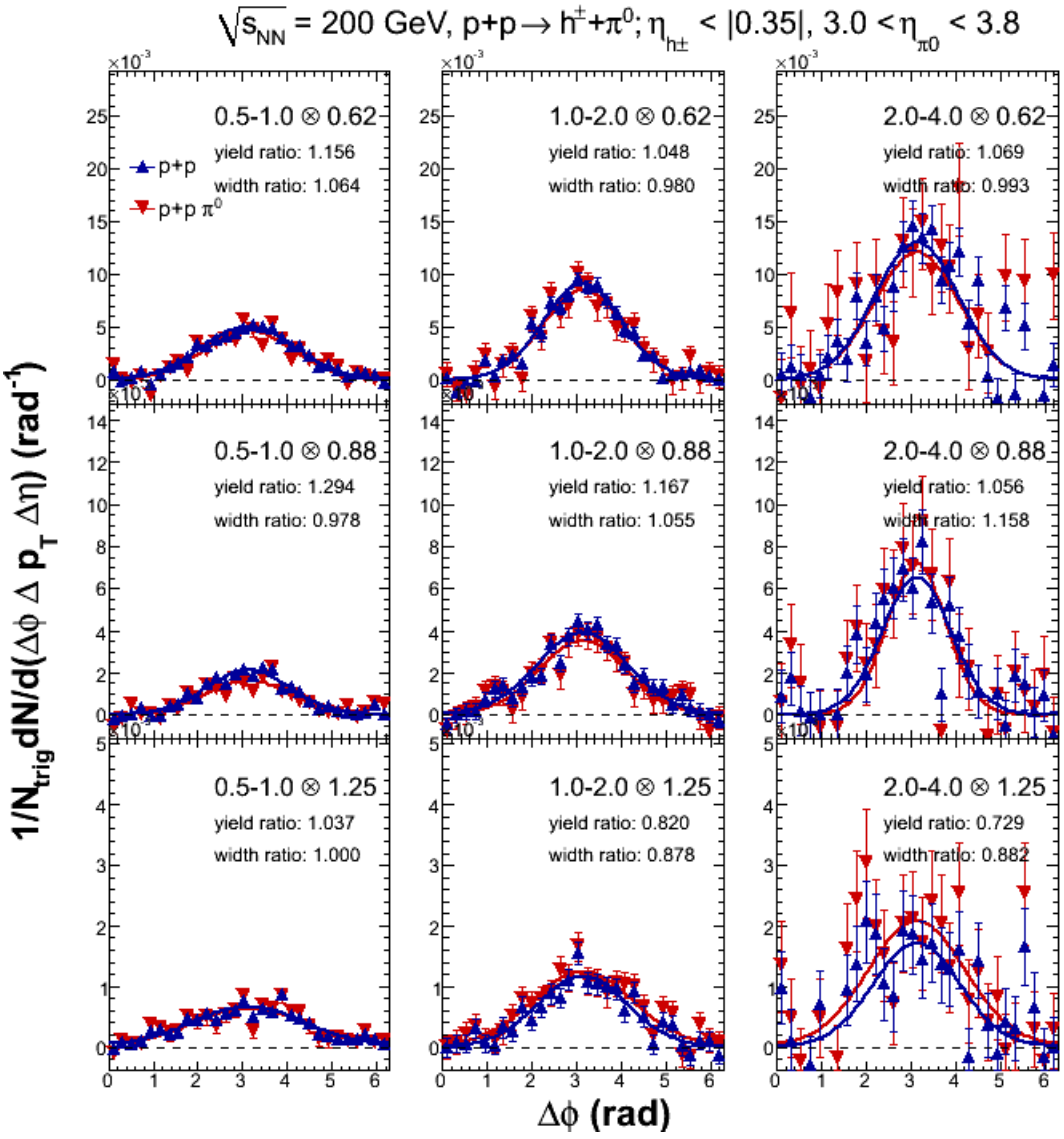

Figure 6.13: Example 2pp (2 embedded p+p events) PYTHIA→PISA $\Delta\phi$ correlation functions for the true π^0 correlation function (red) and our measured (blue). The p_T of the trigger (midrapidity $h^{\pm}$) and associate particle (MPC π^0) are listed as $p_{T,trig} \otimes p_{T,assoc}$.

the background correlation. We know that the true signal has the conditional yield

$$CY_{real} = \frac{Y_{s1s2}}{s_1} = M_A s_2. \tag{6.4}$$

Now, if we assume that $M_A = M_B$, then we just need to scale down our correlation function by a factor $\frac{s_2}{s_2+b_2}$ and we will have the true signal correlation function. Let us now take the ratio of our correlation function to the real correlation function for the signal; we assume that $\frac{M_B}{M_A} = 1 + \Delta_B$, and we obtain

$$\frac{CY_{meas} \times s_2/(s_2+b_2)}{CY_{real}} = 1 + \Delta_B \times \frac{b_2}{s_2+b_2}. \tag{6.5}$$

One arrives at a similar expression given a background b_1 in the trigger particle, $b_2 = 0$ in the associate, and given that $Y_{b1s2} = b_1 s_2 M_C$:

$$\frac{CY_{meas}}{CY_{real}} = 1 + \Delta_C \times \frac{b_1}{s_1+b_1}. \tag{6.6}$$

Note that we do not scale this correlation function as we divide out by the number of signal plus background trigger particles.

If we allow both trigger and background particles to have backgrounds, then a $b_1 b_2$ term with $Y_{b1b2} = b_1 b_2 M_D$ enters the final equation and we get

$$\frac{CY_{meas} \times s_2/(s_2+b_2)}{CY_{real}} = 1 + \frac{1}{(s_1+b_1)(s_2+b_2)}(\Delta_B s_1 b_2 + \Delta_C b_1 s_2 + \Delta_D b_1 b_2). \tag{6.7}$$

Hence with this expression we now can quantify an error on the measured conditional yield. If we assume a 40% error[2] on the values of the Δ_i's, then we can just plug this into the above equation and calculate our error.

As mentioned previously, we have measured the sidebands in both simulation and data. When we use simulation results, one is able to understand exactly how the background contributes to the correlation functions, and hence we can compare the sidebands to the background directly beneath the π^0 peak. Our simulated results are from correlations between a hadron identified at midrapidity correlated with a π^0 detected in the MPC. For statistical reasons, the hadron sample came directly from the PYHIA event record, while the π^0 was reconstructed from the PISA simulations. In Fig. 6.14, we show the ratio of the simulated correlation strength for 1pp (a) and 2pp (b) events of the background underneath the peak

[2]The 40% error is an upper estimate for the level of deviation between the correlation strength of the sidebands and the background under the π^0 peak.

($m_{inv} = 0.08 - 0.18$ GeV/c^2) to correlation strength of the π^0's. For comparison, we also show the ratio of the correlation strength of the sidebands ($m_{inv} = 0.18 - 0.26$ GeV/c^2) to the π^0 correlation strength. A constant line is fit to the measured ratios; the ratios we use for the corrections are from the top set of plots.

In Figs. 6.15-6.16, we show the ratio of the sideband correlation strength to that of the π^0 mass window for $h^{\pm}$/MPC-π^0 and EMC-π^0/MPC-π^0 correlations from the data. These results also seem to indicate that a small correction to the assumptions made in eq. 6.7 is necessary.

We opt to use the simulated fit results for our correction rather than the measured sidebands and include our sizable systematic error on this assumption. Thus, we determine that the correlation strength of the background is 7% larger in p+p and 10% in d+Au than the correlation strength of the peak itself; this measurement still carries a large systematic error. We correct the correlation functions by scaling them with an additional term of $1/(1 + \Delta\frac{b_2}{s_2+b_2})$. In Tables C.1-D.6, the term $\frac{S}{S+B}_{MPC}$ contains this correction. When calculating the systematic error from the sidebands, we do not include this correction.

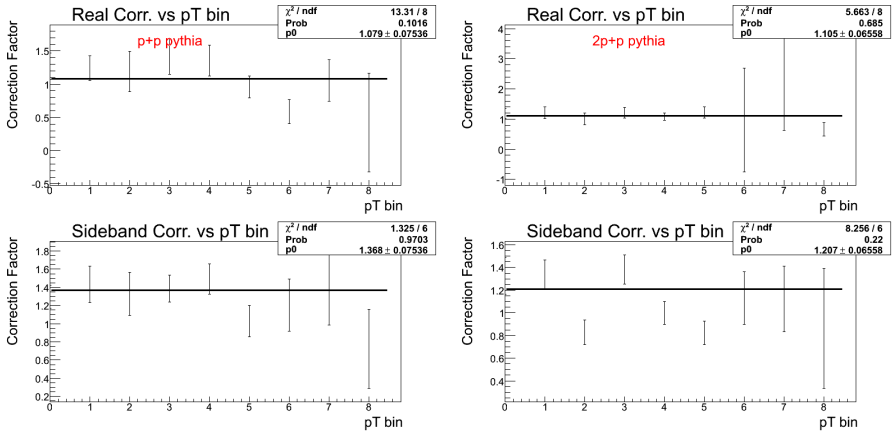

(a) (b)

Figure 6.14: The ratio of real background contribution and the sideband background to the measured yields for **a.)** p+p PYTHIA, **b.)** 2p+p PYTHIA embedded events.

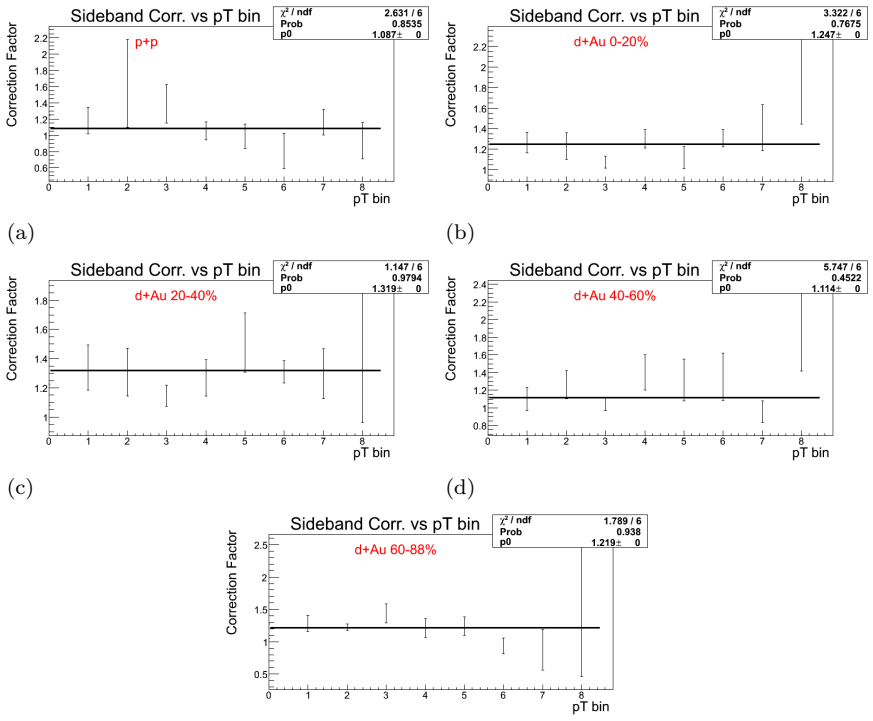

Figure 6.15: **Central-Arm $h^{\pm}$/MPC-π^0:** The ratio of the sideband yields to the measured yields for the mid-forward correlations for **a.)** p+p, **b.)** d+Au 0-20, **c.)** d+Au 20-40, **d.)** d+Au 40-60, **e.)** d+Au 60-88.

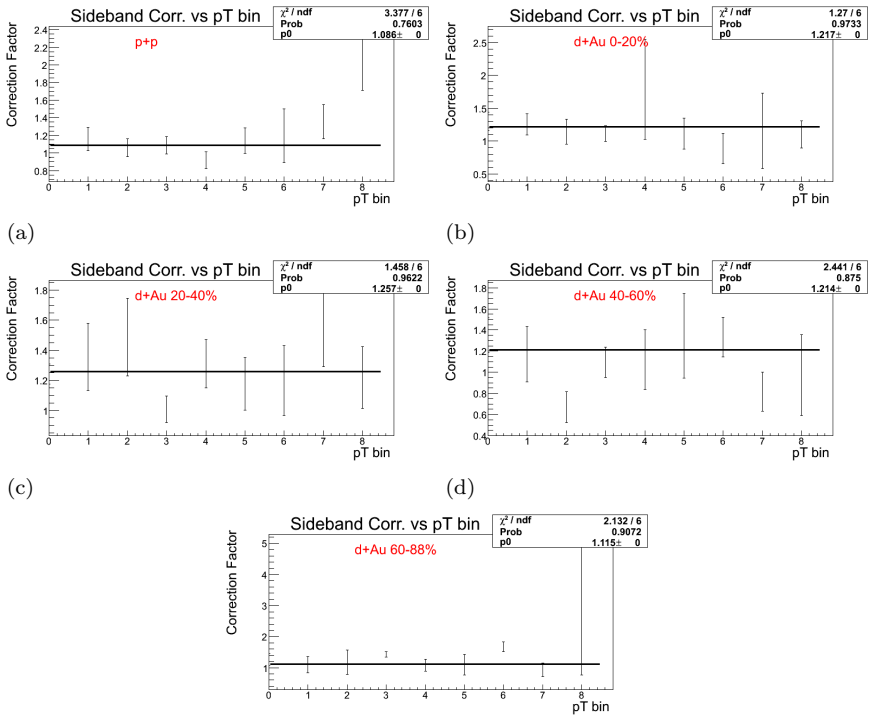

Figure 6.16: **EMCal-π^0/MPC-π^0:** The ratio of the sideband yields to the measured yields for the mid-forward correlations for **a.)** p+p, **b.)** d+Au 0-20, **c.)** d+Au 20-40, **d.)** d+Au 40-60, **e.)** d+Au 60-88.

6.5.3 Efficiency Correction

In section 4.4.2, we calculated the acceptance×efficiency correction for the MPC π^0's for all centrality classes and p_T bins for $p_T \in 0.25 - 2.0$ GeV/c. For the present measurement, the p_T bins needed are $0.5 - 0.75$ GeV/c, $0.75 - 1.0$ GeV/c, and $1.0 - 1.5$ GeV/c (the last bin results from combining two smaller bins). In Table 6.1, we show the rebinned efficiency values and systematic errors that we apply to the data; these efficiencies are used as a correction to the CFs. It should be noted that some portion of the systematic error cancels when taking the ratio between d+Au and p+p, as seen in Table 6.2. In these tables ϵ is the single-π^0 reconstruction efficiency, σ is the statistical error, and s_{mass}, s_{spec}, s_{escale}, and s_{GEANT} correspond to the systematic errors from the yield extraction, shape of the input spectrum, energy scale, and GEANT errors, respectively. The total systematic error is listed as s_{tot} and the *bcorr* corresponds to the up-down correction, $C_{up-down}$.

One small aside is that because our efficiency depends upon the spectral shape, if the shape of the di-hadron measurements differed significantly from the single-particle spectra, we might have to recalculate our efficiencies. However, as seen in Figs. 6.19-6.20, the spectral shapes are quite similar.

Table 6.1: Rebinned efficiencies, **relative** stat, sys errors for $3.0 < \eta < 3.8$.

d+Au 0-20%								
p_T	ϵ	σ_ϵ	s_{mass}	s_{spec}	s_{escale}	s_{GEANT}	s_{tot}	$bcorr$
0.625	0.052	0.016	0.020	0.031	0.067	0.070	0.104	0.964
0.875	0.076	0.014	0.021	0.009	0.086	0.070	0.113	0.962
1.250	0.051	0.015	0.036	0.017	0.104	0.070	0.132	0.875
d+Au 20-40%								
p_T	ϵ	σ_ϵ	s_{mass}	s_{spec}	s_{escale}	s_{GEANT}	s_{tot}	$bcorr$
0.625	0.053	0.015	0.020	0.023	0.067	0.070	0.102	0.964
0.875	0.077	0.014	0.022	0.011	0.085	0.070	0.113	0.963
1.250	0.051	0.015	0.038	0.017	0.104	0.070	0.132	0.878
d+Au 40-60%								
p_T	ϵ	σ_ϵ	s_{mass}	s_{spec}	s_{escale}	s_{GEANT}	s_{tot}	$bcorr$
0.625	0.057	0.015	0.017	0.018	0.067	0.070	0.100	0.964
0.875	0.077	0.014	0.021	0.013	0.084	0.070	0.112	0.965
1.250	0.050	0.015	0.036	0.018	0.106	0.070	0.133	0.874
d+Au 60-88%								
p_T	ϵ	σ_ϵ	s_{mass}	s_{spec}	s_{escale}	s_{GEANT}	s_{tot}	$bcorr$
0.625	0.059	0.012	0.015	0.015	0.069	0.070	0.101	0.961
0.875	0.080	0.012	0.017	0.011	0.089	0.070	0.115	0.960
1.250	0.052	0.012	0.031	0.017	0.110	0.070	0.135	0.861
d+Au MinBias								
p_T	ϵ	σ_ϵ	s_{mass}	s_{spec}	s_{escale}	s_{GEANT}	s_{tot}	$bcorr$
0.625	0.055	0.007	0.019	0.020	0.068	0.070	0.101	0.963
0.875	0.077	0.007	0.020	0.011	0.087	0.070	0.114	0.962
1.250	0.051	0.007	0.035	0.017	0.105	0.070	0.132	0.873
p+p								
p_T	ϵ	σ_ϵ	s_{mass}	s_{spec}	s_{escale}	s_{GEANT}	s_{tot}	$bcorr$
0.625	0.060	0.010	0.013	0.029	0.075	0.070	0.107	0.952
0.875	0.082	0.010	0.019	0.008	0.097	0.070	0.122	0.950
1.250	0.052	0.010	0.030	0.019	0.118	0.070	0.142	0.834

Table 6.2: Rebinned efficiency ratios, **relative** stat, sys errors for $3.0 < \eta < 3.8$.

d+Au 0-20%/p+p								
p_T	$\epsilon_{dA}/\epsilon_{pp}$	$\sigma_{\epsilon rat}$	s_{mass}	s_{spec}	s_{escale}	s_{GEANT}	s_{tot}	$bcorr_{rat}$
0.625	0.863	0.016	0.024	0.042	0.040	0.040	0.074	1.013
0.875	0.935	0.016	0.028	0.012	0.040	0.040	0.064	1.013
1.250	0.989	0.018	0.047	0.025	0.040	0.040	0.078	1.050
d+Au 20-40%/p+p								
p_T	$\epsilon_{dA}/\epsilon_{pp}$	$\sigma_{\epsilon rat}$	s_{mass}	s_{spec}	s_{escale}	s_{GEANT}	s_{tot}	$bcorr_{rat}$
0.625	0.890	0.016	0.024	0.037	0.040	0.040	0.071	1.013
0.875	0.947	0.016	0.029	0.013	0.040	0.040	0.065	1.013
1.250	0.977	0.018	0.049	0.026	0.040	0.040	0.079	1.053
d+Au 40-60%/p+p								
p_T	$\epsilon_{dA}/\epsilon_{pp}$	$\sigma_{\epsilon rat}$	s_{mass}	s_{spec}	s_{escale}	s_{GEANT}	s_{tot}	$bcorr_{rat}$
0.625	0.955	0.017	0.021	0.034	0.040	0.040	0.069	1.013
0.875	0.939	0.016	0.029	0.015	0.040	0.040	0.065	1.016
1.250	0.965	0.018	0.047	0.026	0.040	0.040	0.078	1.049
d+Au 60-88%/p+p								
p_T	$\epsilon_{dA}/\epsilon_{pp}$	$\sigma_{\epsilon rat}$	s_{mass}	s_{spec}	s_{escale}	s_{GEANT}	s_{tot}	$bcorr_{rat}$
0.625	0.990	0.016	0.020	0.033	0.040	0.040	0.068	1.010
0.875	0.975	0.015	0.026	0.014	0.040	0.040	0.064	1.010
1.250	0.994	0.016	0.043	0.025	0.040	0.040	0.076	1.033
d+Au MinBias/p+p								
p_T	$\epsilon_{dA}/\epsilon_{pp}$	$\sigma_{\epsilon rat}$	s_{mass}	s_{spec}	s_{escale}	s_{GEANT}	s_{tot}	$bcorr_{rat}$
0.625	0.917	0.012	0.023	0.035	0.040	0.040	0.071	1.012
0.875	0.949	0.011	0.028	0.013	0.040	0.040	0.065	1.012
1.250	0.981	0.012	0.046	0.026	0.040	0.040	0.077	1.047

6.5.4 Bin-Shift Correction

In section 4.4.4, we derived our formulae for calculating the up-down bin-shift correction and did the calculation for the bins used in the single-particle spectra. The corrections depend upon the spectral shape; we use the same spectral shape for corrections in the di-hadron measurements because as one can see in Figs. 6.19-6.20, the spectral shapes are fairly similar (as evidenced by that agreement of the points with the fit). The $1.0 - 1.5$ GeV/c bin has a larger correction because of the larger bin size. These corrections are listed in Tables C.1-C.3, and D.1-D.3.

6.6 Systematic Errors

In the present correlation analysis, the main systematic errors arise from the fitting procedure and the sideband analysis (see eq. 6.7). We assume a 40% error[3] for the sideband contributions to the correlation functions. The statistical errors from the fit itself contain a combination of statistical and systematic parts (type-A errors [136]), and are incorporated into the statistical errors of the yields. Errors on the yield extraction, efficiency, and energy scale are also incorporated here, and these calculations were shown in sections 4.4.1, 4.4.2, 4.5.1 respectively. The errors from the EMCal-π^0 yield extraction is negligible, as the systematics cancel when taking the ratio. The errors on the midrapidity π^0 and $h^{\pm}$ energy scales are also negligible; this is because the behavior of $I_{\rm dA}$ and $J_{\rm dA}$ versus the midrapidity p_T essentially are linear with a very small slope, and thus the propagated errors become very small.

The main contribution to the global error for the $J_{\rm dA}$ calculation comes from the uncertainty of the total p+p cross section, which we take to be 9.7% [126]. There is also a centrality-class dependent global error that is added in quadrature with the aforementioned error [63]; these global errors are the same as in the MPC π^0 $R_{\rm dA}$ case in Table 4.2.

[3]The 40% error is an upper estimate for the level of deviation between the correlation strength of the sidebands and the background under the π^0 peak.

6.7 Results

6.7.1 Conditional Yields

Our final calculation of the conditional yields (see eq. 5.4) given that we trigger in the midrapidity detector gives us the following expression

$$CY = \frac{N_{pairs} \times C_{up-down} \times C_{leakage}}{N_{trig}\epsilon_{assoc}\Delta p_T \Delta\eta}, \tag{6.8}$$

where $C_{up-down}$ is the up-down bin-shift correction, $C_{leakage}$ accounts for the leakage of the π^0 counts outside the π^0 mass window, and N_{pair} corresponds to the integral number of counts in the awayside peak.

In Figs. 6.17-6.18, we show the background-subtracted correlation functions for all centralities. The supporting correlation functions and fits are shown in Appendices C.2, D.2. In Figs. 6.19-6.20, we show the conditional yields as a function of centrality class, $p_{T,trig}$, and $p_{T,assoc}$ for the midrapidity $h^{\pm}$ and π^0's, respectively. From these figures, one can see a suppression in the yields as the impact parameter decreases (more central collisions). Also, scaled fits to the single-particle spectra are shown along-side the data points, which describe the shape reasonably well; thus we do not attempt to recalculate the efficiencies using the spectral shape of the conditional yields.

In Tables C.1-C.3, D.1-D.3, we show the various factors that go into the calculation of the conditional yields and in Tables C.4-C.6, D.4-D.6, we show the final value of the yields and the errors.

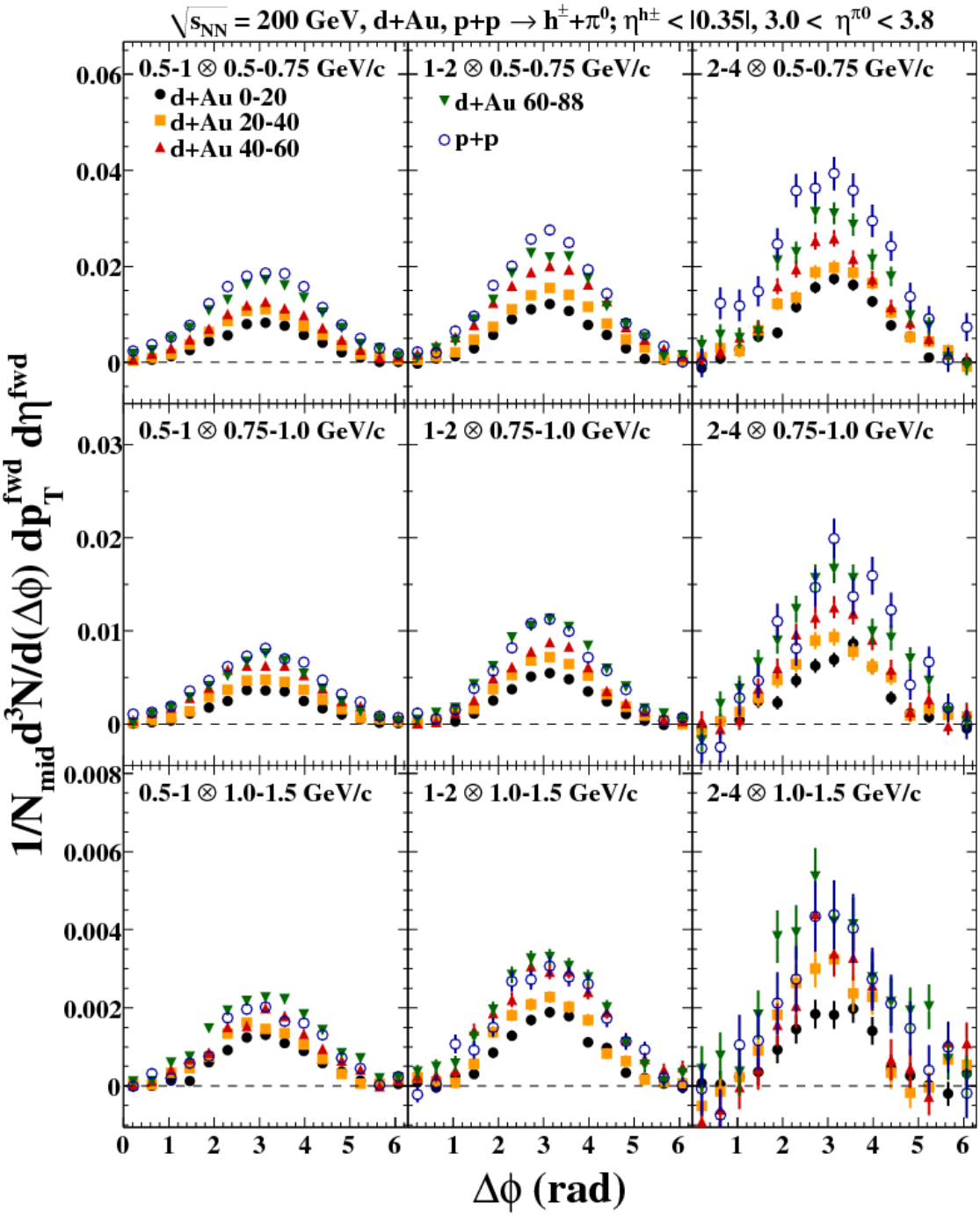

Figure 6.17: Background-subtracted central-arm $h^{\pm}$/MPC-π^0 $\Delta\phi$ correlation functions all centralities. The p_T of the trigger (midrapidity $h^{\pm}$) and associate particle (MPC π^0) are listed as $p_{T,trig} \otimes p_{T,assoc}$.

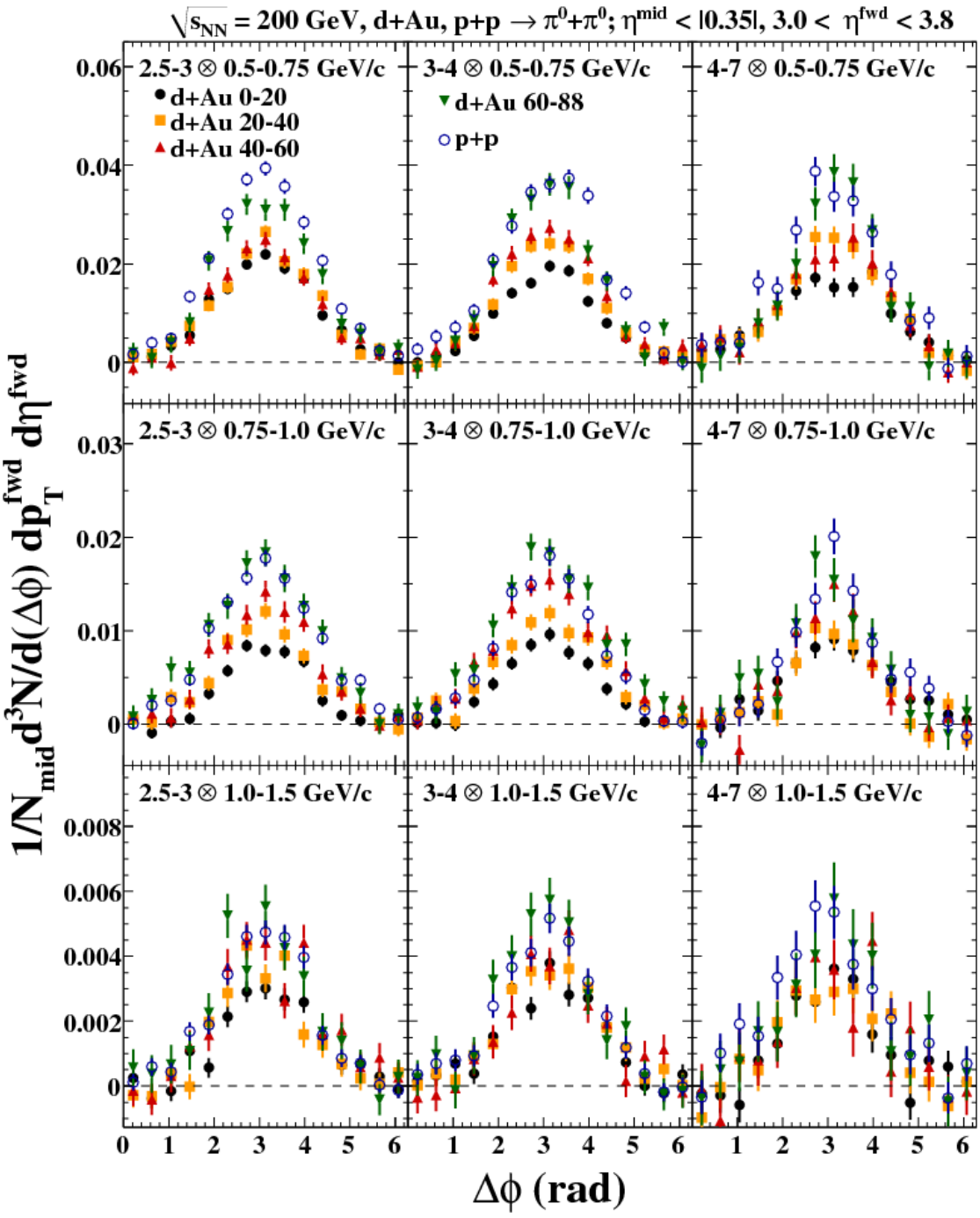

Figure 6.18: Background-subtracted EMCal-π^0/MPC-π^0 $\Delta\phi$ correlation functions all centralities. The p_T of the trigger (EMC π^0) and associate particle (MPC π^0) are listed as $p_{T,trig} \otimes p_{T,assoc}$.

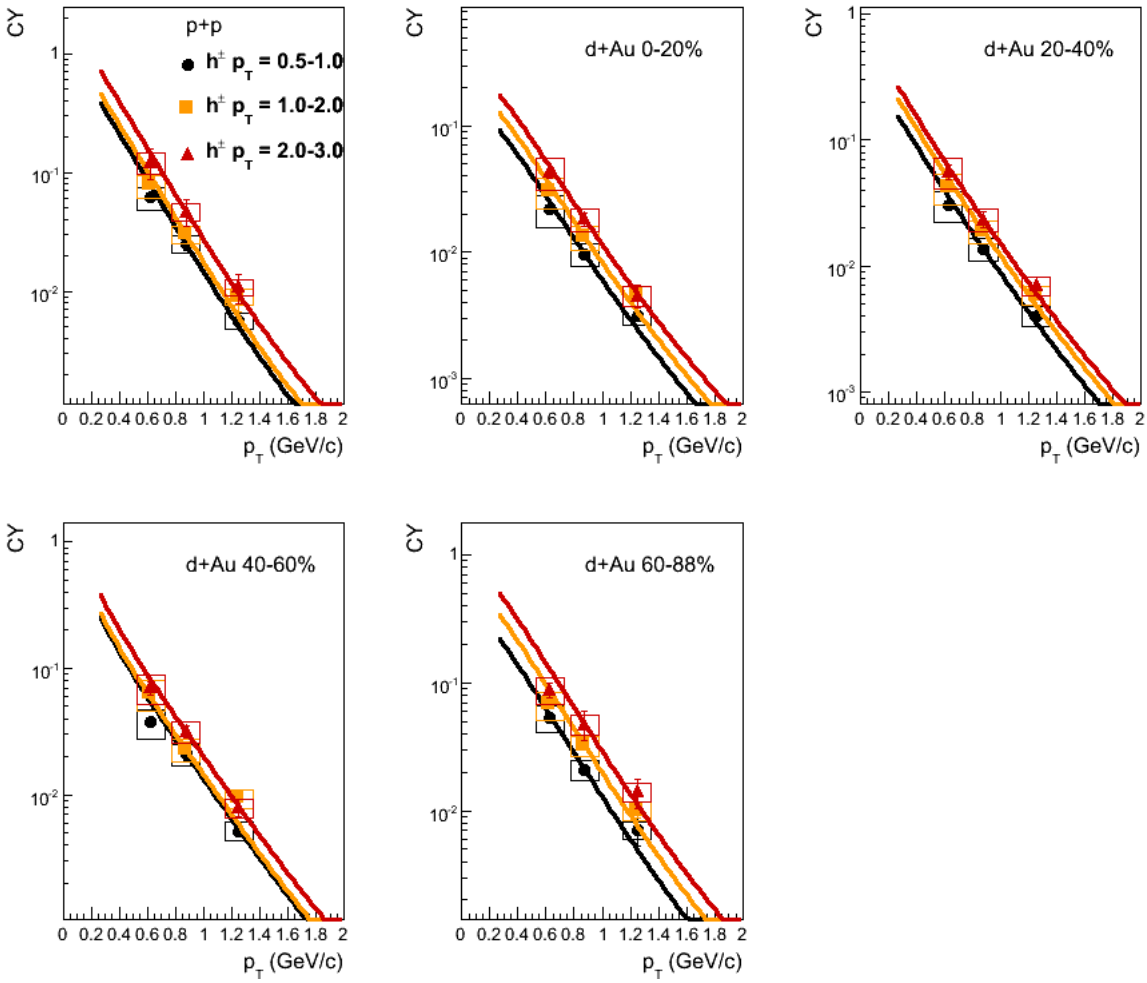

Figure 6.19: Central-arm $h^{\pm}$/MPC-π^0 conditional yields for all centrality classes. The curves in the plot represent the shape of the single-particle p_T spectra for MPC π^0's.

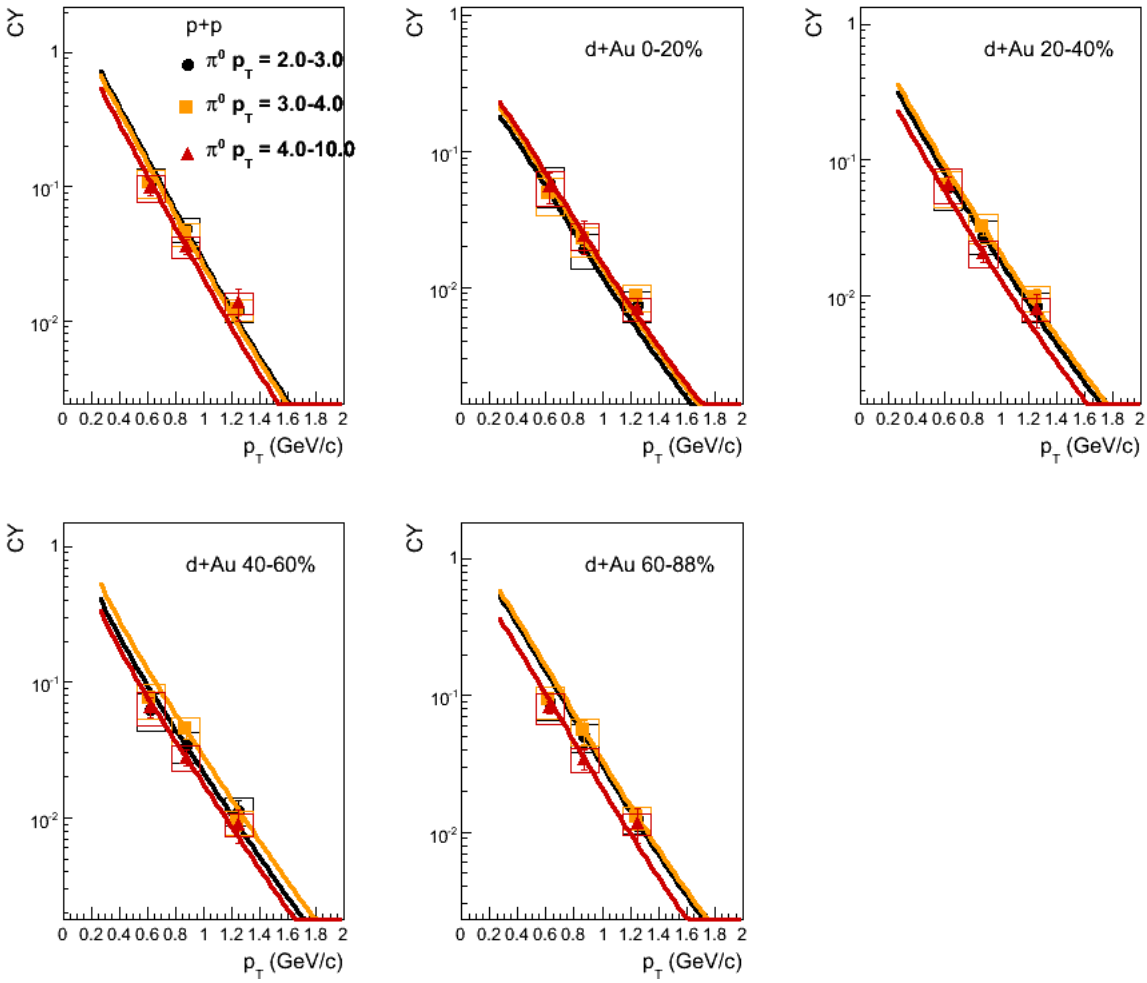

Figure 6.20: EMCal-π^0/MPC-π^0 conditional yields for all centrality classes. The curves in the plot represent the shape of the single-particle p_T spectra for MPC π^0's.

6.7.2 Correlation Widths

In Tables C.4-C.6, D.4-D.6, we also included the correlation widths and their statistical and systematic errors. These widths are interesting because they test CGC hypotheses wherein a broadening of the widths in d+Au as compared to p+p is seen [2, 6]. In addition to the identified π^0's in the MPC, we also add single, high-energy clusters as defined in section 4.2 so that we can reach higher p_T. In Fig. 6.21, we show all the correlation functions for the EMC-π^0/MPC-*cluster* correlations (as opposed to EMC-π^0/MPC-π^0 correlations). No efficiency corrections have been applied, and no background contributions to the correlation functions have been subtracted. We summarize the widths and errors for the cluster correlations in Tables D.7-D.9.

Finally, in Fig. 6.22, we show the correlation widths as a function of $p_{T,assoc}$ for three different $p_{T,trigger}$ bins. One can see that there does not seem to be a larger difference between p+p and d+Au, especially as one moves to the clusters (open points). The widths decrease as the p_T of the MPC particle is increased as expected from jet fragmentation.

6.7.3 I_{dA}, J_{dA}

As a quick reminder, $I_{\rm dA} = \frac{CY_{dA}}{CY_{pp}}$ and for the midrapidity trigger we have

$$J_{dA} = R_{dA,mid} \times I_{dA,mid-trig}. \tag{6.9}$$

We show our results for $J_{\rm dA}$ and $I_{\rm dA}$ in Figs. 6.23-6.24 along with the values of R_{dA} for MPC π^0's. Here we see the interesting trend of increasing suppression as we increase N_{coll}. There also seems to be a decrease in $J_{\rm dA}$ with decreasing $p_{T,trig}$. Because the trigger particle is at midrapidity and the associate at forward rapidity, x^{Au} (Bjorken-x of parton in the Au-nucleus) should depend very strongly on $p_{T,trig}$ and only weakly on $p_{T,assoc}$ (see eq. 1.15 for x_2). Hence we see that the level of suppression in $J_{\rm dA}$ increases as we go to small x, which is qualitatively consistent with shadowing and CGC predictions.

In Tables C.7-C.9 and D.10-D.12, we tabulate the results for J_{dA} and I_{dA}. It should be noted that some of the systematic errors cancel when taking the ratio of conditional yields, including a portion from the sideband errors. Additionally, we used the results for the midrapidity hadron R_{dA} from the 2003 data [68, 137] and these results plus the relative errors are listed in C.10-C.12 and D.13-D.15. In these tables, we also present the values of R_{dA} for MPC π^0's in the p_T bins of this analysis.

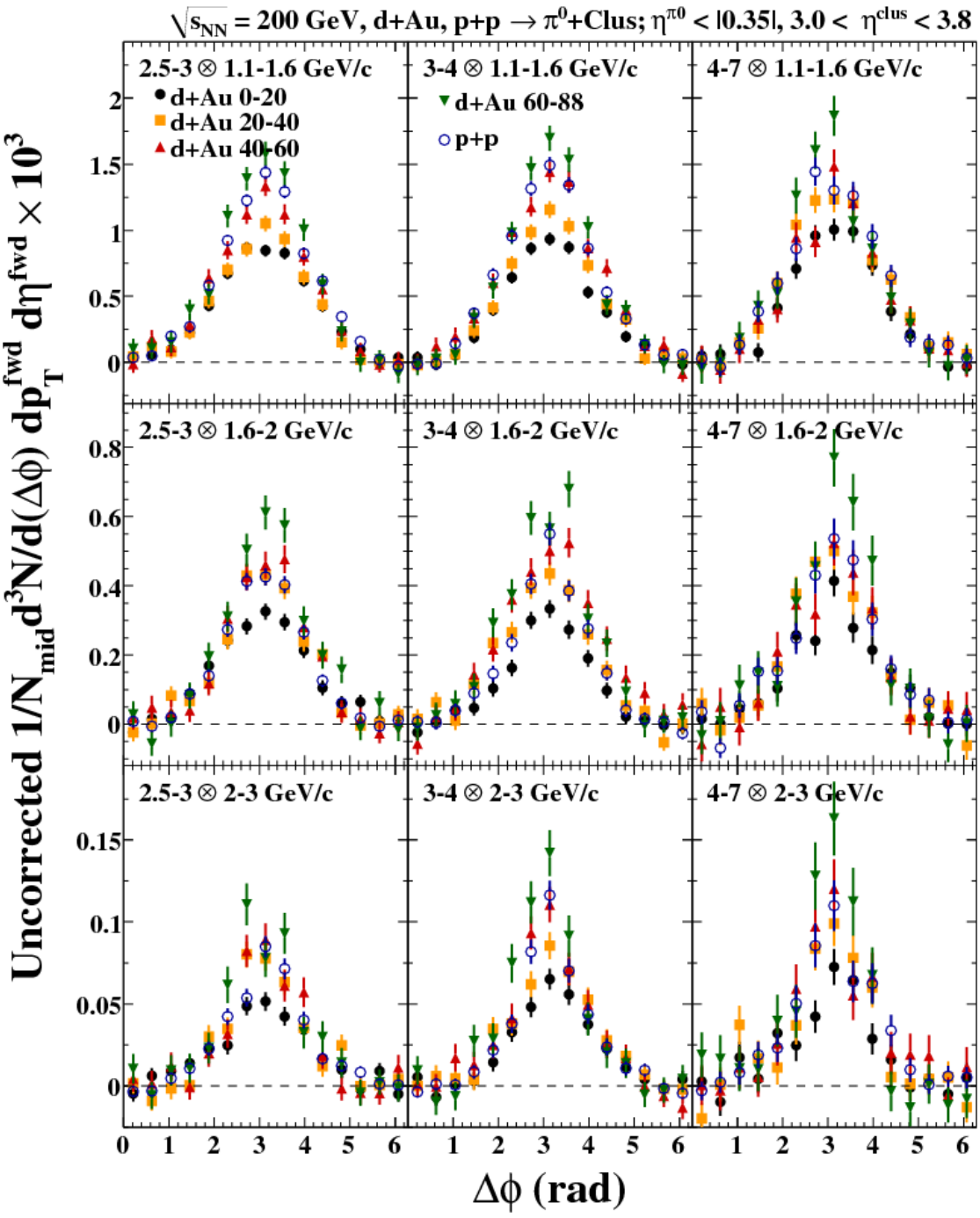

Figure 6.21: Background-subtracted EMCal-π^0/MPC-cluster $\Delta\phi$ correlation functions all centralities. The p_T of the trigger (EMC) and associate particle (MPC) are listed as $p_{T,trig} \otimes p_{T,assoc}$.

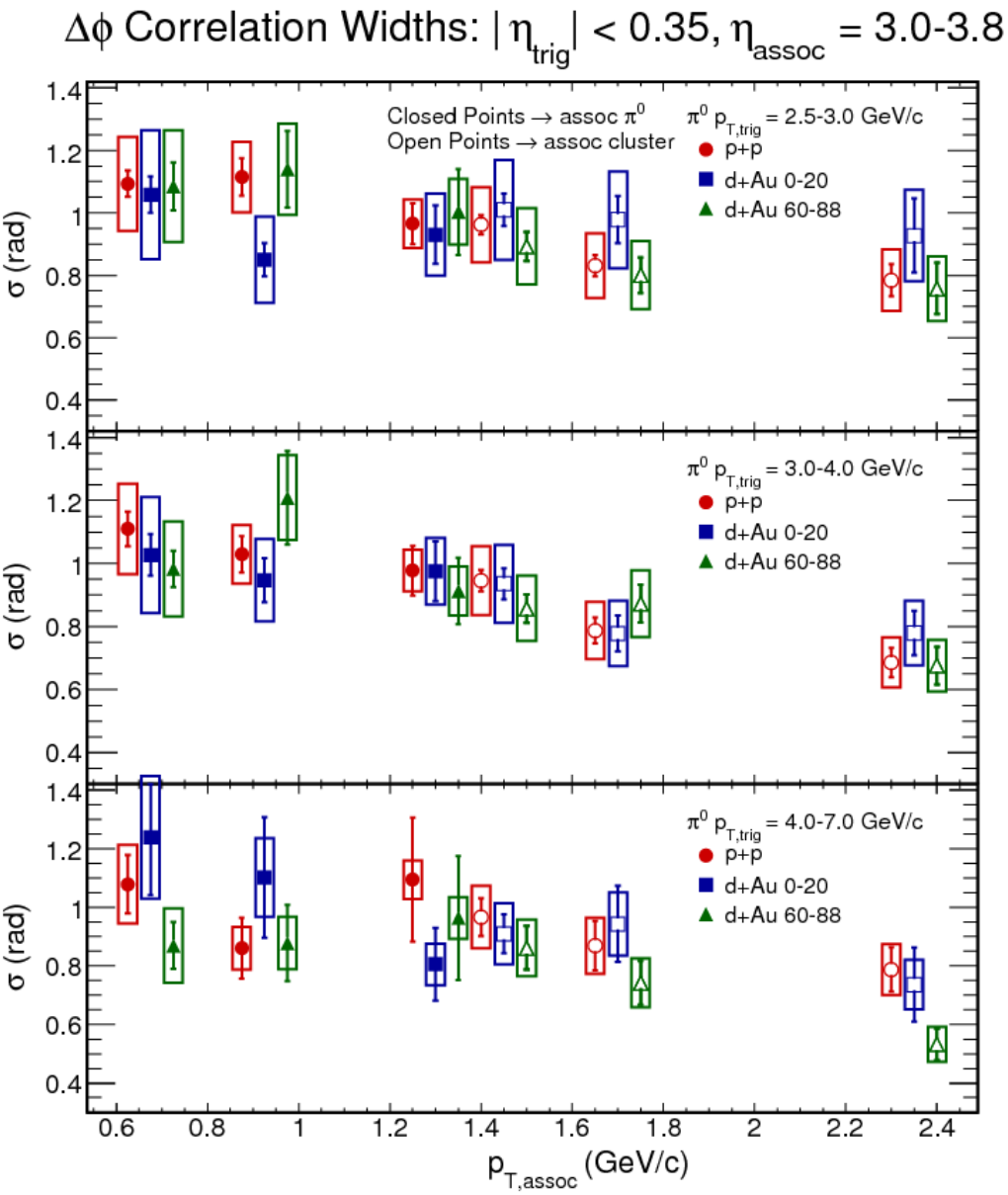

Figure 6.22: Mid-forward widths for EMC-π^0/MPC-π^0 and EMC-π^0/MPC-cluster $\Delta\phi$ correlation functions for p+p, d+Au central and peripheral bins. The MPC-π^0 widths are the closed points while the MPC-cluster widths are the open points. The p+p and d+Au points have a horizontal offset so that one can see the points clearly.

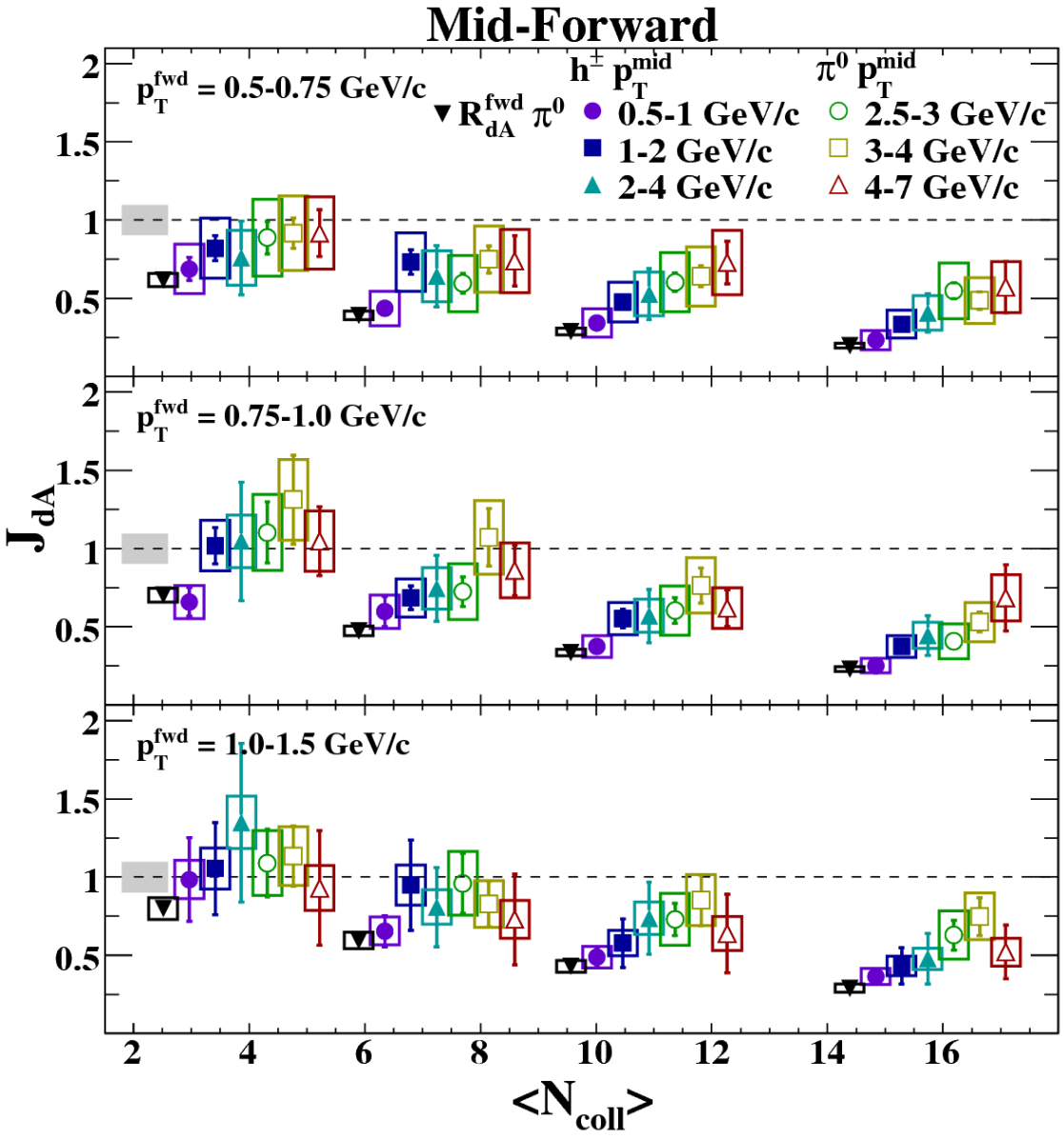

Figure 6.23: J_{dA} versus N_{coll} for all trigger and associate p_T values. The systematic error on each point is shown by the open boxes. The gray error band at the left on each panel represents a global systematic scale error of 9.7%. Additional centrality-dependent systematic errors of 7.5%, 5.1%, 4.1%, and 4.8% for the peripheral to central bins, respectively, are not shown. The $\langle N_{\rm coll}\rangle$ values within a centrality selection are offset from their actual values for visual clarity (see text for actual $\langle N_{\rm coll}\rangle$ values).

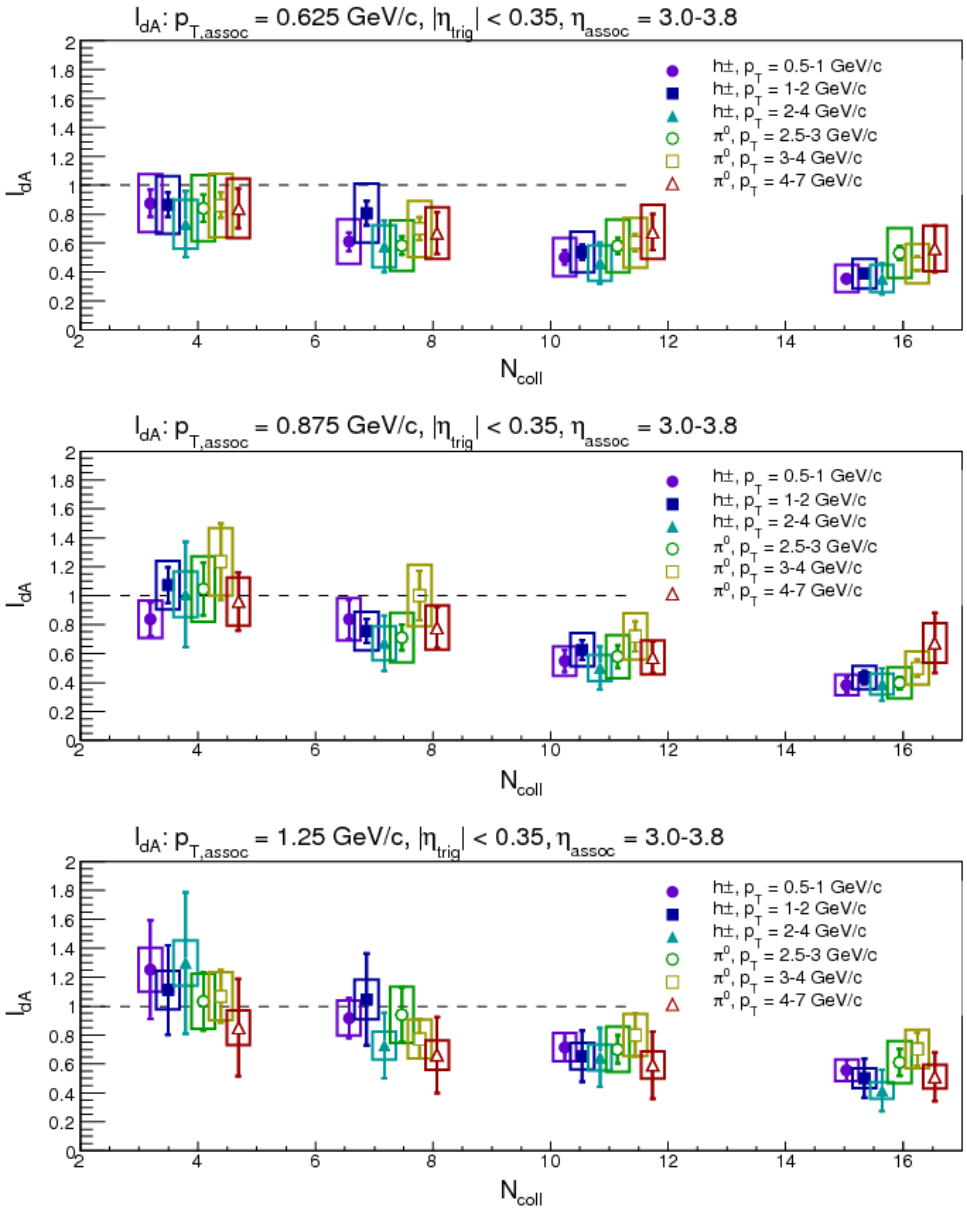

Figure 6.24: I_{dA} versus N_{coll} for all trigger and associate p_T values. The N_{coll} (or horizontal axis) values for each point are offset from the true value for visual clarity.

Chapter 7

Forward-Forward Correlations

We now proceed to discuss correlation functions wherein the trigger particle is a MPC cluster and the associate particle is a MPC π^0 (see section 4.2); these are termed *forward-forward* correlations as both particles are detected in the same, forward MPC. We observe the nearside peak at $\Delta\phi = 0$ in addition to the peak at $\Delta\phi = \pi$ because the particles have very similar rapidities. Given that the two particles come from di-jet production, this is the lowest Bjorken-$x \approx 5 \times 10^{-4}$ achievable in $\sqrt{s_{_{NN}}} = 200$ GeV collisions at PHENIX (and RHIC). Recently, there have been a number of CGC-inspired predictions indicating that a large modification to the width and yield of the awayside peak is expected in central d+Au collisions (especially central collisions wherein the parton densities can be a factor 12 larger than in the proton) but not in p+p [6, 90, 138]. We test these theories with our measurements.

7.1 Data Analysis

7.1.1 Procedural Discussion

In calculating a conditional yield (eq. 5.4) for the forward-forward correlations, we have to make corrections for non-signal contributions to the correlation function, which come from the background underneath the π^0 peak. We have already discussed the methodology (section 6.5.2) for correcting the mid-forward correlation functions; this is applied to the forward-forward correlations along with a correction to the nearside peak, which must be corrected for mass resonance decays. In section 7.1.5, we apply our correction and show that in simulation we attain good agreement with the true π^0 correlation function.

After correcting the correlation functions for the background contributions, they are corrected for the single-particle efficiency and pair efficiency (efficiency loss from having the two particles overlap in the MPC). We also correct for the leakage of the π^0 mass distribution outside the defined window and additionally apply a bin-shift correction.

7.1.2 Cluster-Energy Correction

Usage of the clusters requires that we understand their energy response. Because the cluster sample is dominated by π^0's, we focus on correcting the energy of the clusters to the true π^0 energy. The issue is that for merged π^0's and for those which are almost merged, some of the energy is outside the "core" of the cluster, and hence the energy calculated by the clustering algorithm called ecore (see section 3.6) will not produce the correct energy response. To understand this behavior, we take π^0's embedded into p+p events and calculate the energy response, as seen in Fig. 7.1. From this study, we calculate that our p_T-bin edges change from $1.0 \rightarrow 1.08$, $1.5 \rightarrow 1.57$, and $2.0 \rightarrow 2.04$ GeV/c. The upper bin edge of the $2.0 - 5.0$ GeV/c bins remains the same.

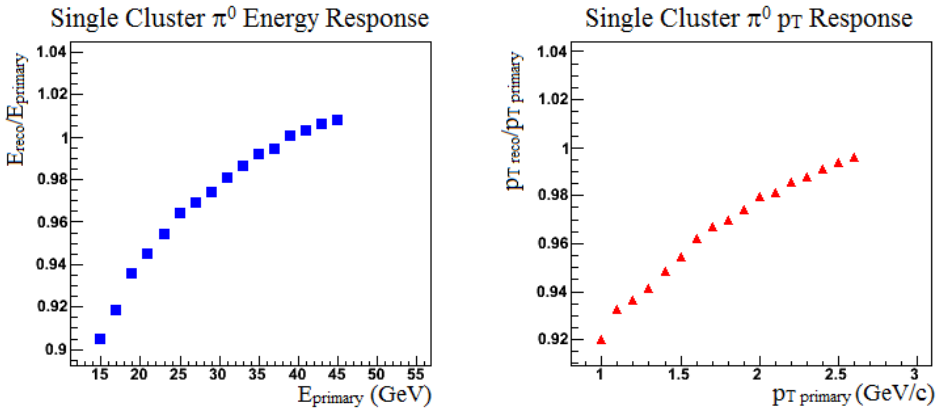

Figure 7.1: Energy and p_T response of single-cluster reconstruction of π^0's

7.1.3 Pedestal Determination

Determination of the constant pedestals of the correlation functions can be performed by using a fit, assuming that the signal has Zero-Yield At the Minimum (ZYAM) [131], or by calculating it explicitly using single-particle distributions of both the trigger and associate particle (known as Mean-Seeds Mean-Partners or MSMP in PHENIX) [139]. Example efficiency-corrected correlation functions for p+p are shown in Fig. 7.2. Please note that the open, red triangles represent the correlations before we apply a correction to the nearside peak (see section 7.1.5). Here we have used the ZYAM assumption to fit the pedestal, which simply means we set the pedestal level to the minimum in the correlation function.

We fit the distribution with a constant plus two Gaussian signals centered at $\Delta\phi = 0$ and π. As with the mid-forward correlations, we have to account for the periodic boundaries of $\Delta\phi \in 0 - 2\pi$. We again

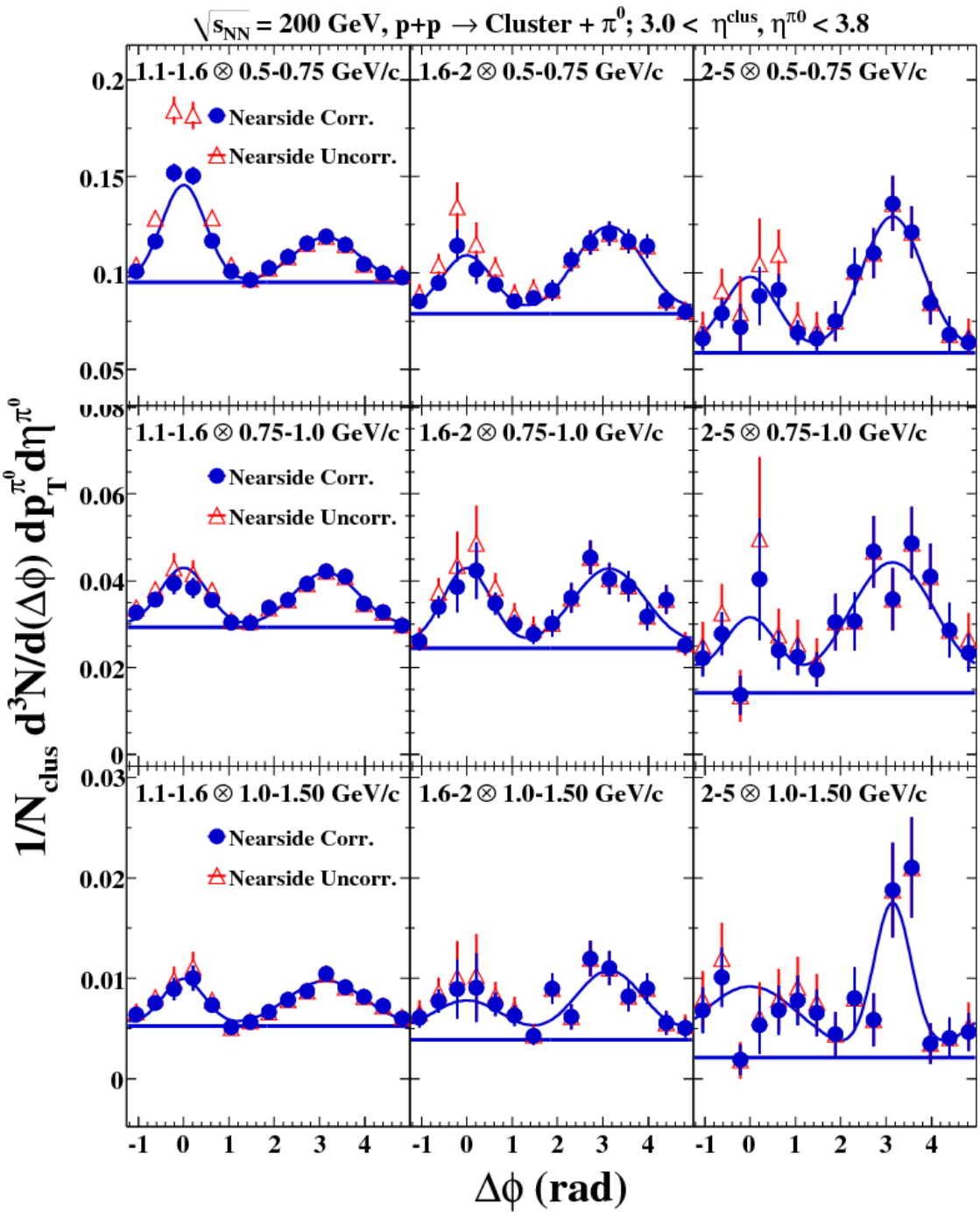

Figure 7.2: **MPC-Cluster/MPC-π^0:** Example p+p $\Delta\phi$ correlation functions. The p_T of the trigger (MPC cluster) and associate particle (MPC π^0) are listed as $p_{T,trig} \otimes p_{T,assoc}$.

use a 5-Gaussian fit, wherein our function is the sum of five sets of two Gaussian-signals atop a constant pedestal, with the Gaussian for the awayside centered at $n\pi$, $n \in \{-3, -1, 1, 3, 5\}$ and for the nearside at $m\pi$, $m \in \{-4, -2, 0, 2, 4\}$, or

$$f(\Delta\phi) = p_0 + \frac{p_1}{\sqrt{2\pi}\sigma_{away}} \sum_{\mu\in\{-3\pi,-\pi,\pi,3\pi,5\pi\}} e^{\frac{(x-\mu)^2}{2\sigma_{away}^2}} + \frac{p_2}{\sqrt{2\pi}\sigma_{near}} \sum_{\mu\in\{-4\pi,-2\pi,0,2\pi,4\pi\}} e^{\frac{(x-\mu)^2}{2\sigma_{near}^2}}. \tag{7.1}$$

One can see in the example (Fig. 7.2) that the nearside peak tends to be narrower than the awayside. To extract the awayside signal and pedestal level, one technique is to simply fit the correlation function with the above fit function. However, because there may be a large region of overlap between the two Gaussian signals, the task of simultaneously fitting the pedestal level along with the two Gaussian signals is difficult; the fit results seem inconsistent and the technique is inadequate to properly calculate the yields and widths of the peaks. Another technique is to fix the nearside width, and perform the fit; however, this still produces a relatively large uncertainty on the background level, as the fit completely depends on the shape of the awayside peak being Gaussian. Any systematic fluctuations in the shape can easily cause the fit to fail.

Alternatively, one can attempt to quantify how incorrect the ZYAM assumption is. To evaluate this, we do a simple exercise: create simulated correlation functions which are the sum of two Gaussian signals as defined in eq. 7.1 and measure how incorrect the awayside yield is when we fit using the ZYAM pedestal. In Fig. 7.3, we show a plot that quantifies how the ZYAM assumption fails as a function of the awayside width and the awayside signal fraction ($\frac{A}{A+N}$, where A is the awayside area and N is the nearside area) given a fixed nearside width of $\sigma_{near} = 0.6$. As one expects, the wider the awayside peak gets, or the smaller its fraction, the larger correction one has to make.

This analysis shows the difficulty in obtaining the awayside width and yield with good precision and accuracy using ZYAM. A better approach would be determining the background level from the particle production rates, such as MSMP [139]. This was tried; however, the results did not seem reasonable, as the background level in some cases was even higher than in ZYAM. One uncertainty with this method is that while it has been used extensively for Au+Au analyses, it has not been used in p+p or d+Au, and hence its validity has not been established. Another issue is the possibility of auto-correlations with the BBC (which sits at a similar pseudorapidity to the MPC) that complicates this analysis.

Thus, the inability to consistently obtain good fit results for the correlation functions, and the failure of the absolute-normalization technique leads us to use the ZYAM-fit method with all of its inadequacies.

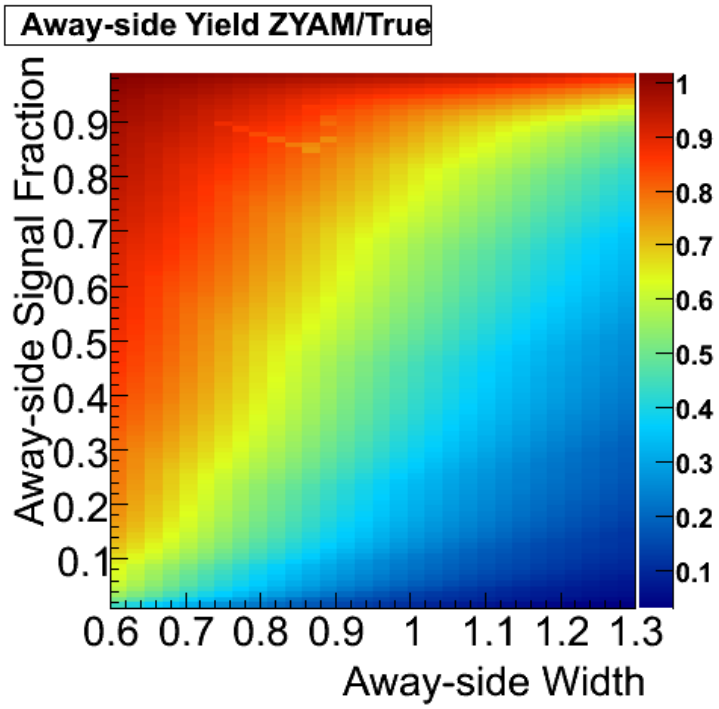

Figure 7.3: Performance of ZYAM as a function of the awayside width and awayside signal fraction ($\frac{A}{A+N}$). The colored axis indicates the ratio of the awayside yield obtained assuming ZYAM background subtraction and the true input yields.

Hence throughout the rest of this chapter, it should be noted that the fits use a ZYAM background, and the background subtracted correlation functions use ZYAM as well.

7.1.4 Pair Cuts

Particle pair cuts are usually made when the correlations involve two particles from the same detector; pair cuts require some minimum spatial separation between particles to ensure that both particles are detected properly. The particle pair cut made in this analysis is a $\Delta r = 4.0$ cm separation between the high-energy cluster and the two clusters of the identified π^0. This cut effectively makes an 8 cm diameter hole around the high-energy cluster, which in turn makes the nearside peak very difficult to measure. In fact, our correlations are performed in a torus of 8 cm ($11 < r < 19$ cm), and hence the nearside is very sensitive to the acceptance. What does this hole do in terms of the physical signal? It will reduce the nearside signal size because we cut a hole in our acceptance at $\Delta\eta \times \Delta\phi = 0 \times 0$. The amount that our signal is reduced depends both upon the hole size as well as our $\Delta\eta$ coverage integrated over in the correlation function.

In Fig. 7.4, we show an example, un-normalized two-particle acceptance function for the forward-forward correlations in p+p. One can see the large hole at $\Delta\phi = 0$ and 2π resulting from the separation cut made amongst the clusters (the so-called pair cuts). In Fig. 7.5, we show the pair efficiency for all $p_{T,trig} \otimes p_{T,assoc}$ bins used in this analysis. The pair efficiency κ is defined as the $\Delta\phi$-integral of the acceptance function with pair cuts divided by the integral of the acceptance function without pair cuts (the $\Delta r = 4$ cm cut). One correction is used for each $p_{T,trig} \otimes p_{T,assoc}$ bin as shown in Table 7.1; the values of κ are averaged over all centralities and collision species.

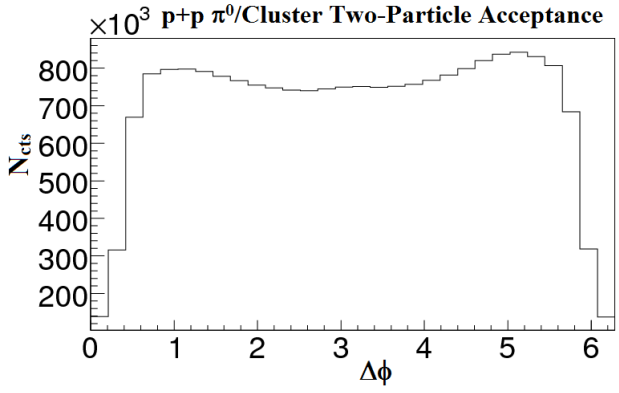

Figure 7.4: Example two-particle forward-forward acceptance function in p+p.

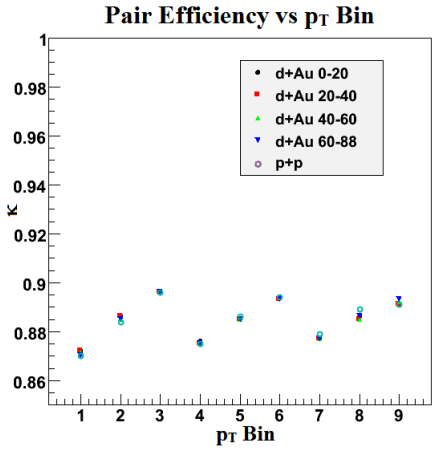

Figure 7.5: Pair acceptance correction versus p_T bin for p+p and d+Au centrality bins.

Table 7.1: Pair acceptance κ.

$p_T bin$	$p_{T,trig}$	$p_{T,assoc}$	κ
1	1.0-1.5	0.625	0.871
2	1.0-1.5	0.875	0.885
3	1.0-1.5	1.25	0.896
4	1.5-2.0	0.625	0.875
5	1.5-2.0	0.875	0.885
6	1.5-2.0	1.25	0.894
7	2.0-5.0	0.625	0.877
8	2.0-5.0	0.875	0.886
9	2.0-5.0	1.25	0.892

7.1.5 Sideband Correction

Similar to the mid-forward correlations, we must correct the forward-forward correlations for background counts underneath the π^0 peak. We employ the procedure outlined in section 6.5.2. We show evidence that our procedure is reasonable in Fig. 7.6. Here we have taken a sample of roughly 500 million p+p PYTHIA→PISA events (the size of our minimum-bias dataset) and measured the same correlation functions. The advantage is that we are able to use the simulations to track the signal (π^0) and background contributions to the correlation functions. Hence we can test our method for subtracting the background contributions to see if it reproduces the true signal correlation functions. In Fig. 7.6, we show these $\Delta\phi$ correlation functions for the true π^0 correlation function (dark blue) and the measured (red). The light blue is the correlation function before correcting the nearside, which will be discussed shortly.

One can see in Fig. 7.6 that the measured awayside peak (red or light blue) almost exactly matches the signal peak (blue), showing that the correlation strength of the signal and background are very similar. However, the nearside peak (light blue) with no other correction is far from the correct value. To correct for this, we try to measure the correlation strength of the background for the nearside peak. The reason we have to do this is that it is possible to have mass resonance decays contributing to the nearside (this will not affect the awayside). Hence we naïvely expect that the correlation strength for the nearside should be larger because of these decays. To correct for this, we try to measure the ratio $C_0 = M_s/M_b$, where M_s is the true signal correlation strength and M_b is the nearside correlation strength of the background. We use the ZYAM subtraction and scale down by a factor F (rather than subtraction). To obtain the correct scaling factor, we must have (note: this is not yet scaled by $\frac{s_2}{s_2+b_2}$)

$$CY_{meas} = M_s s_2 + M_s b_2 = F(M_s s_2 + M_b b_2), \tag{7.2}$$

and hence we define a correction factor to the nearside yield of

$$F \equiv \frac{C_0 \times (s_2 + b_2)}{C_0 s_2 + b_2}. \tag{7.3}$$

Thus by measuring the factor C_0 we can correct the nearside. We measure C_0 in data using the sidebands. In Fig. 7.7, we show this factor as a function of collision centrality measured using the sideband of $m_{inv} = 0.18 - 0.3$ GeV/c^2. To minimize some of the systematics in this procedure, it was decided to only use the first data point for all centrality bins, which has the best statistics. We have two different corrections that we ended up applying: we apply a correction of $C_0 = 0.45$ in p+p and $C_0 = 0.29$ in d+Au. In d+Au we

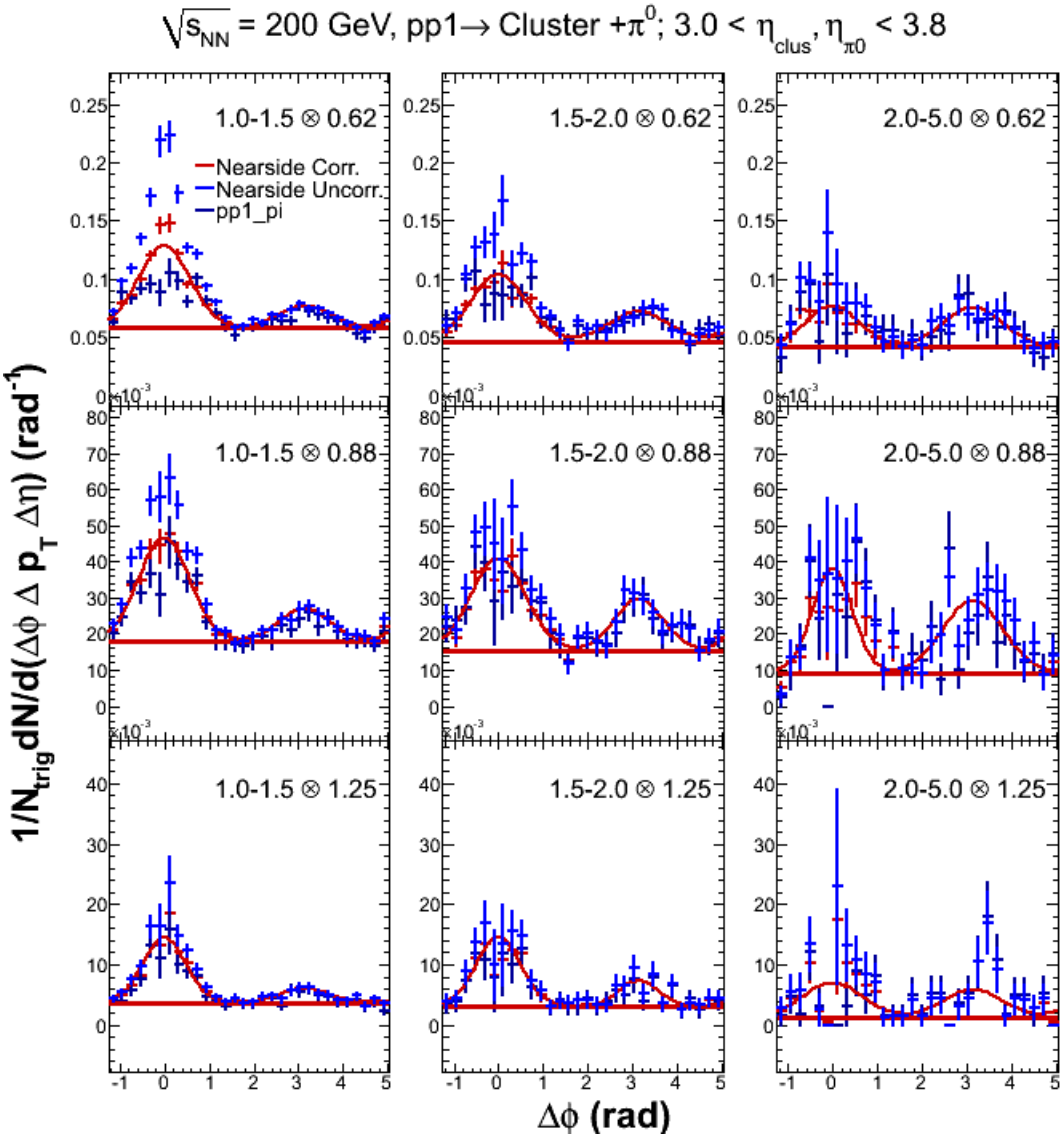

Figure 7.6: Example p+p PYTHIA $\Delta\phi$ correlation functions for the true π^0 correlation function (dark blue) and our measured (red). The light blue is the correlation function before correcting the nearside. The p_T of the trigger (Cluster) and associate particle (MPC π^0) are listed as $p_{T,trig} \otimes p_{T,assoc}$.

measure the factor in all centrality bins and take the average.

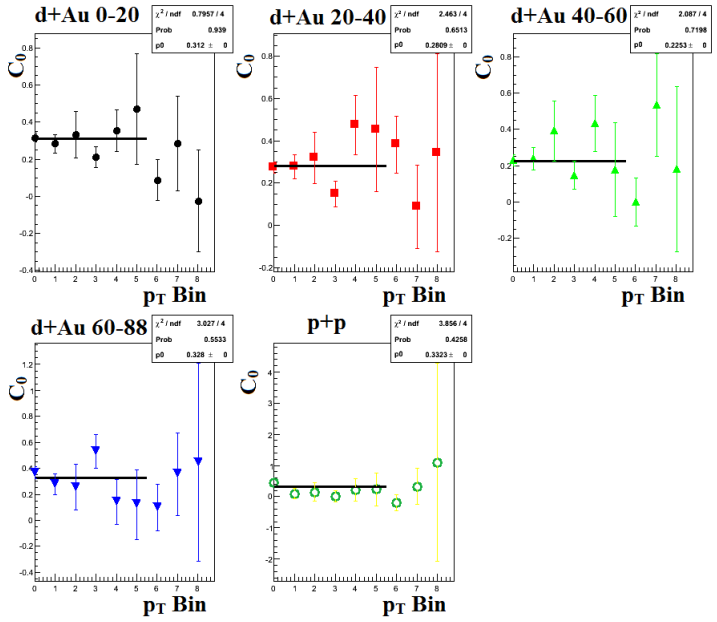

Figure 7.7: Value of $C_0 = \frac{M_s}{M_b}$ for the nearside peak versus p_T bins.

As a test of our procedure and of the correlations in the forward direction, we also embed two p+p events into each other and track the energy depositions across the two events. In Fig. 7.8, we show the corrected correlation functions (red) and the nearside uncorrected (light blue). In Fig. 7.9, we subtract the ZYAM backgrounds and show a comparison of the correlation functions from the two embedded p+p events (red) with the single p+p events (blue) in Fig. 7.9. One can see that there is a good agreement between the true π^0 correlation functions for single p+p events and our measured ones for the two embedded events.

The final corrected correlation functions and background-subtracted correlation functions are shown in Figs. E.1-E.9 in the appendix.

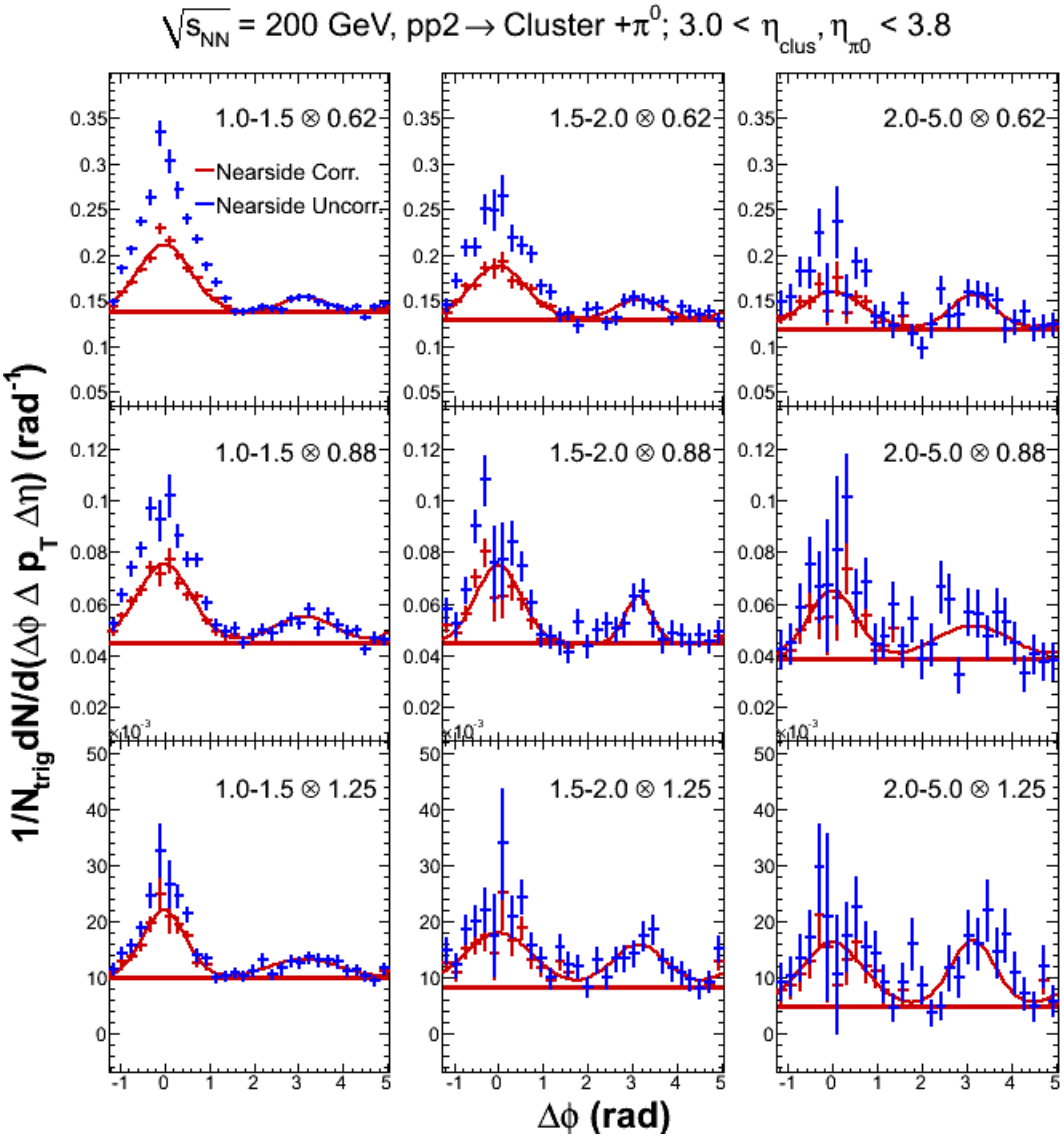

Figure 7.8: Example 2p+p PYTHIA (two p+p events embedded into one another) $\Delta\phi$ correlation functions (red). The light blue is the correlation function before correcting the nearside. The p_T of the trigger (Cluster) and associate particle (MPC π^0) are listed as $p_{T,trig} \otimes p_{T,assoc}$.

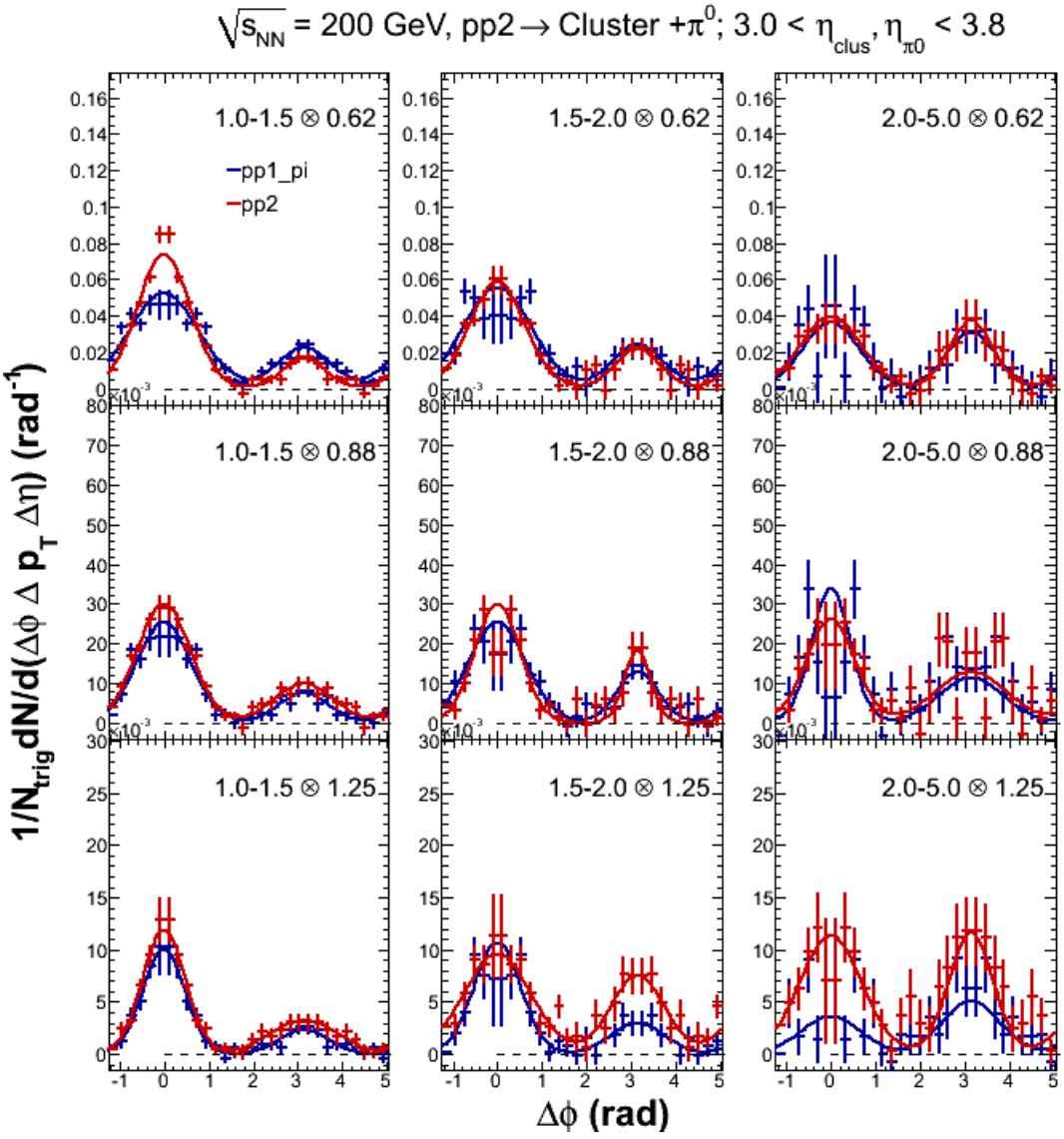

Figure 7.9: Example 2p+p PYTHIA (two p+p events embedded into one another) $\Delta\phi$ correlation functions (red) and the single p+p PYTHIA π^0 correlation functions (blue). The p_T of the trigger (Cluster) and associate particle (MPC π^0) are listed as $p_{T,trig} \otimes p_{T,assoc}$.

7.1.6 Efficiency and Bin-Shift Corrections

We correct the correlation functions with the same efficiency corrections discussed in section 6.5.3 and the bin-shift corrections detailed in section 6.5.4.

7.2 Systematic Errors

The main systematic errors for the forward-forward correlations come from the sideband correction and the ZYAM subtraction procedure. In this section, we detail the errors from each of these sources. In addition, though relatively small, the errors on the yield extraction, efficiency, and energy scale are also incorporated; these calculations were shown in sections 4.4.1, 4.4.2, 4.5.1 respectively.

7.2.1 Sideband Systematics

As with the mid-forward analysis, significant systematic errors arise from the side-band analysis. We assume a 40% error on our assumptions about how the sidebands contribute to the correlation functions in the awayside and a 60% error on the nearside. That is, if we scale down the correlation function by $\frac{s_2}{s_2+b_2}$, then our systematic error on the awayside becomes

$$s_{away} = 0.4 \times \big(1 - \frac{s_2}{s_2 + b_2}\big), \tag{7.4}$$

while the systematic error on the nearside is

$$s_{near} = 0.6 \times \big(1 - \frac{s_2}{s_2 + b_2} \times F\big). \tag{7.5}$$

7.2.2 ZYAM I_{dA} and J_{dA} Systematics

Our procedure for calculating I_{dA} and J_{dA} is made difficult by the fact that our Gaussian peaks are wide. We have resorted to using a ZYAM procedure for the pedestal determination in our measurements of I_{dA} and J_{dA}. ZYAM is a procedure that can be systematically off for calculating the conditional yields, but less so for calculating either I_{dA} or J_{dA}. This is true because the ZYAM estimate for the conditional yield will be systematically low (because the pedestal is too high) in both p+p and d+Au, and thus the ratio of the CYs cancels portions of the systematic errors.

To understand the systematic behavior of ZYAM, we create "simulated correlation functions" by adding

nearside and awayside Gaussian peaks on top of a constant pedestal. We fit the known correlation functions with our ZYAM procedure, and try to understand how systematically off the ZYAM assumption is by varying the widths of the peaks as well as the awayside signal fraction ($f = \frac{A}{A+N}$), where A and N are the area of the awayside and nearside peaks.

Let us define a few variables that will be relevant to this discussion. Let A (N) refer to the true area of the away (near) side Gaussian peak, and σ_A (σ_N) refer to the true width of the peaks. We define A_z (N_z) as the area of the respective ZYAM measured areas.

In our previously shown simulated study (Fig. 7.3), the vertical axis (awayside signal fraction) corresponds to $A/(A+N)$, while the horizontal axis is the true width of the awayside σ_A. We measure A_z and N_z for the correlation functions, and thus we can measure the ratio $A_z/(A_z + N_z)$. We can also reconstruct $\sigma_{A,Z}$ and $\sigma_{N,Z}$ or the ZYAM widths of the peaks, and subsequent studies are performed for different values of σ_N.

In Fig. 7.10, we show the $\sigma_{A,Z}$ (colored scale) as a function of $A/(A+N)$ and σ_A for a fixed nearside width of $\sigma_N = 0.6$.

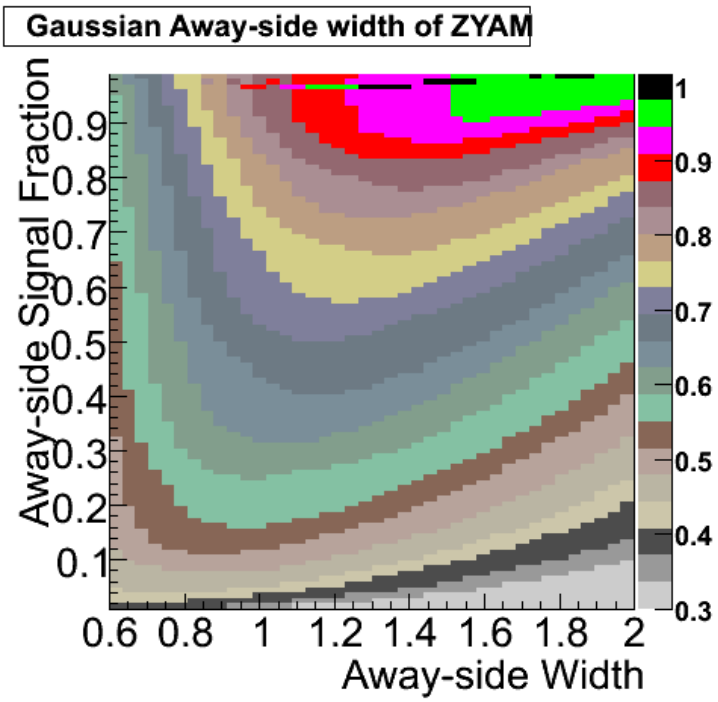

Figure 7.10: ZYAM $\sigma_{A,Z}$ (colored scale) with varying values of σ_A (horizontal axis) and $A/(A+N)$ (vertical axis) for a fixed nearside width of 0.6.

One can see that the measured ZYAM-width level-curves of the awayside are not monotonic, and hence there arises an ambiguity if we attempt to extract the true awayside width from the ZYAM width; this

difficulty propagates to the extraction of the awayside area. It is possible that for very wide peaks there is a significant area hidden underneath the correlation function.

It would thus seem that a significant broadening as well as a suppression in the yields can have the same effect on the correlation functions. We first evaluate the systematic errors under the assumption that the broadening is not so significant and that the awayside peak has widths that are not significantly larger than the mid-forward case as well as the Muon Arm $h^{\pm}$/MPC π^0 case (the Muon Arm/MPC correlations were briefly studied and appear similar to the mid-forward correlations). In both of these sets of CFs, the widths do not rise above 1.3 for virtually any correlation function, and hence we use this as our upper limit when evaluating the systematic error.

Let us now outline the procedure used for calculating the error in the ZYAM assumption; we use this as our systematic error for the conditional yields. From the data, we can measure $A_Z/(A_Z + N_Z)$. For our simulated correlation function, we measure $\frac{A_Z+N_Z}{A+N}$ and A_Z/A for varying values of $A/(A+N)$, σ_A, and σ_N, as shown in Figs. 7.11-7.12.

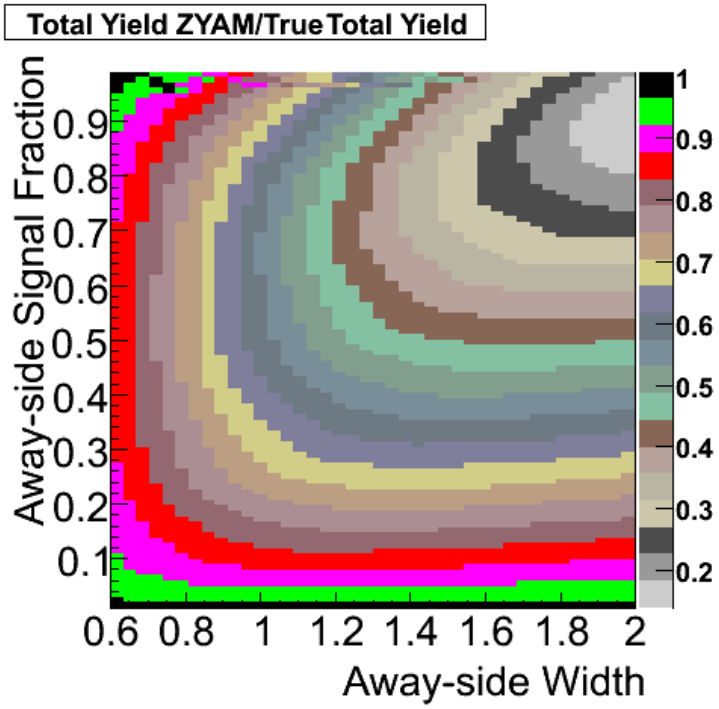

Figure 7.11: Simulated values of $\frac{A_Z+N_Z}{A+N}$ (colored scale) with varying values of σ_A (horizontal axis) and $A/(A+N)$ (vertical axis) for a fixed nearside width of 0.6.

For a given awayside width σ_A, we use our simulation to determine $A/(A+N)$ from our measured ratio and the simulated distributions. A 7^{th} degree polynomial is fit to the 1-dimensional projection of the

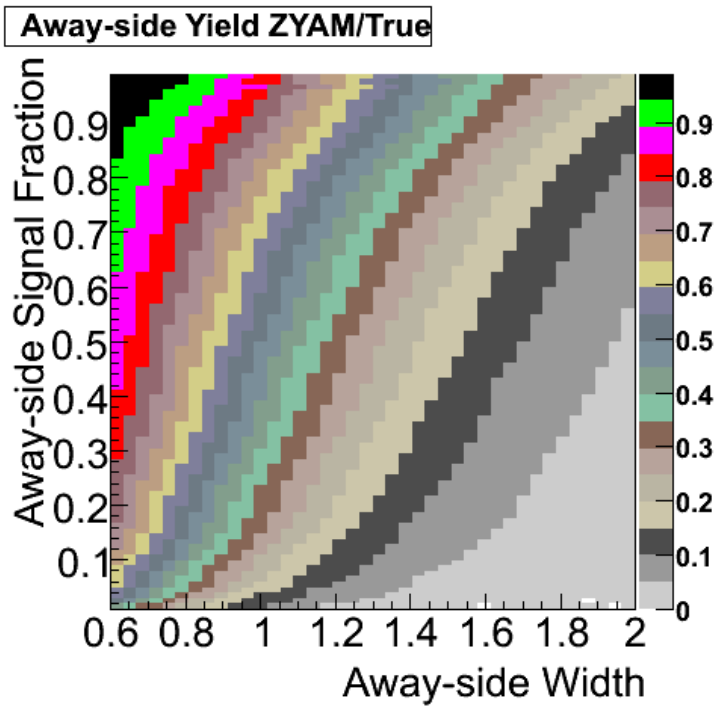

Figure 7.12: Simulated values of $\frac{A_Z}{A}$ (colored scale) with varying values of σ_A (horizontal axis) and $A/(A+N)$ (vertical axis) for a fixed nearside width of 0.6.

$f_1 \equiv A_Z/A$ distribution while a 6^{th} degree polynomial is fit to the $f_2 \equiv \frac{A_Z+N_Z}{A+N}$ distribution; the projections are now a function of $A/(A+N)$. We then calculate the value of $A/(A+N)$ that gives the best match to $\frac{A_Z}{A_Z+N_Z} \times 1/f_1 \times f_2$. We perform this procedure for 13 different values of σ_A distributed uniformly between $0.7 - 1.3$. We additionally vary the nearside width from 0.55, 0.60, and 0.65. Also, we allow our input ratio $A_Z/(A_Z+N_Z)$ to vary by $\pm 20\%$ in 10% increments. Thus we have essentially calculated a (one-sided) distribution which we can call our systematic error. To completely utilize all information from our fit, we also weight by how well the value of $\sigma_{A,Z}$ matches that expected from our simulated study. This does not change the error significantly, as we use a relatively weak weighting function where the width is μ:

$$w(\mu) = (1 + (2/\mu)Gaus(\mu, \sigma = 0.1\mu))^2. \tag{7.6}$$

In this weighting function, we first give all widths from $0.7 - 1.3$ a weight of 1, which corresponds to an area of $0.6 \times 1 = 0.6$. We add on top of this a Gaussian peak and square the entire function. The area of the Gaussian-like function on top of the background is ≈ 1.2. Thus, the peak region has a weight of $\approx 3 - 4$ higher than the rest of the widths.

This ensures that we give more weight to values of σ_A where the ZYAM width between our simulated CFs and measured ones match, but does not weight so heavily that the other cases are not accounted for. Thus we have our one-sided error distributions for the CYs which can be extremely large, and that are measured for all centralities.

The next step is to take the ratio of the CYs to form I_{dA}. The nice thing about using ZYAM in this ratio is that ZYAM will provide an answer for the CY that is too small, and thus by taking the ratio of the ZYAM yields, the systematic error from the ZYAM assumptions cancel. We thus take the (one-sided) systematic error distributions from the CYs above and use these to calculate an asymmetric systematic error for the ratio of the CYs.

Procedurally, we iterate through each bin of the d+Au and p+p CY systematic-error histograms in question, and calculate the ratio of the horizontal values in the two histograms. For instance, let us say the d+Au ZYAM CY is low by a factor of 4, while the p+p ZYAM CY is low by a factor of 2. Then we would say that the systematic error from using the ZYAM assumption on I_{dA} is $s_Z = 4/2 - 1 = +100\%$. Thus we would have an error of 100%. If on the other hand our p+p error was 4 and the d+Au error was 2, then we would have an error of $s_Z = 2/4 - 1 = -50\%$; from this simple example one can see how the asymmetric error bars arise. We use all combinations of the error histograms for the CYs; the weight is the product of the heights in each bin.

At this point, we also use a constraint from the physical system; we have observed that the d+Au peripheral and p+p correlation functions are similar, as the collision systems are very similar. If we allow the range of widths to vary uniformly between 0.7-1.3 for both systems simultaneously, we ignore the fact that the collision systems are so similar, and the error becomes larger; for example, if one has a small width in p+p (say 0.6) and a large width in d+Au (say 1.3), then the ZYAM yield in p+p will be very close to the true value, whereas it will be much different in d+Au. Thus, we choose to create a weighting function that is similar to a step function to try to account for the fact that peripheral d+Au and p+p correlation functions are similar.

$$f(\Delta w) = \begin{cases} 15.0/\Delta w & \Delta w < k \\ 1.0 & \text{else} \end{cases} \tag{7.7}$$

where $\Delta w = w_{dA} - w_{pp}$, and $k = \frac{\langle N_{coll} \rangle}{15.06} \times min(w_{pp}, w_{dA})$. We thus see that for d+Au central collisions, the weighting function is large when the widths are within 100% of each other, while for peripheral collisions the weight is large when the widths are within 20%. Thus our systematic error includes more possible broadening in d+Au central collisions, and less-so for d+Au peripheral collisions.

In Figs. 7.13-7.14, we see the error distributions for d+Au central and peripheral collisions. The systematic error is calculated from these distributions by taking one standard deviation on the left- and right-hand sides of the distribution.

7.3 Results

7.3.1 Correlation Functions

Our final correlation functions are shown as

$$1/N_{trig} \frac{d^3N}{d\Delta\phi dp_T d\eta} = C_{up-down} \times C_{leak} \times \frac{dN/d\Delta\phi}{N_{trig}\epsilon_a \kappa \Delta p_T \Delta\eta} \tag{7.8}$$

where $C_{up-down}$ is the up-down bin-shift correction, C_{leak} accounts for the leakage of the π^0 counts outside the window used in our analysis, κ is the pair-acceptance correction, and ϵ_a is the single-particle efficiency for the MPC π^0's.

In Figs. 7.15-7.16, we show the ZYAM pedestal subtracted correlation functions for d+Au peripheral and central compared to p+p.

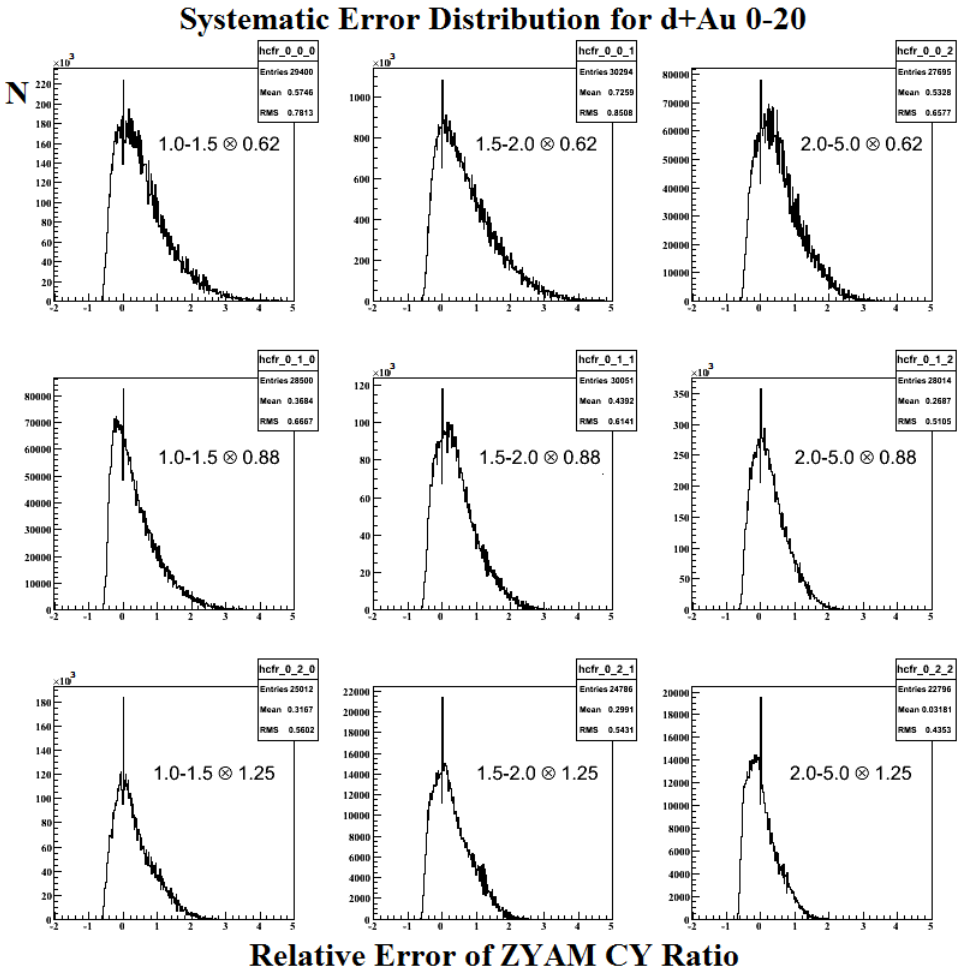

Figure 7.13: Relative error distributions of the ZYAM conditional-yield ratio between d+Au 0-20% and p+p for the different p_T bins.

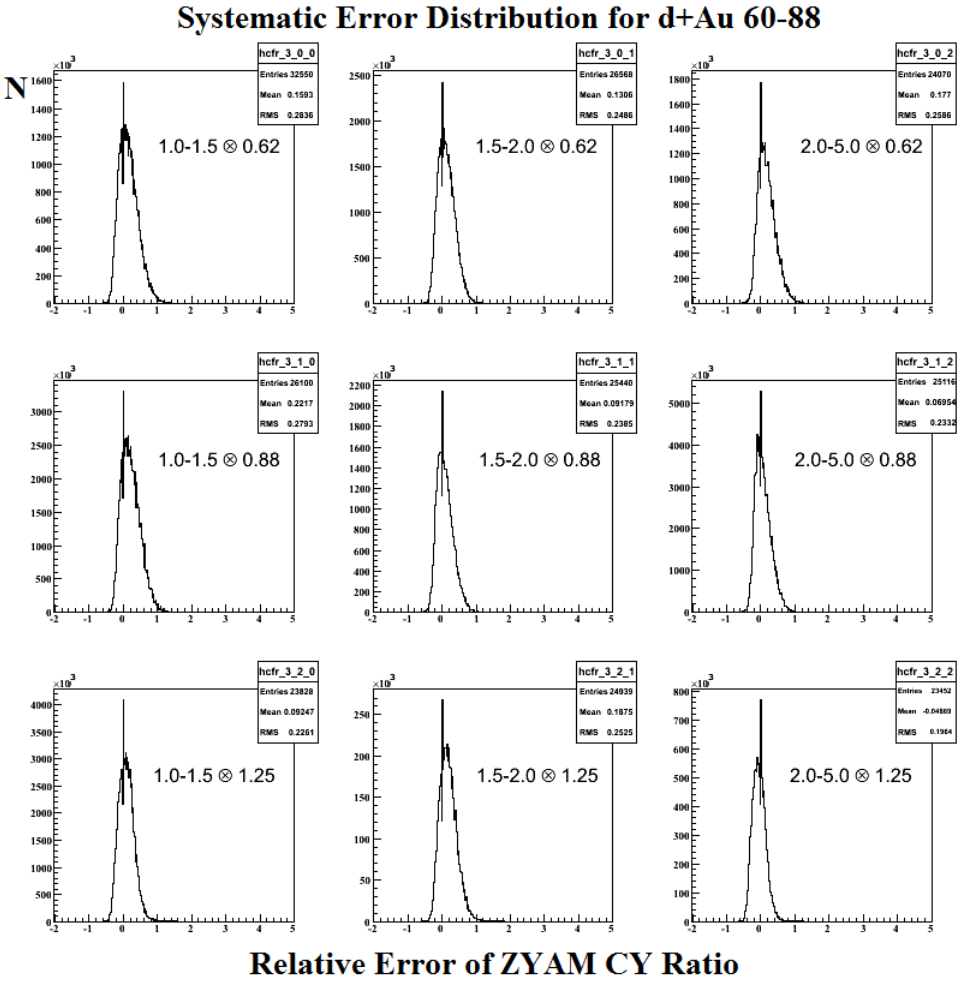

Figure 7.14: Relative error distributions of the ZYAM conditional-yield ratio between d+Au 60-88% and p+p for the different p_T bins.

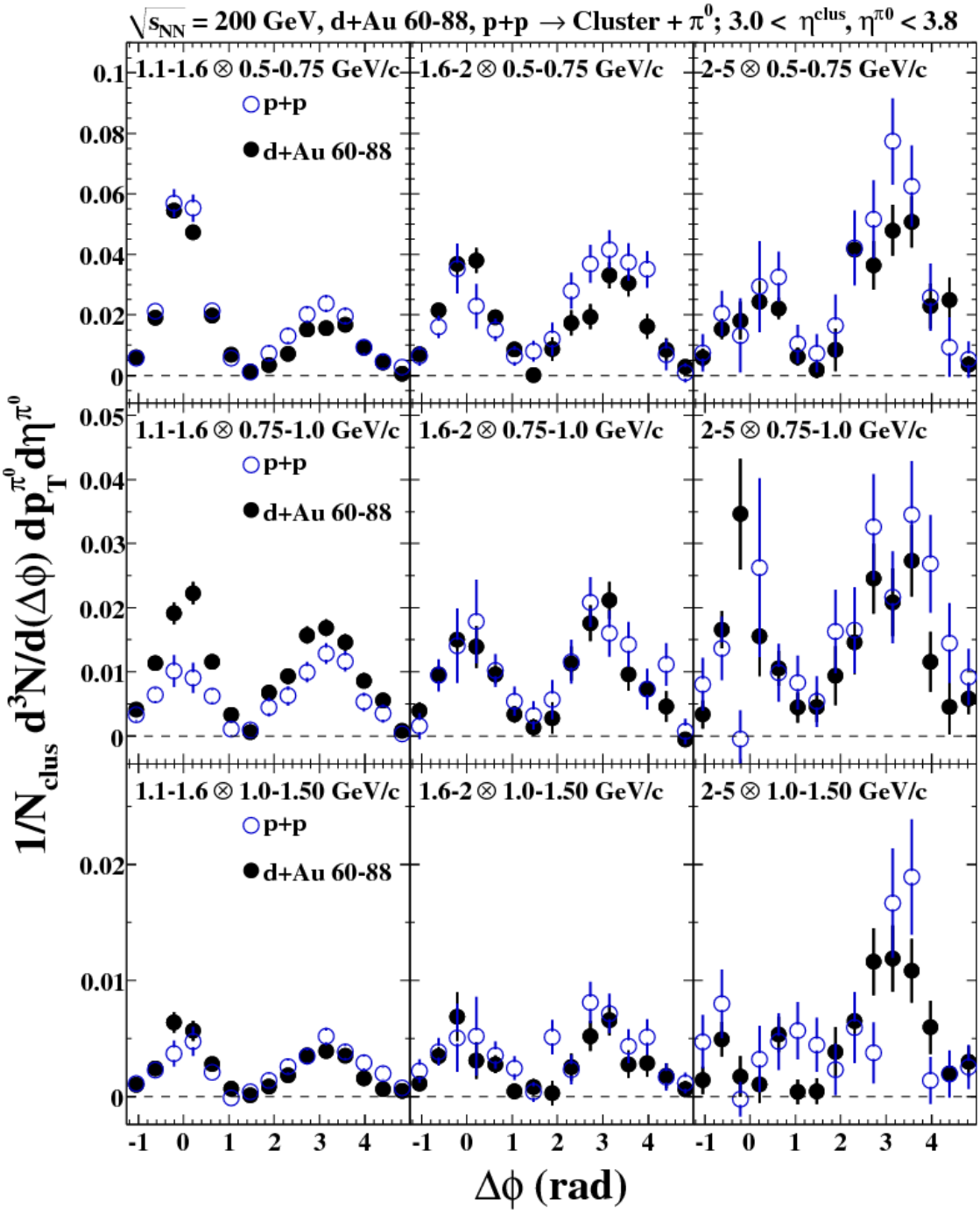

Figure 7.15: ZYAM background-subtracted MPC-cluster/MPC-π^0 $\Delta\phi$ correlation functions for d+Au 60-88% (black, full circles) compared with the p+p correlation functions (blue, open circles). The p_T of the trigger (MPC cluster) and associate particle (MPC π^0) are listed as $p_{T,trig} \otimes p_{T,assoc}$.

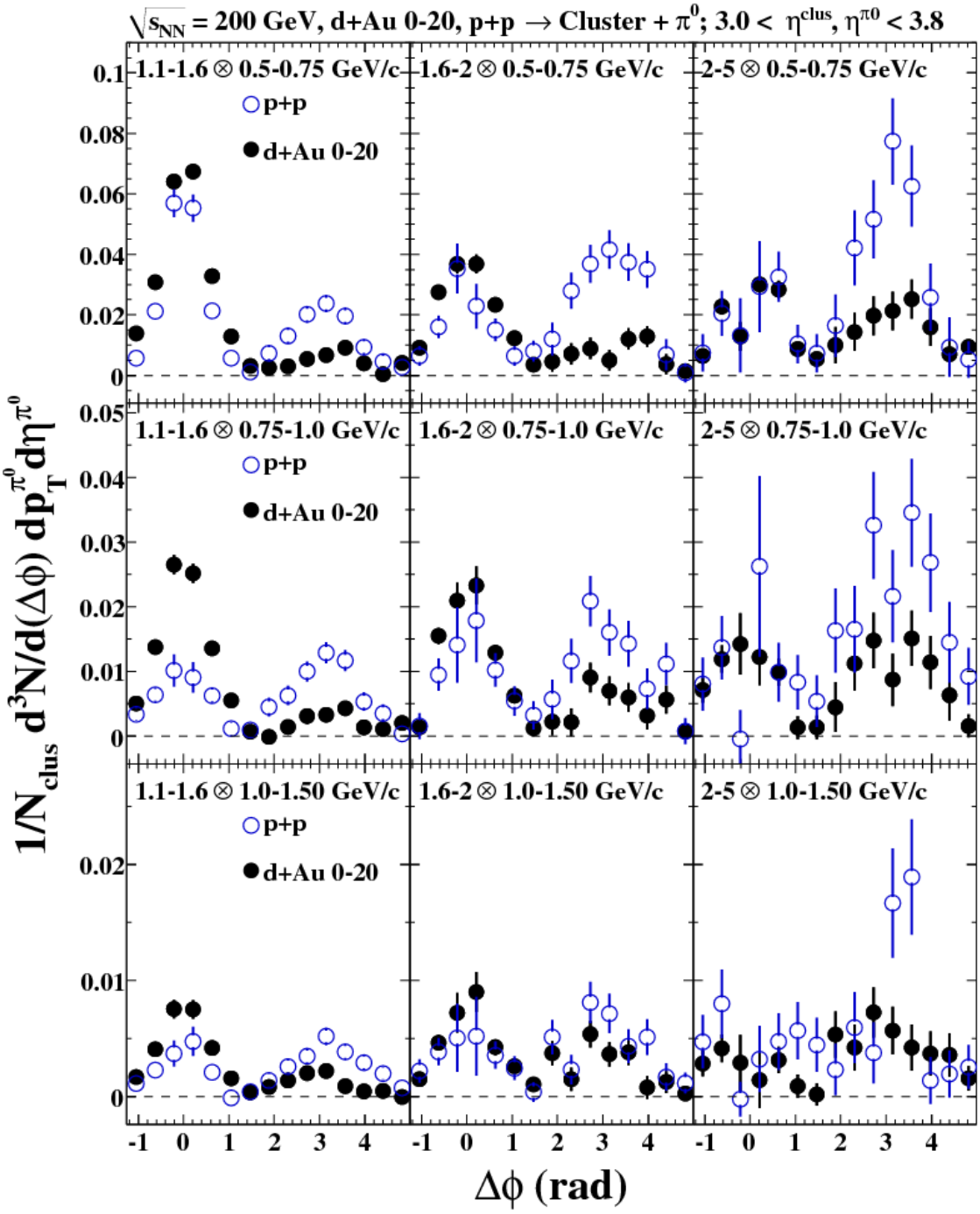

Figure 7.16: ZYAM background-subtracted MPC-cluster/MPC-π^0 $\Delta\phi$ correlation functions for d+Au 0-20% (black, full circles) compared with the p+p correlation functions (blue, open circles). The p_T of the trigger (MPC cluster) and associate particle (MPC π^0) are listed as $p_{T,trig} \otimes p_{T,assoc}$.

One can see that the awayside appears suppressed in central d+Au collisions as compared to p+p (but is similar in peripheral d+Au), and thus there appears to be a di-jet suppression when both jets are forward. Alternatively, if the awayside peak does not come from di-jets[1] but rather other correlations in the forward direction, then this conclusion cannot be drawn.

In Appendix E.2, we show the cluster/π^0 correlation functions for all centrality bins. We show the corrected correlation functions, fit, and a comparison with the nearside uncorrected plots. Then we show the ZYAM subtracted correlation functions and a comparison with the p+p correlation functions.

In Tables E.1-E.3, we show the various factors that go into the calculation of the conditional yields and the relative errors. In Tables E.4-E.6, we show the conditional yields, ZYAM fit widths, and show the contributions to the systematic error (excluding the ZYAM assumption error).

[1] This idea is motivated by a PYTHIA study in appendix A.

7.3.2 $I_{\rm dA}$ and $J_{\rm dA}$

We next show the nuclear modification factor $I_{dA} = CY_{dA}/CY_{pp}$ in Fig. 7.17 for the forward-forward correlations using the ZYAM subtraction and the systematic errors we described previously. It is shown as a function of the number of binary collisions N_{coll}. One can indeed see an increasing suppression with increasing $N_{\rm coll}$.

To calculate J_{dA}, we also need the R_{dA} values for the clusters, which have not yet been measured. It has been found through PYTHIA studies that the clusters are dominated by π^0's, and hence we use the values of the π^0 $R_{\rm dA}$ in this calculation. This is further justified because a comparison of the $R_{\rm dA}$ values of π^0's to those of clusters (without efficiency corrections) shows excellent agreement. The reason we can make this comparison with clusters is that the geometric acceptance of the MPC does not change between d+Au and p+p, and the multiplicity does not significantly differ either. Hence the efficiencies of d+Au and p+p nearly cancel in the $R_{\rm dA}$ ratio, and using the ratio of uncorrected cluster spectra gives a nearly correct answer.

What value of p_T do we use for R_{dA}? From Fig. 7.18 below, we see that R_{dA} looks very linear (i.e. $R_{dA} = \sum a_i p_T^i$ where $i \in \{0, 1\}$). The linearity for $R_{\rm dA}$ simplifies our calculation to using the p+p $\langle p_T \rangle$ values for each bin as we show below. Let us say the p+p spectrum is $f(p_T)$ and the d+Au spectrum scaled by $1/N_{coll}$ is $g(p_T)$. Thus we have

$$g(p_T) = R_{dA}(p_T) f(p_T). \tag{7.9}$$

We define x_0, y_0 such that for a given bin

$$f(x_0) = C \times \int_{p_1}^{p_2} f(x) dx, \tag{7.10}$$

$$g(y_0) = C \times \int_{p_1}^{p_2} g(y) dy, \tag{7.11}$$

where p_1 and p_2 are the lower and upper bin edges and $C = 1.0/(p_2 - p_1)^2$. Thus we have

$$g(y_0) = C \times \int_{p_1}^{p_2} g(y) dy = C \times \int_{p_1}^{p_2} R_{dA}(x) f(x) dx \tag{7.12}$$

$$= C \times \int_{p_1}^{p_2} \sum (a_i x^i) f(x) dx = \sum a_i f(x_0) \langle x^i \rangle \tag{7.13}$$

[2] If $f = g$, then $x_0 = y_0$

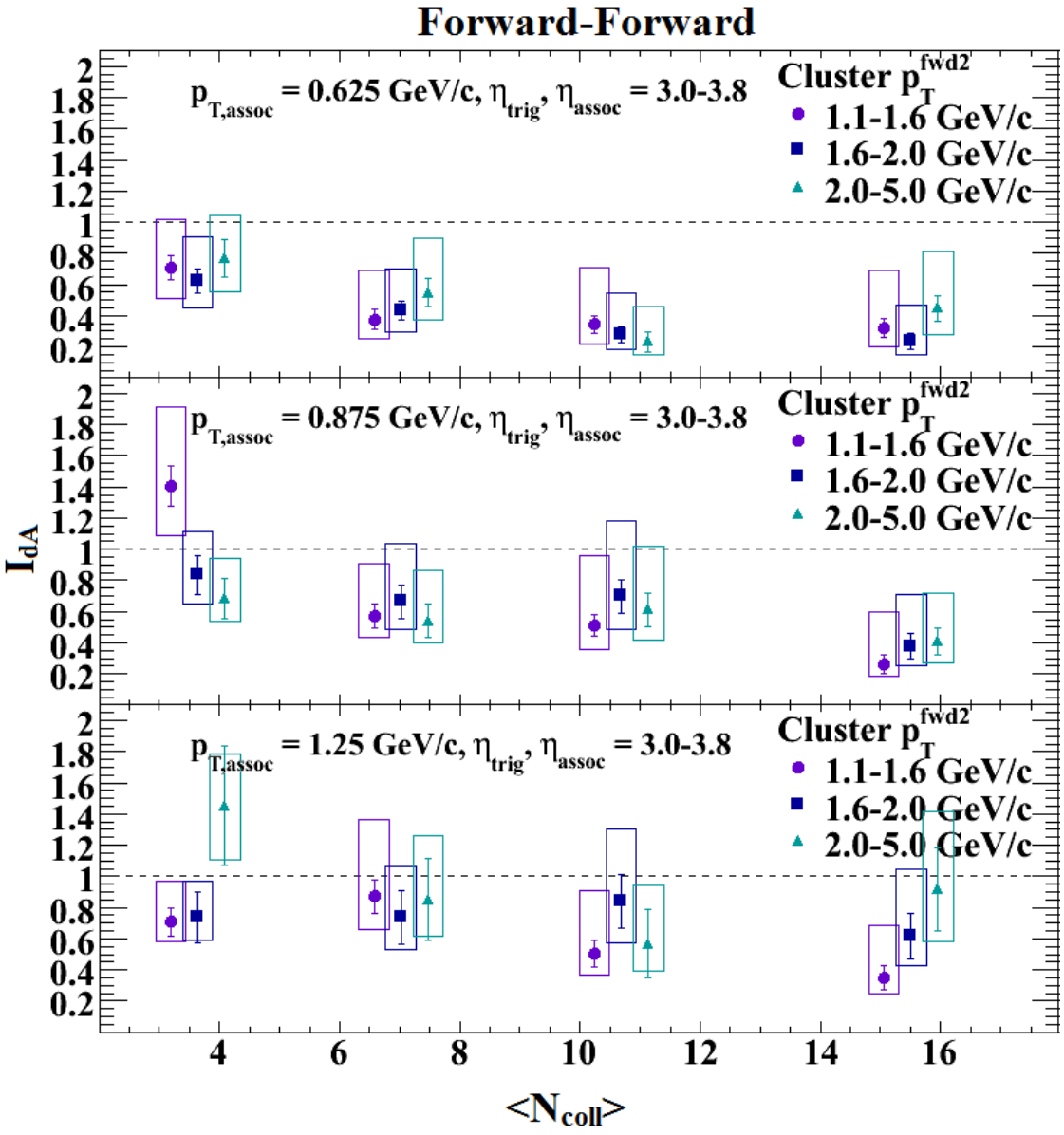

Figure 7.17: I_{dA} versus N_{coll} for all trigger and associate p_T values. The systematic error on each point is shown by the open boxes. The $\langle N_{\rm coll}\rangle$ values within a centrality selection are offset from their actual values for visual clarity (see text for actual $\langle N_{\rm coll}\rangle$ values).

Thus we see that for our bin we have

$$R_{dA} = \sum a_i \langle {p_T}^i \rangle \tag{7.14}$$

where $\langle {p_T}^i \rangle = \frac{\int_{p_1}^{p_2} x^i f(x) dx}{\int_{p_1}^{p_2} x^i dx}$.

Hence, if R_{dA} is linear as a function of p_T, then we simply need to use the average value in this bin of p_T from the p+p spectrum. We employ this procedure for the p_T bins with ranges 1.08-1.57 GeV/c and 1.57-2.04 GeV/c; from a fit to the p+p π^0 spectrum, we determine that the associated p_T-bin averages are $\langle p_T \rangle = 1.25, 1.75$ GeV/c. For the highest p_T bin, we have to extrapolate, since we do not measure the value of R_{dA} here. We have chosen to take the value of $R_{dA}(p_T = 2)$, and thus increase systematic error on this data point. In addition to the systematic error of the points, we add an additional systematic error that is based on the linear fit to R_{dA}. We take the difference between the value we use at $p_T = 2$ and the extrapolated value of R_{dA} from the linear fit at $p_T = 2.5$ GeV/c (see Fig. 7.18).

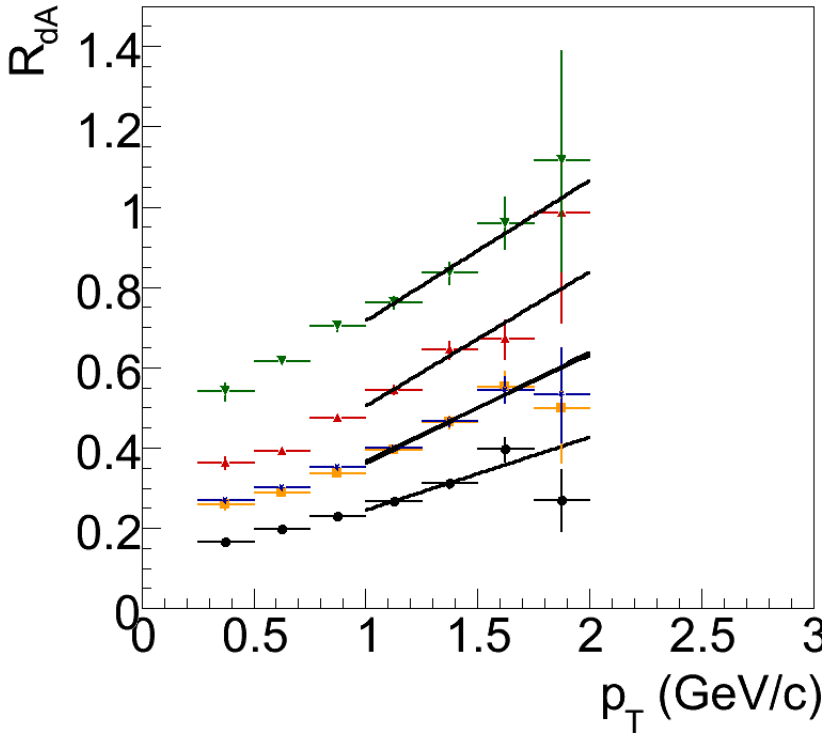

Figure 7.18: Fits to R_{dA} for all centrality bins (d+Au 60-88, top to d+Au 0-20, bottom).

For the statistical and systematic errors we use the two bins for R_{dA} that roughly correspond to the

binning of the cluster p_T range. The errors are calculated based on a simple formula that could be used to combine the bins

$$R = \frac{R_1 p_1 + R_2 p_2}{p_1 + p_2}, \tag{7.15}$$

where R_i are the R_{dA} values for the two bins and p_i are the p+p p_T-spectrum values. We simply propagate the errors using the above formula, adding statistical errors in quadrature and essentially averaging the systematic errors by replacing R_i with s_i in the eq. 7.15 above. The highest p_T bin (2.04-5.0 GeV/c) uses the systematic errors from the $1.57 - 2.04$ GeV/c bin added in quadrature with the error determined by the fit. The final $R_{\rm dA}$ values, statistical errors (σ_{RdA}), and systematic errors (s_{RdA}) are shown in Table 7.2.

Table 7.2: R_{dA} and statistical and systematic errors for the fit.

d+Au 0-20%			
p_T	R_{dA}	σ_{RdA}	s_{RdA}
1.25	0.290	0.00540	0.0233
1.75	0.380	0.0385	0.0625
2	0.426	0	0.0876
d+Au 20-40%			
p_T	R_{dA}	σ_{RdA}	s_{RdA}
1.25	0.431	0.00800	0.0351
1.75	0.567	0.0548	0.0938
2	0.637	0	0.147
d+Au 40-60%			
p_T	R_{dA}	σ_{RdA}	s_{RdA}
1.25	0.589	0.0109	0.0475
1.75	0.754	0.0744	0.115
2	0.838	0	0.200
d+Au 60-88%			
p_T	R_{dA}	σ_{RdA}	s_{RdA}
1.25	0.805	0.0135	0.0630
1.75	0.977	0.0871	0.163
2	1.066	0	0.269

Armed with these values of R_{dA}, we calculate J_{dA}, as seen in Fig. 7.19. J_{dA} follows simply as $J_{dA} = R_{dA,trig} \times I_{dA,trig}$. One can clearly see an even larger suppression in $J_{\rm dA}$ than $I_{\rm dA}$ because of the suppression of $R_{dA,trig}$ in the forward direction.

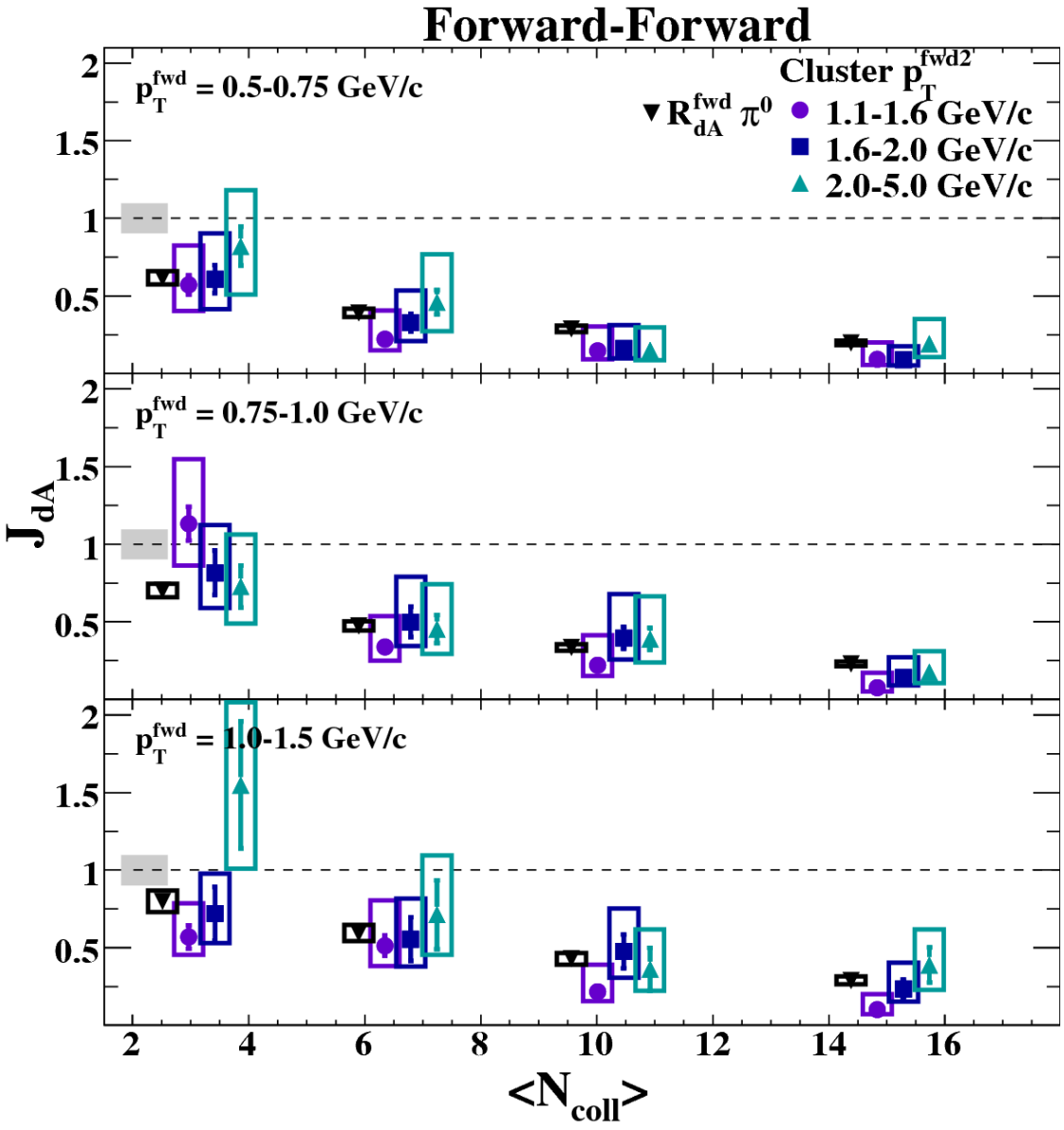

Figure 7.19: J_{dA} versus N_{coll} for all trigger and associate p_T values. The systematic error on each point is shown by the open boxes. The gray error band at the left on each panel represents a global systematic scale error of 9.7%. Additional centrality-dependent systematic errors of 7.5%, 5.1%, 4.1%, and 4.8% for the peripheral to central bins, respectively, are not shown. The $\langle N_{\rm coll}\rangle$ values within a centrality selection are offset from their actual values for visual clarity (see text for actual $\langle N_{\rm coll}\rangle$ values).

Chapter 8

Discussion

We have thus far presented an array of measurements in an attempt to understand different aspects of forward-particle production and probe whether or not gluon saturation can be observed at RHIC. These new single-particle $R_{\rm dA}$ measurements show an increasing suppression with increasing $N_{\rm coll}$ at forward rapidities and add to knowledge from previous measurements at STAR [4] and BRAHMS [3]. As discussed in the introduction, the different shadowing models alone cannot explain the observed suppression in $R_{\rm dA}$.

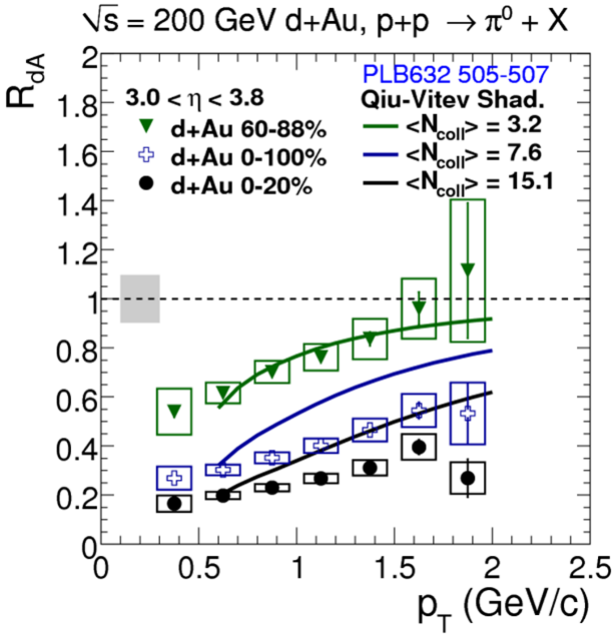

Figure 8.1: Forward π^0 $R_{\rm dA}$ for peripheral, unbiased and central d+Au events compared with shadowing-predictions from the Qiu-Vitev shadowing model [10]. The systematic error on each point is shown by the open boxes. The gray error band at the left represents a global systematic scale error of 9.7%. Additional centrality-dependent systematic errors of 7.5%, 5.1%, 4.1%, and 4.8% for the peripheral to central bins, respectively, are not shown.

In Fig. 8.1, we show a comparison of the forward π^0 $R_{\rm dA}$ measurement presented in this thesis with

the higher-twist shadowing predictions from Qiu and Vitev [10]. One can see that this shadowing cannot account for the observed suppression in the central or unbiased (0-100%) curves, but does match well in the peripheral case where shadowing effects are minimal.

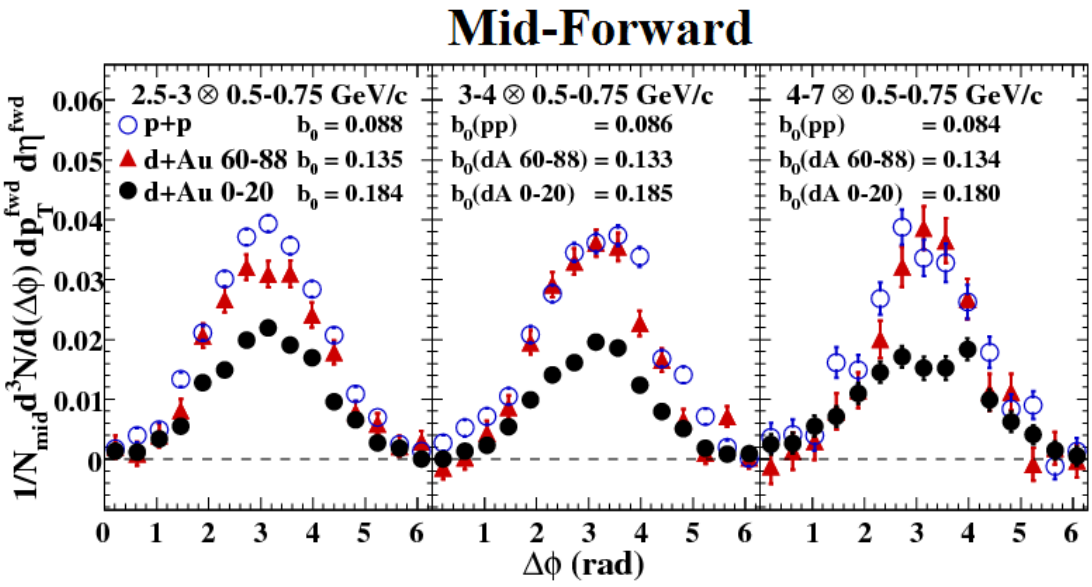

Figure 8.2: Pedestal-subtracted π^0-π^0 per-trigger correlation functions for, as indicated, p+p, d+Au peripheral (60–88% centrality) and d+Au central (0–20% centrality) collisions at $\sqrt{s_{NN}} = 200$ GeV; the associated π^0's of $p_T = 0.5$–0.75 GeV/c are measured at forward rapidity ($3.0 < \eta < 3.8$) and the triggered π^0's are measured at midrapidity ($|\eta| < 0.35$) for the indicated p_T ranges. The subtracted pedestal values, b_0, are also indicated.

In addition to the single-particle probes, we have also presented two sets of correlation functions (mid-forward and forward-forward); a selection of correlation functions from p+p, peripheral d+Au and central d+Au are shown in Figs. 8.2-8.3. We quantify the di-jet modification in d+Au compared to p+p by using $I_{\rm dA}$ and $J_{\rm dA}$. Several PHENIX measurements in both d+Au and Au+Au have been made using $I_{\rm dA}$, the ratio of conditional yields; however, few measurements exist for $J_{\rm dA}$. One of the main reasons we use $J_{\rm dA}$ in this measurement is that the value of $J_{\rm dA}$ does not change if we arbitrarily switch the trigger and associate appellations, as is the case with $I_{\rm dA}$. Also, $J_{\rm dA}$ is the correlated two-particle analogue of $R_{\rm dA}$ and hence one might say that it is a more fundamental quantity than $I_{\rm dA}$. In Ref. [10], the authors use their higher-twist shadowing framework to make predictions for $J_{\rm dA}$ for mid-forward correlations. In Fig. 8.4, we show a comparison with our calculated $J_{\rm dA}$ values and the shadowing predictions.

One can see that the suppression of J_{dA} increases with increasing N_{coll} in a very similar manner to the shadowing predictions. In the most central collisions (largest $N_{\rm coll}$), the shadowing model seems to

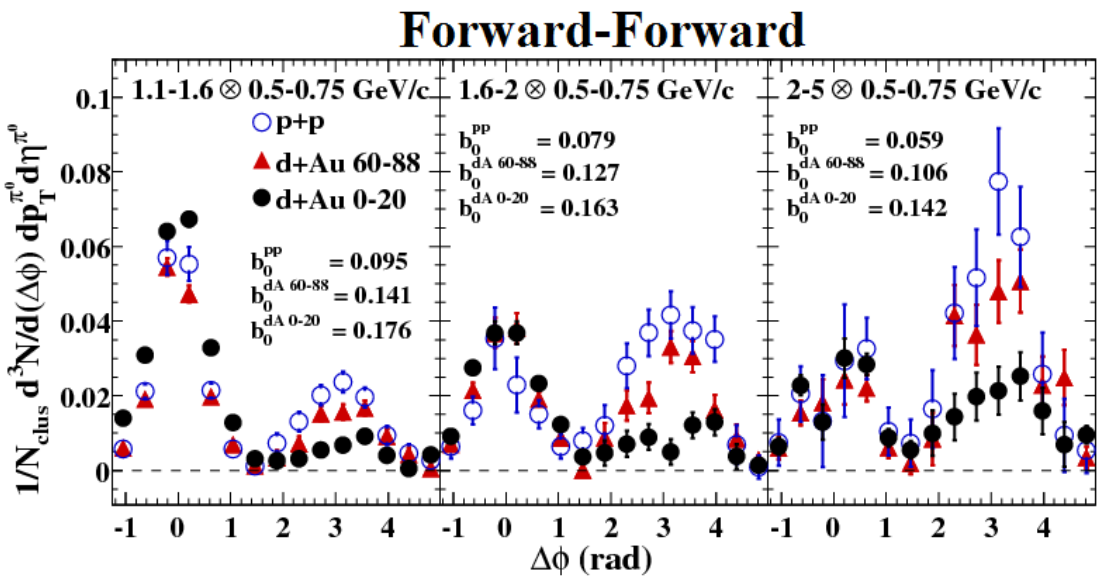

Figure 8.3: Pedestal-subtracted cluster-π^0 per-trigger correlation functions measured at forward rapidity ($3.0 < \eta < 3.8$) for, as indicated, p+p, d+Au peripheral (60–88% centrality) and d+Au central (0-20% centrality) collisions at $\sqrt{s_{NN}} = 200$ GeV; the correlation functions are for associated π^0's of $p_T = 0.5$–0.75 GeV/c and trigger clusters over the indicated p_T ranges. Systematic errors of up to 30% on the nearside ($|\Delta\phi| < 0.5$) are not shown. The subtracted pedestal values, b_0, are also indicated.

underpredict the level of suppression observed, though the match is better than expected. It appears that shadowing can account for much of the observed suppression, though not all of it. The correct theory must be able to simultaneously explain the behavior of $R_{\rm dA}$ as well as $J_{\rm dA}$, and the shadowing model in question still has a relatively large discrepancy with $R_{\rm dA}$ and a smaller one with $J_{\rm dA}$.

As mentioned in the introduction, the addition of initial-state energy-loss to the Qiu-Vitev shadowing model seems to be able to explain the suppression of the STAR $R_{\rm dA}$ data [54], and it would be interesting to see if it could explain both the PHENIX $R_{\rm dA}$ and $J_{\rm dA}$ data. The CGC theory, on the other hand, also seems to be able to explain the suppression in $R_{\rm dA}$ through gluon saturation effects (though there is some question about why at high p_T when $Q^2 >> Q_s^2$ the suppression does not disappear) [52]. Though early CGC predictions for the mid-forward correlations were produced [2], the newer theoretical advancements focus on the forward-forward correlations [6, 90, 138], as the mid-forward do not seem to have a small enough Bjorken-x for the theorists to make accurate predictions [85].

What is interesting about this statement is that the most probable di-jet configuration where one jet is forward is to have the other at midrapidity (the mid-forward system). Hence when calculating the forward-particle cross sections used for the forward $R_{\rm dA}$, one would expect that CGC would integrate over the

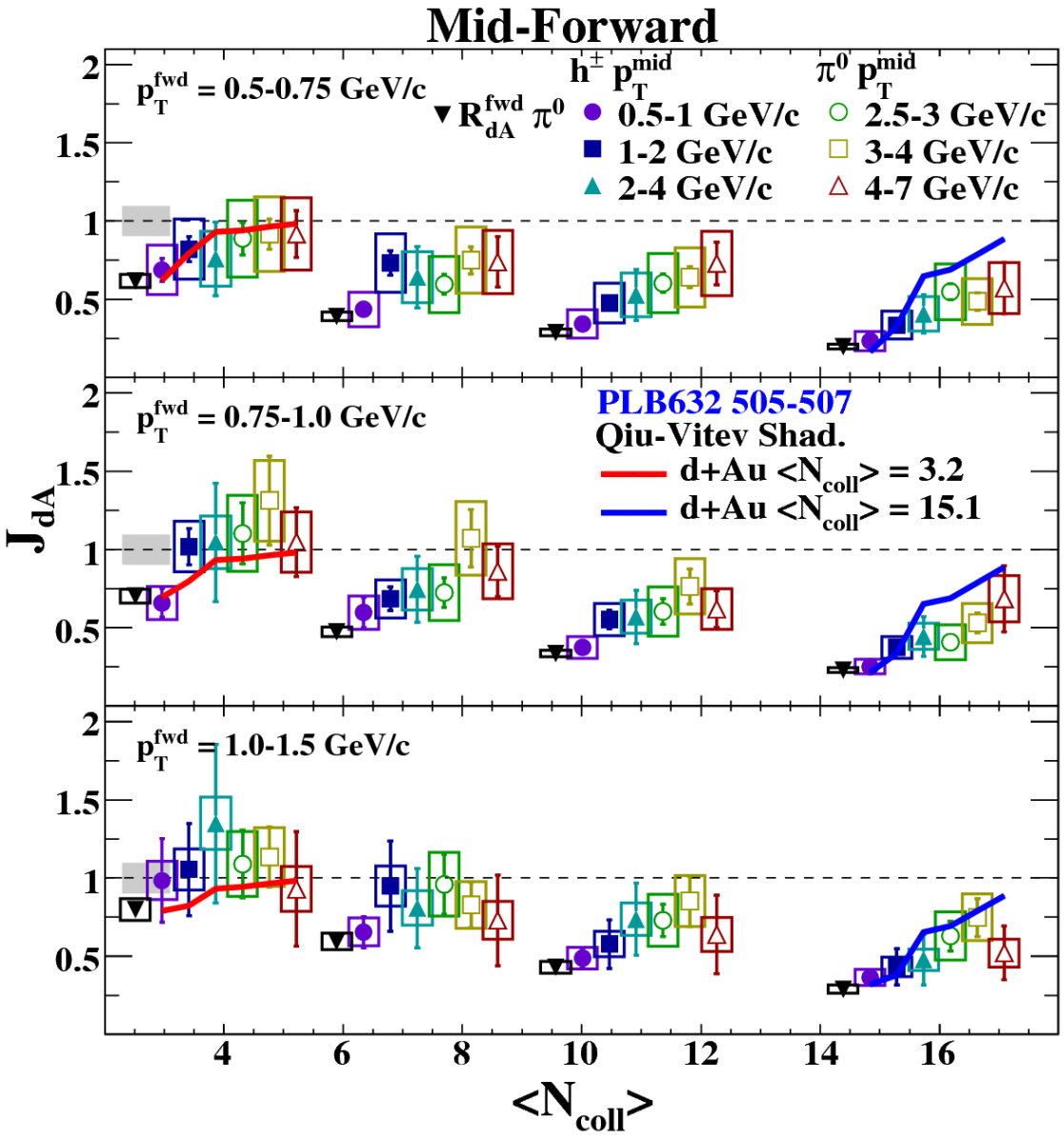

Figure 8.4: Midrapidity-hadron/forward-rapidity π^0 $J_{\rm dA}$ measurements compared with shadowing-predictions from the Qiu-Vitev shadowing model [10]. The systematic error on each point is shown by the open boxes. The gray error band at the left on each panel represents a global systematic scale error of 9.7%. Additional centrality-dependent systematic errors of 7.5%, 5.1%, 4.1%, and 4.8% for the peripheral to central bins, respectively, are not shown. The $\langle N_{\rm coll}\rangle$ values within a centrality selection are offset from their actual values for visual clarity (see text for actual $\langle N_{\rm coll}\rangle$ values).

mid-forward di-jet cross sections (for the $R_{\rm dA}$ predictions), or that these di-jet cross sections would be accounted for in the calculations. However, as stated the theory can produce $R_{\rm dA}$ predictions but does not seem to be not applicable to the mid-forward di-jet system.

To make this point clearer, we now discuss a direct relationship between $J_{\rm dA}$ and $R_{\rm dA}$. Assuming that all hard-scattering interactions appear as di-jet systems (ignoring 3-jet events and different CGC diagrams), one can define the hard-scattering component of $R_{\rm dA}$ as a weighted integral of $J_{\rm dA}$ over one particle's rapidity and p_T. First, we define $R_{\rm dA}$ in terms of the "hard" and "soft" components. Y^{soft} and Y^{hard} are defined as the p_T and η dependent invariant yields per N_{coll} (eq. 4.1) for the hard and soft components of the differential cross section, and we have

$$R_{\rm dA}(p_T,\eta) = \frac{Y_{dA}^{hard}(p_T,\eta) + Y_{dA}^{soft}(p_T,\eta)}{Y_{pp}^{hard}(p_T,\eta) + Y_{pp}^{soft}(p_T,\eta)} = \frac{R_{dA}^{hard}(p_T,\eta)Y_{pp}^{hard} + R_{dA}^{soft}(p_T,\eta)Y_{pp}^{soft}}{Y_{pp}^{hard}(p_T,\eta) + Y_{pp}^{soft}(p_T,\eta)}. \tag{8.1}$$

Next, we can define R_{dA}^{hard} as

$$R_{dA}^{hard}(p_T^a,\eta^a) = \frac{\int dp_T^b d\eta^b J_{dA}(p_T^a,\eta^a,p_T^b,\eta^b) w_{pp}^{hard}(p_T^a,\eta^a,p_T^b,\eta^b)}{\int dp_T^b d\eta^b w_{pp}^{hard}(p_T^a,\eta^a,p_T^b,\eta^b)}, \tag{8.2}$$

where w_{pp}^{hard} is a weighting function (the correlated p+p di-hadron cross section) and a and b are arbitrary particle indices used to distinguish the two particles. In performing the integral over p_T^b and η^b, one should note that the largest weight is given to the lower values of p_T^b at midrapidity; this is where the correlated di-hadron cross section is the largest.

In light of this discussion, we again note that in Fig. 8.4, we show both the mid-forward $J_{\rm dA}$ values as well as the values of the forward $R_{\rm dA}$. We would naïvely expect the lower p_T values of $J_{\rm dA}$ to contribute the most to R_{dA}^{hard}. Interestingly enough, one can see that in the lowest p_T^{mid} bin of $0.5-1.0$ GeV/c for the charged hadrons, the match between $J_{\rm dA}$ and $R_{\rm dA}$ is quite good. As p_T^{mid} increases, the values of $J_{\rm dA}$ increase and move farther away from the $R_{\rm dA}$ values. However, these values have a much smaller weight in eq. 8.2, and hence these values are not so important in determining ${R_{\rm dA}}^{hard}$. It is also interesting to note that in the low-p_T bins ($p_T \lesssim 1$ GeV/c) one would expect to have a very large soft component to $R_{\rm dA}$; even so, we still have a good match between the low-p_T^{mid} $J_{\rm dA}$ values and $R_{\rm dA}$.

One interesting aspect of the suppression is that it seems to increase with decreasing trigger p_T^{mid}, which directly would correspond to a decrease in x, as for these kinematics $x \approx \frac{p_T^{mid}}{\sqrt{s_{NN}}}$. Qualitatively speaking, this phenomenon would be predicted by both nuclear shadowing models and CGC, as both indicate increasing suppression with decreasing x. However, the shadowing models do not seem to account for the observed level

of the suppression, and hence there is likely more at work than leading- or higher-twist shadowing. One can also see that R_{dA} is consistently $< J_{dA}$, though for the small p_T^{mid} values they are similar. This means that per-detected forward particle there are more midrapidity particles produced in d+Au than in the analogous p+p measurement, or in other words $I_{dA,fwd-trig} > 1$ if we trigger in the forward direction as opposed to $I_{dA,mid-trig} < 1$ for the midrapidity trigger. While these results follow naturally from the definition of $J_{\rm dA}$ and the fact that ${R_{\rm dA}}^{mid} \neq {R_{\rm dA}}^{fwd}$ (i.e. $J_{\rm dA} = I_{dA,fwd-trig} \times R_{dA}^{fwd} = I_{dA,mid-trig} \times R_{dA}^{mid}$), this difference in trigger-particle definitions created confusion early on (which probably still exists) when interpreting our $I_{dA,mid-trig}$ results as a suppression. Some thought that the suppression we observed proved CGC, while others were more skeptical. Hence, it was decided that more measurements were needed, as this measurement was not able to distinguish amongst the competing models.

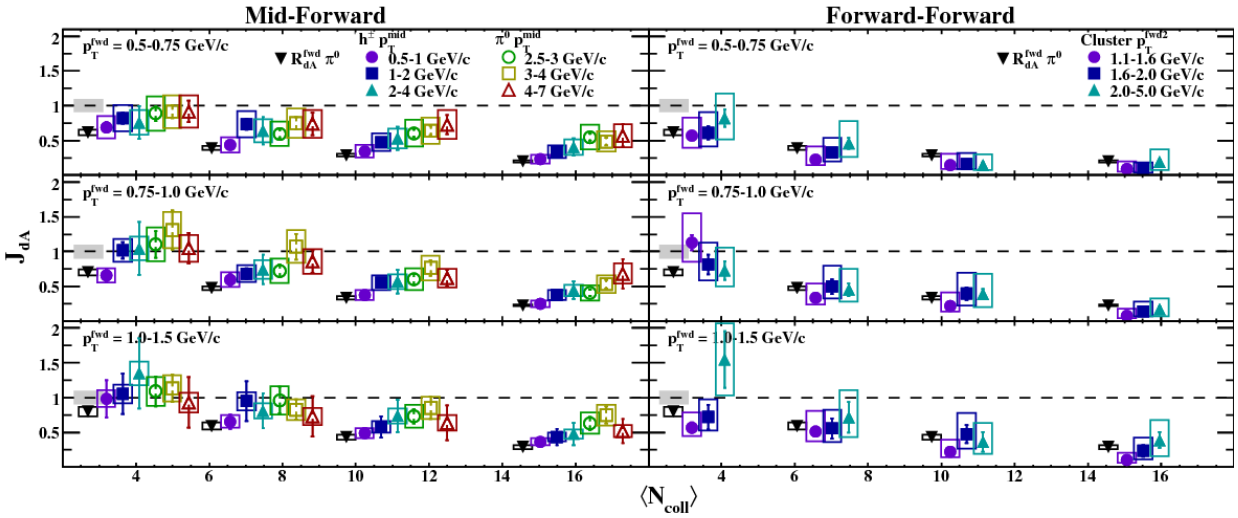

Figure 8.5: J_{dA} versus $\langle N_{\rm coll} \rangle$ for forward rapidity ($3.0 < \eta < 3.8$) π^0's paired with midrapidity ($|\eta| < 0.35$) hadrons and π^0's (left), and for forward rapidity ($3.0 < \eta < 3.8$) cluster-π^0 pairs (right) for the indicated combinations of p_T. Also plotted are the values of the forward π^0 $R_{\rm dA}$. The systematic error on each point is shown by the open boxes. The gray error band at the left on each panel represents a global systematic scale error of 9.7%. Additional centrality-dependent systematic errors of 7.5%, 5.1%, 4.1%, and 4.8% for the peripheral to central bins, respectively, are not shown. The $\langle N_{\rm coll} \rangle$ values within a centrality selection are offset from their actual values for visual clarity (see text for actual $\langle N_{\rm coll} \rangle$ values).

We thus formed correlation functions between MPC π^0's and hadrons detected in the Muon Arm Spectrometers ($1.2 < |\eta| < 2.2$)) to reach smaller values of x. However, after seeing a preliminary STAR result from Les Bland wherein two π^0's were correlated at very forward rapidities ($2.5 < \eta < 4.0$) and what appeared to be a significant modification, it was decided to pursue a similar measurement with the MPC. Thus, in an attempt to observe the effects of gluon saturation, we constructed di-hadron correlation functions

where both particles were at forward rapidities, or $\langle\eta^{1,2}\rangle \approx 3.3$. The reason for choosing this measurement is simple: it can probe the lowest values of x_{Au} achievable at RHIC. From eq 1.15, we see that the value of x_{Au} becomes $x_{Au} \approx \frac{1/30\times(p_{T,1}+p_{T,2})}{\sqrt{s_{NN}}}$ and hence the measurement is sensitive to x values around 5×10^{-4}. The decrease in x causes an increase in the saturation scale Q_s and it is expected that we should be sensitive to saturation effects [90]. In Fig. 8.5 (right panel), we show $J_{\rm dA}$ for the forward-forward correlations versus $N_{\rm coll}$ for varying π^0-p_T^{fwd} and cluster-p_T^{fwd2} values. One can see that the suppression in $J_{\rm dA}$ reaches a factor 10 in some bins. We also display the values of $R_{\rm dA}$ for the π^0's and in the left panel show the mid-forward correlations. This plot essentially summarizes all of the measurements presented in this thesis.

In order to show the explicit x dependence of $J_{\rm dA}$, in Fig. 8.6 we plot $J_{\rm dA}$ against the variable x_{frag}^{Au}, which is essentially the same as x_2 in eq. 1.15, or

$$x_{frag}^{Au} = \frac{\langle p_{T,1}\rangle e^{-\langle y_1\rangle} + \langle p_{T,2}\rangle e^{-\langle y_2\rangle}}{\sqrt{s}}. \tag{8.3}$$

This variable would be the momentum fraction of partons in the Au-nucleus given a $z = 1$ ($z \equiv \frac{p_{hadron}}{p_{parton}}$) fragmentation wherein all jet energies are deposited into the particles used in the correlation functions. At midrapidity, the values of z are $\sim 0.5 - 0.75$ [140], and we would thus expect that x_{frag}^{Au} is slightly smaller than the true value of x_{Au}, though not by more than a factor of 2. In Fig. 8.6 we have plotted $J_{\rm dA}$ for both the forward-forward correlations ($x_{frag}^{Au} < 10^{-3}$) as well as the mid-forward correlations ($x_{frag}^{Au} > 10^{-3}$). The general trend seems to be that the suppression increases with decreasing x and increasing impact parameter, which qualitatively would be predicted by CGC. Hence we have provided the x dependence of the correlated di-hadron nuclear modification factor (one might even say di-jet nuclear modification factor), which is crucial to distinguishing between the competing theories. It will be especially interesting to see if the CGC theory predictions match our observed trends in the data. In Tables 8.1-8.4 we show the data tables of J_{dA} for different values of x as determined by p_T and η combinations of the two particles. The statistical errors, asymmetric systematic errors (s_{low}, s_{high}) and global systematic errors (s_{gl}) are all listed.

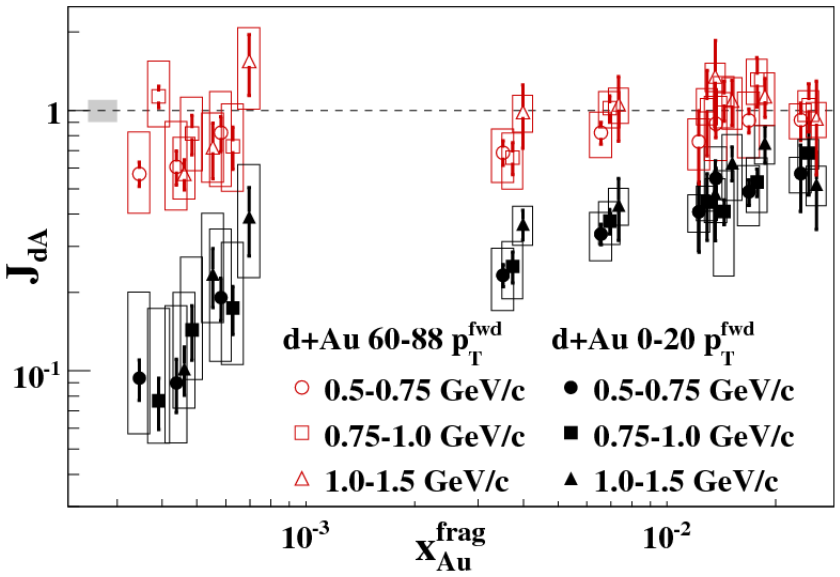

Figure 8.6: J_{dA} versus $x_{\mathrm{Au}}^{\mathrm{frag}}$ for peripheral (60–88%) and central (0–20%) d+Au collisions at $\sqrt{s_{NN}} = 200$ GeV. The systematic and statistical error bars are the same as in Fig. 8.5. Above $x_{\mathrm{Au}}^{\mathrm{frag}} > 10^{-3}$, some data points were offset from their true $x_{\mathrm{Au}}^{\mathrm{frag}}$ to avoid overlap. The leftmost point in each group of three is at the correct $x_{\mathrm{Au}}^{\mathrm{frag}}$.

Table 8.1: J_{dA} vs x, systematic, statistical errors for $3.0 < \eta^{fwd} < 3.8$, d+Au 0-20%.

d+Au 0-20%							
p_T^{trig}	p_T^{assoc}	x_{Au}^{frag}	J_{dA}	σ_{JdA}	s_{Jda}^{low}	s_{Jda}^{high}	$s_{gl,JdA}/J_{dA}$
1.25	0.625	3.46e-04	0.093	0.016	0.036	0.107	0.108
1.75	0.625	4.38e-04	0.090	0.021	0.037	0.088	0.108
2.53	0.625	5.82e-04	0.191	0.035	0.083	0.160	0.108
1.25	0.875	3.92e-04	0.077	0.017	0.024	0.097	0.108
1.75	0.875	4.84e-04	0.144	0.034	0.051	0.129	0.108
2.53	0.875	6.28e-04	0.174	0.037	0.069	0.137	0.108
1.25	1.250	4.61e-04	0.102	0.021	0.030	0.098	0.108
1.75	1.250	5.53e-04	0.235	0.060	0.082	0.168	0.108
2.53	1.250	6.97e-04	0.390	0.114	0.162	0.229	0.108
0.68	0.625	3.52e-03	0.233	0.023	0.062	0.062	0.108
1.29	0.625	6.57e-03	0.335	0.030	0.070	0.070	0.108
2.43	0.625	1.23e-02	0.407	0.122	0.067	0.067	0.108
2.71	0.625	1.37e-02	0.548	0.052	0.178	0.178	0.108
3.35	0.625	1.69e-02	0.486	0.055	0.126	0.126	0.108
4.67	0.625	2.35e-02	0.572	0.163	0.090	0.090	0.108
0.68	0.875	3.56e-03	0.252	0.035	0.062	0.062	0.108
1.29	0.875	6.61e-03	0.375	0.040	0.070	0.070	0.108
2.43	0.875	1.23e-02	0.445	0.128	0.067	0.067	0.108
2.71	0.875	1.37e-02	0.409	0.045	0.178	0.178	0.108
3.35	0.875	1.69e-02	0.531	0.064	0.126	0.126	0.108
4.67	0.875	2.35e-02	0.685	0.212	0.090	0.090	0.108
0.68	1.250	3.63e-03	0.365	0.048	0.062	0.062	0.108
1.29	1.250	6.68e-03	0.432	0.116	0.070	0.070	0.108
2.43	1.250	1.24e-02	0.478	0.162	0.067	0.067	0.108
2.71	1.250	1.38e-02	0.630	0.095	0.178	0.178	0.108
3.35	1.250	1.70e-02	0.748	0.121	0.126	0.126	0.108
4.67	1.250	2.36e-02	0.520	0.172	0.090	0.090	0.108

Table 8.2: J_{dA} vs x, systematic, statistical errors for $3.0 < \eta^{fwd} < 3.8$, d+Au 20-40%.

d+Au 20-40%							
p_T^{trig}	p_T^{assoc}	x_{Au}^{frag}	J_{dA}	σ_{JdA}	s_{Jda}^{low}	s_{Jda}^{high}	$s_{gl,JdA}/J_{dA}$
1.25	0.625	3.46e-04	0.148	0.026	0.055	0.157	0.105
1.75	0.625	4.38e-04	0.160	0.033	0.062	0.153	0.105
2.53	0.625	5.82e-04	0.148	0.040	0.062	0.150	0.105
1.25	0.875	3.92e-04	0.220	0.031	0.069	0.192	0.105
1.75	0.875	4.84e-04	0.397	0.072	0.140	0.282	0.105
2.53	0.875	6.28e-04	0.391	0.070	0.153	0.272	0.105
1.25	1.250	4.61e-04	0.218	0.036	0.061	0.175	0.105
1.75	1.250	5.53e-04	0.476	0.108	0.169	0.278	0.105
2.53	1.250	6.97e-04	0.362	0.139	0.140	0.255	0.105
0.68	0.625	3.52e-03	0.342	0.034	0.091	0.091	0.105
1.29	0.625	6.57e-03	0.476	0.045	0.103	0.103	0.105
2.43	0.625	1.23e-02	0.527	0.164	0.104	0.104	0.105
2.71	0.625	1.37e-02	0.604	0.059	0.190	0.190	0.105
3.35	0.625	1.69e-02	0.641	0.066	0.176	0.176	0.105
4.67	0.625	2.35e-02	0.729	0.136	0.109	0.109	0.105
0.68	0.875	3.56e-03	0.374	0.051	0.091	0.091	0.105
1.29	0.875	6.61e-03	0.553	0.061	0.103	0.103	0.105
2.43	0.875	1.23e-02	0.570	0.170	0.104	0.104	0.105
2.71	0.875	1.37e-02	0.603	0.081	0.190	0.190	0.105
3.35	0.875	1.69e-02	0.765	0.111	0.176	0.176	0.105
4.67	0.875	2.35e-02	0.619	0.117	0.109	0.109	0.105
0.68	1.250	3.63e-03	0.488	0.066	0.091	0.091	0.105
1.29	1.250	6.68e-03	0.578	0.156	0.103	0.103	0.105
2.43	1.250	1.24e-02	0.737	0.230	0.104	0.104	0.105
2.71	1.250	1.38e-02	0.730	0.104	0.190	0.190	0.105
3.35	1.250	1.70e-02	0.852	0.161	0.176	0.176	0.105
4.67	1.250	2.36e-02	0.639	0.251	0.109	0.109	0.105

Table 8.3: J_{dA} vs x, systematic, statistical errors for $3.0 < \eta^{fwd} < 3.8$, d+Au 40-60%.

d+Au 40-60%							
p_T^{trig}	p_T^{assoc}	x_{Au}^{frag}	J_{dA}	σ_{JdA}	s_{Jda}^{low}	s_{Jda}^{high}	$s_{gl,JdA}/J_{dA}$
1.25	0.625	3.46e-04	0.221	0.039	0.072	0.187	0.110
1.75	0.625	4.38e-04	0.327	0.057	0.117	0.209	0.110
2.53	0.625	5.82e-04	0.460	0.079	0.186	0.309	0.110
1.25	0.875	3.92e-04	0.337	0.046	0.086	0.200	0.110
1.75	0.875	4.84e-04	0.500	0.097	0.156	0.292	0.110
2.53	0.875	6.28e-04	0.453	0.090	0.160	0.291	0.110
1.25	1.250	4.61e-04	0.513	0.064	0.130	0.291	0.110
1.75	1.250	5.53e-04	0.556	0.140	0.177	0.263	0.110
2.53	1.250	6.97e-04	0.713	0.221	0.257	0.382	0.110
0.68	0.625	3.52e-03	0.435	0.046	0.111	0.111	0.110
1.29	0.625	6.57e-03	0.732	0.077	0.123	0.123	0.110
2.43	0.625	1.23e-02	0.642	0.197	0.110	0.110	0.110
2.71	0.625	1.37e-02	0.596	0.064	0.180	0.180	0.110
3.35	0.625	1.69e-02	0.749	0.086	0.235	0.235	0.110
4.67	0.625	2.35e-02	0.739	0.161	0.120	0.120	0.110
0.68	0.875	3.56e-03	0.597	0.096	0.111	0.111	0.110
1.29	0.875	6.61e-03	0.685	0.076	0.123	0.123	0.110
2.43	0.875	1.23e-02	0.746	0.210	0.110	0.110	0.110
2.71	0.875	1.37e-02	0.725	0.094	0.180	0.180	0.110
3.35	0.875	1.69e-02	1.073	0.184	0.235	0.235	0.110
4.67	0.875	2.35e-02	0.860	0.160	0.120	0.120	0.110
0.68	1.250	3.63e-03	0.655	0.100	0.111	0.111	0.110
1.29	1.250	6.68e-03	0.948	0.288	0.123	0.123	0.110
2.43	1.250	1.24e-02	0.809	0.253	0.110	0.110	0.110
2.71	1.250	1.38e-02	0.960	0.192	0.180	0.180	0.110
3.35	1.250	1.70e-02	0.828	0.146	0.235	0.235	0.110
4.67	1.250	2.36e-02	0.729	0.290	0.120	0.120	0.110

Table 8.4: J_{dA} vs x, systematic, statistical errors for $3.0 < \eta^{fwd} < 3.8$, d+Au 60-88%.

d+Au 60-88%							
p_T^{trig}	p_T^{assoc}	x_{Au}^{frag}	J_{dA}	σ_{JdA}	s_{Jda}^{low}	s_{Jda}^{high}	$s_{gl,JdA}/J_{dA}$
1.25	0.625	3.46e-04	0.571	0.061	0.168	0.256	0.123
1.75	0.625	4.38e-04	0.607	0.091	0.192	0.297	0.123
2.53	0.625	5.82e-04	0.820	0.125	0.311	0.362	0.123
1.25	0.875	3.92e-04	1.131	0.108	0.267	0.416	0.123
1.75	0.875	4.84e-04	0.816	0.143	0.228	0.308	0.123
2.53	0.875	6.28e-04	0.728	0.135	0.239	0.335	0.123
1.25	1.250	4.61e-04	0.570	0.075	0.114	0.218	0.123
1.75	1.250	5.53e-04	0.720	0.173	0.190	0.256	0.123
2.53	1.250	6.97e-04	1.549	0.408	0.538	0.532	0.123
0.68	0.625	3.52e-03	0.688	0.074	0.160	0.160	0.123
1.29	0.625	6.57e-03	0.821	0.079	0.162	0.162	0.123
2.43	0.625	1.23e-02	0.759	0.236	0.168	0.168	0.123
2.71	0.625	1.37e-02	0.887	0.103	0.245	0.245	0.123
3.35	0.625	1.69e-02	0.916	0.097	0.259	0.259	0.123
4.67	0.625	2.35e-02	0.918	0.151	0.142	0.142	0.123
0.68	0.875	3.56e-03	0.659	0.092	0.160	0.160	0.123
1.29	0.875	6.61e-03	1.019	0.117	0.162	0.162	0.123
2.43	0.875	1.23e-02	1.047	0.379	0.168	0.168	0.123
2.71	0.875	1.37e-02	1.103	0.195	0.245	0.245	0.123
3.35	0.875	1.69e-02	1.312	0.283	0.259	0.259	0.123
4.67	0.875	2.35e-02	1.047	0.220	0.142	0.142	0.123
0.68	1.250	3.63e-03	0.984	0.268	0.160	0.160	0.123
1.29	1.250	6.68e-03	1.054	0.293	0.162	0.162	0.123
2.43	1.250	1.24e-02	1.349	0.508	0.168	0.168	0.123
2.71	1.250	1.38e-02	1.090	0.215	0.245	0.245	0.123
3.35	1.250	1.70e-02	1.134	0.194	0.259	0.259	0.123
4.67	1.250	2.36e-02	0.930	0.367	0.142	0.142	0.123

Appendix A

PYTHIA x-Distribution Study

We have analyzed the forward-forward correlations between two π^0's in p+p PYTHIA simulations run through PISA. We have found that for the p_T bins used in this analysis, the awayside correlation peak in PYTHIA does not seem to arise from di-jets, but rather from some other momentum-conserving process.

We correlate two π^0's in PYTHIA, and hence in what follows particle 1 refers to a particle with a pseudorapidity of $3.0 < \eta_1 < 4.0$, while particle 2 has a pseudorapidity that is allowed to vary. We also look at the PYTHIA event record and find the two outgoing partons that initiate the final-state reaction (both jet and non-jet events).

In Fig. A.1, we show the η_2 versus x_2 distribution of particle 2 given that particle 1 is in the forward region with $3.0 < \eta_1 < 4.0$, $p_{T,1} > 2.0$ GeV/c and particle 2 has $p_{T,2} > 1.0$ GeV/c. One can see a strong correlation between x_2 and η_2. However, as one goes to the largest (and smallest) pseudorapidities on the vertical axis, this correlation weakens and there is no longer a strong peak in the x_2 distribution. In Fig. A.2 we show η_2 slices of the x_2 distribution, and see that the distribution flattens out in the larger η_2 bins.

In Fig. A.3 we show the PYTHIA $\Delta\phi$ distributions for $3.0 < \eta_{1,2} < 4.0$, $p_{T,1} > 2.0$ GeV/c, $p_{T,2} > 1.0$ GeV/c given different cuts on the leading partons. This shows that the awayside correlations do not arise from a di-jet source, as the fraction of the correlations originating from the case when both partons are forward is very small (red and blue histograms) compared to the full correlation function (black). To rephrase, this means that much of the awayside correlation comes from a non-dijet source. On the other hand, this effect seen in simulation could arise from constraints in momentum conservation that were introduced in PYTHIA Tune A to match the underlying event background [124].

Hence when interpreting the forward-forward correlations, one needs to be careful about the interpretation, as PYTHIA suggests these are not di-jet correlations at small x; if this is actually true, CGC phenomenology is not applicable for the correlations.

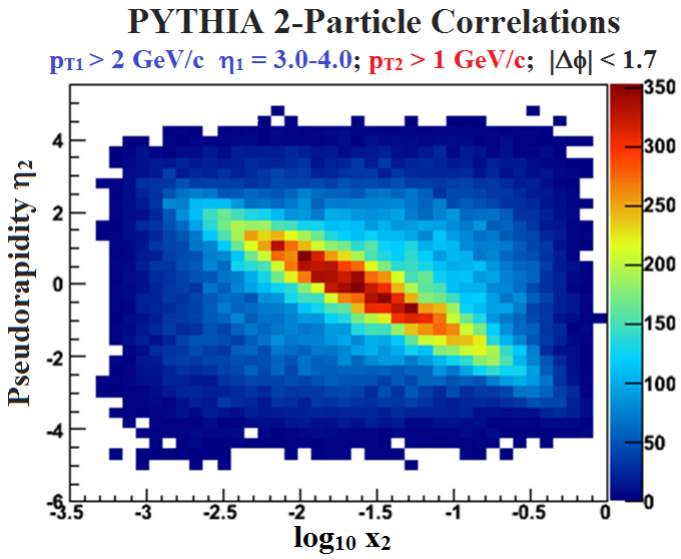

Figure A.1: The η_2 vs x_2 distributions given that particle 1 has $3.0 < \eta_1 < 4.0$, $p_{T,1} > 2.0$ GeV/c and particle 2 has $p_{T,2} > 1.0$ GeV/c.

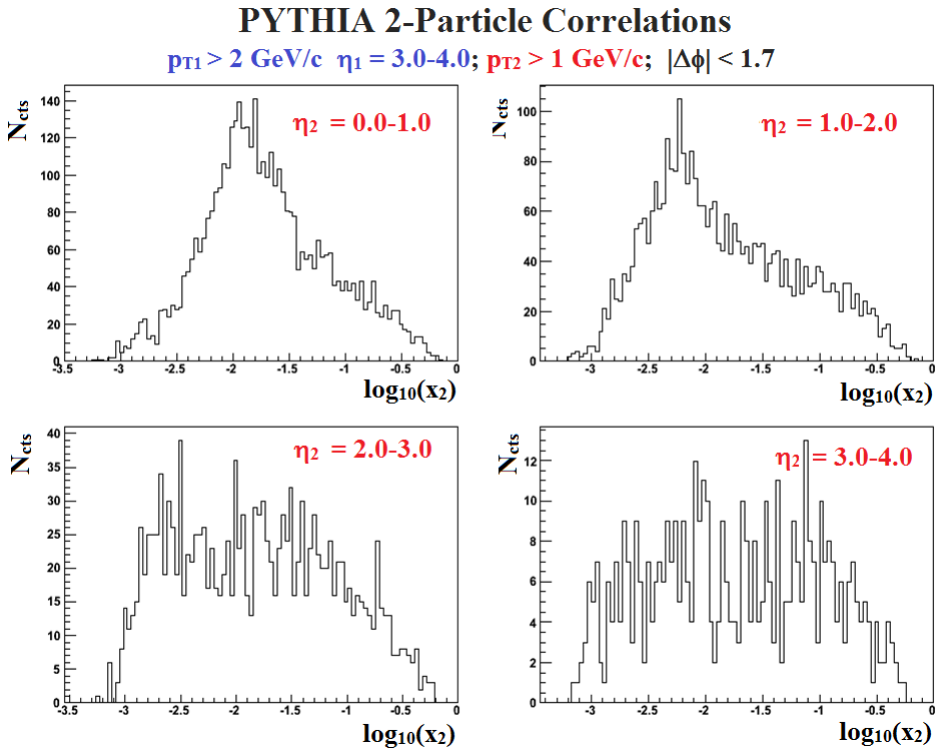

Figure A.2: The x_2 distributions for different slices in η_2 given that particle 1 has $3.0 < \eta_1 < 4.0$, $p_{T,1} > 2.0$ GeV/c and particle 2 has $p_{T,2} > 1.0$ GeV/c.

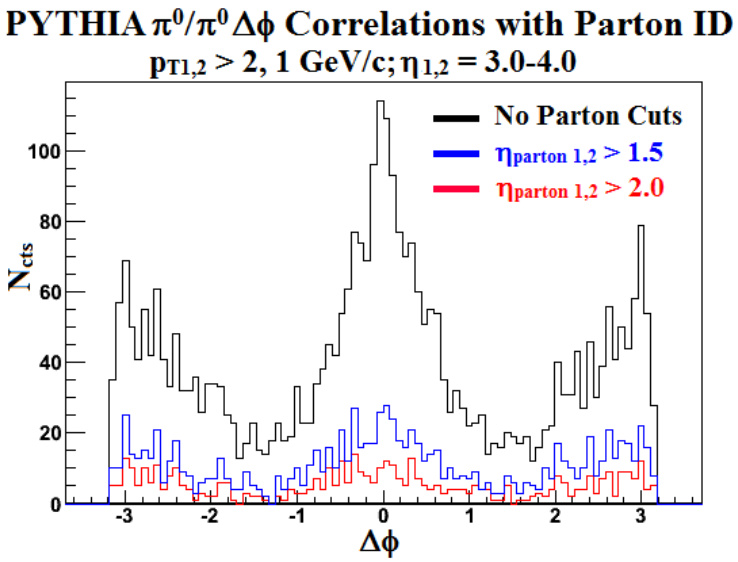

Figure A.3: The PYTHIA $\Delta\phi$ distributions for $3.0 < \eta_{1,2} < 4.0$, $p_{T,1} > 2.0$ GeV/c, $p_{T,2} > 1.0$ GeV/c given different cuts on the leading partons. This shows that the awayside correlations do not arise from a di-jet source.

Appendix B

MPC π^0 R_{dA} and Yield Tables and Figures

B.1 Tabulated Results

In all subsequent tables, σ represents a statistical error, while s represents a systematic error (type B), and the global systematic error is s_{global}.

B.1.1 Yields, Efficiencies, Relative Statistical Errors

In this section, the terms that are present in the tables are as follows:

p_T	Transverse momentum of the bin center,
InvYield	Invariant yield,
$\frac{dN/dpt}{N_{ev}}$	Efficiency-corrected yield in p_T bin normalized per event,
$\frac{N_{raw}}{N_{ev}}$	Uncorrected yield in p_T bin normalized per event,
ϵ	π^0 reconstruction efficiency,
bcorr	Up-down correction, or $C_{up-down}$.

Table B.1: Yields, efficiencies and **relative** stat errors for $3.0 < \eta < 3.4$.

p_T	$InvYield$	σ_{InvY}	$\frac{dN/dpt}{N_{ev}}$	$\sigma_{dN/dpt}$	$\frac{N_{raw}}{N_{ev}}$	σ_{Nraw}	ϵ	σ_ϵ	$bcorr$
d+Au 0-20%, N_{events} = 3.69e+08									
0.375	1.79e+00	0.164	4.68e-01	0.164	1.94e-04	0.024	4.14e-04	0.162	0.960
0.625	4.25e-01	0.023	1.85e-01	0.023	6.80e-03	0.003	3.68e-02	0.023	0.960
0.875	1.01e-01	0.020	6.19e-02	0.020	4.31e-03	0.003	6.97e-02	0.019	0.956
1.125	3.19e-02	0.022	2.49e-02	0.022	1.60e-03	0.004	6.43e-02	0.022	0.963
1.375	1.12e-02	0.030	1.06e-02	0.030	4.29e-04	0.010	4.05e-02	0.028	0.970
1.625	4.43e-03	0.058	4.93e-03	0.058	6.47e-05	0.024	1.31e-02	0.053	0.975
1.875	1.37e-03	0.220	1.75e-03	0.220	2.65e-06	0.143	1.52e-03	0.167	0.979
d+Au 20-40%, N_{events} = 3.68e+08									
0.375	1.73e+00	0.160	4.25e-01	0.160	1.90e-04	0.035	4.47e-04	0.156	0.960
0.625	4.10e-01	0.023	1.68e-01	0.023	6.55e-03	0.004	3.91e-02	0.023	0.960
0.875	9.97e-02	0.020	5.73e-02	0.020	4.06e-03	0.003	7.08e-02	0.019	0.956
1.125	3.13e-02	0.022	2.30e-02	0.022	1.49e-03	0.005	6.49e-02	0.022	0.963
1.375	1.10e-02	0.030	9.79e-03	0.030	3.97e-04	0.010	4.05e-02	0.028	0.970
1.625	4.13e-03	0.056	4.33e-03	0.056	5.83e-05	0.025	1.35e-02	0.051	0.975
1.875	1.69e-03	0.198	2.04e-03	0.198	2.86e-06	0.102	1.41e-03	0.170	0.979
d+Au 40-60%, N_{events} = 3.68e+08									
0.375	1.64e+00	0.158	3.90e-01	0.158	1.81e-04	0.026	4.63e-04	0.155	0.960
0.625	3.51e-01	0.023	1.39e-01	0.023	5.81e-03	0.003	4.18e-02	0.022	0.960
0.875	8.70e-02	0.019	4.83e-02	0.019	3.49e-03	0.003	7.22e-02	0.019	0.957
1.125	2.68e-02	0.022	1.90e-02	0.022	1.25e-03	0.005	6.58e-02	0.022	0.964
1.375	9.63e-03	0.030	8.31e-03	0.030	3.26e-04	0.010	3.92e-02	0.029	0.968
1.625	3.11e-03	0.058	3.15e-03	0.058	4.68e-05	0.028	1.48e-02	0.051	0.972
1.875	2.07e-03	0.208	2.42e-03	0.208	2.27e-06	0.096	9.39e-04	0.184	0.976
d+Au 60-88%, N_{events} = 5.16e+08									
0.375	9.59e-01	0.118	2.29e-01	0.118	1.43e-04	0.024	6.24e-04	0.116	0.958
0.625	2.51e-01	0.019	9.99e-02	0.019	4.47e-03	0.004	4.47e-02	0.018	0.958
0.875	6.10e-02	0.016	3.41e-02	0.016	2.57e-03	0.003	7.54e-02	0.016	0.954
1.125	1.79e-02	0.019	1.28e-02	0.019	8.65e-04	0.005	6.76e-02	0.018	0.959
1.375	6.08e-03	0.027	5.27e-03	0.027	2.12e-04	0.013	4.02e-02	0.024	0.966
1.625	2.15e-03	0.051	2.19e-03	0.051	2.95e-05	0.026	1.35e-02	0.043	0.973
1.875	1.14e-03	0.165	1.33e-03	0.165	1.59e-06	0.075	1.19e-03	0.147	0.979
d+Au MinBias, N_{events} = 1.62e+09									
0.375	1.35e+00	0.076	3.72e-01	0.076	1.78e-04	0.021	4.78e-04	0.073	0.959
0.625	3.12e-01	0.011	1.44e-01	0.011	5.78e-03	0.003	4.02e-02	0.011	0.959
0.875	7.61e-02	0.010	4.93e-02	0.010	3.53e-03	0.003	7.18e-02	0.009	0.955
1.125	2.33e-02	0.011	1.93e-02	0.011	1.26e-03	0.005	6.56e-02	0.010	0.962
1.375	8.17e-03	0.017	8.20e-03	0.017	3.29e-04	0.009	4.02e-02	0.014	0.969
1.625	2.99e-03	0.036	3.52e-03	0.036	4.80e-05	0.026	1.36e-02	0.025	0.975
1.875	1.33e-03	0.125	1.80e-03	0.125	2.31e-06	0.091	1.28e-03	0.086	0.979
p+p, N_{events} = 4.21e+08									
0.375	5.68e-01	0.107	2.04e-01	0.107	1.09e-04	0.030	5.33e-04	0.103	0.950
0.625	1.21e-01	0.016	7.22e-02	0.016	3.11e-03	0.004	4.31e-02	0.016	0.950
0.875	2.61e-02	0.014	2.20e-02	0.014	1.67e-03	0.004	7.61e-02	0.013	0.947
1.125	7.21e-03	0.016	7.76e-03	0.016	5.11e-04	0.006	6.58e-02	0.015	0.952
1.375	2.18e-03	0.024	2.85e-03	0.024	1.14e-04	0.013	4.00e-02	0.020	0.959
1.625	6.73e-04	0.047	1.03e-03	0.047	1.42e-05	0.031	1.38e-02	0.035	0.966
1.875	3.04e-04	0.184	5.34e-04	0.184	6.68e-07	0.131	1.25e-03	0.128	0.972

Table B.2: Yields, efficiencies and **relative** stat errors for $3.4 < \eta < 3.8$.

d+Au 0-20%, N_{events} = 3.69e+08									
p_T	$InvYield$	σ_{InvY}	$\frac{dN/dpt}{N_{ev}}$	$\sigma_{dN/dpt}$	$\frac{N_{raw}}{N_{ev}}$	σ_{Nraw}	ϵ	σ_ϵ	$bcorr$
0.375	6.95e-01	0.042	1.79e-01	0.042	2.38e-03	0.009	1.33e-02	0.041	0.972
0.625	1.70e-01	0.021	7.29e-02	0.021	6.36e-03	0.004	8.72e-02	0.021	0.972
0.875	5.45e-02	0.021	3.27e-02	0.021	2.93e-03	0.003	8.96e-02	0.021	0.975
1.125	1.85e-02	0.029	1.43e-02	0.029	7.43e-04	0.006	5.20e-02	0.029	0.971
1.375	6.05e-03	0.066	5.74e-03	0.066	7.84e-05	0.022	1.37e-02	0.063	0.968
d+Au 20-40%, N_{events} = 3.68e+08									
p_T	$InvYield$	σ_{InvY}	$\frac{dN/dpt}{N_{ev}}$	$\sigma_{dN/dpt}$	$\frac{N_{raw}}{N_{ev}}$	σ_{Nraw}	ϵ	σ_ϵ	$bcorr$
0.375	8.24e-01	0.042	2.00e-01	0.042	2.46e-03	0.009	1.23e-02	0.041	0.969
0.625	1.90e-01	0.021	7.69e-02	0.021	6.34e-03	0.004	8.25e-02	0.021	0.969
0.875	5.63e-02	0.021	3.20e-02	0.021	2.85e-03	0.003	8.92e-02	0.021	0.969
1.125	1.97e-02	0.029	1.43e-02	0.029	7.18e-04	0.006	5.02e-02	0.028	0.973
1.375	7.24e-03	0.069	6.41e-03	0.069	7.44e-05	0.024	1.16e-02	0.065	0.975
d+Au 40-60%, N_{events} = 3.68e+08									
p_T	$InvYield$	σ_{InvY}	$\frac{dN/dpt}{N_{ev}}$	$\sigma_{dN/dpt}$	$\frac{N_{raw}}{N_{ev}}$	σ_{Nraw}	ϵ	σ_ϵ	$bcorr$
0.375	8.08e-01	0.040	1.90e-01	0.040	2.41e-03	0.007	1.27e-02	0.040	0.969
0.625	1.78e-01	0.020	6.99e-02	0.020	5.95e-03	0.004	8.51e-02	0.020	0.969
0.875	5.53e-02	0.021	3.03e-02	0.021	2.54e-03	0.003	8.41e-02	0.021	0.971
1.125	1.80e-02	0.030	1.27e-02	0.030	6.15e-04	0.008	4.84e-02	0.029	0.970
1.375	6.09e-03	0.067	5.26e-03	0.067	6.22e-05	0.023	1.18e-02	0.063	0.968
d+Au 60-88%, N_{events} = 5.16e+08									
p_T	$InvYield$	σ_{InvY}	$\frac{dN/dpt}{N_{ev}}$	$\sigma_{dN/dpt}$	$\frac{N_{raw}}{N_{ev}}$	σ_{Nraw}	ϵ	σ_ϵ	$bcorr$
0.375	6.77e-01	0.033	1.61e-01	0.033	2.11e-03	0.006	1.31e-02	0.032	0.963
0.625	1.52e-01	0.017	6.02e-02	0.017	5.02e-03	0.003	8.34e-02	0.016	0.963
0.875	4.18e-02	0.018	2.31e-02	0.018	1.98e-03	0.003	8.57e-02	0.017	0.964
1.125	1.27e-02	0.025	9.05e-03	0.025	4.57e-04	0.007	5.05e-02	0.024	0.963
1.375	3.90e-03	0.060	3.39e-03	0.060	4.09e-05	0.025	1.21e-02	0.054	0.963
d+Au MinBias, N_{events} = 1.62e+09									
p_T	$InvYield$	σ_{InvY}	$\frac{dN/dpt}{N_{ev}}$	$\sigma_{dN/dpt}$	$\frac{N_{raw}}{N_{ev}}$	σ_{Nraw}	ϵ	σ_ϵ	$bcorr$
0.375	6.68e-01	0.021	1.83e-01	0.021	2.33e-03	0.007	1.28e-02	0.019	0.968
0.625	1.51e-01	0.010	6.89e-02	0.010	5.83e-03	0.003	8.46e-02	0.010	0.968
0.875	4.53e-02	0.010	2.89e-02	0.010	2.52e-03	0.003	8.73e-02	0.010	0.971
1.125	1.50e-02	0.015	1.23e-02	0.015	6.19e-04	0.006	5.04e-02	0.014	0.969
1.375	4.86e-03	0.039	4.88e-03	0.039	6.07e-05	0.023	1.24e-02	0.031	0.967
p+p, N_{events} = 4.21e+08									
p_T	$InvYield$	σ_{InvY}	$\frac{dN/dpt}{N_{ev}}$	$\sigma_{dN/dpt}$	$\frac{N_{raw}}{N_{ev}}$	σ_{Nraw}	ϵ	σ_ϵ	$bcorr$
0.375	4.44e-01	0.026	1.59e-01	0.026	2.13e-03	0.007	1.33e-02	0.025	0.951
0.625	8.73e-02	0.014	5.22e-02	0.014	4.28e-03	0.004	8.19e-02	0.013	0.951
0.875	2.00e-02	0.014	1.68e-02	0.014	1.49e-03	0.004	8.89e-02	0.014	0.948
1.125	5.43e-03	0.021	5.83e-03	0.021	3.07e-04	0.009	5.27e-02	0.019	0.954
1.375	1.61e-03	0.053	2.10e-03	0.053	2.59e-05	0.030	1.23e-02	0.043	0.960

Table B.3: Yields, efficiencies and **relative** stat errors for $3.0 < \eta < 3.8$.

p_T	$InvYield$	σ_{InvY}	$\frac{dN/dpt}{N_{ev}}$	$\sigma_{dN/dpt}$	$\frac{N_{raw}}{N_{ev}}$	σ_{Nraw}	ϵ	σ_ϵ	$bcorr$
d+Au 0-20%, N_{events} = 3.69e+08									
0.375	1.24e+00	0.041	6.47e-01	0.041	2.64e-03	0.009	4.08e-03	0.040	0.964
0.625	2.97e-01	0.016	2.57e-01	0.016	1.33e-02	0.002	5.18e-02	0.016	0.964
0.875	7.91e-02	0.015	9.61e-02	0.015	7.32e-03	0.002	7.62e-02	0.014	0.962
1.125	2.52e-02	0.018	3.92e-02	0.018	2.35e-03	0.004	5.98e-02	0.017	0.965
1.375	8.55e-03	0.027	1.62e-02	0.027	5.03e-04	0.010	3.11e-02	0.026	0.969
1.625	3.32e-03	0.058	7.41e-03	0.058	6.47e-05	0.024	8.74e-03	0.053	0.973
1.875	9.97e-04	0.220	2.56e-03	0.220	2.65e-06	0.143	1.04e-03	0.167	0.976
d+Au 20-40%, N_{events} = 3.68e+08									
0.375	1.33e+00	0.041	6.48e-01	0.041	2.71e-03	0.008	4.19e-03	0.040	0.964
0.625	2.93e-01	0.016	2.39e-01	0.016	1.28e-02	0.002	5.34e-02	0.015	0.964
0.875	7.84e-02	0.014	8.95e-02	0.014	6.91e-03	0.002	7.72e-02	0.014	0.963
1.125	2.54e-02	0.018	3.71e-02	0.018	2.20e-03	0.004	5.94e-02	0.017	0.966
1.375	8.67e-03	0.028	1.55e-02	0.028	4.65e-04	0.009	3.01e-02	0.026	0.969
1.625	3.15e-03	0.056	6.62e-03	0.056	5.83e-05	0.025	8.81e-03	0.051	0.972
1.875	1.26e-03	0.199	3.03e-03	0.199	2.86e-06	0.102	9.43e-04	0.171	0.976
d+Au 40-60%, N_{events} = 3.68e+08									
0.375	1.20e+00	0.039	5.65e-01	0.039	2.61e-03	0.007	4.62e-03	0.038	0.964
0.625	2.55e-01	0.015	2.01e-01	0.015	1.15e-02	0.002	5.73e-02	0.015	0.964
0.875	7.12e-02	0.014	7.84e-02	0.014	6.01e-03	0.002	7.66e-02	0.014	0.965
1.125	2.24e-02	0.018	3.17e-02	0.018	1.86e-03	0.004	5.88e-02	0.017	0.966
1.375	7.73e-03	0.028	1.34e-02	0.028	3.83e-04	0.009	2.87e-02	0.026	0.967
1.625	2.46e-03	0.058	5.00e-03	0.058	4.68e-05	0.028	9.35e-03	0.051	0.969
1.875	1.59e-03	0.208	3.73e-03	0.208	2.27e-06	0.096	6.09e-04	0.184	0.973
d+Au 60-88%, N_{events} = 5.16e+08									
0.375	8.65e-01	0.031	4.11e-01	0.031	2.24e-03	0.006	5.46e-03	0.031	0.961
0.625	1.96e-01	0.013	1.55e-01	0.013	9.22e-03	0.002	5.94e-02	0.012	0.961
0.875	5.12e-02	0.012	5.70e-02	0.012	4.53e-03	0.002	7.95e-02	0.012	0.960
1.125	1.52e-02	0.015	2.17e-02	0.015	1.31e-03	0.004	6.04e-02	0.014	0.961
1.375	4.88e-03	0.025	8.48e-03	0.025	2.47e-04	0.012	2.91e-02	0.022	0.964
1.625	1.71e-03	0.051	3.50e-03	0.051	2.95e-05	0.026	8.45e-03	0.043	0.969
1.875	8.77e-04	0.166	2.06e-03	0.166	1.59e-06	0.075	7.72e-04	0.148	0.974
d+Au MinBias, N_{events} = 1.62e+09									
0.375	1.02e+00	0.020	5.63e-01	0.020	2.54e-03	0.007	4.51e-03	0.019	0.963
0.625	2.28e-01	0.008	2.09e-01	0.008	1.15e-02	0.002	5.51e-02	0.007	0.963
0.875	6.09e-02	0.007	7.84e-02	0.007	6.06e-03	0.002	7.73e-02	0.007	0.962
1.125	1.90e-02	0.009	3.14e-02	0.009	1.87e-03	0.004	5.97e-02	0.008	0.965
1.375	6.45e-03	0.015	1.29e-02	0.015	3.86e-04	0.009	2.98e-02	0.013	0.968
1.625	2.30e-03	0.036	5.44e-03	0.036	4.80e-05	0.026	8.82e-03	0.025	0.972
1.875	9.94e-04	0.126	2.70e-03	0.126	2.31e-06	0.091	8.55e-04	0.086	0.975
p+p, N_{events} = 4.21e+08									
0.375	5.01e-01	0.026	3.59e-01	0.026	2.22e-03	0.007	6.17e-03	0.025	0.952
0.625	9.93e-02	0.011	1.19e-01	0.011	7.13e-03	0.003	6.00e-02	0.010	0.952
0.875	2.28e-02	0.010	3.83e-02	0.010	3.12e-03	0.003	8.15e-02	0.010	0.950
1.125	6.25e-03	0.013	1.35e-02	0.013	8.11e-04	0.005	6.02e-02	0.012	0.952
1.375	1.83e-03	0.022	4.77e-03	0.022	1.37e-04	0.013	2.87e-02	0.018	0.958
1.625	5.57e-04	0.047	1.71e-03	0.047	1.42e-05	0.031	8.33e-03	0.035	0.964
1.875	2.46e-04	0.183	8.65e-04	0.183	6.68e-07	0.131	7.72e-04	0.128	0.971

B.1.2 Invariant Yields and Relative Errors

In this section, the terms that are present in the tables are as follows:

p_T	Transverse momentum of the bin center,
InvYield	Invariant yield,
s_{mass}	Systematic error from yield extraction,
s_{spec}	Systematic error from shape of input spectrum,
s_{escale}	Systematic error from energy scale,
s_{GEANT}	Systematic error from GEANT description of MPC,
s_{tot}	Total sum of type B systematic errors (those listed above),
s_{global}	Global systematic error.

Table B.4: Yields, **relative** systematic errors for $3.0 < \eta < 3.4$.

p_T	$InvYield$	σ_{InvY}	s_{mass}	s_{spec}	s_{escale}	s_{GEANT}	s_{tot}	s_{global}
d+Au 0-20%								
0.375	1.79e+00	0.164	0.057	0.078	0.050	0.070	0.130	0.011
0.625	4.25e-01	0.023	0.037	0.045	0.070	0.070	0.115	0.011
0.875	1.01e-01	0.020	0.020	0.015	0.090	0.070	0.116	0.011
1.125	3.19e-02	0.022	0.026	0.016	0.101	0.070	0.127	0.011
1.375	1.12e-02	0.030	0.048	0.015	0.109	0.070	0.139	0.011
1.625	4.43e-03	0.058	0.071	0.009	0.116	0.070	0.154	0.011
1.875	1.37e-03	0.220	0.168	0.048	0.121	0.070	0.224	0.011
d+Au 20-40%								
0.375	1.73e+00	0.160	0.080	0.052	0.050	0.070	0.128	0.006
0.625	4.10e-01	0.023	0.040	0.045	0.070	0.070	0.116	0.006
0.875	9.97e-02	0.020	0.018	0.014	0.089	0.070	0.116	0.006
1.125	3.13e-02	0.022	0.031	0.018	0.101	0.070	0.128	0.006
1.375	1.10e-02	0.030	0.052	0.015	0.110	0.070	0.141	0.006
1.625	4.13e-03	0.056	0.071	0.010	0.116	0.070	0.153	0.006
1.875	1.69e-03	0.198	0.169	0.046	0.121	0.070	0.224	0.006
d+Au 40-60%								
0.375	1.64e+00	0.158	0.096	0.053	0.050	0.070	0.139	0.016
0.625	3.51e-01	0.023	0.044	0.029	0.070	0.070	0.112	0.016
0.875	8.70e-02	0.019	0.017	0.020	0.089	0.070	0.116	0.016
1.125	2.68e-02	0.022	0.027	0.022	0.102	0.070	0.128	0.016
1.375	9.63e-03	0.030	0.055	0.023	0.113	0.070	0.146	0.016
1.625	3.11e-03	0.058	0.053	0.004	0.122	0.070	0.151	0.016
1.875	2.07e-03	0.208	0.136	0.028	0.129	0.070	0.203	0.016
d+Au 60-88%								
0.375	9.59e-01	0.118	0.100	0.043	0.051	0.070	0.139	0.053
0.625	2.51e-01	0.019	0.042	0.021	0.071	0.070	0.110	0.053
0.875	6.10e-02	0.016	0.015	0.022	0.093	0.070	0.119	0.053
1.125	1.79e-02	0.019	0.024	0.031	0.106	0.070	0.133	0.053
1.375	6.08e-03	0.027	0.051	0.027	0.113	0.070	0.145	0.053
1.625	2.15e-03	0.051	0.060	0.006	0.117	0.070	0.149	0.053
1.875	1.14e-03	0.165	0.183	0.053	0.120	0.070	0.235	0.053
d+Au MinBias								
0.375	1.35e+00	0.076	0.074	0.058	0.050	0.070	0.128	0.001
0.625	3.12e-01	0.011	0.039	0.032	0.070	0.070	0.111	0.001
0.875	7.61e-02	0.010	0.018	0.019	0.090	0.070	0.117	0.001
1.125	2.33e-02	0.011	0.027	0.020	0.102	0.070	0.128	0.001
1.375	8.17e-03	0.017	0.050	0.017	0.110	0.070	0.141	0.001
1.625	2.99e-03	0.036	0.053	0.004	0.116	0.070	0.145	0.001
1.875	1.33e-03	0.125	0.158	0.047	0.119	0.070	0.215	0.001
p+p								
0.375	5.68e-01	0.107	0.111	0.050	0.053	0.070	0.150	0.097
0.625	1.21e-01	0.016	0.031	0.032	0.076	0.070	0.112	0.097
0.875	2.61e-02	0.014	0.013	0.025	0.099	0.070	0.124	0.097
1.125	7.21e-03	0.016	0.023	0.034	0.114	0.070	0.140	0.097
1.375	2.18e-03	0.024	0.048	0.037	0.125	0.070	0.155	0.097
1.625	6.73e-04	0.047	0.031	0.017	0.132	0.070	0.153	0.097
1.875	3.04e-04	0.184	0.072	0.023	0.136	0.070	0.170	0.097

Table B.5: Yields, **relative** systematic errors for $3.4 < \eta < 3.8$.

d+Au 0-20%								
p_T	$InvYield$	σ_{InvY}	s_{mass}	s_{spec}	s_{escale}	s_{GEANT}	s_{tot}	s_{global}
0.375	6.95e-01	0.042	0.100	0.112	0.045	0.070	0.171	0.011
0.625	1.70e-01	0.021	0.022	0.108	0.061	0.070	0.144	0.011
0.875	5.45e-02	0.021	0.023	0.041	0.077	0.070	0.114	0.011
1.125	1.85e-02	0.029	0.041	0.045	0.098	0.070	0.135	0.011
1.375	6.05e-03	0.066	0.101	0.071	0.116	0.070	0.183	0.011
d+Au 20-40%								
p_T	$InvYield$	σ_{InvY}	s_{mass}	s_{spec}	s_{escale}	s_{GEANT}	s_{tot}	s_{global}
0.375	8.24e-01	0.042	0.073	0.086	0.046	0.070	0.140	0.006
0.625	1.90e-01	0.021	0.031	0.073	0.063	0.070	0.123	0.006
0.875	5.63e-02	0.021	0.023	0.039	0.079	0.070	0.115	0.006
1.125	1.97e-02	0.029	0.043	0.043	0.092	0.070	0.130	0.006
1.375	7.24e-03	0.069	0.096	0.082	0.104	0.070	0.178	0.006
d+Au 40-60%								
p_T	$InvYield$	σ_{InvY}	s_{mass}	s_{spec}	s_{escale}	s_{GEANT}	s_{tot}	s_{global}
0.375	8.08e-01	0.040	0.047	0.071	0.046	0.070	0.120	0.016
0.625	1.78e-01	0.020	0.018	0.058	0.064	0.070	0.112	0.016
0.875	5.53e-02	0.021	0.024	0.038	0.079	0.070	0.115	0.016
1.125	1.80e-02	0.030	0.037	0.046	0.098	0.070	0.134	0.016
1.375	6.09e-03	0.067	0.093	0.084	0.116	0.070	0.184	0.016
d+Au 60-88%								
p_T	$InvYield$	σ_{InvY}	s_{mass}	s_{spec}	s_{escale}	s_{GEANT}	s_{tot}	s_{global}
0.375	6.77e-01	0.033	0.042	0.036	0.049	0.070	0.101	0.053
0.625	1.52e-01	0.017	0.015	0.034	0.068	0.070	0.104	0.053
0.875	4.18e-02	0.018	0.020	0.036	0.087	0.070	0.119	0.053
1.125	1.27e-02	0.025	0.038	0.045	0.106	0.070	0.140	0.053
1.375	3.90e-03	0.060	0.079	0.080	0.121	0.070	0.179	0.053
d+Au MinBias								
p_T	$InvYield$	σ_{InvY}	s_{mass}	s_{spec}	s_{escale}	s_{GEANT}	s_{tot}	s_{global}
0.375	6.68e-01	0.021	0.057	0.073	0.047	0.070	0.125	0.001
0.625	1.51e-01	0.010	0.017	0.068	0.064	0.070	0.118	0.001
0.875	4.53e-02	0.010	0.022	0.040	0.080	0.070	0.116	0.001
1.125	1.50e-02	0.015	0.041	0.045	0.099	0.070	0.136	0.001
1.375	4.86e-03	0.039	0.091	0.072	0.117	0.070	0.179	0.001
p+p								
p_T	$InvYield$	σ_{InvY}	s_{mass}	s_{spec}	s_{escale}	s_{GEANT}	s_{tot}	s_{global}
0.375	4.44e-01	0.026	0.053	0.010	0.053	0.070	0.103	0.097
0.625	8.73e-02	0.014	0.019	0.027	0.075	0.070	0.108	0.097
0.875	2.00e-02	0.014	0.026	0.030	0.097	0.070	0.127	0.097
1.125	5.43e-03	0.021	0.036	0.048	0.113	0.070	0.146	0.097
1.375	1.61e-03	0.053	0.075	0.083	0.124	0.070	0.181	0.097

Table B.6: Yields, **relative** systematic errors for $3.0 < \eta < 3.8$.

p_T	$InvYield$	σ_{InvY}	s_{mass}	s_{spec}	s_{escale}	s_{GEANT}	s_{tot}	s_{global}
d+Au 0-20%								
0.375	1.24e+00	0.041	0.090	0.113	0.048	0.070	0.168	0.011
0.625	2.97e-01	0.016	0.020	0.031	0.067	0.070	0.104	0.011
0.875	7.91e-02	0.015	0.021	0.009	0.086	0.070	0.113	0.011
1.125	2.52e-02	0.018	0.032	0.012	0.101	0.070	0.127	0.011
1.375	8.55e-03	0.027	0.054	0.029	0.112	0.070	0.146	0.011
1.625	3.32e-03	0.058	0.071	0.051	0.121	0.070	0.165	0.011
1.875	9.97e-04	0.220	0.168	0.078	0.128	0.070	0.236	0.011
d+Au 20-40%								
0.375	1.33e+00	0.041	0.065	0.095	0.048	0.070	0.143	0.006
0.625	2.93e-01	0.016	0.020	0.023	0.067	0.070	0.102	0.006
0.875	7.84e-02	0.014	0.022	0.011	0.085	0.070	0.113	0.006
1.125	2.54e-02	0.018	0.035	0.011	0.100	0.070	0.127	0.006
1.375	8.67e-03	0.028	0.056	0.032	0.112	0.070	0.147	0.006
1.625	3.15e-03	0.056	0.071	0.052	0.122	0.070	0.166	0.006
1.875	1.26e-03	0.199	0.169	0.084	0.130	0.070	0.240	0.006
d+Au 40-60%								
0.375	1.20e+00	0.039	0.046	0.095	0.048	0.070	0.136	0.016
0.625	2.55e-01	0.015	0.017	0.018	0.067	0.070	0.100	0.016
0.875	7.12e-02	0.014	0.021	0.013	0.084	0.070	0.112	0.016
1.125	2.24e-02	0.018	0.032	0.012	0.102	0.070	0.128	0.016
1.375	7.73e-03	0.028	0.057	0.032	0.117	0.070	0.151	0.016
1.625	2.46e-03	0.058	0.053	0.055	0.128	0.070	0.165	0.016
1.875	1.59e-03	0.208	0.136	0.084	0.135	0.070	0.221	0.016
d+Au 60-88%								
0.375	8.65e-01	0.031	0.042	0.094	0.050	0.070	0.134	0.053
0.625	1.96e-01	0.013	0.015	0.015	0.069	0.070	0.101	0.053
0.875	5.12e-02	0.012	0.017	0.011	0.089	0.070	0.115	0.053
1.125	1.52e-02	0.015	0.028	0.011	0.106	0.070	0.131	0.053
1.375	4.88e-03	0.025	0.047	0.032	0.119	0.070	0.149	0.053
1.625	1.71e-03	0.051	0.060	0.055	0.128	0.070	0.167	0.053
1.875	8.77e-04	0.166	0.183	0.106	0.133	0.070	0.260	0.053
d+Au MinBias								
0.375	1.02e+00	0.020	0.053	0.095	0.049	0.070	0.138	0.001
0.625	2.28e-01	0.008	0.019	0.020	0.068	0.070	0.101	0.001
0.875	6.09e-02	0.007	0.020	0.011	0.087	0.070	0.114	0.001
1.125	1.90e-02	0.009	0.031	0.012	0.102	0.070	0.128	0.001
1.375	6.45e-03	0.015	0.053	0.031	0.114	0.070	0.147	0.001
1.625	2.30e-03	0.036	0.053	0.054	0.124	0.070	0.161	0.001
1.875	9.94e-04	0.126	0.158	0.088	0.130	0.070	0.234	0.001
p+p								
0.375	5.01e-01	0.026	0.052	0.116	0.053	0.070	0.154	0.097
0.625	9.93e-02	0.011	0.013	0.029	0.075	0.070	0.107	0.097
0.875	2.28e-02	0.010	0.019	0.008	0.097	0.070	0.122	0.097
1.125	6.25e-03	0.013	0.027	0.013	0.115	0.070	0.138	0.097
1.375	1.83e-03	0.022	0.045	0.035	0.127	0.070	0.156	0.097
1.625	5.57e-04	0.047	0.031	0.073	0.134	0.070	0.171	0.097
1.875	2.46e-04	0.183	0.072	0.121	0.138	0.070	0.209	0.097

B.1.3 R_{dA} and Relative Errors

In this section, the terms that are present in the tables are as follows:

p_T	Transverse momentum of the bin center,
R_{dA}	Single hadron nuclear modification factor,
s_{mass}	Systematic error from yield extraction,
s_{spec}	Systematic error from shape of input spectrum,
s_{escale}	Systematic error from energy scale,
s_{GEANT}	Systematic error from GEANT description of MPC,
s_{tot}	Total sum of type B systematic errors (those listed above),
s_{global}	Global systematic error.

Table B.7: R_{dA}, p+p cross-section, **relative** stat, sys errors for $3.0 < \eta < 3.4$.

d+Au 0-20%								
p_T	R_{dA}	σ_{Rda}	s_{mass}	s_{spec}	s_{escale}	s_{GEANT}	s_{tot}	s_{global}
0.375	2.10e-01	0.196	0.125	0.093	0.040	0.040	0.165	0.108
0.625	2.34e-01	0.028	0.048	0.055	0.040	0.040	0.093	0.108
0.875	2.58e-01	0.024	0.024	0.029	0.040	0.040	0.068	0.108
1.125	2.94e-01	0.027	0.035	0.037	0.040	0.040	0.076	0.108
1.375	3.41e-01	0.039	0.067	0.040	0.040	0.040	0.097	0.108
1.625	4.37e-01	0.075	0.078	0.019	0.040	0.040	0.098	0.108
1.875	2.99e-01	0.287	0.183	0.053	0.040	0.040	0.199	0.108
d+Au 20-40%								
0.375	2.98e-01	0.193	0.137	0.072	0.040	0.040	0.164	0.105
0.625	3.32e-01	0.028	0.051	0.056	0.040	0.040	0.094	0.105
0.875	3.73e-01	0.024	0.023	0.029	0.040	0.040	0.067	0.105
1.125	4.24e-01	0.027	0.038	0.038	0.040	0.040	0.078	0.105
1.375	4.92e-01	0.039	0.071	0.040	0.040	0.040	0.099	0.105
1.625	5.99e-01	0.073	0.077	0.019	0.040	0.040	0.098	0.105
1.875	5.43e-01	0.270	0.184	0.051	0.040	0.040	0.199	0.105
d+Au 40-60%								
0.375	4.40e-01	0.191	0.146	0.073	0.040	0.040	0.173	0.110
0.625	4.43e-01	0.028	0.054	0.043	0.040	0.040	0.089	0.110
0.875	5.06e-01	0.024	0.021	0.032	0.040	0.040	0.068	0.110
1.125	5.64e-01	0.027	0.036	0.040	0.040	0.040	0.078	0.110
1.375	6.71e-01	0.039	0.072	0.044	0.040	0.040	0.102	0.110
1.625	7.01e-01	0.075	0.062	0.017	0.040	0.040	0.085	0.110
1.875	1.04e+00	0.277	0.154	0.037	0.040	0.040	0.168	0.110
d+Au 60-88%								
0.375	5.29e-01	0.160	0.149	0.066	0.040	0.040	0.173	0.123
0.625	6.52e-01	0.025	0.052	0.039	0.040	0.040	0.086	0.123
0.875	7.31e-01	0.021	0.020	0.033	0.040	0.040	0.069	0.123
1.125	7.76e-01	0.025	0.033	0.046	0.040	0.040	0.080	0.123
1.375	8.71e-01	0.036	0.070	0.046	0.040	0.040	0.101	0.123
1.625	1.00e+00	0.069	0.068	0.018	0.040	0.040	0.090	0.123
1.875	1.17e+00	0.247	0.196	0.058	0.040	0.040	0.212	0.123
d+Au MinBias								
0.375	3.12e-01	0.132	0.133	0.077	0.040	0.040	0.164	0.103
0.625	3.41e-01	0.020	0.050	0.045	0.040	0.040	0.088	0.103
0.875	3.84e-01	0.017	0.022	0.031	0.040	0.040	0.069	0.103
1.125	4.26e-01	0.020	0.036	0.039	0.040	0.040	0.078	0.103
1.375	4.94e-01	0.029	0.069	0.041	0.040	0.040	0.098	0.103
1.625	5.85e-01	0.059	0.061	0.017	0.040	0.040	0.085	0.103
1.875	5.78e-01	0.222	0.174	0.052	0.040	0.040	0.190	0.103
p+p								
p_T	X-section	σ_{xc}	s_{mass}	s_{spec}	s_{escale}	s_{GEANT}	s_{tot}	s_{global}
0.375	2.39e+01	0.107	0.111	0.050	0.053	0.070	0.150	0.097
0.625	5.09e+00	0.016	0.031	0.032	0.076	0.070	0.112	0.097
0.875	1.10e+00	0.014	0.013	0.025	0.099	0.070	0.124	0.097
1.125	3.04e-01	0.016	0.023	0.034	0.114	0.070	0.140	0.097
1.375	9.20e-02	0.024	0.048	0.037	0.125	0.070	0.155	0.097
1.625	2.84e-02	0.047	0.031	0.017	0.132	0.070	0.153	0.097
1.875	1.28e-02	0.184	0.072	0.023	0.136	0.070	0.170	0.097

Table B.8: R_{dA}, p+p cross-section, **relative** stat, sys errors for $3.4 < \eta < 3.8$.

d+Au 0-20%								
p_T	R_{dA}	σ_{Rda}	s_{mass}	s_{spec}	s_{escale}	s_{GEANT}	s_{tot}	s_{global}
0.375	1.04e-01	0.049	0.113	0.112	0.040	0.040	0.169	0.108
0.625	1.29e-01	0.025	0.029	0.111	0.040	0.040	0.128	0.108
0.875	1.81e-01	0.026	0.035	0.051	0.040	0.040	0.084	0.108
1.125	2.26e-01	0.036	0.055	0.066	0.040	0.040	0.103	0.108
1.375	2.49e-01	0.085	0.126	0.109	0.040	0.040	0.176	0.108
d+Au 20-40%								
p_T	R_{dA}	σ_{Rda}	s_{mass}	s_{spec}	s_{escale}	s_{GEANT}	s_{tot}	s_{global}
0.375	1.81e-01	0.049	0.090	0.086	0.040	0.040	0.137	0.105
0.625	2.12e-01	0.025	0.036	0.078	0.040	0.040	0.103	0.105
0.875	2.75e-01	0.025	0.035	0.050	0.040	0.040	0.083	0.105
1.125	3.54e-01	0.036	0.056	0.065	0.040	0.040	0.103	0.105
1.375	4.38e-01	0.087	0.122	0.117	0.040	0.040	0.178	0.105
d+Au 40-60%								
p_T	R_{dA}	σ_{Rda}	s_{mass}	s_{spec}	s_{escale}	s_{GEANT}	s_{tot}	s_{global}
0.375	2.77e-01	0.048	0.071	0.072	0.040	0.040	0.116	0.110
0.625	3.11e-01	0.025	0.026	0.064	0.040	0.040	0.089	0.110
0.875	4.21e-01	0.025	0.035	0.048	0.040	0.040	0.082	0.110
1.125	5.05e-01	0.036	0.052	0.067	0.040	0.040	0.102	0.110
1.375	5.74e-01	0.085	0.119	0.118	0.040	0.040	0.177	0.110
d+Au 60-88%								
p_T	R_{dA}	σ_{Rda}	s_{mass}	s_{spec}	s_{escale}	s_{GEANT}	s_{tot}	s_{global}
0.375	4.77e-01	0.042	0.067	0.037	0.040	0.040	0.095	0.123
0.625	5.45e-01	0.022	0.024	0.043	0.040	0.040	0.075	0.123
0.875	6.54e-01	0.023	0.033	0.047	0.040	0.040	0.081	0.123
1.125	7.32e-01	0.032	0.052	0.066	0.040	0.040	0.102	0.123
1.375	7.55e-01	0.080	0.109	0.115	0.040	0.040	0.168	0.123
d+Au MinBias								
p_T	R_{dA}	σ_{Rda}	s_{mass}	s_{spec}	s_{escale}	s_{GEANT}	s_{tot}	s_{global}
0.375	1.98e-01	0.033	0.078	0.074	0.040	0.040	0.121	0.103
0.625	2.28e-01	0.017	0.025	0.073	0.040	0.040	0.096	0.103
0.875	2.99e-01	0.018	0.035	0.050	0.040	0.040	0.083	0.103
1.125	3.64e-01	0.026	0.054	0.066	0.040	0.040	0.103	0.103
1.375	3.97e-01	0.066	0.119	0.110	0.040	0.040	0.171	0.103
p+p								
p_T	X-section	σ_{xc}	s_{mass}	s_{spec}	s_{escale}	s_{GEANT}	s_{tot}	s_{global}
0.375	1.87e+01	0.026	0.053	0.010	0.053	0.070	0.103	0.097
0.625	3.68e+00	0.014	0.019	0.027	0.075	0.070	0.108	0.097
0.875	8.43e-01	0.014	0.026	0.030	0.097	0.070	0.127	0.097
1.125	2.29e-01	0.021	0.036	0.048	0.113	0.070	0.146	0.097
1.375	6.81e-02	0.053	0.075	0.083	0.124	0.070	0.181	0.097

Table B.9: R_{dA}, p+p cross-section, **relative** stat, sys errors for $3.0 < \eta < 3.8$.

d+Au 0-20%								
p_T	R_{dA}	σ_{Rda}	s_{mass}	s_{spec}	s_{escale}	s_{GEANT}	s_{tot}	s_{global}
0.375	1.65e-01	0.048	0.104	0.162	0.040	0.040	0.201	0.108
0.625	1.98e-01	0.019	0.024	0.042	0.040	0.040	0.074	0.108
0.875	2.30e-01	0.018	0.028	0.012	0.040	0.040	0.064	0.108
1.125	2.68e-01	0.022	0.042	0.018	0.040	0.040	0.073	0.108
1.375	3.11e-01	0.035	0.070	0.046	0.040	0.040	0.101	0.108
1.625	3.96e-01	0.075	0.078	0.090	0.040	0.040	0.132	0.108
1.875	2.69e-01	0.287	0.183	0.144	0.040	0.040	0.240	0.108
d+Au 20-40%								
0.375	2.58e-01	0.048	0.084	0.150	0.040	0.040	0.181	0.105
0.625	2.88e-01	0.019	0.024	0.037	0.040	0.040	0.071	0.105
0.875	3.35e-01	0.018	0.029	0.013	0.040	0.040	0.065	0.105
1.125	3.96e-01	0.022	0.044	0.017	0.040	0.040	0.074	0.105
1.375	4.63e-01	0.035	0.072	0.047	0.040	0.040	0.103	0.105
1.625	5.52e-01	0.073	0.077	0.090	0.040	0.040	0.132	0.105
1.875	4.99e-01	0.271	0.184	0.147	0.040	0.040	0.242	0.105
d+Au 40-60%								
0.375	3.63e-01	0.047	0.069	0.150	0.040	0.040	0.175	0.110
0.625	3.91e-01	0.018	0.021	0.034	0.040	0.040	0.069	0.110
0.875	4.74e-01	0.017	0.029	0.015	0.040	0.040	0.065	0.110
1.125	5.44e-01	0.022	0.042	0.018	0.040	0.040	0.073	0.110
1.375	6.44e-01	0.035	0.072	0.047	0.040	0.040	0.103	0.110
1.625	6.70e-01	0.074	0.062	0.092	0.040	0.040	0.124	0.110
1.875	9.86e-01	0.277	0.154	0.148	0.040	0.040	0.221	0.110
d+Au 60-88%								
0.375	5.40e-01	0.041	0.067	0.150	0.040	0.040	0.173	0.123
0.625	6.16e-01	0.016	0.020	0.033	0.040	0.040	0.068	0.123
0.875	7.02e-01	0.016	0.026	0.014	0.040	0.040	0.064	0.123
1.125	7.62e-01	0.020	0.039	0.017	0.040	0.040	0.071	0.123
1.375	8.36e-01	0.033	0.065	0.048	0.040	0.040	0.099	0.123
1.625	9.60e-01	0.069	0.068	0.092	0.040	0.040	0.127	0.123
1.875	1.12e+00	0.247	0.196	0.161	0.040	0.040	0.260	0.123
d+Au MinBias								
0.375	2.69e-01	0.032	0.075	0.150	0.040	0.040	0.177	0.103
0.625	3.03e-01	0.013	0.023	0.035	0.040	0.040	0.071	0.103
0.875	3.52e-01	0.012	0.028	0.013	0.040	0.040	0.065	0.103
1.125	4.01e-01	0.016	0.042	0.017	0.040	0.040	0.072	0.103
1.375	4.65e-01	0.027	0.070	0.047	0.040	0.040	0.101	0.103
1.625	5.45e-01	0.059	0.061	0.091	0.040	0.040	0.123	0.103
1.875	5.33e-01	0.222	0.174	0.150	0.040	0.040	0.236	0.103
p+p								
p_T	X-section	σ_{xc}	s_{mass}	s_{spec}	s_{escale}	s_{GEANT}	s_{tot}	s_{global}
0.375	2.11e+01	0.026	0.052	0.116	0.053	0.070	0.154	0.097
0.625	4.19e+00	0.011	0.013	0.029	0.075	0.070	0.107	0.097
0.875	9.63e-01	0.010	0.019	0.008	0.097	0.070	0.122	0.097
1.125	2.64e-01	0.013	0.027	0.013	0.115	0.070	0.138	0.097
1.375	7.70e-02	0.022	0.045	0.035	0.127	0.070	0.156	0.097
1.625	2.35e-02	0.047	0.031	0.073	0.134	0.070	0.171	0.097
1.875	1.04e-02	0.183	0.072	0.121	0.138	0.070	0.209	0.097

B.2 Invariant Mass Distributions and Background Determination

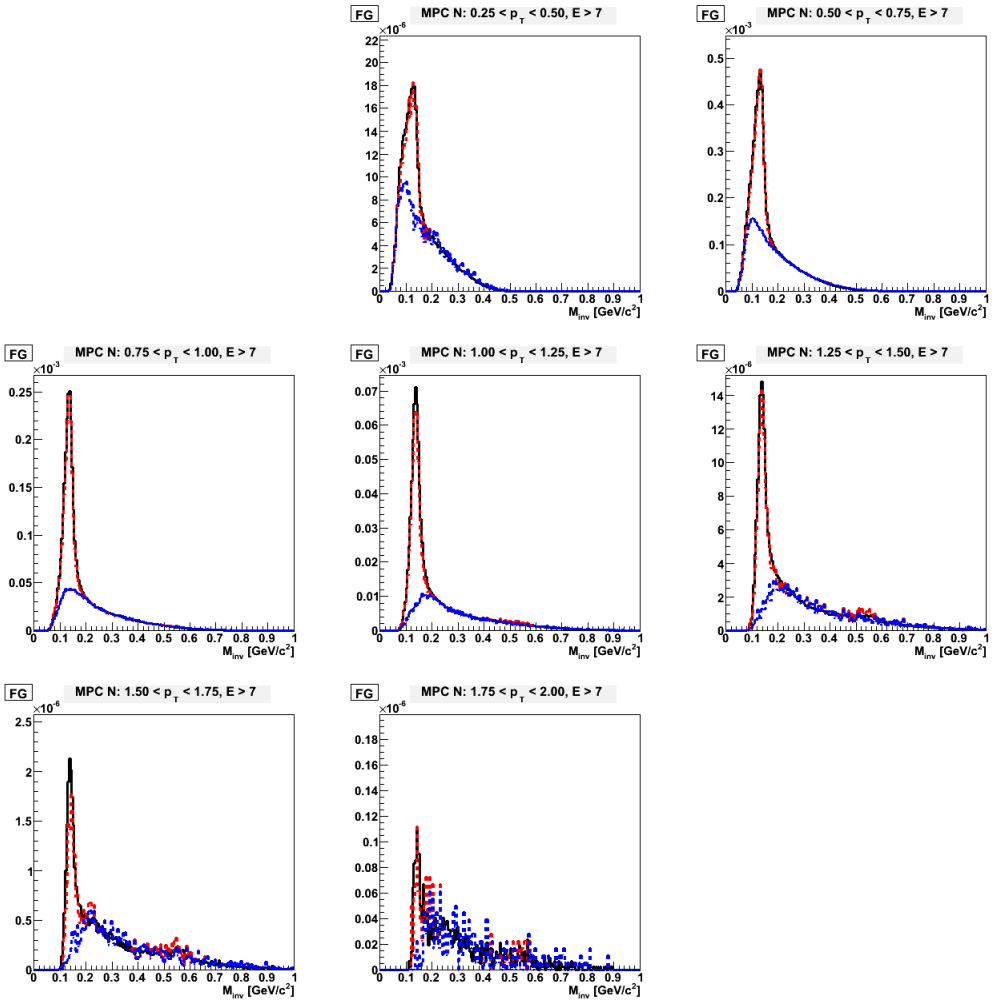

Figure B.1: **pp, Rapidity = 3.0-3.4:** This plot illustrates how the background was formed. The invariant mass distributions for data (black), linear combinations of 1pp, 2pp, and 3pp shapes that match simulation to the data (red), and the background for this linear combination are all plotted together.

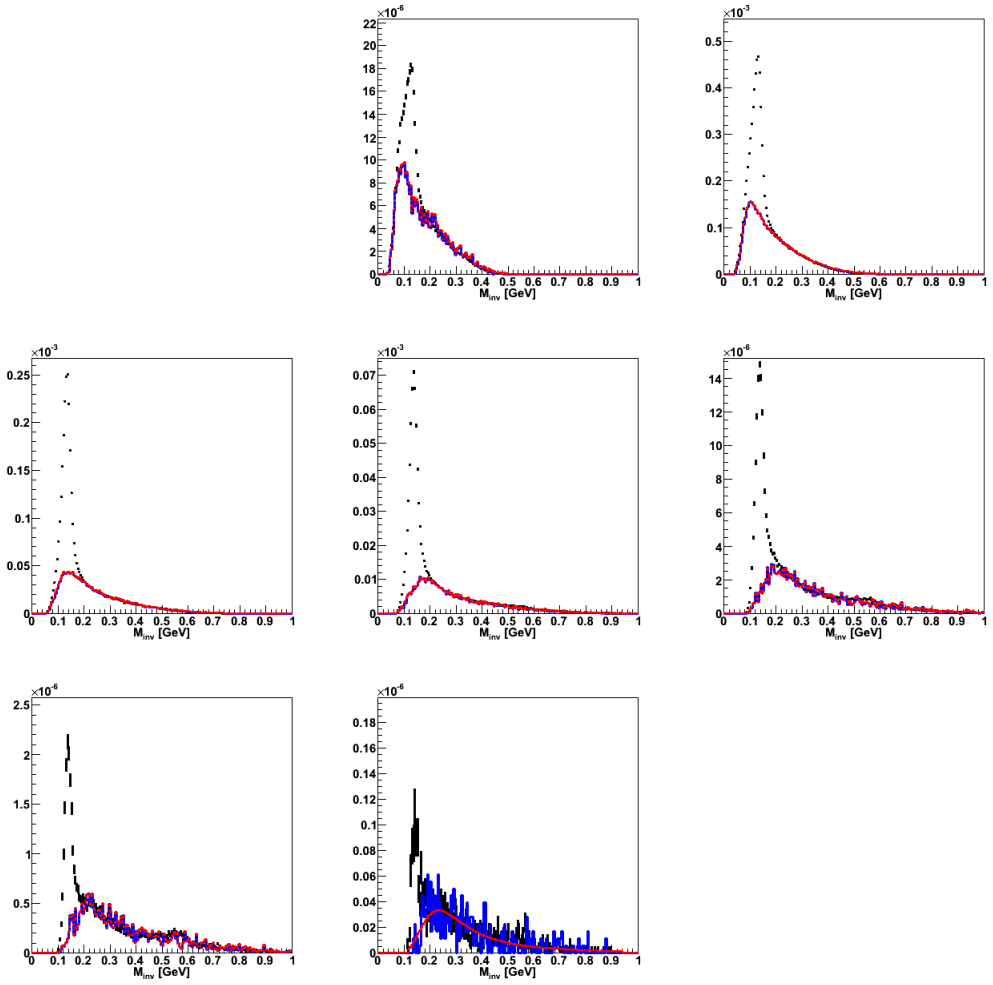

Figure B.2: **pp, Rapidity = 3.0-3.4:** Invariant mass foreground (black) and final background (red) distributions.

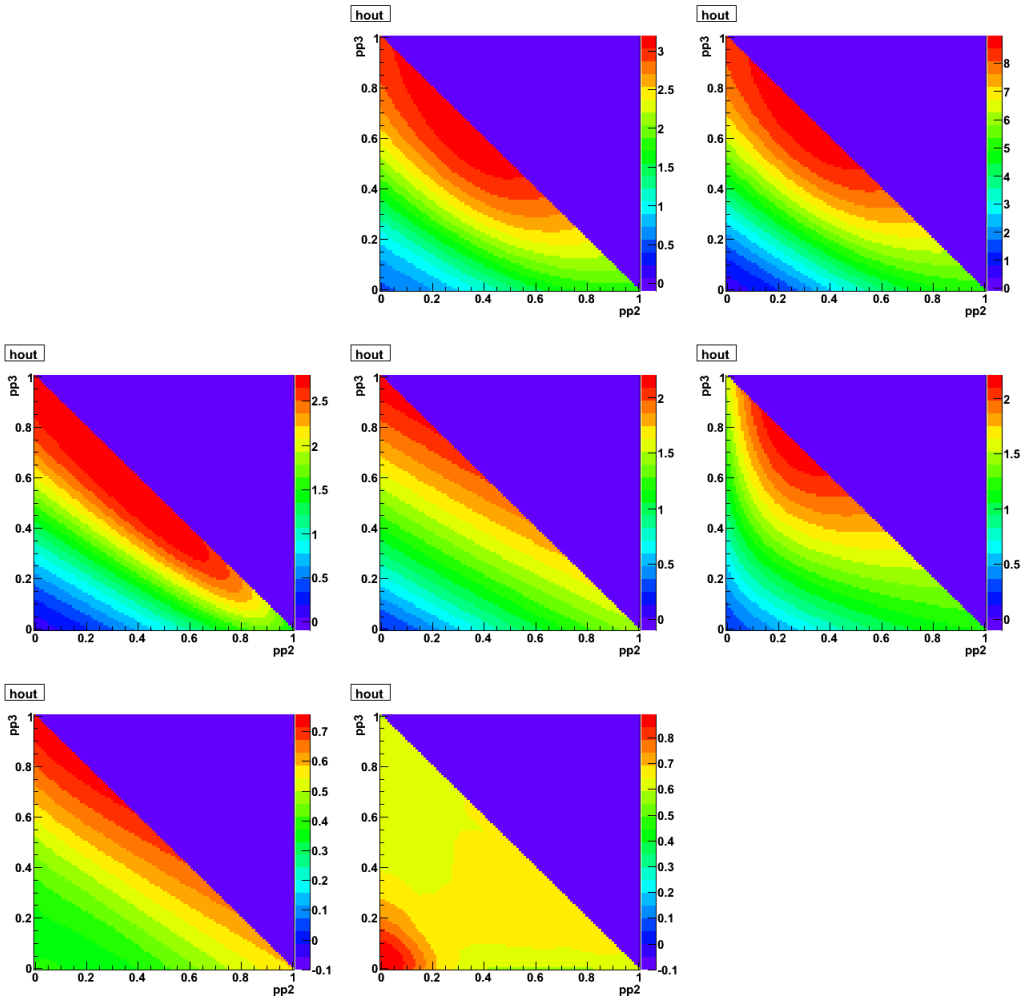

Figure B.3: **pp, Rapidity = 3.0-3.4:** The minimization contours for the difference between invariant mass shapes of the data and linear combinations 1pp, 2pp, and 3pp Pythia shapes. The background is determined by using the linear combination of the Pythia background shapes that minimizes this quantity.

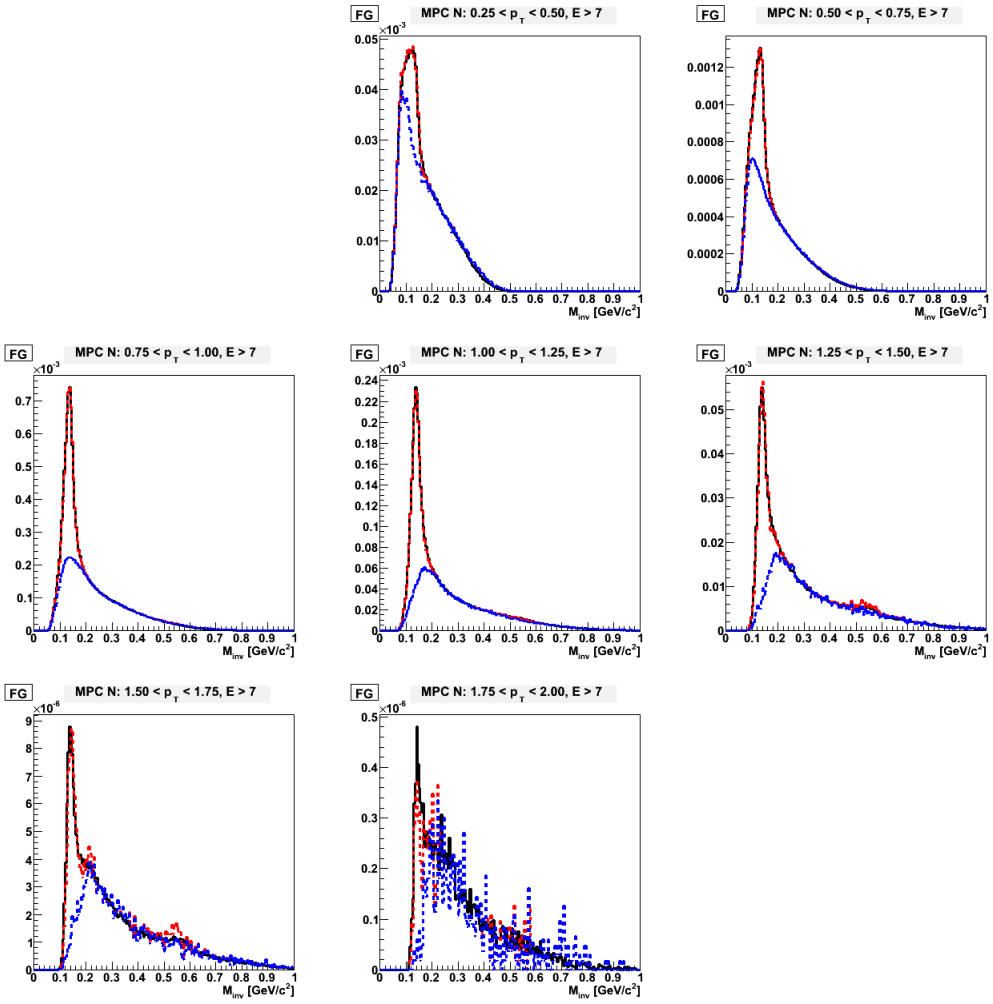

Figure B.4: **dAu 0-20, Rapidity = 3.0-3.4:** This plot illustrates how the background was formed. The invariant mass distributions for data (black), linear combinations of 1pp, 2pp, and 3pp shapes that match simulation to the data (red), and the background for this linear combination are all plotted together.

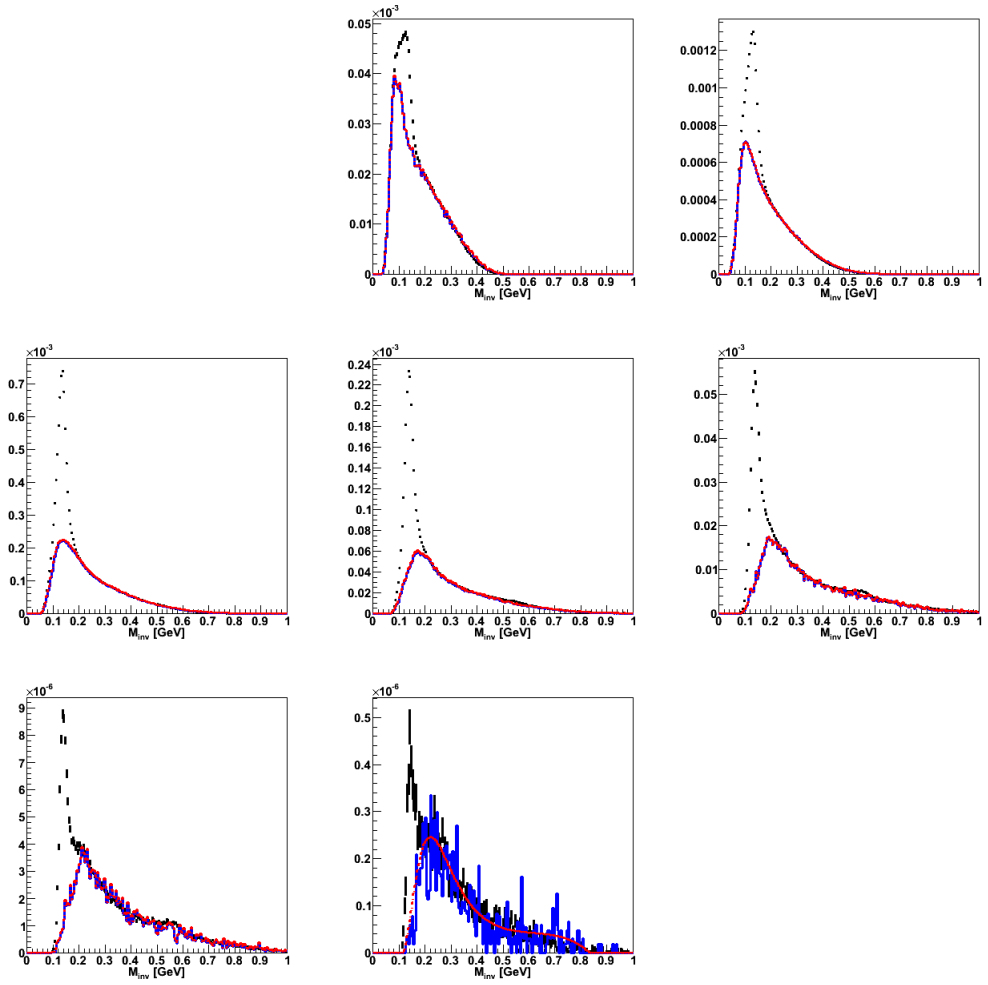

Figure B.5: **dAu 0-20, Rapidity = 3.0-3.4:** Invariant mass foreground (black) and final background (red) distributions.

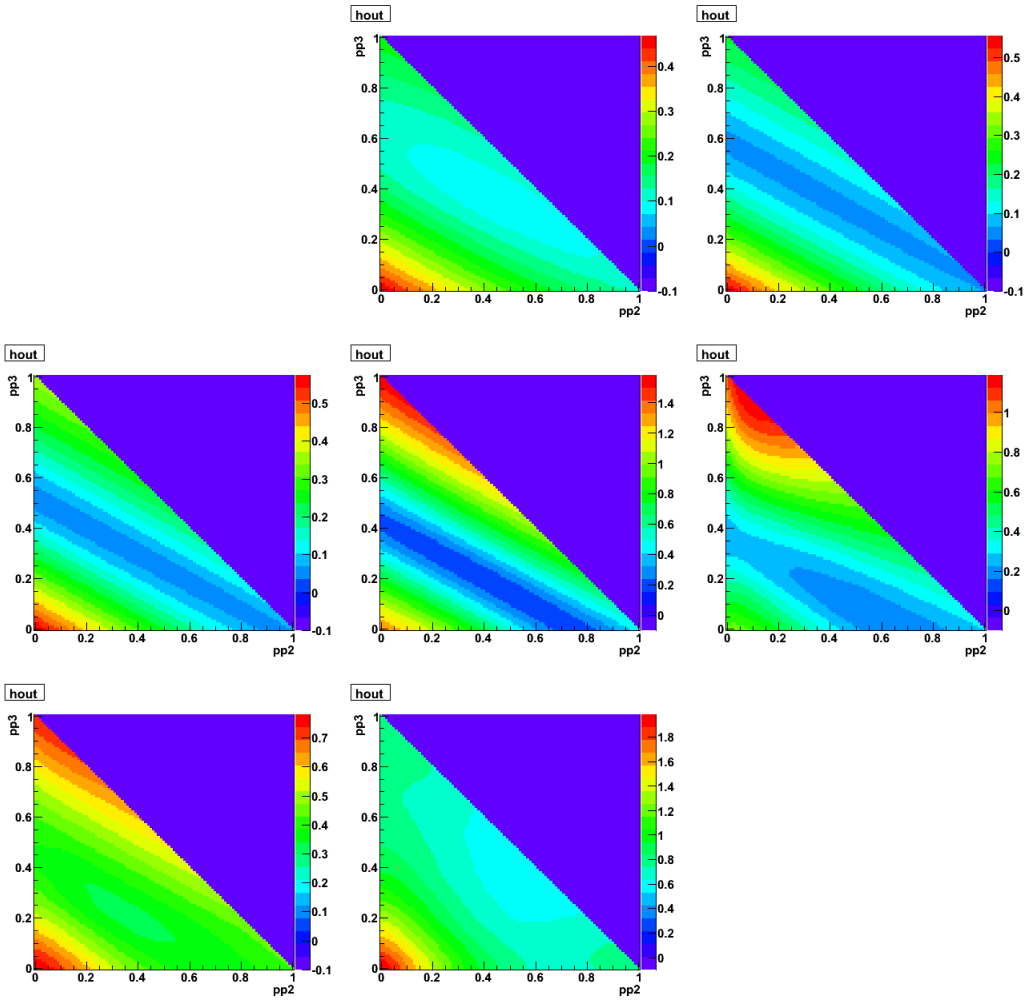

Figure B.6: **dAu 0-20, Rapidity = 3.0-3.4:** The minimization contours for the difference between invariant mass shapes of the data and linear combinations 1pp, 2pp, and 3pp Pythia shapes. The background is determined by using the linear combination of the Pythia background shapes that minimizes this quantity.

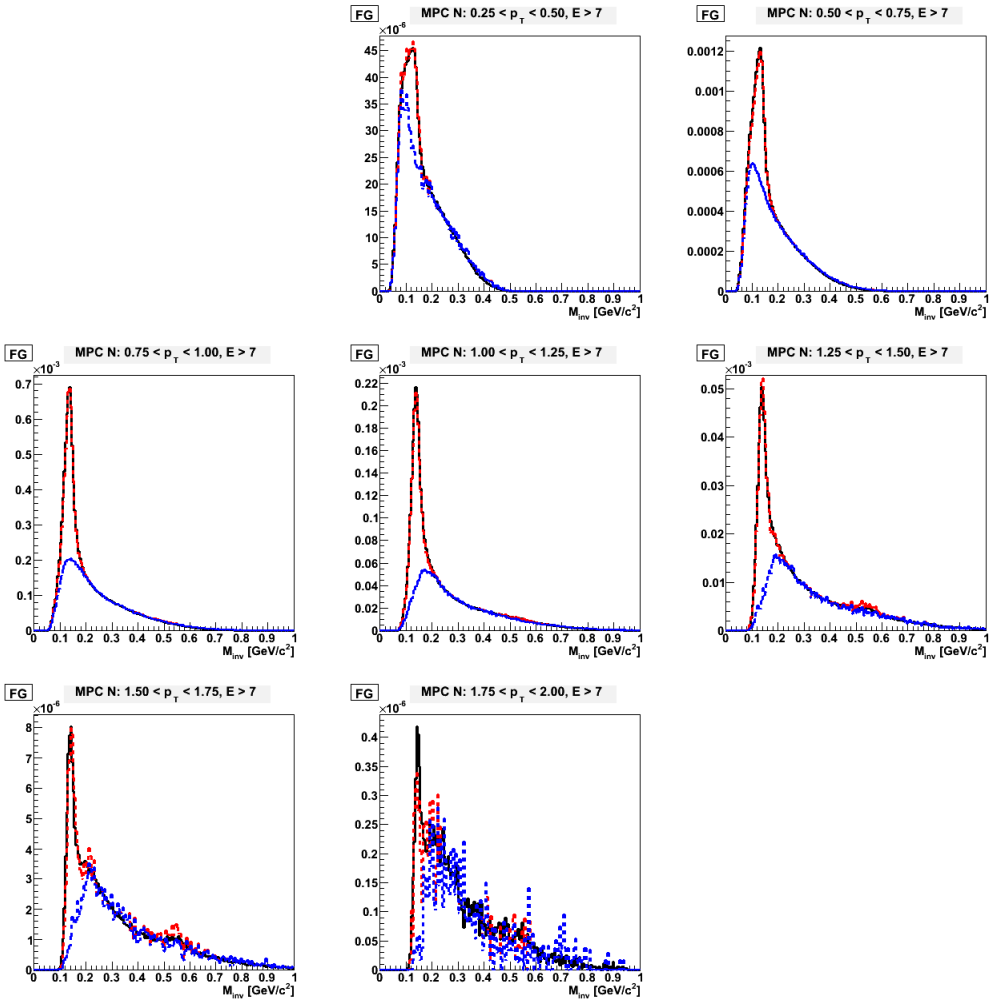

Figure B.7: **dAu 20-40, Rapidity = 3.0-3.4:** This plot illustrates how the background was formed. The invariant mass distributions for data (black), linear combinations of 1pp, 2pp, and 3pp shapes that match simulation to the data (red), and the background for this linear combination are all plotted together.

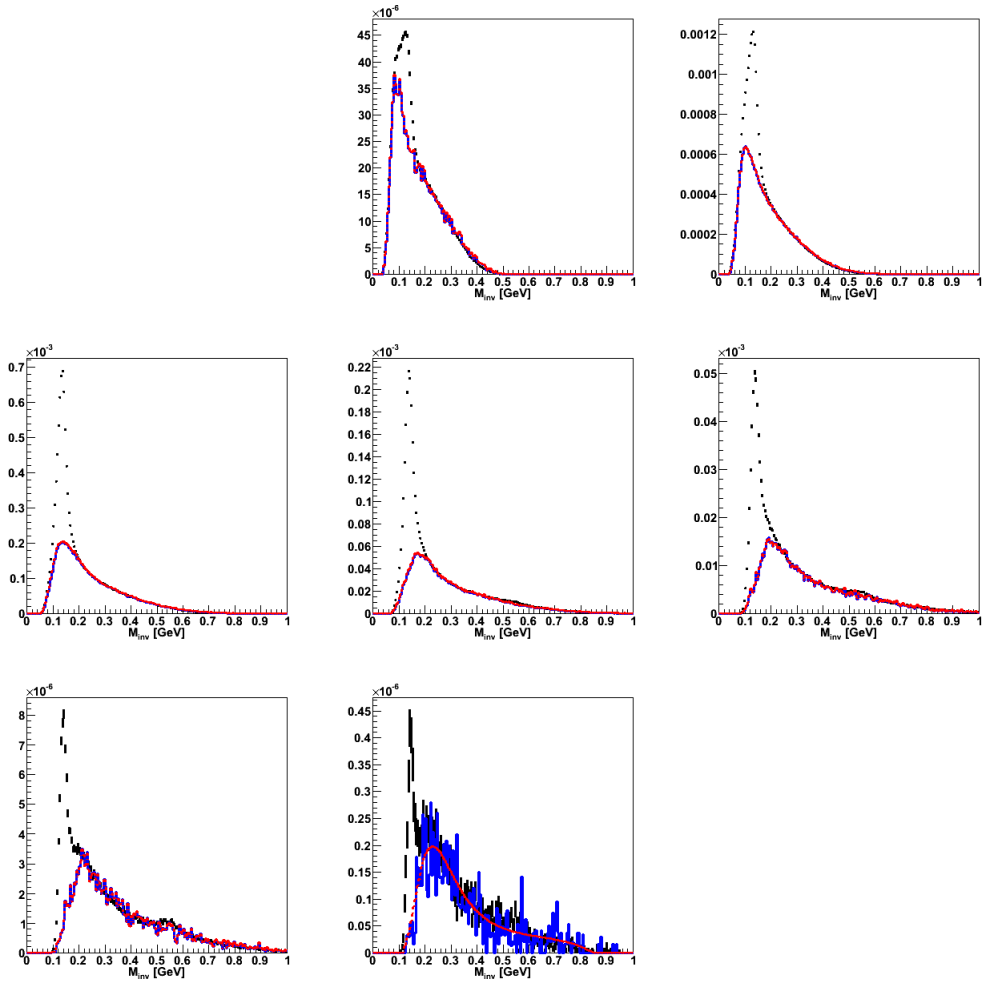

Figure B.8: **dAu 20-40, Rapidity = 3.0-3.4:** Invariant mass foreground (black) and final background (red) distributions.

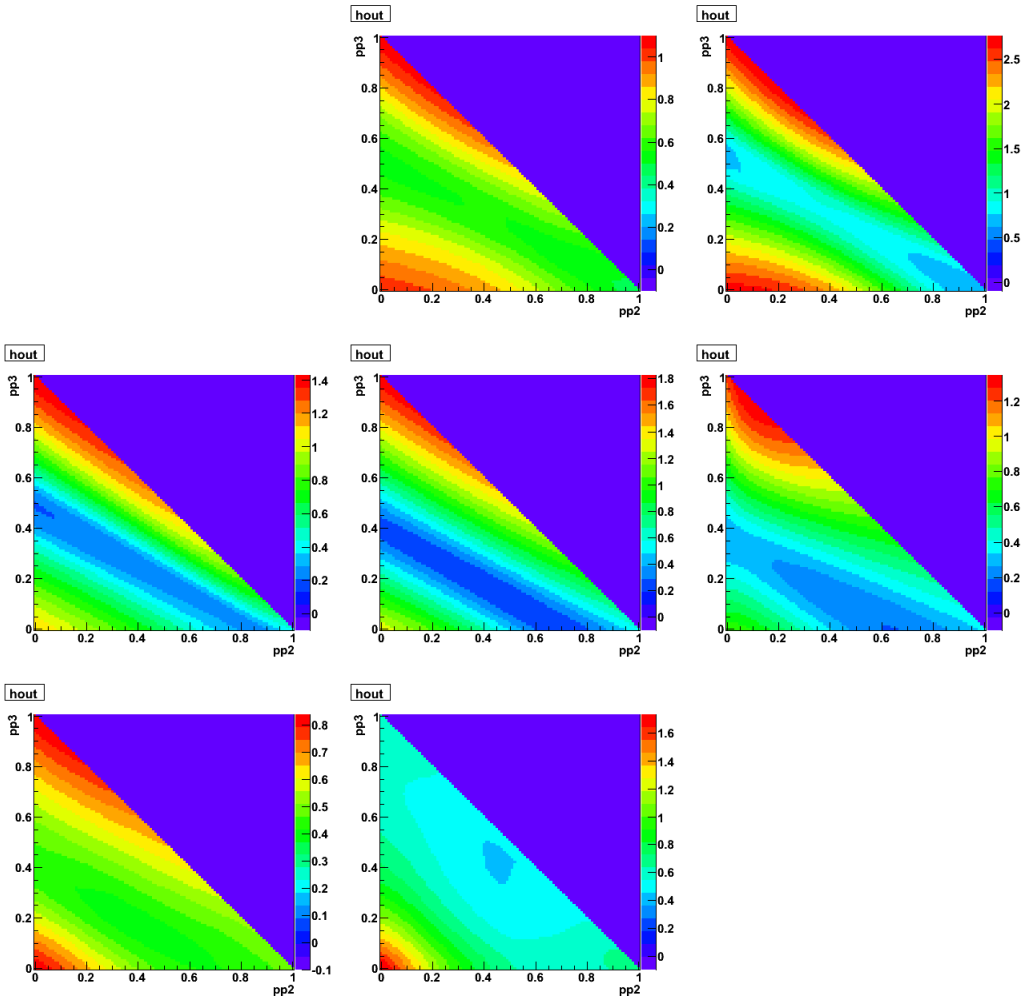

Figure B.9: **dAu 20-40, Rapidity = 3.0-3.4:** The minimization contours for the difference between invariant mass shapes of the data and linear combinations 1pp, 2pp, and 3pp Pythia shapes. The background is determined by using the linear combination of the Pythia background shapes that minimizes this quantity.

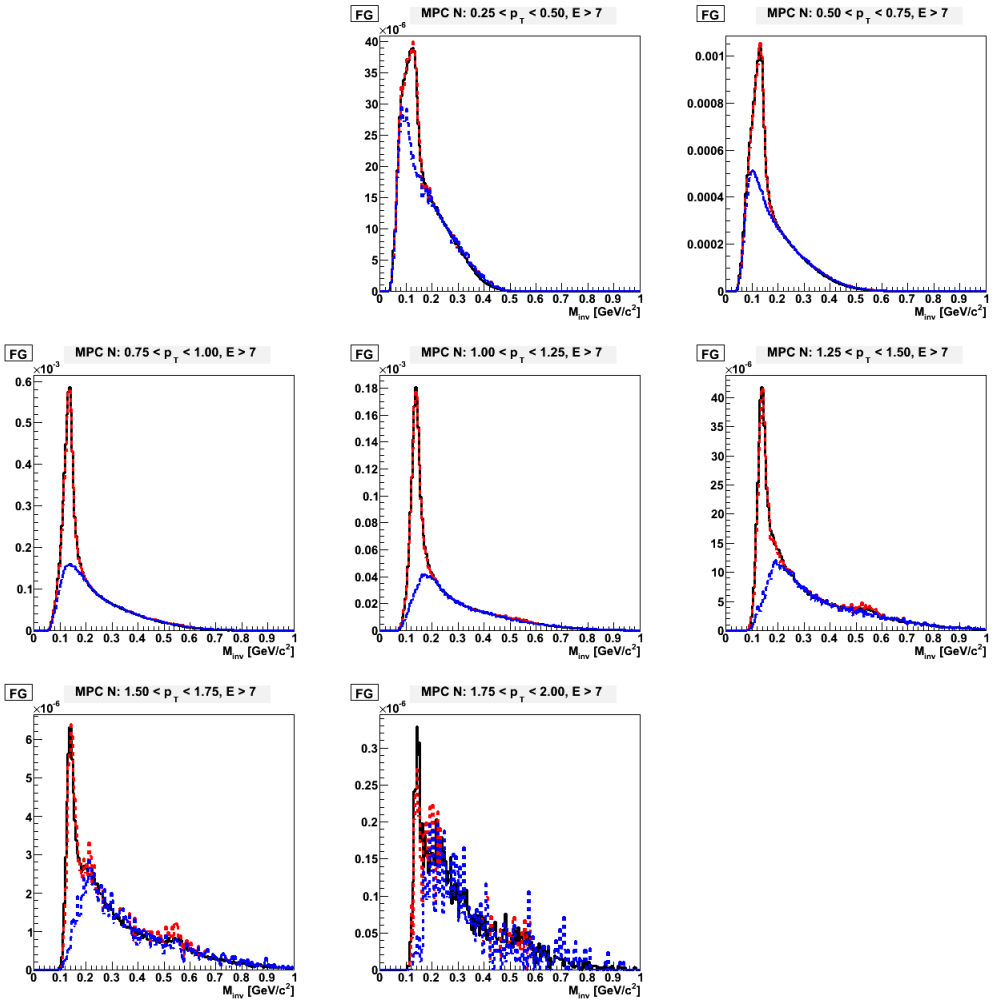

Figure B.10: **dAu 40-60, Rapidity = 3.0-3.4:** This plot illustrates how the background was formed. The invariant mass distributions for data (black), linear combinations of 1pp, 2pp, and 3pp shapes that match simulation to the data (red), and the background for this linear combination are all plotted together.

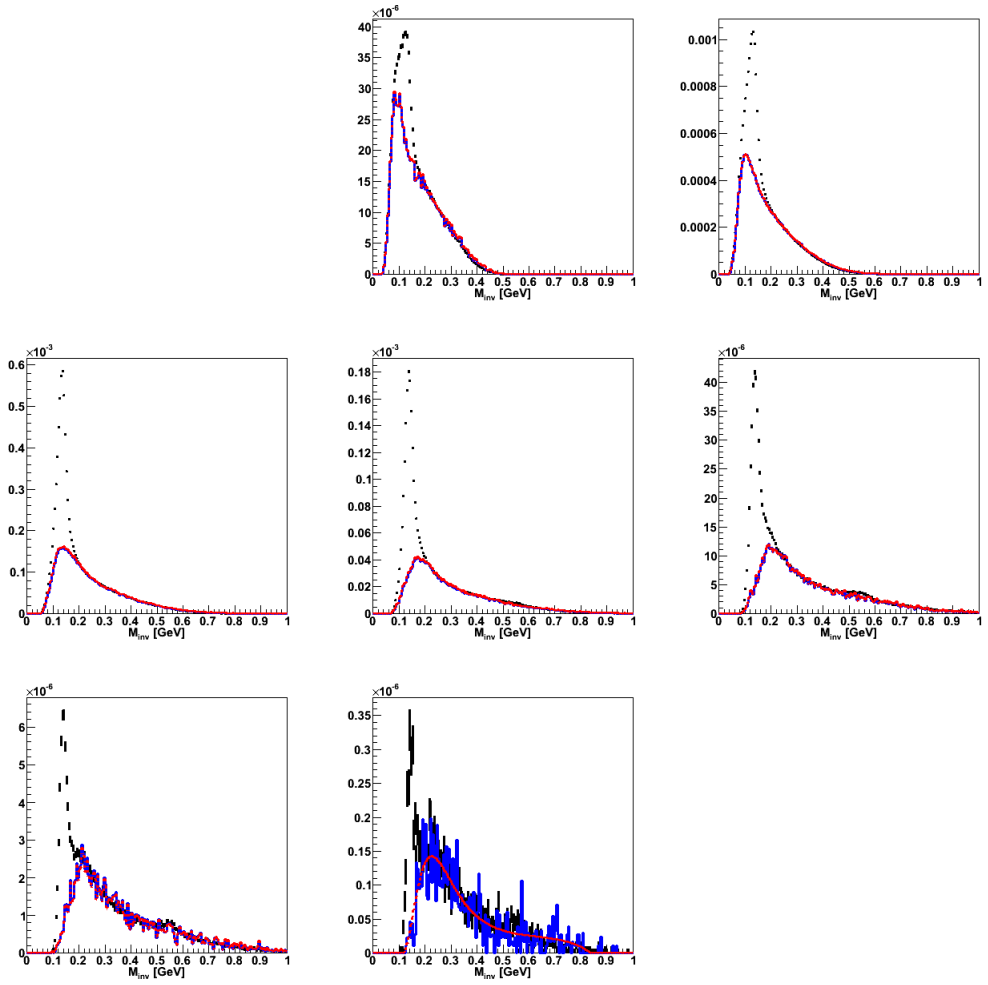

Figure B.11: **dAu 40-60, Rapidity = 3.0-3.4:** Invariant mass foreground (black) and final background (red) distributions.

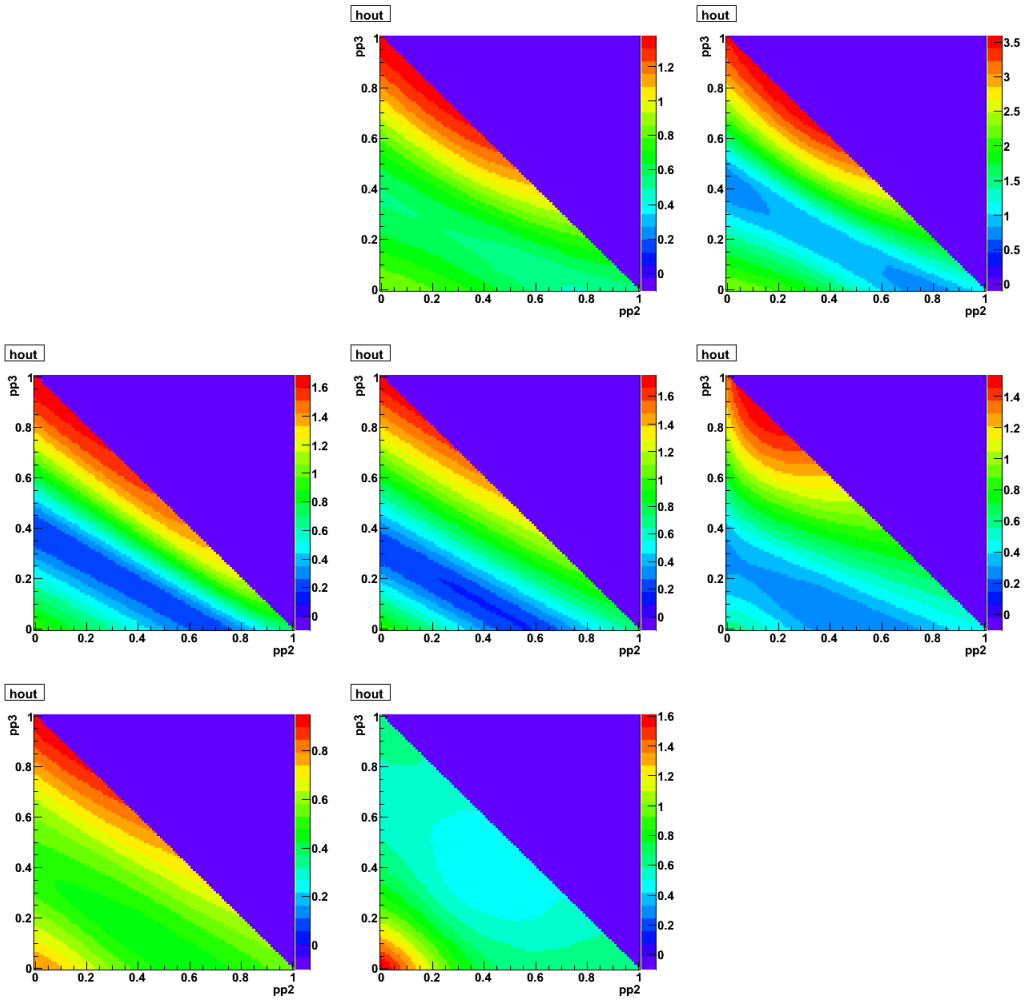

Figure B.12: **dAu 40-60, Rapidity = 3.0-3.4:** The minimization contours for the difference between invariant mass shapes of the data and linear combinations 1pp, 2pp, and 3pp Pythia shapes. The background is determined by using the linear combination of the Pythia background shapes that minimizes this quantity.

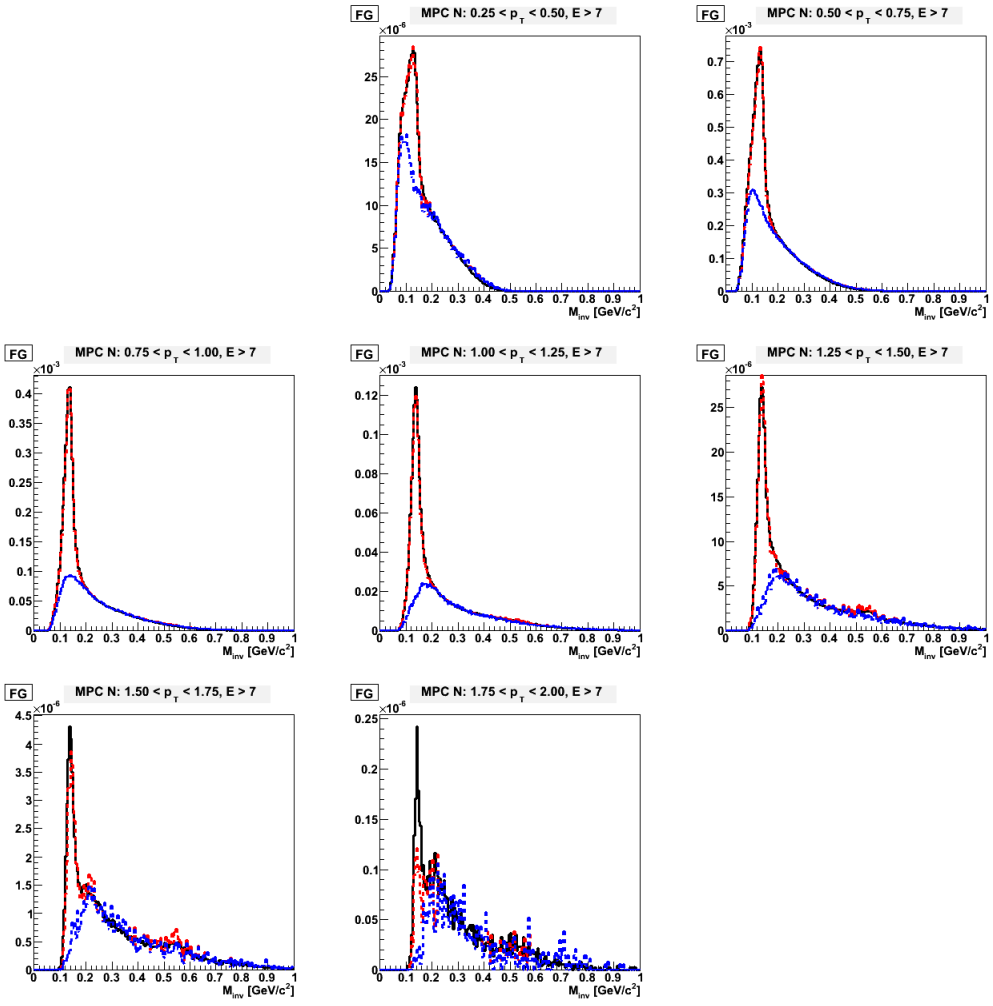

Figure B.13: **dAu 60-88, Rapidity = 3.0-3.4:** This plot illustrates how the background was formed. The invariant mass distributions for data (black), linear combinations of 1pp, 2pp, and 3pp shapes that match simulation to the data (red), and the background for this linear combination are all plotted together.

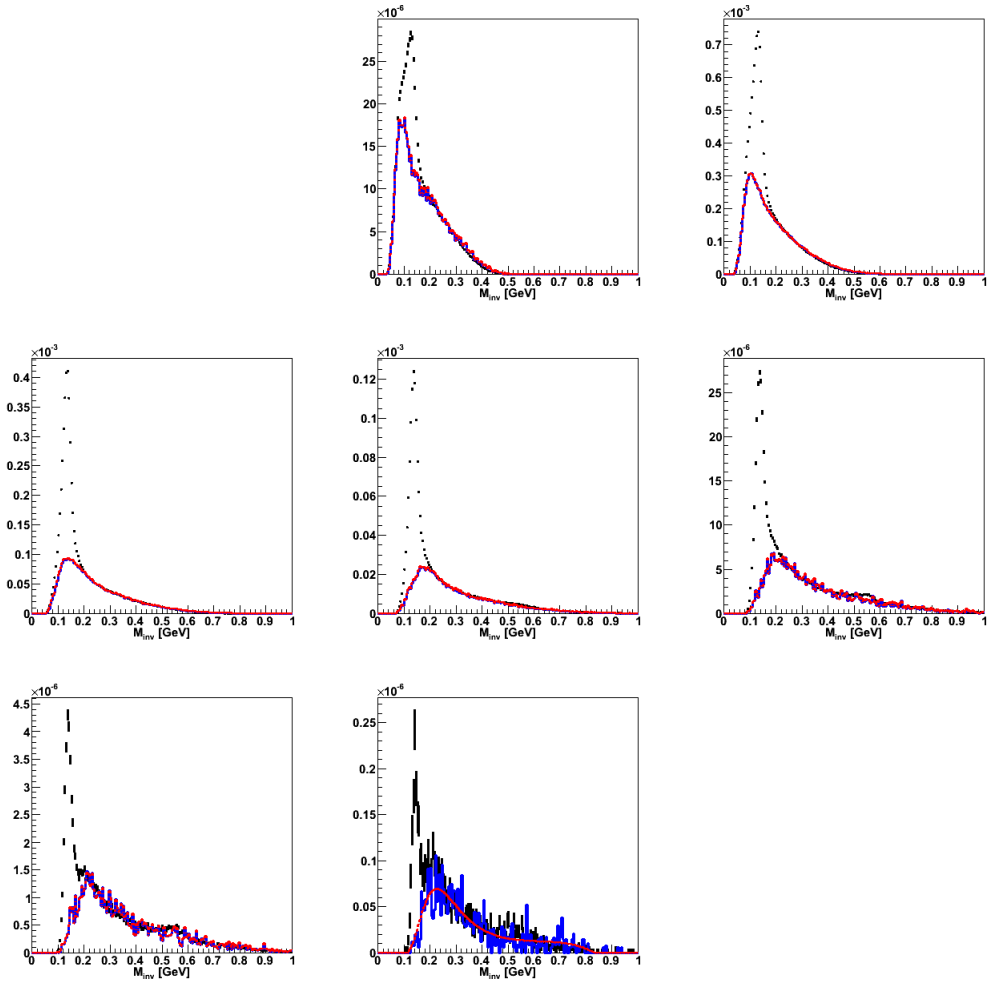

Figure B.14: **dAu 60-88, Rapidity = 3.0-3.4:** Invariant mass foreground (black) and final background (red) distributions.

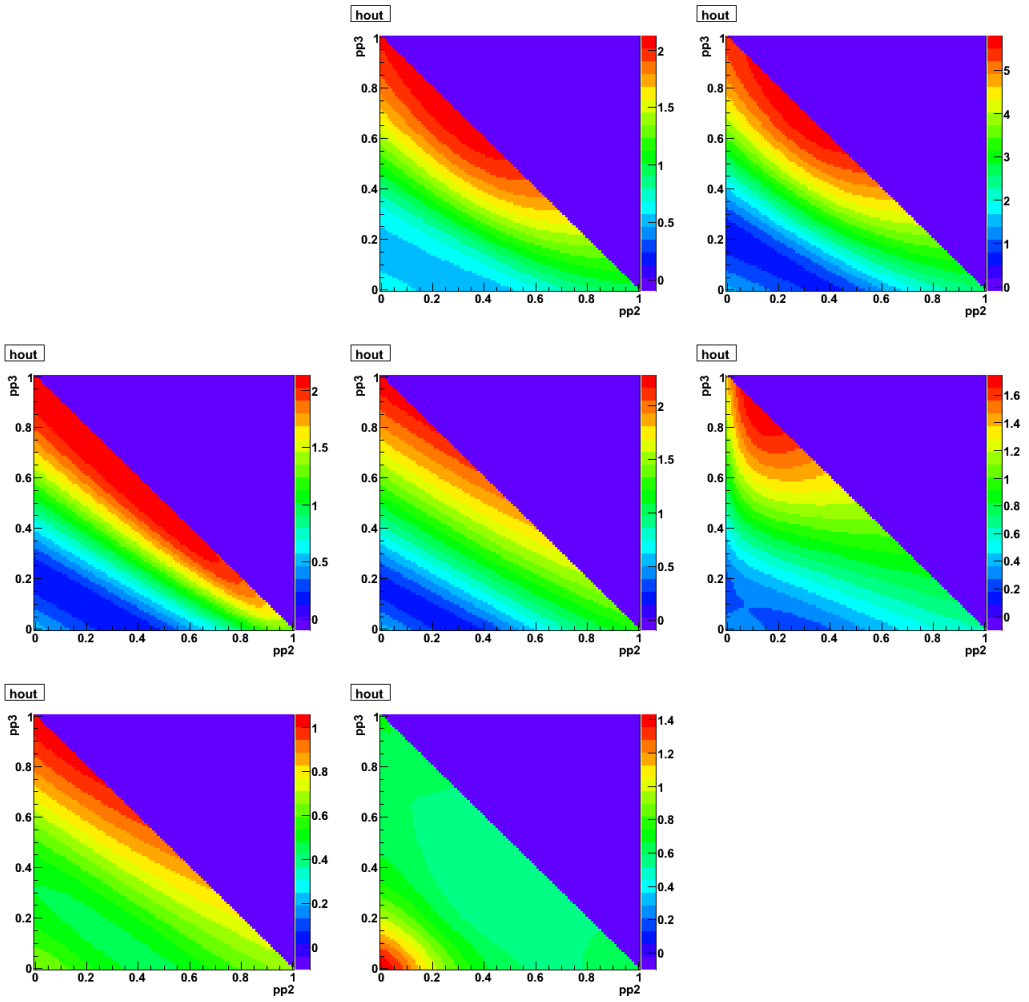

Figure B.15: **dAu 60-88, Rapidity = 3.0-3.4:** The minimization contours for the difference between invariant mass shapes of the data and linear combinations 1pp, 2pp, and 3pp Pythia shapes. The background is determined by using the linear combination of the Pythia background shapes that minimizes this quantity.

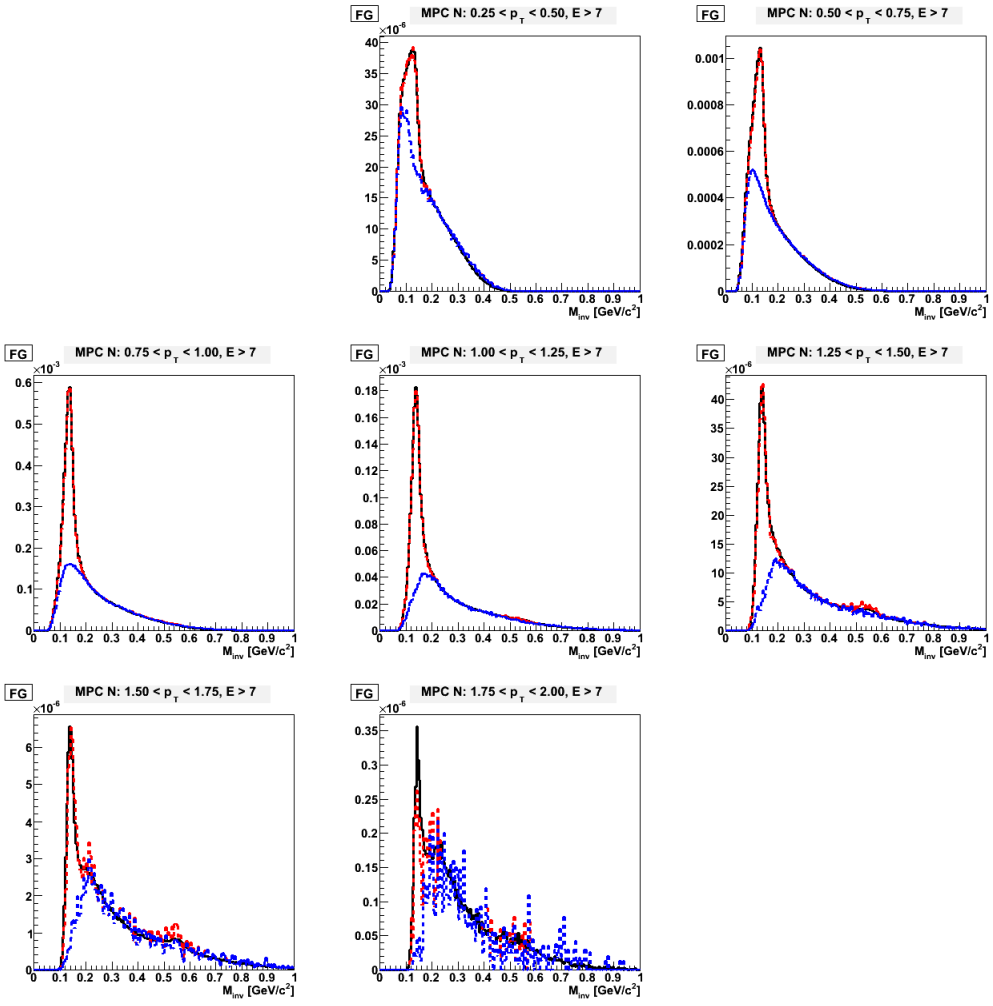

Figure B.16: **dAu MinBias, Rapidity = 3.0-3.4:** This plot illustrates how the background was formed. The invariant mass distributions for data (black), linear combinations of 1pp, 2pp, and 3pp shapes that match simulation to the data (red), and the background for this linear combination are all plotted together.

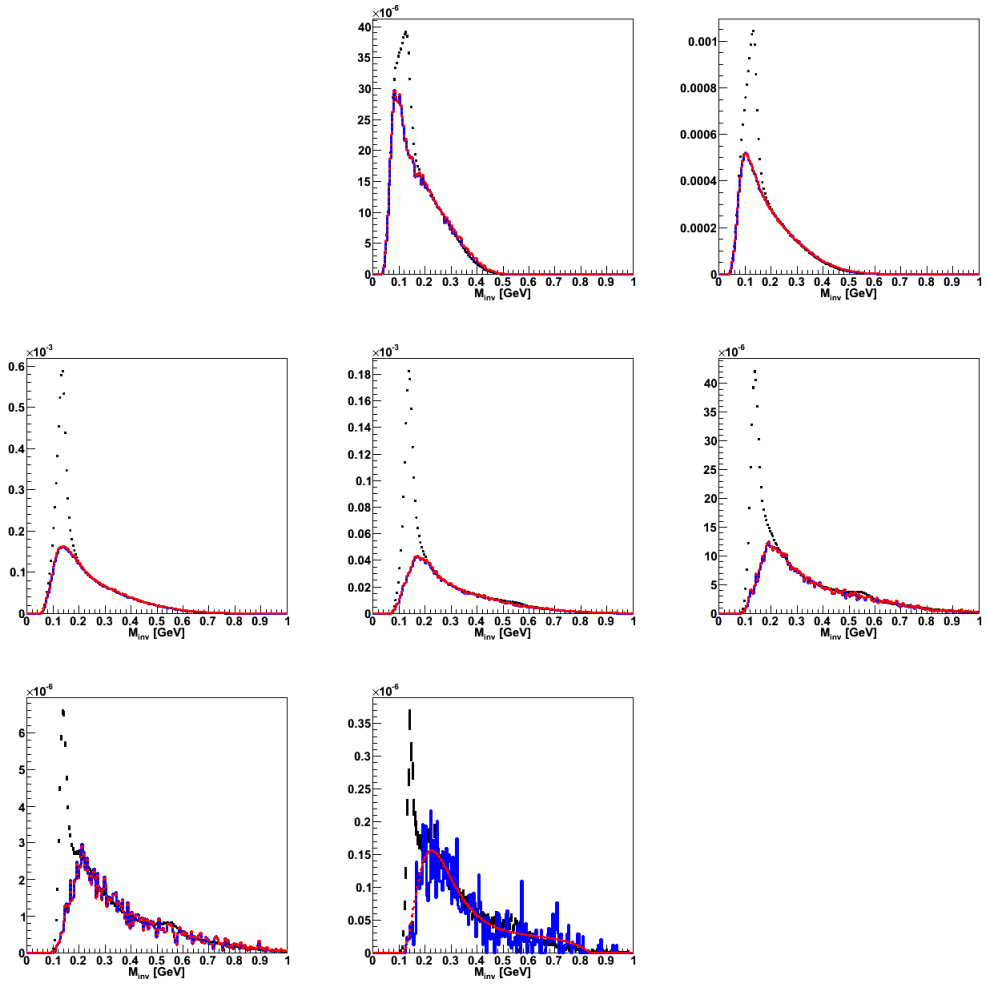

Figure B.17: **dAu MinBias, Rapidity = 3.0-3.4:** Invariant mass foreground (black) and final background (red) distributions.

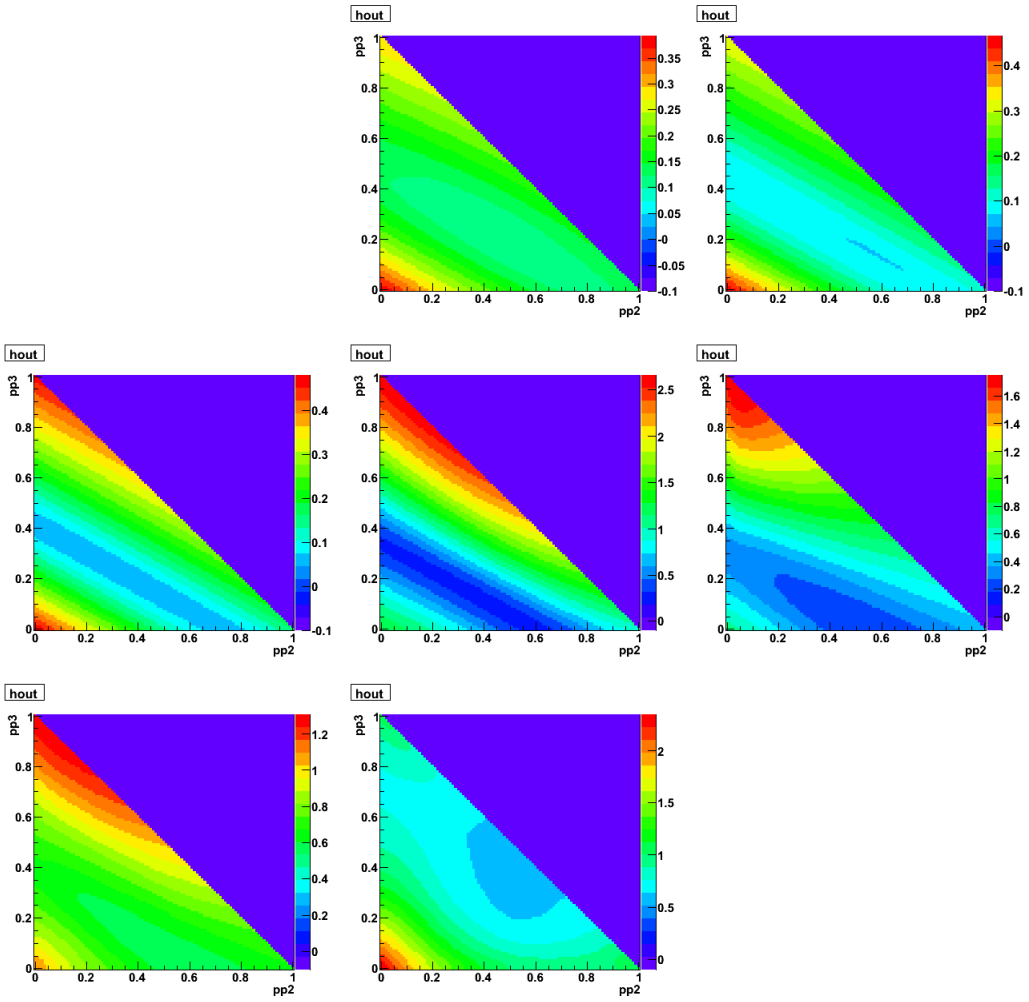

Figure B.18: **dAu MinBias, Rapidity = 3.0-3.4:** The minimization contours for the difference between invariant mass shapes of the data and linear combinations 1pp, 2pp, and 3pp Pythia shapes. The background is determined by using the linear combination of the Pythia background shapes that minimizes this quantity.

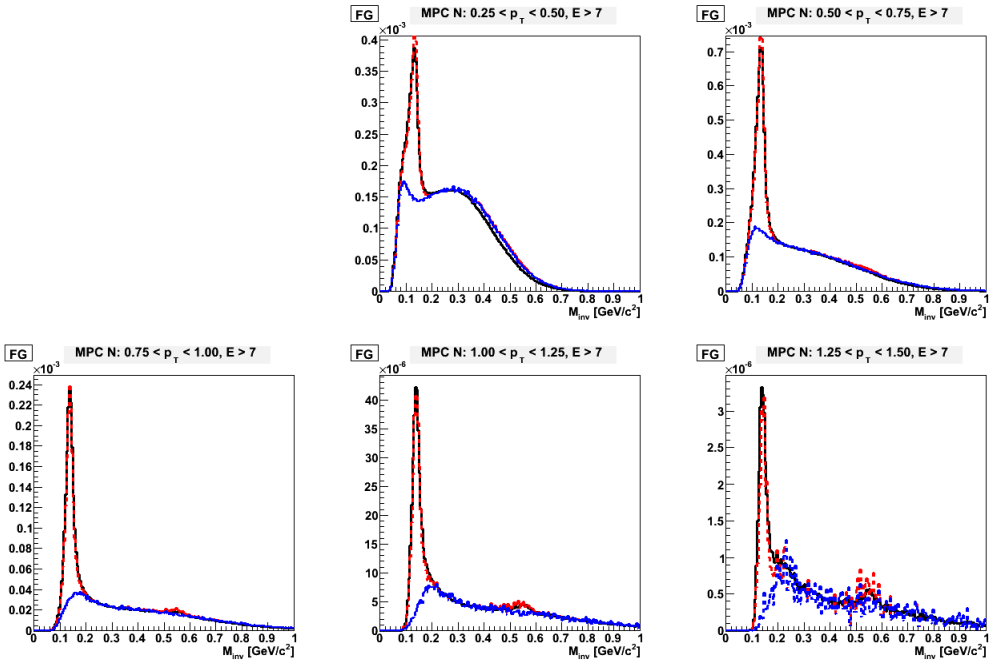

Figure B.19: **pp, Rapidity = 3.4-3.8:** This plot illustrates how the background was formed. The invariant mass distributions for data (black), linear combinations of 1pp, 2pp, and 3pp shapes that match simulation to the data (red), and the background for this linear combination are all plotted together.

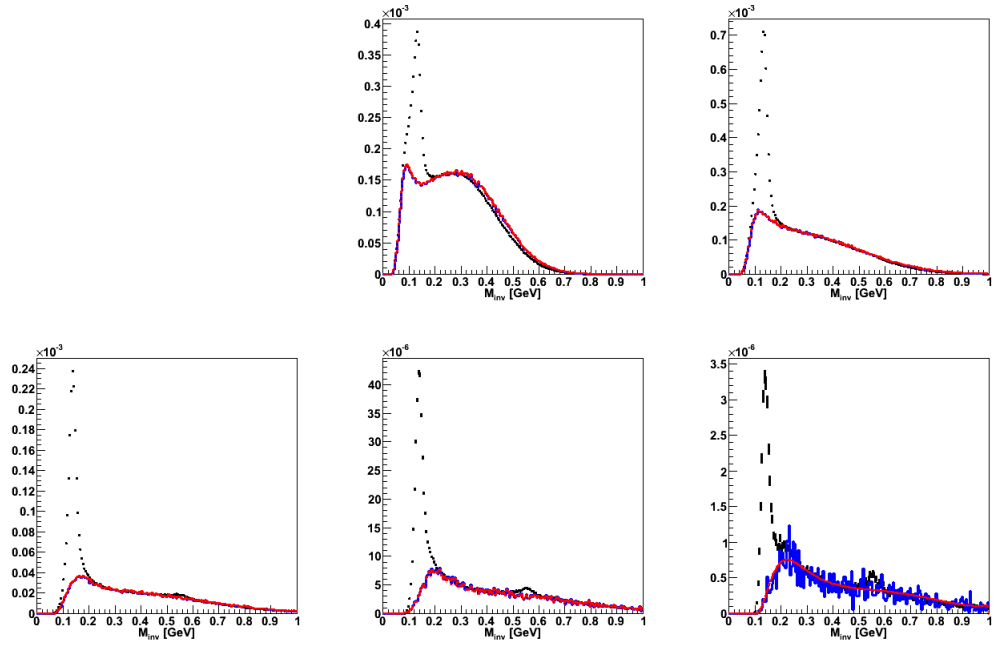

Figure B.20: **pp, Rapidity = 3.4-3.8:** Invariant mass foreground (black) and final background (red) distributions.

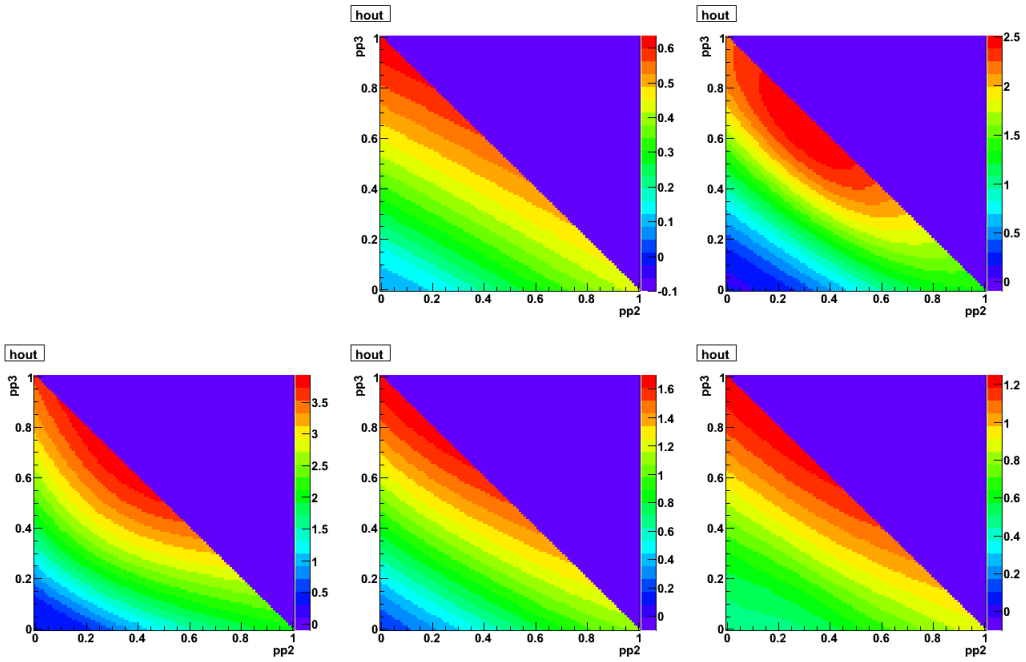

Figure B.21: **pp, Rapidity = 3.4-3.8:** The minimization contours for the difference between invariant mass shapes of the data and linear combinations 1pp, 2pp, and 3pp Pythia shapes. The background is determined by using the linear combination of the Pythia background shapes that minimizes this quantity.

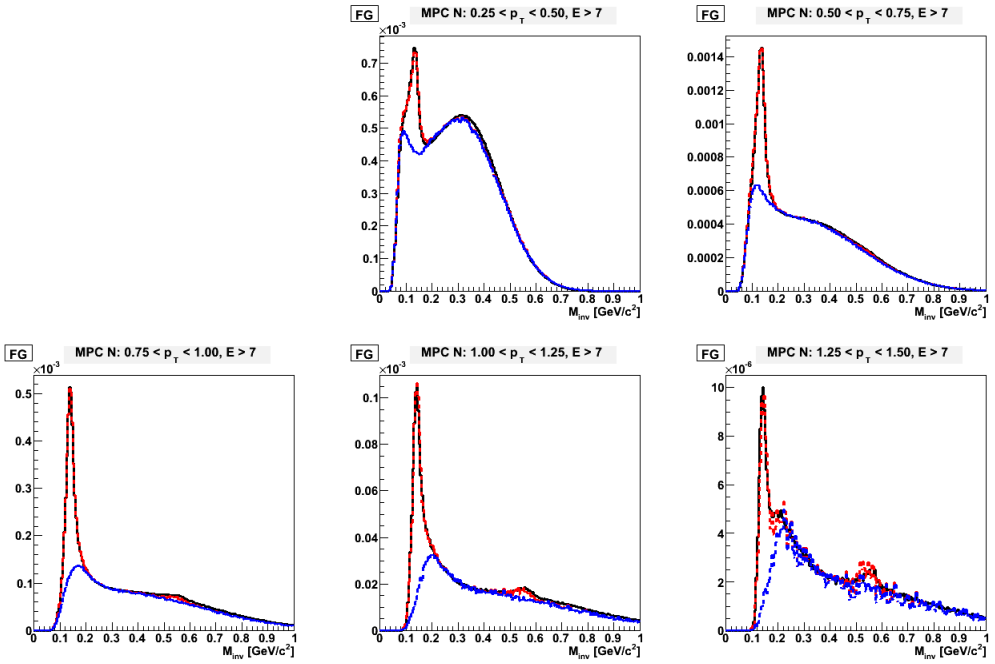

Figure B.22: **dAu 0-20, Rapidity = 3.4-3.8:** This plot illustrates how the background was formed. The invariant mass distributions for data (black), linear combinations of 1pp, 2pp, and 3pp shapes that match simulation to the data (red), and the background for this linear combination are all plotted together.

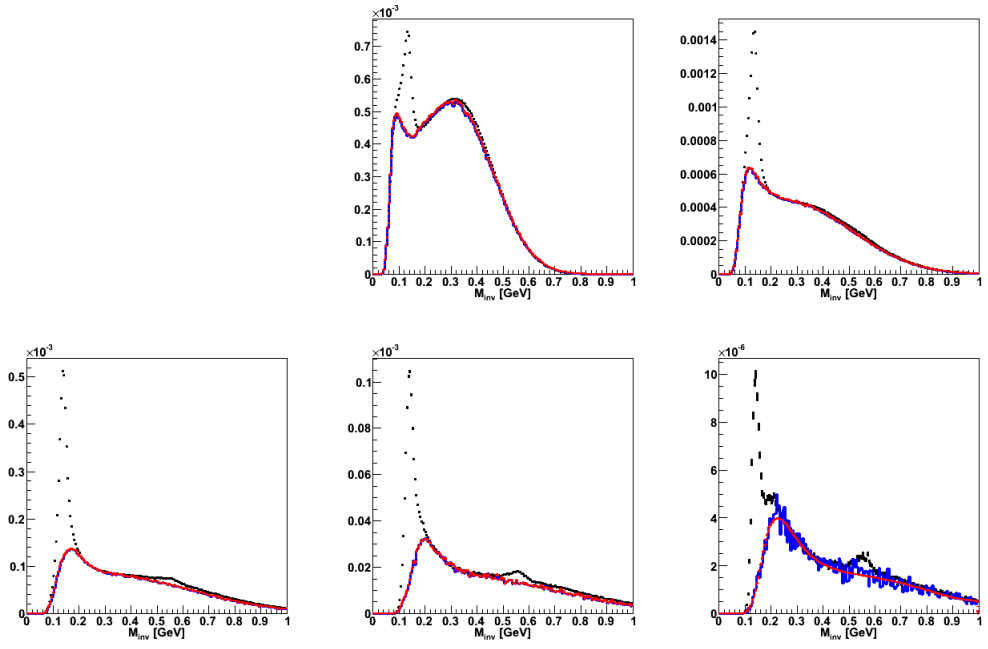

Figure B.23: **dAu 0-20, Rapidity = 3.4-3.8:** Invariant mass foreground (black) and final background (red) distributions.

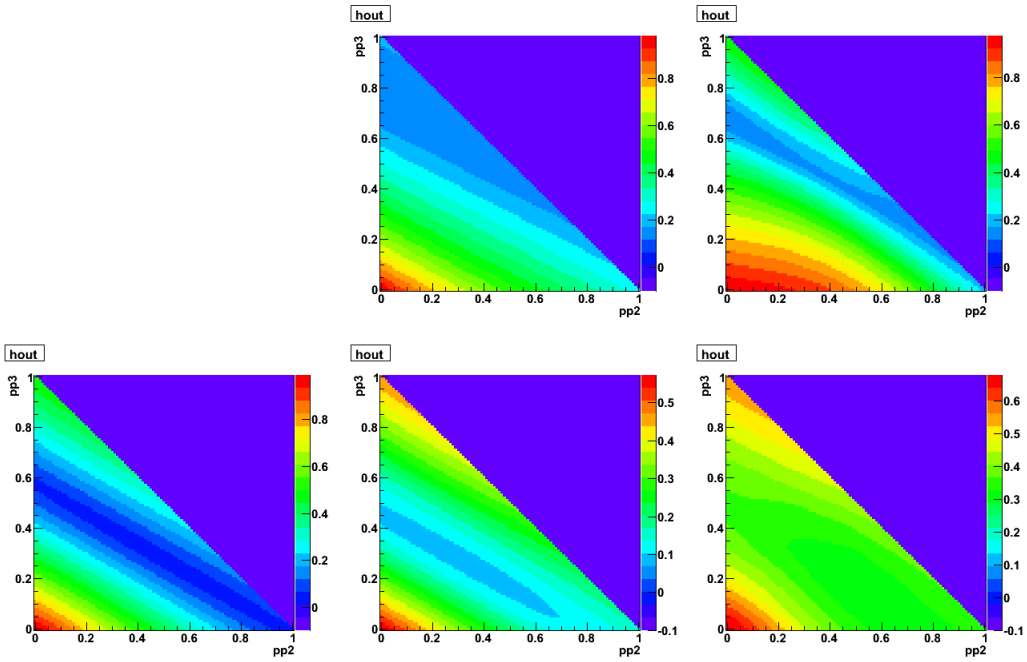

Figure B.24: **dAu 0-20, Rapidity = 3.4-3.8:** The minimization contours for the difference between invariant mass shapes of the data and linear combinations 1pp, 2pp, and 3pp Pythia shapes. The background is determined by using the linear combination of the Pythia background shapes that minimizes this quantity.

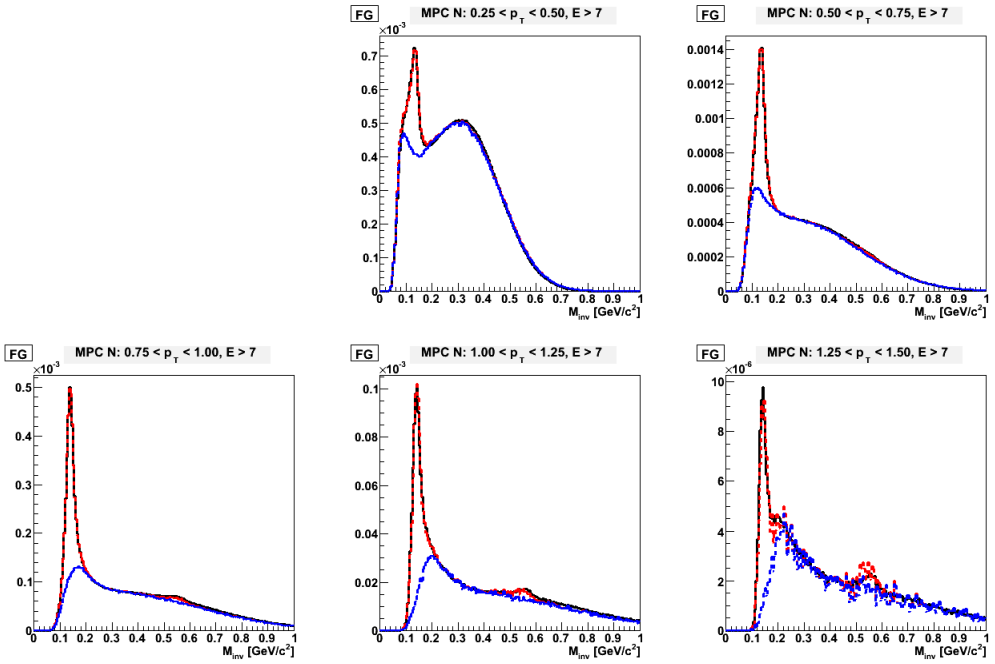

Figure B.25: **dAu 20-40, Rapidity = 3.4-3.8:** This plot illustrates how the background was formed. The invariant mass distributions for data (black), linear combinations of 1pp, 2pp, and 3pp shapes that match simulation to the data (red), and the background for this linear combination are all plotted together.

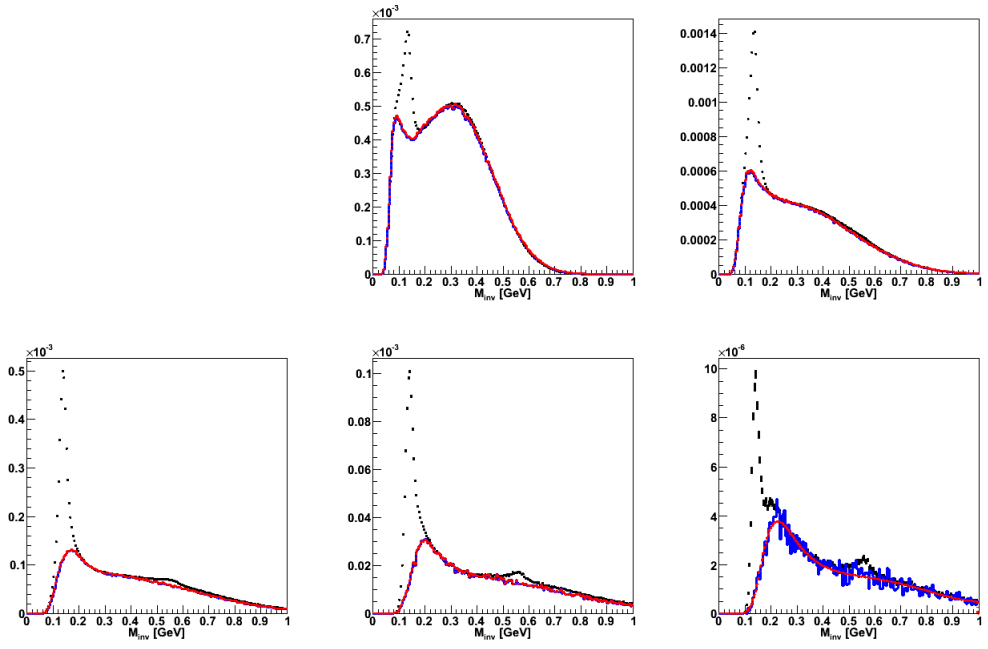

Figure B.26: **dAu 20-40, Rapidity = 3.4-3.8:** Invariant mass foreground (black) and final background (red) distributions.

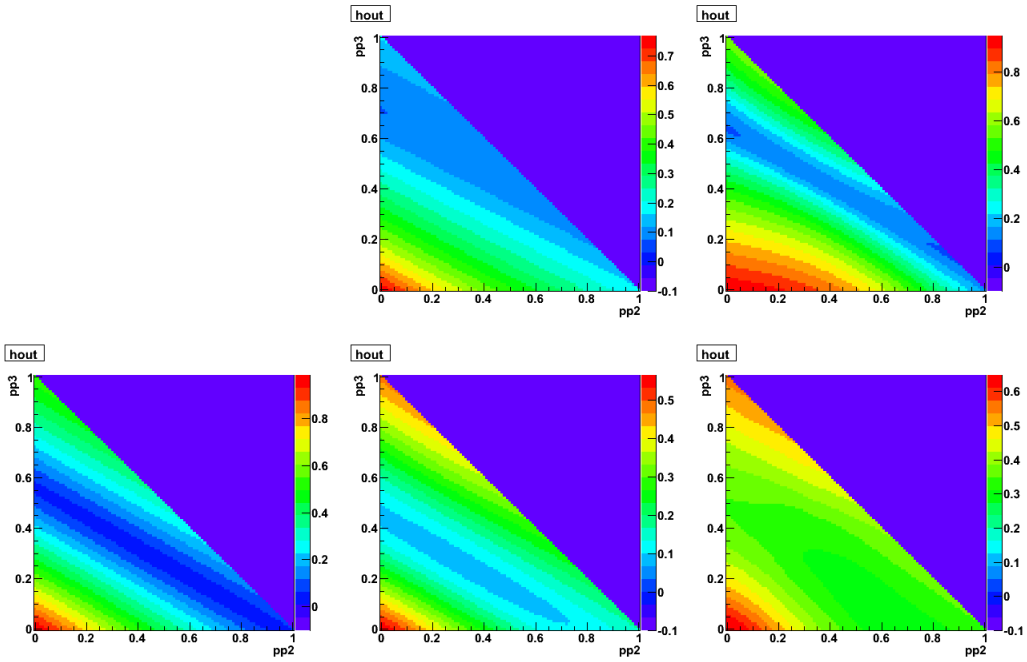

Figure B.27: **dAu 20-40, Rapidity = 3.4-3.8:** The minimization contours for the difference between invariant mass shapes of the data and linear combinations 1pp, 2pp, and 3pp Pythia shapes. The background is determined by using the linear combination of the Pythia background shapes that minimizes this quantity.

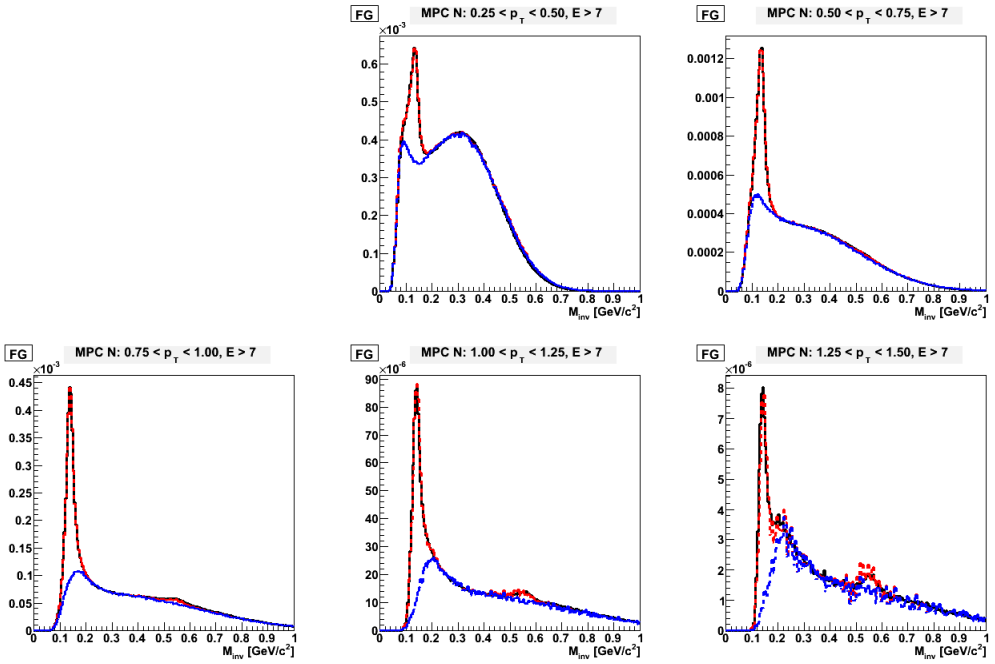

Figure B.28: **dAu 40-60, Rapidity = 3.4-3.8:** This plot illustrates how the background was formed. The invariant mass distributions for data (black), linear combinations of 1pp, 2pp, and 3pp shapes that match simulation to the data (red), and the background for this linear combination are all plotted together.

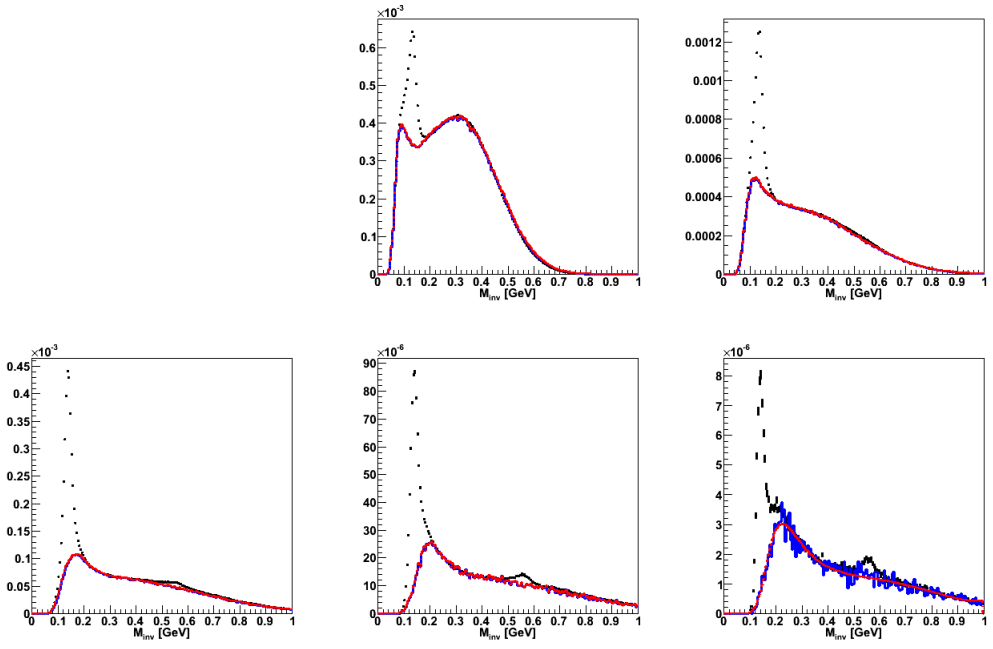

Figure B.29: **dAu 40-60, Rapidity = 3.4-3.8:** Invariant mass foreground (black) and final background (red) distributions.

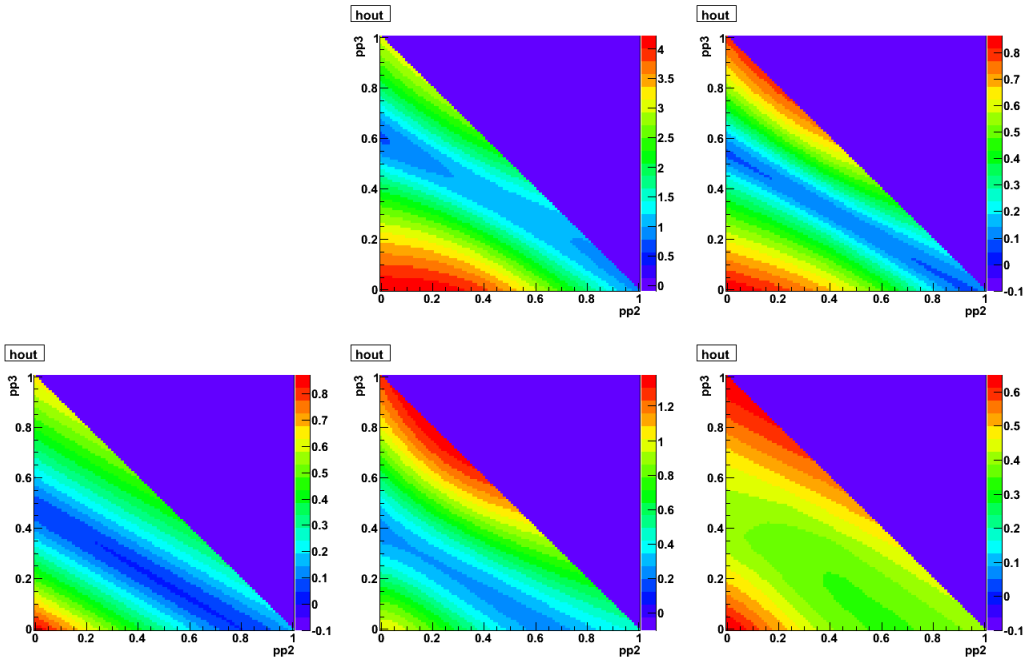

Figure B.30: **dAu 40-60, Rapidity = 3.4-3.8:** The minimization contours for the difference between invariant mass shapes of the data and linear combinations 1pp, 2pp, and 3pp Pythia shapes. The background is determined by using the linear combination of the Pythia background shapes that minimizes this quantity.

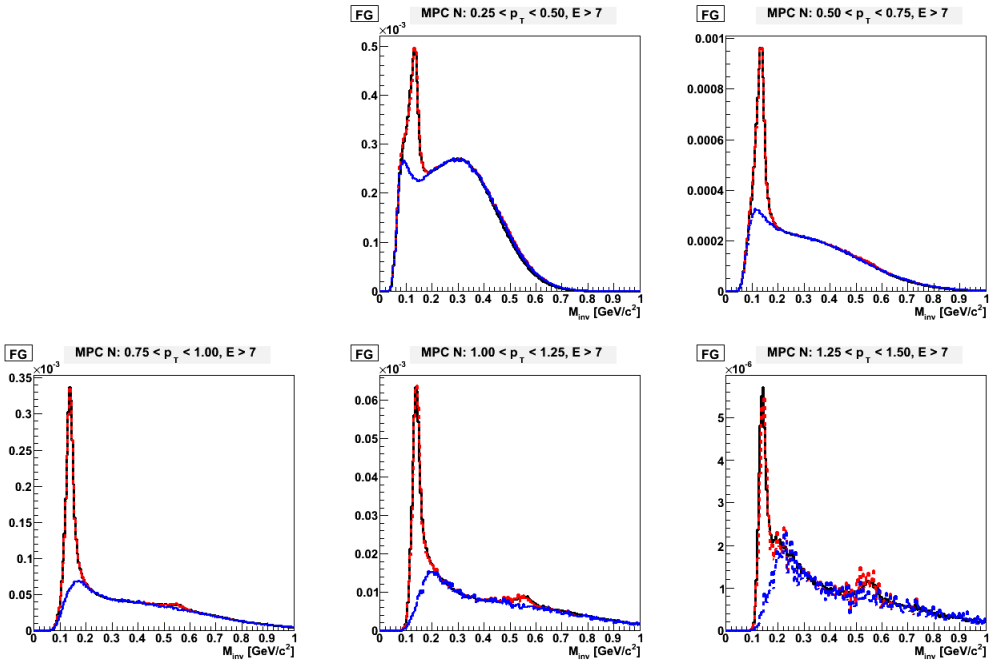

Figure B.31: **dAu 60-88, Rapidity = 3.4-3.8:** This plot illustrates how the background was formed. The invariant mass distributions for data (black), linear combinations of 1pp, 2pp, and 3pp shapes that match simulation to the data (red), and the background for this linear combination are all plotted together.

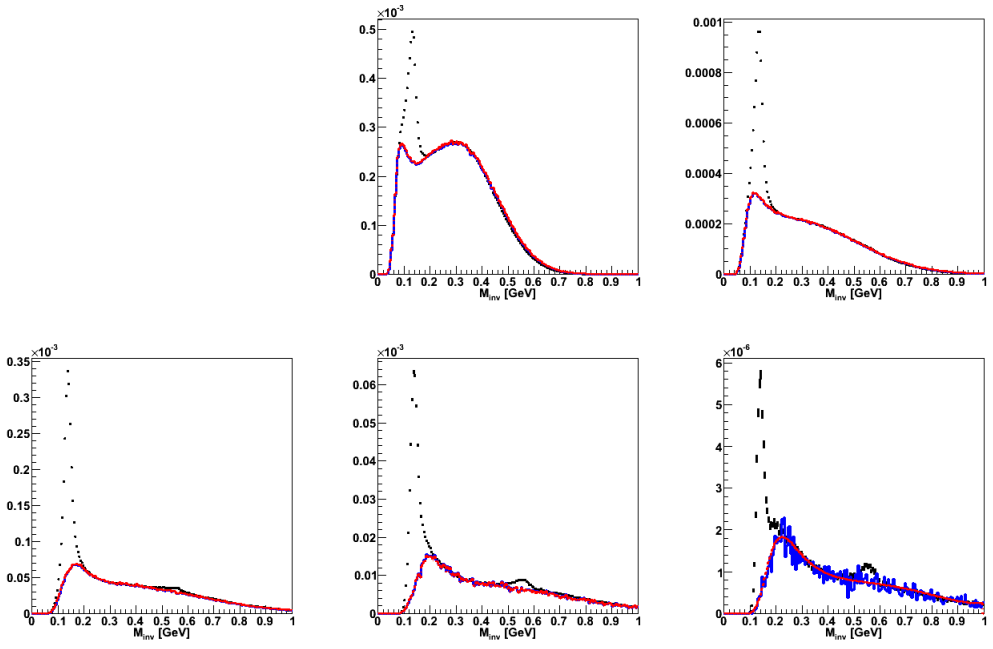

Figure B.32: **dAu 60-88, Rapidity = 3.4-3.8:** Invariant mass foreground (black) and final background (red) distributions.

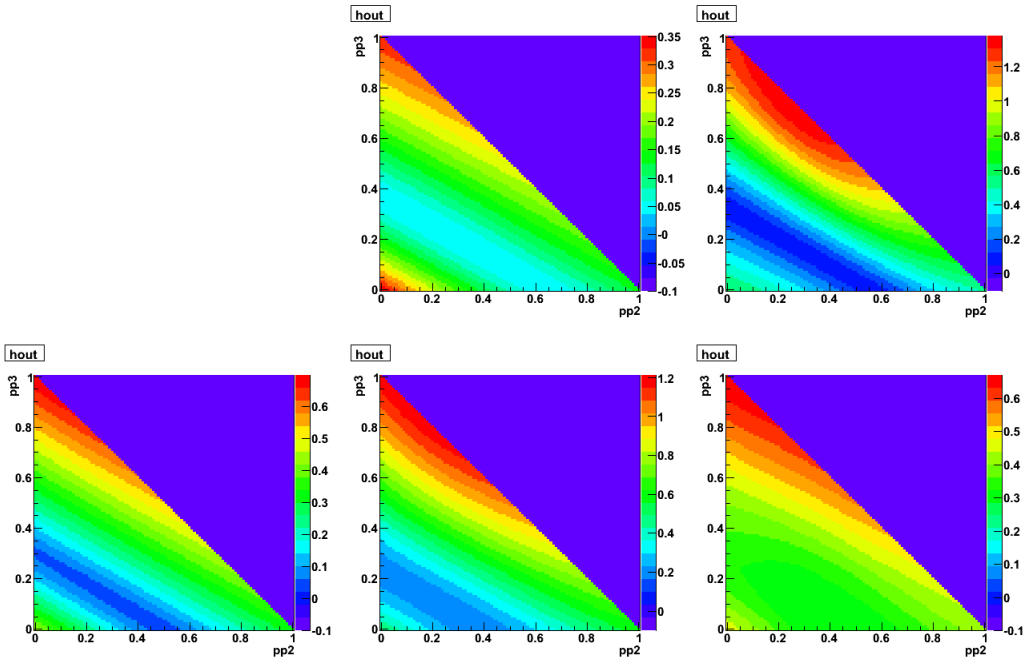

Figure B.33: **dAu 60-88, Rapidity = 3.4-3.8:** The minimization contours for the difference between invariant mass shapes of the data and linear combinations 1pp, 2pp, and 3pp Pythia shapes. The background is determined by using the linear combination of the Pythia background shapes that minimizes this quantity.

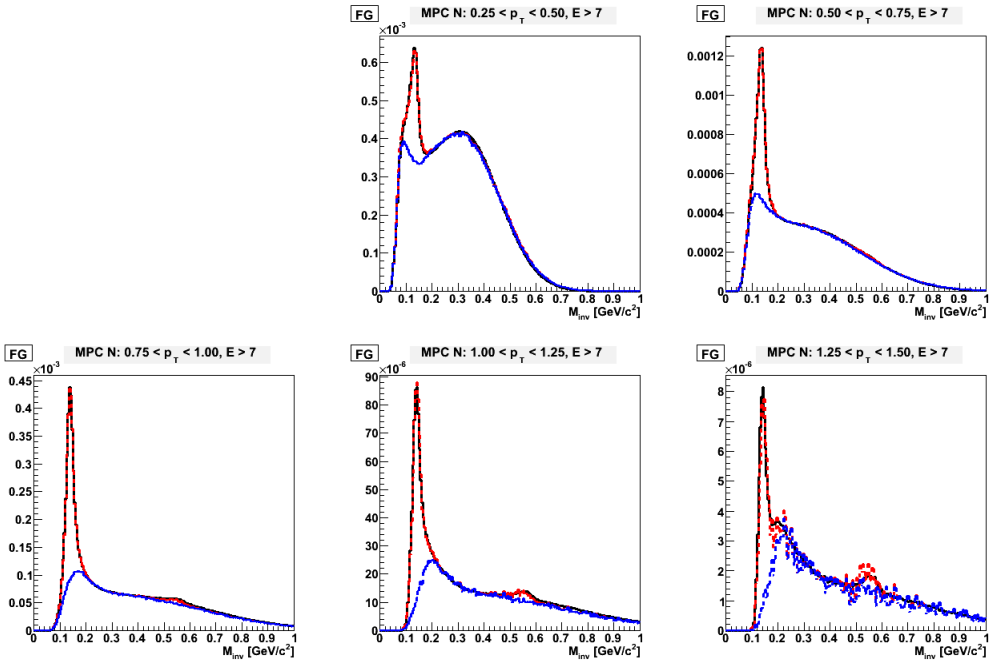

Figure B.34: **dAu MinBias, Rapidity = 3.4-3.8:** This plot illustrates how the background was formed. The invariant mass distributions for data (black), linear combinations of 1pp, 2pp, and 3pp shapes that match simulation to the data (red), and the background for this linear combination are all plotted together.

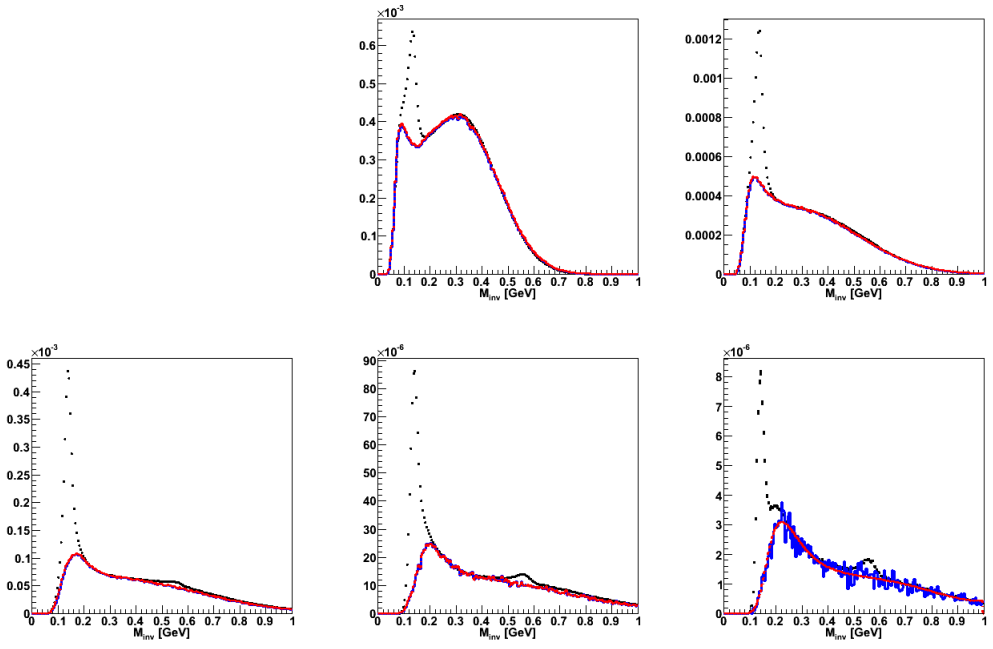

Figure B.35: **dAu MinBias, Rapidity = 3.4-3.8:** Invariant mass foreground (black) and final background (red) distributions.

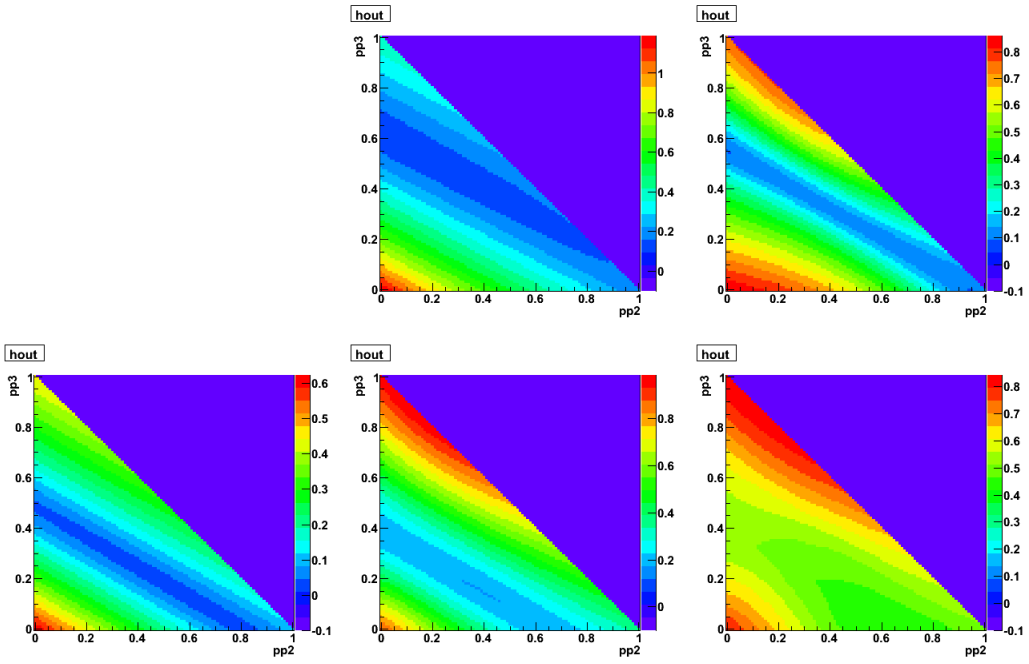

Figure B.36: **dAu MinBias, Rapidity = 3.4-3.8:** The minimization contours for the difference between invariant mass shapes of the data and linear combinations 1pp, 2pp, and 3pp Pythia shapes. The background is determined by using the linear combination of the Pythia background shapes that minimizes this quantity.

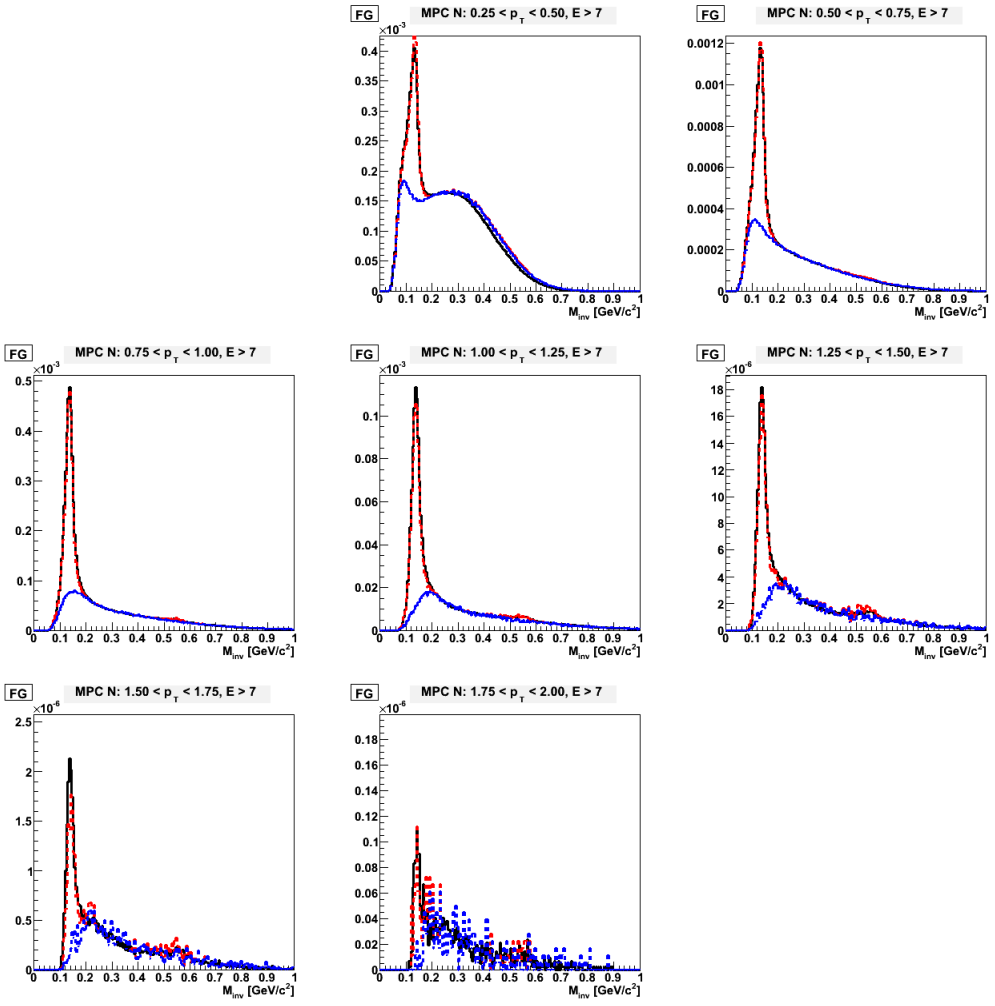

Figure B.37: **pp, Rapidity = 3.0-3.8:** This plot illustrates how the background was formed. The invariant mass distributions for data (black), linear combinations of 1pp, 2pp, and 3pp shapes that match simulation to the data (red), and the background for this linear combination are all plotted together.

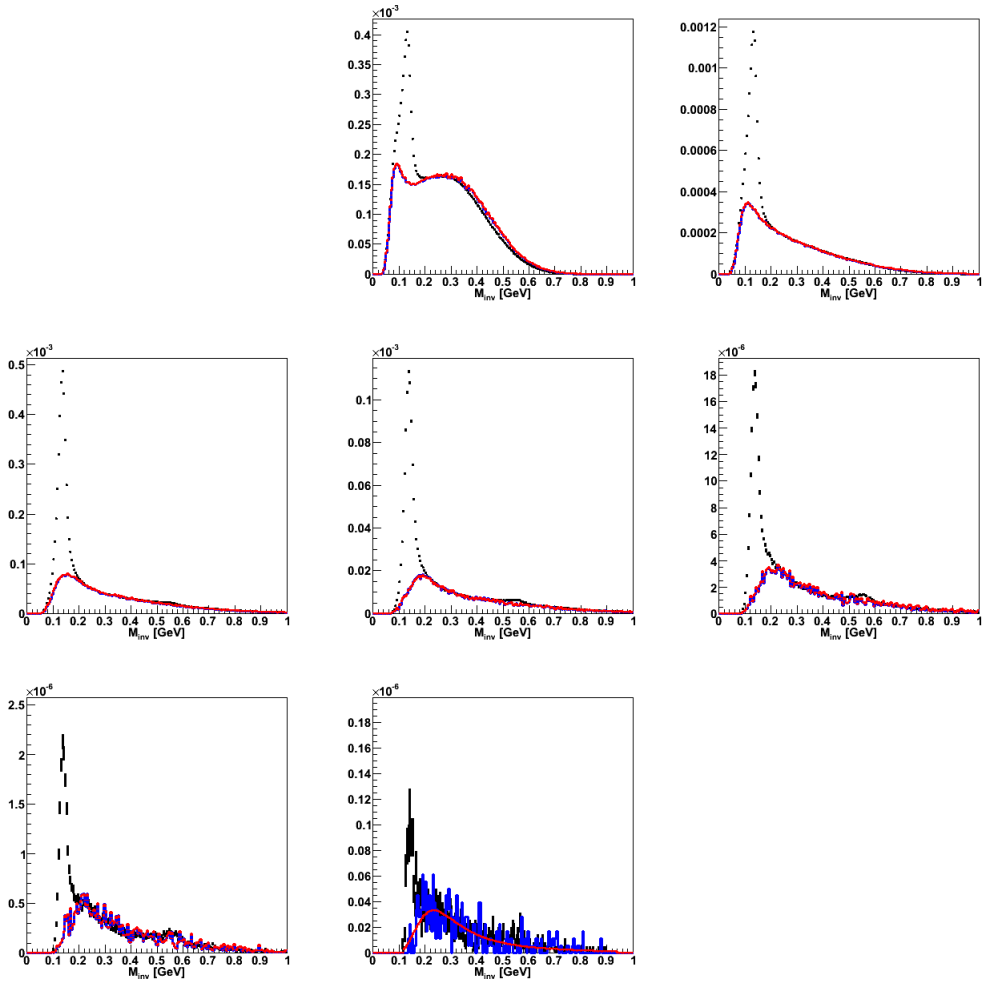

Figure B.38: **pp, Rapidity = 3.0-3.8:** Invariant mass foreground (black) and final background (red) distributions.

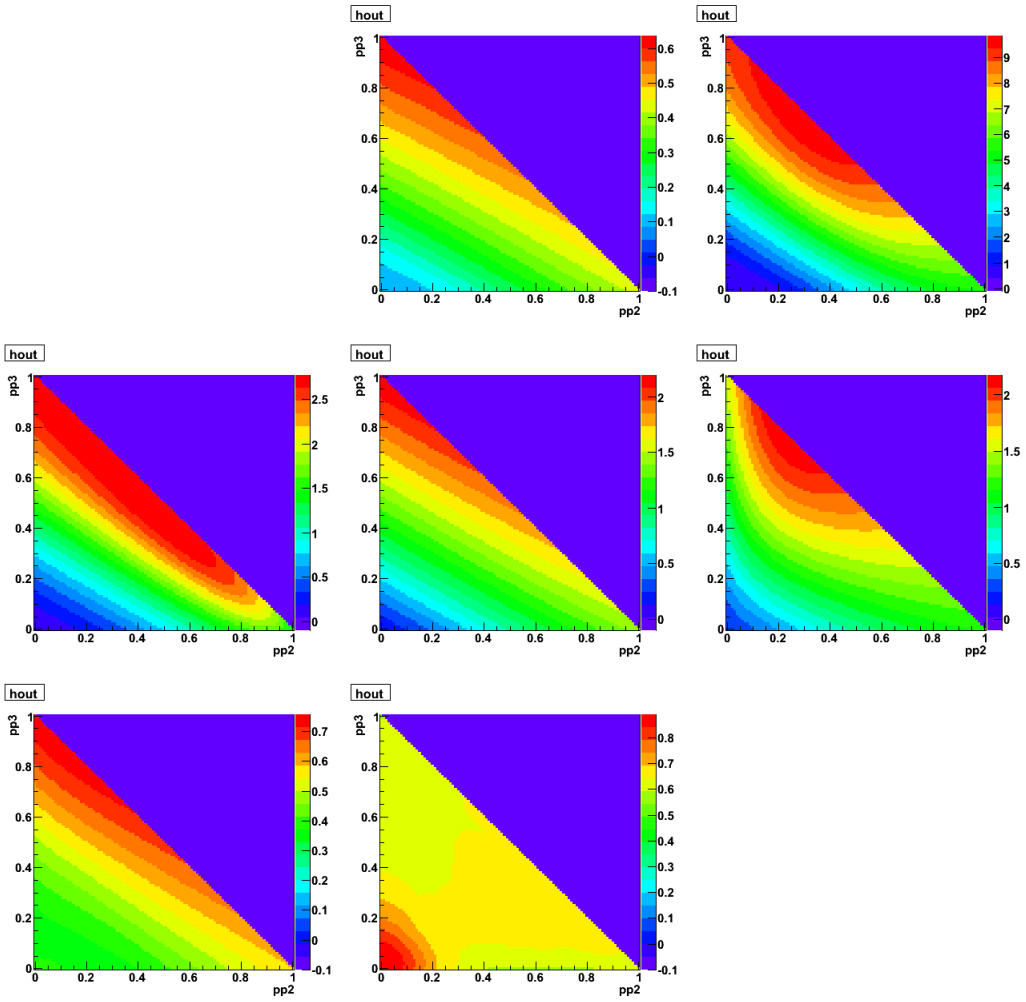

Figure B.39: **pp, Rapidity = 3.0-3.8:** The minimization contours for the difference between invariant mass shapes of the data and linear combinations 1pp, 2pp, and 3pp Pythia shapes. The background is determined by using the linear combination of the Pythia background shapes that minimizes this quantity.

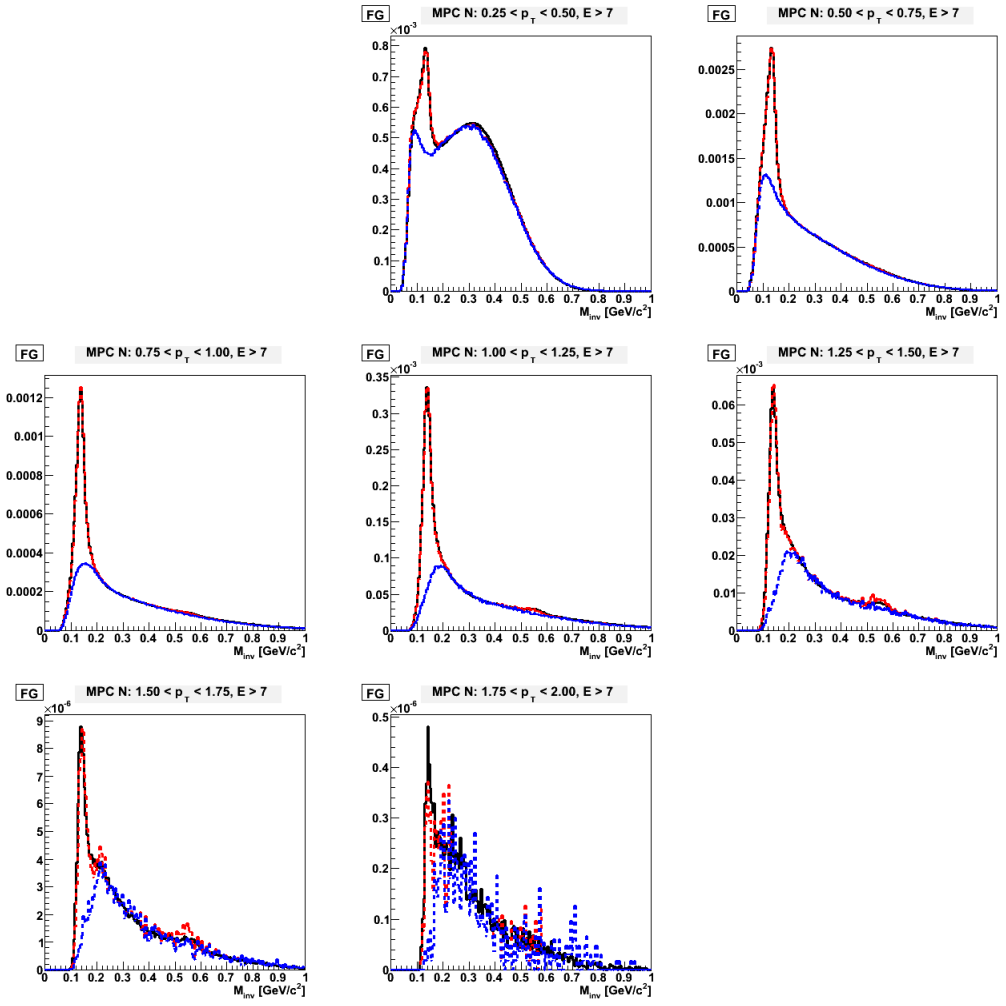

Figure B.40: **dAu 0-20, Rapidity = 3.0-3.8:** This plot illustrates how the background was formed. The invariant mass distributions for data (black), linear combinations of 1pp, 2pp, and 3pp shapes that match simulation to the data (red), and the background for this linear combination are all plotted together.

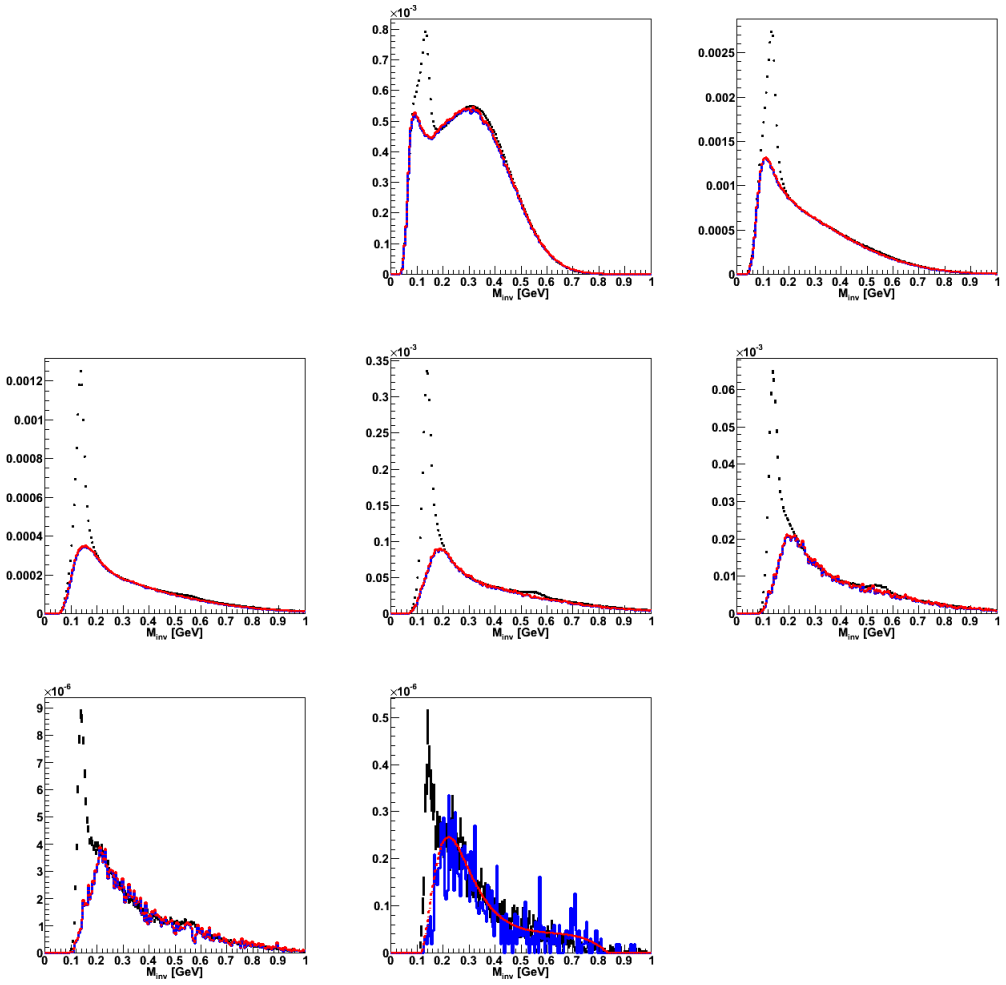

Figure B.41: **dAu 0-20, Rapidity = 3.0-3.8:** Invariant mass foreground (black) and final background (red) distributions.

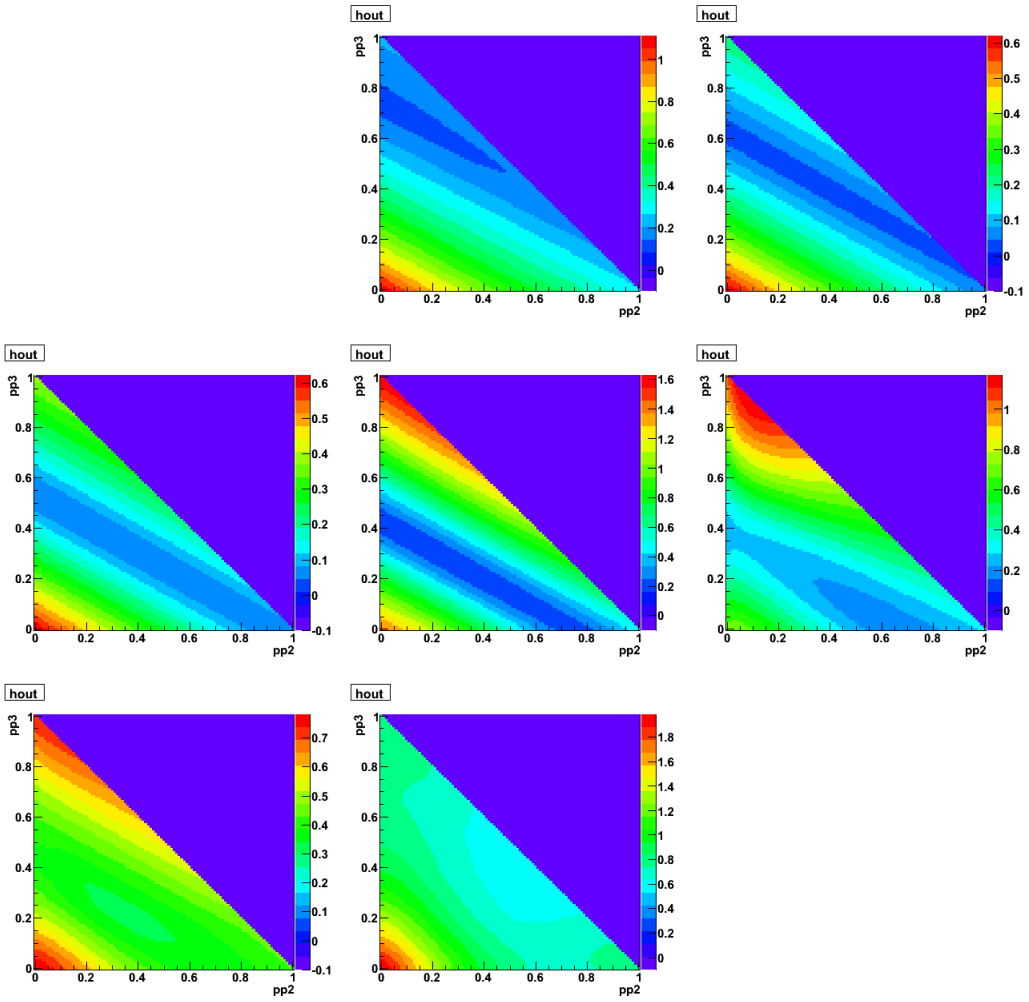

Figure B.42: **dAu 0-20, Rapidity = 3.0-3.8:** The minimization contours for the difference between invariant mass shapes of the data and linear combinations 1pp, 2pp, and 3pp Pythia shapes. The background is determined by using the linear combination of the Pythia background shapes that minimizes this quantity.

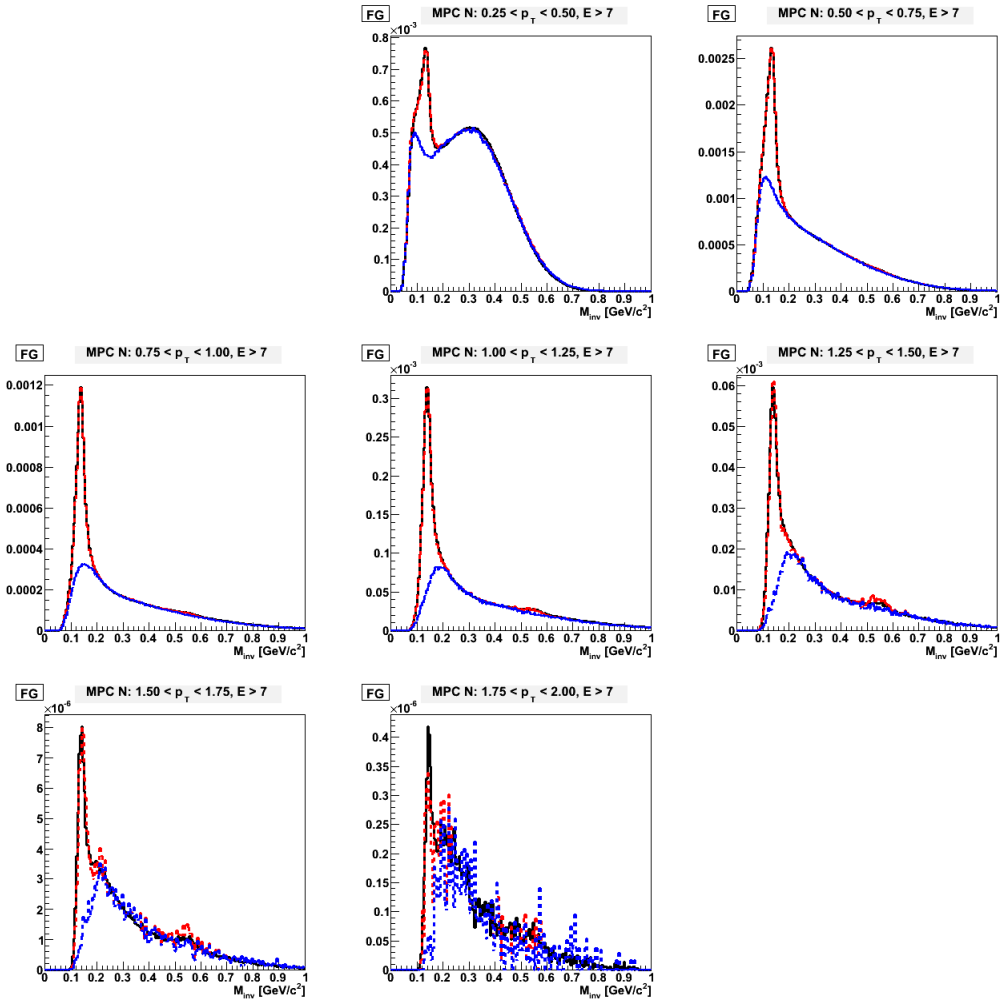

Figure B.43: **dAu 20-40, Rapidity = 3.0-3.8:** This plot illustrates how the background was formed. The invariant mass distributions for data (black), linear combinations of 1pp, 2pp, and 3pp shapes that match simulation to the data (red), and the background for this linear combination are all plotted together.

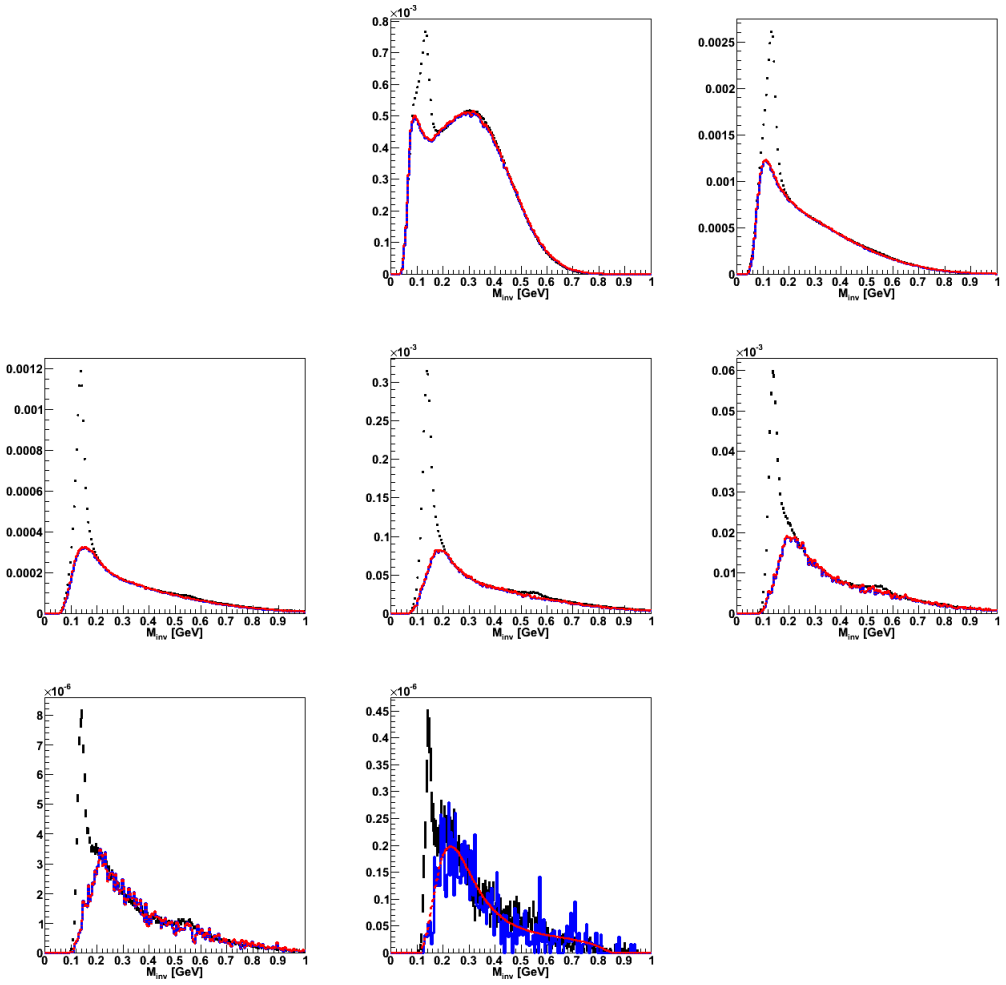

Figure B.44: **dAu 20-40, Rapidity = 3.0-3.8:** Invariant mass foreground (black) and final background (red) distributions.

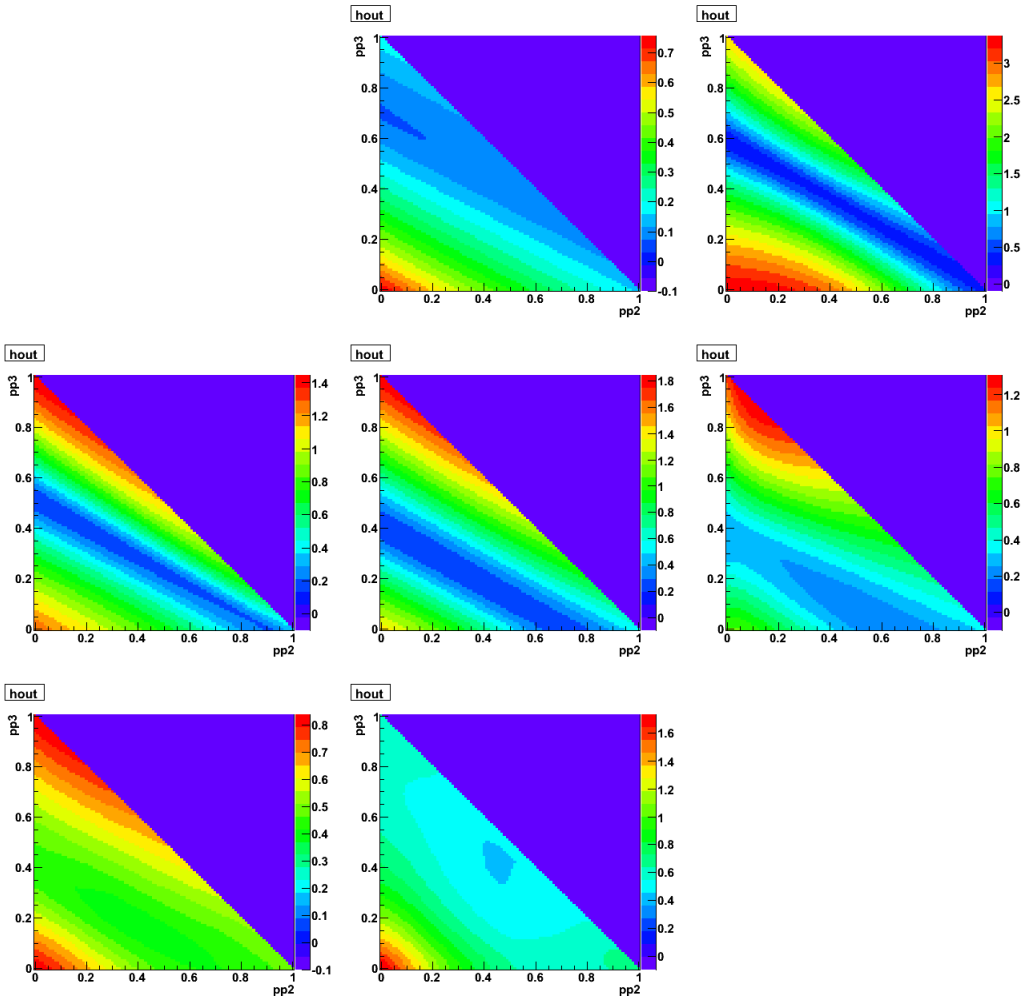

Figure B.45: **dAu 20-40, Rapidity = 3.0-3.8:** The minimization contours for the difference between invariant mass shapes of the data and linear combinations 1pp, 2pp, and 3pp Pythia shapes. The background is determined by using the linear combination of the Pythia background shapes that minimizes this quantity.

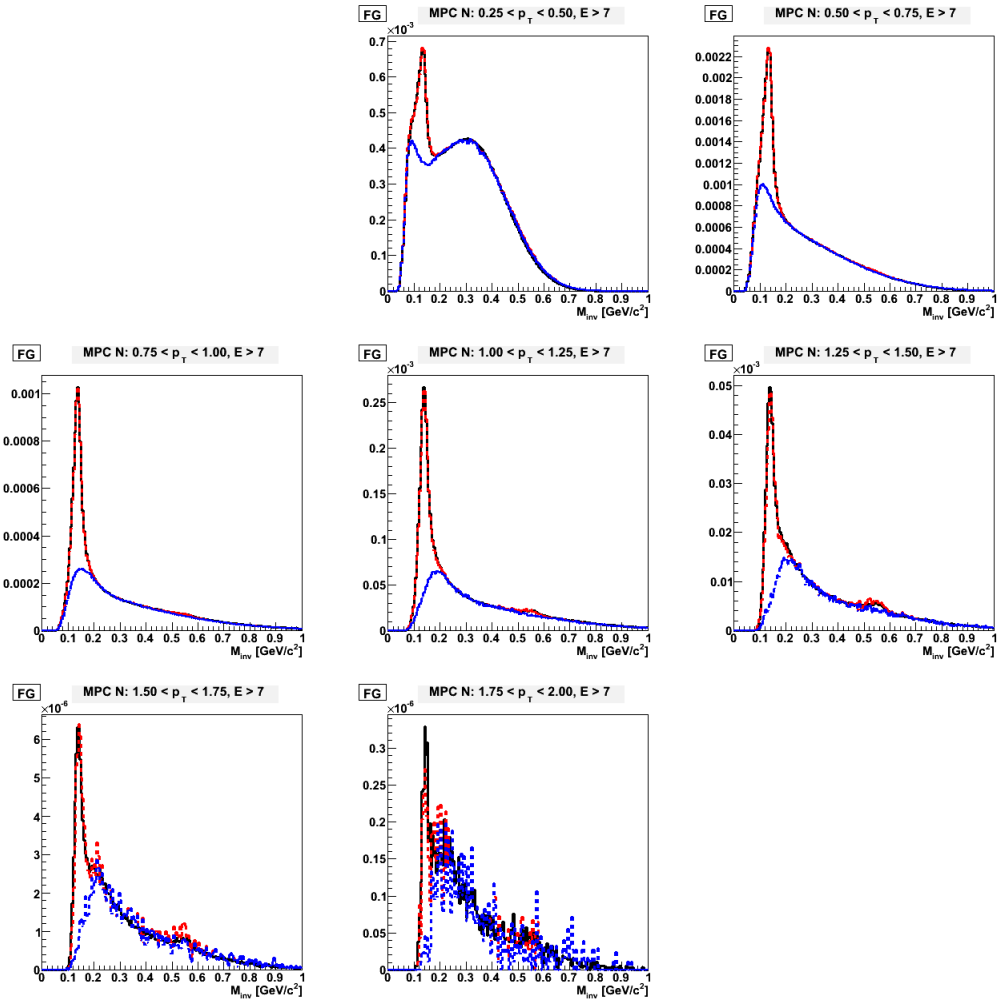

Figure B.46: **dAu 40-60, Rapidity = 3.0-3.8:** This plot illustrates how the background was formed. The invariant mass distributions for data (black), linear combinations of 1pp, 2pp, and 3pp shapes that match simulation to the data (red), and the background for this linear combination are all plotted together.

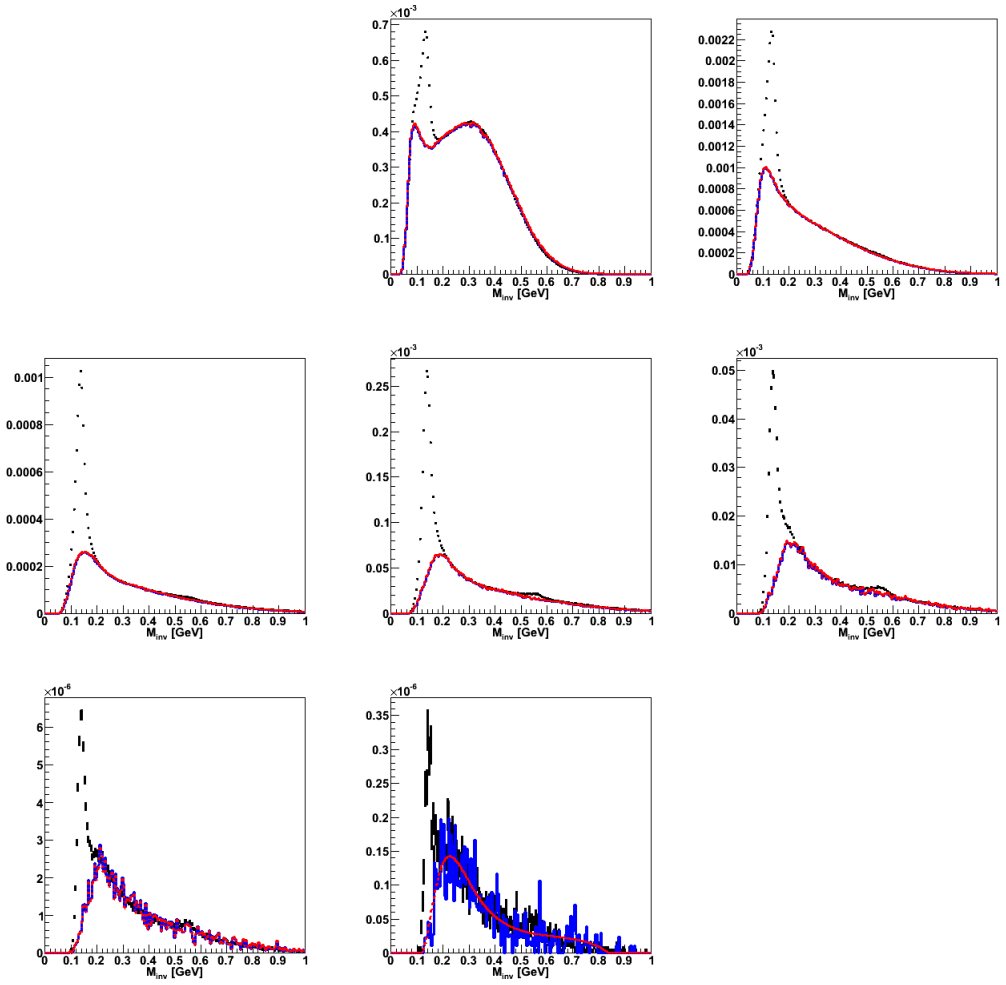

Figure B.47: **dAu 40-60, Rapidity = 3.0-3.8:** Invariant mass foreground (black) and final background (red) distributions.

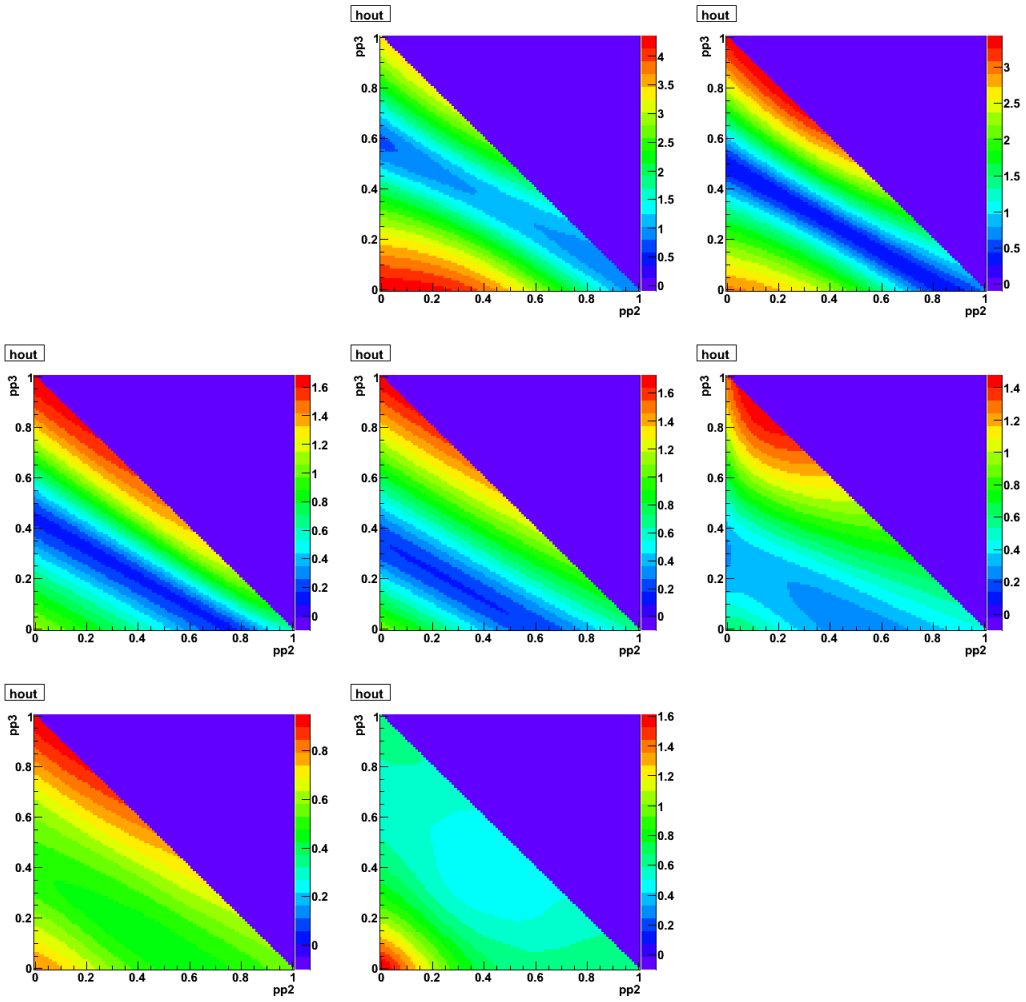

Figure B.48: **dAu 40-60, Rapidity = 3.0-3.8:** The minimization contours for the difference between invariant mass shapes of the data and linear combinations 1pp, 2pp, and 3pp Pythia shapes. The background is determined by using the linear combination of the Pythia background shapes that minimizes this quantity.

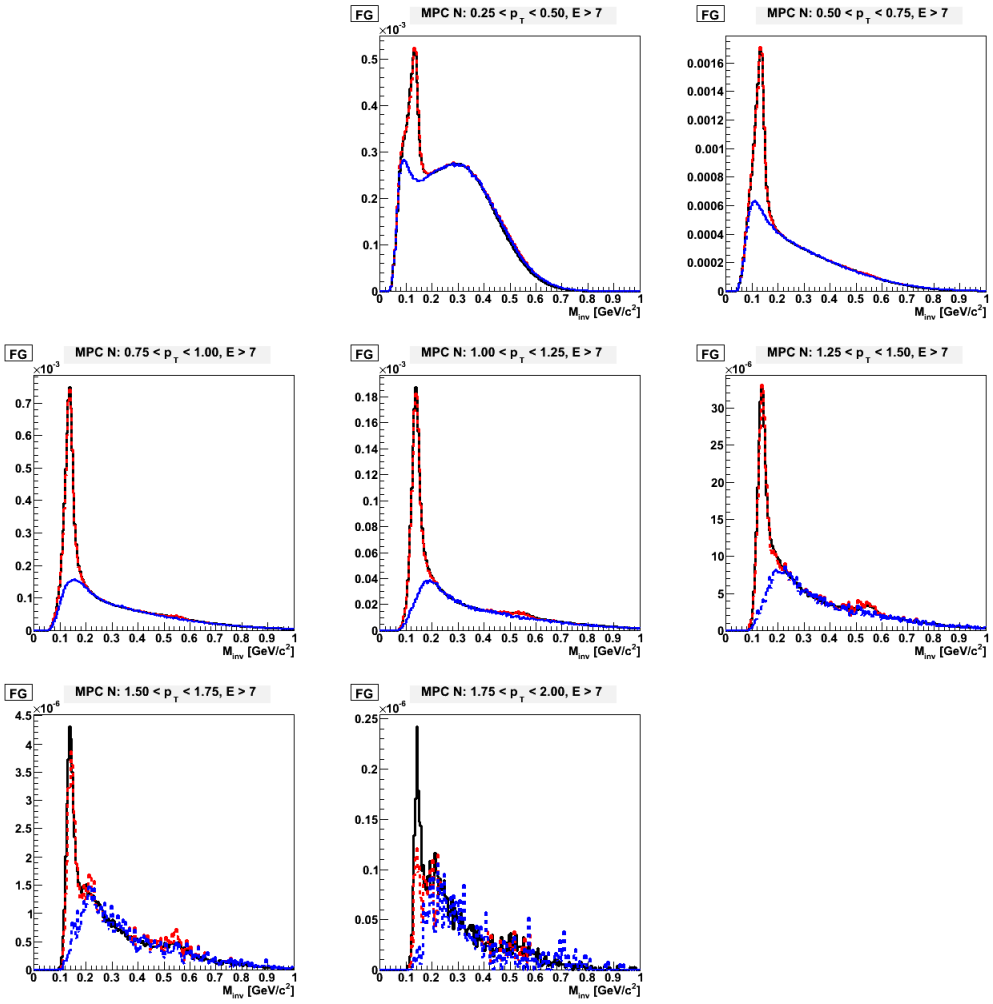

Figure B.49: **dAu 60-88, Rapidity = 3.0-3.8:** This plot illustrates how the background was formed. The invariant mass distributions for data (black), linear combinations of 1pp, 2pp, and 3pp shapes that match simulation to the data (red), and the background for this linear combination are all plotted together.

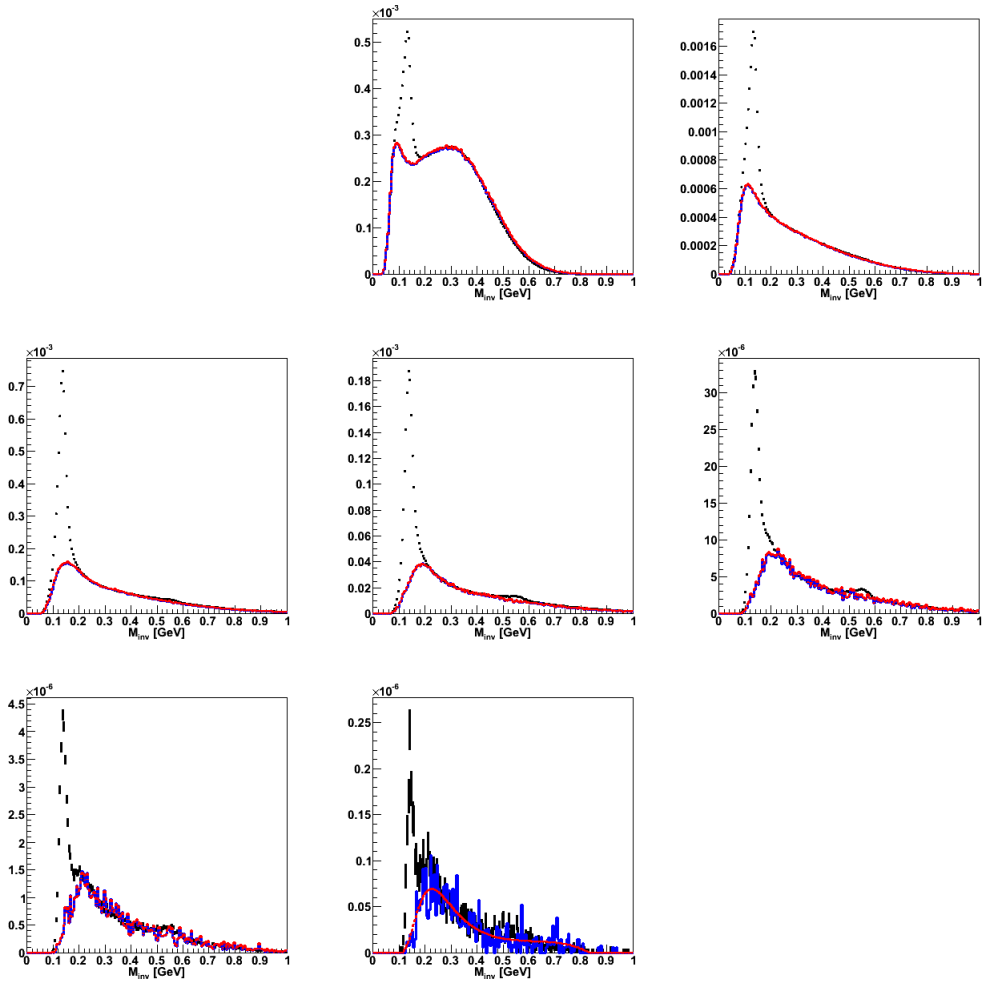

Figure B.50: **dAu 60-88, Rapidity = 3.0-3.8:** Invariant mass foreground (black) and final background (red) distributions.

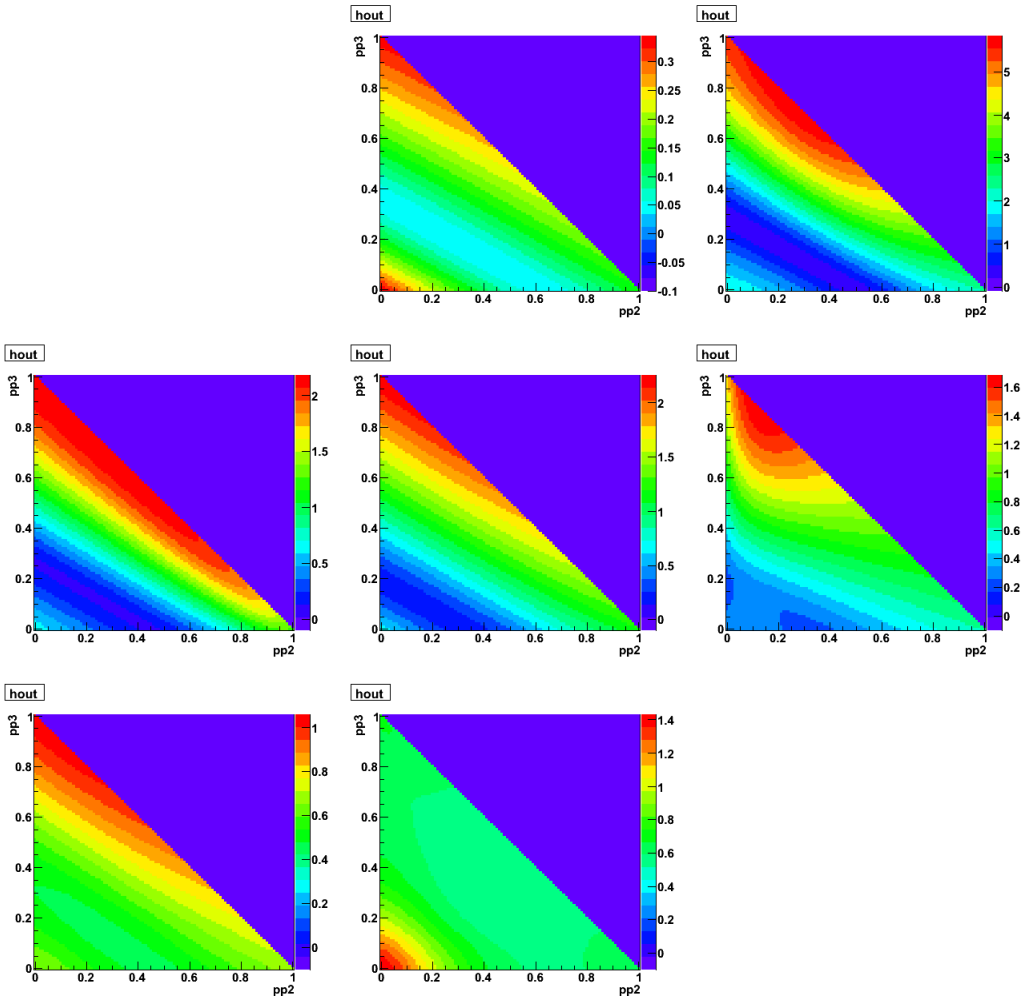

Figure B.51: **dAu 60-88, Rapidity = 3.0-3.8:** The minimization contours for the difference between invariant mass shapes of the data and linear combinations 1pp, 2pp, and 3pp Pythia shapes. The background is determined by using the linear combination of the Pythia background shapes that minimizes this quantity.

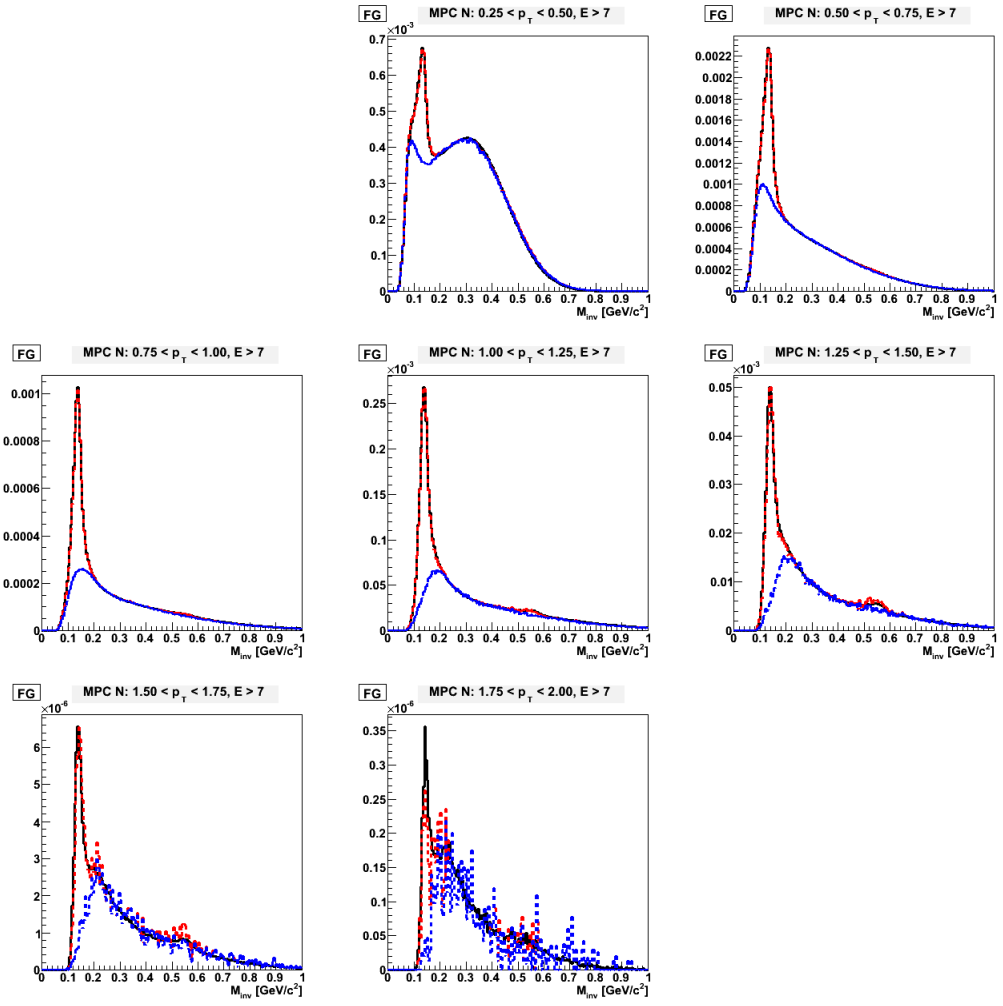

Figure B.52: **dAu MinBias, Rapidity = 3.0-3.8:** This plot illustrates how the background was formed. The invariant mass distributions for data (black), linear combinations of 1pp, 2pp, and 3pp shapes that match simulation to the data (red), and the background for this linear combination are all plotted together.

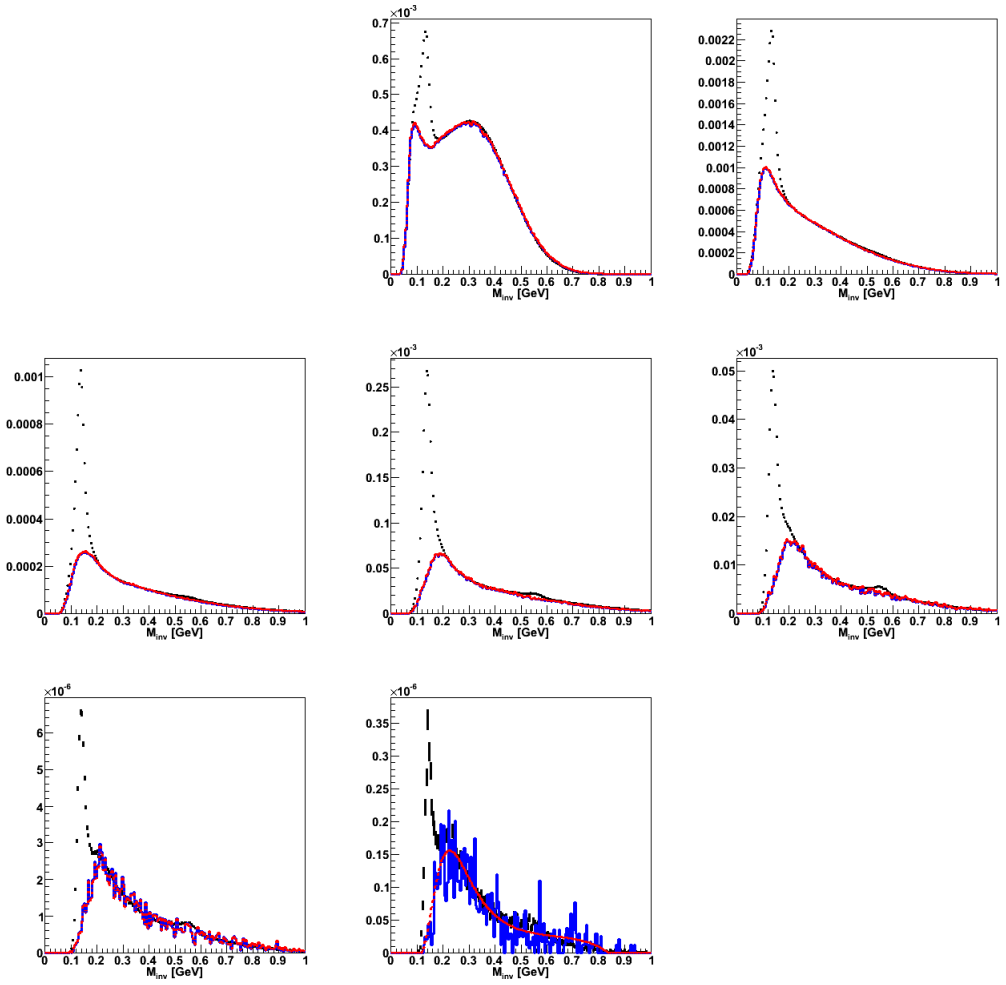

Figure B.53: **dAu MinBias, Rapidity = 3.0-3.8:** Invariant mass foreground (black) and final background (red) distributions.

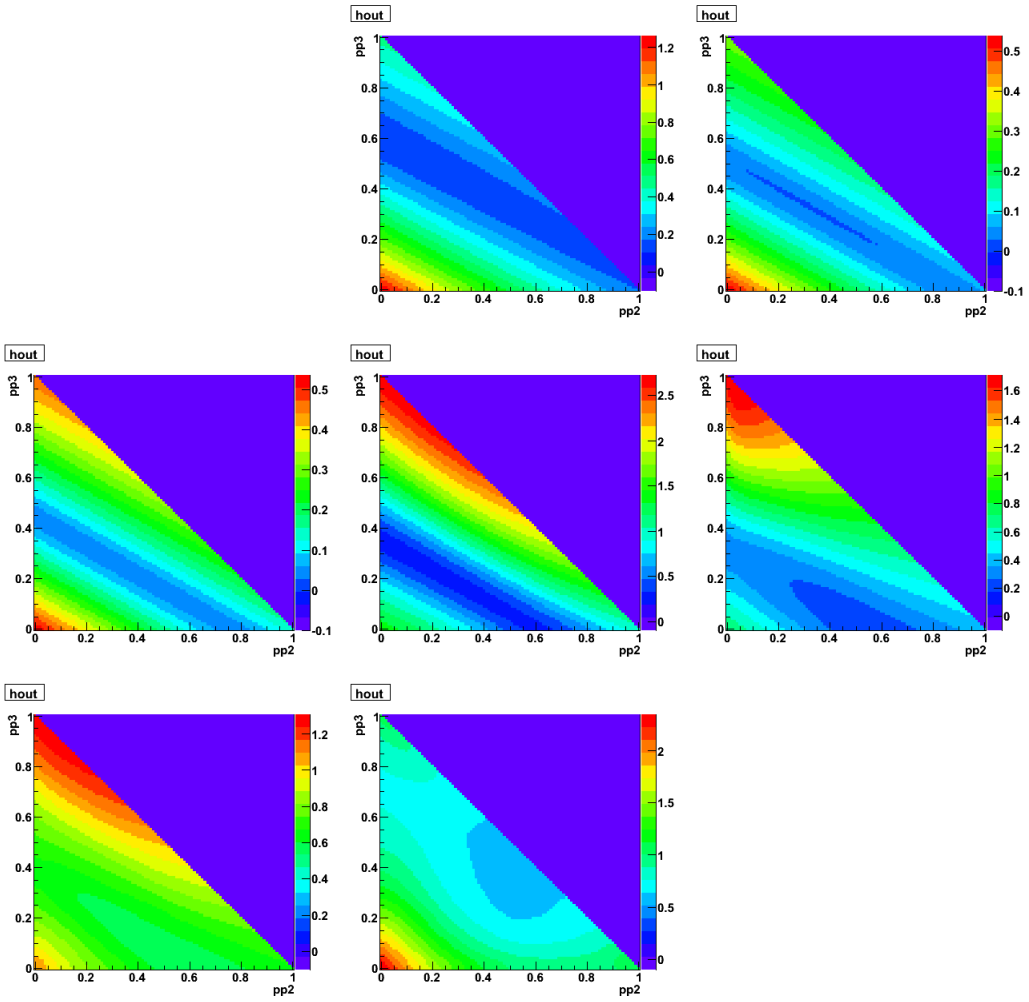

Figure B.54: **dAu MinBias, Rapidity = 3.0-3.8:** The minimization contours for the difference between invariant mass shapes of the data and linear combinations 1pp, 2pp, and 3pp Pythia shapes. The background is determined by using the linear combination of the Pythia background shapes that minimizes this quantity.

Appendix C

Mid-Forward $h^{\pm}/\pi^0$ Azimuthal Correlations Tables and Figures

C.1 Tabulated Results

In all subsequent tables, σ represents a statistical error, while s represents a systematic error (type B), and the global systematic error is s_{global}.

C.1.1 Raw and Conditional Errors, Relative Stat. Errors

In this section, the terms that are present in the tables are as follows:

p_T	Transverse momentum of the bin center,
Y	Number of correlated particle pairs,
CY	Conditional yield, or the area of the correlated di-hadron signal per trigger particle detected,
ϵ	π^0 reconstruction efficiency,
$\frac{S}{S+B}MPC$	Fraction of counts in π^0 mass window, $0.08 < m_{inv} < 0.18$ GeV/c^2 that are actually signal π^0's (as opposed to background counts),
C_{leak}	Accounts for leakage of the π^0 yield outside the defined window of $0.08 < m_{inv} < 0.18$ GeV/c^2,
C_{bcorr}	Up-down correction, or $C_{up-down}$,
$\Delta p_T \Delta\eta$	Corrects for p_T and η bin widths (e.g. $\Delta p_T \Delta\eta = 0.25 \times 0.8 = 0.2$).

Table C.1: Conditional and Raw Yields, N_{trig}, efficiencies, corrections, and **Relative** stat errors for $3.0 < \eta < 3.8$, central $h^{\pm} p_T = 0.5 - 1.0$ GeV/c.

d+Au 0-20%, $N_{trig} = 2.561e+08$										
p_T	CY	σ_{CY}	Y	σ_Y	ϵ	σ_ϵ	$\frac{S}{S+B}_{MPC}$	C_{leak}	C_{bcorr}	$\Delta p_T \Delta\eta$
0.625	2.18e-02	0.048	1.71e+05	0.046	0.052	0.016	0.34	1.04	0.96	0.20
0.875	9.58e-03	0.066	6.98e+04	0.065	0.076	0.014	0.54	1.02	0.96	0.20
1.250	3.15e-03	0.080	2.60e+04	0.078	0.051	0.015	0.70	1.04	0.88	0.40
d+Au 20-40%, $N_{trig} = 1.806e+08$										
p_T	CY	σ_{CY}	Y	σ_Y	ϵ	σ_ϵ	$\frac{S}{S+B}_{MPC}$	C_{leak}	C_{bcorr}	$\Delta p_T \Delta\eta$
0.625	3.09e-02	0.051	1.73e+05	0.048	0.053	0.015	0.34	1.03	0.96	0.20
0.875	1.37e-02	0.067	7.11e+04	0.066	0.077	0.014	0.55	1.02	0.96	0.20
1.250	4.05e-03	0.085	2.30e+04	0.084	0.051	0.015	0.70	1.05	0.88	0.40
d+Au 40-60%, $N_{trig} = 1.236e+08$										
p_T	CY	σ_{CY}	Y	σ_Y	ϵ	σ_ϵ	$\frac{S}{S+B}_{MPC}$	C_{leak}	C_{bcorr}	$\Delta p_T \Delta\eta$
0.625	3.75e-02	0.063	1.44e+05	0.061	0.057	0.015	0.37	1.03	0.96	0.20
0.875	2.09e-02	0.107	7.11e+04	0.106	0.077	0.014	0.57	1.02	0.97	0.20
1.250	5.20e-03	0.111	1.97e+04	0.110	0.050	0.015	0.71	1.04	0.87	0.40
d+Au 60-88%, $N_{trig} = 8.957e+07$										
p_T	CY	σ_{CY}	Y	σ_Y	ϵ	σ_ϵ	$\frac{S}{S+B}_{MPC}$	C_{leak}	C_{bcorr}	$\Delta p_T \Delta\eta$
0.625	5.38e-02	0.068	1.36e+05	0.067	0.059	0.012	0.43	1.03	0.96	0.20
0.875	2.10e-02	0.072	4.92e+04	0.071	0.080	0.012	0.62	1.02	0.96	0.20
1.250	7.09e-03	0.251	1.96e+04	0.251	0.052	0.012	0.75	1.04	0.86	0.40
p+p, $N_{trig} = 4.309e+07$										
p_T	CY	σ_{CY}	Y	σ_Y	ϵ	σ_ϵ	$\frac{S}{S+B}_{MPC}$	C_{leak}	C_{bcorr}	$\Delta p_T \Delta\eta$
0.625	6.15e-02	0.084	6.26e+04	0.083	0.060	0.010	0.52	1.03	0.95	0.20
0.875	2.50e-02	0.120	2.60e+04	0.120	0.082	0.010	0.70	1.02	0.95	0.20
1.250	5.66e-03	0.105	7.28e+03	0.104	0.052	0.010	0.80	1.04	0.83	0.40

Table C.2: Conditional and Raw Yields, N_{trig}, efficiencies, corrections, and **Relative** stat errors for $3.0 < \eta < 3.8$, central $h^{\pm} p_T = 1.0 - 2.0$ GeV/c.

d+Au 0-20%, $N_{trig} = 9.978e+07$										
p_T	CY	σ_{CY}	Y	σ_Y	ϵ	σ_ϵ	$\frac{S}{S+B}_{MPC}$	C_{leak}	C_{bcorr}	$\Delta p_T \Delta\eta$
0.625	3.02e-02	0.047	9.22e+04	0.044	0.052	0.016	0.34	1.04	0.96	0.20
0.875	1.31e-02	0.060	3.73e+04	0.058	0.076	0.014	0.54	1.02	0.96	0.20
1.250	4.50e-03	0.086	1.45e+04	0.085	0.051	0.015	0.70	1.04	0.88	0.40
d+Au 20-40%, $N_{trig} = 6.748e+07$										
p_T	CY	σ_{CY}	Y	σ_Y	ϵ	σ_ϵ	$\frac{S}{S+B}_{MPC}$	C_{leak}	C_{bcorr}	$\Delta p_T \Delta\eta$
0.625	4.18e-02	0.056	8.78e+04	0.053	0.053	0.015	0.34	1.03	0.96	0.20
0.875	1.89e-02	0.067	3.65e+04	0.065	0.077	0.014	0.55	1.02	0.96	0.20
1.250	5.86e-03	0.092	1.25e+04	0.091	0.051	0.015	0.70	1.05	0.88	0.40
d+Au 40-60%, $N_{trig} = 4.351e+07$										
p_T	CY	σ_{CY}	Y	σ_Y	ϵ	σ_ϵ	$\frac{S}{S+B}_{MPC}$	C_{leak}	C_{bcorr}	$\Delta p_T \Delta\eta$
0.625	6.27e-02	0.074	8.50e+04	0.073	0.057	0.015	0.37	1.03	0.96	0.20
0.875	2.28e-02	0.067	2.72e+04	0.065	0.077	0.014	0.57	1.02	0.97	0.20
1.250	9.38e-03	0.168	1.25e+04	0.168	0.050	0.015	0.71	1.04	0.87	0.40
d+Au 60-88%, $N_{trig} = 2.803e+07$										
p_T	CY	σ_{CY}	Y	σ_Y	ϵ	σ_ϵ	$\frac{S}{S+B}_{MPC}$	C_{leak}	C_{bcorr}	$\Delta p_T \Delta\eta$
0.625	6.72e-02	0.061	5.30e+04	0.059	0.059	0.012	0.43	1.03	0.96	0.20
0.875	3.24e-02	0.073	2.38e+04	0.072	0.080	0.012	0.62	1.02	0.96	0.20
1.250	9.97e-03	0.115	8.60e+03	0.115	0.052	0.012	0.75	1.04	0.86	0.40
p+p, $N_{trig} = 1.163e+07$										
p_T	CY	σ_{CY}	Y	σ_Y	ϵ	σ_ϵ	$\frac{S}{S+B}_{MPC}$	C_{leak}	C_{bcorr}	$\Delta p_T \Delta\eta$
0.625	7.76e-02	0.075	2.13e+04	0.074	0.060	0.010	0.52	1.03	0.95	0.20
0.875	3.01e-02	0.089	8.45e+03	0.088	0.082	0.010	0.70	1.02	0.95	0.20
1.250	8.97e-03	0.253	3.11e+03	0.253	0.052	0.010	0.80	1.04	0.83	0.40

Table C.3: Conditional and Raw Yields, N_{trig}, efficiencies, corrections, and **Relative** stat errors for $3.0 < \eta < 3.8$, central $h^{\pm} p_T = 2.0 - 3.0$ GeV/c.

d+Au 0-20%, $N_{trig} = 1.165e+07$										
p_T	CY	σ_{CY}	Y	σ_Y	ϵ	σ_ϵ	$\frac{S}{S+B}_{MPC}$	C_{leak}	C_{bcorr}	$\Delta p_T \Delta\eta$
0.625	4.31e-02	0.099	1.54e+04	0.097	0.052	0.016	0.34	1.04	0.96	0.20
0.875	1.83e-02	0.128	6.06e+03	0.127	0.076	0.014	0.54	1.02	0.96	0.20
1.250	4.53e-03	0.202	1.70e+03	0.202	0.051	0.015	0.70	1.04	0.88	0.40
d+Au 20-40%, $N_{trig} = 7.668e+06$										
p_T	CY	σ_{CY}	Y	σ_Y	ϵ	σ_ϵ	$\frac{S}{S+B}_{MPC}$	C_{leak}	C_{bcorr}	$\Delta p_T \Delta\eta$
0.625	5.61e-02	0.130	1.34e+04	0.129	0.053	0.015	0.34	1.03	0.96	0.20
0.875	2.35e-02	0.151	5.18e+03	0.150	0.077	0.014	0.55	1.02	0.96	0.20
1.250	7.02e-03	0.152	1.69e+03	0.151	0.051	0.015	0.70	1.05	0.88	0.40
d+Au 40-60%, $N_{trig} = 4.704e+06$										
p_T	CY	σ_{CY}	Y	σ_Y	ϵ	σ_ϵ	$\frac{S}{S+B}_{MPC}$	C_{leak}	C_{bcorr}	$\Delta p_T \Delta\eta$
0.625	7.01e-02	0.122	1.03e+04	0.121	0.057	0.015	0.37	1.03	0.96	0.20
0.875	3.16e-02	0.114	4.09e+03	0.113	0.077	0.014	0.57	1.02	0.97	0.20
1.250	7.90e-03	0.154	1.14e+03	0.153	0.050	0.015	0.71	1.04	0.87	0.40
d+Au 60-88%, $N_{trig} = 2.771e+06$										
p_T	CY	σ_{CY}	Y	σ_Y	ϵ	σ_ϵ	$\frac{S}{S+B}_{MPC}$	C_{leak}	C_{bcorr}	$\Delta p_T \Delta\eta$
0.625	8.87e-02	0.133	6.92e+03	0.133	0.059	0.012	0.43	1.03	0.96	0.20
0.875	4.75e-02	0.254	3.45e+03	0.254	0.080	0.012	0.62	1.02	0.96	0.20
1.250	1.41e-02	0.260	1.20e+03	0.260	0.052	0.012	0.75	1.04	0.86	0.40
p+p, $N_{trig} = 1.016e+06$										
p_T	CY	σ_{CY}	Y	σ_Y	ϵ	σ_ϵ	$\frac{S}{S+B}_{MPC}$	C_{leak}	C_{bcorr}	$\Delta p_T \Delta\eta$
0.625	1.21e-01	0.281	2.91e+03	0.281	0.060	0.010	0.52	1.03	0.95	0.20
0.875	4.71e-02	0.257	1.15e+03	0.257	0.082	0.010	0.70	1.02	0.95	0.20
1.250	1.09e-02	0.272	3.29e+02	0.272	0.052	0.010	0.80	1.04	0.83	0.40

C.1.2 Conditional Yields, Widths and Relative Errors

In this section, the terms that are present in the tables are as follows:

p_T	Transverse momentum of the bin center,
CY	Conditional yield, or the area of the correlated di-hadron signal per trigger particle detected,
$\frac{S}{S+B}MPC$	Fraction of counts in π^0 mass window, $0.08 < m_{inv} < 0.18$ GeV/c^2 that are actually signal π^0's (as opposed to background counts),
$\frac{S}{S+B}trig$	1 for charged hadrons,
s_{eff}	Systematic error from yield extraction, input spectrum shape, energy scale, and GEANT,
s_{sb}	Systematic error from contributions of the background under the π^0 peak to the CF,
s_{tot}	Total systematic error on the CY,
W	Gaussian width of the awayside peak,
s_w	Systematic error on the Gaussian width of the awayside peak.

Table C.4: Conditional Yields, widths, **Relative** sys, stat errors for MPC π^0 $3.0 < \eta < 3.8$, central $h^{\pm}p_T = 0.5 - 1.0$ GeV/c.

d+Au 0-20%										
p_T	CY	σ_{CY}	$\frac{S}{S+B}_{MPC}$	$\frac{S}{S+B}_{trig}$	s_{eff}	s_{sb}	s_{tot}	W	σ_w	s_w
0.625	2.18e-02	0.048	0.338	1.000	0.104	0.256	0.276	1.044	0.034	0.160
0.875	9.58e-03	0.066	0.545	1.000	0.113	0.173	0.207	1.024	0.049	0.108
1.250	3.15e-03	0.080	0.697	1.000	0.132	0.113	0.174	0.965	0.061	0.071
d+Au 20-40%										
p_T	CY	σ_{CY}	$\frac{S}{S+B}_{MPC}$	$\frac{S}{S+B}_{trig}$	s_{eff}	s_{sb}	s_{tot}	W	σ_w	s_w
0.625	3.09e-02	0.051	0.345	1.000	0.102	0.253	0.273	1.121	0.034	0.158
0.875	1.37e-02	0.067	0.548	1.000	0.113	0.171	0.205	1.107	0.046	0.107
1.250	4.05e-03	0.085	0.700	1.000	0.132	0.112	0.173	1.024	0.062	0.070
d+Au 40-60%										
p_T	CY	σ_{CY}	$\frac{S}{S+B}_{MPC}$	$\frac{S}{S+B}_{trig}$	s_{eff}	s_{sb}	s_{tot}	W	σ_w	s_w
0.625	3.75e-02	0.063	0.369	1.000	0.100	0.243	0.263	1.195	0.039	0.152
0.875	2.09e-02	0.107	0.567	1.000	0.112	0.164	0.198	1.269	0.062	0.102
1.250	5.20e-03	0.111	0.714	1.000	0.133	0.107	0.171	1.110	0.077	0.067
d+Au 60-88%										
p_T	CY	σ_{CY}	$\frac{S}{S+B}_{MPC}$	$\frac{S}{S+B}_{trig}$	s_{eff}	s_{sb}	s_{tot}	W	σ_w	s_w
0.625	5.38e-02	0.068	0.427	1.000	0.101	0.220	0.242	1.264	0.040	0.137
0.875	2.10e-02	0.072	0.622	1.000	0.115	0.142	0.183	1.155	0.048	0.089
1.250	7.09e-03	0.251	0.749	1.000	0.135	0.094	0.164	1.203	0.152	0.058
p+p										
p_T	CY	σ_{CY}	$\frac{S}{S+B}_{MPC}$	$\frac{S}{S+B}_{trig}$	s_{eff}	s_{sb}	s_{tot}	W	σ_w	s_w
0.625	6.15e-02	0.084	0.519	1.000	0.107	0.186	0.214	1.281	0.048	0.116
0.875	2.50e-02	0.120	0.698	1.000	0.122	0.115	0.167	1.277	0.069	0.072
1.250	5.66e-03	0.105	0.803	1.000	0.142	0.075	0.160	1.111	0.073	0.047

Table C.5: Conditional Yields, widths, **Relative** sys, stat errors for MPC π^0 $3.0 < \eta < 3.8$, central $h^{\pm} p_T = 1.0 - 2.0$ GeV/c.

d+Au 0-20%										
p_T	CY	σ_{CY}	$\frac{S}{S+B}_{MPC}$	$\frac{S}{S+B}_{trig}$	s_{eff}	s_{sb}	s_{tot}	W	σ_w	s_w
0.625	3.02e-02	0.047	0.338	1.000	0.104	0.256	0.276	0.990	0.034	0.160
0.875	1.31e-02	0.060	0.545	1.000	0.113	0.173	0.207	0.951	0.046	0.108
1.250	4.50e-03	0.086	0.697	1.000	0.132	0.113	0.174	0.947	0.067	0.071
d+Au 20-40%										
p_T	CY	σ_{CY}	$\frac{S}{S+B}_{MPC}$	$\frac{S}{S+B}_{trig}$	s_{eff}	s_{sb}	s_{tot}	W	σ_w	s_w
0.625	4.18e-02	0.056	0.345	1.000	0.102	0.253	0.273	1.094	0.038	0.158
0.875	1.89e-02	0.067	0.548	1.000	0.113	0.171	0.205	1.044	0.048	0.107
1.250	5.86e-03	0.092	0.700	1.000	0.132	0.112	0.173	1.010	0.069	0.070
d+Au 40-60%										
p_T	CY	σ_{CY}	$\frac{S}{S+B}_{MPC}$	$\frac{S}{S+B}_{trig}$	s_{eff}	s_{sb}	s_{tot}	W	σ_w	s_w
0.625	6.27e-02	0.074	0.369	1.000	0.100	0.243	0.263	1.233	0.045	0.152
0.875	2.28e-02	0.067	0.567	1.000	0.112	0.164	0.198	1.037	0.049	0.102
1.250	9.38e-03	0.168	0.714	1.000	0.133	0.107	0.171	1.227	0.100	0.067
d+Au 60-88%										
p_T	CY	σ_{CY}	$\frac{S}{S+B}_{MPC}$	$\frac{S}{S+B}_{trig}$	s_{eff}	s_{sb}	s_{tot}	W	σ_w	s_w
0.625	6.72e-02	0.061	0.427	1.000	0.101	0.220	0.242	1.152	0.040	0.137
0.875	3.24e-02	0.073	0.622	1.000	0.115	0.142	0.183	1.130	0.050	0.089
1.250	9.97e-03	0.115	0.749	1.000	0.135	0.094	0.164	1.151	0.076	0.058
p+p										
p_T	CY	σ_{CY}	$\frac{S}{S+B}_{MPC}$	$\frac{S}{S+B}_{trig}$	s_{eff}	s_{sb}	s_{tot}	W	σ_w	s_w
0.625	7.76e-02	0.075	0.519	1.000	0.107	0.186	0.214	1.152	0.050	0.116
0.875	3.01e-02	0.089	0.698	1.000	0.122	0.115	0.167	1.097	0.063	0.072
1.250	8.97e-03	0.253	0.803	1.000	0.142	0.075	0.160	1.151	0.155	0.047

Table C.6: Conditional Yields, widths, **Relative** sys, stat errors for MPC π^0 $3.0 < \eta < 3.8$, central $h^{\pm} p_T = 2.0 - 3.0$ GeV/c.

d+Au 0-20%										
p_T	CY	σ_{CY}	$\frac{S}{S+B}_{MPC}$	$\frac{S}{S+B}_{trig}$	s_{eff}	s_{sb}	s_{tot}	W	σ_w	s_w
0.625	4.31e-02	0.099	0.338	1.000	0.104	0.256	0.276	1.002	0.075	0.160
0.875	1.83e-02	0.128	0.545	1.000	0.113	0.173	0.207	0.942	0.102	0.108
1.250	4.53e-03	0.202	0.697	1.000	0.132	0.113	0.174	0.875	0.162	0.071
d+Au 20-40%										
p_T	CY	σ_{CY}	$\frac{S}{S+B}_{MPC}$	$\frac{S}{S+B}_{trig}$	s_{eff}	s_{sb}	s_{tot}	W	σ_w	s_w
0.625	5.61e-02	0.130	0.345	1.000	0.102	0.253	0.273	1.116	0.089	0.158
0.875	2.35e-02	0.151	0.548	1.000	0.113	0.171	0.205	1.023	0.113	0.107
1.250	7.02e-03	0.152	0.700	1.000	0.132	0.112	0.173	0.858	0.121	0.070
d+Au 40-60%										
p_T	CY	σ_{CY}	$\frac{S}{S+B}_{MPC}$	$\frac{S}{S+B}_{trig}$	s_{eff}	s_{sb}	s_{tot}	W	σ_w	s_w
0.625	7.01e-02	0.122	0.369	1.000	0.100	0.243	0.263	1.101	0.085	0.152
0.875	3.16e-02	0.114	0.567	1.000	0.112	0.164	0.198	0.964	0.089	0.102
1.250	7.90e-03	0.154	0.714	1.000	0.133	0.107	0.171	0.805	0.128	0.067
d+Au 60-88%										
p_T	CY	σ_{CY}	$\frac{S}{S+B}_{MPC}$	$\frac{S}{S+B}_{trig}$	s_{eff}	s_{sb}	s_{tot}	W	σ_w	s_w
0.625	8.87e-02	0.133	0.427	1.000	0.101	0.220	0.242	1.121	0.091	0.137
0.875	4.75e-02	0.254	0.622	1.000	0.115	0.142	0.183	1.168	0.157	0.089
1.250	1.41e-02	0.260	0.749	1.000	0.135	0.094	0.164	1.245	0.168	0.058
p+p										
p_T	CY	σ_{CY}	$\frac{S}{S+B}_{MPC}$	$\frac{S}{S+B}_{trig}$	s_{eff}	s_{sb}	s_{tot}	W	σ_w	s_w
0.625	1.21e-01	0.281	0.519	1.000	0.107	0.186	0.214	1.242	0.154	0.116
0.875	4.71e-02	0.257	0.698	1.000	0.122	0.115	0.167	1.090	0.161	0.072
1.250	1.09e-02	0.272	0.803	1.000	0.142	0.075	0.160	1.056	0.187	0.047

C.1.3 $I_{\rm dA}$, $J_{\rm dA}$ and Relative Errors

In this section, the terms that are present in the tables are as follows:

p_T	Transverse momentum of the bin center,
$I_{\rm dA}$	Ratio of CYs between d+Au and p+p,
$J_{\rm dA}$	Correlated di-hadron nuclear modification factor formed by taking the ratio between measured di-hadron yields in d+Au per $N_{\rm coll}$ and di-hadron yields in p+p. In practice, the formula $J_{\rm dA} = I_{dA,trig} \times R_{dA,trig}$ is used,
$s_{eff,IdA}$	Systematic error from yield extraction, input spectrum shape, energy scale, and GEANT with cancellations taken into account for $I_{\rm dA}$,
$s_{SB,IdA}$	Systematic error from contributions of the background under the π^0 peak to the CF with cancellations taken into account for $I_{\rm dA}$,
$s_{tot,IdA}$	Total systematic error on $I_{\rm dA}$,
$s_{gl,IdA}$	Zero global systematic error for $I_{\rm dA}$,
$s_{tot,JdA}$	Total systematic error on $J_{\rm dA}$,
$s_{gl,JdA}$	Global systematic error for $I_{\rm dA}$.

Table C.7: I_{dA}, J_{dA} **relative** sys, stat errors for $3.0 < \eta < 3.8$, central $h^{\pm} p_T = 0.5 - 1.0$ GeV/c.

d+Au 0-20%, $R_{dA} = 0.657 \pm 0.0017$ **(stat)** ± 0.032 **(sys)**										
p_T	I_{dA}	σ_{IdA}	J_{dA}	σ_{JdA}	$s_{eff,IdA}$	$s_{SB,IdA}$	$s_{tot,IdA}$	$s_{gl,Ida}$	$s_{tot,JdA}$	$s_{gl,JdA}$
0.625	0.354	0.097	0.233	0.097	0.074	0.256	0.267	0.000	0.269	0.100
0.875	0.383	0.137	0.252	0.137	0.064	0.173	0.184	0.000	0.187	0.100
1.250	0.556	0.132	0.365	0.132	0.078	0.113	0.137	0.000	0.141	0.100
d+Au 20-40%, $R_{dA} = 0.681 \pm 0.0018$ **(stat)** ± 0.032 **(sys)**										
p_T	I_{dA}	σ_{IdA}	J_{dA}	σ_{JdA}	$s_{eff,IdA}$	$s_{SB,IdA}$	$s_{tot,IdA}$	$s_{gl,Ida}$	$s_{tot,JdA}$	$s_{gl,JdA}$
0.625	0.502	0.098	0.342	0.098	0.071	0.253	0.263	0.000	0.265	0.100
0.875	0.549	0.138	0.374	0.138	0.065	0.171	0.183	0.000	0.186	0.100
1.250	0.716	0.135	0.488	0.135	0.079	0.112	0.137	0.000	0.141	0.100
d+Au 40-60%, $R_{dA} = 0.714 \pm 0.0020$ **(stat)** ± 0.032 **(sys)**										
p_T	I_{dA}	σ_{IdA}	J_{dA}	σ_{JdA}	$s_{eff,IdA}$	$s_{SB,IdA}$	$s_{tot,IdA}$	$s_{gl,Ida}$	$s_{tot,JdA}$	$s_{gl,JdA}$
0.625	0.610	0.105	0.435	0.105	0.069	0.243	0.253	0.000	0.255	0.100
0.875	0.837	0.161	0.597	0.161	0.065	0.164	0.176	0.000	0.179	0.100
1.250	0.917	0.153	0.655	0.153	0.078	0.107	0.132	0.000	0.136	0.100
d+Au 60-88%, $R_{dA} = 0.786 \pm 0.0022$ **(stat)** ± 0.032 **(sys)**										
p_T	I_{dA}	σ_{IdA}	J_{dA}	σ_{JdA}	$s_{eff,IdA}$	$s_{SB,IdA}$	$s_{tot,IdA}$	$s_{gl,Ida}$	$s_{tot,JdA}$	$s_{gl,JdA}$
0.625	0.875	0.108	0.688	0.108	0.068	0.220	0.230	0.000	0.232	0.100
0.875	0.838	0.140	0.659	0.140	0.064	0.142	0.156	0.000	0.159	0.100
1.250	1.252	0.272	0.984	0.272	0.076	0.094	0.120	0.000	0.124	0.100

Table C.8: I_{dA}, J_{dA} **relative** sys, stat errors for $3.0 < \eta < 3.8$, central $h^{\pm} p_T = 1.0 - 2.0$ GeV/c.

d+Au 0-20%, $R_{dA} = 0.861 \pm 0.0025$ **(stat)** ± 0.032 **(sys)**										
p_T	I_{dA}	σ_{IdA}	J_{dA}	σ_{JdA}	$s_{eff,IdA}$	$s_{SB,IdA}$	$s_{tot,IdA}$	$s_{gl,Ida}$	$s_{tot,JdA}$	$s_{gl,JdA}$
0.625	0.389	0.089	0.335	0.089	0.074	0.256	0.267	0.000	0.269	0.100
0.875	0.436	0.107	0.375	0.107	0.064	0.173	0.184	0.000	0.187	0.100
1.250	0.502	0.267	0.432	0.267	0.078	0.113	0.137	0.000	0.141	0.100
d+Au 20-40%, $R_{dA} = 0.884 \pm 0.0026$ **(stat)** ± 0.032 **(sys)**										
p_T	I_{dA}	σ_{IdA}	J_{dA}	σ_{JdA}	$s_{eff,IdA}$	$s_{SB,IdA}$	$s_{tot,IdA}$	$s_{gl,Ida}$	$s_{tot,JdA}$	$s_{gl,JdA}$
0.625	0.539	0.093	0.476	0.093	0.071	0.253	0.263	0.000	0.265	0.100
0.875	0.625	0.111	0.553	0.111	0.065	0.171	0.183	0.000	0.186	0.100
1.250	0.654	0.270	0.578	0.270	0.079	0.112	0.137	0.000	0.141	0.100
d+Au 40-60%, $R_{dA} = 0.907 \pm 0.0028$ **(stat)** ± 0.032 **(sys)**										
p_T	I_{dA}	σ_{IdA}	J_{dA}	σ_{JdA}	$s_{eff,IdA}$	$s_{SB,IdA}$	$s_{tot,IdA}$	$s_{gl,Ida}$	$s_{tot,JdA}$	$s_{gl,JdA}$
0.625	0.807	0.106	0.732	0.106	0.069	0.243	0.253	0.000	0.255	0.100
0.875	0.755	0.111	0.685	0.111	0.065	0.164	0.176	0.000	0.179	0.100
1.250	1.046	0.304	0.948	0.304	0.078	0.107	0.132	0.000	0.136	0.100
d+Au 60-88%, $R_{dA} = 0.949 \pm 0.0030$ **(stat)** ± 0.032 **(sys)**										
p_T	I_{dA}	σ_{IdA}	J_{dA}	σ_{JdA}	$s_{eff,IdA}$	$s_{SB,IdA}$	$s_{tot,IdA}$	$s_{gl,Ida}$	$s_{tot,JdA}$	$s_{gl,JdA}$
0.625	0.865	0.097	0.821	0.097	0.068	0.220	0.230	0.000	0.232	0.100
0.875	1.074	0.115	1.019	0.115	0.064	0.142	0.156	0.000	0.159	0.100
1.250	1.111	0.278	1.054	0.278	0.076	0.094	0.120	0.000	0.124	0.100

Table C.9: I_{dA}, J_{dA} **relative** sys, stat errors for $3.0 < \eta < 3.8$, central $h^{\pm} p_T = 2.0 - 4.0$ GeV/c.

d+Au 0-20%, $R_{dA} = 1.147 \pm 0.0086$ **(stat)** ± 0.032 **(sys)**										
p_T	I_{dA}	σ_{IdA}	J_{dA}	σ_{JdA}	$s_{eff,IdA}$	$s_{SB,IdA}$	$s_{tot,IdA}$	$s_{gl,Ida}$	$s_{tot,JdA}$	$s_{gl,JdA}$
0.625	0.355	0.298	0.407	0.298	0.074	0.256	0.267	0.000	0.269	0.100
0.875	0.388	0.287	0.445	0.287	0.064	0.173	0.184	0.000	0.187	0.100
1.250	0.417	0.339	0.478	0.339	0.078	0.113	0.137	0.000	0.141	0.100
d+Au 20-40%, $R_{dA} = 1.141 \pm 0.0089$ **(stat)** ± 0.032 **(sys)**										
p_T	I_{dA}	σ_{IdA}	J_{dA}	σ_{JdA}	$s_{eff,IdA}$	$s_{SB,IdA}$	$s_{tot,IdA}$	$s_{gl,Ida}$	$s_{tot,JdA}$	$s_{gl,JdA}$
0.625	0.462	0.310	0.527	0.310	0.071	0.253	0.263	0.000	0.265	0.100
0.875	0.500	0.298	0.570	0.298	0.065	0.171	0.183	0.000	0.186	0.100
1.250	0.646	0.311	0.737	0.312	0.079	0.112	0.137	0.000	0.141	0.100
d+Au 40-60%, $R_{dA} = 1.111 \pm 0.0093$ **(stat)** ± 0.032 **(sys)**										
p_T	I_{dA}	σ_{IdA}	J_{dA}	σ_{JdA}	$s_{eff,IdA}$	$s_{SB,IdA}$	$s_{tot,IdA}$	$s_{gl,Ida}$	$s_{tot,JdA}$	$s_{gl,JdA}$
0.625	0.577	0.307	0.642	0.307	0.069	0.243	0.253	0.000	0.255	0.100
0.875	0.671	0.281	0.746	0.281	0.065	0.164	0.176	0.000	0.179	0.100
1.250	0.728	0.313	0.809	0.313	0.078	0.107	0.132	0.000	0.136	0.100
d+Au 60-88%, $R_{dA} = 1.038 \pm 0.0100$ **(stat)** ± 0.032 **(sys)**										
p_T	I_{dA}	σ_{IdA}	J_{dA}	σ_{JdA}	$s_{eff,IdA}$	$s_{SB,IdA}$	$s_{tot,IdA}$	$s_{gl,Ida}$	$s_{tot,JdA}$	$s_{gl,JdA}$
0.625	0.731	0.311	0.759	0.312	0.068	0.220	0.230	0.000	0.232	0.100
0.875	1.008	0.362	1.047	0.362	0.064	0.142	0.156	0.000	0.159	0.100
1.250	1.299	0.376	1.349	0.377	0.076	0.094	0.120	0.000	0.124	0.100

C.1.4 Central Arm $h^{\pm}$ and MPC π^0 $R_{\rm dA}$ values

In this section, the terms that are present in the tables are as follows:

p_T	Transverse momentum of the bin center,
$R_{\rm dA}$	Single hadron nuclear modification factor for central arm $h^{\pm}$'s,
s_{RdA}	Systematic error for central arm $h^{\pm}$ $R_{\rm dA}$,
$R_{dA,MPC}$	Single hadron nuclear modification factor for forward MPC π^0's,
$s_{RdA,MPC}$	Systematic error for forward MPC π^0's.

Table C.10: R_{dA} **relative** sys, stat errors for central $h^{\pm} p_T = 0.5 - 1.0$ GeV/c.

d+Au 0-20%						
p_T	R_{dA}	σ_{RdA}	s_{RdA}	$R_{dA,MPC}$	$\sigma_{RdA,MPC}$	$s_{RdA,MPC}$
0.625	0.657	0.002	0.032	0.198	0.019	0.074
0.875	0.657	0.002	0.032	0.230	0.018	0.064
1.250	0.657	0.002	0.032	0.289	0.030	0.088
d+Au 20-40%						
p_T	R_{dA}	σ_{RdA}	s_{RdA}	$R_{dA,MPC}$	$\sigma_{RdA,MPC}$	$s_{RdA,MPC}$
0.625	0.681	0.002	0.032	0.288	0.019	0.071
0.875	0.681	0.002	0.032	0.335	0.018	0.065
1.250	0.681	0.002	0.032	0.430	0.031	0.090
d+Au 40-60%						
p_T	R_{dA}	σ_{RdA}	s_{RdA}	$R_{dA,MPC}$	$\sigma_{RdA,MPC}$	$s_{RdA,MPC}$
0.625	0.714	0.002	0.032	0.391	0.018	0.069
0.875	0.714	0.002	0.032	0.474	0.017	0.065
1.250	0.714	0.002	0.032	0.594	0.031	0.089
d+Au 60-88%						
p_T	R_{dA}	σ_{RdA}	s_{RdA}	$R_{dA,MPC}$	$\sigma_{RdA,MPC}$	$s_{RdA,MPC}$
0.625	0.786	0.002	0.032	0.616	0.016	0.068
0.875	0.786	0.002	0.032	0.702	0.016	0.064
1.250	0.786	0.002	0.032	0.799	0.028	0.085

Table C.11: R_{dA} **relative** sys, stat errors for central $h^{\pm} p_T = 1.0 - 2.0$ GeV/c.

d+Au 0-20%						
p_T	R_{dA}	σ_{RdA}	s_{RdA}	$R_{dA,MPC}$	$\sigma_{RdA,MPC}$	$s_{RdA,MPC}$
0.625	0.861	0.003	0.032	0.198	0.019	0.074
0.875	0.861	0.003	0.032	0.230	0.018	0.064
1.250	0.861	0.003	0.032	0.289	0.030	0.088
d+Au 20-40%						
p_T	R_{dA}	σ_{RdA}	s_{RdA}	$R_{dA,MPC}$	$\sigma_{RdA,MPC}$	$s_{RdA,MPC}$
0.625	0.884	0.003	0.032	0.288	0.019	0.071
0.875	0.884	0.003	0.032	0.335	0.018	0.065
1.250	0.884	0.003	0.032	0.430	0.031	0.090
d+Au 40-60%						
p_T	R_{dA}	σ_{RdA}	s_{RdA}	$R_{dA,MPC}$	$\sigma_{RdA,MPC}$	$s_{RdA,MPC}$
0.625	0.907	0.003	0.032	0.391	0.018	0.069
0.875	0.907	0.003	0.032	0.474	0.017	0.065
1.250	0.907	0.003	0.032	0.594	0.031	0.089
d+Au 60-88%						
p_T	R_{dA}	σ_{RdA}	s_{RdA}	$R_{dA,MPC}$	$\sigma_{RdA,MPC}$	$s_{RdA,MPC}$
0.625	0.949	0.003	0.032	0.616	0.016	0.068
0.875	0.949	0.003	0.032	0.702	0.016	0.064
1.250	0.949	0.003	0.032	0.799	0.028	0.085

Table C.12: R_{dA} **relative** sys, stat errors for central $h^{\pm} p_T = 2.0 - 4.0$ GeV/c.

d+Au 0-20%						
p_T	R_{dA}	σ_{RdA}	s_{RdA}	$R_{dA,MPC}$	$\sigma_{RdA,MPC}$	$s_{RdA,MPC}$
0.625	1.147	0.009	0.032	0.198	0.019	0.074
0.875	1.147	0.009	0.032	0.230	0.018	0.064
1.250	1.147	0.009	0.032	0.289	0.030	0.088
d+Au 20-40%						
p_T	R_{dA}	σ_{RdA}	s_{RdA}	$R_{dA,MPC}$	$\sigma_{RdA,MPC}$	$s_{RdA,MPC}$
0.625	1.141	0.009	0.032	0.288	0.019	0.071
0.875	1.141	0.009	0.032	0.335	0.018	0.065
1.250	1.141	0.009	0.032	0.430	0.031	0.090
d+Au 40-60%						
p_T	R_{dA}	σ_{RdA}	s_{RdA}	$R_{dA,MPC}$	$\sigma_{RdA,MPC}$	$s_{RdA,MPC}$
0.625	1.111	0.009	0.032	0.391	0.018	0.069
0.875	1.111	0.009	0.032	0.474	0.017	0.065
1.250	1.111	0.009	0.032	0.594	0.031	0.089
d+Au 60-88%						
p_T	R_{dA}	σ_{RdA}	s_{RdA}	$R_{dA,MPC}$	$\sigma_{RdA,MPC}$	$s_{RdA,MPC}$
0.625	1.038	0.010	0.032	0.616	0.016	0.068
0.875	1.038	0.010	0.032	0.702	0.016	0.064
1.250	1.038	0.010	0.032	0.799	0.028	0.085

C.2 Correlation Functions

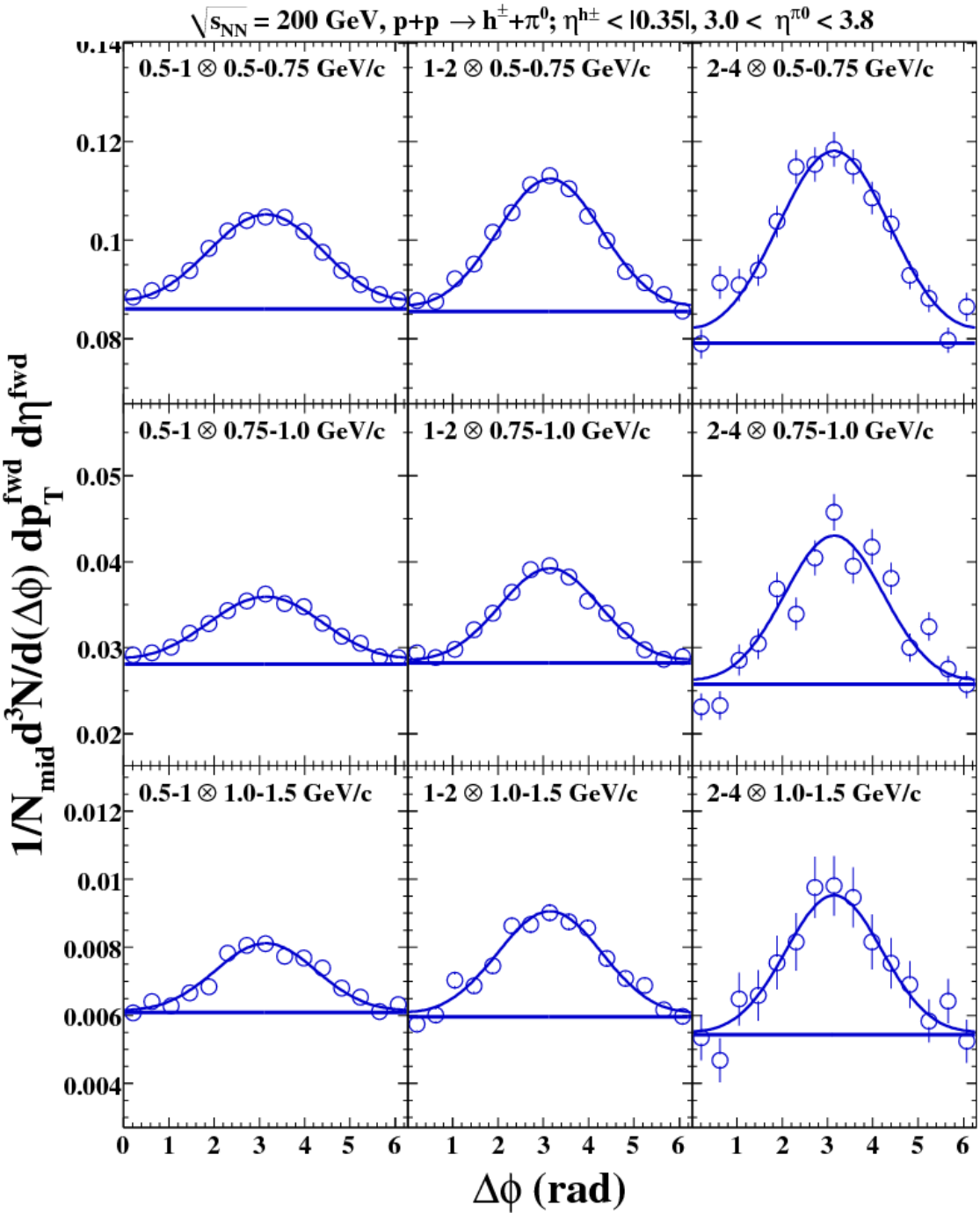

Figure C.1: **p+p, Rapidity = 3.0-3.8:** Correlation functions and fits for all p_T bins.

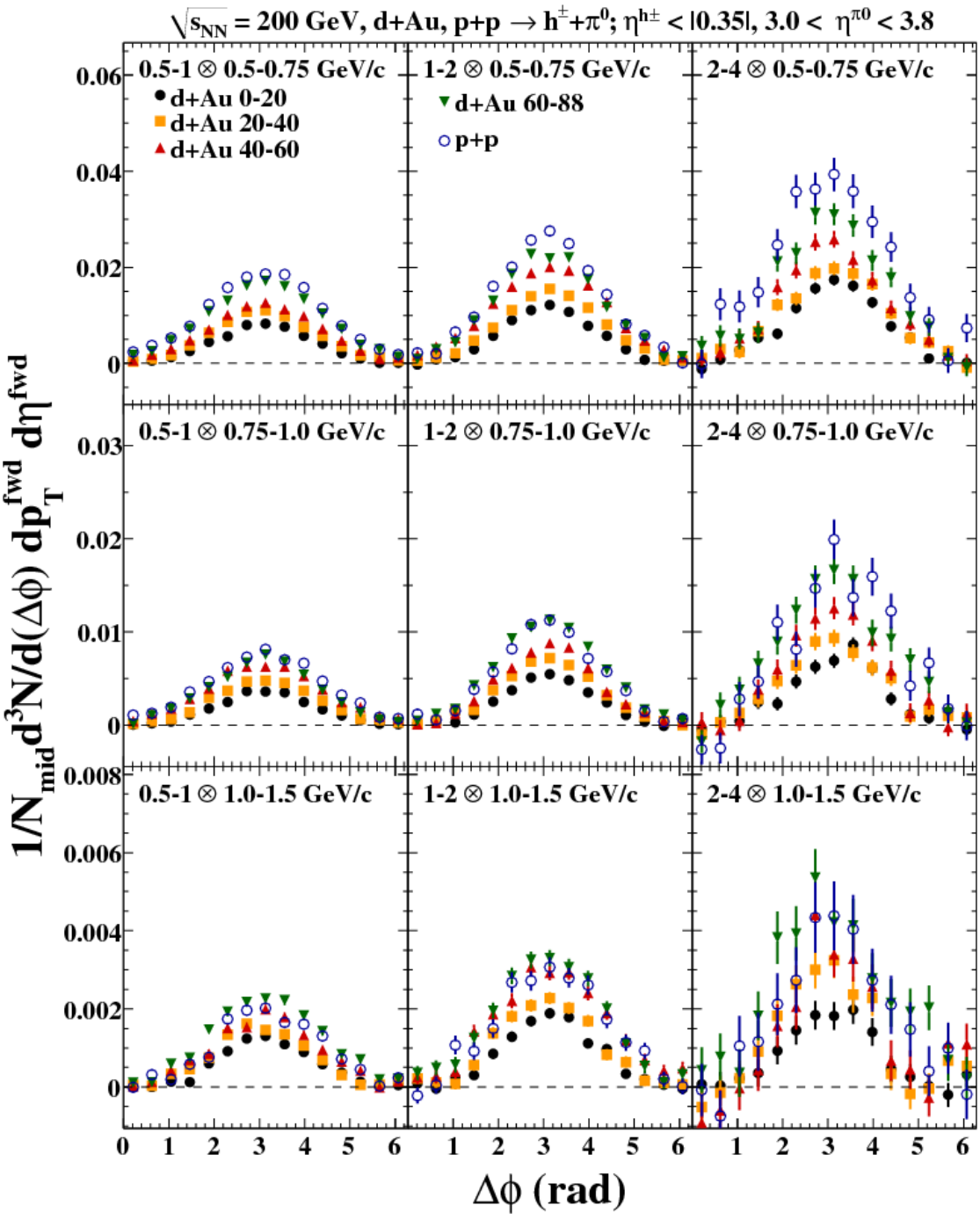

Figure C.2: **Rapidity = 3.0-3.8:** Background subtracted correlation functions and fits for all centralities and p_T bins.

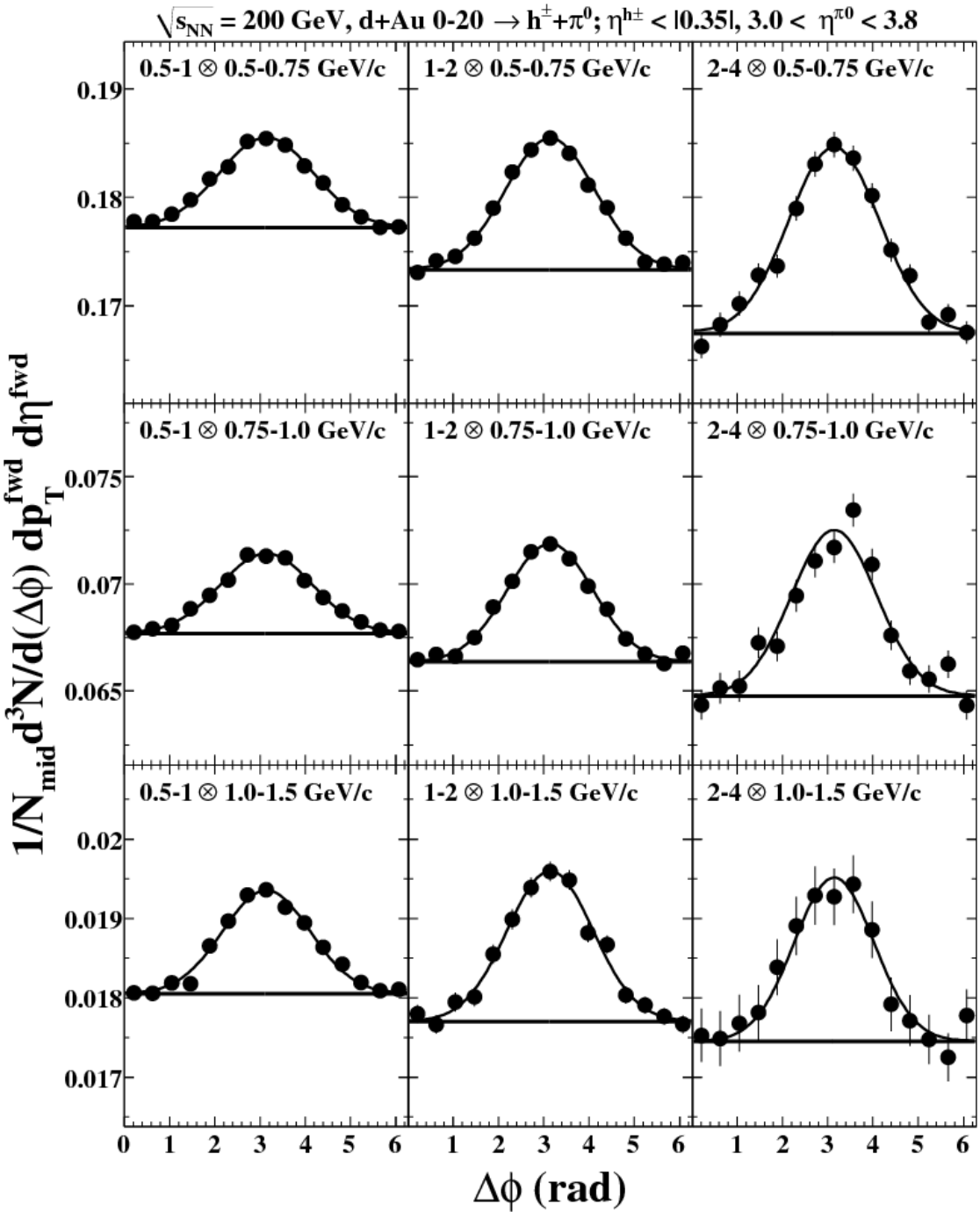

Figure C.3: **d+Au 0-20%, Rapidity = 3.0-3.8:** Correlation functions and fits for all p_T bins.

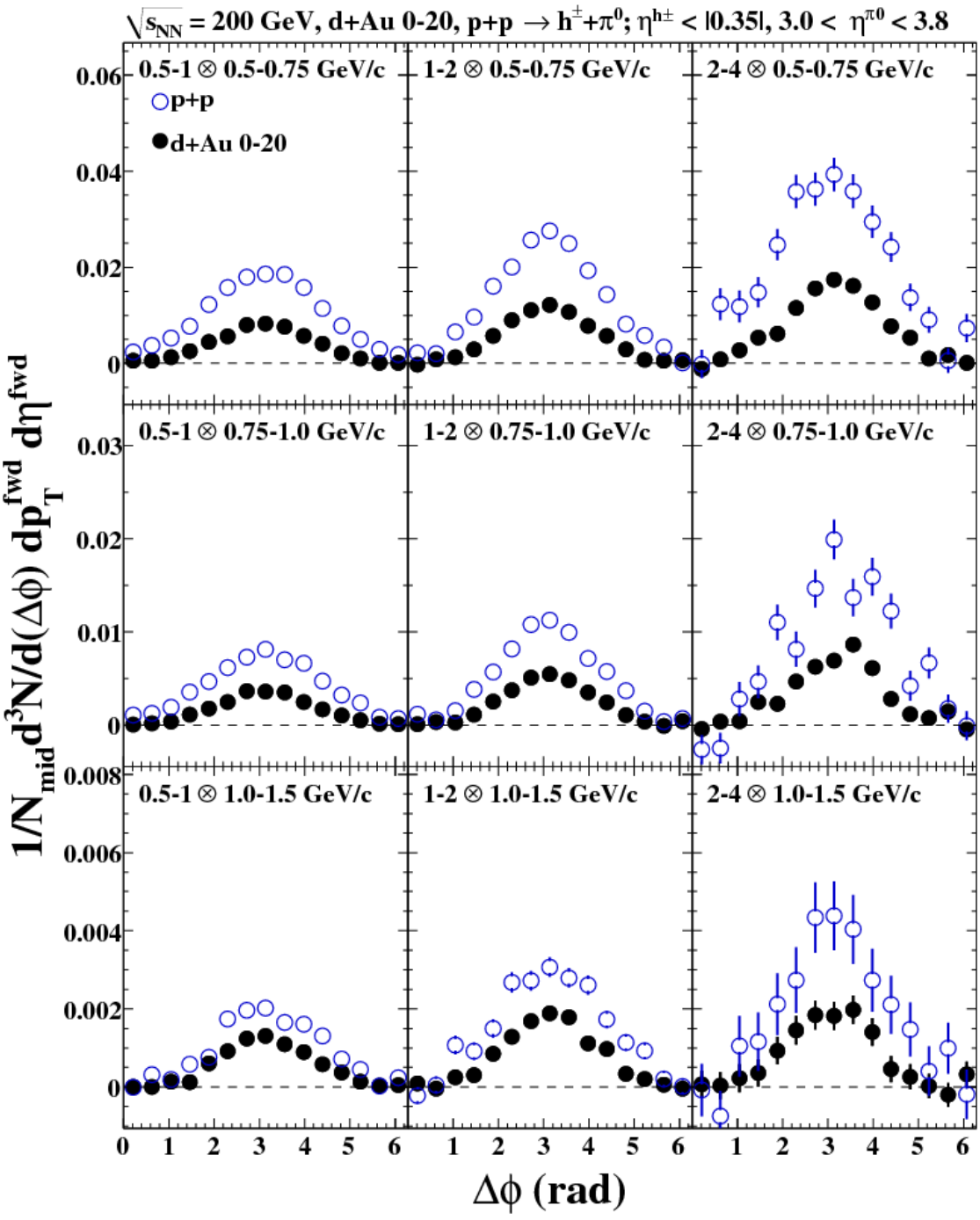

Figure C.4: **d+Au 0-20%, Rapidity = 3.0-3.8:** Background subtracted correlation functions and fits for all p_T bins. The p+p reference is in blue.

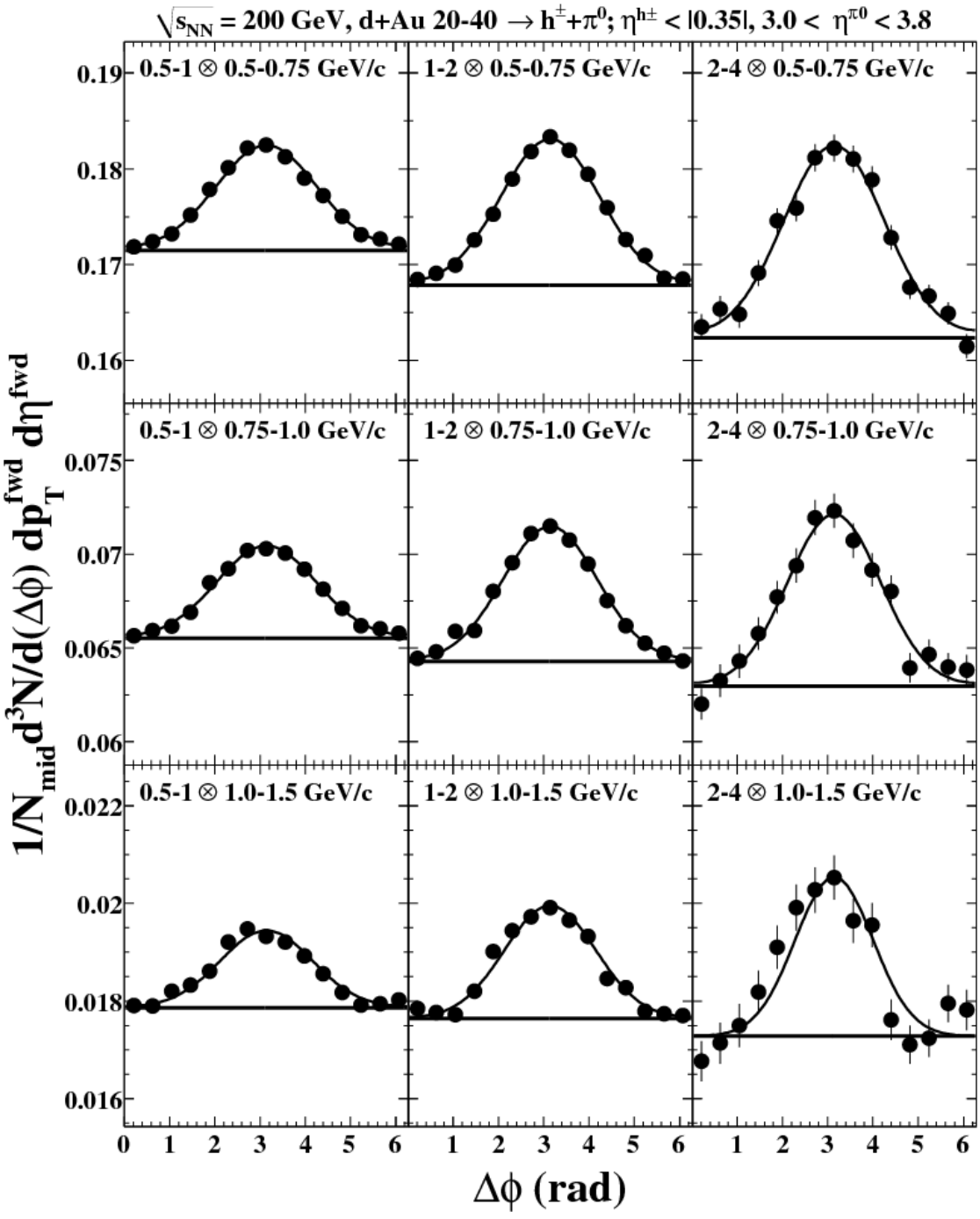

Figure C.5: **dAu 20-40%, Rapidity = 3.0-3.8:** Correlation functions and fits for all p_T bins.

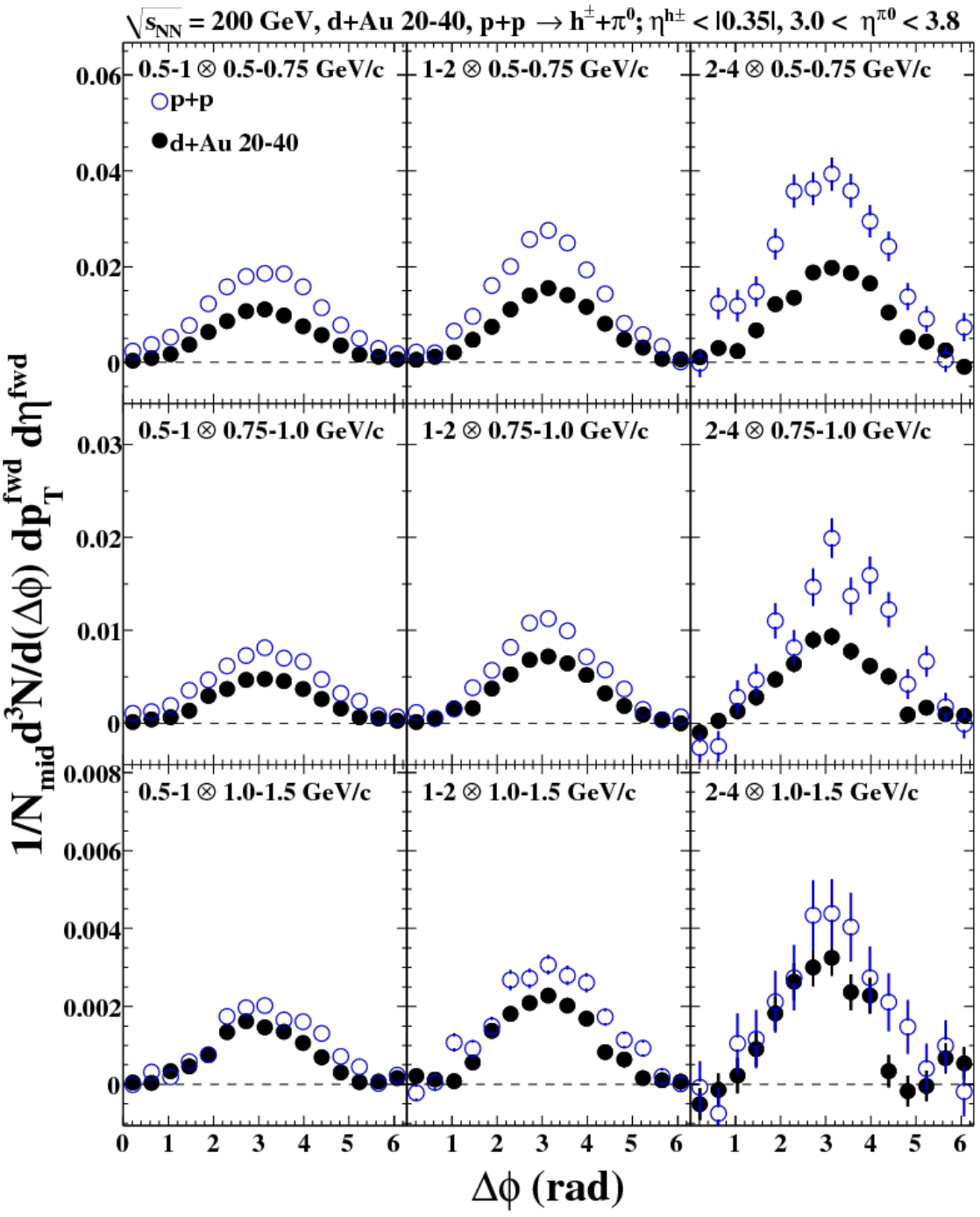

Figure C.6: **dAu 20-40%, Rapidity = 3.0-3.8:** Background subtracted correlation functions and fits for all p_T bins. The p+p reference is in blue.

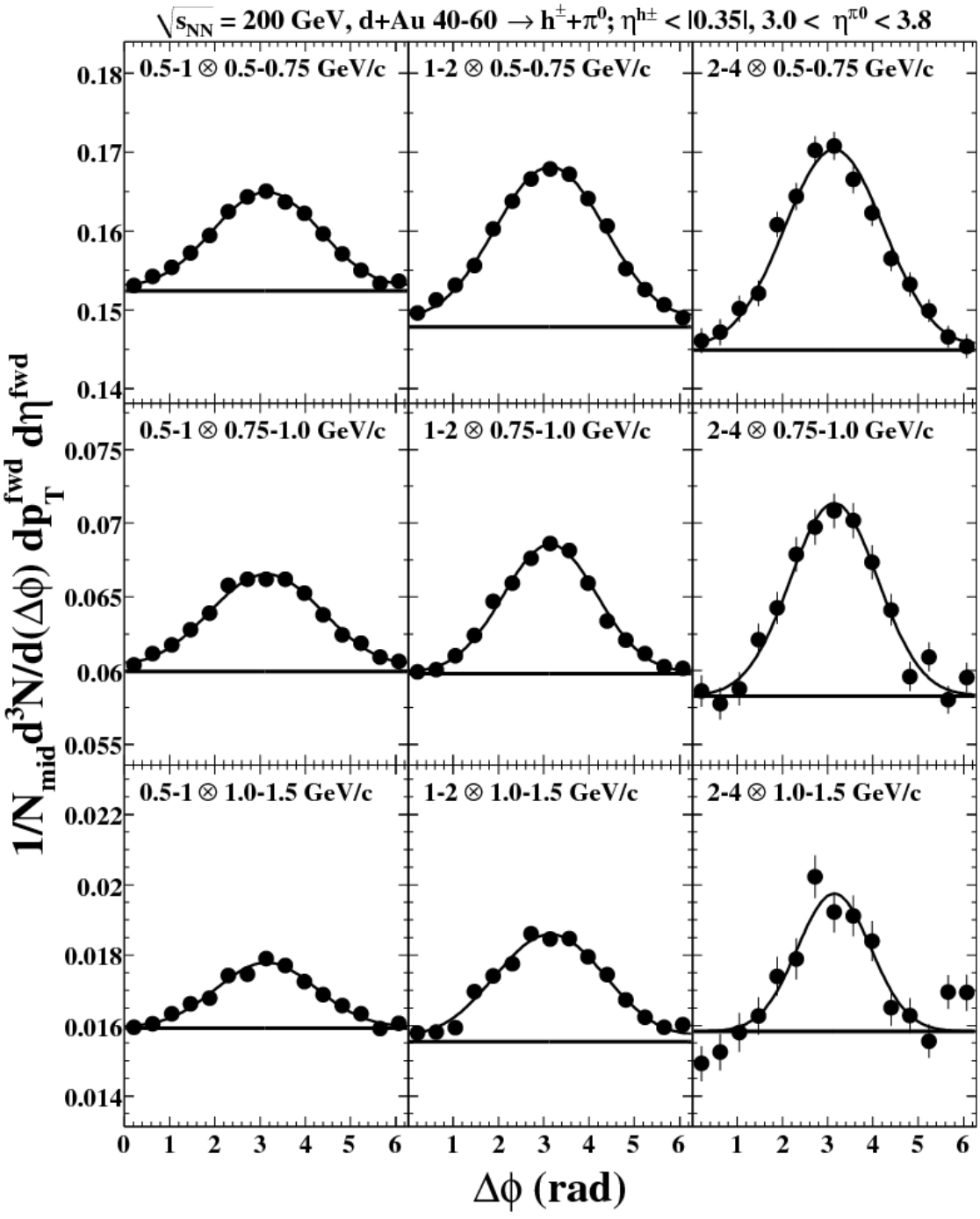

Figure C.7: **dAu 40-60%, Rapidity = 3.0-3.8:** Correlation functions and fits for all p_T bins.

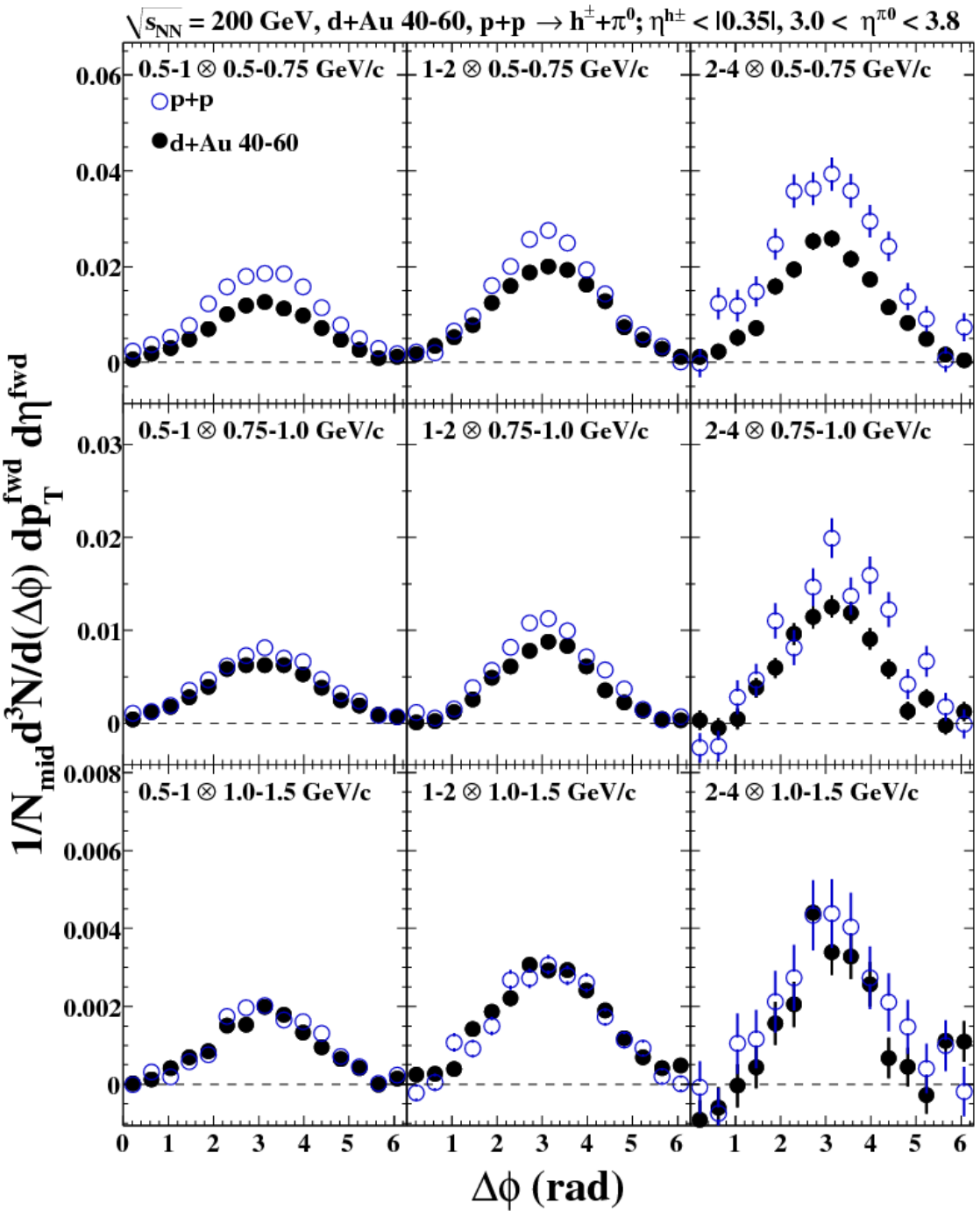

Figure C.8: **dAu 40-60%, Rapidity = 3.0-3.8:** Background subtracted correlation functions and fits for all p_T bins. The p+p reference is in blue.

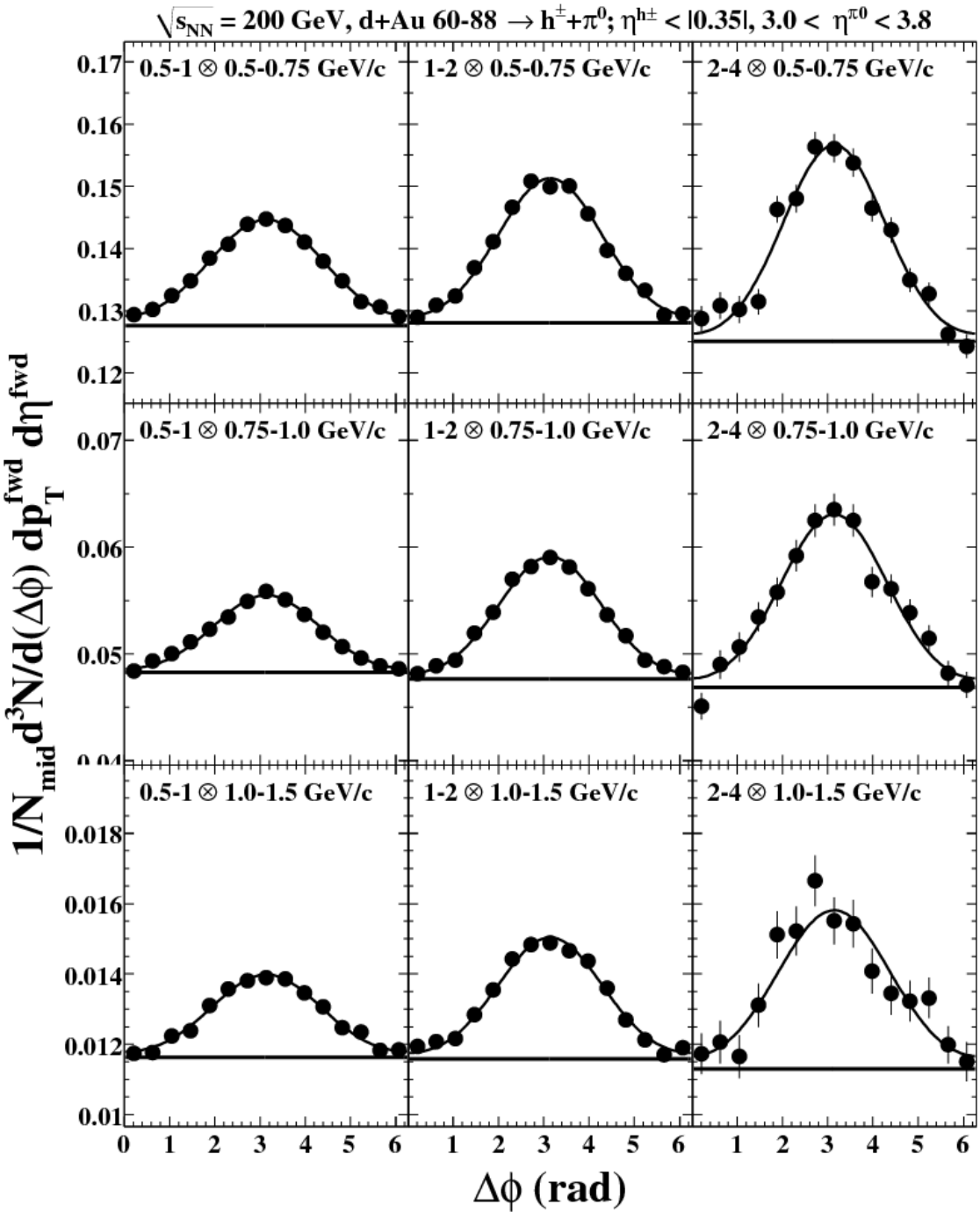

Figure C.9: **dAu 60-88%, Rapidity = 3.0-3.8:** Correlation functions and fits for all p_T bins.

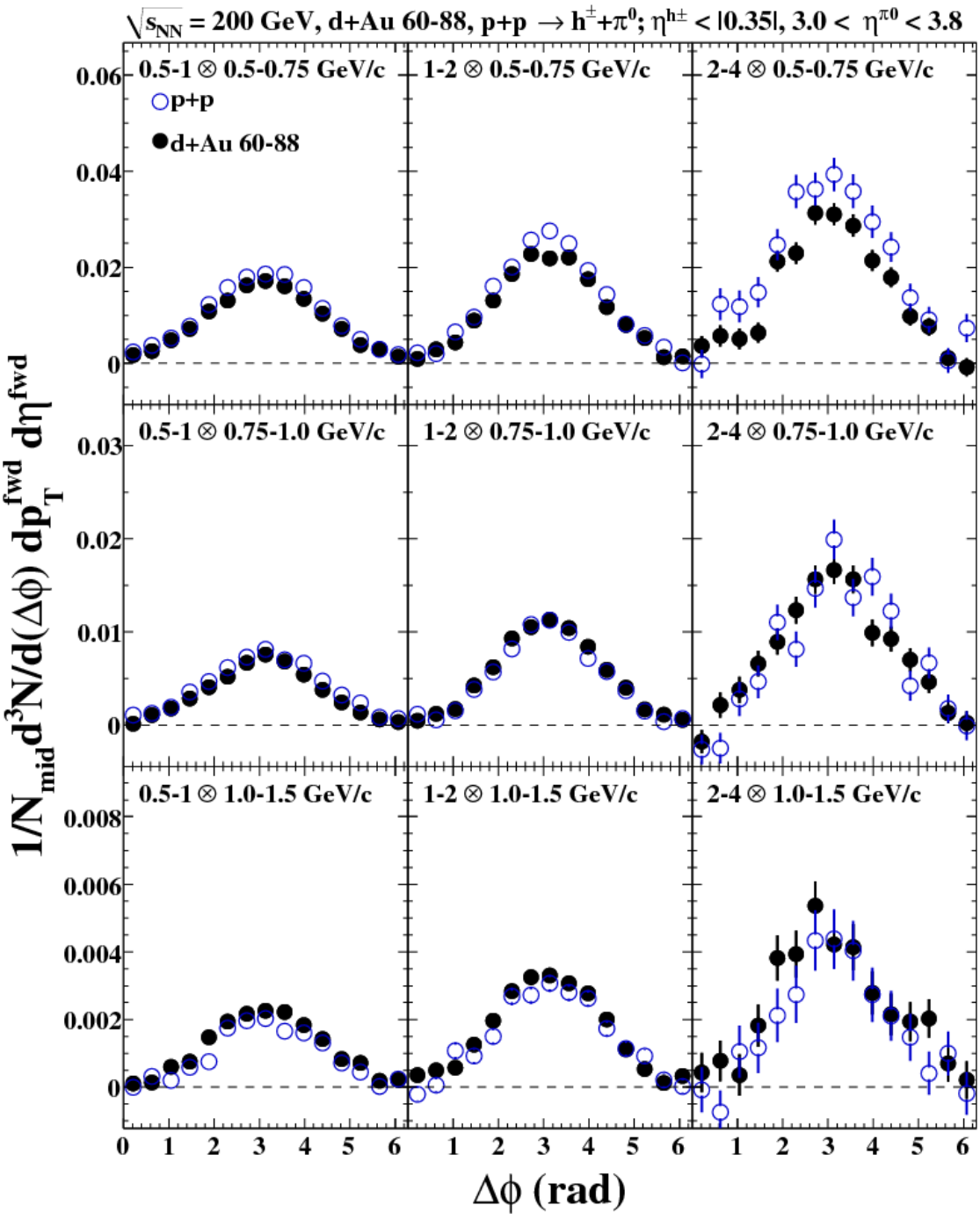

Figure C.10: **dAu 60-88%, Rapidity = 3.0-3.8:** Background subtracted correlation functions and fits for all p_T bins. The p+p reference is in blue.

Appendix D

Mid-Forward π^0/π^0 Azimuthal Correlations Tables and Figures

D.1 Tabulated Results

In all subsequent tables, σ represents a statistical error, while s represents a systematic error (type B), and the global systematic error is s_{global}.

D.1.1 Raw and Conditional Errors, Relative Stat. Errors

In this section, the terms that are present in the tables are as follows:

p_T	Transverse momentum of the bin center,
Y	Number of correlated particle pairs,
CY	Conditional yield, or the area of the correlated di-hadron signal per trigger particle detected,
ϵ	π^0 reconstruction efficiency,
$\frac{S}{S+B}MPC$	Fraction of counts in π^0 mass window, $0.08 < m_{inv} < 0.18$ GeV/c^2 that are actually signal π^0's (as opposed to background counts),
C_{leak}	Accounts for leakage of the π^0 yield outside the defined window of $0.08 < m_{inv} < 0.18$ GeV/c^2,
C_{bcorr}	Up-down correction, or $C_{up-down}$,
$\Delta p_T \Delta\eta$	Corrects for p_T and η bin widths (e.g. $\Delta p_T \Delta\eta = 0.25 \times 0.8 = 0.2$).

Table D.1: Conditional and Raw Yields, N_{trig}, efficiencies, corrections, and **Relative** stat errors for $3.0 < \eta < 3.8$, central $\pi^0 p_T = 2.5 - 3.0$ GeV/c.

d+Au 0-20%, $N_{trig} = 1.508e+07$										
p_T	CY	σ_{CY}	Y	σ_Y	ϵ	σ_ϵ	$\frac{S}{S+B}_{MPC}$	C_{leak}	C_{bcorr}	$\Delta p_T \Delta\eta$
0.625	5.76e-02	0.076	2.66e+04	0.074	0.052	0.016	0.34	1.04	0.96	0.20
0.875	1.90e-02	0.080	8.18e+03	0.078	0.076	0.014	0.54	1.02	0.96	0.20
1.250	7.35e-03	0.126	3.58e+03	0.125	0.051	0.015	0.70	1.04	0.88	0.40
d+Au 20-40%, $N_{trig} = 9.239e+06$										
p_T	CY	σ_{CY}	Y	σ_Y	ϵ	σ_ϵ	$\frac{S}{S+B}_{MPC}$	C_{leak}	C_{bcorr}	$\Delta p_T \Delta\eta$
0.625	6.27e-02	0.079	1.80e+04	0.078	0.053	0.015	0.34	1.03	0.96	0.20
0.875	2.78e-02	0.110	7.38e+03	0.109	0.077	0.014	0.55	1.02	0.96	0.20
1.250	8.43e-03	0.115	2.45e+03	0.114	0.051	0.015	0.70	1.05	0.88	0.40
d+Au 40-60%, $N_{trig} = 5.442e+06$										
p_T	CY	σ_{CY}	Y	σ_Y	ϵ	σ_ϵ	$\frac{S}{S+B}_{MPC}$	C_{leak}	C_{bcorr}	$\Delta p_T \Delta\eta$
0.625	6.31e-02	0.090	1.07e+04	0.089	0.057	0.015	0.37	1.03	0.96	0.20
0.875	3.41e-02	0.103	5.09e+03	0.102	0.077	0.014	0.57	1.02	0.97	0.20
1.250	1.13e-02	0.181	1.89e+03	0.181	0.050	0.015	0.71	1.04	0.87	0.40
d+Au 60-88%, $N_{trig} = 3.149e+06$										
p_T	CY	σ_{CY}	Y	σ_Y	ϵ	σ_ϵ	$\frac{S}{S+B}_{MPC}$	C_{leak}	C_{bcorr}	$\Delta p_T \Delta\eta$
0.625	9.10e-02	0.100	8.07e+03	0.099	0.059	0.012	0.43	1.03	0.96	0.20
0.875	5.02e-02	0.158	4.14e+03	0.158	0.080	0.012	0.62	1.02	0.96	0.20
1.250	1.24e-02	0.178	1.20e+03	0.178	0.052	0.012	0.75	1.04	0.86	0.40
p+p, $N_{trig} = 7.109e+06$										
p_T	CY	σ_{CY}	Y	σ_Y	ϵ	σ_ϵ	$\frac{S}{S+B}_{MPC}$	C_{leak}	C_{bcorr}	$\Delta p_T \Delta\eta$
0.625	1.08e-01	0.053	1.82e+04	0.052	0.060	0.010	0.52	1.03	0.95	0.20
0.875	4.80e-02	0.074	8.22e+03	0.074	0.082	0.010	0.70	1.02	0.95	0.20
1.250	1.20e-02	0.080	2.55e+03	0.080	0.052	0.010	0.80	1.04	0.83	0.40

Table D.2: Conditional and Raw Yields, N_{trig}, efficiencies, corrections, and **Relative** stat errors for $3.0 < \eta < 3.8$, central $\pi^0 p_T = 3.0 - 4.0$ GeV/c.

d+Au 0-20%, $N_{trig} = 1.306e+07$										
p_T	CY	σ_{CY}	Y	σ_Y	ϵ	σ_ϵ	$\frac{S}{S+B}_{MPC}$	C_{leak}	C_{bcorr}	$\Delta p_T \Delta\eta$
0.625	4.87e-02	0.087	1.95e+04	0.085	0.052	0.016	0.34	1.04	0.96	0.20
0.875	2.22e-02	0.095	8.26e+03	0.094	0.076	0.014	0.54	1.02	0.96	0.20
1.250	8.47e-03	0.127	3.57e+03	0.127	0.051	0.015	0.70	1.04	0.88	0.40
d+Au 20-40%, $N_{trig} = 8.449e+06$										
p_T	CY	σ_{CY}	Y	σ_Y	ϵ	σ_ϵ	$\frac{S}{S+B}_{MPC}$	C_{leak}	C_{bcorr}	$\Delta p_T \Delta\eta$
0.625	6.41e-02	0.074	1.68e+04	0.072	0.053	0.015	0.34	1.03	0.96	0.20
0.875	3.20e-02	0.124	7.76e+03	0.124	0.077	0.014	0.55	1.02	0.96	0.20
1.250	9.63e-03	0.160	2.56e+03	0.159	0.051	0.015	0.70	1.05	0.88	0.40
d+Au 40-60%, $N_{trig} = 5.160e+06$										
p_T	CY	σ_{CY}	Y	σ_Y	ϵ	σ_ϵ	$\frac{S}{S+B}_{MPC}$	C_{leak}	C_{bcorr}	$\Delta p_T \Delta\eta$
0.625	7.44e-02	0.089	1.20e+04	0.088	0.057	0.015	0.37	1.03	0.96	0.20
0.875	4.46e-02	0.154	6.32e+03	0.153	0.077	0.014	0.57	1.02	0.97	0.20
1.250	9.29e-03	0.145	1.47e+03	0.144	0.050	0.015	0.71	1.04	0.87	0.40
d+Au 60-88%, $N_{trig} = 3.097e+06$										
p_T	CY	σ_{CY}	Y	σ_Y	ϵ	σ_ϵ	$\frac{S}{S+B}_{MPC}$	C_{leak}	C_{bcorr}	$\Delta p_T \Delta\eta$
0.625	9.17e-02	0.075	7.99e+03	0.074	0.059	0.012	0.43	1.03	0.96	0.20
0.875	5.50e-02	0.202	4.46e+03	0.201	0.080	0.012	0.62	1.02	0.96	0.20
1.250	1.28e-02	0.137	1.22e+03	0.137	0.052	0.012	0.75	1.04	0.86	0.40
p+p, $N_{trig} = 4.942e+06$										
p_T	CY	σ_{CY}	Y	σ_Y	ϵ	σ_ϵ	$\frac{S}{S+B}_{MPC}$	C_{leak}	C_{bcorr}	$\Delta p_T \Delta\eta$
0.625	1.06e-01	0.069	1.24e+04	0.068	0.060	0.010	0.52	1.03	0.95	0.20
0.875	4.45e-02	0.072	5.30e+03	0.071	0.082	0.010	0.70	1.02	0.95	0.20
1.250	1.20e-02	0.098	1.77e+03	0.098	0.052	0.010	0.80	1.04	0.83	0.40

Table D.3: Conditional and Raw Yields, N_{trig}, efficiencies, corrections, and **Relative** stat errors for $3.0 < \eta < 3.8$, central $\pi^0 p_T = 4.0 - 7.0$ GeV/c.

d+Au 0-20%, $N_{trig} = 4.684e+06$										
p_T	CY	σ_{CY}	Y	σ_Y	ϵ	σ_ϵ	$\frac{S}{S+B}_{MPC}$	C_{leak}	C_{bcorr}	$\Delta p_T \Delta\eta$
0.625	5.51e-02	0.255	7.91e+03	0.255	0.052	0.016	0.34	1.04	0.96	0.20
0.875	2.41e-02	0.282	3.21e+03	0.282	0.076	0.014	0.54	1.02	0.96	0.20
1.250	6.93e-03	0.181	1.05e+03	0.180	0.051	0.015	0.70	1.04	0.88	0.40
d+Au 20-40%, $N_{trig} = 3.202e+06$										
p_T	CY	σ_{CY}	Y	σ_Y	ϵ	σ_ϵ	$\frac{S}{S+B}_{MPC}$	C_{leak}	C_{bcorr}	$\Delta p_T \Delta\eta$
0.625	6.64e-02	0.136	6.61e+03	0.135	0.053	0.015	0.34	1.03	0.96	0.20
0.875	2.05e-02	0.139	1.89e+03	0.139	0.077	0.014	0.55	1.02	0.96	0.20
1.250	8.04e-03	0.278	8.11e+02	0.277	0.051	0.015	0.70	1.05	0.88	0.40
d+Au 40-60%, $N_{trig} = 2.019e+06$										
p_T	CY	σ_{CY}	Y	σ_Y	ϵ	σ_ϵ	$\frac{S}{S+B}_{MPC}$	C_{leak}	C_{bcorr}	$\Delta p_T \Delta\eta$
0.625	6.57e-02	0.177	4.14e+03	0.176	0.057	0.015	0.37	1.03	0.96	0.20
0.875	2.79e-02	0.134	1.55e+03	0.133	0.077	0.014	0.57	1.02	0.97	0.20
1.250	8.97e-03	0.284	5.57e+02	0.284	0.050	0.015	0.71	1.04	0.87	0.40
d+Au 60-88%, $N_{trig} = 1.263e+06$										
p_T	CY	σ_{CY}	Y	σ_Y	ϵ	σ_ϵ	$\frac{S}{S+B}_{MPC}$	C_{leak}	C_{bcorr}	$\Delta p_T \Delta\eta$
0.625	8.24e-02	0.104	2.93e+03	0.104	0.059	0.012	0.43	1.03	0.96	0.20
0.875	3.43e-02	0.168	1.13e+03	0.167	0.080	0.012	0.62	1.02	0.96	0.20
1.250	1.16e-02	0.280	4.49e+02	0.280	0.052	0.012	0.75	1.04	0.86	0.40
p+p, $N_{trig} = 1.476e+06$										
p_T	CY	σ_{CY}	Y	σ_Y	ϵ	σ_ϵ	$\frac{S}{S+B}_{MPC}$	C_{leak}	C_{bcorr}	$\Delta p_T \Delta\eta$
0.625	9.81e-02	0.124	3.42e+03	0.124	0.060	0.010	0.52	1.03	0.95	0.20
0.875	3.57e-02	0.124	1.27e+03	0.124	0.082	0.010	0.70	1.02	0.95	0.20
1.250	1.36e-02	0.276	5.97e+02	0.276	0.052	0.010	0.80	1.04	0.83	0.40

D.1.2 Conditional Yields, Widths and Relative Errors

In this section, the terms that are present in the tables are as follows:

p_T	Transverse momentum of the bin center,
CY	Conditional yield, or the area of the correlated di-hadron signal per trigger particle detected,
$\frac{S}{S+B}MPC$	Fraction of counts in π^0 mass window, $0.08 < m_{inv} < 0.18$ GeV/c^2 that are actually signal π^0's (as opposed to background counts),
$\frac{S}{S+B}trig$	Fraction of counts in π^0 mass window, $0.1 < m_{inv} < 0.18$ GeV/c^2 that are actually signal π^0's (as opposed to background counts),
s_{eff}	Systematic error from yield extraction, input spectrum shape, energy scale, and GEANT,
s_{sb}	Systematic error from contributions of the background under the π^0 peak to the CF,
s_{tot}	Total systematic error on the CY,
W	Gaussian width of the awayside peak,
s_w	Systematic error on the Gaussian width of the awayside peak.

Table D.4: Conditional Yields, widths, **Relative** sys, stat errors for $3.0 < \eta < 3.8$, central $\pi^0 p_T = 2.5 - 3.0$ GeV/c.

d+Au 0-20%										
p_T	CY	σ_{CY}	$\frac{S}{S+B}_{MPC}$	$\frac{S}{S+B}_{trig}$	s_{eff}	s_{sb}	s_{tot}	W	σ_w	s_w
0.625	5.76e-02	0.076	0.338	0.610	0.104	0.312	0.329	1.058	0.055	0.195
0.875	1.90e-02	0.080	0.545	0.610	0.113	0.261	0.285	0.849	0.063	0.163
1.250	7.35e-03	0.126	0.697	0.610	0.132	0.225	0.261	0.930	0.100	0.141
d+Au 20-40%										
p_T	CY	σ_{CY}	$\frac{S}{S+B}_{MPC}$	$\frac{S}{S+B}_{trig}$	s_{eff}	s_{sb}	s_{tot}	W	σ_w	s_w
0.625	6.27e-02	0.079	0.345	0.664	0.102	0.303	0.319	1.022	0.060	0.189
0.875	2.78e-02	0.110	0.548	0.664	0.113	0.248	0.273	0.996	0.086	0.155
1.250	8.43e-03	0.115	0.700	0.664	0.132	0.209	0.247	0.838	0.096	0.131
d+Au 40-60%										
p_T	CY	σ_{CY}	$\frac{S}{S+B}_{MPC}$	$\frac{S}{S+B}_{trig}$	s_{eff}	s_{sb}	s_{tot}	W	σ_w	s_w
0.625	6.31e-02	0.090	0.369	0.706	0.100	0.289	0.306	1.011	0.068	0.181
0.875	3.41e-02	0.103	0.567	0.706	0.112	0.233	0.259	0.983	0.080	0.146
1.250	1.13e-02	0.181	0.714	0.706	0.133	0.193	0.235	1.028	0.134	0.121
d+Au 60-88%										
p_T	CY	σ_{CY}	$\frac{S}{S+B}_{MPC}$	$\frac{S}{S+B}_{trig}$	s_{eff}	s_{sb}	s_{tot}	W	σ_w	s_w
0.625	9.10e-02	0.100	0.427	0.755	0.101	0.264	0.282	1.085	0.071	0.165
0.875	5.02e-02	0.158	0.622	0.755	0.115	0.205	0.236	1.140	0.107	0.128
1.250	1.24e-02	0.178	0.749	0.755	0.135	0.169	0.216	1.003	0.137	0.105
p+p										
p_T	CY	σ_{CY}	$\frac{S}{S+B}_{MPC}$	$\frac{S}{S+B}_{trig}$	s_{eff}	s_{sb}	s_{tot}	W	σ_w	s_w
0.625	1.08e-01	0.053	0.519	0.835	0.107	0.221	0.246	1.093	0.038	0.138
0.875	4.80e-02	0.074	0.698	0.835	0.122	0.162	0.203	1.115	0.054	0.101
1.250	1.20e-02	0.080	0.803	0.835	0.142	0.128	0.191	0.965	0.068	0.080

Table D.5: Conditional Yields, widths, **Relative** sys, stat errors for $3.0 < \eta < 3.8$, central $\pi^0 p_T = 3.0 - 4.0$ GeV/c.

d+Au 0-20%										
p_T	CY	σ_{CY}	$\frac{S}{S+B}_{MPC}$	$\frac{S}{S+B}_{trig}$	s_{eff}	s_{sb}	s_{tot}	W	σ_w	s_w
0.625	4.87e-02	0.087	0.338	0.788	0.104	0.287	0.305	1.027	0.064	0.179
0.875	2.22e-02	0.095	0.545	0.788	0.113	0.221	0.248	0.948	0.074	0.138
1.250	8.47e-03	0.127	0.697	0.788	0.132	0.174	0.218	0.975	0.097	0.109
d+Au 20-40%										
p_T	CY	σ_{CY}	$\frac{S}{S+B}_{MPC}$	$\frac{S}{S+B}_{trig}$	s_{eff}	s_{sb}	s_{tot}	W	σ_w	s_w
0.625	6.41e-02	0.074	0.345	0.818	0.102	0.280	0.298	0.999	0.056	0.175
0.875	3.20e-02	0.124	0.548	0.818	0.113	0.213	0.241	1.093	0.087	0.133
1.250	9.63e-03	0.160	0.700	0.818	0.132	0.165	0.211	1.009	0.120	0.103
d+Au 40-60%										
p_T	CY	σ_{CY}	$\frac{S}{S+B}_{MPC}$	$\frac{S}{S+B}_{trig}$	s_{eff}	s_{sb}	s_{tot}	W	σ_w	s_w
0.625	7.44e-02	0.089	0.369	0.839	0.100	0.268	0.286	1.055	0.065	0.168
0.875	4.46e-02	0.154	0.567	0.839	0.112	0.202	0.231	1.160	0.101	0.126
1.250	9.29e-03	0.145	0.714	0.839	0.133	0.154	0.204	0.843	0.128	0.096
d+Au 60-88%										
p_T	CY	σ_{CY}	$\frac{S}{S+B}_{MPC}$	$\frac{S}{S+B}_{trig}$	s_{eff}	s_{sb}	s_{tot}	W	σ_w	s_w
0.625	9.17e-02	0.075	0.427	0.861	0.101	0.245	0.265	0.983	0.058	0.153
0.875	5.50e-02	0.202	0.622	0.861	0.115	0.178	0.212	1.209	0.123	0.111
1.250	1.28e-02	0.137	0.749	0.861	0.135	0.136	0.192	0.913	0.116	0.085
p+p										
p_T	CY	σ_{CY}	$\frac{S}{S+B}_{MPC}$	$\frac{S}{S+B}_{trig}$	s_{eff}	s_{sb}	s_{tot}	W	σ_w	s_w
0.625	1.06e-01	0.069	0.519	0.897	0.107	0.208	0.234	1.110	0.049	0.130
0.875	4.45e-02	0.072	0.698	0.897	0.122	0.144	0.189	1.030	0.056	0.090
1.250	1.20e-02	0.098	0.803	0.897	0.142	0.108	0.178	0.978	0.080	0.068

Table D.6: Conditional Yields, widths, **Relative** sys, stat errors for $3.0 < \eta < 3.8$, central $\pi^0 p_T = 4.0 - 7.0$ GeV/c.

d+Au 0-20%										
p_T	CY	σ_{CY}	$\frac{S}{S+B}_{MPC}$	$\frac{S}{S+B}_{trig}$	s_{eff}	s_{sb}	s_{tot}	W	σ_w	s_w
0.625	5.51e-02	0.255	0.338	0.904	0.104	0.270	0.289	1.238	0.159	0.169
0.875	2.41e-02	0.282	0.545	0.904	0.113	0.194	0.225	1.101	0.186	0.121
1.250	6.93e-03	0.181	0.697	0.904	0.132	0.141	0.193	0.805	0.154	0.088
d+Au 20-40%										
p_T	CY	σ_{CY}	$\frac{S}{S+B}_{MPC}$	$\frac{S}{S+B}_{trig}$	s_{eff}	s_{sb}	s_{tot}	W	σ_w	s_w
0.625	6.64e-02	0.136	0.345	0.912	0.102	0.266	0.285	1.044	0.102	0.166
0.875	2.05e-02	0.139	0.548	0.912	0.113	0.192	0.222	0.768	0.121	0.120
1.250	8.04e-03	0.278	0.700	0.912	0.132	0.137	0.190	0.990	0.191	0.086
d+Au 40-60%										
p_T	CY	σ_{CY}	$\frac{S}{S+B}_{MPC}$	$\frac{S}{S+B}_{trig}$	s_{eff}	s_{sb}	s_{tot}	W	σ_w	s_w
0.625	6.57e-02	0.177	0.369	0.917	0.100	0.256	0.275	1.082	0.123	0.160
0.875	2.79e-02	0.134	0.567	0.917	0.112	0.183	0.215	0.790	0.117	0.115
1.250	8.97e-03	0.284	0.714	0.917	0.133	0.131	0.187	1.035	0.198	0.082
d+Au 60-88%										
p_T	CY	σ_{CY}	$\frac{S}{S+B}_{MPC}$	$\frac{S}{S+B}_{trig}$	s_{eff}	s_{sb}	s_{tot}	W	σ_w	s_w
0.625	8.24e-02	0.104	0.427	0.920	0.101	0.234	0.255	0.870	0.091	0.146
0.875	3.43e-02	0.168	0.622	0.920	0.115	0.163	0.200	0.878	0.147	0.102
1.250	1.16e-02	0.280	0.749	0.920	0.135	0.118	0.179	0.963	0.220	0.074
p+p										
p_T	CY	σ_{CY}	$\frac{S}{S+B}_{MPC}$	$\frac{S}{S+B}_{trig}$	s_{eff}	s_{sb}	s_{tot}	W	σ_w	s_w
0.625	9.81e-02	0.124	0.519	0.932	0.107	0.200	0.227	1.079	0.092	0.125
0.875	3.57e-02	0.124	0.698	0.932	0.122	0.135	0.181	0.860	0.121	0.084
1.250	1.36e-02	0.276	0.803	0.932	0.142	0.097	0.172	1.094	0.193	0.061

D.1.3 EMC Cluster/MPC π^0 Correlation Widths and Relative Errors

In this section, the terms that are present in the tables are as follows:

p_T	Transverse momentum of the bin center,
$\frac{S}{S+B}trig$	Fraction of counts in π^0 mass window, $0.1 < m_{inv} < 0.18$ GeV/c^2 that are actually signal π^0's (as opposed to background counts),
W	Gaussian width of the awayside peak,
s_w	Systematic error on the Gaussian width of the awayside peak.

Table D.7: Widths, **Relative** sys, stat errors for $3.0 < \eta < 3.8$, central $\pi^0 p_T = 2.5 - 3.0$ GeV/c.

d+Au 0-20%				
p_T	$\frac{S}{S+B}_{trig}$	W	σ_w	s_w
1.300	0.609	1.010	0.051	0.159
1.650	0.609	0.978	0.077	0.159
2.300	0.609	0.927	0.127	0.159
d+Au 20-40%				
p_T	$\frac{S}{S+B}_{trig}$	W	σ_w	s_w
1.300	0.662	0.923	0.054	0.151
1.650	0.662	0.832	0.066	0.151
2.300	0.662	0.735	0.092	0.151
d+Au 40-60%				
p_T	$\frac{S}{S+B}_{trig}$	W	σ_w	s_w
1.300	0.704	0.958	0.058	0.144
1.650	0.704	0.805	0.065	0.144
2.300	0.704	0.689	0.090	0.144
d+Au 60-88%				
p_T	$\frac{S}{S+B}_{trig}$	W	σ_w	s_w
1.300	0.754	0.893	0.052	0.137
1.650	0.754	0.800	0.073	0.137
2.300	0.754	0.757	0.109	0.137
p+p				
p_T	$\frac{S}{S+B}_{trig}$	W	σ_w	s_w
1.300	0.835	0.962	0.033	0.125
1.650	0.835	0.831	0.042	0.125
2.300	0.835	0.784	0.066	0.125

Table D.8: Widths, **Relative** sys, stat errors for $3.0 < \eta < 3.8$, central $\pi^0 p_T = 3.0 - 4.0$ GeV/c.

d+Au 0-20%				
p_T	$\frac{S}{S+B}_{trig}$	W	σ_w	s_w
1.300	0.787	0.936	0.053	0.132
1.650	0.787	0.779	0.073	0.132
2.300	0.787	0.780	0.089	0.132
d+Au 20-40%				
p_T	$\frac{S}{S+B}_{trig}$	W	σ_w	s_w
1.300	0.817	0.927	0.053	0.128
1.650	0.817	0.906	0.071	0.128
2.300	0.817	0.859	0.099	0.128
d+Au 40-60%				
p_T	$\frac{S}{S+B}_{trig}$	W	σ_w	s_w
1.300	0.838	1.004	0.058	0.124
1.650	0.838	1.001	0.080	0.124
2.300	0.838	0.709	0.123	0.124
d+Au 60-88%				
p_T	$\frac{S}{S+B}_{trig}$	W	σ_w	s_w
1.300	0.860	0.858	0.053	0.121
1.650	0.860	0.873	0.068	0.121
2.300	0.860	0.676	0.088	0.121
p+p				
p_T	$\frac{S}{S+B}_{trig}$	W	σ_w	s_w
1.300	0.897	0.946	0.036	0.115
1.650	0.897	0.788	0.052	0.115
2.300	0.897	0.686	0.068	0.115

Table D.9: Widths, **Relative** sys, stat errors for $3.0 < \eta < 3.8$, central $\pi^0 p_T = 4.0 - 7.0$ GeV/c.

d+Au 0-20%				
p_T	$\frac{S}{S+B}_{trig}$	W	σ_w	s_w
1.300	0.904	0.910	0.072	0.114
1.650	0.904	0.943	0.138	0.114
2.300	0.904	0.736	0.171	0.114
d+Au 20-40%				
p_T	$\frac{S}{S+B}_{trig}$	W	σ_w	s_w
1.300	0.911	1.005	0.079	0.113
1.650	0.911	0.838	0.091	0.113
2.300	0.911	0.636	0.130	0.113
d+Au 40-60%				
p_T	$\frac{S}{S+B}_{trig}$	W	σ_w	s_w
1.300	0.916	0.925	0.093	0.113
1.650	0.916	0.845	0.112	0.113
2.300	0.916	0.798	0.147	0.113
d+Au 60-88%				
p_T	$\frac{S}{S+B}_{trig}$	W	σ_w	s_w
1.300	0.920	0.861	0.086	0.112
1.650	0.920	0.742	0.102	0.112
2.300	0.920	0.532	0.101	0.112
p+p				
p_T	$\frac{S}{S+B}_{trig}$	W	σ_w	s_w
1.300	0.931	0.967	0.067	0.110
1.650	0.931	0.869	0.096	0.110
2.300	0.931	0.788	0.097	0.110

D.1.4 $I_{\rm dA}$, $J_{\rm dA}$ and Relative Errors

In this section, the terms that are present in the tables are as follows:

p_T	Transverse momentum of the bin center,
$I_{\rm dA}$	Ratio of CYs between d+Au and p+p,
$J_{\rm dA}$	Correlated di-hadron nuclear modification factor formed by taking the ratio between measured di-hadron yields in d+Au per $N_{\rm coll}$ and di-hadron yields in p+p. In practice, the formula $J_{\rm dA} = I_{dA,trig} \times R_{dA,trig}$ is used,
$s_{eff,IdA}$	Systematic error from yield extraction, input spectrum shape, energy scale, and GEANT with cancellations taken into account for $I_{\rm dA}$,
$s_{SB,IdA}$	Systematic error from contributions of the background under the π^0 peak to the CF with cancellations taken into account for $I_{\rm dA}$,
$s_{tot,IdA}$	Total systematic error on $I_{\rm dA}$,
$s_{gl,IdA}$	Zero global systematic error for $I_{\rm dA}$,
$s_{tot,JdA}$	Total systematic error on $J_{\rm dA}$,
$s_{gl,JdA}$	Global systematic error for $I_{\rm dA}$.

Table D.10: I_{dA},J_{dA} **relative** sys, stat errors for $3.0 < \eta < 3.8$, central $\pi^0 p_T = 2.5 - 3.0$ GeV/c.

d+Au 0-20%, $R_{dA} = 1.029 \pm 0.0198$ **(stat)** ± 0.048 **(sys)**										
p_T	I_{dA}	σ_{IdA}	J_{dA}	σ_{JdA}	$s_{eff,IdA}$	$s_{SB,IdA}$	$s_{tot,IdA}$	$s_{gl,Ida}$	$s_{tot,JdA}$	$s_{gl,JdA}$
0.625	0.532	0.092	0.548	0.095	0.074	0.312	0.321	0.000	0.324	0.100
0.875	0.397	0.109	0.409	0.111	0.064	0.261	0.269	0.000	0.273	0.100
1.250	0.612	0.150	0.630	0.151	0.078	0.225	0.238	0.000	0.243	0.100
d+Au 20-40%, $R_{dA} = 1.040 \pm 0.0214$ **(stat)** ± 0.047 **(sys)**										
p_T	I_{dA}	σ_{IdA}	J_{dA}	σ_{JdA}	$s_{eff,IdA}$	$s_{SB,IdA}$	$s_{tot,IdA}$	$s_{gl,Ida}$	$s_{tot,JdA}$	$s_{gl,JdA}$
0.625	0.580	0.095	0.604	0.097	0.071	0.303	0.311	0.000	0.315	0.100
0.875	0.580	0.133	0.603	0.135	0.065	0.248	0.257	0.000	0.261	0.100
1.250	0.701	0.140	0.730	0.142	0.079	0.209	0.223	0.000	0.228	0.100
d+Au 40-60%, $R_{dA} = 1.021 \pm 0.0234$ **(stat)** ± 0.046 **(sys)**										
p_T	I_{dA}	σ_{IdA}	J_{dA}	σ_{JdA}	$s_{eff,IdA}$	$s_{SB,IdA}$	$s_{tot,IdA}$	$s_{gl,Ida}$	$s_{tot,JdA}$	$s_{gl,JdA}$
0.625	0.584	0.105	0.596	0.107	0.069	0.289	0.298	0.000	0.301	0.100
0.875	0.710	0.127	0.725	0.129	0.065	0.233	0.242	0.000	0.247	0.100
1.250	0.940	0.198	0.960	0.200	0.078	0.193	0.208	0.000	0.213	0.100
d+Au 60-88%, $R_{dA} = 1.054 \pm 0.0262$ **(stat)** ± 0.046 **(sys)**										
p_T	I_{dA}	σ_{IdA}	J_{dA}	σ_{JdA}	$s_{eff,IdA}$	$s_{SB,IdA}$	$s_{tot,IdA}$	$s_{gl,Ida}$	$s_{tot,JdA}$	$s_{gl,JdA}$
0.625	0.842	0.113	0.887	0.116	0.068	0.264	0.273	0.000	0.276	0.100
0.875	1.046	0.175	1.103	0.177	0.064	0.205	0.215	0.000	0.220	0.100
1.250	1.034	0.196	1.090	0.197	0.076	0.169	0.185	0.000	0.190	0.100

Table D.11: I_{dA},J_{dA} **relative** sys, stat errors for $3.0 < \eta < 3.8$, central $\pi^0 p_T = 3.0 - 4.0$ GeV/c.

d+Au 0-20%, $R_{dA} = 1.063 \pm 0.0191$ **(stat)** ± 0.057 **(sys)**										
p_T	I_{dA}	σ_{IdA}	J_{dA}	σ_{JdA}	$s_{eff,IdA}$	$s_{SB,IdA}$	$s_{tot,IdA}$	$s_{gl,Ida}$	$s_{tot,JdA}$	$s_{gl,JdA}$
0.625	0.458	0.111	0.486	0.112	0.074	0.287	0.296	0.000	0.302	0.100
0.875	0.499	0.119	0.531	0.120	0.064	0.221	0.230	0.000	0.237	0.100
1.250	0.704	0.161	0.748	0.162	0.078	0.174	0.191	0.000	0.199	0.100
d+Au 20-40%, $R_{dA} = 1.064 \pm 0.0227$ **(stat)** ± 0.057 **(sys)**										
p_T	I_{dA}	σ_{IdA}	J_{dA}	σ_{JdA}	$s_{eff,IdA}$	$s_{SB,IdA}$	$s_{tot,IdA}$	$s_{gl,Ida}$	$s_{tot,JdA}$	$s_{gl,JdA}$
0.625	0.603	0.101	0.641	0.104	0.071	0.280	0.289	0.000	0.295	0.100
0.875	0.719	0.144	0.765	0.145	0.065	0.213	0.223	0.000	0.230	0.100
1.250	0.801	0.188	0.852	0.189	0.079	0.165	0.183	0.000	0.191	0.100
d+Au 40-60%, $R_{dA} = 1.072 \pm 0.0240$ **(stat)** ± 0.056 **(sys)**										
p_T	I_{dA}	σ_{IdA}	J_{dA}	σ_{JdA}	$s_{eff,IdA}$	$s_{SB,IdA}$	$s_{tot,IdA}$	$s_{gl,Ida}$	$s_{tot,JdA}$	$s_{gl,JdA}$
0.625	0.699	0.113	0.749	0.115	0.069	0.268	0.277	0.000	0.283	0.100
0.875	1.001	0.170	1.073	0.171	0.065	0.202	0.212	0.000	0.219	0.100
1.250	0.772	0.175	0.828	0.177	0.078	0.154	0.172	0.000	0.181	0.100
d+Au 60-88%, $R_{dA} = 1.062 \pm 0.0285$ **(stat)** ± 0.056 **(sys)**										
p_T	I_{dA}	σ_{IdA}	J_{dA}	σ_{JdA}	$s_{eff,IdA}$	$s_{SB,IdA}$	$s_{tot,IdA}$	$s_{gl,Ida}$	$s_{tot,JdA}$	$s_{gl,JdA}$
0.625	0.862	0.101	0.916	0.105	0.068	0.245	0.254	0.000	0.260	0.100
0.875	1.235	0.214	1.312	0.216	0.064	0.178	0.189	0.000	0.197	0.100
1.250	1.067	0.169	1.134	0.171	0.076	0.136	0.156	0.000	0.165	0.100

Table D.12: I_{dA},J_{dA} **relative** sys, stat errors for $3.0 < \eta < 3.8$, central $\pi^0 p_T = 4.0 - 7.0$ GeV/c.

d+Au 0-20%, $R_{dA} = 1.018 \pm 0.0236$ **(stat)** ± 0.063 **(sys)**										
p_T	I_{dA}	σ_{IdA}	J_{dA}	σ_{JdA}	$s_{eff,IdA}$	$s_{SB,IdA}$	$s_{tot,IdA}$	$s_{gl,Ida}$	$s_{tot,JdA}$	$s_{gl,JdA}$
0.625	0.562	0.284	0.572	0.285	0.074	0.270	0.280	0.000	0.287	0.100
0.875	0.673	0.308	0.685	0.309	0.064	0.194	0.205	0.000	0.214	0.100
1.250	0.511	0.330	0.520	0.331	0.078	0.141	0.161	0.000	0.173	0.100
d+Au 20-40%, $R_{dA} = 1.078 \pm 0.0286$ **(stat)** ± 0.062 **(sys)**										
p_T	I_{dA}	σ_{IdA}	J_{dA}	σ_{JdA}	$s_{eff,IdA}$	$s_{SB,IdA}$	$s_{tot,IdA}$	$s_{gl,Ida}$	$s_{tot,JdA}$	$s_{gl,JdA}$
0.625	0.677	0.184	0.729	0.186	0.071	0.266	0.276	0.000	0.283	0.100
0.875	0.574	0.187	0.619	0.189	0.065	0.192	0.202	0.000	0.212	0.100
1.250	0.593	0.392	0.639	0.393	0.079	0.137	0.158	0.000	0.170	0.100
d+Au 40-60%, $R_{dA} = 1.103 \pm 0.0321$ **(stat)** ± 0.062 **(sys)**										
p_T	I_{dA}	σ_{IdA}	J_{dA}	σ_{JdA}	$s_{eff,IdA}$	$s_{SB,IdA}$	$s_{tot,IdA}$	$s_{gl,Ida}$	$s_{tot,JdA}$	$s_{gl,JdA}$
0.625	0.670	0.216	0.739	0.219	0.069	0.256	0.265	0.000	0.273	0.100
0.875	0.780	0.183	0.860	0.186	0.065	0.183	0.195	0.000	0.204	0.100
1.250	0.661	0.396	0.729	0.397	0.078	0.131	0.153	0.000	0.165	0.100
d+Au 60-88%, $R_{dA} = 1.093 \pm 0.0252$ **(stat)** ± 0.062 **(sys)**										
p_T	I_{dA}	σ_{IdA}	J_{dA}	σ_{JdA}	$s_{eff,IdA}$	$s_{SB,IdA}$	$s_{tot,IdA}$	$s_{gl,Ida}$	$s_{tot,JdA}$	$s_{gl,JdA}$
0.625	0.840	0.162	0.918	0.164	0.068	0.234	0.244	0.000	0.252	0.100
0.875	0.959	0.209	1.047	0.210	0.064	0.163	0.175	0.000	0.186	0.100
1.250	0.851	0.393	0.930	0.394	0.076	0.118	0.140	0.000	0.153	0.100

D.1.5 Central Arm π^0 and MPC π^0 $R_{\rm dA}$ values

In this section, the terms that are present in the tables are as follows:

p_T	Transverse momentum of the bin center,
$R_{\rm dA}$	Single hadron nuclear modification factor for central arm π^0's,
s_{RdA}	Systematic error for central arm π^0 $R_{\rm dA}$,
$R_{dA,MPC}$	Single hadron nuclear modification factor for forward MPC π^0's,
$s_{RdA,MPC}$	Systematic error for forward MPC π^0's.

Table D.13: R_{dA} **relative** sys, stat errors for central $\pi^0 p_T = 2.5 - 3.0$ GeV/c.

d+Au 0-20%						
p_T	R_{dA}	σ_{RdA}	s_{RdA}	$R_{dA,MPC}$	$\sigma_{RdA,MPC}$	$s_{RdA,MPC}$
0.625	1.029	0.020	0.048	0.198	0.019	0.074
0.875	1.029	0.020	0.048	0.230	0.018	0.064
1.250	1.029	0.020	0.048	0.289	0.030	0.088
d+Au 20-40%						
p_T	R_{dA}	σ_{RdA}	s_{RdA}	$R_{dA,MPC}$	$\sigma_{RdA,MPC}$	$s_{RdA,MPC}$
0.625	1.040	0.021	0.047	0.288	0.019	0.071
0.875	1.040	0.021	0.047	0.335	0.018	0.065
1.250	1.040	0.021	0.047	0.430	0.031	0.090
d+Au 40-60%						
p_T	R_{dA}	σ_{RdA}	s_{RdA}	$R_{dA,MPC}$	$\sigma_{RdA,MPC}$	$s_{RdA,MPC}$
0.625	1.021	0.023	0.046	0.391	0.018	0.069
0.875	1.021	0.023	0.046	0.474	0.017	0.065
1.250	1.021	0.023	0.046	0.594	0.031	0.089
d+Au 60-88%						
p_T	R_{dA}	σ_{RdA}	s_{RdA}	$R_{dA,MPC}$	$\sigma_{RdA,MPC}$	$s_{RdA,MPC}$
0.625	1.054	0.026	0.046	0.616	0.016	0.068
0.875	1.054	0.026	0.046	0.702	0.016	0.064
1.250	1.054	0.026	0.046	0.799	0.028	0.085

Table D.14: R_{dA} **relative** sys, stat errors for central $\pi^0 p_T = 3.0 - 4.0$ GeV/c.

d+Au 0-20%						
p_T	R_{dA}	σ_{RdA}	s_{RdA}	$R_{dA,MPC}$	$\sigma_{RdA,MPC}$	$s_{RdA,MPC}$
0.625	1.063	0.019	0.057	0.198	0.019	0.074
0.875	1.063	0.019	0.057	0.230	0.018	0.064
1.250	1.063	0.019	0.057	0.289	0.030	0.088
d+Au 20-40%						
p_T	R_{dA}	σ_{RdA}	s_{RdA}	$R_{dA,MPC}$	$\sigma_{RdA,MPC}$	$s_{RdA,MPC}$
0.625	1.064	0.023	0.057	0.288	0.019	0.071
0.875	1.064	0.023	0.057	0.335	0.018	0.065
1.250	1.064	0.023	0.057	0.430	0.031	0.090
d+Au 40-60%						
p_T	R_{dA}	σ_{RdA}	s_{RdA}	$R_{dA,MPC}$	$\sigma_{RdA,MPC}$	$s_{RdA,MPC}$
0.625	1.072	0.024	0.056	0.391	0.018	0.069
0.875	1.072	0.024	0.056	0.474	0.017	0.065
1.250	1.072	0.024	0.056	0.594	0.031	0.089
d+Au 60-88%						
p_T	R_{dA}	σ_{RdA}	s_{RdA}	$R_{dA,MPC}$	$\sigma_{RdA,MPC}$	$s_{RdA,MPC}$
0.625	1.062	0.029	0.056	0.616	0.016	0.068
0.875	1.062	0.029	0.056	0.702	0.016	0.064
1.250	1.062	0.029	0.056	0.799	0.028	0.085

Table D.15: R_{dA} **relative** sys, stat errors for central $\pi^0 p_T = 4.0 - 7.0$ GeV/c.

d+Au 0-20%						
p_T	R_{dA}	σ_{RdA}	s_{RdA}	$R_{dA,MPC}$	$\sigma_{RdA,MPC}$	$s_{RdA,MPC}$
0.625	1.018	0.024	0.063	0.198	0.019	0.074
0.875	1.018	0.024	0.063	0.230	0.018	0.064
1.250	1.018	0.024	0.063	0.289	0.030	0.088
d+Au 20-40%						
p_T	R_{dA}	σ_{RdA}	s_{RdA}	$R_{dA,MPC}$	$\sigma_{RdA,MPC}$	$s_{RdA,MPC}$
0.625	1.078	0.029	0.062	0.288	0.019	0.071
0.875	1.078	0.029	0.062	0.335	0.018	0.065
1.250	1.078	0.029	0.062	0.430	0.031	0.090
d+Au 40-60%						
p_T	R_{dA}	σ_{RdA}	s_{RdA}	$R_{dA,MPC}$	$\sigma_{RdA,MPC}$	$s_{RdA,MPC}$
0.625	1.103	0.032	0.062	0.391	0.018	0.069
0.875	1.103	0.032	0.062	0.474	0.017	0.065
1.250	1.103	0.032	0.062	0.594	0.031	0.089
d+Au 60-88%						
p_T	R_{dA}	σ_{RdA}	s_{RdA}	$R_{dA,MPC}$	$\sigma_{RdA,MPC}$	$s_{RdA,MPC}$
0.625	1.093	0.025	0.062	0.616	0.016	0.068
0.875	1.093	0.025	0.062	0.702	0.016	0.064
1.250	1.093	0.025	0.062	0.799	0.028	0.085

D.2 Correlation Functions

D.2.1 EMC π^0/MPC π^0 Correlations

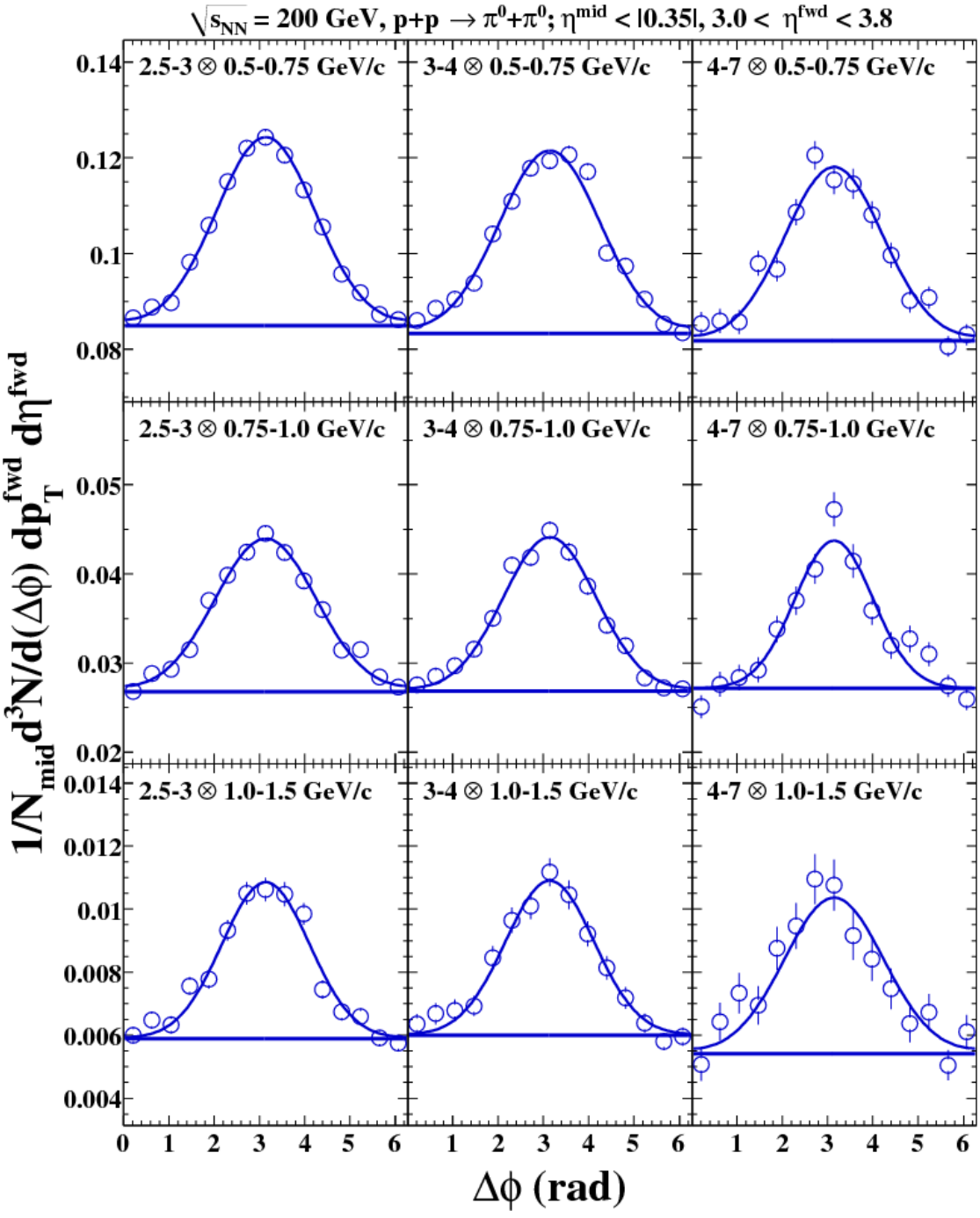

Figure D.1: **p+p, Rapidity = 3.0-3.8:** Correlation functions and fits for all p_T bins.

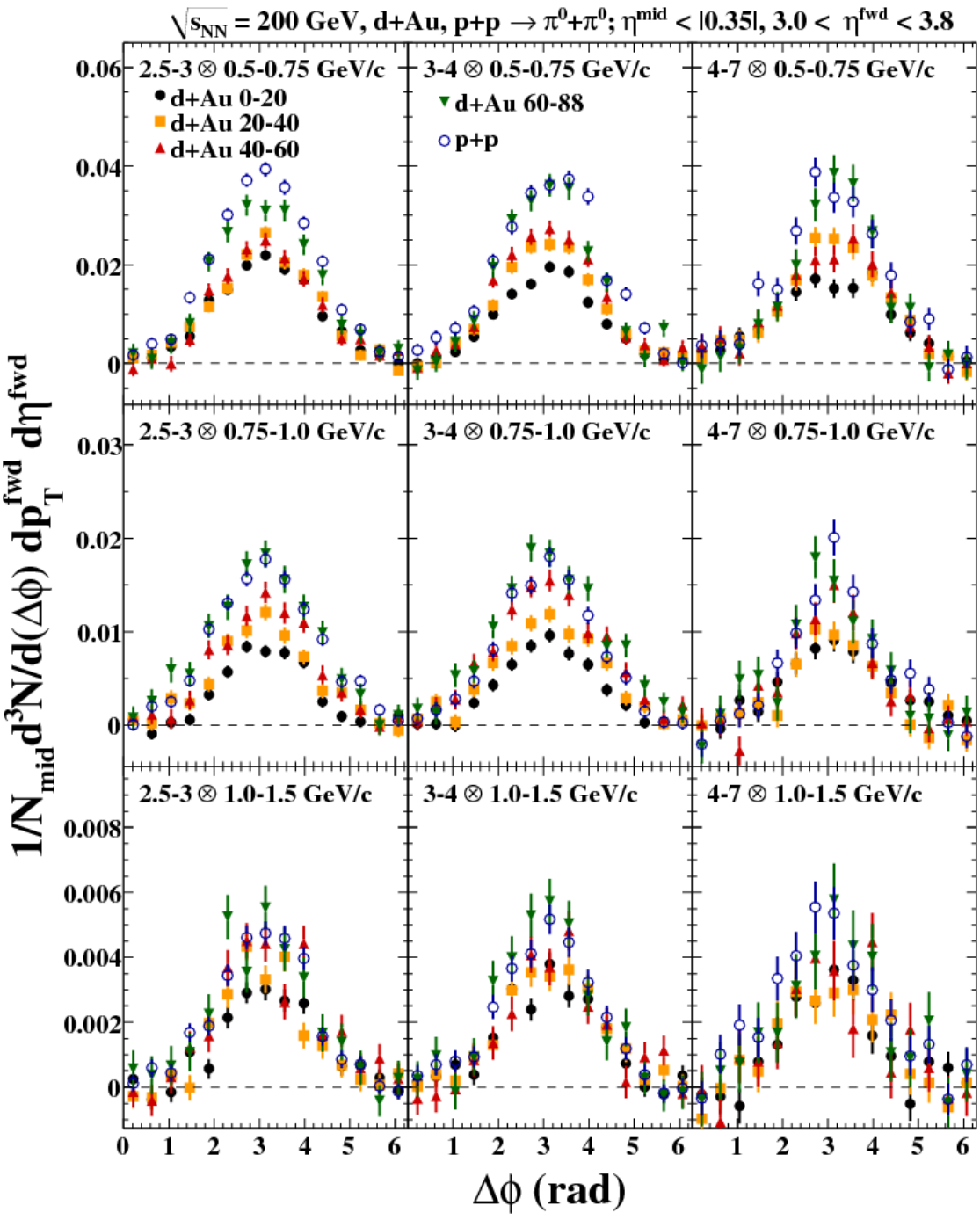

Figure D.2: **Rapidity = 3.0-3.8:** Background subtracted correlation functions and fits for all centralities and p_T bins.

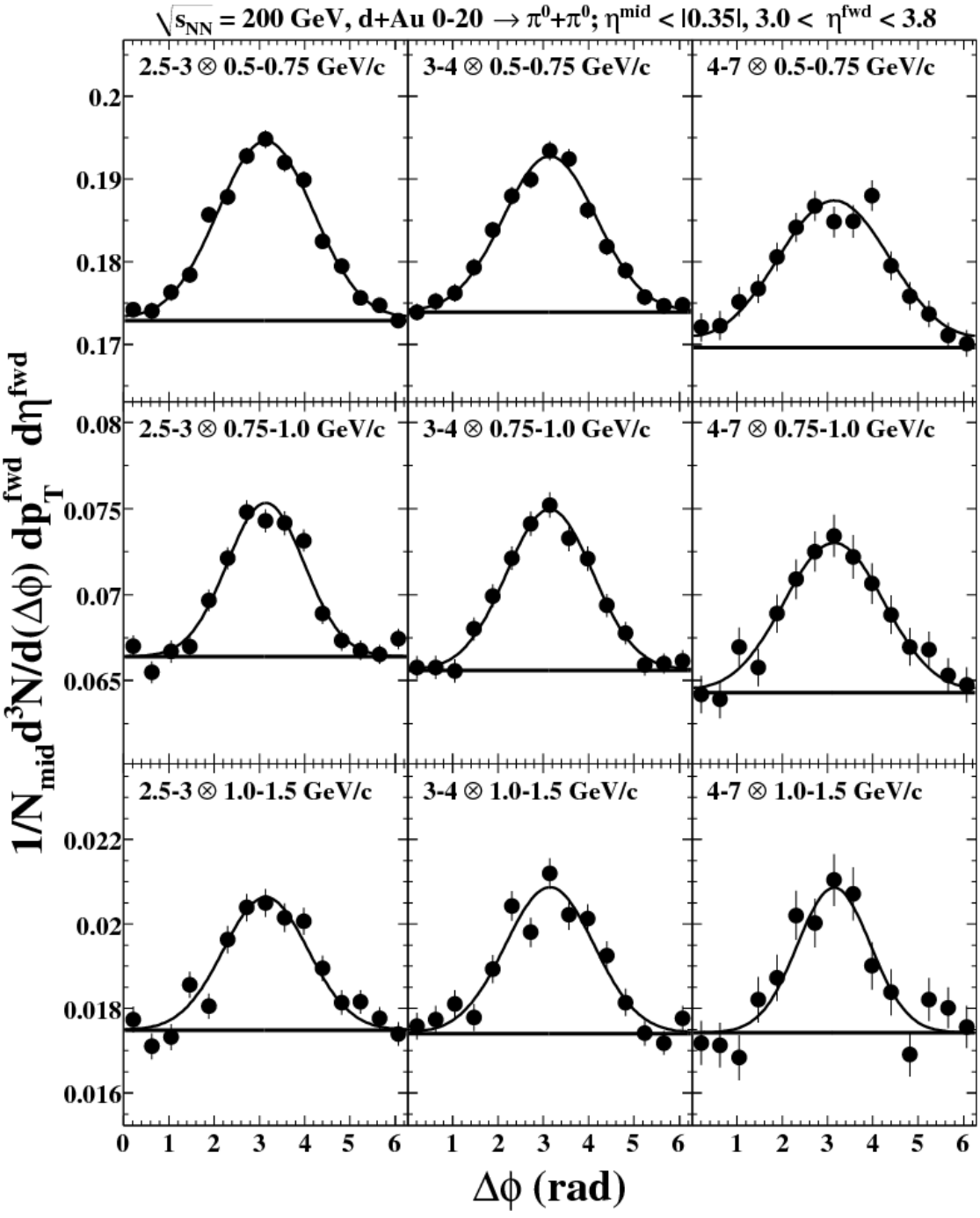

Figure D.3: **d+Au 0-20%, Rapidity = 3.0-3.8:** Correlation functions and fits for all p_T bins.

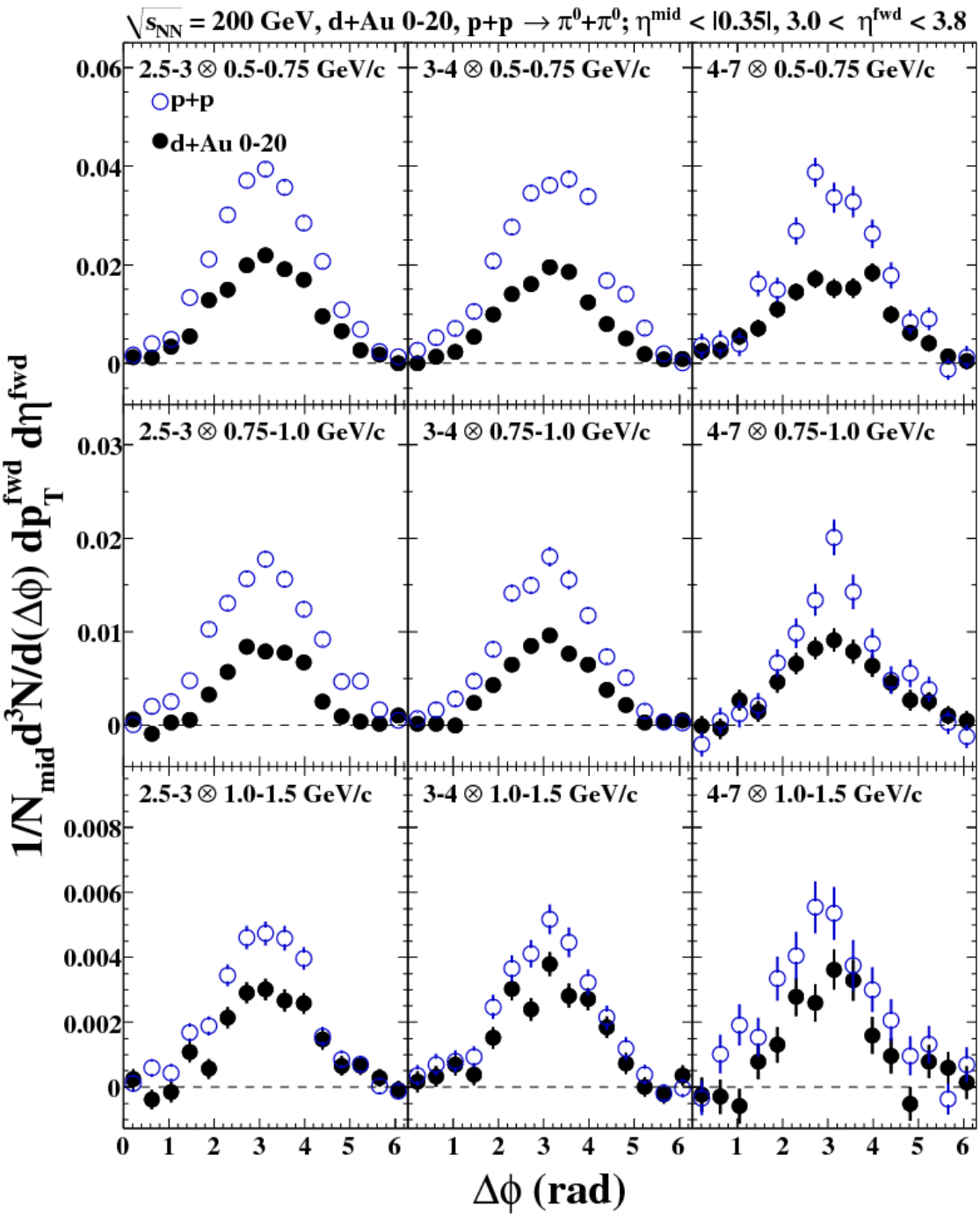

Figure D.4: **d+Au 0-20%, Rapidity = 3.0-3.8:** Background subtracted correlation functions and fits for all p_T bins. The p+p reference is in blue.

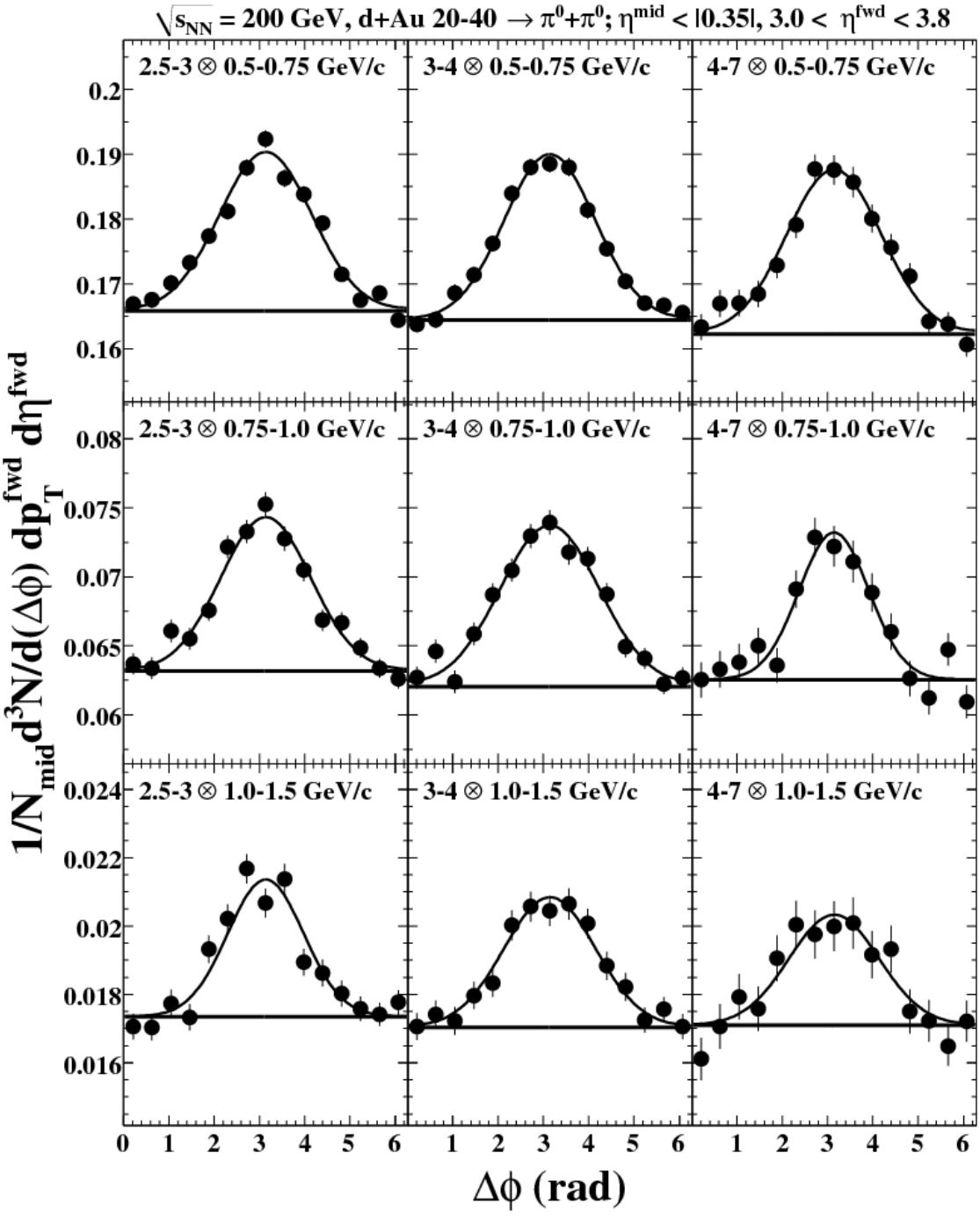

Figure D.5: **dAu 20-40%, Rapidity = 3.0-3.8:** Correlation functions and fits for all p_T bins.

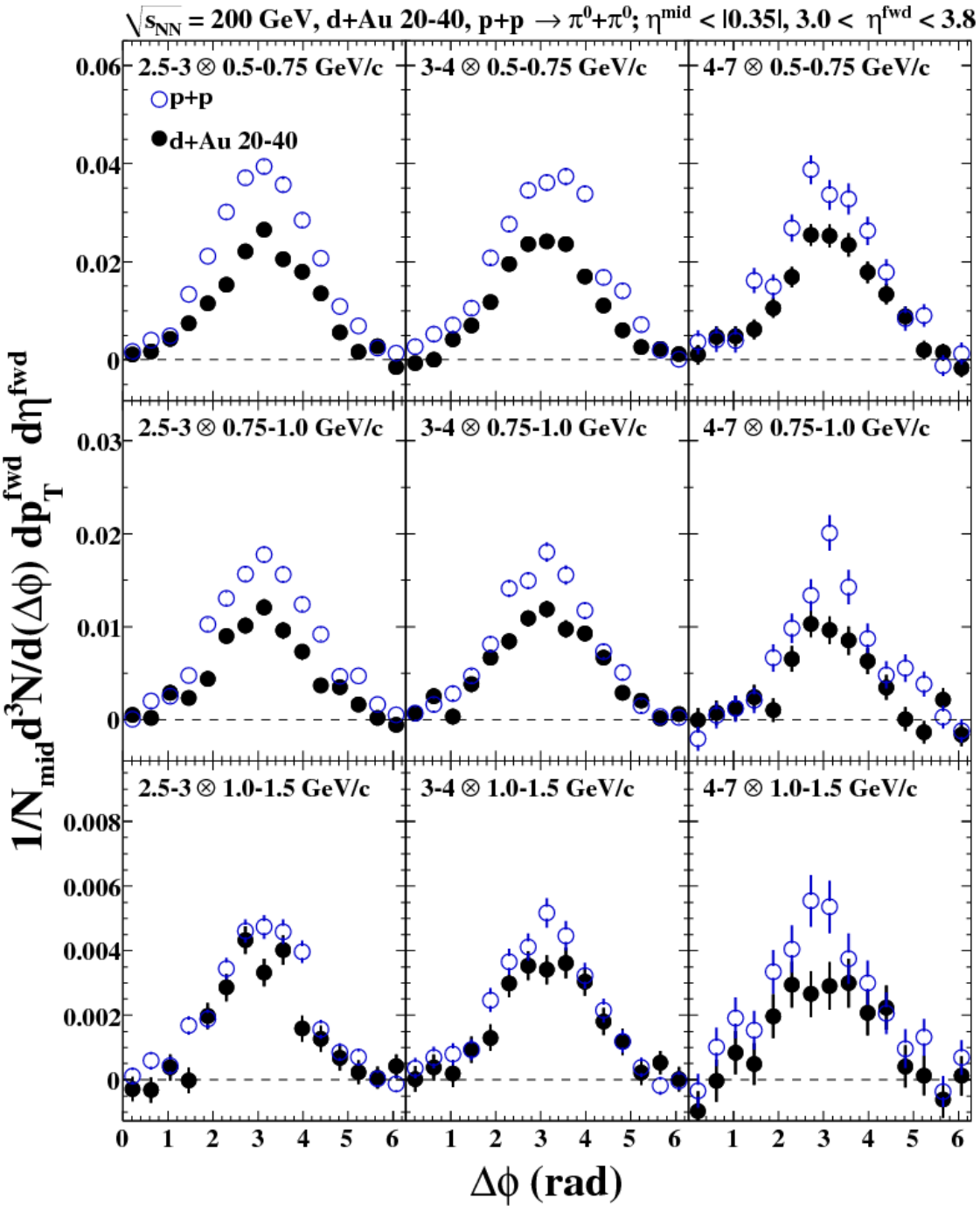

Figure D.6: **dAu 20-40%, Rapidity = 3.0-3.8:** Background subtracted correlation functions and fits for all p_T bins. The p+p reference is in blue.

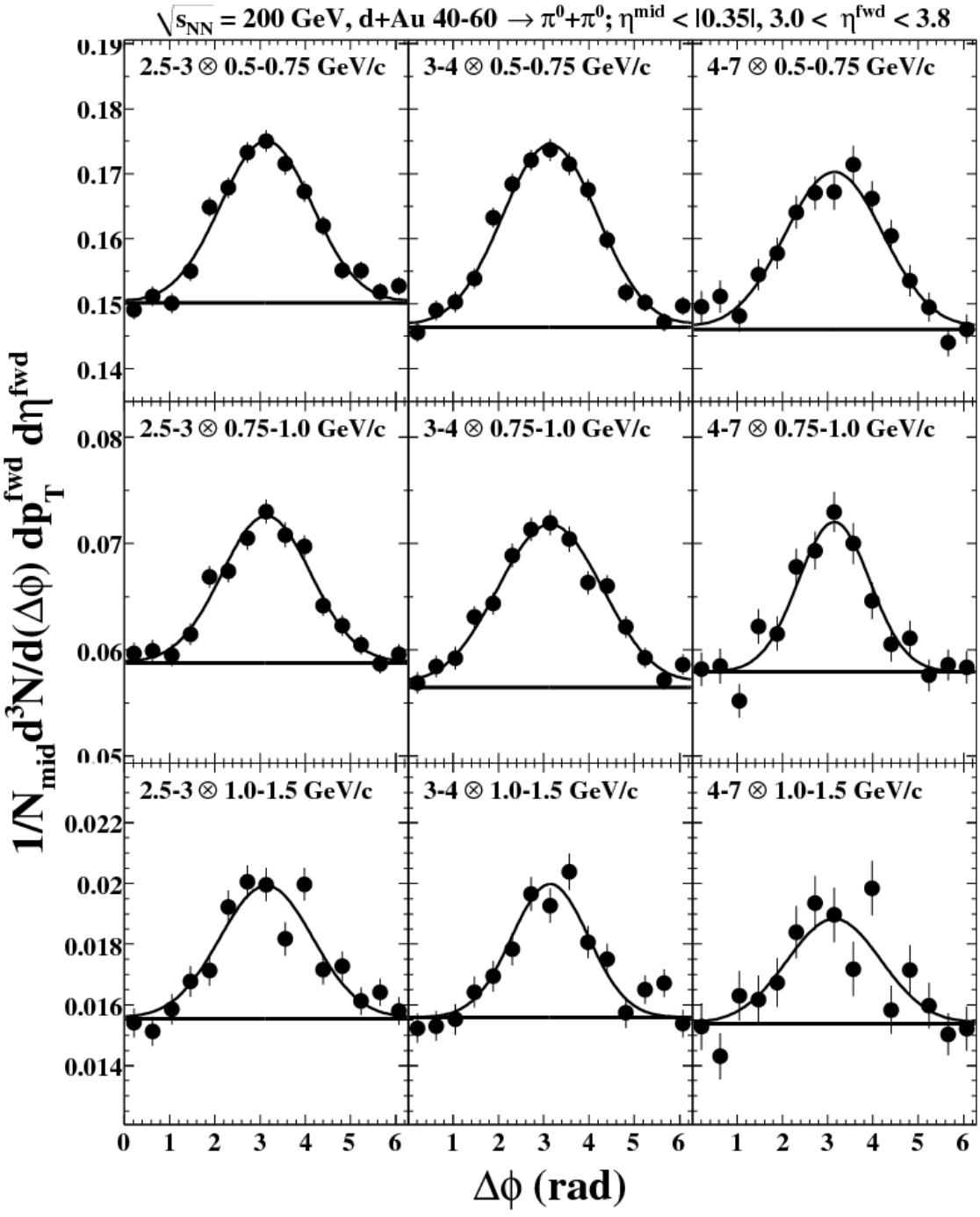

Figure D.7: **dAu 40-60%, Rapidity = 3.0-3.8:** Correlation functions and fits for all p_T bins.

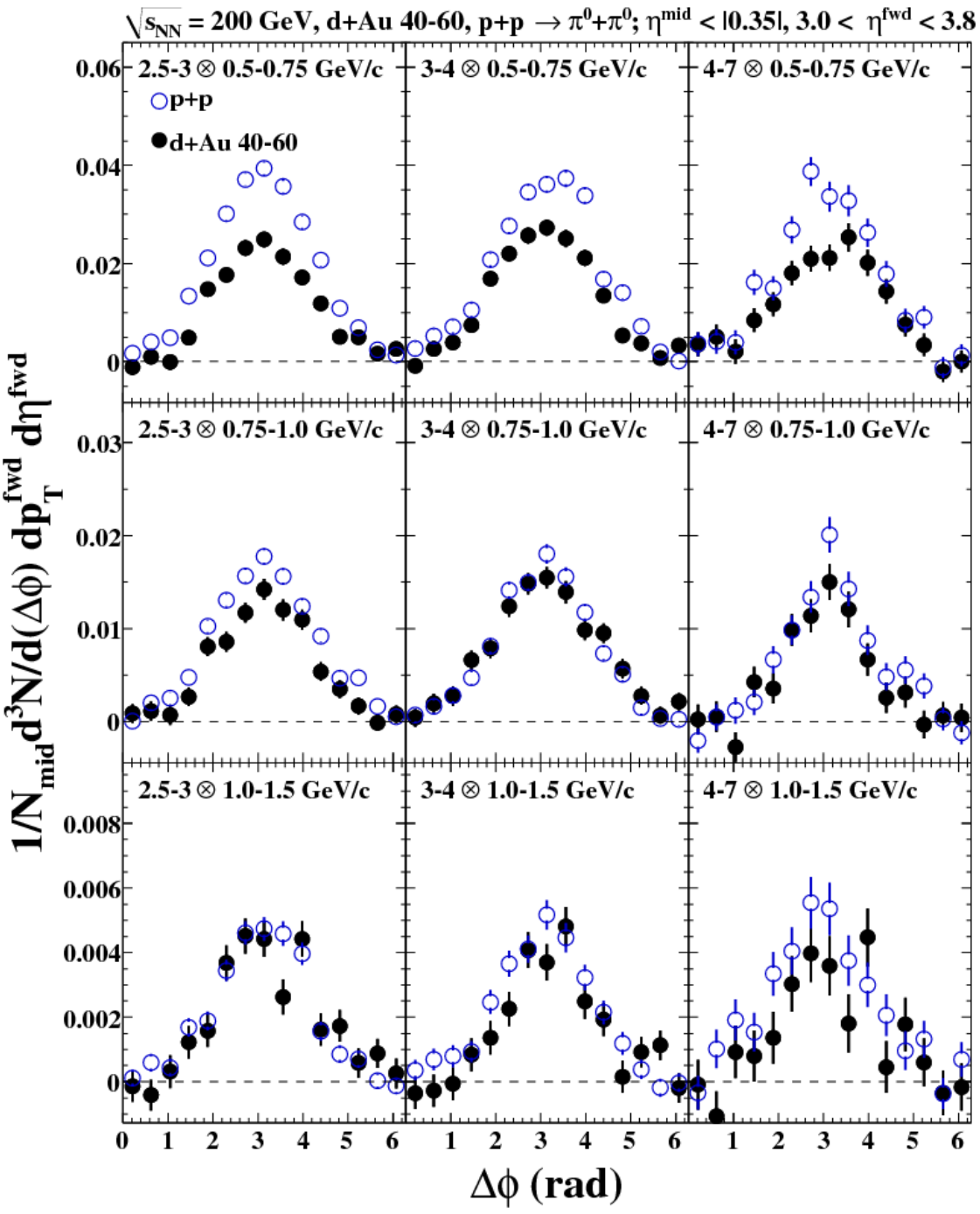

Figure D.8: **dAu 40-60%, Rapidity = 3.0-3.8:** Background subtracted correlation functions and fits for all p_T bins. The p+p reference is in blue.

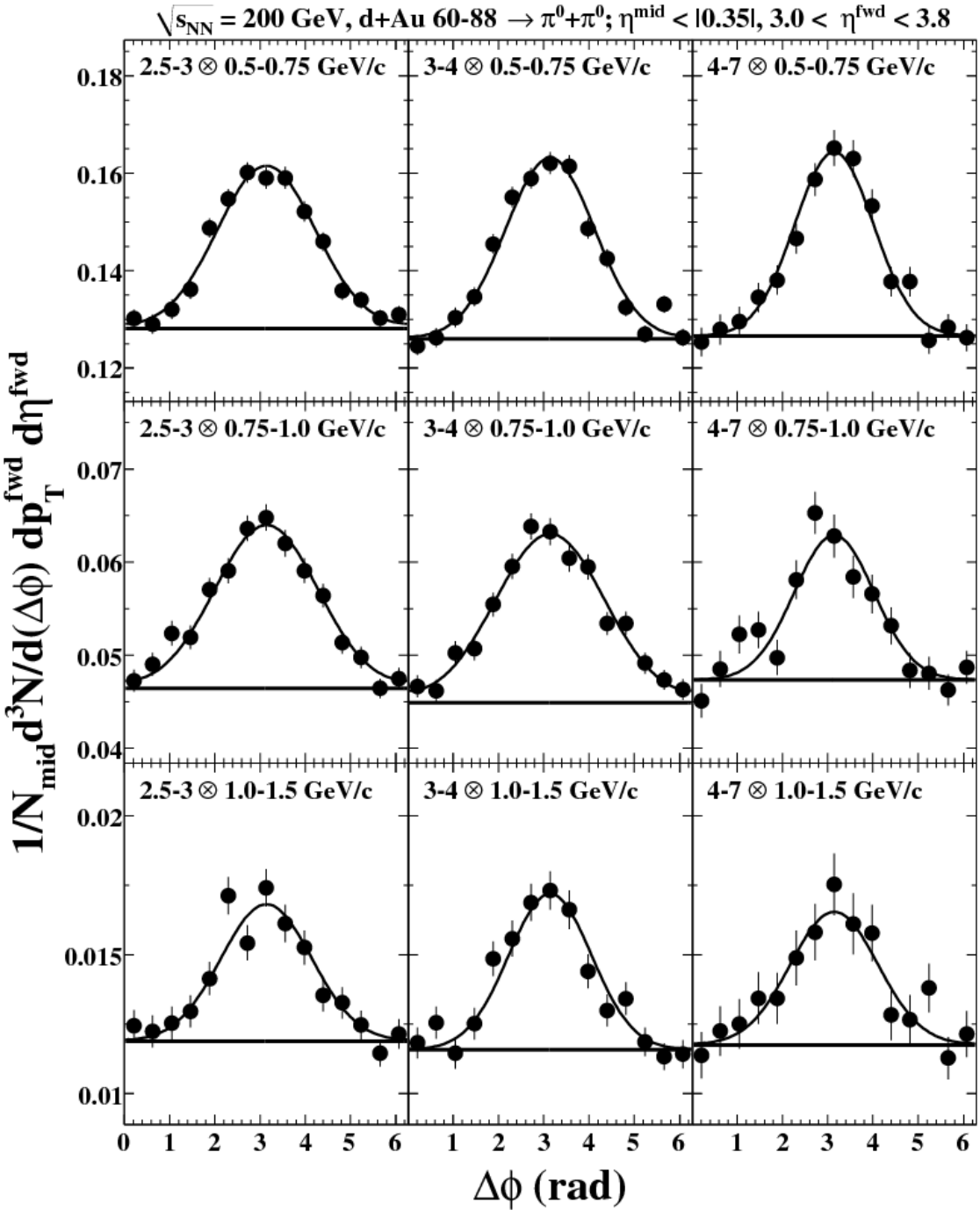

Figure D.9: **dAu 60-88%, Rapidity = 3.0-3.8:** Correlation functions and fits for all p_T bins.

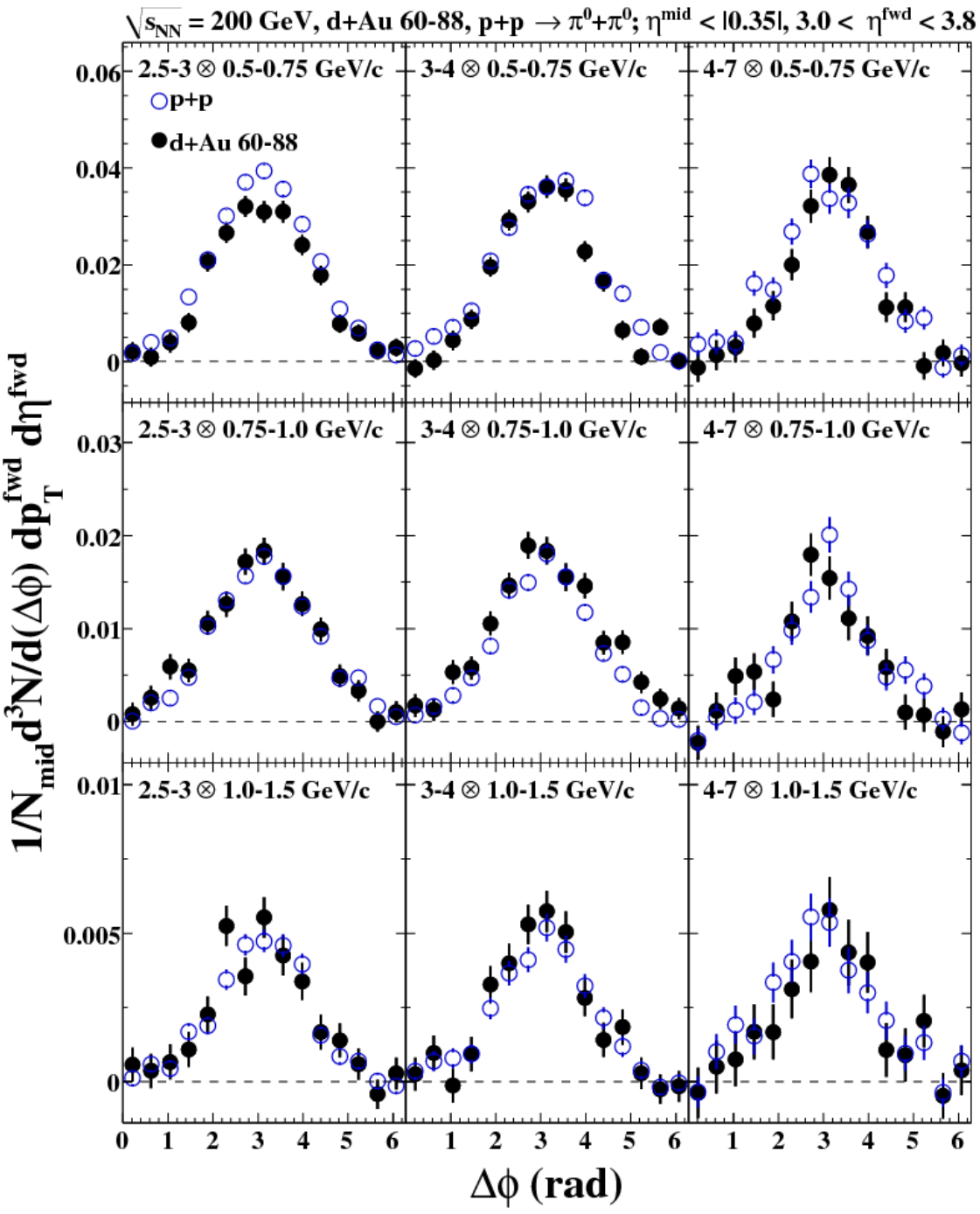

Figure D.10: **dAu 60-88%, Rapidity = 3.0-3.8:** Background subtracted correlation functions and fits for all p_T bins. The p+p reference is in blue.

D.2.2 EMC π^0/MPC Cluster Correlations

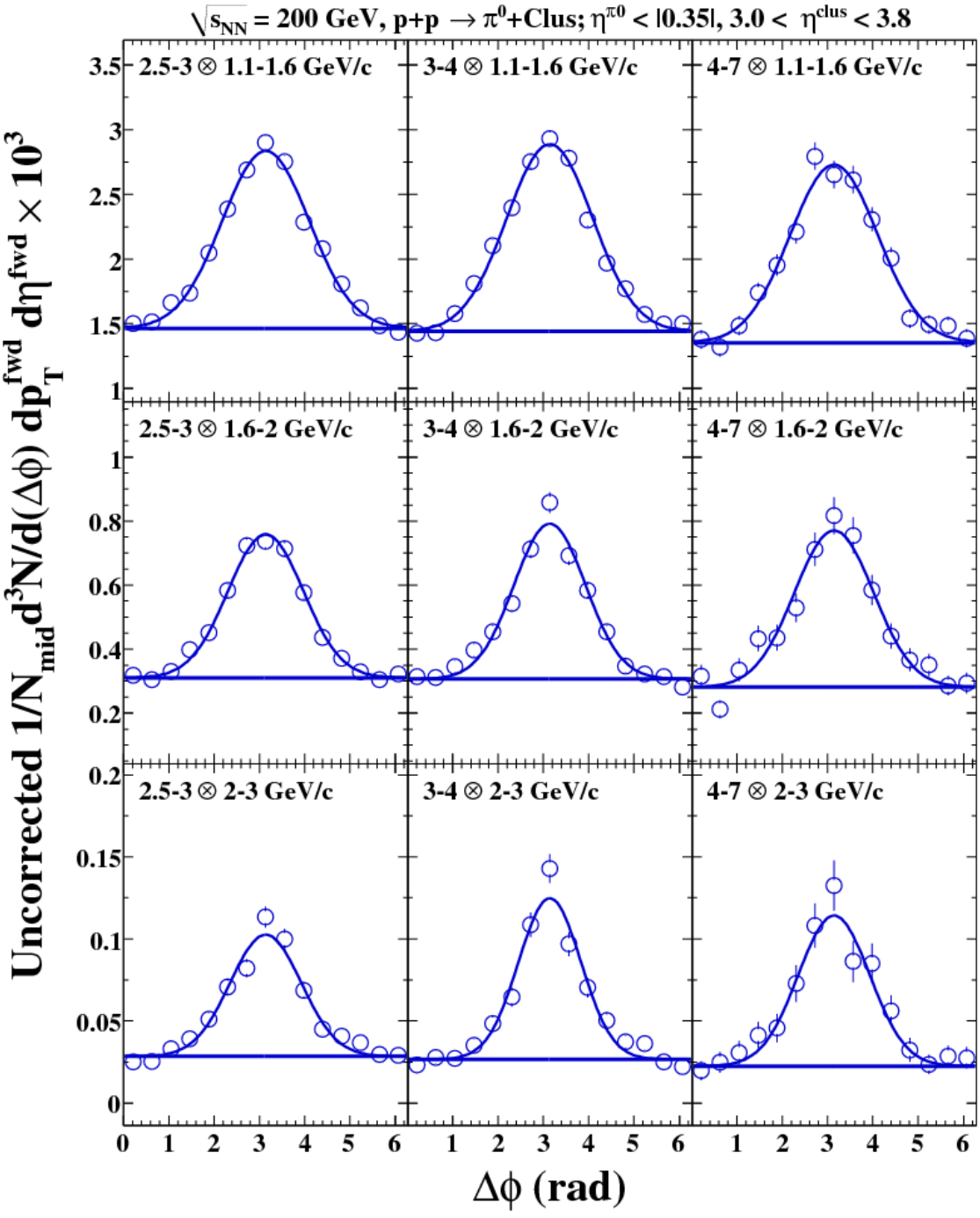

Figure D.11: **p+p, Rapidity = 3.0-3.8:** Correlation functions and fits for all p_T bins.

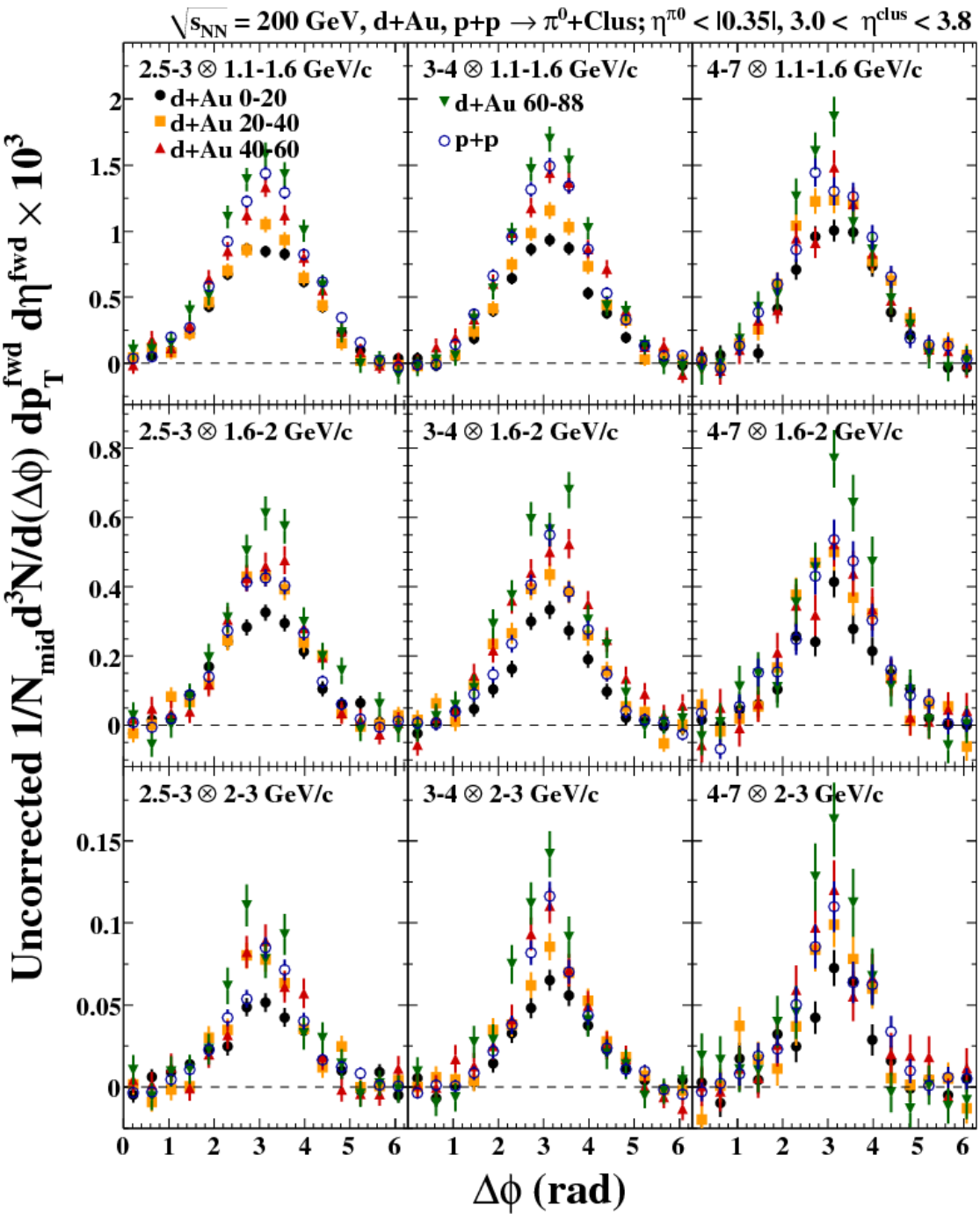

Figure D.12: **Rapidity = 3.0-3.8:** Background subtracted correlation functions and fits for all centralities and p_T bins.

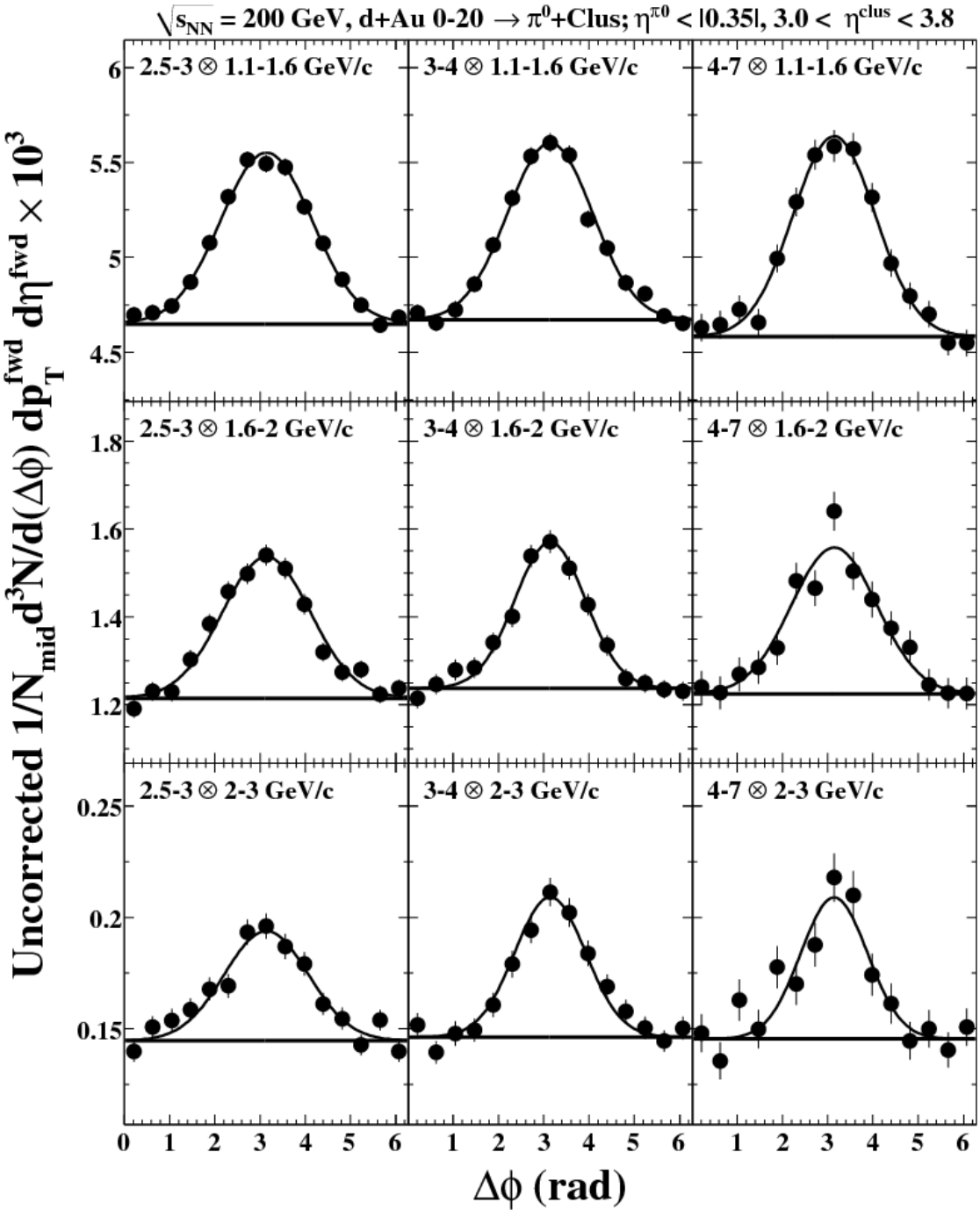

Figure D.13: **d+Au 0-20%, Rapidity = 3.0-3.8:** Correlation functions and fits for all p_T bins.

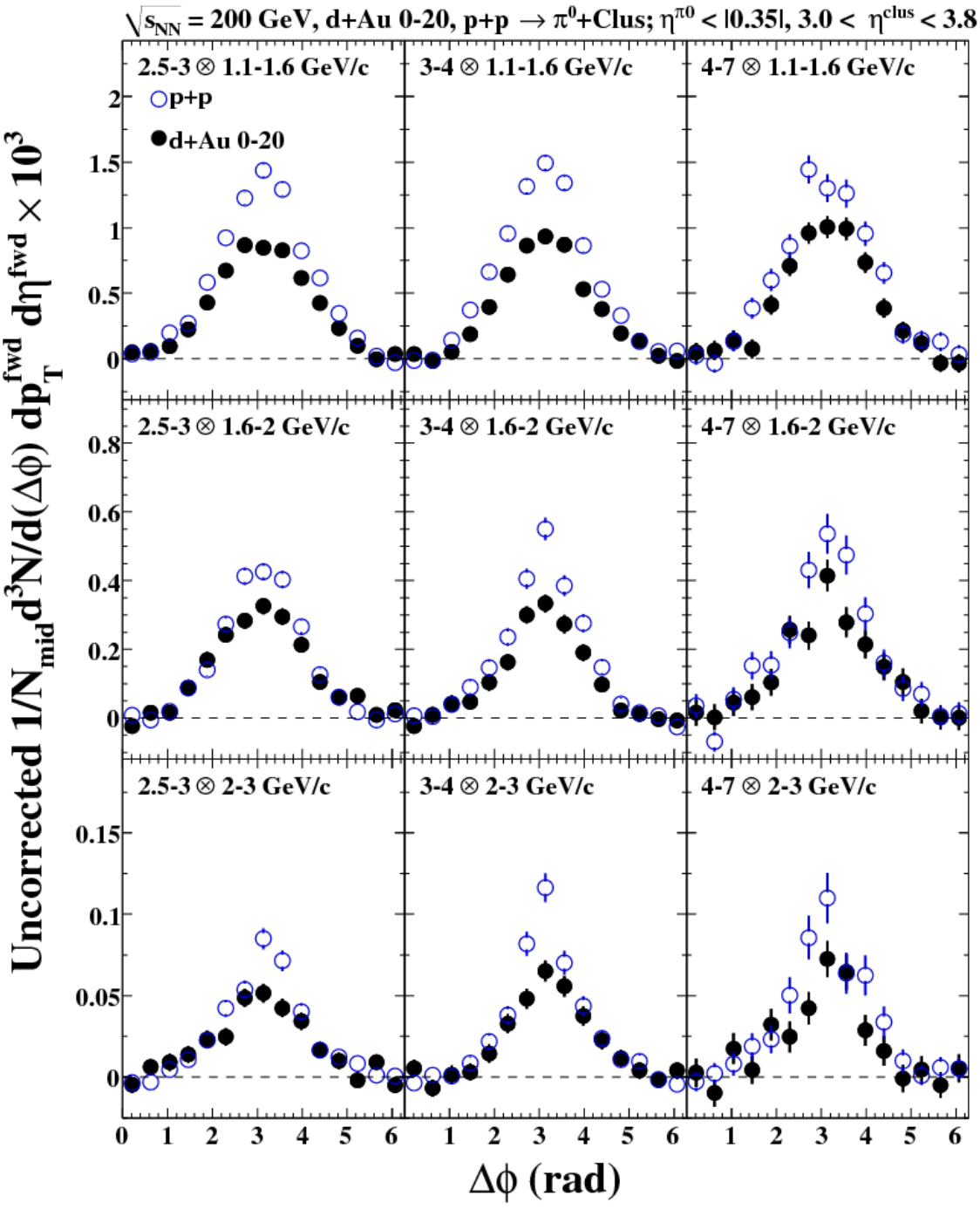

Figure D.14: **d+Au 0-20%, Rapidity = 3.0-3.8:** Background subtracted correlation functions and fits for all p_T bins. The p+p reference is in blue.

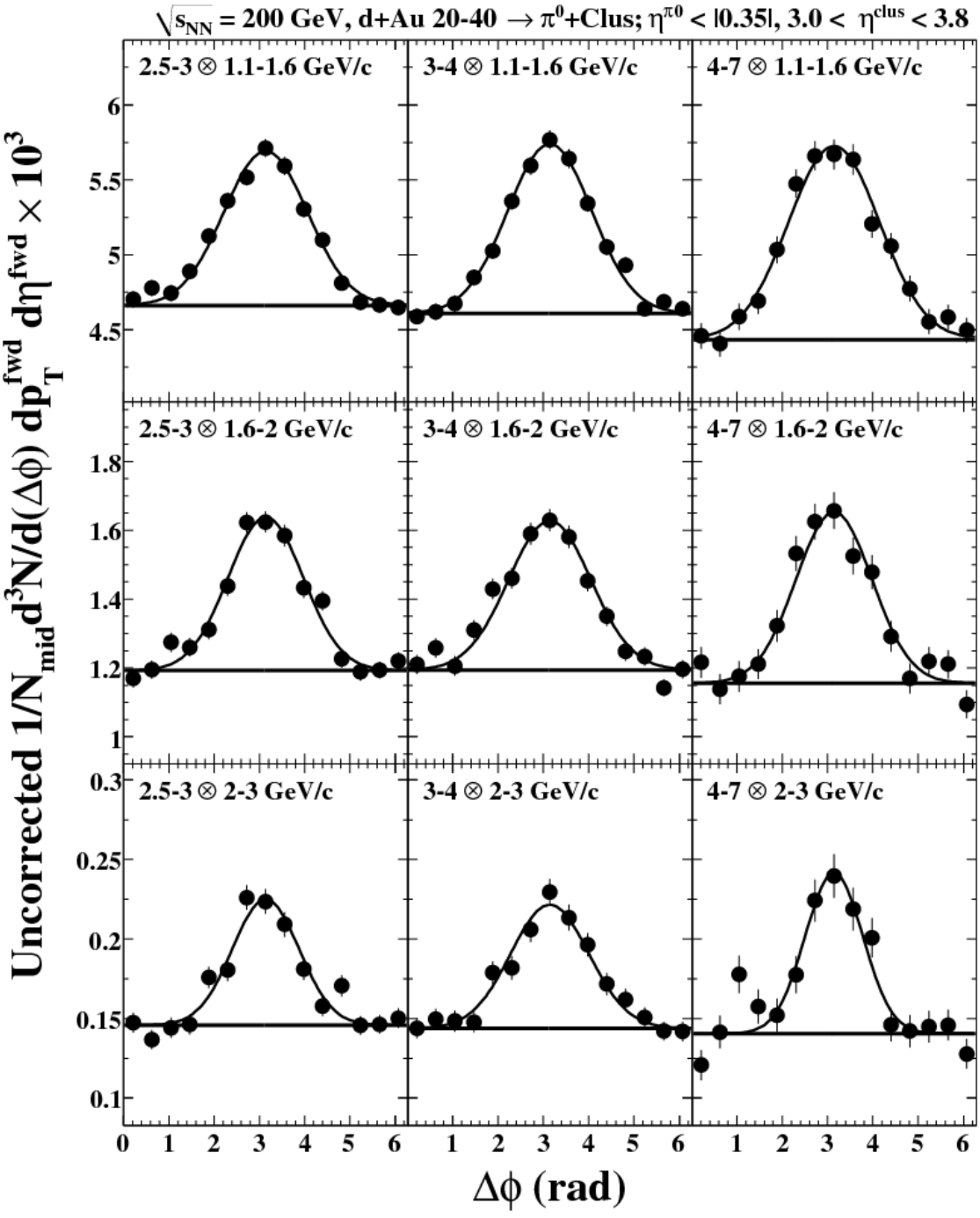

Figure D.15: **dAu 20-40%, Rapidity = 3.0-3.8:** Correlation functions and fits for all p_T bins.

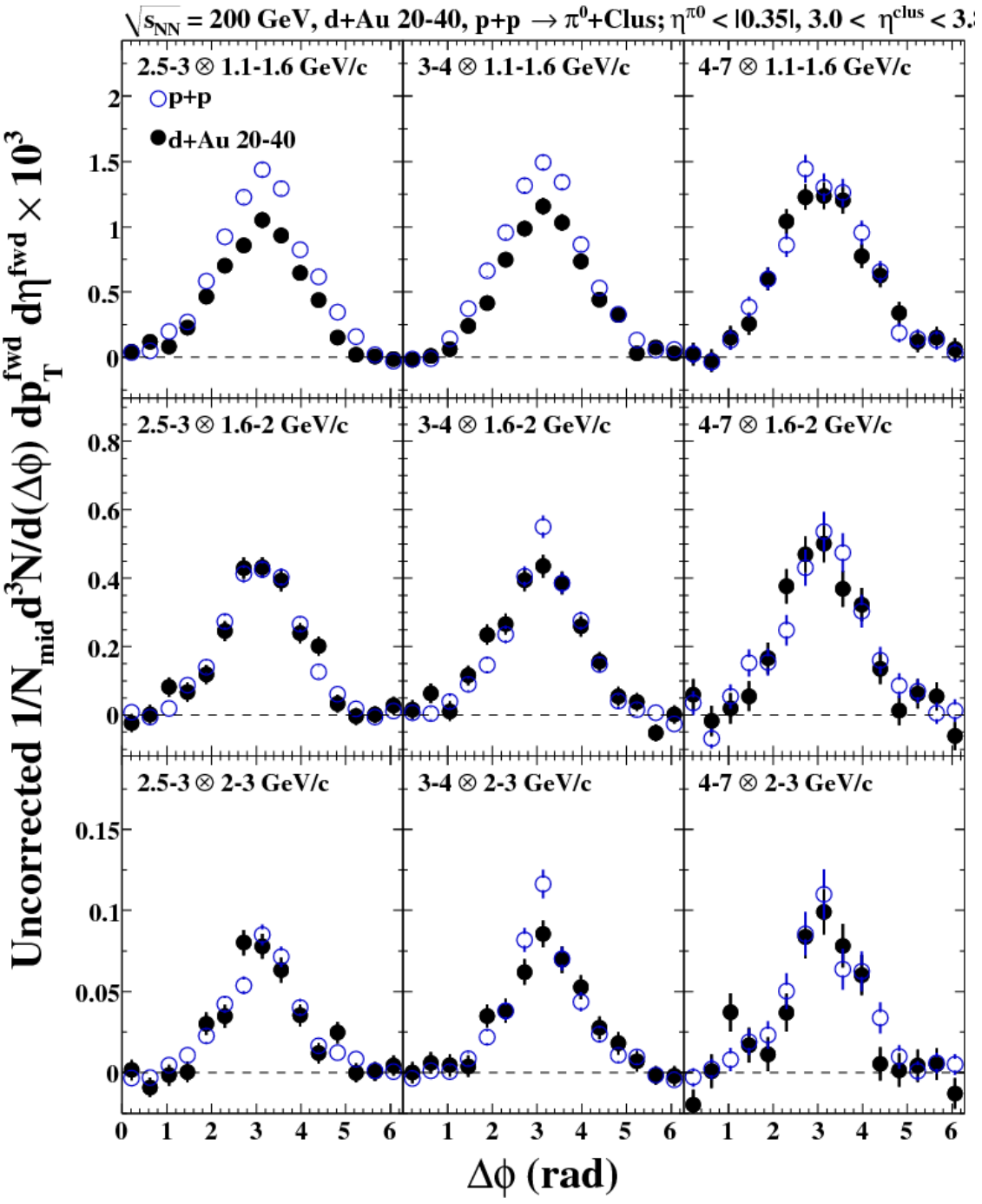

Figure D.16: **dAu 20-40%, Rapidity = 3.0-3.8:** Background subtracted correlation functions and fits for all p_T bins. The p+p reference is in blue.

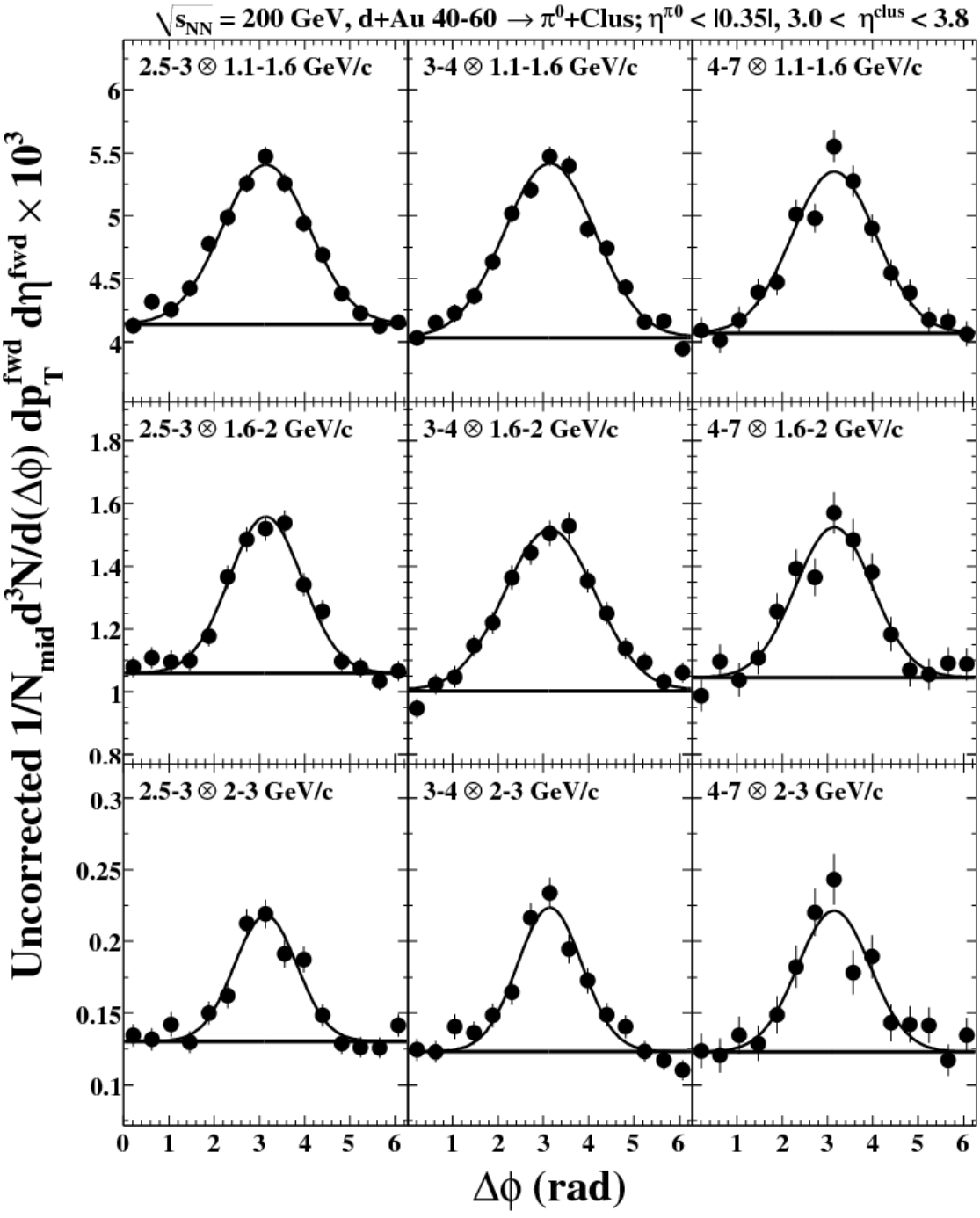

Figure D.17: **dAu 40-60%, Rapidity = 3.0-3.8:** Correlation functions and fits for all p_T bins.

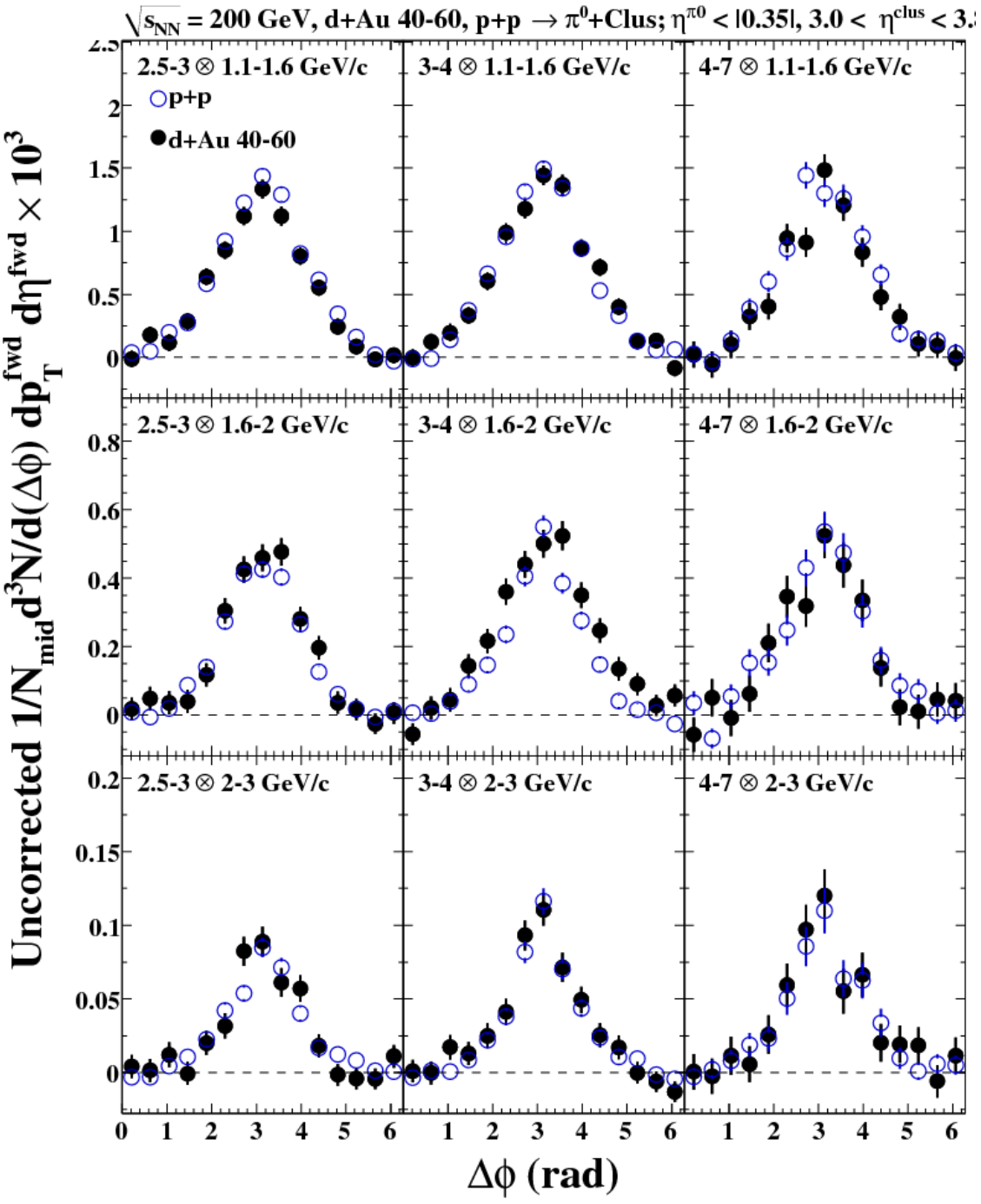

Figure D.18: **dAu 40-60%, Rapidity = 3.0-3.8:** Background subtracted correlation functions and fits for all p_T bins. The p+p reference is in blue.

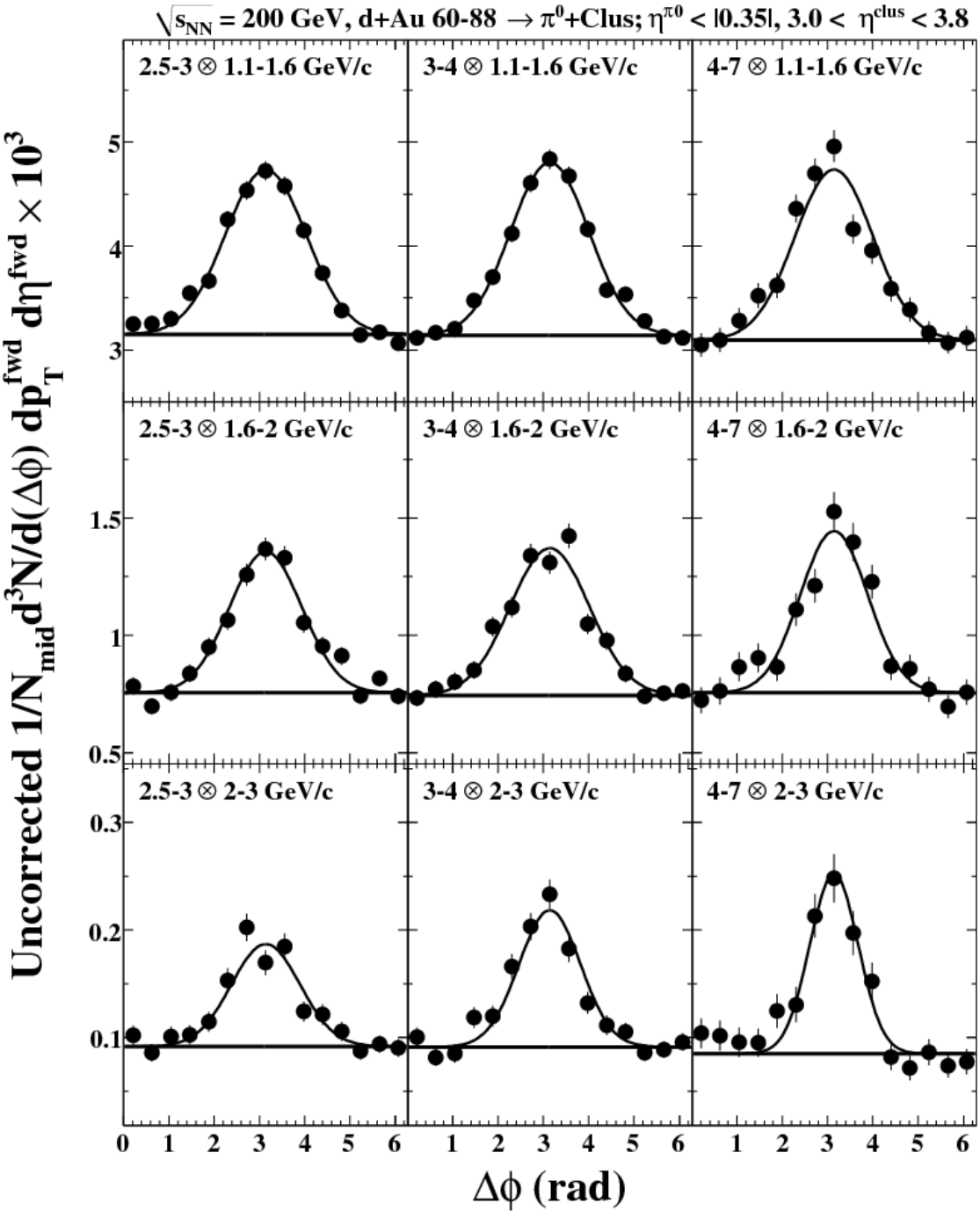

Figure D.19: **dAu 60-88%, Rapidity = 3.0-3.8:** Correlation functions and fits for all p_T bins.

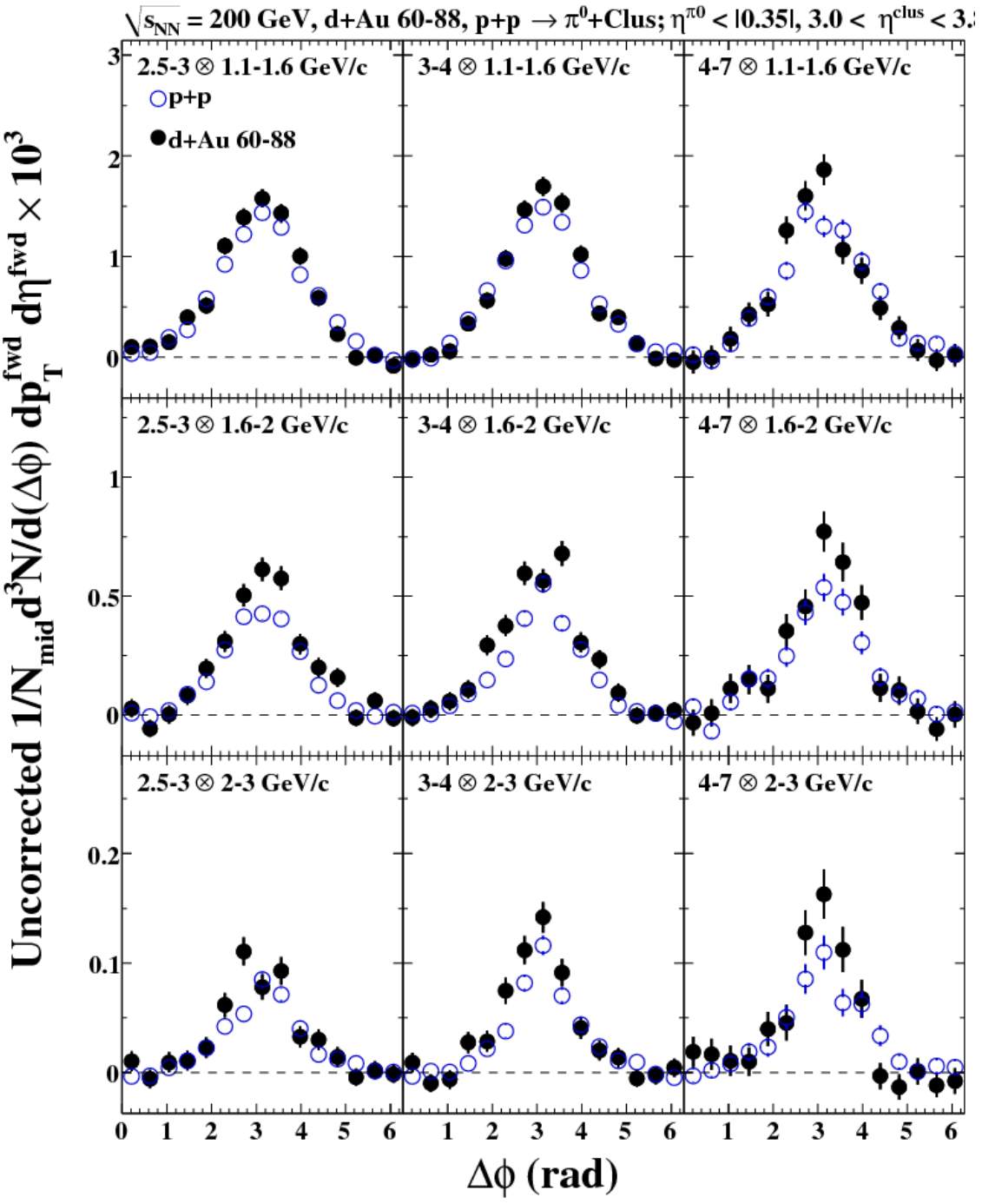

Figure D.20: **dAu 60-88%, Rapidity = 3.0-3.8:** Background subtracted correlation functions and fits for all p_T bins. The p+p reference is in blue.

Appendix E

Forward-Forward Azimuthal Correlations Tables and Figures

E.1 Tabulated Results

In all subsequent tables, σ represents a statistical error, while s represents a systematic error (type B), and the global systematic error is s_{global}.

E.1.1 Conditional and Raw Yields, Relative Statistical Errors

In this section, the terms that are present in the tables are as follows:

p_T	Transverse momentum of the bin center,
Y	Number of correlated particle pairs,
CY	Conditional yield, or the area of the correlated di-hadron signal per trigger particle detected,
ϵ	π^0 reconstruction efficiency,
$\frac{S}{S+B}MPC$	Fraction of counts in π^0 mass window, $0.08 < m_{inv} < 0.18$ GeV/c^2 that are actually signal π^0's (as opposed to background counts),
C_{leak}	Accounts for leakage of the π^0 yield outside the defined window of $0.08 < m_{inv} < 0.18$ GeV/c^2,
C_{bcorr}	Up-down correction, or $C_{up-down}$,
$\Delta p_T \Delta\eta$	Corrects for p_T and η bin widths (e.g. $\Delta p_T \Delta\eta = 0.25 \times 0.8 = 0.2$).

Table E.1: Conditional and Raw Yields, N_{trig}, efficiencies, corrections, and **Relative** stat errors for $3.0 < \eta < 3.8$, Cluster $p_T = 1.0 - 1.5$ GeV/c.

d+Au 0-20%, $N_{trig} = 5.011e+06$										
p_T	CY	σ_{CY}	Y	σ_Y	ϵ	σ_ϵ	$\frac{S}{S+B}_{MPC}$	C_{leak}	C_{bcorr}	$\Delta p_T \Delta\eta$
0.625	1.18e-02	0.258	1.48e+03	0.257	0.052	0.016	0.36	1.04	0.96	0.20
0.875	5.18e-03	0.303	6.27e+02	0.302	0.076	0.014	0.57	1.02	0.96	0.20
1.250	4.66e-03	0.212	6.56e+02	0.212	0.051	0.015	0.72	1.04	0.88	0.40
d+Au 20-40%, $N_{trig} = 4.762e+06$										
p_T	CY	σ_{CY}	Y	σ_Y	ϵ	σ_ϵ	$\frac{S}{S+B}_{MPC}$	C_{leak}	C_{bcorr}	$\Delta p_T \Delta\eta$
0.625	9.32e-03	0.259	1.13e+03	0.259	0.053	0.015	0.37	1.03	0.96	0.20
0.875	1.13e-02	0.155	1.32e+03	0.155	0.077	0.014	0.57	1.02	0.96	0.20
1.250	5.08e-03	0.183	6.63e+02	0.182	0.051	0.015	0.72	1.05	0.88	0.40
d+Au 40-60%, $N_{trig} = 3.981e+06$										
p_T	CY	σ_{CY}	Y	σ_Y	ϵ	σ_ϵ	$\frac{S}{S+B}_{MPC}$	C_{leak}	C_{bcorr}	$\Delta p_T \Delta\eta$
0.625	1.54e-02	0.176	1.57e+03	0.175	0.057	0.015	0.39	1.03	0.96	0.20
0.875	1.30e-02	0.154	1.21e+03	0.153	0.077	0.014	0.59	1.02	0.97	0.20
1.250	7.75e-03	0.129	8.27e+02	0.129	0.050	0.015	0.73	1.04	0.87	0.40
d+Au 60-88%, $N_{trig} = 3.739e+06$										
p_T	CY	σ_{CY}	Y	σ_Y	ϵ	σ_ϵ	$\frac{S}{S+B}_{MPC}$	C_{leak}	C_{bcorr}	$\Delta p_T \Delta\eta$
0.625	2.81e-02	0.113	2.44e+03	0.112	0.059	0.012	0.45	1.03	0.96	0.20
0.875	3.33e-02	0.063	2.79e+03	0.062	0.080	0.012	0.64	1.02	0.96	0.20
1.250	6.79e-03	0.138	6.84e+02	0.138	0.052	0.012	0.77	1.04	0.86	0.40
p+p, $N_{trig} = 1.716e+06$										
p_T	CY	σ_{CY}	Y	σ_Y	ϵ	σ_ϵ	$\frac{S}{S+B}_{MPC}$	C_{leak}	C_{bcorr}	$\Delta p_T \Delta\eta$
0.625	4.53e-02	0.099	1.55e+03	0.098	0.060	0.010	0.54	1.03	0.95	0.20
0.875	2.29e-02	0.117	8.21e+02	0.117	0.082	0.010	0.71	1.02	0.95	0.20
1.250	8.86e-03	0.123	4.01e+02	0.123	0.052	0.010	0.81	1.04	0.83	0.40

Table E.2: Conditional and Raw Yields, N_{trig}, efficiencies, corrections, and **Relative** stat errors for $3.0 < \eta < 3.8$, Cluster $p_T = 1.5 - 2.0$ GeV/c.

d+Au 0-20%, $N_{trig} = 1.312e+06$										
p_T	CY	σ_{CY}	Y	σ_Y	ϵ	σ_ϵ	$\frac{S}{S+B}_{MPC}$	C_{leak}	C_{bcorr}	$\Delta p_T \Delta\eta$
0.625	1.96e-02	0.318	6.48e+02	0.318	0.052	0.016	0.36	1.04	0.96	0.20
0.875	1.52e-02	0.217	4.82e+02	0.217	0.076	0.014	0.57	1.02	0.96	0.20
1.250	1.01e-02	0.224	3.71e+02	0.224	0.051	0.015	0.72	1.04	0.88	0.40
d+Au 20-40%, $N_{trig} = 1.228e+06$										
p_T	CY	σ_{CY}	Y	σ_Y	ϵ	σ_ϵ	$\frac{S}{S+B}_{MPC}$	C_{leak}	C_{bcorr}	$\Delta p_T \Delta\eta$
0.625	2.75e-02	0.250	8.65e+02	0.250	0.053	0.015	0.37	1.03	0.96	0.20
0.875	2.86e-02	0.132	8.56e+02	0.132	0.077	0.014	0.57	1.02	0.96	0.20
1.250	9.92e-03	0.195	3.34e+02	0.194	0.051	0.015	0.72	1.05	0.88	0.40
d+Au 40-60%, $N_{trig} = 9.918e+05$										
p_T	CY	σ_{CY}	Y	σ_Y	ϵ	σ_ϵ	$\frac{S}{S+B}_{MPC}$	C_{leak}	C_{bcorr}	$\Delta p_T \Delta\eta$
0.625	4.36e-02	0.142	1.11e+03	0.142	0.057	0.015	0.39	1.03	0.96	0.20
0.875	2.57e-02	0.164	5.95e+02	0.163	0.077	0.014	0.59	1.02	0.97	0.20
1.250	5.02e-03	0.440	1.33e+02	0.440	0.050	0.015	0.73	1.04	0.87	0.40
d+Au 60-88%, $N_{trig} = 8.714e+05$										
p_T	CY	σ_{CY}	Y	σ_Y	ϵ	σ_ϵ	$\frac{S}{S+B}_{MPC}$	C_{leak}	C_{bcorr}	$\Delta p_T \Delta\eta$
0.625	4.70e-02	0.133	9.56e+02	0.133	0.059	0.012	0.45	1.03	0.96	0.20
0.875	3.53e-02	0.124	6.87e+02	0.124	0.080	0.012	0.64	1.02	0.96	0.20
1.250	1.02e-02	0.195	2.39e+02	0.195	0.052	0.012	0.77	1.04	0.86	0.40
p+p, $N_{trig} = 3.370e+05$										
p_T	CY	σ_{CY}	Y	σ_Y	ϵ	σ_ϵ	$\frac{S}{S+B}_{MPC}$	C_{leak}	C_{bcorr}	$\Delta p_T \Delta\eta$
0.625	8.57e-02	0.132	5.78e+02	0.132	0.060	0.010	0.54	1.03	0.95	0.20
0.875	3.99e-02	0.155	2.81e+02	0.154	0.082	0.010	0.71	1.02	0.95	0.20
1.250	8.27e-03	0.357	7.33e+01	0.357	0.052	0.010	0.81	1.04	0.83	0.40

Table E.3: Conditional and Raw Yields, N_{trig}, efficiencies, corrections, and **Relative** stat errors for $3.0 < \eta < 3.8$, Cluster $p_T > 2.0$ GeV/c.

d+Au 0-20%, $N_{trig} = 3.654e+05$										
p_T	CY	σ_{CY}	Y	σ_Y	ϵ	σ_ϵ	$\frac{S}{S+B}_{MPC}$	C_{leak}	C_{bcorr}	$\Delta p_T \Delta\eta$
0.625	4.39e-02	0.241	4.05e+02	0.241	0.052	0.016	0.36	1.04	0.96	0.20
0.875	3.31e-02	0.203	2.93e+02	0.202	0.076	0.014	0.57	1.02	0.96	0.20
1.250	1.27e-02	0.264	1.30e+02	0.263	0.051	0.015	0.72	1.04	0.88	0.40
d+Au 20-40%, $N_{trig} = 3.389e+05$										
p_T	CY	σ_{CY}	Y	σ_Y	ϵ	σ_ϵ	$\frac{S}{S+B}_{MPC}$	C_{leak}	C_{bcorr}	$\Delta p_T \Delta\eta$
0.625	2.82e-02	0.340	2.45e+02	0.339	0.053	0.015	0.37	1.03	0.96	0.20
0.875	4.03e-02	0.172	3.32e+02	0.172	0.077	0.014	0.57	1.02	0.96	0.20
1.250	6.80e-03	0.468	6.30e+01	0.467	0.051	0.015	0.72	1.05	0.88	0.40
d+Au 40-60%, $N_{trig} = 2.672e+05$										
p_T	CY	σ_{CY}	Y	σ_Y	ϵ	σ_ϵ	$\frac{S}{S+B}_{MPC}$	C_{leak}	C_{bcorr}	$\Delta p_T \Delta\eta$
0.625	6.77e-02	0.167	4.67e+02	0.167	0.057	0.015	0.39	1.03	0.96	0.20
0.875	4.60e-02	0.182	2.87e+02	0.181	0.077	0.014	0.59	1.02	0.97	0.20
1.250	1.81e-02	0.217	1.29e+02	0.216	0.050	0.015	0.73	1.04	0.87	0.40
d+Au 60-88%, $N_{trig} = 2.227e+05$										
p_T	CY	σ_{CY}	Y	σ_Y	ϵ	σ_ϵ	$\frac{S}{S+B}_{MPC}$	C_{leak}	C_{bcorr}	$\Delta p_T \Delta\eta$
0.625	8.81e-02	0.141	4.60e+02	0.141	0.059	0.012	0.45	1.03	0.96	0.20
0.875	4.78e-02	0.200	2.38e+02	0.200	0.080	0.012	0.64	1.02	0.96	0.20
1.250	2.13e-02	0.189	1.27e+02	0.189	0.052	0.012	0.77	1.04	0.86	0.40
p+p, $N_{trig} = 7.558e+04$										
p_T	CY	σ_{CY}	Y	σ_Y	ϵ	σ_ϵ	$\frac{S}{S+B}_{MPC}$	C_{leak}	C_{bcorr}	$\Delta p_T \Delta\eta$
0.625	1.25e-01	0.169	1.89e+02	0.169	0.060	0.010	0.54	1.03	0.95	0.20
0.875	6.97e-02	0.217	1.10e+02	0.217	0.082	0.010	0.71	1.02	0.95	0.20
1.250	9.96e-03	0.448	1.97e+01	0.448	0.052	0.010	0.81	1.04	0.83	0.40

E.1.2 Conditional Yields and Relative Errors

In this section, the terms that are present in the tables are as follows:

p_T	Transverse momentum of the bin center,
CY	Conditional yield, or the area of the correlated di-hadron signal per trigger particle detected,
$\frac{S}{S+B}MPC$	Fraction of counts in π^0 mass window, $0.08 < m_{inv} < 0.18$ GeV/c^2 that are actually signal π^0's (as opposed to background counts),
$\frac{S}{S+B}trig$	1 for clusters,
s_{eff}	Systematic error from yield extraction, input spectrum shape, energy scale, and GEANT,
s_{sb}	Systematic error from contributions of the background under the π^0 peak to the CF,
s_{zyam}	Systematic error from ZYAM subtraction, some of which cancels when taking the ratio between p+p and d+Au,
s_{tot}	Total systematic error on the CY,
W	Gaussian width of the awayside peak.

Table E.4: Conditional Yields, widths, **Relative** sys, stat errors for $3.0 < \eta < 3.8$, Cluster $p_T = 1.0 - 1.5$ GeV/c.

d+Au 0-20%										
p_T	CY	σ_{CY}	$\frac{S}{S+B}_{MPC}$	$\frac{S}{S+B}_{trig}$	s_{eff}	s_{sb}	s_{zyam}	s_{tot}	W	σ_w
0.625	1.18e-02	0.258	0.360	1.000	0.104	0.256	2.705	0.276	0.754	0.303
0.875	5.18e-03	0.303	0.568	1.000	0.113	0.173	2.416	0.207	0.523	0.273
1.250	4.66e-03	0.212	0.717	1.000	0.132	0.113	1.503	0.174	0.852	0.241
d+Au 20-40%										
p_T	CY	σ_{CY}	$\frac{S}{S+B}_{MPC}$	$\frac{S}{S+B}_{trig}$	s_{eff}	s_{sb}	s_{zyam}	s_{tot}	W	σ_w
0.625	9.32e-03	0.259	0.367	1.000	0.102	0.253	2.345	0.273	0.428	0.291
0.875	1.13e-02	0.155	0.571	1.000	0.113	0.171	2.034	0.205	0.627	0.134
1.250	5.08e-03	0.183	0.720	1.000	0.132	0.112	1.767	0.173	0.675	0.189
d+Au 40-60%										
p_T	CY	σ_{CY}	$\frac{S}{S+B}_{MPC}$	$\frac{S}{S+B}_{trig}$	s_{eff}	s_{sb}	s_{zyam}	s_{tot}	W	σ_w
0.625	1.54e-02	0.176	0.392	1.000	0.100	0.243	1.627	0.263	0.446	0.210
0.875	1.30e-02	0.154	0.591	1.000	0.112	0.164	1.292	0.198	0.538	0.180
1.250	7.75e-03	0.129	0.733	1.000	0.133	0.107	1.539	0.171	0.650	0.136
d+Au 60-88%										
p_T	CY	σ_{CY}	$\frac{S}{S+B}_{MPC}$	$\frac{S}{S+B}_{trig}$	s_{eff}	s_{sb}	s_{zyam}	s_{tot}	W	σ_w
0.625	2.81e-02	0.113	0.451	1.000	0.101	0.220	1.955	0.242	0.656	0.113
0.875	3.33e-02	0.063	0.644	1.000	0.115	0.142	1.409	0.183	0.715	0.061
1.250	6.79e-03	0.138	0.766	1.000	0.135	0.094	1.386	0.164	0.682	0.140
p+p										
p_T	CY	σ_{CY}	$\frac{S}{S+B}_{MPC}$	$\frac{S}{S+B}_{trig}$	s_{eff}	s_{sb}	s_{zyam}	s_{tot}	W	σ_w
0.625	4.53e-02	0.099	0.536	1.000	0.107	0.186	1.522	0.214	0.677	0.107
0.875	2.29e-02	0.117	0.712	1.000	0.122	0.115	1.198	0.167	0.774	0.128
1.250	8.86e-03	0.123	0.813	1.000	0.142	0.075	1.042	0.160	0.710	0.130

Table E.5: Conditional Yields, widths, **Relative** sys, stat errors for $3.0 < \eta < 3.8$, Cluster $p_T = 1.5 - 2.0$ GeV/c.

d+Au 0-20%										
p_T	CY	σ_{CY}	$\frac{S}{S+B}_{MPC}$	$\frac{S}{S+B}_{trig}$	s_{eff}	s_{sb}	s_{zyam}	s_{tot}	W	σ_w
0.625	1.96e-02	0.318	0.360	1.000	0.104	0.256	1.888	0.276	0.869	0.402
0.875	1.52e-02	0.217	0.568	1.000	0.113	0.173	1.063	0.207	0.520	0.235
1.250	1.01e-02	0.224	0.717	1.000	0.132	0.113	1.331	0.174	0.833	0.311
d+Au 20-40%										
p_T	CY	σ_{CY}	$\frac{S}{S+B}_{MPC}$	$\frac{S}{S+B}_{trig}$	s_{eff}	s_{sb}	s_{zyam}	s_{tot}	W	σ_w
0.625	2.75e-02	0.250	0.367	1.000	0.102	0.253	1.863	0.273	0.759	0.319
0.875	2.86e-02	0.132	0.571	1.000	0.113	0.171	1.548	0.205	0.671	0.145
1.250	9.92e-03	0.195	0.720	1.000	0.132	0.112	1.200	0.173	0.857	0.199
d+Au 40-60%										
p_T	CY	σ_{CY}	$\frac{S}{S+B}_{MPC}$	$\frac{S}{S+B}_{trig}$	s_{eff}	s_{sb}	s_{zyam}	s_{tot}	W	σ_w
0.625	4.36e-02	0.142	0.392	1.000	0.100	0.243	1.272	0.263	0.858	0.120
0.875	2.57e-02	0.164	0.591	1.000	0.112	0.164	1.575	0.198	0.759	0.153
1.250	5.02e-03	0.440	0.733	1.000	0.133	0.107	1.279	0.171	1.186	0.385
d+Au 60-88%										
p_T	CY	σ_{CY}	$\frac{S}{S+B}_{MPC}$	$\frac{S}{S+B}_{trig}$	s_{eff}	s_{sb}	s_{zyam}	s_{tot}	W	σ_w
0.625	4.70e-02	0.133	0.451	1.000	0.101	0.220	1.568	0.242	0.626	0.123
0.875	3.53e-02	0.124	0.644	1.000	0.115	0.142	1.257	0.183	0.711	0.123
1.250	1.02e-02	0.195	0.766	1.000	0.135	0.094	0.567	0.164	0.554	0.249
p+p										
p_T	CY	σ_{CY}	$\frac{S}{S+B}_{MPC}$	$\frac{S}{S+B}_{trig}$	s_{eff}	s_{sb}	s_{zyam}	s_{tot}	W	σ_w
0.625	8.57e-02	0.132	0.536	1.000	0.107	0.186	1.175	0.214	0.794	0.153
0.875	3.99e-02	0.155	0.712	1.000	0.122	0.115	1.132	0.167	0.738	0.169
1.250	8.27e-03	0.357	0.813	1.000	0.142	0.075	1.104	0.160	0.411	0.390

Table E.6: Conditional Yields, widths, **Relative** sys, stat errors for $3.0 < \eta < 3.8$, Cluster $p_T > 2.0$ GeV/c.

d+Au 0-20%										
p_T	CY	σ_{CY}	$\frac{S}{S+B}_{MPC}$	$\frac{S}{S+B}_{trig}$	s_{eff}	s_{sb}	s_{zyam}	s_{tot}	W	σ_w
0.625	4.39e-02	0.241	0.360	1.000	0.104	0.256	1.203	0.276	1.012	0.257
0.875	3.31e-02	0.203	0.568	1.000	0.113	0.173	1.359	0.207	0.742	0.196
1.250	1.27e-02	0.264	0.717	1.000	0.132	0.113	0.883	0.174	0.912	0.238
d+Au 20-40%										
p_T	CY	σ_{CY}	$\frac{S}{S+B}_{MPC}$	$\frac{S}{S+B}_{trig}$	s_{eff}	s_{sb}	s_{zyam}	s_{tot}	W	σ_w
0.625	2.82e-02	0.340	0.367	1.000	0.102	0.253	1.905	0.273	0.645	0.275
0.875	4.03e-02	0.172	0.571	1.000	0.113	0.171	1.318	0.205	0.747	0.147
1.250	6.80e-03	0.468	0.720	1.000	0.132	0.112	1.254	0.173	0.609	0.530
d+Au 40-60%										
p_T	CY	σ_{CY}	$\frac{S}{S+B}_{MPC}$	$\frac{S}{S+B}_{trig}$	s_{eff}	s_{sb}	s_{zyam}	s_{tot}	W	σ_w
0.625	6.77e-02	0.167	0.392	1.000	0.100	0.243	1.395	0.263	0.701	0.161
0.875	4.60e-02	0.182	0.591	1.000	0.112	0.164	1.315	0.198	0.807	0.197
1.250	1.81e-02	0.217	0.733	1.000	0.133	0.107	0.574	0.171	0.571	0.256
d+Au 60-88%										
p_T	CY	σ_{CY}	$\frac{S}{S+B}_{MPC}$	$\frac{S}{S+B}_{trig}$	s_{eff}	s_{sb}	s_{zyam}	s_{tot}	W	σ_w
0.625	8.81e-02	0.141	0.451	1.000	0.101	0.220	1.210	0.242	0.691	0.125
0.875	4.78e-02	0.200	0.644	1.000	0.115	0.142	1.182	0.183	0.867	0.233
1.250	2.13e-02	0.189	0.766	1.000	0.135	0.094	1.064	0.164	0.730	0.167
p+p										
p_T	CY	σ_{CY}	$\frac{S}{S+B}_{MPC}$	$\frac{S}{S+B}_{trig}$	s_{eff}	s_{sb}	s_{zyam}	s_{tot}	W	σ_w
0.625	1.25e-01	0.169	0.536	1.000	0.107	0.186	0.995	0.214	0.729	0.178
0.875	6.97e-02	0.217	0.712	1.000	0.122	0.115	0.940	0.167	0.899	0.265
1.250	9.96e-03	0.448	0.813	1.000	0.142	0.075	1.124	0.160	0.300	0.201

E.1.3 $I_{\rm dA}$, $J_{\rm dA}$ and Relative Errors

In this section, the terms that are present in the tables are as follows:

p_T	Transverse momentum of the bin center,
$I_{\rm dA}$	Ratio of CYs between d+Au and p+p,
$J_{\rm dA}$	Correlated di-hadron nuclear modification factor formed by taking the ratio between measured di-hadron yields in d+Au per $N_{\rm coll}$ and di-hadron yields in p+p. In practice, the formula $J_{\rm dA} = I_{dA,trig} \times R_{dA,trig}$ is used,
$s_{eff,IdA}$	Systematic error from yield extraction, input spectrum shape, energy scale, and GEANT with cancellations taken into account for $I_{\rm dA}$,
$s_{SB,IdA}$	Systematic error from contributions of the background under the π^0 peak to the CF with cancellations taken into account for $I_{\rm dA}$,
$s_{ZYAM,IdA}$	Asymmetric error from ZYAM subtraction to $I_{\rm dA}$,
$s_{tot,IdA}$	Total asymmetric systematic error on $I_{\rm dA}$,
$s_{tot,JdA}$	Total asymmetric systematic error on $J_{\rm dA}$.

Table E.7: I_{dA},J_{dA} **relative** sys, stat errors for $3.0 < \eta < 3.8$, Cluster $p_T = 1.0 - 1.5$ GeV/c.

d+Au 0-20%, $R_{dA} = 0.291 \pm 0.0186$ **(stat)** ± 0.080 **(sys)**									
p_T	I_{dA}	σ_{IdA}	J_{dA}	σ_{JdA}	$s_{eff,IdA}$	$s_{SB,IdA}$	$s_{ZYAM,IdA}$	$s_{tot,IdA}$	$s_{tot,JdA}$
0.625	0.321	0.175	0.093	0.176	0.074	0.256	-0.272/1.113	-0.381/1.145	-0.389/1.148
0.875	0.263	0.222	0.077	0.223	0.064	0.173	-0.239/1.248	-0.302/1.261	-0.312/1.264
1.250	0.350	0.210	0.102	0.210	0.078	0.113	-0.248/0.952	-0.283/0.962	-0.295/0.966
d+Au 20-40%, $R_{dA} = 0.431 \pm 0.0186$ **(stat)** ± 0.082 **(sys)**									
p_T	I_{dA}	σ_{IdA}	J_{dA}	σ_{JdA}	$s_{eff,IdA}$	$s_{SB,IdA}$	$s_{ZYAM,IdA}$	$s_{tot,IdA}$	$s_{tot,JdA}$
0.625	0.343	0.173	0.148	0.174	0.071	0.253	-0.254/1.023	-0.366/1.057	-0.375/1.060
0.875	0.511	0.141	0.220	0.142	0.065	0.171	-0.239/0.849	-0.302/0.869	-0.312/0.873
1.250	0.505	0.163	0.218	0.164	0.079	0.112	-0.230/0.788	-0.268/0.800	-0.280/0.804
d+Au 40-60%, $R_{dA} = 0.589 \pm 0.0186$ **(stat)** ± 0.081 **(sys)**									
p_T	I_{dA}	σ_{IdA}	J_{dA}	σ_{JdA}	$s_{eff,IdA}$	$s_{SB,IdA}$	$s_{ZYAM,IdA}$	$s_{tot,IdA}$	$s_{tot,JdA}$
0.625	0.375	0.175	0.221	0.176	0.069	0.243	-0.191/0.803	-0.317/0.842	-0.327/0.846
0.875	0.573	0.134	0.337	0.135	0.065	0.164	-0.164/0.558	-0.241/0.586	-0.254/0.591
1.250	0.871	0.123	0.513	0.125	0.078	0.107	-0.202/0.546	-0.241/0.562	-0.254/0.568
d+Au 60-88%, $R_{dA} = 0.805 \pm 0.0169$ **(stat)** ± 0.078 **(sys)**									
p_T	I_{dA}	σ_{IdA}	J_{dA}	σ_{JdA}	$s_{eff,IdA}$	$s_{SB,IdA}$	$s_{ZYAM,IdA}$	$s_{tot,IdA}$	$s_{tot,JdA}$
0.625	0.709	0.106	0.571	0.108	0.068	0.220	-0.167/0.377	-0.284/0.441	-0.295/0.448
0.875	1.405	0.094	1.131	0.096	0.064	0.142	-0.159/0.324	-0.223/0.359	-0.236/0.368
1.250	0.708	0.131	0.570	0.132	0.076	0.094	-0.138/0.355	-0.183/0.375	-0.199/0.383

Table E.8: I_{dA},J_{dA} **relative** sys, stat errors for $3.0 < \eta < 3.8$, Cluster $p_T = 1.5 - 2.0$ GeV/c.

d+Au 0-20%, $R_{dA} = 0.381 \pm 0.1012$ **(stat)** ± 0.164 **(sys)**									
p_T	I_{dA}	σ_{IdA}	J_{dA}	σ_{JdA}	$s_{eff,IdA}$	$s_{SB,IdA}$	$s_{ZYAM,IdA}$	$s_{tot,IdA}$	$s_{tot,JdA}$
0.625	0.236	0.209	0.090	0.232	0.074	0.256	-0.266/0.927	-0.377/0.965	-0.411/0.979
0.875	0.377	0.213	0.144	0.236	0.064	0.173	-0.258/0.866	-0.317/0.886	-0.357/0.901
1.250	0.617	0.235	0.235	0.256	0.078	0.113	-0.274/0.684	-0.306/0.698	-0.347/0.717
d+Au 20-40%, $R_{dA} = 0.568 \pm 0.0966$ **(stat)** ± 0.165 **(sys)**									
p_T	I_{dA}	σ_{IdA}	J_{dA}	σ_{JdA}	$s_{eff,IdA}$	$s_{SB,IdA}$	$s_{ZYAM,IdA}$	$s_{tot,IdA}$	$s_{tot,JdA}$
0.625	0.282	0.184	0.160	0.208	0.071	0.253	-0.229/0.903	-0.349/0.941	-0.386/0.955
0.875	0.699	0.153	0.397	0.181	0.065	0.171	-0.251/0.665	-0.311/0.690	-0.352/0.710
1.250	0.838	0.206	0.476	0.228	0.079	0.112	-0.283/0.543	-0.315/0.560	-0.355/0.584
d+Au 40-60%, $R_{dA} = 0.754 \pm 0.0988$ **(stat)** ± 0.153 **(sys)**									
p_T	I_{dA}	σ_{IdA}	J_{dA}	σ_{JdA}	$s_{eff,IdA}$	$s_{SB,IdA}$	$s_{ZYAM,IdA}$	$s_{tot,IdA}$	$s_{tot,JdA}$
0.625	0.434	0.144	0.327	0.175	0.069	0.243	-0.203/0.564	-0.324/0.618	-0.359/0.637
0.875	0.663	0.168	0.500	0.194	0.065	0.164	-0.207/0.535	-0.272/0.564	-0.312/0.584
1.250	0.737	0.232	0.556	0.252	0.078	0.107	-0.246/0.427	-0.279/0.447	-0.319/0.473
d+Au 60-88%, $R_{dA} = 0.978 \pm 0.0891$ **(stat)** ± 0.168 **(sys)**									
p_T	I_{dA}	σ_{IdA}	J_{dA}	σ_{JdA}	$s_{eff,IdA}$	$s_{SB,IdA}$	$s_{ZYAM,IdA}$	$s_{tot,IdA}$	$s_{tot,JdA}$
0.625	0.621	0.120	0.607	0.149	0.068	0.220	-0.138/0.398	-0.268/0.460	-0.316/0.490
0.875	0.835	0.151	0.816	0.175	0.064	0.142	-0.160/0.301	-0.223/0.339	-0.279/0.378
1.250	0.737	0.224	0.720	0.241	0.076	0.094	-0.163/0.289	-0.203/0.313	-0.263/0.355

Table E.9: I_{dA},J_{dA} **relative** sys, stat errors for $3.0 < \eta < 3.8$, Cluster $p_T = 2.0 - 5.0$ GeV/c.

d+Au 0-20%, $R_{dA} = 0.427 \pm 0.0000$ **(stat)** ± 0.205 **(sys)**									
p_T	I_{dA}	σ_{IdA}	J_{dA}	σ_{JdA}	$s_{eff,IdA}$	$s_{SB,IdA}$	$s_{ZYAM,IdA}$	$s_{tot,IdA}$	$s_{tot,JdA}$
0.625	0.448	0.185	0.191	0.185	0.074	0.256	-0.271/0.764	-0.380/0.810	-0.432/0.835
0.875	0.409	0.210	0.174	0.210	0.064	0.173	-0.281/0.736	-0.336/0.759	-0.394/0.786
1.250	0.914	0.293	0.390	0.293	0.078	0.113	-0.333/0.534	-0.360/0.551	-0.415/0.588
d+Au 20-40%, $R_{dA} = 0.638 \pm 0.0000$ **(stat)** ± 0.232 **(sys)**									
p_T	I_{dA}	σ_{IdA}	J_{dA}	σ_{JdA}	$s_{eff,IdA}$	$s_{SB,IdA}$	$s_{ZYAM,IdA}$	$s_{tot,IdA}$	$s_{tot,JdA}$
0.625	0.232	0.270	0.148	0.270	0.071	0.253	-0.225/0.948	-0.346/0.984	-0.417/1.011
0.875	0.613	0.178	0.391	0.178	0.065	0.171	-0.256/0.629	-0.315/0.655	-0.391/0.695
1.250	0.567	0.385	0.362	0.385	0.079	0.112	-0.280/0.651	-0.312/0.666	-0.388/0.705
d+Au 40-60%, $R_{dA} = 0.839 \pm 0.0000$ **(stat)** ± 0.239 **(sys)**									
p_T	I_{dA}	σ_{IdA}	J_{dA}	σ_{JdA}	$s_{eff,IdA}$	$s_{SB,IdA}$	$s_{ZYAM,IdA}$	$s_{tot,IdA}$	$s_{tot,JdA}$
0.625	0.549	0.171	0.460	0.171	0.069	0.243	-0.207/0.575	-0.327/0.628	-0.405/0.672
0.875	0.540	0.199	0.453	0.199	0.065	0.164	-0.191/0.570	-0.260/0.597	-0.353/0.643
1.250	0.850	0.309	0.713	0.309	0.078	0.107	-0.236/0.461	-0.271/0.480	-0.361/0.536
d+Au 60-88%, $R_{dA} = 1.066 \pm 0.0000$ **(stat)** ± 0.253 **(sys)**									
p_T	I_{dA}	σ_{IdA}	J_{dA}	σ_{JdA}	$s_{eff,IdA}$	$s_{SB,IdA}$	$s_{ZYAM,IdA}$	$s_{tot,IdA}$	$s_{tot,JdA}$
0.625	0.769	0.153	0.820	0.153	0.068	0.220	-0.163/0.279	-0.282/0.362	-0.379/0.441
0.875	0.682	0.185	0.728	0.185	0.064	0.142	-0.139/0.351	-0.209/0.384	-0.328/0.460
1.250	1.452	0.263	1.549	0.263	0.076	0.094	-0.205/0.198	-0.238/0.232	-0.347/0.343

E.2 MPC Cluster/π^0 Correlation Functions

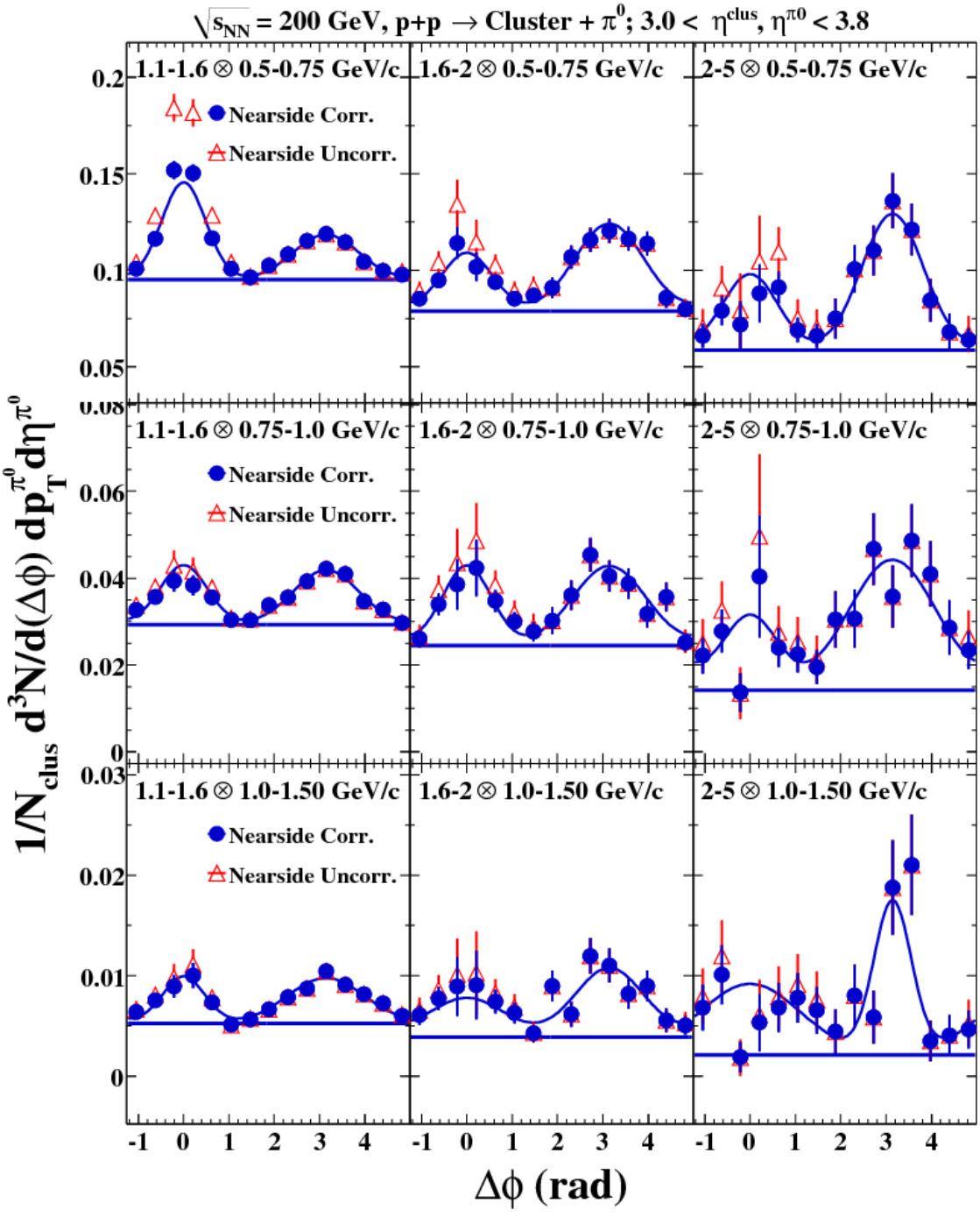

Figure E.1: **p+p, Rapidity = 3.0-3.8:** MPC Cluster/π^0 correlation functions and fits for all p_T bins.

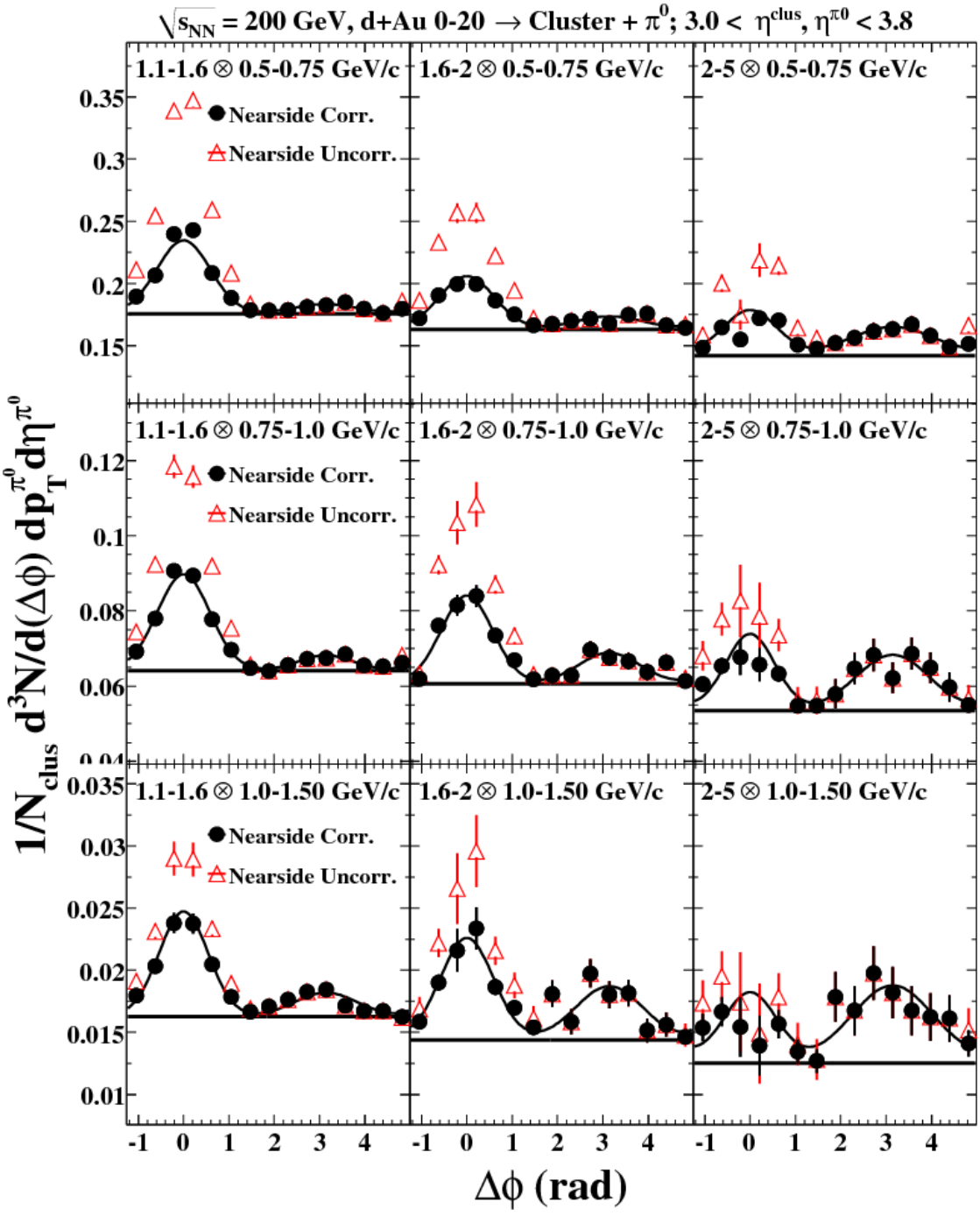

Figure E.2: **d+Au 0-20%, Rapidity = 3.0-3.8:** MPC Cluster/π^0 correlation functions and fits for all p_T bins.

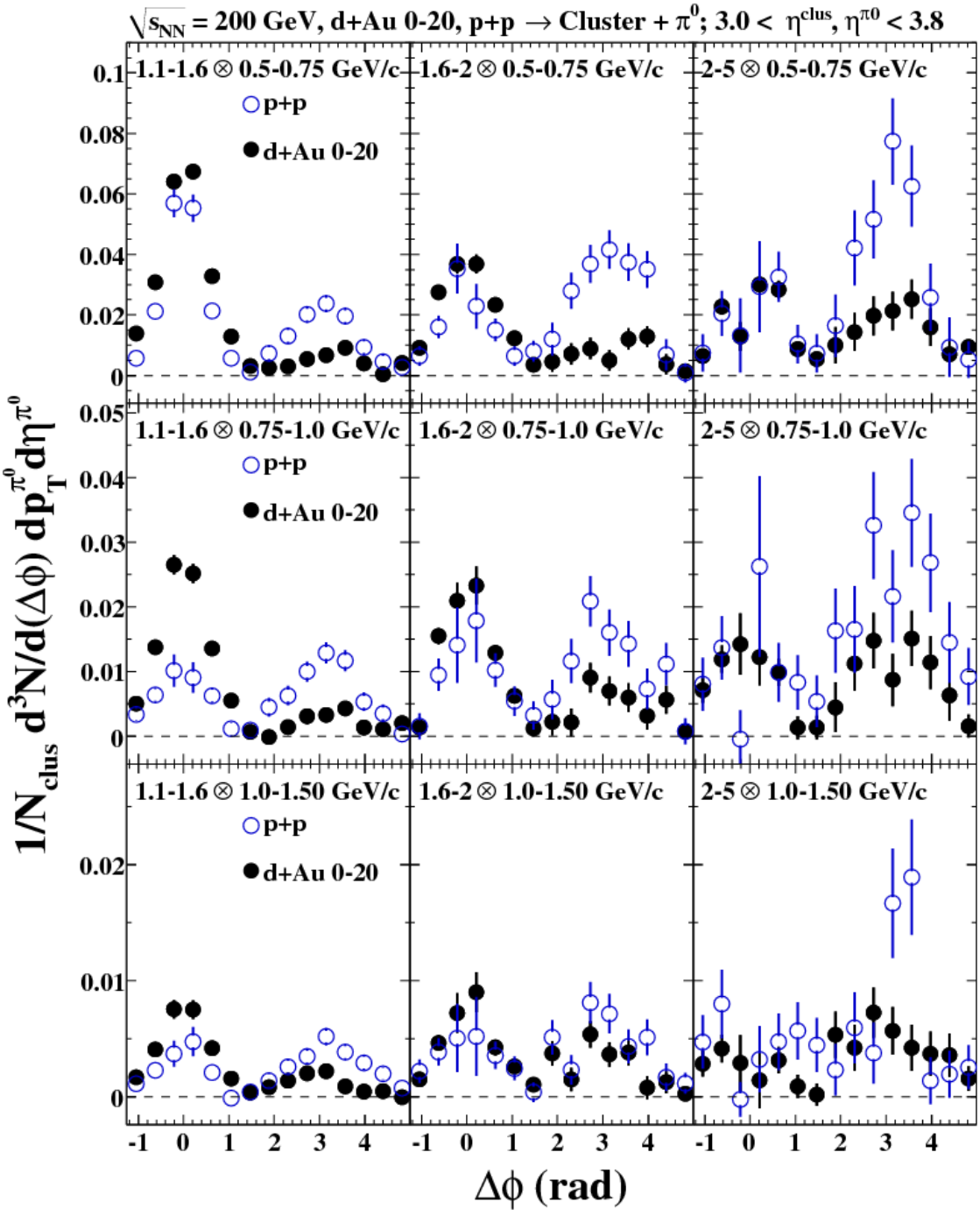

Figure E.3: **d+Au 0-20%, Rapidity = 3.0-3.8:** MPC Cluster/π^0 Background subtracted correlation functions and fits for all p_T bins. The p+p reference is in blue.

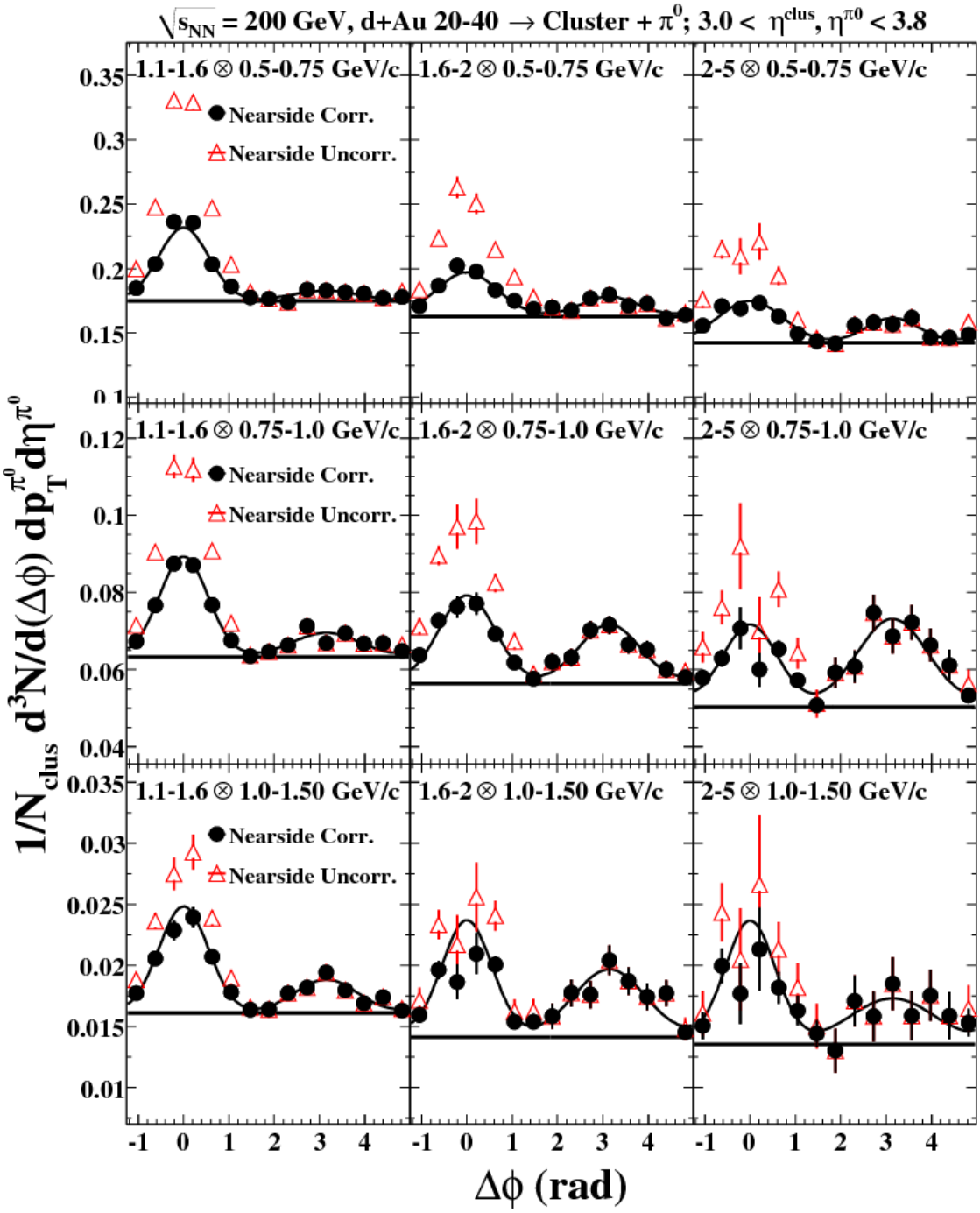

Figure E.4: **dAu 20-40%, Rapidity = 3.0-3.8:** MPC Cluster/π^0 correlation functions and fits for all p_T bins.

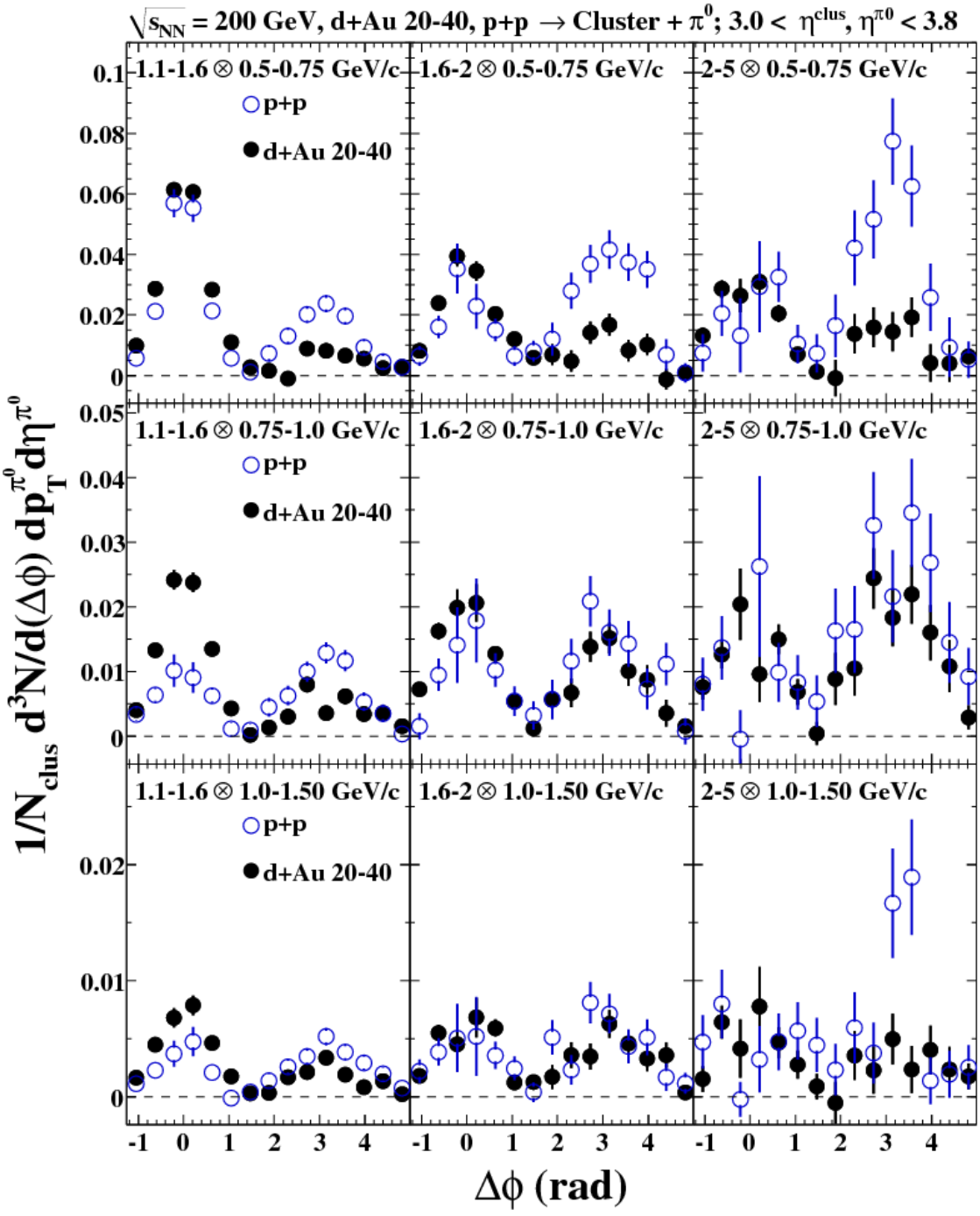

Figure E.5: **dAu 20-40%, Rapidity = 3.0-3.8:** MPC Cluster/π^0 Background subtracted correlation functions and fits for all p_T bins. The p+p reference is in blue.

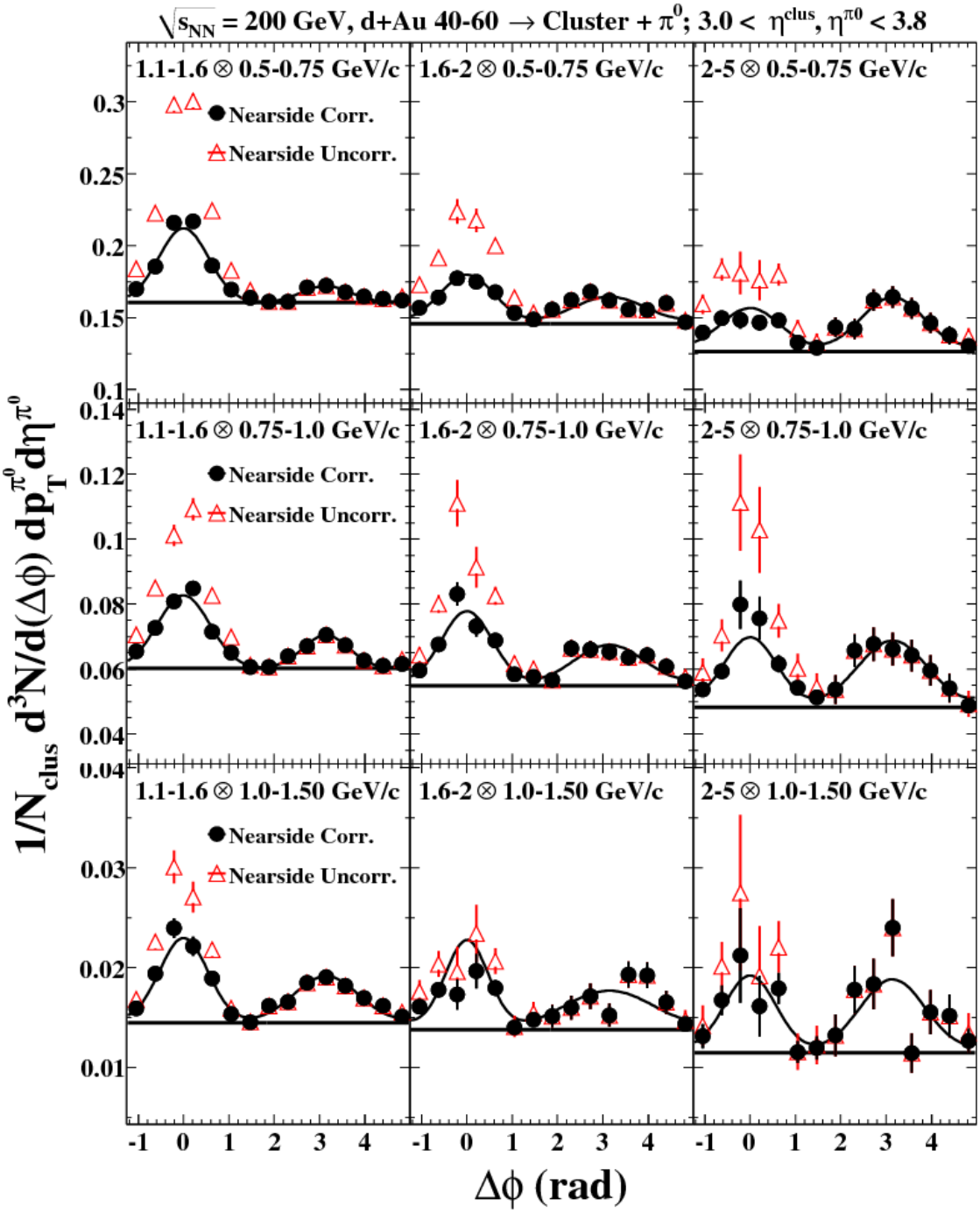

Figure E.6: **dAu 40-60%, Rapidity = 3.0-3.8:** MPC Cluster/π^0 correlation functions and fits for all p_T bins.

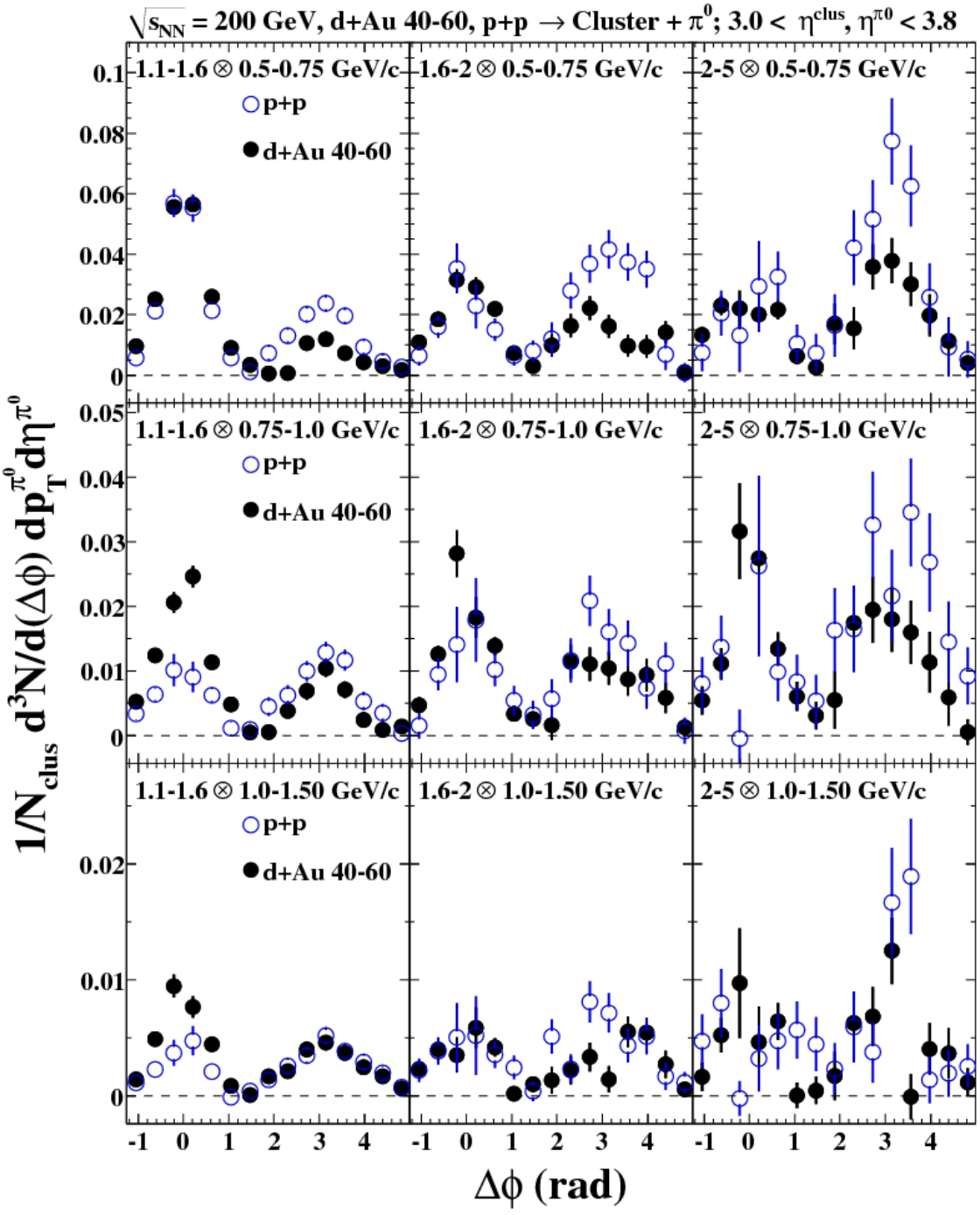

Figure E.7: **dAu 40-60%, Rapidity = 3.0-3.8:** MPC Cluster/π^0 Background subtracted correlation functions and fits for all p_T bins. The p+p reference is in blue.

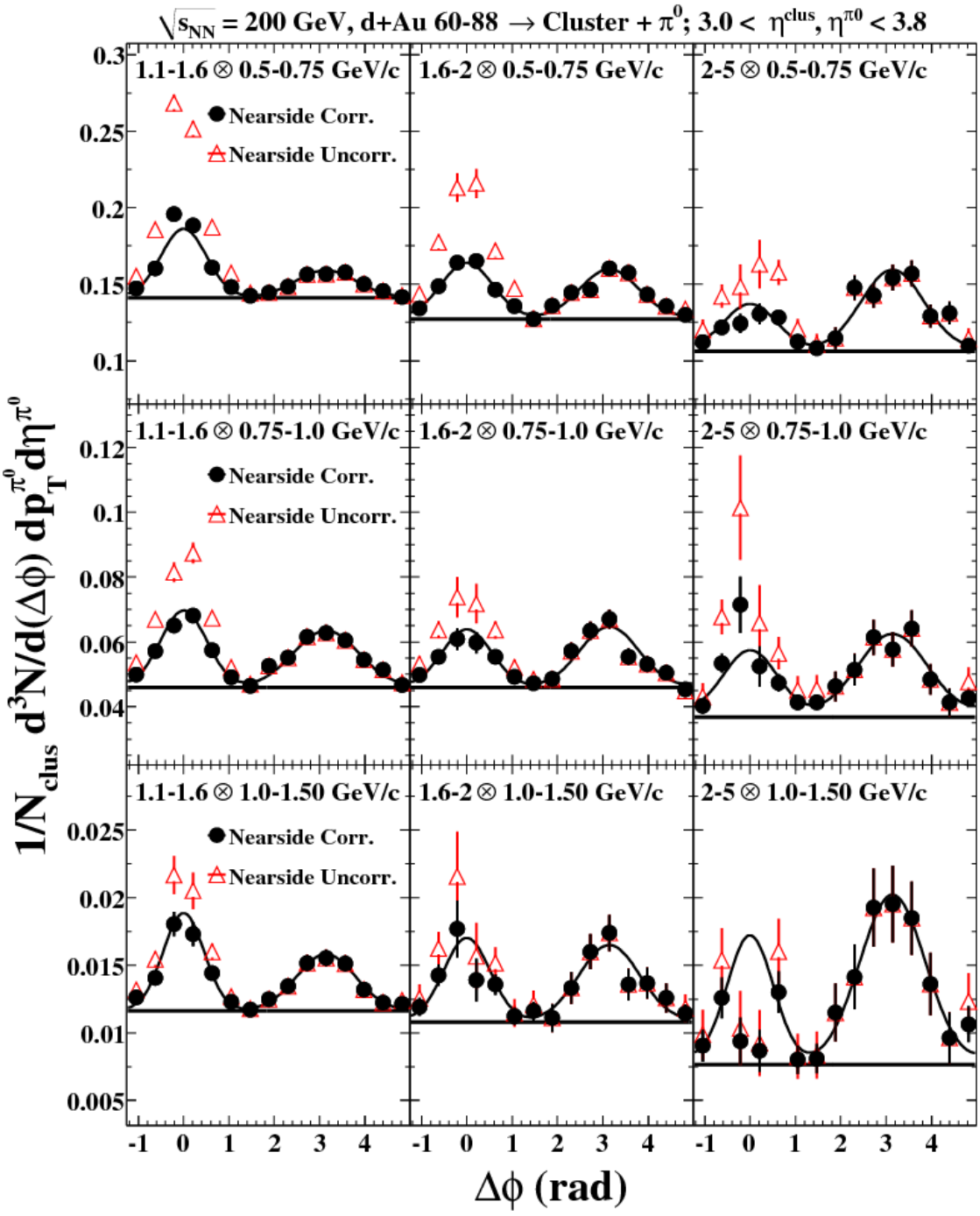

Figure E.8: **dAu 60-88%, Rapidity = 3.0-3.8:** MPC Cluster/π^0 correlation functions and fits for all p_T bins.

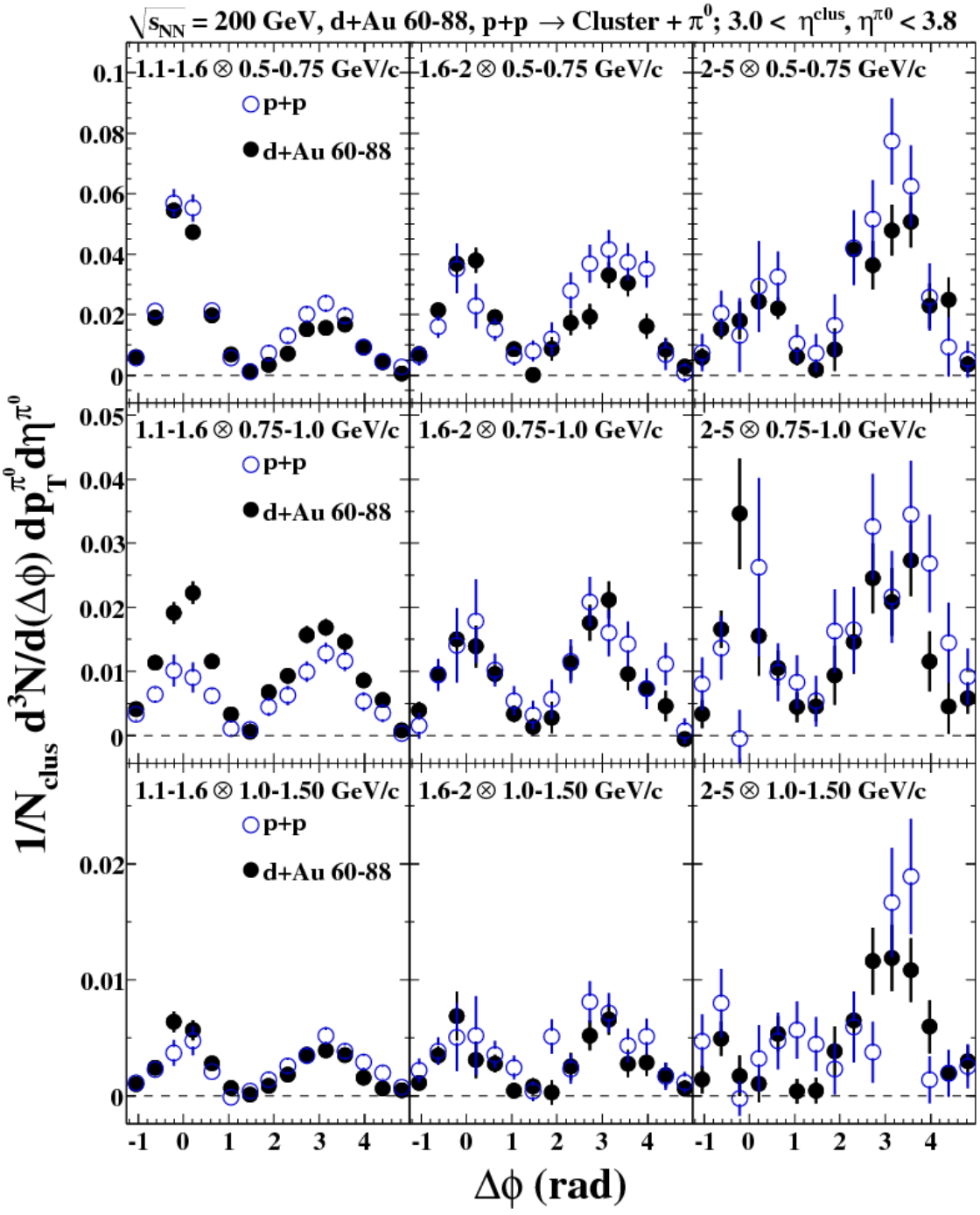

Figure E.9: **dAu 60-88%, Rapidity = 3.0-3.8:** MPC Cluster/π^0 Background subtracted correlation functions and fits for all p_T bins. The p+p reference is in blue.

References

[1] L. McLerran and R. Venugopalan *Phys. Rev.* **D49** no. 7, (1994) 3352–3355.

[2] D. Kharzeev, E. Levin, and L. McLerran *Nucl. Phys.* **A748** (2005) 627–640, arXiv:hep-ph/0403271.

[3] I. Arsene *et al.*, (**BRAHMS** Collaboration) *Phys. Rev. Lett.* **93** (2004) 242303, arXiv:nucl-ex/0403005.

[4] J. Adams *et al.*, (**STAR** Collaboration) *Phys. Rev. Lett.* **97** (2006) 152302, arXiv:nucl-ex/0602011.

[5] J.-w. Qiu and I. Vitev, "Resummed QCD power corrections to nuclear shadowing," *Phys. Rev. Lett.* **93** (2004) 262301, arXiv:hep-ph/0309094.

[6] C. Marquet, "Forward inclusive dijet production and azimuthal correlations in pA collisions," *Nucl. Phys.* **A796** (2007) 41–60.

[7] L. V. Gribov, E. M. Levin, and M. G. Ryskin, "Semihard Processes in QCD," *Phys. Rept.* **100** (1983) 1–150.

[8] A. H. Mueller and J.-w. Qiu, "Gluon Recombination and Shadowing at Small Values of x," *Nucl. Phys.* **B268** (1986) 427.

[9] V. Guzey, M. Strikman, and W. Vogelsang *Phys. Lett.* **B603** (2004) 173–183, arXiv:hep-ph/0407201.

[10] J.-w. Qiu and I. Vitev, "Coherent QCD multiple scattering in proton nucleus collisions," *Phys. Lett.* **B632** (2006) 507–511, arXiv:hep-ph/0405068.

[11] N. Armesto, "Nuclear shadowing," *J. Phys.* **G32** (2006) R367–R394, arXiv:hep-ph/0604108.

[12] I. Vitev *Phys. Rev.* **C75** no. 6, (2007) 064906.

[13] L. Frankfurt and M. Strikman *Phys. Lett.* **B645** (2007) 412–421, arXiv:nucl-th/0603049.

[14] M. E. Peskin and D. V. Schroeder, "An introduction to quantum field theory,". Reading, USA: Addison-Wesley (1995) 842 p.

[15] D. J. Gross and F. Wilczek, "Ultraviolet behavior of non-Abelian gauge theories," *Phys. Rev. Lett.* **30** (1973) 1343–1346.

[16] H. D. Politzer, "Reliable perturbative results for strong interactions?," *Phys. Rev. Lett.* **30** (1973) 1346–1349.

[17] K. G. Wilson, "Confinement of quarks," *Phys. Rev.* **D10** (1974) 2445–2459.

[18] J. W. Harris and B. Muller *Ann. Rev. Nucl. Part. Sci.* **46** (1996) 71–107, arXiv:hep-ph/9602235.

[19] K. Adcox *et al.*, (**PHENIX** Collaboration), "Formation of dense partonic matter in relativistic nucleus nucleus collisions at RHIC: Experimental evaluation by the PHENIX collaboration," *Nucl. Phys.* **A757** (2005) 184–283, arXiv:nucl-ex/0410003.

[20] J. Adams *et al.*, (**STAR** Collaboration), "Experimental and theoretical challenges in the search for the quark gluon plasma: The STAR collaboration's critical assessment of the evidence from RHIC collisions," *Nucl. Phys.* **A757** (2005) 102–183, arXiv:nucl-ex/0501009.

[21] I. Arsene *et al.*, (**BRAHMS** Collaboration), "Quark Gluon Plasma an Color Glass Condensate at RHIC? The perspective from the BRAHMS experiment," *Nucl. Phys.* **A757** (2005) 1–27, arXiv:nucl-ex/0410020.

[22] B. B. Back *et al.*, "The PHOBOS perspective on discoveries at RHIC," *Nucl. Phys.* **A757** (2005) 28–101, arXiv:nucl-ex/0410022.

[23] S. Bethke, "Experimental tests of asymptotic freedom," *Prog. Part. Nucl. Phys.* **58** (2007) 351–386, arXiv:hep-ex/0606035.

[24] F. Halzen and A. D. Martin, "Quarks and leptons: an introductory course in modern particle physics,". ISBN-9780471887416 (1984).

[25] J. D. Bjorken, "Asymptotic Sum Rules at Infinite Momentum," *Phys. Rev.* **179** (1969) 1547–1553.

[26] R. P. Feynman, "Very high-energy collisions of hadrons," *Phys. Rev. Lett.* **23** (1969) 1415–1417.

[27] C. Adloff *et al.*, (**H1** Collaboration), "Measurement and QCD analysis of neutral and charged current cross sections at HERA," *Eur. Phys. J.* **C30** (2003) 1–32, arXiv:hep-ex/0304003.

[28] C. Adloff *et al.*, (**H1** Collaboration), "Deep-inelastic inclusive e p scattering at low x and a determination of alpha(s)," *Eur. Phys. J.* **C21** (2001) 33–61, arXiv:hep-ex/0012053.

[29] S. Chekanov *et al.*, (**ZEUS** Collaboration), "Measurement of the neutral current cross section and F2 structure function for deep inelastic e+ p scattering at HERA," *Eur. Phys. J.* **C21** (2001) 443–471, arXiv:hep-ex/0105090.

[30] F. D. Aaron *et al.*, (**H1 and ZEUS** Collaboration), "Combined Measurement and QCD Analysis of the Inclusive ep Scattering Cross Sections at HERA," *JHEP* **01** (2010) 109, arXiv:0911.0884 [hep-ex].

[31] M. Arneodo *et al.*, (**New Muon.** Collaboration), "Measurement of the proton and the deuteron structure functions, F2(p) and F2(d)," *Phys. Lett.* **B364** (1995) 107–115, arXiv:hep-ph/9509406.

[32] A. C. Benvenuti *et al.*, (**BCDMS** Collaboration), "Test of QCD and a measurement of lambda from scaling violations in the proton structure function $F_2(x, Q^2)$ at high Q^2," *Phys. Lett.* **B223** (1989) 490.

[33] V. N. Gribov and L. N. Lipatov, "e+ e- pair annihilation and deep inelastic e p scattering in perturbation theory," *Sov. J. Nucl. Phys.* **15** (1972) 675–684.

[34] V. N. Gribov and L. N. Lipatov, "Deep inelastic e p scattering in perturbation theory," *Sov. J. Nucl. Phys.* **15** (1972) 438–450.

[35] Y. L. Dokshitzer, "Calculation of the Structure Functions for Deep Inelastic Scattering and e+ e- Annihilation by Perturbation Theory in Quantum Chromodynamics," *Sov. Phys. JETP* **46** (1977) 641–653.

[36] G. Altarelli and G. Parisi, "Asymptotic Freedom in Parton Language," *Nucl. Phys.* **B126** (1977) 298.

[37] K. J. Eskola, H. Honkanen, V. J. Kolhinen, J.-w. Qiu, and C. A. Salgado, "Nonlinear corrections to the DGLAP equations in view of the HERA data," *Nucl. Phys.* **B660** (2003) 211–224, arXiv:hep-ph/0211239.

[38] Y. V. Kovchegov, "Unitarization of the BFKL pomeron on a nucleus," *Phys. Rev.* **D61** (2000) 074018, arXiv:hep-ph/9905214.

[39] F. Gelis, E. Iancu, J. Jalilian-Marian, and R. Venugopalan, "The Color Glass Condensate," *Ann. Rev. Nucl. Part. Sci.* **60** (2010) 463–489, arXiv:1002.0333 [hep-ph].

[40] J. Pumplin *et al.*, "New generation of parton distributions with uncertainties from global QCD analysis," *JHEP* **07** (2002) 012, arXiv:hep-ph/0201195.

[41] J. Gomez *et al.*, "Measurement of the A-dependence of deep inelastic electron scattering," *Phys. Rev.* **D49** (1994) 4348–4372.

[42] P. Amaudruz *et al.*, (**New Muon** Collaboration), "A Reevaluation of the nuclear structure function ratios for D, He, Li-6, C and Ca," *Nucl. Phys.* **B441** (1995) 3–11, arXiv:hep-ph/9503291.

[43] M. Arneodo *et al.*, (**New Muon.** Collaboration), "The Structure Function ratios F2(li) / F2(D) and F2(C) / F2(D) at small x," *Nucl. Phys.* **B441** (1995) 12–30, arXiv:hep-ex/9504002.

[44] M. Arneodo *et al.*, (**New Muon** Collaboration), "The A dependence of the nuclear structure function ratios," *Nucl. Phys.* **B481** (1996) 3–22.

[45] M. Arneodo *et al.*, (**New Muon** Collaboration), "The Q**2 dependence of the structure function ratio F2 Sn / F2 C and the difference R Sn - R C in deep inelastic muon scattering," *Nucl. Phys.* **B481** (1996) 23–39.

[46] J. Ashman et al. [European Muon Collaboration], Z. Phys. **C 57**, 211 (1993).

[47] K. J. Eskola, H. Paukkunen, and C. A. Salgado, "EPS09 - a New Generation of NLO and LO Nuclear Parton Distribution Functions," *JHEP* **04** (2009) 065, arXiv:0902.4154 [hep-ph].

[48] Glauber R.J., 1959 Lectures in Theoretical Physics, Vol 1, ed. W.E. Brittin et al. (New York: Interscience), 315 (1959); Gribov V.N., Sov. Phys. JETP **29**, 483 (1969); Gribov V.N., Sov. Phys. JETP **30**, 709 (1970).

[49] R. G. Roberts. Cambridge University Press, 1990.

[50] L. Frankfurt, V. Guzey, and M. Strikman, "Leading twist nuclear shadowing: Uncertainties, comparison to experiments, and higher twist effects.," *Phys. Rev.* **D71** (2005) 054001, arXiv:hep-ph/0303022.

[51] J. L. Albacete, N. Armesto, J. G. Milhano, and C. A. Salgado, "A Global Analysis of DIS Data at Small-x with Running Coupling BK Evolution," arXiv:0906.2721 [hep-ph].

[52] J. L. Albacete and C. Marquet, "Single Inclusive Hadron Production at RHIC and the LHC from the Color Glass Condensate," *Phys. Lett.* **B687** (2010) 174–179, arXiv:1001.1378 [hep-ph].

[53] J. Jalilian-Marian, A. Kovner, L.D. McLerran, H. Weigert, Phys. Rev. **D 55**, 5414 (1997); J. Jalilian-Marian, A. Kovner, A. Leonidov, H. Weigert, Nucl. Phys. **B 504**, 415 (1997), Phys. Rev. **D 59**, 014014 (1999), *ibid.* 034007 (1999), *ibid.* erratum, 099903 (1999); E. Iancu, A. Leonidov, L.D. McLerran, Nucl. Phys. **A 692**, 583 (2001), Phys. Lett. **B 510**, 133 (2001); E. Ferreiro, E. Iancu, A. Leonidov, L.D. McLerran, Nucl. Phys. **A 703**, 489 (2002).

[54] R. B. Neufeld, I. Vitev, and B.-W. Zhang, "Toward a determination of the shortest radiation length in nature," arXiv:1010.3708 [hep-ph].

[55] C. Bourrely and J. Soffer, "Do we understand the single-spin asymmetry for pi0 inclusive production in p+p collisions?," *Eur. Phys. J.* **C36** (2004) 371–374, arXiv:hep-ph/0311110.

[56] D. de Florian, W. Vogelsang, and F. Wagner, "Single-Inclusive Hadron Production in Polarized pp Scattering at Next-to-Leading Logarithmic Accuracy," *Phys. Rev.* **D76** (2007) 094021, arXiv:0708.3060 [hep-ph].

[57] R. C. Hwa, C. B. Yang, and R. J. Fries *Phys. Rev.* **C71** (2005) 024902, arXiv:nucl-th/0410111.

[58] E. Iancu and R. Venugopalan, "The color glass condensate and high energy scattering in QCD," arXiv:hep-ph/0303204.

[59] M. Harrison, S. G. Peggs, and T. Roser, "The RHIC accelerator," *Ann. Rev. Nucl. Part. Sci.* **52** (2002) 425–469.

[60] S. A. Bass *et al.*, "Systematic Comparison of Jet Energy-Loss Schemes in a realistic hydrodynamic medium," *Phys. Rev.* **C79** (2009) 024901, arXiv:0808.0908 [nucl-th].

[61] R. J. Glauber and G. Matthiae, "High-energy scattering of protons by nuclei," *Nucl. Phys.* **B21** (1970) 135–157.

[62] K. Reygers, PHENIX Internal Analysis Note 078.

[63] J. Nagle, PHENIX Internal Analysis Note 900.

[64] S. S. Adler *et al.*, (**PHENIX** Collaboration), "Suppressed pi0 production at large transverse momentum in central Au + Au collisions at s(NN)**(1/2) = 200-GeV," *Phys. Rev. Lett.* **91** (2003) 072301, arXiv:nucl-ex/0304022.

[65] S. S. Adler *et al.*, (**PHENIX** Collaboration), "High p(T) charged hadron suppression in Au + Au collisions at s(NN)**1/2 = 200-GeV," *Phys. Rev.* **C69** (2004) 034910, arXiv:nucl-ex/0308006.

[66] S. S. Adler *et al.*, (**PHENIX** Collaboration), "Absence of suppression in particle production at large transverse momentum in s(NN)**(1/2) = 200-GeV d + Au collisions," *Phys. Rev. Lett.* **91** (2003) 072303, arXiv:nucl-ex/0306021.

[67] S. S. Adler *et al.*, (**PHENIX** Collaboration), "Centrality dependence of direct photon production in s(NN)**(1/2) = 200-GeV Au + Au collisions," *Phys. Rev. Lett.* **94** (2005) 232301, arXiv:nucl-ex/0503003.

[68] S. S. Adler *et al.*, (**PHENIX** Collaboration) *Phys. Rev. Lett.* **98** (2007) 172302, arXiv:nucl-ex/0610036.

[69] S. Chekanov *et al.*, (**ZEUS** Collaboration), "A ZEUS next-to-leading-order QCD analysis of data on deep inelastic scattering," *Phys. Rev.* **D67** (2003) 012007, arXiv:hep-ex/0208023.

[70] J. Jalilian-Marian and Y. V. Kovchegov, "Saturation physics and deuteron gold collisions at RHIC," *Prog. Part. Nucl. Phys.* **56** (2006) 104–231, arXiv:hep-ph/0505052.

[71] I. Balitsky, "Operator expansion for high-energy scattering," *Nucl. Phys.* **B463** (1996) 99–160, arXiv:hep-ph/9509348.

[72] J. L. Albacete and Y. V. Kovchegov, "Solving High Energy Evolution Equation Including Running Coupling Corrections," *Phys. Rev.* **D75** (2007) 125021, arXiv:0704.0612 [hep-ph].

[73] E. Gardi, J. Kuokkanen, K. Rummukainen, and H. Weigert, "Running coupling and power corrections in nonlinear evolution at the high-energy limit," *Nucl. Phys.* **A784** (2007) 282–340, arXiv:hep-ph/0609087.

[74] J. L. Albacete and A. Dumitru, "A model for gluon production in heavy-ion collisions at the LHC with rcBK unintegrated gluon densities," arXiv:1011.5161 [hep-ph].

[75] D. N. Triantafyllopoulos, "The energy dependence of the saturation momentum from RG improved BFKL evolution," *Nucl. Phys.* **B648** (2003) 293–316, arXiv:hep-ph/0209121.

[76] J. L. Albacete, N. Armesto, J. G. Milhano, C. A. Salgado, and U. A. Wiedemann, "Numerical analysis of the Balitsky-Kovchegov equation with running coupling: Dependence of the saturation scale on nuclear size and rapidity," *Phys. Rev.* **D71** (2005) 014003, arXiv:hep-ph/0408216.

[77] A. Stasto, K. J. Golec-Biernat, and J. Kwiecinski, "Geometric scaling for the total gamma* p cross-section in the low x region," *Phys.Rev.Lett.* **86** (2001) 596–599, arXiv:hep-ph/0007192 [hep-ph].

[78] J.-P. Blaizot and F. Gelis, "Searching evidence for the color glass condensate at RHIC," *Nucl. Phys.* **A750** (2005) 148–165, arXiv:hep-ph/0405305.

[79] M. Chiu, (**PHENIX** Collaboration), "Charged particle angular correlations from leading photons at RHIC," *Nucl. Phys.* **A715** (2003) 761–764, arXiv:nucl-ex/0211008.

[80] S. S. Adler *et al.*, (**PHENIX** Collaboration), "Jet properties from dihadron correlations in p+p collisions at s**(1/2) = 200-GeV," *Phys. Rev.* **D74** (2006) 072002, arXiv:hep-ex/0605039.

[81] J.-y. Jia, "Probing jet properties via two particle correlation method," *J. Phys.* **G31** (2005) S521–S532, arXiv:nucl-ex/0409024.

[82] A. Adare *et al.*, (**PHENIX Collaboration** Collaboration) *Phys. Rev.* **C78** no. 1, (2008) 014901.

[83] A. H. Mueller and H. Navelet, "An Inclusive Minijet Cross-Section and the Bare Pomeron in QCD," *Nucl. Phys.* **B282** (1987) 727.

[84] C. Marquet, "Azimuthal correlations of forward dijets in d+Au collisions at RHIC," *J. Phys.* **G35** (2008) 104049, arXiv:0804.4893 [hep-ph].

[85] C. Marquet, Private Communication.

[86] S. S. Adler *et al.*, (**PHENIX** Collaboration) *Phys. Rev. Lett.* **96** (2006) 222301, arXiv:nucl-ex/0603017.

[87] B. Meredith, "Probing High Parton Densities at Low-x in d+Au Collisions at PHENIX Using the New Forward and Backward Muon Piston Calorimeters," *Nucl. Phys.* **A830** (2009) 595c–598c, arXiv:0907.4832 [nucl-ex].

[88] B. A. Meredith, (**PHENIX** Collaboration), "Searching for gluon saturation in d+Au collisions at PHENIX," *PoS* **DIS2010** (2010) 081.

[89] E. Braidot, (**STAR** Collaboration), "Two Particle Correlations at Forward Rapidity in STAR," *Nucl. Phys.* **A854** (2011) 168–174, arXiv:1008.3989 [nucl-ex].

[90] J. L. Albacete and C. Marquet, "Azimuthal correlations of forward di-hadrons in d+Au collisions at RHIC in the Color Glass Condensate," *Phys. Rev. Lett.* **105** (2010) 162301, arXiv:1005.4065 [hep-ph].

[91] T. Satogata *et al.*, "Commissioning of RHIC Deuteron Gold Collisions,". Particle Accelerator Conference (PAC 03) 12-16 May 2003, Portland, Oregon.

[92] K. Adcox *et al.*, "PHENIX detector overview," *Nuclear Instruments and Methods in Physics Research Section A: Accelerators, Spectrometers, Detectors and Associated Equipment* **499** no. 2-3, (2003) 469 – 479.

[93] L. Aphecetche *et al.*, "PHENIX calorimeter," *Nuclear Instruments and Methods in Physics Research Section A: Accelerators, Spectrometers, Detectors and Associated Equipment* **499** no. 2-3, (2003) 521 – 536.

[94] K. Adcox *et al.*, "PHENIX central arm tracking detectors," *Nuclear Instruments and Methods in Physics Research Section A: Accelerators, Spectrometers, Detectors and Associated Equipment* **499** no. 2-3, (2003) 489 – 507.

[95] M. Aizawa *et al.*, "PHENIX central arm particle ID detectors," *Nuclear Instruments and Methods in Physics Research Section A: Accelerators, Spectrometers, Detectors and Associated Equipment* **499** no. 2-3, (2003) 508 – 520.

[96] H. Akikawa *et al.*, "PHENIX Muon Arms," *Nuclear Instruments and Methods in Physics Research Section A: Accelerators, Spectrometers, Detectors and Associated Equipment* **499** no. 2-3, (2003) 537 – 548.

[97] M. Chiu, (**PHENIX** Collaboration) *AIP Conf. Proc.* **915** (2007) 539–542, `arXiv:nucl-ex/0701031`.

[98] J. Koster, Ph. D. Thesis, UIUC (2010).

[99] A. Adare *et al.*, (**PHENIX** Collaboration), "Suppression of back-to-back hadron pairs at forward rapidity in d+Au Collisions at $\sqrt{s_{NN}} = 200$ GeV," `arXiv:1105.5112 [nucl-ex]`. submitted to Phys. Rev. Lett.

[100] Z. Citron, (**PHENIX** Collaboration), "Forward and backward to mid-rapidity correlations measured in d + Au collisions at s(NN)**(1/2) = 200 with the PHENIX detector," *Nucl. Phys.* **A855** (2011) 257–260.

[101] M. Allen *et al.*, "PHENIX inner detectors," *Nuclear Instruments and Methods in Physics Research Section A: Accelerators, Spectrometers, Detectors and Associated Equipment* **499** no. 2-3, (2003) 549 – 559.

[102] E. Richardson *et al.*, "A reaction plane detector for PHENIX at RHIC," *Nuclear Instruments and Methods in Physics Research Section A: Accelerators, Spectrometers, Detectors and Associated Equipment* **636** no. 1, (2011) 99 – 107.

[103] J. Jia et al, PHENIX Internal Analysis Notes 117, 177.

[104] J.-P. Peigneux, NIM A351 197-200 (1994).

[105] M. Ippolitov et al., NIM A486 121-125 (2002).

[106] Hamamatsu Photonics, "Si PIN photodiode S1233 Series.".

[107] ALICE Collaboration, Technical Design Report of the Photon Spectrometer (PHOS), CERN/LHCC 99-4, March 1999, URL: https://edms.cern.ch/document/398934/1.

[108] D. Aleksandrov *et al.*, "A high resolution electromagnetic calorimeter based on lead-tungstate crystals," *Nuclear Instruments and Methods in Physics Research Section A: Accelerators, Spectrometers, Detectors and Associated Equipment* **550** no. 1-2, (2005) 169 – 184.

[109] J. Koster, M. Chiu, A. Kazantsev, PHENIX Internal Technical Note 440.

[110] J. Koster, B. Meredith, M. Chiu, M. Perdekamp, S. Wolin, PHENIX Internal Analysis Note 927.

[111] S. S. Adler *et al.*, "PHENIX on-line and off-line computing," *Nuclear Instruments and Methods in Physics Research Section A: Accelerators, Spectrometers, Detectors and Associated Equipment* **499** no. 2-3, (2003) 593 – 602.

[112] M. L. Purschke, (**PHENIX Collaboration** Collaboration), "Online and offline computing systems in the PHENIX experiment," arXiv:hep-ex/0305103 [hep-ex].

[113] S. S. Adler *et al.*, "PHENIX on-line and off-line computing," *Nuclear Instruments and Methods in Physics Research Section A: Accelerators, Spectrometers, Detectors and Associated Equipment* **499** no. 2-3, (2003) 560–592.

[114] R. Yang, Ph. D. Thesis, UIUC (2010).

[115] C. W. Fabjan and F. Gianotti, "Calorimetry for particle physics," *Rev. Mod. Phys.* **75** (2003) 1243–1286.

[116] A.A. Lednev, IHEP Preprint 93-153, Protvino (1993).

[117] T. Sjostrand, S. Mrenna, and P. Z. Skands, "PYTHIA 6.4 Physics and Manual," *JHEP* **0605** (2006) 026.

[118] R. Brun *et al.*, "GEANT3,". CERN-DD-EE-84-1.

[119] G. Grindhammer and S. Peters, "The parameterized simulation of electromagnetic showers in homogeneous and sampling calorimeters," arXiv:hep-ex/0001020.

[120] F. Berger, M. Purshke et al., NIM A321 152-164 (1992).

[121] A. Kazantsev, Personal Communication concerning Fermilab Beam Test.

[122] A. Bazilevsky, Personal Communication.

[123] S. Wolin, Private Communication.

[124] R. D. Field, (**CDF** Collaboration), "The underlying event in hard scattering processes," arXiv:hep-ph/0201192.

[125] Rousseeuw, P. J. "Least Median of Squares Regression" Journal of the American Statistical Association, 79, 871880, 1984.

[126] S. Belikov et al, PHENIX Internal Analysis Note 184.

[127] S. Bazilevsky, PHENIX Internal Analysis Note 358.

[128] T. Awes et al, PHENIX Internal Analysis Note 073.

[129] J. Adams *et al.*, (**STAR** Collaboration), "Evidence from d + Au measurements for final-state suppression of high p(T) hadrons in Au + Au collisions at RHIC," *Phys. Rev. Lett.* **91** (2003) 072304, arXiv:nucl-ex/0306024.

[130] S. S. Adler *et al.*, (**PHENIX** Collaboration) *Phys. Rev.* **C73** (2006) 054903, arXiv:nucl-ex/0510021.

[131] N. N. Ajitanand *et al.*, "Decomposition of harmonic and jet contributions to particle-pair correlations at ultra-relativistic energies," *Phys. Rev.* **C72** (2005) 011902, arXiv:nucl-ex/0501025.

[132] K. Adcox *et al.*, (**PHENIX** Collaboration), "Flow measurements via two-particle azimuthal correlations in Au + Au collisions at s(NN)**(1/2) = 130-GeV," *Phys. Rev. Lett.* **89** (2002) 212301, arXiv:nucl-ex/0204005.

[133] D. Triantafyllopoulos, Private Communication.

[134] N. Grau, Z. Citron, and J. Jia, PHENIX Internal Analysis Note 816.

[135] B. Sahlmuller, S. Klamor, S. Bathe, PHENIX Internal Analysis Note 978.

[136] D. d'Enterria, PHENIX Internal Analysis Note 380.

[137] S. S. Adler *et al.*, (**PHENIX** Collaboration), "Centrality dependence of charged hadron production in deuteron+gold and nucleon+gold collisions at $\sqrt{s_{NN}}$=200 GeV," *Phys. Rev.* **C77** (2008) 014905, arXiv:0708.2416 [nucl-ex].

[138] K. Tuchin, "Rapidity and centrality dependence of azimuthal correlations in Deuteron-Gold collisions at RHIC," *Nucl.Phys.* **A846** (2010) 83–94, arXiv:0912.5479 [hep-ph].

[139] A. Sickles, M. P. McCumber, and A. Adare, "Extraction of Correlated Jet Pair Signals in Relativistic Heavy Ion Collisions," *Phys. Rev.* **C81** (2010) 014908, arXiv:0907.4113 [nucl-ex].

[140] S. S. Adler *et al.*, (**PHENIX** Collaboration), "Jet properties from dihadron correlations in p+p collisions at s**(1/2) = 200-GeV," *Phys. Rev.* **D74** (2006) 072002, arXiv:hep-ex/0605039.